UNIVERSITÀ DEGLI STUDI DI PISA
DIPARTIMENTO DI FISICA

TESI DI DOTTORATO DI RICERCA IN
FISICA APPLICATA
ANNO ACCADEMICO 2000-2001
(Tesi completata nel 2004)

TITOLO:
A FAST ROTATING DIFFERENTIAL ACCELEROMETER FOR TESTING THE EQUIVALENCE PRINCIPLE: PRELIMINARY RESULTS.

DOTTORANDO
GIAN LUCA COMANDI

TUTORE
PROF.SSA ANNA M. NOBILI

REFEREES:

PROF. MASSIMO BASSAN, UNIVERSITÀ TOR VERGATA, ROMA, ITALIA

PROF. EPHRAIM FISCHBACH, PURDUE UNIVERSITY, USA

TABLE OF CONTENTS

A FAST ROTATING DIFFERENTIAL ACCELEROMETER FOR TESTING THE EQUIVALENCE PRINCIPLE: PRELIMINARY RESULTS

by

Gian Luca Comandi

University of Pisa, Italy

INTRODUCTION

General Relativity is based on the *"hypothesis of complete physical equivalence"* between a gravitational field and an accelerated frame formulated by Einstein in 1907. This *hypothesis* is usually referred to as the Weak Equivalence *"Principle"* and its experimental consequence is the Universality of Free Fall, namely the fact that in a gravitational field all bodies fall with the same acceleration regardless of their mass and composition. So far the best experimental proof of the equivalence principle have been obtained by the "Eöt-Wash" group at the University of Washington with test masses suspended on a slowly rotating torsion balance, reaching a sensitivity of 1 part in 10^{12} in their relative fractional acceleration. An experiment in space, with the test masses orbiting the Earth at low altitude, would take advantage of the much stronger signal (by about 3 orders of magnitude), the absence of weight and the long experiment duration, and can therefore potentially provide a much more accurate test. However, a torsion balance is not appropriate for space because it is based on the existence of a preferential direction provided on the surface of the Earth by the local gravitational acceleration. An experiment named "Galileo Galilei"- GG has been designed for testing the equivalence principle in space with concentric co-axial hollow test cylinders weakly coupled to form a differential accelerometer and fast rotating around their symmetry axis for high frequency modulation of the expected signal. GGG ("GG on the Ground") is a differential accelerometer based on the same concepts as the one proposed for space, but modified to work in the laboratory at 1-g. To this end the spin/symmetry axis is used to suspend the test cylinders against local gravity and the test cylinders are weakly coupled in the horizontal plane in order to be sensitive to differential forces acting in this plane, hence also to the horizontal component of a possible violation of equivalence. Like in the space experiment, the read out consists of two capacitance bridges (spinning with the system) whose plates are located half way in between the test cylinders to measure the relative displacements of the test cylinders along the orthogonal directions of the plane perpendicular to the spin axis.

This thesis reports the results of my work on the GGG experiment since the year 2000. My previous work on GGG has been reported in my "laurea" degree thesis under the title: *"Verifica del Principio di Equivalenza a terra e nello spazio con masse di prova in rotazione veloce"*, where I developed a physical model of the gyroscopic effects on the test masses of the GGG rotating accelerometer showing that these effects cannot be distinguished from the signal of an equivalence principle violation in the field of the Earth, whereby coming to the conclusion that a variant of the GG accelerometer modified to work on the Earth can be used only for equivalence principle tests in the field of the Sun. The theoretical predictions of the model were compared with extensive experimental measurements of the gyroscopic effects at various spin frequencies showing the validity of the physical model.

This thesis is based on the work I have carried out on the GGG experiment after that. The first aim was to be able to rotate the system at high frequency with the test cylinders undergoing very small displacements relative to one other, in spite of their weak coupling and large mass. The theory of supercritical rotors underlying such a dynamical system is well known. However, the number of bodies involved, the differential character of the apparatus and the high sensitivity required make GGG a very new and peculiar instrument for which no past experience is available. The goal of having good measurement runs was therefore a primary goal. At the same time, I have developed a full scale multi-body mathematical model of the rotating GGG accelerometer allowing us to perform realistic numerical simulation of the dynamical behaviour of the actual system. The model provides quantitative predictions for the actual system, and also guidelines on how to improve the apparatus design for better performances. The natural frequencies of the system as predicted in dependence of the spin frequency are all confirmed by the experimental measurements. In addition, the model allows us to quantify two crucial properties of the accelerometer, namely its common mode rejection factor (i.e. how good it is as a differential accelerometer) and self-centring of the test cylinders on the spin axis (the theoretical property of weakly suspended rotors which makes fast rotation rates and small relative displacements of the spinning cylinders possible at all).

A physical quantity of the outmost importance in any small force experiment is the quality factor Q of the system, which must be measured for the full apparatus and at the frequency which is relevant for the experiment. For a sufficiently low pressure of the residual air inside the vacuum chamber we have measured the Q of the mechanical suspensions at all natural frequencies of the GGG system, fully assembled and not rotating. The best Q value of 95000 was obtained at the highest natural frequency of the system, of about 1.4 Hz. A well established theory of damping and rotordynamics for fast spinning weakly suspended rotors predicts, in the presence of non zero dissipation in the reference frame of the rotor (namely, of dissipation in the rotating parts of the system, primarily in the mechanical suspensions), the onset of the so called whirl motions at frequencies very close to the natural frequencies of the system. The same theory predicts that the higher is the Q of the system at the spin frequency, the slower is the growth rate of the whirl instabilities. A mathematical model of the whirl motions in GGG was used to fit the whirl motions as measured by the capacitance bridges of the read out, so as to derive the Q of the rotating system which turned out to be affected by losses in non rigid parts of the apparatus besides the suspensions, which all need to be identified so as to apply appropriate changes to the system. Since the frequencies of whirl are

well identified and fitted, much smaller relative displacements of the test cylinders at low frequency can be detected. The smaller is the amplitude of the whirl, the more sensitive is the accelerometer to low frequency differential forces such as a 24-hr violation of the equivalence principle in the field of the Sun. This requires that whirl is not allowed to grow and in point of fact that it is stabilized to remain as small as possible. It is well known that whirl motion can be stabilized by introducing in the system a sufficient amount of non-rotating damping. This can be done passively, which is what we do during the initial acceleration phase from zero spin to the nominal spin frequency above the natural ones. When the spin rate equals each natural frequency the system passes through the corresponding resonance, and in absence of an adequate passive damper the resulting disturbances could be too unacceptable. The passive damper has been designed in such a way not to leave any moving or dissipating part on the rotor after all resonances have been crossed. During rotation above the natural frequencies a finer whirl damping can be achieved actively using specific capacitance sensors and actuators. It was part of my thesis work to theoretically design the control laws for the active stabilization of whirl motion in GGG and to implement the full control system which so far has provided a reduction of the amplitude of the whirl at the natural differential frequency to a few tenths of μm.

The GGG experiment is affected by the local terrain tilts, because by tilting the spin/symmetry axis of the accelerometer they produce spurious relative displacements of the test cylinders. The largest and most dangerous ones while aiming at testing the equivalence principle in the field of the Sun are the disturbances caused by temperature and pressure variations during the day. Terrain tilts and horizontal seismic accelerations are indistinguishable from each other because of the equivalence principle. Horizontal accelerations change the direction of the local vertical; however, in GGG these absolute changes are not relevant because the signal is a relative displacement of the test cylinders around the local vertical at the time, and for this reason it is possible to achieve a good reduction of both disturbances together. From 2 to 3 orders of magnitude of low frequency seismic noise attenuation can be achieved actively, using as sensor a small tiltmeter and piezoceramics as fine actuators. I have designed the control laws for this system and realized the electronic circuit needed for this purpose. A further noise reduction is planned for the future using a cardanic suspension of the whole system; it turns out that by exploiting the lever effect the stiffness required to obtain 4 orders of magnitude reduction is similar to that one of the suspensions currently in use.

As mentioned at the beginning, the GGG experiment has started as a ground variant of the GG space experiment, in particular because of the novelties involved in the GG concept and the need for them to be tested. Both experiments need to be investigated if aiming to a very high accuracy test of the equivalence principle, though GG only theoretically and with numerical simulations at this phase. As far as GG is concerned, I have contributed to redesigning the experiment for a high inclination sun-synchronous orbit (for which more and cheaper launch opportunities are available). In particular, I have worked on the stabilization of whirl motions for a GG-like system of bodies in a spinning spacecraft and in realistic errors. Related to that is the issue of tidal effects due to the presence of whirl motion, which I have

investigated in detail showing how they can be distinguished from an equivalence principle violation signal.

This thesis is organized as follows:

- Chapter 1 gives the required basic concepts of rotordynamics, introducing concepts such as “whirl motion”, “self centring” and “critical speed.
- Chapter 2 contains a qualitative description of the GGG experiment (mechanical design, how it works, read-out, adjustments and settings…).
- The dynamical model of the GGG system of rotors is developed in Chapters 3 and 4 (normal modes, common mode rejection factor, self centring and comparison between predictions and measurements).
- Whirl motions and Q of the system are the subject of Chapter 5: theory, experiments and analysis of measurement data.
- Chapter 6 is concerned with the active linear control of whirl motion while Chapter 7 deals with the active control of terrain tilts and seismic horizontal accelerations. In both Chapters the theoretical predictions of the control scheme are compared to the experimental results.
- Chapter 8 concludes on the state and perspectives of the GGG experiment.
- Chapter 9 is devoted to the GG space experiment. It contains a brief description of the experiment and reports my specific contribution on whirl control and tidal effects.

Various Chapters have Appendices where specific issues are discussed whose results are important but can be looked at separately. Appendix 9 deals with the PGB (Pico Gravity Box) noise attenuator. In its passive version it is simply an intermediate stage used in the GG experiment. However, I have chosen to report also the results on a passive/active PGB noise attenuator to be used on the space station, a project of the Italian Space Agency later cancelled after the Columbia disaster. My expertise on actively controlled systems for space was initially developed for this project and this Appendix may in fact be helpful for interested readers.

Symbols

Latin Letters

A	state matrix
B	input matrix
C	output matrix
C_0	initial value of the capacitance
C_i	value of the i-th capacitance changed due to the displacement
c_{cr}	critical value of the coefficient c
c_{eq}	equivalent viscous damping coefficient
CMR	common mode rejection
c_{NR}	coefficient of non rotating damping
c_R	coefficient of rotating damping
D	coupling input – output matrix
E	energy
E_w	energy of whirl motion
EP	equivalence principle
ESS	sun elevation sensors
$\vec{F}$	force
F_{com}	force acting in a common manner on the two test bodies
F_{dif}	force acting in a differential manner on the two test bodies
FFT	fast Fourier transform
$\vec{F}_g$	vector of the generalized forces
F_i	generalized force
fit_WF(t)	theoretical function used to fit the forward whirl
$\vec{F}_{xy}^{NR}$	force due to non-rotating damping in the non-rotating frame S
$\vec{F}_{\xi\eta}^{NR}$	force due to non-rotating damping in the rotating frame S_R
$\vec{F}_{xy}^{R}$	force due to rotating damping in the non-rotating frame S
$\vec{F}_{\xi\eta}^{R}$	force due to rotating damping in the rotating frame S_R
$\Im_Z(k)$	discrete Fourier transform of the discrete time signal Z(k)
$\Im_Z(\omega)$	Fourier transform of the continuous time signal Z(t)
$\vec{g}$	local gravity
GG	“Galileo Galilei” space experiment
GGG	“Galileo Galilei on the ground” experiment
$H^{NR}(s)$	transfer functions matrix in the non-rotating reference frame S
$H_{com}^{NR}(s)$	transfer functions matrix in the non-rotating reference frame S in presence of a common input force
$H_{dif}^{NR}(s)$	transfer functions matrix in the non-rotating reference frame S in presence of a differential input force
$H_n(s)$	transfer function from ϑ_n and the output ϑ

$H_{Vn}(s)$	transfer function from the electrical noise V_{noise_tilt} and the output ϑ
$H^{NR}_{\alpha,\beta}(s)$	α,β component of the transfer functions matrix $H^{NR}(s)$ in the non-rotating reference frame S
$H^{Rot}(s)$	transfer functions matrix in the rotating reference frame S_R
$H^{Rot}_{\alpha,\beta}(s)$	α,β component of the transfer functions matrix $H^{Rot}(s)$ in the rotating reference frame S_R
$H_{\vartheta}(s)$	transfer function from the input disturbance ϑ_d and the output signal ϑ
I	moment of inertia
$\Im m$	imaginary part of a complex quantity
I(s)	transfer function of the integrator unit
ISS	international space station
j	imaginary unit
k	elastic constant
k_d	deviatoric stiffness
k_{din}	dynamic stiffness of the system with structural damping
k_m	mean stiffness
K_{PZT}	DC gain of the PZT converting the input voltage into an angle
K_{ref}	scale factor introduced to convert the reference angle ϑ_{ref} into a voltage
K_{tilt}	DC scale factor of the tiltmeter converting angles into voltage signals
k_x	elastic constant along the x direction in the non rotating frame
k_y	elastic constant along the y direction in the non rotating frame
k_ξ	elastic constant along the ξ direction in the non rotating frame
k_η	elastic constant along the η direction in the non rotating frame
ℓ	length of the flexible part of the laminar suspension
L	distance from the central suspension and one end of the balancing arm
$\vec{L}$	angular momentum
L	Lagrange function
L′	effective length of the rotor
L_1	distance of the centre of mass of the inner cylinder from its suspension point
L_2	distance of the centre of mass of the outer cylinder from its suspension point
m	mass of a body
[M]	mass matrix
$\vec{M}$	torque
m_a	mass of the balancing arm
m_1	mass of the inner cylinder
m_2	mass of the outer cylinder
m^g	gravitational mass
m^i	inertial mass
m_r	reduced mass
$M_\odot$	mass of the Sun
O	origin of the reference frames S and S_R
PGB	pico gravity box
$p_i^{\alpha\beta}$	i-th pole of the transfer function $H^{NR}_{\alpha,\beta}(s)$
PM	phase margin
P(s)	transfer function of the PZT
PZT	piezoceramic

Q'	vector of the generalized coordinates q'_i
Q'^0	vector of the generalized coordinates q'_i at equilibrium
Q	vector of the new generalized coordinates representing small oscillations around the equilibrium position Q'^0
$\dot{Q}'$	vector of the generalized velocities $\dot{q}'_i$
$\dot{Q}'^0$	vector of the generalized velocities $\dot{q}'_i$ at equilibrium
$\dot{Q}$	vector of the new generalized velocities representing small oscillations around the equilibrium position $\dot{Q}'^0$
Q	quality factor
Q_w	quality factor of the whirl motion
q'_i	i-th generalized coordinate
q'^0_i	value of q'_i at equilibrium
q_i	new generalized coordinate representing the small oscillation around the equilibrium angle q'^0_i
$\dot{q}'_i$	i-th generalized velocity
$\dot{q}'^0_i$	value of $\dot{q}'_i$ at equilibrium
$\dot{q}_i$	new generalized velocity representing the small oscillation around $\dot{q}'^0_i$
Q_S	quality factor at the spin frequency
$\vec{r}$	position vector
$\hat{r}$	unit vector
$\Re e$	real part of a complex quantity
r_w	whirl radius
R_ξ	reconstructed signal in the rotating frame obtained from Φ_ξ
R_η	reconstructed signal in the rotating frame obtained from Φ_η
$R_\oplus$	radius of the Earth
$R_{\oplus\odot}$	Earth-Sun distance
s	Laplace variable
S	(O,x,y,z) non rotating reference frame
S_B	(Ξ,Π,Υ) reference frame fixed with the body
S_R	(O,ξ,η,z) rotating reference frame
T	kinetic energy
T_C	sampling period
T_d	natural differential period, inverse of ν_d
T_{int}	integration time
TP(s)	transfer function of the system piezo+tiltmeter
T_s	spin period
T(s)	transfer function of the tiltmeter
T_w	whirl period
U	potential energy
$\vec{u}$	input vector
UFF	universality of free falling
U_g	gravitational potential energy
u_i^{Rot}	i-th input of the transfer functions matrix $H^{Rot}(s)$ in the rotating frame S_R
U_k	elastic potential energy
U_c	centrifugal potential energy

U_{cc}	"Coriolis" potential energy
V_{noise_tilt}	electrical noise affecting the tiltmeter
Wb(t)	backward whirl continuous time signal
Wb(k)	forward whirl discrete time signal
Wf(t)	forward whirl continuous time signal
Wf(k)	forward whirl discrete time signal
x	coordinate in the inertial frame S
$\vec{x}$	state space vector
X_{nr}^{e}	experimental discrete time signals in the x direction of the laboratory frame
X_{nr}^{t}	experimental continuous time signals in the x direction of the laboratory frame
y	coordinate in the inertial frame S
$\vec{y}$	output vector
y_i^{NR}	i-th output of the transfer functions matrix $H^{NR}(s)$ in the non rotating frame
y_i^{Rot}	i-th output of the transfer functions matrix $H^{Rot}(s)$ in the rotating frame
Y_{nr}^{e}	experimental discrete time signals in the y direction of the laboratory frame
Y_{nr}^{t}	experimental continuous time signals in the y direction of the laboratory frame
z	coordinate in the inertial frame S - vertical axis of the inertial frame S, coinciding with the rotation axis
z'	complex coordinate in the non rotating frame
z'_h	solution of the homogeneous equation
$z_i^{\alpha\beta}$	i-th zero of the transfer function $H_{\alpha,\beta}^{NR}(s)$
z'_p	particular solution of the general equation

Greek Letters

χ	common mode rejection factor
χ_0	static (DC) value of the common mode rejection factor $\chi(s)$ in the limit $s\rightarrow 0$
$\left\|1/\chi_0\right\|_{\nu_s}$	absolute value of $1/\chi_0$ as a function of the spin frequency ν_s
$\chi_x(s)$	common mode rejection factor in x direction as a function of frequencies
$\chi_y(s)$	common mode rejection factor in x direction as a function of frequencies
$\delta_{i,k}$	Dirac's delta
$\delta\nu$	small shift of a natural frequency due to the anisotropy of the cardanic suspensions
ΔL	adjustable distance used to regulate the differential period
$\Delta\vec{x}_{com}$	common mode displacement
$\Delta\vec{x}_{dif}$	differential mode displacement
Δx_{EP}	differential displacement of the expected EP violation signal
$\Delta\xi$	distance of the centre of mass from the motor axis
$\Delta\xi_{rel}$	relative distance between the centres of mass of the cylinders
$\vec{\varepsilon}$	the eccentricity or unbalance or offset
$\vec{\varepsilon}_2$	second offset

Φ_ξ	vector of data acquired by the capacitance bridge sensitive along ξ direction in the rotating frame
$\Phi_\xi(k)$	k-th component of Φ_ξ
Φ_η	vector of data acquired by the capacitance bridge sensitive along η direction in the rotating frame
$\Phi_\eta(k)$	k-th component of Φ_η
ϕ_i'	angle from the ξ axis and the projection of the vector pointing to the centre of mass of the i-th body on the ξ–η plane
$\phi_i'^0$	value of ϕ_i' at equilibrium
ϕ_i	new angle representing the small oscillation around the equilibrium angle $\phi_i'^0$
γ_k	loss factor
γ_{NR}	loss factor connected to the non-rotating damping
γ_R	loss factor connected to the rotating damping
η	coordinate in the rotating frame S_R
$\boldsymbol{\eta}$	Eötvös parameter
φ	phase
ϑ	angular deviation of the horizontal plane from the initial position ϑ_{ref}
$\vartheta_d(\nu)$	seismic disturbance as a function of frequency
ϑ_d^{24h}	peak value of the total seismic disturbances at frequency ν_{24h}
ϑ_i'	angle between the vertical axis z and the vector pointing to the centre of mass of the i-th body
$\vartheta_i'^0$	value of ϑ_i' at equilibrium
ϑ_i	new angle representing the small oscillation around the equilibrium angle $\vartheta_i'^0$
ϑ_n^{24h}	peak value of the electrical noise affecting the tiltmeter at frequency ν_{24h}
ϑ_{noise}^{24h}	peak value of the seismic noise at frequency ν_{24h}
ϑ_{noise_tilt}	electrical noise affecting the tiltmeter converted into an angle
ϑ_{pk}^{24h}	peak value of the tidal effect at frequency ν_{24h}
ϑ_{ref}	reference angle
λ	eigenvalue
λ_L	latitude of the laboratory
λ^{NR}	dimensionless natural frequency
Λ	elastic anisotropy
Λ'	elastic anisotropy in the rotating frame S_R
ν	frequency [Hz]
$\nu(\nu_s)$	natural frequency ν as a function of the spin speed
ν_C	sampling frequency
ν_{c1}	lowest natural frequency corresponding to a common mode in which the centres of mass of the two cylinders oscillate in phase
ν_{c1}^0	value of the common mode natural frequency ν_{c1} at zero spin rate
ν_{c2}	highest natural frequency corresponding to a common mode in which the centres of mass of the two cylinders oscillate in phase
ν_{c2}^0	value of the common mode natural frequency ν_{c2} at zero spin rate

ν_d	natural differential frequency corresponding to a mode of oscillation in which the centres of mass of the two cylinders oscillate in opposition of phase
ν_d^0	value of the differential natural frequency ν_d at zero spin rate
ν_{d+}	the differential natural frequency split up by $+\delta\nu$
ν_{d-}	the differential natural frequency split up by $-\delta\nu$
ν_n	natural frequency
ν_n^0	natural frequency at zero spin rate
$\nu_{pole}(\nu_s)$	pole of the transfer function $H_{\alpha,\beta}^{NR}(s)$ as a function of the spin speed
ν_{pole}^0	value of $\nu_{pole}(\nu_s)$ at $\nu_s=0$
ν_s	spin frequency
$\overline{\nu}_s$	spin frequency at which the best performances against common mode external disturbances are obtained
$\nu_{zero}(\nu_s)$	zero of the transfer function $H_{\alpha,\beta}^{NR}(s)$ as a function of the spin speed
ν_{zero}^0	value of $\nu_{zero}(\nu_s)$ at $\nu_s=0$
ν_{12h}	frequency at which the tidal disturbances spectrum has the second peak
ν_{24h}	frequency at which the tidal disturbances spectrum has the highest peak
Π	coordinate in the reference frame fixed with the body
$\sigma+$	Fourier transform of the forward whirling motion signal
$\sigma-$	Fourier transform of the backward whirling motion signal
τ	time constant
τ_w	time constant of the whirl motion
τ_1	time constant of the backward whirl motion
τ_2	time constant of the forward whirl motion
Υ	coordinate in the reference frame fixed with the body
ω	angular velocity [rad/s]
ω'	dimensionless angular velocity
ω_1	backward whirl frequency
ω_2	forward whirl frequency
ω_B	band limit
ω_{cr}	critical speed
ω_{cr2}	second critical speed
ω_{min}	smaller frequency component which can be identified with the FFT
ω_n	natural angular velocity
$\vec{\omega}_s$	angular velocity about the axis of rotation; it is also referred to as spin speed or spin frequency
ω_w	whirl frequency
$\omega_\oplus$	angular velocity of the Earth
$\vec{\xi}$	relative position vector
ξ_i	i-th component of $\vec{\xi}$
Ξ	coordinate in the reference frame fixed with the body
$\psi(k)$	discrete vector in the frequency domain used to define the σ_+ and σ_- functions
ζ	complex coodinate in the rotating frame

CHAPTER 1

INTRODUCTION TO THE DYNAMICAL BEHAVIOUR OF ROTORS.

1.1: GENERAL CONSIDERATIONS.

The present chapter originates from the need to give the required basic concepts of rotordynamics to the reader. The intention is to prepare the reader to the following chapters by introducing concepts such as "whirl motion", "self centring" and "critical speed". In the references, the author gives a list of books and papers oriented towards the subjects of the dynamics of rotating machinery here discussed. In particular, the presentation of the subject in the present chapter is widely inspired by [1].
A rotor is a body suspended through a set of cylindrical bearings and rotating around an axis whose direction is fixed in the inertial space[1] ([1 - 3]). The part of the machine that does not rotate will be referred to stator. In the undeformed configuration, the rotation axis is well defined and fixed, and it coincides with one of the principal axis of inertia. Unfortunately, this is true only approximately, and the centre of mass of the suspended body does not coincide with the suspension point.

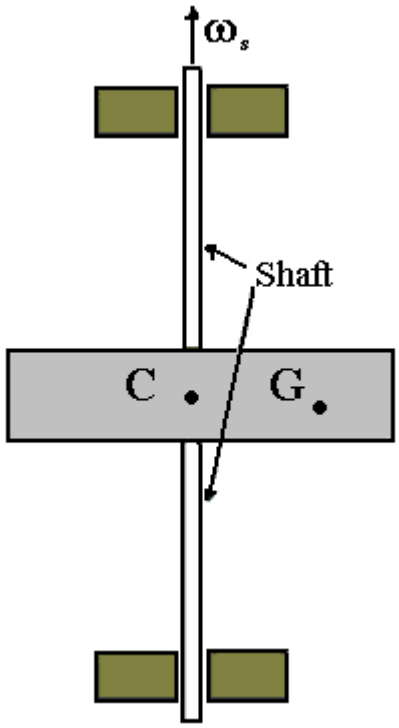

Figure 1.1: Longitudinal section of a rotor spinning at angular frequency ω_s. The centre of mass G does not coincide with the geometrical centre C of the disk. The shaft is elastic.

A simple model of rotor is shown in figure 1.1. The model is sketched in its undeformed configuration. $\vec{\omega}_s$ is the angular velocity about the axis of rotation and it is usually referred to as spin speed or spin frequency. G is the centre of mass of the suspended body. C is the suspension point of the body. In real world, the centre of mass G is not coincident with the

[1] ISO definition.

centre C; the distance between the two points $\vec{\varepsilon}$ is said eccentricity (or unbalance) and it can strongly affect the system. $\vec{\varepsilon}$ is a constant vector in the rotating frame fixed to the rigid body. In the non-rotating frame (inertial frame) the eccentricity rotates with angular velocity ω_s.
Forces due to the unbalance of the rotor itself can be described as vector rotating with the spin angular speed in the inertial reference frame. The spin velocities at which one of the forces acting on the rotor has a frequency coinciding with one of the natural frequencies[2] of the system are referred as critical speeds[3]. If the natural mode of the system is uncoupled to the forcing function no resonance occurs. However, the resonance takes place at critical speeds: the amplitude of the vibration grows linearly in time and the rotor can incur a failure. In particular, the coincidence of the spin speed with one of the natural frequencies of the rotor is very dangerous. The range of frequencies spanning from 0Hz to the first critical speed ω_{cr} is referred to as subcritical regime. Above ω_{cr}, the supercritical range starts. Working in the supercritical regime offers some advantages but at least one of the critical speeds must be crossed. Note that the concept of critical frequency can be defined only in the case of linear systems (or in the case of linearized systems)[4].
Rotors develop an unstable behaviour in certain velocity range. In the study of non-rotating damped linear system the amplitude of free oscillations decays in time because of dissipation due to damping. In the case of rotors, instead, the centrifugal field can cause a growth in time of the amplitude of free vibrations. The frequency range in which these self excited vibrations can develop is said instability range: the kinetic energy stored in the rotor is some orders of magnitude greater than the elastic potential energy the system can store before failure and it can sustain vibrations with increasing amplitude. The instability regions are always located in the supercritical range and working in the instability range is impossible. Critical speeds are very different from instability ranges: they occur at well-defined spin frequencies and can be passed if adequate damping is present.
If the time history of the system is expressed in the form $\underline{x}=\underline{x}_0 e^{st}$, the system is stable when the real part of the complex eigenvalues s is negative. We adopt the definition of stability introduced by Liapunov [4]: let us consider the vector $\underline{R}(t)$ in the state space, i.e. $\underline{R}(t)=(\underline{x}(t),\underline{v}(t))$, and use the expression $|\underline{R}(t)|$ for its norm. An equilibrium position $\underline{R}_0=(\underline{x}_0,\underline{0})$ is stable if $\forall\varepsilon>0\ \exists\delta>0$ such that the inequality $|\underline{R}(t)-\underline{R}_0|<\varepsilon$ holds $\forall t\in[0,\infty]$ if $|\underline{R}(t=0)-\underline{R}_0|<\delta$, i.e. if any trajectory starting within a circle of radius δ centred in the equilibrium point $\underline{R}_0=(\underline{x}_0,\underline{0})$ remains within a circle of radius ε for all values of time. The equilibrium position is asymptotically stable if $|\underline{R}(t)-\underline{R}_0|\to 0$ when $t\to\infty$.
Once the inertial reference frame is stated, the six equations of motion under the action of the generic force $\vec{F}$ and torque $\vec{M}$ can be written in the form:

$$\begin{cases} m\ddot{\vec{r}}=\vec{F} \\ \vec{M}=\dfrac{d\vec{L}}{dt} \end{cases} \qquad (1.1)$$

[2] The natural frequencies are the solutions of the characteristic equation associated to the equation of motion of the system. The natural frequencies of a rotor can depend on the spin speed.
[3] The coincidence between the critical speed with the natural frequency of the undamped system is not a general feature of the rotors. It is a characteristic of those rotors in which the natural frequencies do not change with the spin velocity.
[4] Because only in this case the concept of natural frequency can be applied.

The assumptions of small unbalance and small displacement allow the equations of motion to be linearized. This chapter will be devoted to the study of the dynamic behaviour of simple rotors. In particular, some mathematical model that are not too complex will be discussed in order to introduce some of the most important characteristics of the rotors.

1.2: THE LINEAR JEFFCOTT ROTOR.

The simplest system that can be used to describe the dynamic behaviour of rotors is the so called Jeffcott rotor. The Jeffcott rotor consists of a point mass rigidly attached to a mass-less shaft. k is the stiffness of the elastic shaft and m the mass of the suspended body. A simple sketch of a Jeffcott rotor is depicted in figure 1.2: G is the point mass and C is the centre of the cross section of the shaft. The distance between the two points is the eccentricity $\vec{\varepsilon}=\overrightarrow{CG}$. The point G is always contained in the x-y plane[5]. $\vec{r}$ is the position vector of the point C with respect to the centre O of the undeformed shaft (O is also the origin of the (x,y,z) inertial reference frame). $\vec{r}_G = \vec{r} + \vec{\varepsilon}$ is the position vector of the point mass G. The line AOB coincides with the undeformed spin axis (shaft) along z direction; the line ACB is the deformed shaft. The assumptions of small unbalance and small displacement allow the equations of motion to be linearized. In the non-rotating frame (inertial frame) the eccentricity rotates with angular velocity ω_s ($\vec{\omega}_s = \omega_s \hat{z}$ is the angular spin speed of the rotor). $\varphi=\omega_s t$ is the angle between the eccentricity and the x axis of the inertial frame.

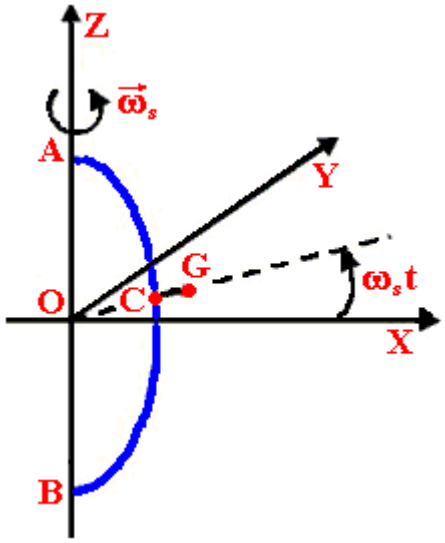

Figure 1.2: Sketch of the Jeffcott rotor. G is the point mass and C is the centre of the cross section of the shaft. The distance between the two points is the eccentricity $\vec{\varepsilon}=\overrightarrow{CG}$. $\vec{r}$ is the position vector of the point C with respect to the centre O of the undeformed shaft. $\vec{r}_G = \vec{r} + \vec{\varepsilon}$ is the position vector of the point mass G. The line AOB coincides with the undeformed spin axis (shaft); the line ACB is the deformed shaft.

Let us assume the displacements x and y of the point C as generalized coordinates (two degrees of freedom), i.e.:

$$\vec{r}=\overrightarrow{OC}=(x,y) \qquad (1.2)$$

The position and velocity of point G are:

[5] This simplification is true in the limit of small displacements.

$$\vec{r}_G=\overrightarrow{OG}=\begin{pmatrix} x+\varepsilon\cos(\omega_s t) \\ y+\varepsilon\sin(\omega_s t) \end{pmatrix} \tag{1.3}$$

$$\dot{\vec{r}}_G=\begin{pmatrix} \dot{x}-\varepsilon\omega_s\sin(\omega_s t) \\ \dot{y}+\varepsilon\omega_s\cos(\omega_s t) \end{pmatrix} \tag{1.4}$$

The Lagrange function is then:

$$L=\frac{1}{2}m\left[\dot{x}^2+\dot{y}^2+\varepsilon^2\omega_s^2+2\varepsilon\omega_s\left(\dot{y}\cos(\omega_s t)-\dot{x}\sin(\omega_s t)\right)\right]-\frac{1}{2}k\left(x^2+y^2\right) \tag{1.5}$$

Making the assumption of constant spin speed (i.e. $\dot{\varphi}=\omega_s$), the following equations of motion are obtained through the lagrangean of the system:

$$\begin{cases} m\left[\ddot{x}-\varepsilon\omega_s^2\cos(\omega_s t)\right]+kx=0 \\ m\left[\ddot{y}-\varepsilon\omega_s^2\sin(\omega_s t)\right]+ky=0 \end{cases} \tag{1.6}$$

By introducing the complex coordinate $z' = x+jy$, the equation (1.7) is easily obtained from (1.6).

$$m\ddot{z}'+kz'=m\varepsilon\omega_s^2 e^{j\omega_s t} \tag{1.7}$$

The general solution of the homogeneous equation is then:

$$z'_h=z_1 e^{j\omega_{cr}t}+z_2 e^{-j\omega_{cr}t} \tag{1.8}$$

where $\omega_{cr}=\sqrt{k/m}$ is the critical speed of the system[6], often called whirl speed. Equation (1.8) shows that z' is a vector that rotates in the horizontal plane. The motion is the superimposition of a circular forward motion (also called forward whirl or direct whirl), occurring in the same direction as the spin angular velocity[7], and a backward motion (backward or indirect whirl). The resulting whirl motion can be circular, elliptic or rectilinear. The particular solution of equation (1.7) is:

$$z'_p=z_0 e^{j\omega_s t}=\varepsilon\frac{\omega_s^2}{\omega_{cr}^2-\omega_s^2}e^{j\omega_s t} \tag{1.9}$$

Equation (1.9) shows that the vector $\vec{r}$ (i.e. the point C) rotates in the plane with angular velocity ω_s, remaining in line with the vector $\overrightarrow{CG}=\varepsilon\left(\cos(\omega_s t),\sin(\omega_s t)\right)$, being z_0 the distance from the origin O of the reference frame[8]. Combining the equation (1.3) with (1.9), the position $\vec{r}_G$ of the point mass G reduces to:

$$\vec{r}_G=\varepsilon\frac{\omega_{cr}^2}{\omega_{cr}^2-\omega_s^2}\left(\cos(\omega_s t),\sin(\omega_s t)\right) \tag{1.10}$$

---

[6] It coincides with the natural frequency of the non rotating system.

[7] In this study the spin speed will be considered positive if anticlockwise.

[8] $z_0=\left|\vec{r}\right|$.

The value of the amplitude of r_G as a function of the spin speed is shown in figure 1.3. The point mass G rotates in the horizontal plane of the inertial frame with angular velocity ω_s. Instead, in a reference frame rotating with angular velocity $\vec{\omega}_s = \omega_s \hat{z}$, with the origin in O and z-axis coinciding with that of the preceding frame, the point mass G is in equilibrium. In subcritical regime, i.e. at spin speed lower than the critical one, the amplitude of $\vec{r}_G$ grows from ε to an infinite value (in coincidence with the critical speed ω_{cr}). In supercritical regime, (i.e. $\omega_s > \omega_{cr}$), G lies between O and C. The value of the amplitude is negative and it decreases with the spin angular velocity:

$$\vec{r} \cong -\vec{\varepsilon} \quad , \quad \vec{r}_G \cong -\left(\frac{\omega_{cr}}{\omega_s}\right)^2 \vec{\varepsilon} \cong 0 \quad \text{if} \quad \omega_s >> \omega_{cr} \tag{1.11}$$

Equation (1.11) means that in supercritical region there is a self-centring of the body on the rotation axis (i.e. G is practically coincident with O). The phenomenon is known as auto-centring in supercritical rotation[9]: the rotor rotates about its centre of mass instead of its geometrical centre.

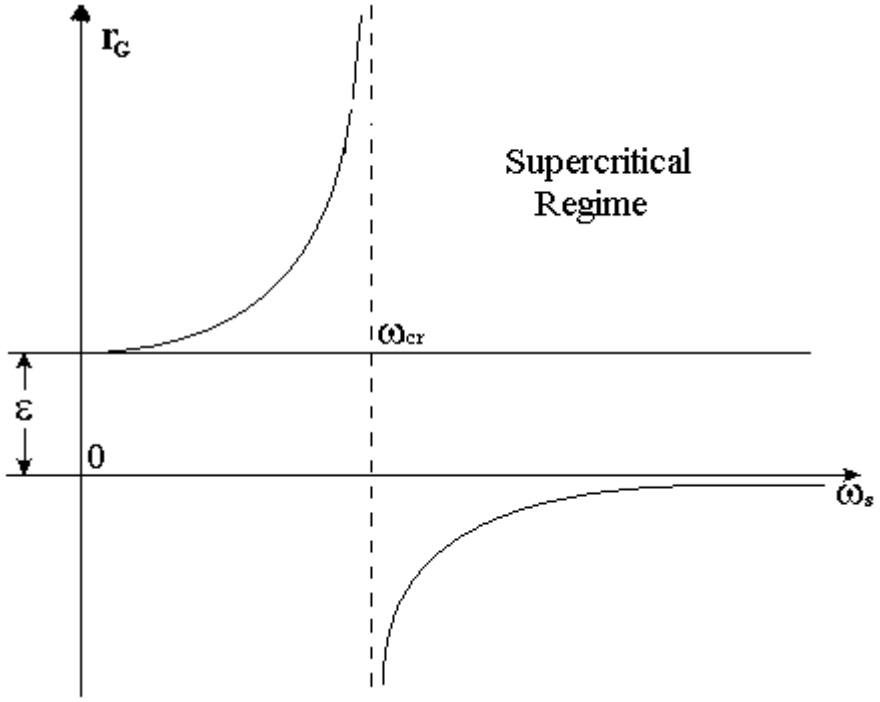

Figure 1.3 : Amplitude of the position vector $\vec{r}_G$ as a function of the spin speed. The amplitude grows from ε to an infinite value in coincidence with the critical speed ω_{cr}. In the supercritical range, i.e. at frequencies higher than the critical one, the value is negative and it decreases with the speed.

The final motion of the point C is the superimposition of a free whirl (circular, elliptic or linear) at frequency $\omega_{cr} = \sqrt{k/m}$ (see equation (1.8)) and a circular motion with angular velocity ω_s (see equation (1.9)).

[9]In order for the system to reach its equilibrium position on the opposite side with respect to the offset vector $\vec{\varepsilon}$, it must have two degrees of freedom. Indeed, it is well known that 1D systems are highly unstable if spinning at frequencies above the critical one. On this argument see section 1.11.

1.3: VISCOUS DAMPING.

Energy dissipation in rotating machines can cause the free motion to decay in time or increase ([1], [5 - 8]). When considering a damped system, it is important to distinguish between two different kinds of damping:

- the so called non-rotating damping, associated to the stationary parts of the apparatus
- the so called rotating damping, associated to the energy dissipation inside the rotor.

In the following we will show that non-rotating damping is stabilizing at any speeds. Instead, we will show that rotating damping reduces the amplitude of oscillations in case of subcritical rotation ($\omega_s<\omega_{cr}$), but it has destabilizing effects (whirling motions) when the rotor is in supercritical rotation. The force due to non-rotating damping is given in the non-rotating frame by (viscous damping model proportional to the velocity):

$$\vec{F}_{xy}^{NR}=-c_{NR}\left(\dot{x},\dot{y}\right) \tag{1.12}$$

where c_{NR} is the non-rotating damping coefficient. By using the complex notation, the force reduces to:

$$\vec{F}^{NR}=F_x^{NR}+jF_y^{NR}=-c_{NR}\dot{z}' \tag{1.13}$$

Let us now introduce the rotating reference frame (O,ξ,η,z) with the origin O and the z axis coinciding with that of the inertial frame. Axes ξ and η rotate in the x-y plane with angular velocity ω_s. The force due to rotating (viscous) damping is expressed in the rotating frame by:

$$\vec{F}_{\xi\eta}^{R}=-c_R\begin{pmatrix}\dot{\xi}\\ \dot{\eta}\end{pmatrix} \tag{1.14}$$

Introducing the complex position vector in the rotating frame $\zeta=\xi+j\eta$, it is readily obtained $\zeta=z'\,e^{-j\omega st}$. The derivative of the complex coordinate ζ is then:

$$\dot{\zeta}=\left(\dot{z}'-j\omega_s z'\right)e^{-j\omega_s t} \tag{1.15}$$

Combining equations (1.14) and (1.15), the force due to rotating damping in the rotating frame is obtained:

$$\vec{F}_{\xi\eta}^{R}=-c_R\dot{\zeta}=-c_R\left(\dot{z}'-j\omega_s z'\right)e^{-j\omega_s t} \tag{1.16}$$

In the inertial frame it reads:

$$\vec{F}_{xy}^{R}=-c_R\left(\dot{z}'-j\omega_s z'\right) \tag{1.17}$$

1.4: THE JEFFCOTT ROTOR WITH VISCOUS DAMPING.

By introducing the forces (1.13) and (1.17) at the right-hand side of the equation of motion (1.7), it follows[10]:

$$m\ddot{z}'+(c_R+c_{NR})\dot{z}'+(k-j\omega_s c_R)z'=m\varepsilon\omega_s^2 e^{j\omega_s t} \tag{1.18}$$

[10] If the angular frequency of the rotor is not constant, the equation that describes the motion of even a simple body is more complex and it is easier to perform the numerical integration. This problem will be shown in section 1.6.

The characteristic equation of the associated homogeneous equation gives the values of the λ eigenvalues:

$$\lambda=j\frac{c_R+c_{NR}}{2m}\pm\sqrt{\frac{4m\left(k-j\omega_s c_R\right)-\left(c_R+c_{NR}\right)^2}{4m^2}} \tag{1.19}$$

The eigenvalues (1.19) may be written in a more manageable manner by separating the real parts of the complex frequencies from the imaginary parts.
After introducing the three parameters $a=\left(4mk-\left(c_R+c_{NR}\right)^2\right)\Big/4m^2$, $b=-c_R\omega_s/m$ and $c=\left(c_R+c_{NR}\right)/2m$ the first eigenvalue is obtained as[11]:

$$\lambda_1=-\sqrt{\frac{\sqrt{a^2+b^2}+a}{2}}+j\left(c+\sqrt{\frac{\sqrt{a^2+b^2}-a}{2}}\right) \tag{1.20}$$

It has a negative real part, namely $\Re e(\lambda_1)<0$[12]. Hence, the corresponding motion $z'=z_1e^{-\Im m(\lambda_1)t}e^{j\Re e(\lambda_1)t}$ is a backward whirl mode. The imaginary part is always positive in the whole range of frequency. It corresponds then to a damped backward whirl with amplitude decreasing in time with exponential law. The centre of mass of the rotor spiralises toward the centre of rotation, i.e. the origin O of the reference frame. This whirl damps out quickly and has little practical interest. The second eigenvalue is:

$$\lambda_2=\sqrt{\frac{\sqrt{a^2+b^2}+a}{2}}+j\left(c-\sqrt{\frac{\sqrt{a^2+b^2}-a}{2}}\right) \tag{1.21}$$

It has a positive real part and corresponds to a forward whirl motion. The imaginary part can be either positive or negative and the corresponding whirl can be either damped or excited. The condition for stability in terms of the sign of λ_2 is $\Im m(\lambda_2)>0$. With simple algebra it can be shown to be:

$$\omega_s<\omega_{cr}\left(1+c_{NR}/c_R\right) \tag{1.22}$$

If only rotating damping is present the motion is unstable in whole supercritical regime. In case of highly supercritical rotation the condition for stability means:

$$c_{NR}>c_R\,\omega_s/\omega_{cr} \tag{1.23}$$

Equation (1.23) means that non-rotating damping has a stabilizing effect on the rotor. The condition is easy to fulfil due to the very low level of the rotating damping of real rotors. The particular integral of the non-homogeneous equation (1.18) is connected to the presence of the unbalance and can be written in the form:

---

[11] $\sqrt{a+jb}=\sqrt{\frac{a+\sqrt{a^2+b^2}}{2}}+j\sqrt{\frac{-a+\sqrt{a^2+b^2}}{2}}$

[12] In the limit $\omega_s>>\sqrt{(k/m)}$ and $Q>>1$ it is easily found: $\Re e(\lambda_1)=-\omega_{c\,r}$ and $\Re e(\lambda_2)=\omega_{c\,r}$.

$$z'_p = z_0 e^{j\omega_s t} = \varepsilon \frac{\omega_s^2}{\omega_{cr}^2 - \omega_s^2 + j\omega_s c_{NR}/m} e^{j\omega_s t} \tag{1.24}$$

Starting from equation (1.24) the motion of the centre of mass[13] is readily obtained. In particular, we can write the value of the amplitude as a function of the spin speed:

$$\left|z_G(j\omega_s)\right| = \varepsilon \left| \frac{\omega_s^2}{\omega_{cr}^2 - \omega_s^2 + j\frac{\omega_s c_R}{m}} + 1 \right| \tag{1.25}$$

By introducing the dimensionless parameter

$$\gamma_R = c_R/(2m\omega_{cr}) = 1/Q \tag{1.26}$$

equation (1.25) can be written as:

$$\left|z_G(j\omega_s)\right| = \varepsilon \sqrt{1 + 4\gamma_R^2 \frac{\omega_s^2}{\omega_{cr}^2}} \Bigg/ \sqrt{\left(1 - \frac{\omega_s^2}{\omega_{cr}^2}\right)^2 + \left(2\gamma_R \frac{\omega_s}{\omega_{cr}}\right)^2} \tag{1.27}$$

Figure 1.4 shows the dependence of the amplitude of z_G (1.27) as a function of the angular spin frequency.

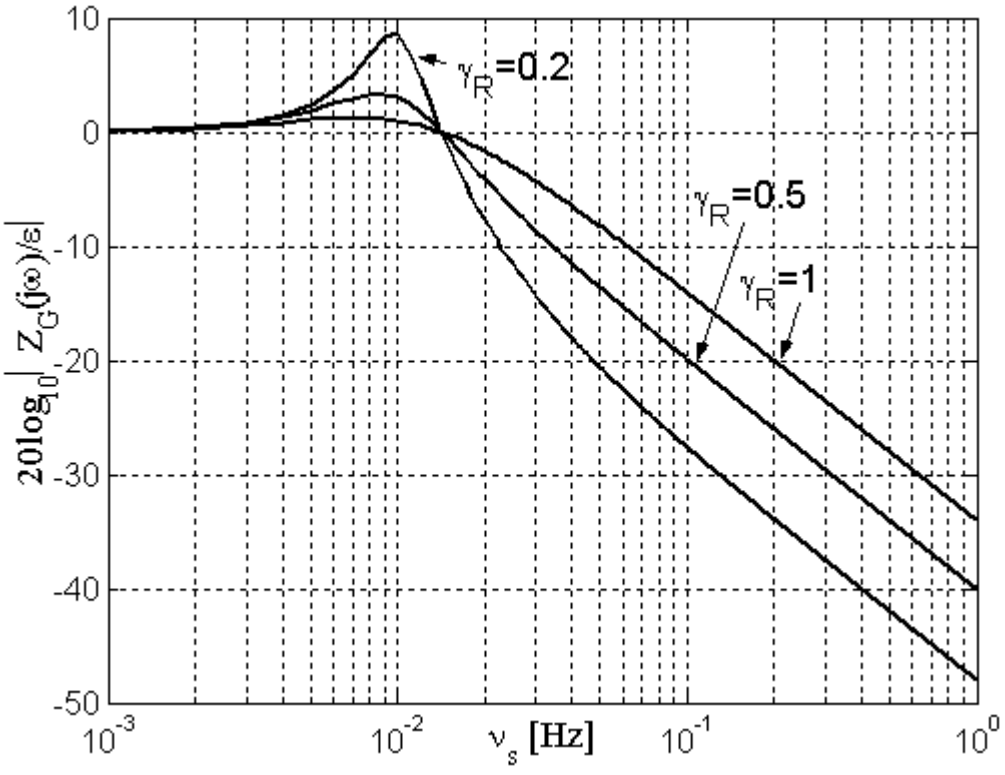

Figure 1.4: Dimensionless amplitude of the distance of the point mass G from the rotation axis for three different values of rotating damping.

[13] $z_G = x_G + jy_G = z' + \varepsilon e^{j\omega_s t}$

In supercritical regime it decreases with the spin angular velocity and vanishes in the limit $\omega_s \to \infty$, i.e. there is a self-centring of the suspended body on the rotation axis. If the stability condition (1.23) is satisfied, the general solution of the equation (1.18) can be considered as the superimposition of a backward whirl motion (the solution corresponding to the eigenvalue (1.20)), which decays in time, a forward motion, with decreasing amplitude (the solution corresponding to (1.21)) and a circular motion at the spin frequency with constant amplitude (corresponding to (1.24)). There is a self-centring of the point mass G, instead, on the rotation axis, at distance $\sim \varepsilon \omega_{cr}^2 / \omega_s^2 \ll \varepsilon$.

1.5: STRUCTURAL DAMPING.

Many materials, when subjected to cyclic loading, show a behaviour that can be described in terms of a hysteresis cycle. In these cases the damping is called "structural". Structural damping is due to the relative motions of different parts in the material when subject to deformations. Let us introduce the complex stiffness $k^*=k^R+jk^I$ ([1], [9]): the real part k^R is linked with the elastic stiffness of the material, while the imaginary part k^I is connected to the damping. $\gamma_k=k^I/k^R$ is the loss factor. The expression of the complex stiffness may be written as $k^*=k(1+j\gamma_k)$. For simplicity, we consider a model with only one degree of freedom, that is simple but demonstrates, at least qualitatively, the behaviour of more complex systems: on the point mass m can act a force function of time f(t) and the supporting point can move in the x direction. The equation of motion can be solved in the frequency domain:

$$k_{din} X(j\omega) = F(j\omega) \tag{1.28}$$

In equation (1.28) we have introduced the dynamic stiffness of the system with structural damping:

$$k_{din} = -m\omega^2 + k(1 + j\gamma_k) \tag{1.29}$$

The dynamic stiffness is a function of the forcing frequency, and in case of damped system, it is complex. The complex frequency of the free oscillations can be obtained by equating to zero the dynamic stiffness:

$$\omega_c = \sqrt{k/m}\sqrt{1 + j\gamma_k} = \omega_n \sqrt{1 + j\gamma_k} \tag{1.30}$$

where ω_n is the natural frequency of the undamped system.
After some simple algebra[14], the real and the imaginary parts of the complex frequency can be easily separated:

$$\omega_c = \omega_n \sqrt{\frac{1 + \sqrt{1 + \gamma_k^2}}{2}} + j\omega_n \sqrt{\frac{-1 + \sqrt{1 + \gamma_k^2}}{2}} \tag{1.31}$$

The loss factor is typically very small ($\gamma_k << 1$); in this limit it follows:

$$\Re e(\omega_c) \approx \omega_n \tag{1.32}$$

[14] $\sqrt{2(a + jb)} = \sqrt{a + \sqrt{a^2 + b^2}} + j\sqrt{-a + \sqrt{a^2 + b^2}}$

$$\Im m(\omega_c) \approx \omega_n \frac{\gamma_k}{2} \tag{1.33}$$

Relations (1.32) and (1.33) show that the frequency shift due to the presence of structural damping is negligible for lightly damped systems.
The ratio between the elastic stiffness and the dynamic stiffness is usually referred to as the frequency response H of the system. The expressions for the real and imaginary parts, its amplitude and phase are:

$$\Re e(H(j\omega)) = k\frac{k - m\omega^2}{\sqrt{\left(k - m\omega^2\right)^2 + k^2\gamma_k^2}} \tag{1.34}$$

$$\Im m(H(j\omega)) = -\frac{k^2\gamma_k}{\sqrt{\left(k - m\omega^2\right)^2 + k^2\gamma_k^2}} \tag{1.35}$$

$$\left|H(j\omega)\right| = \frac{k}{\sqrt{\left(k - m\omega^2\right)^2 + k^2\gamma_k^2}} = \frac{1}{\sqrt{\left(1 - \omega^2/\omega_n^2\right)^2 + \gamma_k^2}} \tag{1.36}$$

$$\Phi(j\omega) = \operatorname{arctg}\left(-\frac{k\gamma_k}{k - m\omega^2}\right) = \operatorname{arctg}\left(-\gamma_k \Big/ \left(1 - \omega^2/\omega_n^2\right)\right) \tag{1.37}$$

Figure 1.5 shows the amplitude and phase of H as function of the forcing frequency for different values of the loss factor.

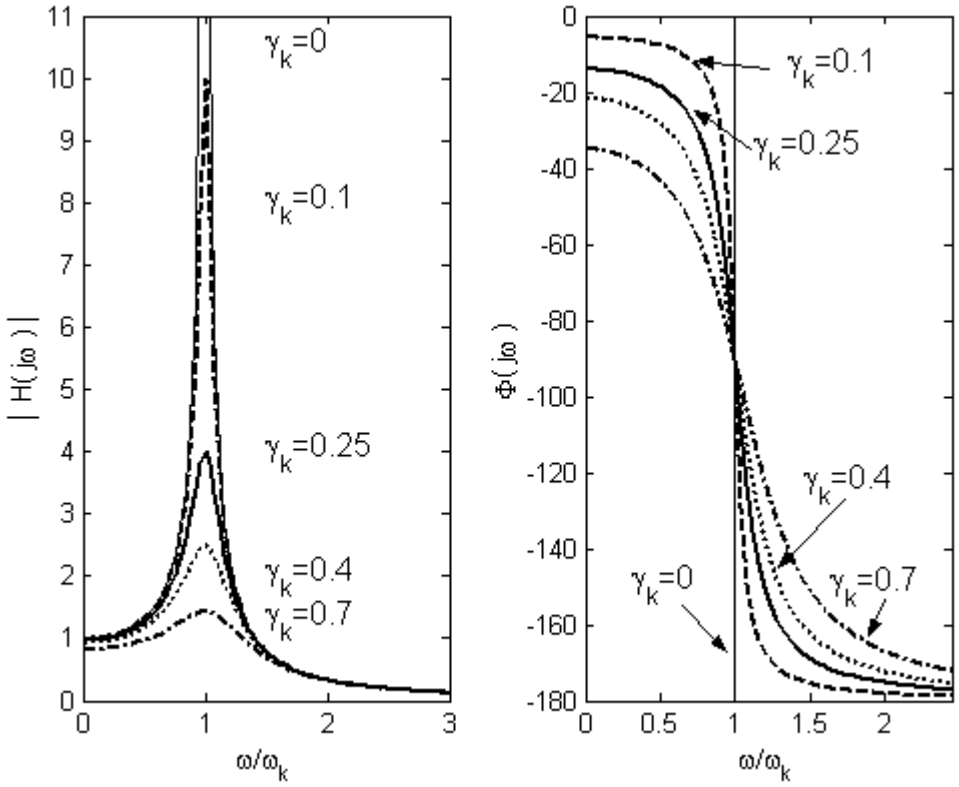

Figure 1.5: Amplitude and phase of H(jω) as function of the forcing frequency. For different values of the loss factor.

The quality factor of the system with structural damping is defined as:

$$Q = \left|H(j\omega)\right|_{max} = \frac{1}{\gamma_k} \tag{1.38}$$

Structural damping is then a form of linear damping and it can be assimilated with viscous damping through the equivalent viscous damping coefficient:

$$c_{eq} = k\gamma_k / \omega \tag{1.39}$$

In equation (1.39) ω is the frequency at which the material goes through the hysteresis cycle. By inserting the relation (1.38) into the (1.39), it follows:

$$c_{eq} = \frac{k}{\omega Q} \tag{1.40}$$

On the basis of experiences with many rotating machines it is concluded that friction inside rotating parts (the suspensions) is essentially of structural nature. Hence, a structural damping model is usually better suited for the rotating damping. Note that the frequency at which the hysteresis cycle is gone through is now $|\omega_n - \omega_s|$ with ω_s the spin speed:

$$c_R = \frac{k}{Q|\omega_n - \omega|}$$ [15] (1.41)

In case of highly supercritical rotation, the relation (1.41) can be simplified in $c_R \approx k/Q\omega$, i.e. energy is dissipated at the high spin angular velocity and not at the low natural frequency.

1.6: ACCELERATING JEFFCOTT ROTOR.

If the spin speed is constant, the terms in $\dot{\omega}_s$ in equation (1.18) are neglected. However, when the rotational speed is not constant, the angle between the two reference frames (inertial and rotating; see section 1.2) can not be written as $\varphi=\omega_s t$. φ is now a third generalized coordinate linked with the rotation about the z axis. A driving torque M_z is assumed to be applied to the shaft of the rotor (torsionally stiff) and the lagrangean of the system is expressed by the relation:

$$L = \frac{1}{2}m\left[\dot{x}^2+\dot{y}^2+\varepsilon^2\dot{\varphi}^2+2\varepsilon\dot{\varphi}\left(\dot{y}\cos(\varphi)-\dot{x}\sin(\varphi)\right)\right]-\frac{1}{2}k\left(x^2+y^2\right)+\frac{1}{2}J_z\dot{\varphi}^2 \tag{1.42}$$

The equations of motion are determined from (1.42) in the standard manner:

$$m\ddot{z}'+(c_R+c_{NR})\dot{z}'+(k-j\dot{\varphi}c_R)z'=m\varepsilon\left(\dot{\varphi}^2-j\ddot{\varphi}\right)e^{j\varphi}$$ [16] (1.43)

$$\left(J_z+m\varepsilon^2\right)\ddot{\varphi}+m\varepsilon\left(-\ddot{x}\sin(\varphi)+\ddot{y}\cos(\varphi)\right)=M_z$$ [17] (1.44)

---

[15] For the non-rotating damping the equivalent coefficient is $c_{NR} = k/Q\omega_n$.

[16] If the spin speed is constant, equation (1.18) is easily obtained from (1.43) by performing the substitutions $\varphi \rightarrow \omega_s t$, $d\varphi/dt \rightarrow \omega_s$, $d^2\varphi/dt^2 \rightarrow 0$.

In this case it is better to introduce a rotating frame (which, however, does not rotate at constant speed). The position, velocity and acceleration of point C can be expressed as functions of complex coordinate ζ:

$$z' = \zeta e^{j\varphi} \tag{1.45}$$

$$\dot{z}' = \left(\dot{\zeta} + j\dot{\varphi}\zeta\right)e^{j\varphi} \tag{1.46}$$

$$\ddot{z}' = \left(\ddot{\zeta} + j\ddot{\varphi}\zeta + 2j\dot{\varphi}\dot{\zeta} - \varphi^2\zeta\right)e^{j\varphi} \tag{1.47}$$

By introducing the relations (1.45), (1.46) and (1.47) into the equations (1.43) and (1.44) it follows:

$$m\ddot{\zeta}+(c_R+c_{NR}+2mj\dot{\varphi})\dot{\zeta}+(k+j\dot{\varphi}c_{NR}+j\ddot{\varphi}-\varphi^2)\zeta=m\varepsilon\left(\dot{\varphi}^2-j\ddot{\varphi}\right) \tag{1.48}$$

$$\left(J_z+m\varepsilon^2\right)\ddot{\varphi}+m\varepsilon\left(\ddot{\eta}+2\dot{\varphi}\dot{\xi}+\ddot{\varphi}\xi-\dot{\varphi}^2\eta\right)=M_z\ ^{18} \tag{1.49}$$

When the time history of the driving torque is known, equations (1.48) and (1.49) can be solved by performing a numerical integration.
We want, now, to evaluate the torque needed to operate at constant speed ω_s. In this limit ($\ddot{\varphi}=0$), equations (1.48) coincide with equations (1.18) and the displacement ζ is constant at the value expressed by (1.24), namely:

$$\zeta_{\ddot{\varphi}=0}=\varepsilon\omega_s^2\Big/\left(\omega_{cr}^2-\omega_s^2+j\omega_s c_{NR}/m\right) \tag{1.50}$$

By stating $\ddot{\varphi}=0, \dot{\varphi}=\omega_S, \varphi=\omega_S t$, equation (1.49) can be written in the form:

$$-m\varepsilon\omega_s^2\eta_{\ddot{\varphi}=0}=M_z\ ^{19} \tag{1.51}$$

By combining equations (1.50) with (1.51), the torque needed to operate at constant speed ω_s is obtained:

$$M_z=\frac{c_{NR}\varepsilon^2\omega_s^5}{\left(\omega_{cr}^2-\omega_s^2\right)^2+\dfrac{\omega_s^2c_{NR}^2}{m^2}}\ ^{20} \tag{1.52}$$

---

[17] The equation (1.44) is obtained in the standard manner: $\dfrac{d}{dt}\dfrac{\partial L}{\partial\dot{\varphi}}-\dfrac{\partial L}{\partial\varphi}=M_Z$.

[18] In sections 1.2 and 1.3 we have introduced the complex variables $z'=x+jy$ and $\zeta=\xi+j\eta$. After some simple algebra, it follows: $\zeta=z'e^{-j\varphi}$ and $\Im m(\ddot{z}'e^{-j\varphi})=-\ddot{x}\sin(\varphi)+\ddot{y}\cos(\varphi)$. Equation (1.44) can be written as $(J_z+m\varepsilon^2)\ddot{\varphi}+m\varepsilon\Im m\left(\ddot{z}'e^{-j\varphi}\right)=M_z$. By noticing that $\Im m\left(\ddot{z}'e^{-j\varphi}\right)=\ddot{\eta}+2\dot{\varphi}\dot{\xi}+\ddot{\varphi}\xi-\dot{\varphi}^2\eta$, equation (1.49) is readily obtained.

[19] We have equated to zero all derivatives of the generalized coordinates: $\ddot{\varphi}=\dot{\xi}=\ddot{\xi}=\dot{\eta}=\ddot{\eta}=0$.

[20] $\eta_{\ddot{\varphi}=0}=\Im m\left(\zeta_{\ddot{\varphi}=0}\right)=-\dfrac{c_{NR}\varepsilon\omega_s^3/m}{\left[\left(\omega_{cr}^2-\omega_s^2\right)^2+\dfrac{\omega_s^2c_{NR}^2}{m^2}\right]}$

Let us introduce the loss factors:

$$\gamma_R = \frac{c_R}{2\sqrt{km}}; \gamma_{NR} = \frac{c_{NR}}{2\sqrt{km}} \tag{1.53}$$

The driving torque may be written in terms of non-dimensional parameters:

$$M_z = 2\gamma_{NR} k\varepsilon^2 \frac{\omega_s^5 / \omega_{cr}^5}{\left(1-\omega_s^2/\omega_{cr}^2\right)^2 + 4\gamma_{NR}^2 \omega_s^2/\omega_{cr}^2} = 2k\varepsilon^2 M_z^* \tag{1.54}$$

Figure 1.6 shows the non-dimensional driving torque M_Z^* as a function of the ratio ω_s/ω_{cr}.

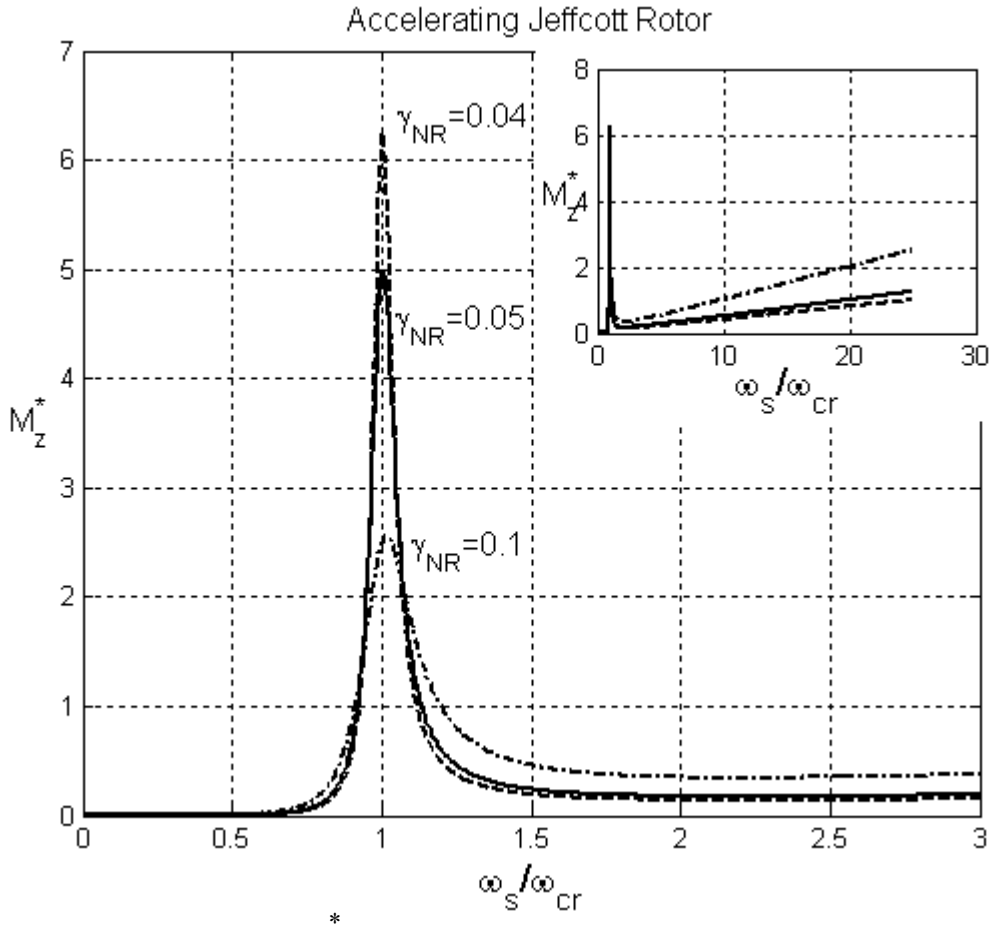

Figure 1.6: Non-dimensional torque M_Z^* as a function of the ratio ω_s/ω_{cr}. The torque has a peak at the critical speed. Inset: value of the torque at high spin speed.

The torque has a peak at the critical frequency:

$$M_{cr} = M_z(\omega_s = \omega_{cr}) = \frac{k\varepsilon^2}{2\gamma_{NR}} \tag{1.55}$$

and, in case of highly supercritical rotation, the torque needed to operate at constant speed grows linearly with the spin angular velocity:

$$\lim_{\omega_s \to \infty} M_z = 2k\varepsilon^2 \gamma_{NR} \omega_s \tag{1.56}$$

Note that M_{cr} is also the smaller torque needed to operate at speed higher than the critical speed.

1.7: COUPLED ROTORS.

In order to investigate the properties of coupled rotors ([10 - 11]), we examine the simple problem of two bodies connected by dissipative springs. Two concentric, co-axial, hollow cylinders with mass $m_1=m_2=m$, weakly coupled by dissipative mechanical suspensions with elastic stiffness k, rotates around their symmetry axis (z axis) at constant spin speed ω_s higher than the natural frequency of the system (supercritical regime). The rotation is counter-clockwise[21].

In supercritical rotation mechanical suspensions are known to undergo deformation (and therefore to dissipate energy) at the spin frequency. Energy dissipation makes the spin rate to decrease, together with the spin angular momentum. Since the total angular momentum must be conserved, the bodies develop a whirl motion of increasing amplitude around each other at a frequency close to the natural differential[22] one due to the coupling. In figure 1.7 a sketch of the two coupled cylinders is shown. Since the springs are very weak and their masses are negligible compared to the mass of the rotor, they will be obliged to follow the motion of the attachment points which rotate at ω_s around the centre of mass of the respective test mass. The centres of mass of the springs will rotate around O at ω_s. When the springs are going from position 1 to position 3 in figure 1.7, they will be forced to expand by $4r_w$ (r_w is the radius of the whirl motion), and when going from position 3 to 1 to contract by the same amount.

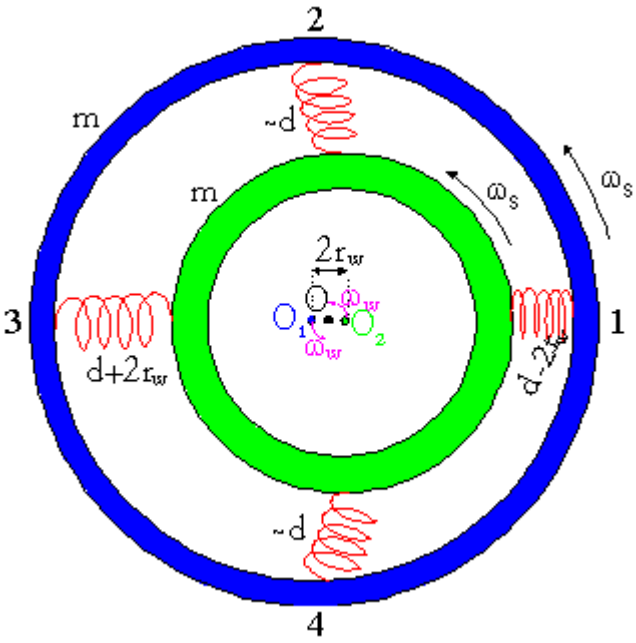

Figure 1.7: Simple model of a system made of two bodies of mass m, coupled by weak springs. Both bodies are spinning at the same angular velocity ω_s around their respective centres of mass O_1 and O_2. O_1 and O_2 are whirling around the centre of mass O of the whole system at the natural frequency $\omega_w=\omega_n$.

[21] This is a simplified model for the system spacecraft – PGB which will be studied in chapters 7,8 and 9.

[22] Natural differential frequency: the cylinders' centres of mass move within the horizontal plane in opposition of phase while their symmetry axis remains aligned with the vertical z

The centres of mass O_1 and O_2 of the two cylinders rotate around O with angular frequency $\omega_w=\omega_n$ (ω_n is the natural frequency of the system). After the spring, starting from position 1, has completed one turn in the time $T_s=2\pi/\omega_s$, the whirling motion will have displaced position 1 by an angle $\pm 2\pi\omega_w/\omega_s$ (the sign + refers to the forward whirling and the sign – to the backward one). Therefore, in order to reach again the position 1 of maximum contraction, the spring takes a time slightly different from T_s. This means that each spring is forced to oscillate at the frequency $\omega_s \pm \omega_w$. As a consequence, by considering the dissipation of the whole system as expressed by the quality factor *Q*, the coefficient of rotating damping is given as $c_R=k/(Q\,|\omega_s \pm \omega_w|)$ in agreement with equation (1.41). Let us consider $\vec{r}_1$ the position vector of the cylinder 1, $\vec{r}_2$ the position vector of body 2, $\vec{\varepsilon}$ (eccentricity) the vector locating the suspension point of the spring with respect to the centre of the outer body 2 (see figure 1.8).

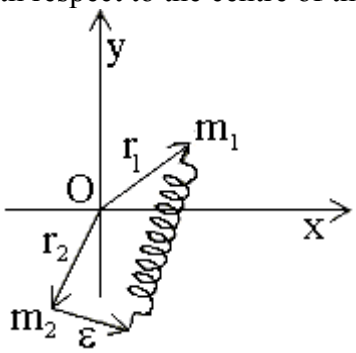

Figure 1.8: Simplified model of the system. $\vec{r}_1$ is the position vector of the cylinder 1, $\vec{r}_2$ the position vector of body 2, $\vec{\varepsilon}$ (eccentricity) the vector locating the suspension point of the spring with respect to the centre of the outer body 2.

In the inertial reference frame the equations of motion of the centres of mass are:

$$\begin{cases} m_1\ddot{\vec{r}}_1=-k(\vec{r}_1-\vec{r}_2+\vec{\varepsilon})-c_R\left(\dot{\vec{r}}_1-\dot{\vec{r}}_2-\vec{\omega}_s\times(\vec{r}_1-\vec{r}_2)\right) \\ m_2\ddot{\vec{r}}_2=-k(\vec{r}_2-\vec{r}_1-\vec{\varepsilon})-c_R\left(\dot{\vec{r}}_2-\dot{\vec{r}}_1-\vec{\omega}_s\times(\vec{r}_2-\vec{r}_1)\right) \end{cases} \tag{1.57}$$

where the rotating damping (1.17) has been introduced. By defining the relative position vector $\vec{\xi}=\vec{r}_2-\vec{r}_1=(\xi_1,\xi_2)$, the reduced mass $m_r=(m_1m_2)/(m_1+m_2)$ and the natural frequency $\omega_n^2=k/m_r$, we can write the equation for the relative motion of the cylinders:

$$\ddot{\vec{\xi}}=-\omega_n^2\left(\vec{\xi}-\vec{\varepsilon}\right)-\frac{c_R}{m_r}\left(\dot{\vec{\xi}}-\vec{\omega}_s\times\vec{\xi}\right) \tag{1.58}$$

By noticing that for a highly spinning rotor the coefficient of rotating damping takes the value $c_R = m_r\,\omega_n^2/(Q\omega_s)$ and being the vector $\vec{\varepsilon}=\vec{\varepsilon}(t)=\varepsilon(\cos(\omega_s t),\sin(\omega_s t))$ a rotating vector in the inertial reference frame (it is fixed in the reference frame co-rotating with the rotor), it follows:

$$\ddot{\vec{\xi}}+\frac{\omega_n^2}{Q\omega_s}\dot{\vec{\xi}}+\left[\omega_n^2\vec{\xi}-\frac{\omega_n^2}{Q\omega_s}\left(\vec{\omega}_s\times\vec{\xi}\right)\right]=\omega_n^2\vec{\varepsilon}(t) \tag{1.59}$$

Equation (1.59) can be written in terms of the complex coordinate $z'=\xi_1+j\xi_2$:

$$\ddot{z}'+\frac{\omega_n^2}{Q\omega_s}\dot{z}'+\left(\omega_n^2-j\frac{\omega_n^2}{Q}\right)z'=\omega_n^2\varepsilon e^{j\omega_s t} \tag{1.60}$$

Before finding the solutions of equation (1.60), let us replace the right-hand side of this equation with the forcing function[23] $f(t)=\alpha e^{j\omega t}$. The transfer function is now:

$$H(j\omega)=\frac{Z(j\omega)}{F(j\omega)}=1\Big/\left[\left(\omega_n^2-\omega^2\right)+j\left(\frac{\omega-\omega_s}{\omega_s}\right)\frac{\omega_n^2}{Q}\right] \tag{1.61}$$

In the particular case of equation (1.60) (i.e. when $\omega=\omega_s$, $\alpha=\omega_n^2\varepsilon$ and the forcing function $f(t)=\omega_n^2\varepsilon e^{j\omega_s t}$) the transfer function (1.61) can be written as:

$$H(j\omega_s)=1\Big/\left(\omega_n^2-\omega_s^2\right) \tag{1.62}$$

The particular integral of the non-homogeneous equation (1.59) can be readily obtained from (1.62):

$$\vec{\xi}_\varepsilon(t)=\frac{\omega_n^2}{\left(\omega_n^2-\omega_s^2\right)}\vec{\varepsilon}(t) \tag{1.63}$$

Equation (1.10) obtained in the case of the Jeffcott rotor and equation (1.63) are very similar. In supercritical regime, the amplitude of the vector $\vec{\xi}_\varepsilon(t)$ decreases with the spin speed. The equation (1.60) is like equation (1.18) and its solution are obtained in the same manner. In the limit of highly supercritical rotation $\omega_s>>\omega_n$ and high quality factor $Q>>1$, its eigenvalues are:

$$\lambda_{1,2}=\mp\omega_n\left[1-j/(2Q)\right]$$ [24] (1.64)

Having the eigenvalues (1.64), the general solution of the homogeneous equation associated with (1.59) may be easily written in the form:

$$\vec{\xi}_w(t)=Ae^{-\omega_n t/2Q}\begin{pmatrix}\cos(-\omega_n t+\varphi_A)\\ \sin(-\omega_n t+\varphi_A)\end{pmatrix}+Be^{\omega_n t/2Q}\begin{pmatrix}\cos(\omega_n t+\varphi_B)\\ \sin(\omega_n t+\varphi_B)\end{pmatrix} \tag{1.65}$$

---

[23] We want to solve the general equation: $\ddot{z}'+\frac{\omega_n^2}{Q\omega_s}\dot{z}'+\left(\omega_n^2-j\frac{\omega_n^2}{Q}\right)z'=f(t)$

[24] We Start from equations (1.20) and (1.21) for the Jeffcott rotor. If $c_{NR}=0$ the eigenvalues are:

$$\lambda_{1,2}=\mp\frac{1}{\sqrt{2}}\sqrt{\omega_n^2+\sqrt{\omega_n^4+\left(\frac{k}{m_r Q}\right)^2}}+j\left[\frac{k/m_r}{2Q\omega_s}\pm\frac{1}{\sqrt{2}}\sqrt{-\omega_n^2+\sqrt{\omega_n^4+\left(\frac{k}{m_r Q}\right)^2}}\right]$$

Remembering the definition of the natural frequency ω_n, it follows:

$$\lambda_{1,2}=\mp\frac{1}{\sqrt{2}}\sqrt{\omega_n^2+\sqrt{\omega_n^4\left(1+\frac{1}{Q^2}\right)}}+j\left[\frac{\omega_n^2}{2Q\omega_s}\pm\frac{1}{\sqrt{2}}\sqrt{-\omega_n^2+\sqrt{\omega_n^4\left(1+\frac{1}{Q^2}\right)}}\right]$$

In the limit $x>>1$, we have $\sqrt{\left(1+1/x^2\right)}\approx 1+1/(2x^2)$.

Then, the following approximated relations for the eigenvalues are obtained:

$$\lambda_{1,2}\approx\mp\frac{1}{\sqrt{2}}\sqrt{2\omega_n^2\left(1+\frac{1}{4Q^2}\right)}+j\left[\frac{\omega_n^2}{2Q\omega_s}\pm\sqrt{\frac{\omega_n^2}{2Q^2}}\right]\approx\mp\omega_n\left(1+\frac{1}{8Q^2}\right)+j\left[\frac{\omega_n^2}{2Q\omega_s}\pm\frac{\omega_n}{2Q}\right]\approx\mp\omega_n\pm j\frac{\omega_n}{2Q}$$

$\vec{\xi}_w(t)$ in (1.65) is the so called whirl motion. It is the superimposition of a circular forward whirl motion (i.e. occurring in the same direction of the spin speed) which is self-excited, and a circular backward whirl motion which is damped. They both occur at an angular velocity equal to the natural frequency of the non-rotating system.
The solution of equation (1.59) can be obtained by adding the general solution of the homogeneous equation (1.65) to the particular integral (1.63) of the complete equation:

$$\vec{\xi}=\vec{\xi}_\varepsilon(t)+\vec{\xi}_w(t)$$
$$=\frac{\omega_n^2}{\left(\omega_n^2-\omega_s^2\right)}\vec{\varepsilon}(t)+Ae^{-\omega_n t/2Q}\begin{pmatrix}\cos(-\omega_n t+\varphi_A)\\ \sin(-\omega_n t+\varphi_A)\end{pmatrix}+Be^{\omega_n t/2Q}\begin{pmatrix}\cos(\omega_n t+\varphi_B)\\ \sin(\omega_n t+\varphi_B)\end{pmatrix} \quad (1.66)$$

Clearly, the damping time constant of the system due to the dissipation is proportional to the quality factor Q, namely $\tau = 2Q/\omega_n$. If Q is large, whirl growth is very slow. Equation (1.59) has been integrated numerically and the results are shown in figures 1.9, 1.10 and 1.11.

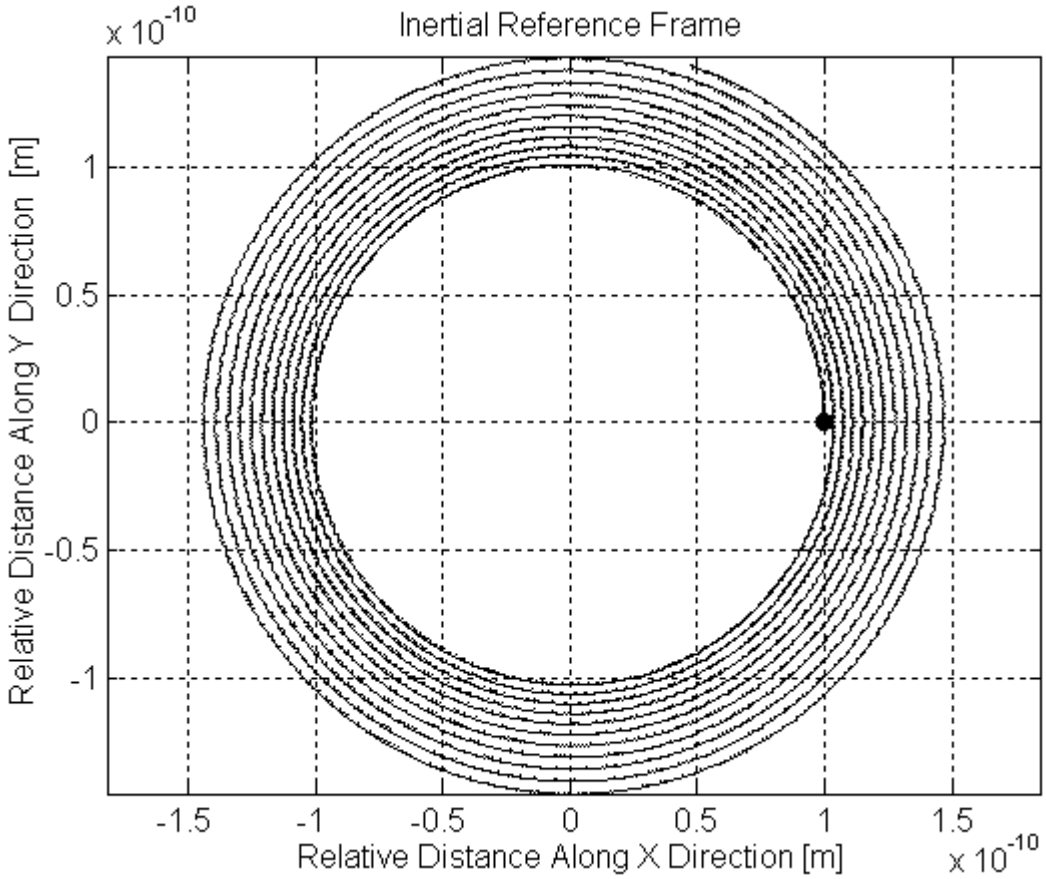

Figure 1.9: Simulation of the two body system.A forward whirl growing in amplitude. For demonstration purposes the numerical integration is carried with a bad quality factor (Q=10) to have a short time constant. Black circle: starting point.

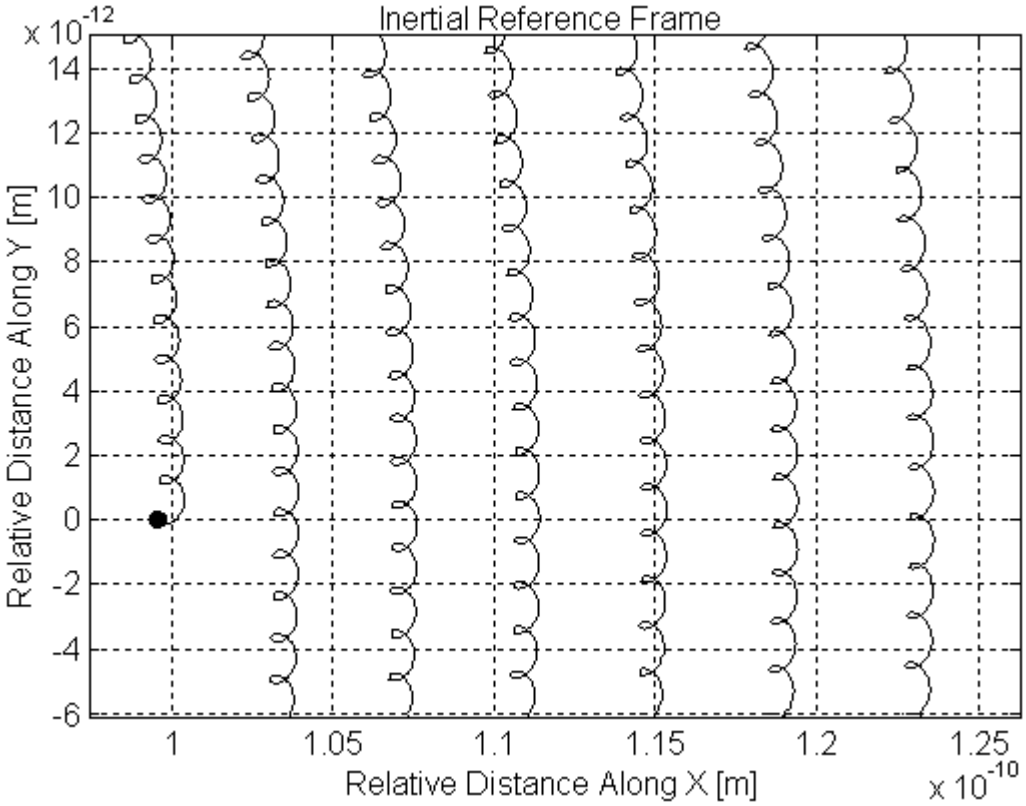

Figure 1.10: Enlargement of the previous figure. Black circle: starting point. Small oscillations at the spin frequency are visible.

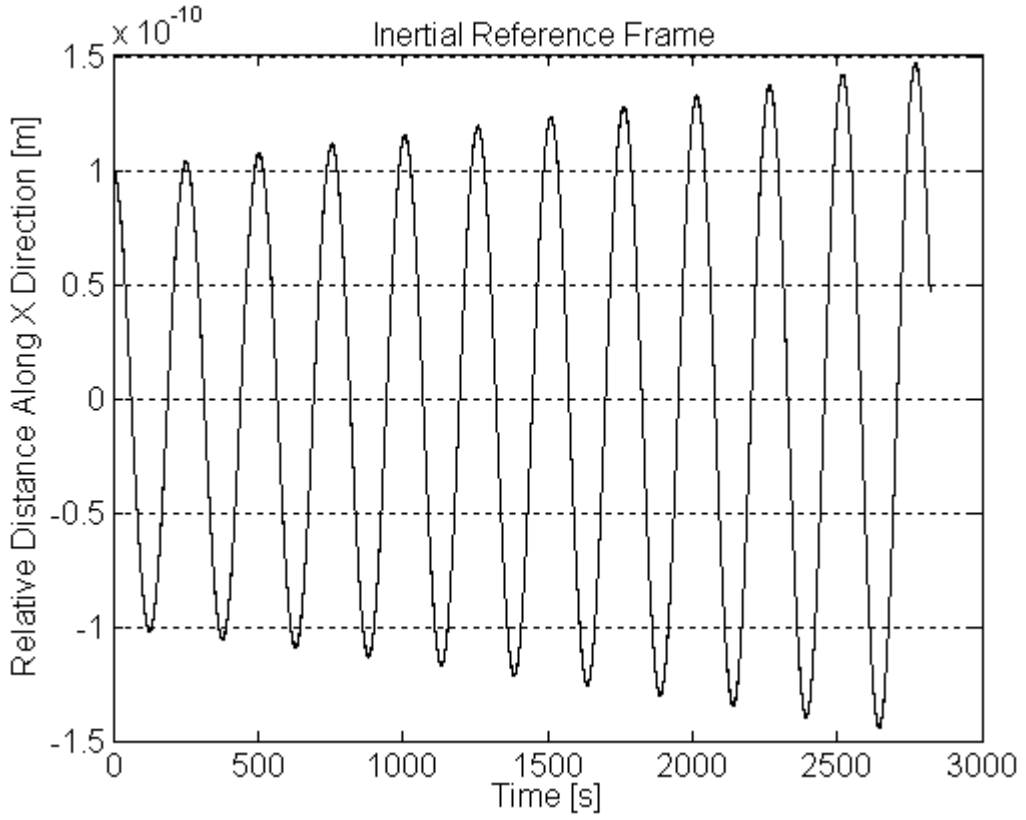

Figure 1.11: Simulation of the two body system. Relative distance along y direction as a function of time. The growth of the amplitude is evident.

We can now complete the mathematical model specializing here to the introduction of an external force F_e (constant or slowly variable) acting on body 1; the solution is the superimposition of three relative displacements:

$$\vec{\xi}=\vec{\xi}_{\varepsilon}(t)+\vec{\xi}_{w}(t)+\vec{\xi}_{Fe}(t) \tag{1.67}$$

with:

$$\vec{\xi}_{Fe}(t)=-\frac{m_1}{k/m_r+\omega_s^2 c_r^2/km_r}\vec{F}_e(t)-\frac{m_1}{k/m_r+\omega_s^2 c_r^2/km_r}\frac{1}{Q}\hat{z}\times\vec{F}_e(t) \tag{1.68}$$

$\vec{\xi}_{Fe}(t)$ in (1.68) is the vector describing the displacement of the equilibrium position due to the action of the external force. This result is interesting. For example, even though the external force has been applied along the x direction, finite differential displacements occurs along the y direction, due to the rotation and to the dissipative nature of the suspensions (the quality factor *Q* is finite. See figure 1.12).

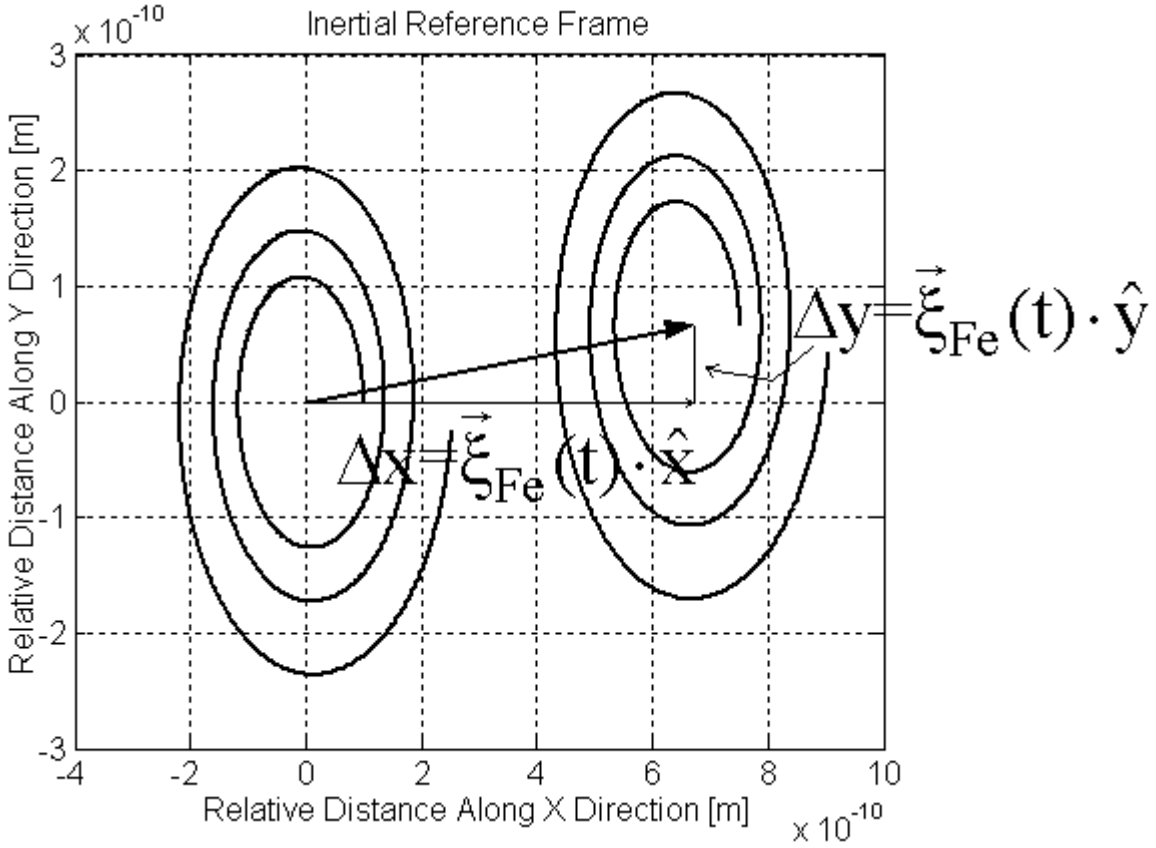

Figure 1.12: Simulation of the two body system. Relative motion in the inertial reference frame. The figure shows the plane of motion in two cases: with (right) and without (left) the inertial force acting on body 2. It shows how the effect of an external force is that of displacing the equilibrium position of the system. A small phase lag ($\Delta y/\Delta x$) appears due to energy losses in the suspensions (i.e. finite quality factor Q=10). Due to these losses, whirl motion at the natural frequency of the system arises in either case around the corresponding equilibrium position.

However, the magnitude of the displacement along the y direction ("orthogonal") is depressed by a factor $1/Q$ <<1 with respect to that along x. Hence, the two degrees of freedom are

coupled from the energy dissipation only because Q has a finite value. The 2 body system is unstable. The simplest way to stabilize it is adding some non-rotating damping which is mathematically expressed by the terms containing the non-rotating damping coefficient c_{NR}. To this aim, we introduce the force (1.12) and then recast this equation in the rotating reference frame:

$$\ddot{\vec{\zeta}}=-\omega_n^2\left(\vec{\zeta}-\vec{\varepsilon}\right)-\frac{c_{NR}}{m_r}\left(\dot{\vec{\zeta}}+\vec{\omega}_s\times\vec{\zeta}\right)-\frac{\omega_n^2}{\omega_s Q}\dot{\vec{\zeta}}+\omega_s^2\vec{\zeta}-2\vec{\omega}_s\times\dot{\vec{\zeta}} \qquad (1.69)$$

$\vec{\zeta}$ is the relative displacement between the bodies in the rotating reference frame. In agreement with (1.23), the condition for stability is $c_{NR}=c_R\ \omega_s/\omega_n$. Equation (1.69) has been integrated numerically and the result is shown in figure 1.13. This plot shows the approaching of the relative displacement to the equilibrium position.

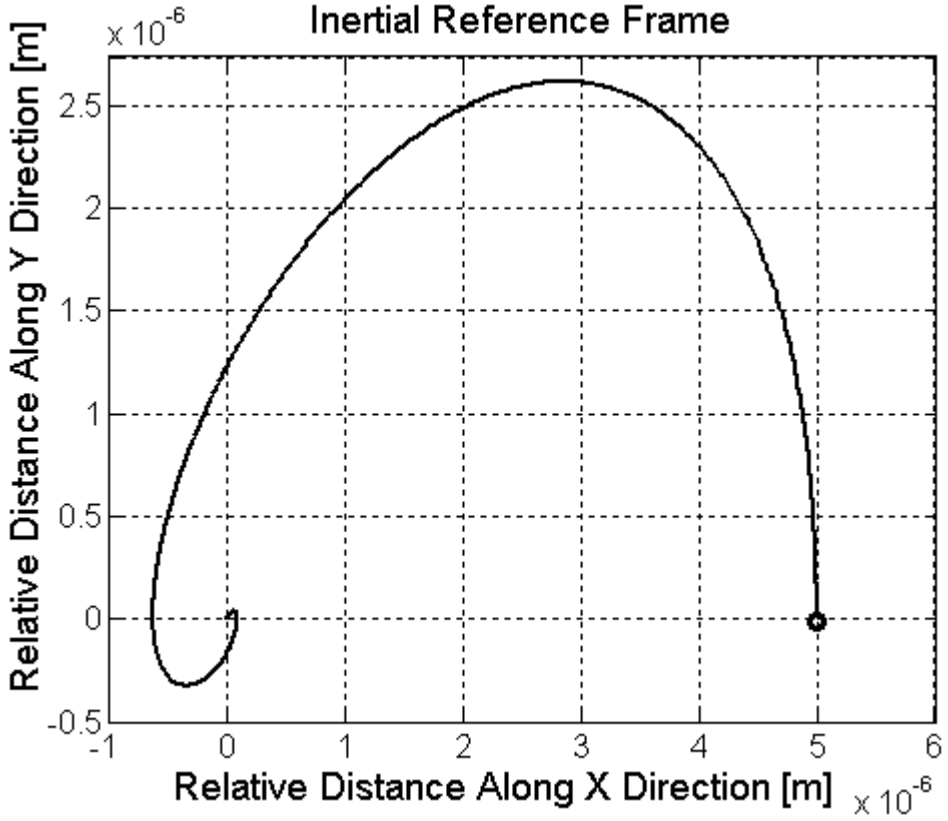

Figure 1.13: Simulation of the two body system. Polar plot of the relative displacement in the inertial reference frame. Forward whirl is damped. $c_{NR}=100\ c_R\ \omega_s/\omega_n$.

1.8: WHIRLING MOTION AND STABILIZING FORCE.

If there is friction inside rotating parts of the system this amounts to a non zero coefficient of rotating damping. Rotating damping has a destabilizing effect because it produces a spin down of the system and a corresponding forward whirling motion of the rotating bodies with an exponentially increasing amplitude.

In the inertial frame, the frequency of the whirling motions is essentially the natural frequency of the non-rotating system $\omega_w=\omega_n$ (ω_n is the natural frequency of the system). In the rotating

frame, the deformations of the springs occur at the frequency $\omega_s \pm \omega_w$. As a consequence, whirl motions grows in amplitude at a rate which depends on the *Q* of the system at the frequency $\omega_s \pm \omega_w$, which is essentially the spin frequency: the higher the *Q* at this frequency, the slower the growth rate of the whirl. More precisely, rotor dynamics predicts that whirl grows with a negative *Q* opposite to the *Q* of the system at its spin frequency. This means that if r_w is the amplitude of the whirling motion, it increases in time as follows:

$$r_w(t) = r_w(0) e^{\frac{\omega_n t}{2Q}} \tag{1.70}$$

and its relative variation in one natural period T_n (if $Q >> 1$) is:

$$\frac{\Delta r_w}{r_w(0)} \cong \frac{\omega_n}{2Q} T_n \tag{1.71}$$

This increase in the amplitude can be interpreted as due to an increasing of the along track velocity, caused by a destabilizing acceleration a_d such that:

$$\frac{1}{2} a_d T_n^2 \cong 2\pi \Delta r_w \tag{1.72}$$

or

$$a_d \cong \frac{1}{Q} \omega_n^2 r_w(0) \tag{1.73}$$

The destabilizing force [12] connected to the acceleration a_d can be written as:

$$\left|\vec{F}_d\right| = \frac{1}{Q} m \omega_n^2 r_w(0) = \frac{1}{Q} \left|\vec{F}_{centrifugal}\right| = \frac{1}{Q} \left|\vec{F}_{spring}\right| \tag{1.74}$$

where $\vec{F}_{centrifugal}$ is the centrifugal force and $\vec{F}_{spring}$ the elastic force of the spring. The destabilizing force is, then, a small fraction $1/Q << 1$ of the elastic force. An active damping force opposite to $\vec{F}_d$ (1.74) and slightly larger is required to stabilize the system.

1.9: ENERGY DISSIPATION IN WHIRLING MOTION.

At this point we want to evaluate how much energy is gained by the whirling motion as fraction of the energy lost by the spinning rotor [13]. The spin energy of the rotor is:

$$E_{rotor} = \frac{1}{2} I \omega_s^2 \tag{1.75.a}$$

with I the moment of inertia. The along track velocity is $v_w = \omega_n r_w$ and the energy of whirl motion is:

$$E_w = E_{kinetic} + E_{elastic} = \frac{1}{2} m \omega_n^2 r_w^2 + \frac{1}{2} \frac{k}{m} m r_w^2 = m \omega_n^2 r_w^2 \tag{1.75.b}$$

The time derivatives of the two energies (1.75.a) and (1.75.b) are:

$$\dot{E}_{rotor}=I\omega_s\dot{\omega}_s \quad ; \quad \dot{E}_w=2m\omega_w^2 r_w\dot{r}_w \tag{1.76}$$

Since the total angular momentum (the spin angular momentum of the rotor L_{rotor} plus the angular momentum of the whirl motion L_w) has to be conserved it must be:

$$L_{rotor}=I\omega_s; \quad L_w=m\omega_n r_w^2; \quad \dot{L}_w+\dot{L}_{rotor}=0 \tag{1.77}$$

Since the frequency ω_n is constant, it follows:

$$I\dot{\omega}_s+2m\omega_n r_w\dot{r}_w=0 \tag{1.78}$$

from which the derivative of the spin speed $\dot{\omega}_s$ can be obtained. By combining (1.77) with (1.78) we obtain:

$$\dot{E}_w=-\frac{\omega_n}{\omega_s}\dot{E}_{rotor} \tag{1.79}$$

Equation (1.79) shows that, in highly supercritical regime ($\omega_s>>\omega_n$), the energy gained by the whirling motion is a very small fraction of the energy lost by the rotor. All the rest is dissipated as heat inside the springs.

1.10: ISOTROPIC JEFFCOTT ROTOR ON NON-ISOTROPIC SUPPORTS.

In the study of rotating machinery a common assumption is that of axial symmetry of the rotor. If both stator and rotor are isotropic with respect to the rotation axis, particularly simple models can be built. On the contrary, if the rotor cannot be considered axially symmetrical, the study can become very complicated. In the following, we will study the simple model of the non-isotropic Jeffcott rotor [1]. With respect to the model in section 1.2, the only difference is, now, that the stiffness of the supports is not isotropic in the x-y plane. Assuming that the elastic constant along the x direction $k_x=k$ is lower than that along the y direction k_y, we introduce the non-dimensional parameter $\Lambda>1$ so that $k_y=\Lambda k_x$ and $k_x=k$.
The Lagrangean of the system is expressed by the relation:

$$L=\frac{1}{2}m\left[\dot{x}^2+\dot{y}^2+\varepsilon^2\omega_s^2+2\varepsilon\omega_s\left(\dot{y}\cos(\omega_s t)-\dot{x}\sin(\omega_s t)\right)\right]-\frac{1}{2}k\left(x^2+\Lambda^2 y^2\right) \tag{1.80}$$

By performing the relevant derivatives , the following equations of motion are obtained:

$$\begin{cases} m\left[\ddot{x}-\varepsilon\omega_s^2\cos(\omega_s t)\right]+kx=0 \\ m\left[\ddot{y}-\varepsilon\omega_s^2\sin(\omega_s t)\right]+\Lambda ky=0 \end{cases} \tag{1.81}$$

The homogeneous equations of motion associated with the system (1.81) are coincident with the equations of the free motion of two system with one degree of freedom and their solutions are two harmonic motions with frequencies:

$$\omega_x=\sqrt{k/m} \quad ; \quad \omega_y=\sqrt{\Lambda k/m}=\sqrt{\Lambda}\omega_x \tag{1.82}$$

The two natural frequencies are independent from the spin speed and coincide with the two critical speeds of the system. The particular solution related to the presence of the unbalance is readily obtained imposing $\ddot{x}=0$ and $\ddot{y}=0$.

$$\begin{bmatrix} x_p(t) \\ y_p(t) \end{bmatrix} = \begin{bmatrix} \dfrac{\varepsilon\omega_s^2}{\omega_x^2-\omega_s^2}\cos(\omega_s t) \\ \dfrac{\varepsilon\omega_s^2}{\omega_y^2-\omega_s^2}\sin(\omega_s t) \end{bmatrix} \tag{1.83}$$

Starting from the definition of the centre of mass $\vec{r}_G$, it follows:

$$\begin{bmatrix} x_{Gp}(t) \\ y_{Gp}(t) \end{bmatrix} = \begin{bmatrix} \dfrac{\varepsilon\omega_x^2}{\omega_x^2-\omega_s^2}\cos(\omega_s t) \\ \dfrac{\varepsilon\omega_y^2}{\omega_y^2-\omega_s^2}\sin(\omega_s t) \end{bmatrix} = \varepsilon \begin{bmatrix} \dfrac{1}{1-\omega_s^2/\omega_x^2}\cos(\omega_s t) \\ \dfrac{1}{\Lambda}\dfrac{1}{1-\omega_s^2/\left(\Lambda\omega_x^2\right)}\sin(\omega_s t) \end{bmatrix} \tag{1.84}$$

Let us now introduce the complex coordinate z′=x+jy and define the elastic constants k_m and k_d:

$$k_m = \left(k_x + k_y\right)/2 \tag{1.85.a}$$

$$k_d = \left(k_x - k_y\right)/2 = k_x(1-\Lambda)/2 \tag{1.85.b}$$

the particular solution can be written in the form:

$$z_p'(t) = \frac{\varepsilon m\omega_s^2}{\left(k-m\omega_s^2\right)\left(\Lambda k-m\omega_s^2\right)}\left\{\left[k_m - m\omega_s^2\right]e^{j\omega_s t} - k_d e^{-j\omega_s t}\right\}^{25} \tag{1.86}$$

When the equality $k_m - m\omega_s^2 = 0$ is satisfied (i.e. $\omega_s = \sqrt{k_m/m}$), the amplitude of the forward whirl vanishes and the motion is a circular backward whirl with amplitude $\varepsilon k_m/k_d$. This is an important result: in presence of anisotropy, backward whirling motions can be self-excited. The amplitude of motion of the point mass G and the components of the vector $\vec{r}_G$ are reported as a function of the spin speed in the non-dimensional plot of figure 1.14. This figure shows the presence of three different speed ranges:

- in the range from 0Hz to the first critical speed (1.82.a) the components of the vector $\vec{r}_G$ are positive and they are out of phase from each other by 90° (see equation (1.84)

---

[25] Starting from (1.81) $z_p' = x_p + jy_p = \varepsilon\omega_s^2\left[\cos(\omega_s t)/\left(\omega_x^2-\omega_s^2\right) + j\sin(\omega_s t)/\left(\omega_y^2-\omega_s^2\right)\right]$. Thanks to the well known formula $\cos(\omega_s t) = \left(e^{j\omega_s t} + e^{-j\omega_s t}\right)/2$ and $\sin(\omega_s t) = \left(e^{j\omega_s t} - e^{-j\omega_s t}\right)/(2j)$, it follows:

$z_p' = \varepsilon\omega_s^2\left\{\left[(\omega_x^2+\omega_y^2)/2 - \omega_s^2\right]e^{j\omega_s t} + (\omega_y^2-\omega_x^2)e^{-j\omega_s t}/2\right\}\Big/\left[\left(\omega_x^2-\omega_s^2\right)\left(\omega_y^2-\omega_s^2\right)\right]$.

By replacing $\omega_x = \sqrt{k/m}$ and $\omega_y = \sqrt{\Lambda k/m} = \sqrt{\Lambda}\omega_x$, equation (1.86) is easily obtained.

or equation (1.86)). The orbit in the x-y plane is elliptic. The x component grows from ε to a value tending to infinity at the first critical speed, while the y component has a finite value. Hence, in the limit $\omega_s \to \omega_x$, the axis of orbit along the x direction tends to infinity.

- In the range from the first to the second critical speed, x_G is negative and y_G is positive. At the frequency $\omega_s = \sqrt{k_m / m}$ (see equation (1.86)) the amplitude of the forward whirl vanishes and the motion is a circular backward whirl with amplitude $\varepsilon k_m / k_d$. In the range from the first critical speed to $\omega_s = \sqrt{k_m / m}$, the ellipse is much elongated along the x direction. In the range from $\omega_s = \sqrt{k_m / m}$ to the second critical speed the ellipse is much elongated along the y direction. In the limit $\omega_s \to \omega_y$, the axis of orbit along the y direction tends to infinity.

- In the supercritical region ($\omega_s > \omega_y$), the components of the vector $\vec{r}_G$ are negative and they tend to zero when the spin speed tends to infinity. Hence, in supercritical region there is a self-centring of the body on the rotation axis and the elastic anisotropy has negligible effect on the rotor.

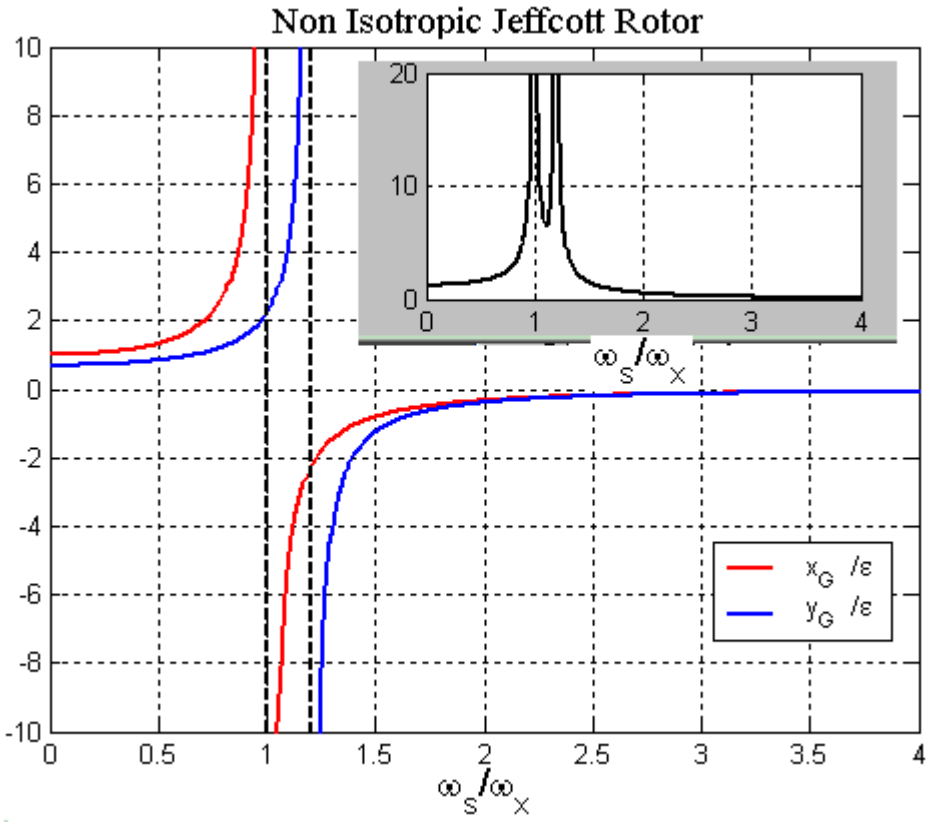

Figure 1.14:Non dimensional response of the Jeffcott Rotor on non-isotropic supports. Red curve: x_G/ε. Blue curve: y_G/ε. Inset: amplitude of the vector $\vec{r}_G$. Λ=1.5.

1.11: NON-ISOTROPIC JEFFCOTT ROTOR. NATURAL FREQUENCIES.

In this section, we will consider a Jeffcott rotor in which the shaft is not isotropic (the elastic constants along the direction ξ and η of the rotating frame are k_ξ and $k_\eta = \Lambda' k_\xi$). Since the deviation from symmetry concern the rotor (not the stator), better evidence can be obtained by writing the equation of motion with reference to the rotating frame (O,ξ,η,z).
Starting from the Lagrange function, the equations of motion[26] can be written in a compact matrix form as:

$$\begin{bmatrix} m & 0 \\ 0 & m \end{bmatrix}\begin{bmatrix} \ddot{\xi} \\ \ddot{\eta} \end{bmatrix}+\begin{bmatrix} 0 & -2m\omega_s \\ 2m\omega_s & 0 \end{bmatrix}\begin{bmatrix} \dot{\xi} \\ \dot{\eta} \end{bmatrix}+\begin{bmatrix} k_\xi - m\omega_s^2 & 0 \\ 0 & k_\eta - m\omega_s^2 \end{bmatrix}\begin{bmatrix} \xi \\ \eta \end{bmatrix} = m\varepsilon\omega_s^2\begin{bmatrix} \cos(\alpha) \\ \sin(\alpha) \end{bmatrix} \tag{1.87}$$

After performing the relevant derivatives with the assumptions $\ddot{\xi} = \ddot{\eta} = \dot{\xi} = \dot{\eta} = 0$, the (1.87) yields two homogeneous algebraic equations:

$$\begin{bmatrix} k_\xi - m\omega_s^2 & 0 \\ 0 & k_\eta - m\omega_s^2 \end{bmatrix}\begin{bmatrix} \xi \\ \eta \end{bmatrix} = m\varepsilon\omega_s^2\begin{bmatrix} \cos(\alpha) \\ \sin(\alpha) \end{bmatrix} \tag{1.88}$$

The equilibrium position in the rotating frame is easily obtained:

$$\begin{bmatrix} \xi_{eq} \\ \eta_{eq} \end{bmatrix} = \begin{bmatrix} \dfrac{m\varepsilon\omega_s^2\cos(\alpha)}{k_\xi - m\omega_s^2} \\ \dfrac{m\varepsilon\omega_s^2\sin(\alpha)}{k_\eta - m\omega_s^2} \end{bmatrix} \tag{1.89}$$

The critical speeds are the frequencies at which the two denominators in (1.89) vanish:

---

[26] Let us start by defining the relevant quantities for this problem; the eccentricity is $\vec{\varepsilon} = \varepsilon(\cos(\alpha),\sin(\alpha))$ where α is the angle between the ξ axis and the direction of the vector. The position vector of the point mass G is $\vec{r}_G = \vec{\varepsilon} + (\xi,\eta,0)$. The spin angular velocity is $\vec{\omega}_s = \omega_s(0,0,1)$, i.e. it is aligned with the vertical axis z. We have to write the potential and kinetic energies in order to write the lagrangean function of the system: the kinetic energy is $T = m\dot{\vec{r}}_G^2/2 = m\left(\dot{\xi}^2 + \dot{\eta}^2\right)/2$ while the centrifugal potential energy can be written in the form: $U_c = m\left(\vec{\omega}_s \times \vec{r}_G\right)^2/2 = m\omega_s^2\left(\xi^2 + \eta^2 + 2\varepsilon\xi\cos(\alpha) + 2\varepsilon\eta\sin(\alpha)\right)/2$ (see appendix 3.A for the definition of the "centrifugal" term of the lagrangean function of a body spinning in a rotating reference frame; note that $\vec{\varepsilon}$ is constant in the rotating frame, hence the term $m\omega_s^2\varepsilon^2/2$, can be neglected); the "Coriolis" potential energy $U_{cc} = m\dot{\vec{r}}_G \cdot \left(\vec{\omega}_s \times \vec{r}_G\right) = -m\omega_s\left(\dot{\xi}\eta - \dot{\eta}\xi\right)$ (see appendix 3.A for the definition of the "Coriolis" term of the lagrangian function of the system); the elastic potential energy $U_k = k_\xi\xi^2/2 + k_\eta\eta^2/2$. The operative expression for the Lagrange's function in the rotating frame is then: $L = T + U_c + U_{cc} - U_k$.

$$\omega_\xi = \sqrt{\frac{k_\xi}{m}} \tag{1.90.a}$$

$$\omega_\eta = \sqrt{\frac{k_\eta}{m}} = \sqrt{\Lambda'}\omega_\xi \tag{1.90.b}$$

The characteristic equation associated with equation (1.87) is:

$$\left\| \begin{bmatrix} -\omega^2 + \omega_\xi^2 - \omega_s^2 & -2j\omega_s\omega \\ 2j\omega_s\omega & -\omega^2 + \omega_\eta^2 - \omega_s^2 \end{bmatrix} \right\| = 0 \tag{1.91}$$

By introducing the non-dimensional parameters:

$$\lambda_\xi = \frac{\omega}{\omega_\xi},\ \omega' = \frac{\omega_s}{\omega_\xi}\ ^{27} \tag{1.92}$$

equation (1.91) can be written in the form:

$$\lambda_\xi^4 - \lambda_\xi^2\left[\Lambda' + 2\omega'^2 + 1\right] + \left(1 - \omega'^2\right)\left(\Lambda' - \omega'^2\right) = 0 \tag{1.93}$$

By solving equation (1.93) in λ_ξ^2 it follows:

$$\lambda_\xi^2 = \omega'^2 + \frac{1+\Lambda'}{2} \pm \sqrt{2\omega'^2\left(1+\Lambda'\right) + \frac{\left(\Lambda'-1\right)^2}{4}} \tag{1.94}$$

The expression under the radical sign $\Delta^2 = 2\omega'^2\left(1+\Lambda'\right) + \left(\Lambda'-1\right)^2/4$ is always positive and the solutions λ_ξ^2 of (1.94) are always real. The one with the sign + is positive, hence there are two real solutions in λ_ξ:

$$\lambda_{\xi,1,2} = \pm\sqrt{\omega'^2 + \frac{1+\Lambda'}{2} + \Delta} \tag{1.95}$$

The root with sign – is positive only if $\omega'^2 + \left(1+\Lambda'\right)/2 - \Delta > 0$; after some simple algebra, this condition can be written as:

$$\omega'^4 - \omega'^2\left(1+\Lambda'\right) + \Lambda' > 0 \tag{1.96}$$

Let us define the function $f(\omega') = \omega'^4 - \omega'^2\left(1+\Lambda'\right) + \Lambda'$. It is easy to show that it can be written as the product of two polynomials of second order in ω':

$$f(\omega') = \left(\omega'^2 - 1\right)\left(\omega'^2 - \Lambda'\right) \tag{1.97}$$

If $f(\omega')$ is positive, the characteristic equation (1.93) has 4 real roots and the system is stable. If $f(\omega')$ is negative (i.e. when $1 < |\omega'| < \sqrt{\Lambda'}$), the characteristic equation (1.93) has 2 real and 2 complex roots. One of the two complex roots has a negative imaginary part which corresponds to an unstable behaviour of the system.

---

[27] $\omega'=1$ means that the system rotates at angular speed $\omega_s=\omega_\xi$. $\omega'=\sqrt{\Lambda'}$ means that the system rotates at angular speed $\omega_s=\omega_\eta$. In the same manner: $\lambda_\xi=1 \Rightarrow \omega=\omega_\xi$ and $\lambda_\xi=\sqrt{\Lambda'} \Rightarrow \omega=\omega_\eta$.

$f(\omega')>0$	$\lvert\omega'\rvert<1 \vee \lvert\omega'\rvert>\sqrt{\Lambda'}$	4 Real Roots	Stable
$f(\omega')<0$	$1<\lvert\omega'\rvert<\sqrt{\Lambda'}$	2 Real Roots 2 Complex Roots	Unstable

Table 1.1:Roots of the characteristic equation (1.93).

The presence of the anisotropy causes the occurrence of an instability range that spans from ω_ξ to ω_η[28]. Rotating and non-rotating damping reduce the instability range between the two critical speeds. In the inertial frame we can introduce the non-dimensional parameter:

$$\lambda^{NR} = \omega^{NR} \big/ \omega_\xi \tag{1.98}$$

that is the non dimensional whirl speed in the x-y plane. λ^{NR} is linked with λ_ξ by the relationship:

$$\lambda^{NR} = \lambda_\xi + \omega' \tag{1.99}$$

By combining equation (1.94) with (1.99), the whirl frequencies in the inertial frame are easily obtained:

$$\lambda^{NR} = \omega' \pm \sqrt{\omega'^2 + \frac{1+\Lambda'}{2} \pm \sqrt{2\omega'^2\left(1+\Lambda'\right) + \frac{\left(\Lambda'-1\right)^2}{4}}} \tag{1.100}$$

The dynamical behaviour of the system (Λ'=1.5) is summarized by figure 1.15 where the natural frequencies are shown as function of the non-dimensional spin speed ω' in the inertial reference frame. Only the first and the fourth quadrant are depicted, because they give a complete picture of the situation (the second and the third quadrant refer to the case of clockwise spin frequency). The frequency range between ω' =1 and ω' =$\sqrt{\Lambda'}$=1.22 is the instability range (we have seen that the system is unstable when (1.97) is negative, i.e. when $1<\lvert\omega'\rvert<\sqrt{\Lambda'}$). The cyan dashed line $\lambda^{NR}=\omega'$ separates the supercritical ($\lambda<\omega'$) from the subcritical ($\lambda^{NR}>\omega'$) region. There are four natural frequencies (the four solutions of equation (1.93)) that form four branches (yellow, blue, violet, red lines).
For example, if $\omega'=\varpi$ the equation (1.93) has four roots (open circles 1,2,3,4 in figure): they are found by the intersection between the vertical black line and the 4 coloured branches (yellow, blue, violet, red lines). The root numbered as 1 in figure 1.15 corresponds to a backward whirling motion (the corresponding value of λ^{NR} is negative). The roots numbered as 2,3,4 correspond to forward whirling motions. In the high supercritical range ($\omega'>>1$), two

[28] In section 1.2 we have stated that self-centring is possible only if the system has al least two degrees of freedom. 1D systems are highly unstable if spinning at frequencies higher than the natural one. This is a consequence of the previous result. In fact, a system with one degree of freedom can be considered a limiting case of asymmetrical rotor. The stiffness along the η axis can be considered infinitely high and the corresponding critical speed is infinitely high too. The instability range spans from ω_ξ to $\omega_\eta=\infty$, i.e. it extends for all values of spin speeds that are above the critical frequency ω_ξ.

natural frequencies grow linearly with $2\nu_s$, and the other two solutions are approximately constant[29]:

- $\omega' \to \infty$ $$\lambda^{NR} = \begin{cases} 2\omega' \pm \sqrt{(1+\Lambda')/2} \simeq 2\omega' \\ \pm\sqrt{(1+\Lambda')/2} = \pm\sqrt{k_m / k_\xi} \end{cases} \quad (1.101)$$

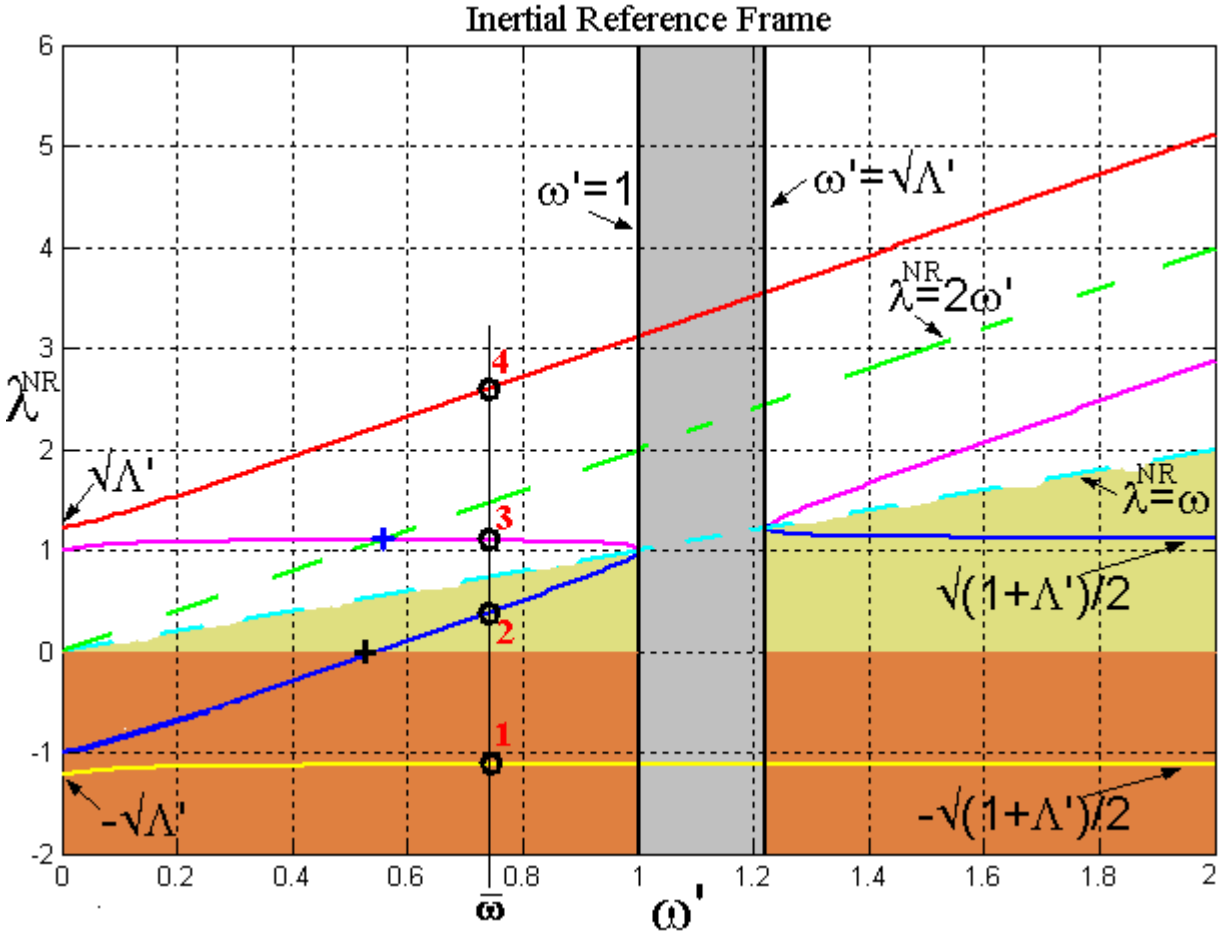

Figure 1.15: Non-isotropic (Λ'=1.5) Jeffcott rotor. Non-dimensional natural frequencies shown as function of the non-dimensional spin speed ω′ in the inertial reference frame. The frequency range between ω′ =1 and ω′ =√Λ'=1.22 is the instability range. The cyan dashed line $\lambda^{NR}=\omega'$ separates the supercritical ($\lambda^{NR}<\omega'$) from the subcritical ($\lambda^{NR}>\omega'$) region. There are four natural frequencies (yellow, blue, violet, red lines) at each spin speed (the four solutions of equation (1.93)). For example, if $\omega'=\bar{\omega}$ the equation (1.93) has four roots (1,2,3,4): they are found by the intersection between the vertical black line and the 4 coloured branches (yellow, blue, violet, red lines). The root numbered as 1 corresponds to a backward whirling motion (the corresponding value of λ^{NR} is

[29] In the limit $\omega' \to \infty$, from equation (1.100) we obtain $\lambda^{NR} \simeq \omega' \pm \sqrt{\omega'^2 \pm \omega'\sqrt{2(1+\Lambda')}}$. Sign + before the radical sign: $\lambda^{NR} \simeq \omega' + \sqrt{\omega'^2 \pm \omega'\sqrt{2(1+\Lambda')}} = \omega' + \omega'\left(1 \pm \sqrt{(1+\Lambda')/2}/\omega'\right) = 2\omega' \pm \sqrt{(1+\Lambda')/2}$. Sign - before the radical sign:
$\lambda^{NR} \simeq \omega' - \sqrt{\omega'^2 \pm \omega'\sqrt{2(1+\Lambda')}} = \omega' - \omega'\sqrt{1 \pm \sqrt{2(1+\Lambda')}/\omega'} = \omega' - \omega'\left(1 \pm \sqrt{(1+\Lambda')/2}/\omega'\right) = \pm\sqrt{(1+\Lambda')/2}$

negative). The root numbered as 2 corresponds to a forward whirling motion. Roots numbered as 3 and 4 are subcritical (forward). In the high supercritical range (ω′>>1) two natural frequencies grow linearly with $2\nu_s$, and the other two solutions are approximately constant ($\pm\sqrt{(1+\Lambda')/2}$). In the low frequency regime (ω′<<1) the natural frequencies are coincident with the critical frequencies. Blue cross: the second critical speed ω_{cr2} located at the intersection of the violet branch with the λ=2ω′ axis. Black cross: the intersection of the blue branch with the λ=0 axis.

where we have used the mean constant $k_m = (k_\xi + k_\eta)/2$. In the low frequency range (ω′<<1), the natural frequencies are coincident with the critical frequencies[30]:

- ω′=0 $$\lambda^{NR} = \begin{cases} \pm\sqrt{\Lambda'} \\ \pm 1 \end{cases} \tag{1.102}$$

In figure 1.15 a second critical spin speed ω'_{cr2} is shown at the intersection of the free whirling violet branch with the straight line $\lambda^{NR}=2\omega'$. All second critical frequency occur in the subcritical region and can not produce unstable whirl. Figure 1.15 also shows an intersection between the blue branch and the $\lambda^{NR}=0$ axis. The value of the spin frequency at which this intersection occur is[31]:

$$\omega'_{\lambda^{NR}=0} = \sqrt{\frac{1}{2}\frac{\Lambda'}{(1+\Lambda')}} \tag{1.103}$$

This frequency is about half of the primary critical speed ω_ξ[32]:

$$\omega_{\lambda^{NR}=0} = \omega'_{\lambda^{NR}=0}\cdot\omega_\xi = \sqrt{\frac{1}{2m}\frac{k_\xi k_\eta}{k_\xi + k_\eta}} \approx \frac{\omega_\xi}{2} \tag{1.104}$$

There is then, at a well-determined spin speed, a natural frequency that vanishes ($\lambda^{NR}\to 0$). At this speed the system is resonant with a static force (DC force), i.e. with a force constant in modulus and direction.

1.12: CONCLUSIONS.

In this chapter we have introduced the Jeffcott rotor to model the dynamical behaviour of the rotors. This simple model allows an understanding of the most important phenomena typical of rotor dynamic. The self-centring in supercritical rotation has been described in section 1.2 (see figure 1.3): the system will spin at a frequency either below or above the natural one. From (1.10), it follows that in the first case the equilibrium position will be farther away from the spin axis than the original offset ε, while in the second case equilibrium will take place

[30] By inserting ω′=0 in equation (1.100), it follows $\lambda^{NR} = \pm\sqrt{1+\Lambda' \pm (\Lambda'-1)}/\sqrt{2}$.

[31] By inserting $\lambda = 0$ into (1.100) the value of the speed is obtained.

[32] $$\omega_{\lambda^{NR}=0} = \omega'\omega_\xi = \sqrt{\frac{1}{2}\frac{\Lambda'}{(1+\Lambda')}\frac{k_\xi}{k_\xi}}\sqrt{\frac{k_\xi}{m}} = \sqrt{\frac{1}{2m}\frac{k_\xi k_\eta}{k_\xi + k_\eta}}$$

closer than ε to the spin axis. The higher the spin speed, the lower the distance of the centre of mass of the suspended body from the undeformed rotation axis. In supercritical regime, the rotors tend to rotate about their centre of mass instead of their geometrical centre. The final motion of the centre of mass is the superimposition of a free whirl (circular, elliptic or linear) at frequency ω_{cr} (see equation (1.8)) and a circular motion with angular velocity ω_s (see equation (1.10)).

In section 1.4 we have shown that rotating damping has a destabilizing effect on the rotor. In presence of rotating damping, the amplitude of whirling motions changes in time with exponential law: backward whirls (1.20) are stable, with decreasing amplitude, while forward whirl can be either damped or self excited (1.21). The condition for stability is given by the inequality (1.22): if only rotating damping is present the motion is unstable in whole supercritical regime; instead, non-rotating damping has a stabilizing effect on the rotor. The rotating damping is the friction (viscous plus structural) between the rotating parts of the rotor. The corresponding losses produce the instabilities in weakly suspended rotors in supercritical regime. The non-rotating damping is the friction between two non-rotating parts of the stator. It is effective in damping transverse translational oscillations of the spin axis without slowing down its rotation. A third kind of damping is the friction in the bearings. This is a friction between the rotor and the stator, which is effective in slowing down the rotation but it is ineffective at damping whirling motion.

In section 1.7 we have studied the problem of two weakly coupled rotors: energy dissipation makes the spin rate to decrease, together with the spin angular momentum. Since the total angular momentum must be conserved, the bodies develop a whirl motion. In supercritical regime, the final motion is the superimposition of a circular forward whirl motion (i.e. occurring in the same direction of the spin speed) which is self-excited (1.65), a circular backward whirl motion (1.65) which is damped (they both occur at an angular velocity equal to the natural frequency of the non-rotating system) and a circular motion with amplitude decreasing with the spin speed (1.63).

In section 1.8 we have evaluated the destabilizing force connected to the energy dissipation in the suspensions (1.74), showing that it is a small fraction ($1/Q<<1$) of the elastic force of the springs. Note that the growth rate of whirls is determined by losses in the system, essentially in the mechanical suspensions as they undergo deformations at the frequency spin and the relevant Q is that measured at the spin speed.

In section 1.9 we have evaluated the fraction of the energy lost by the spinning rotor gained by the whirling motion, showing that, in highly supercritical regime ($\omega_s>>\omega_n$), almost all the energy is dissipated as heat inside the springs (1.80) and do not contribute to the growth of the whirl.

In sections 1.10 and 1.11 we have studied the problem of the non-isotropic Jeffcott rotor. Equation (1.86) shows that, in the case of non-isotropic support (non-isotropic stator), backward whirling motions can be self-excited.

In section 1.11 we have considered a Jeffcott rotor in which the shaft is not isotropic. In the case of the non-rotating system ((1.102), (1.90.a) and (1.90.b)), the natural frequency is expected to split up (the system has two critical speeds ω_ξ and ω_η). In the high supercritical range (1.101), two natural frequencies grows linearly with $2\nu_s$, and the other two solutions are approximately constant. The presence of this anisotropy causes the occurrence of an instability range that spans from the first critical speed ω_ξ to the second critical speed ω_η

(figure 1.15 and table 1.1) which can be reduced by introducing non-rotating damping. The system has, then, at a well-determined spin speed (1.104), a natural frequency that vanishes and then a resonance with a DC force is possible.

CHAPTER 2:

THE GGG –"GG (GALILEO GALILEI) ON THE GROUND" DIFFERENTIAL ACCELEROMETER FOR TESTING THE EQUIVALENCE PRINCIPLE. OVERVIEW OF THE EXPERIMENT.

2.1: INTRODUCTION.

The Equivalence Principle (EP) is the founding principle of General Relativity. It can be tested from its most direct consequence, the universality of free fall (UFF), whereby all bodies fall with the same acceleration regardless the mass and composition. The most accurate experiments have been carried out with test bodies of different composition suspended on a torsion balance ([14 - 15]). These experiments have been aimed at obtaining increasing levels of accuracy ever since the landmark experiment by Eötvös [16], which has verified the EP with an accuracy $\eta = \Delta a/a = 10^{-9}$. This result has been improved to about 10^{-12} by Dicke *et al.* [17] and Braginsky and Panov [18] using signal modulation techniques. In a recent article by Adelberger and co-workers [19], the differential acceleration between test cylinders with an average composition similar to those respectively of the Earth and the Moon is reported with 1σ statistical uncertainty $\Delta a_{\odot} = 5.6\times10^{-13}$ cm s^{-2}, hence $\Delta a_{\odot}/a_{\odot} \simeq 9.3\times10^{-13}$. The relevant theoretical question for a zero-test experiment is at which accuracy level, if any, a violation is to be expected. In an earlier work by Damour and Polyakov, based on string theory and the existence of the dilaton ([20 - 21]) the η values to observe a violation have been bracketed in the range $10^{-18} < \eta < 10^{-13}$. Fischbach and co-workers [22] have derived a non-perturbative rigorous result, according to which a violation at the level of $\eta \simeq 10^{-17}$ must be expected, due to the coupling between gravity and processes of $\nu - \bar{\nu}$ exchange which would then differently affect masses of different nuclei. More recent work by Damour, Piazza and Veneziano [23] reverts back to the dilaton scenario and predicts a violation at the level $\eta \simeq 10^{-12} \div 10^{-13}$. While an $\eta = 10^{-13}$ is in principle accessible in a ground experiment, a sensitivity as high as $\eta = 10^{-17}$ could be achieved only within a space mission: test bodies in low Earth orbit are subject to a driving signal by about 3 orders of magnitude stronger than on torsion balances on the ground. Another main advantage of space is weightlessness: the gravitational attraction of the Earth is largely compensated by the centrifugal force due to the orbital motion of the spacecraft so the main 1g local acceleration of gravity is absent. Three space experiments, aiming to test the equivalence principle, are under investigation by space agencies: μSCOPE ([24 - 25]) with the goal $\eta = 10^{-15}$, "GALILEO GALILEI" (GG) ([10 - 11], [26 - 29]) with the goal $\eta = 10^{-17}$ and STEP ([30 - 31]), with the goal $\eta = 10^{-18}$. In all these experiments, the test bodies are weakly coupled, concentric, co-axial, hollow cylinders of different composition. The modulation of the signal at a frequency higher than the orbital one, reduce electrical and mechanical $1/f$ noises. The GG experiment (see chapters 8 and 9) is distinguished for being specifically conceived around these concepts. We have built a full-scale ground based prototype (GGG) for the proposed GG space experiment. We devote this chapter to describe the general aspects of the GGG experiment ([32 - 35]); some sections are taken from the

articles [33] and [34] available in Appendix_Articles. A mathematical model of the apparatus has been developed and it will be described in chapters 3 and 4 ([36 - 37]).

2.2: BASIC CONCEPTS OF THE GGG MECHANICAL DESIGN.

The GGG differential accelerometer is made of concentric coaxial hollow[1] test cylinders operated in a vacuum chamber, that are weakly coupled by a balancing arm to form a vertical beam balance, with the arm suspended by its midpoint. The apparatus is schematically presented in figure 2.1; figure shows a section of the apparatus through the spin symmetry axis $\hat{z}$ inside the vacuum chamber VC. At the top-centre of the frame is a shaft turning inside ball bearings, indicated by **x** symbols in the figure, to which rotation is transmitted from the motor MO (drawn in brown) by means of O-rings OR mounted on pulleys[2]. The shaft holds the suspension tube ST (yellow)[3], inside which the coupling arm (drawn in cyan) with mass m_a=0.3kg and length 2L+ΔL (about 0.38m), is suspended from its midpoint MP by means of a laminar suspension LS, with elastic constant k (about 10^{-3} J/m^2) and length $\ell = 5 \cdot 10^{-3}$m. The centre of mass of the coupling arm is displaced from the arm suspension point MP by a quantity ΔL/2. ΔL can be adjusted to be either slightly positive or negative. This is accomplished after moving in the vertical direction $\hat{z}$ a small solid ring mounted around the lower half of the coupling arm. The central laminar suspension carries on the whole weight of the arm and of the test masses, suspended from the arm as follows. The inner cylinder m_1 (green in figure 2.1) is suspended from the bottom of the coupling arm, that is at distance L_1 from the cylinder's centre of mass (the green body in figure, with mass m_1=10kg). The outer cylinder (blue), with mass m_2=10kg, is suspended from the top of the coupling arm, that is at distance L_2 from the cylinder's centre of mass. The two corresponding suspensions LS (orange) with elastic constant $k_1=k_2=k$, nominally manufactured with identical characteristics, have a laminar shape (the flexible part has length $\ell = 5 \cdot 10^{-3}$m) and a metallic composition (CuBe), thereby ensuring passive electrostatic discharging of the test masses. The laminar suspensions (cardanic suspensions) are designed to be stiff against local gravity in the vertical (axial) direction $\hat{z}$, and soft in the $\hat{x}, \hat{y}$ directions determining the horizontal-sensitivity plane perpendicular to the spin axis. Figure 2.2 shows two photos (photo a) and b)) of the laminar-cardanic suspensions. Photo a) shows one of the old suspension used in GGG; they were smaller than the ones used at the present time and shown in photo b). The suspensions are carved out of a solid bar of CuBe and properly treated to ensure an high quality factor. Each suspension is composed of 4 thin laminar sheets (70 μm). Two sheets lie in the x-z plane and allow oscillations along the y-axis. The other two sheets lie in the y-z plane and allow oscillations along the x-axis. Photo c) in figure 2.2 shows the coupling arm inside the suspension tube ST. Finally a non-rotating passive damper is present under the lowest laminar suspension, and is used only for stabilization purposes in passing through the rotor critical speeds and instability regions. After reaching the final rotation speed, the passive damper can

[1] For simplicity, we will omit from now on the term "hollow" when referring to the test cylinders.
[2] A new prototype with the motor located on the spin axis is under construction. In fact, we think that the rubber O-ring used to transmit rotation from the motor to the rotating suspension shaft may be a dangerous source of rotating damping (for details see chapter 5).
[3] In the new prototype, the shaft is an extension of the motor's axis.

be disconnected and the finer active damper can be employed. From now on, the label λ=a,1,2 will be used to refer to the coupling arm, inner and outer body parameters.

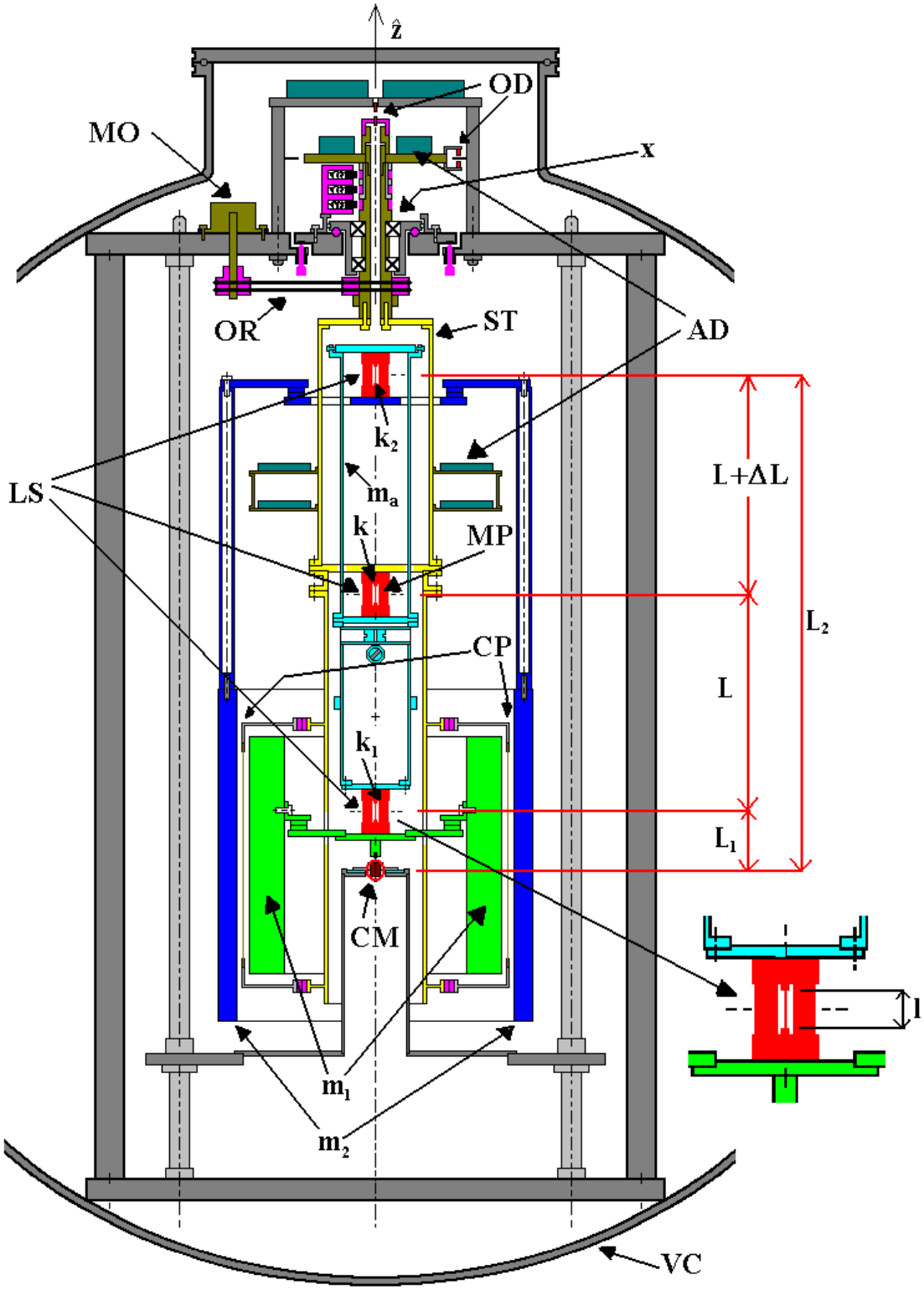

Figure 2.1: GGG. Section through the spin axis of the differential accelerometer inside the vacuum chamber. VC: vacuum chamber. **x**: the ball bearings. OR: O-rings. AD: annular dishes with the read-out electronics. CP: capacitance plates. OD : optical devices. MO: motor (brown). m_1: inner test mass (green). m_2: outer test mass (blue). LS: laminar suspensions (orange). m_a: coupling arm (cyan). ST : suspension tube (yellow). The open red circle indicate the position of the bodies centre of mass CM. The relevant distances L_1 and L_2 of the centres of

mass of the inner and outer bodies from their suspension points are also sketched, along with the arm length 2L+ΔL. The drawing is to scale, as the inner diameter of the vacuum chamber is 1m.

a)

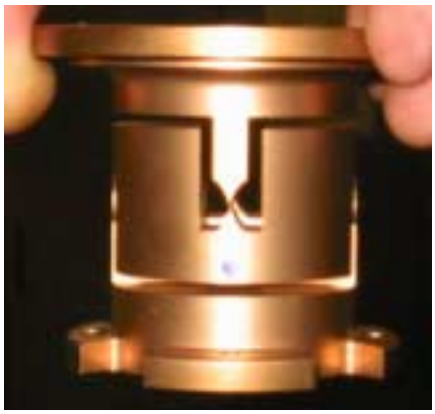

b)

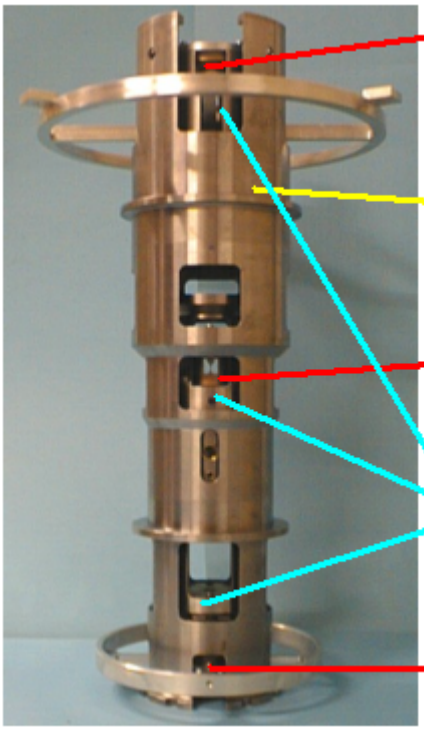

c)

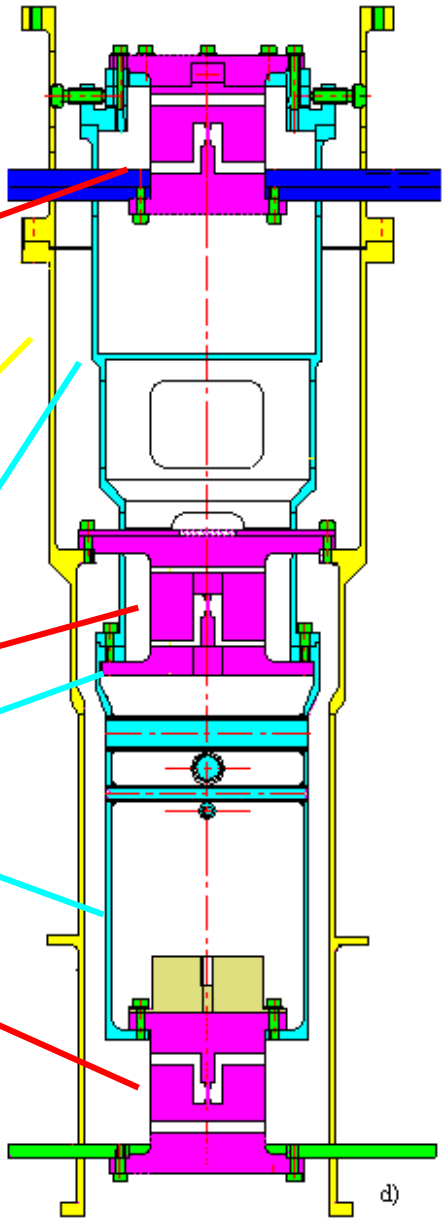

Figure 2.2: Laminar suspensions in the GGG experiment. a) old design b) new design, larger than the previous one c) the coupling arm inside the suspension tube ST, d) section through the spin axis of the suspension tube.

2.3: HOW IT WORKS.

The GGG experiment has been designed to test the Universality of Free Fall, which is the most direct consequence of the EP. Typically, the non-dimensional Eötvös parameter η (see equation 2.1) is used to quantify the violation of equivalence for two bodies of composition A and B, inertial mass m_i and gravitational mass m_g.

$$\eta = 2\left[\left(\frac{m_g}{m_i}\right)_A - \left(\frac{m_g}{m_i}\right)_B\right] \Bigg/ \left[\left(\frac{m_g}{m_i}\right)_A + \left(\frac{m_g}{m_i}\right)_B\right] \qquad (2.1)$$

In presence of an EP violation (i.e. $\eta \neq 0$) a differential acceleration between the two test cylinders is expected. Hence, the GGG accelerometer is designed to be particularly sensitive to differential accelerations acting in the x-y plane perpendicular to the spin axis. In essence, the two test masses of GGG are coupled as in an ordinary beam balance, but here the beam is built vertical so as to obtain a differential coupling in the horizontal plane. Figure 2.3.a shows a schematic model of a vertical beam balance. After having described the real instrument in section 2.2, we are now in a position to outline the minimal model used to describe its dynamical behaviour and obtain an approximated formula for the natural period of oscillation. In figure 2.3.b the bodies are not rotating and are placed at the ends of the coupling arm of length 2L+ ΔL. Three identical laminar suspensions with elastic constant k (i.e. $k_1=k_2=k_a=k$) and length ℓ are used to couple the bodies (as in the real instrument). The arms L_1 and L_2 are depicted in figure 2.3.b but do not play any role in this content. The system in figure has just one degree of freedom. In chapter 3 we will develop a complete mathematical model (with 6 degrees of freedom) and we will demonstrate that, in the differential mode, at zero spin rate, the coupling arm oscillates and the cylinders' centres of mass move within the horizontal plane in opposition of phase while their symmetry axis remains aligned with the vertical z. In section 3.11, we will also show that the minimal model in figure 2.3.b is able to predict with great accuracy the natural (differential) period of free oscillation of the GGG accelerometer (but it is not able to predict the other natural modes at higher frequency), namely[4]:

$$T_d = 2\pi \Bigg/ \sqrt{\frac{3k\ell^2}{(m_1+m_2)L^2} - \frac{g\Delta L}{2L^2}} \qquad (2.2)$$

[4] ϑ is the angle between the coupling arm and the vertical axis z. ϑ_1 (ϑ_2) the angle between L_1 (L_2) and the vertical axis z. Under the reasonable assumption that $\vartheta_1=\vartheta_2=0$ (their symmetry axis remains aligned with the vertical z; see section 3.11) the analytical (approximated) formula of the differential period (inverse of the differential frequency) can be derived from the general equations of motion describing the small oscillations of the angles with respect the equilibrium position $\vartheta_a=0$. To this aim, let us begin with writing the total potential energy $U = 0.5(k_1+k_2+k_a)\ell^2 \sin^2\vartheta_a + [m_2(L+\Delta L) - m_1 L]g\cos\vartheta_a + (m_2L_2 - m_1L_1)g$. By expanding it to the 2nd order and neglecting the term $(m_2L_2 - m_1L_1)g$, it can be written as: $U = \left[(k_1+k_2+k_a)\ell^2 - m_2 g\Delta L\right]\vartheta_a^2/2$. In the same manner the total kinetic energy of the system can be readily written as $T = \left[m_1L^2 + m_2(L+\Delta L)^2\right]\dot{\vartheta}_a^2/2$. The equation of motion is determined from the Langrange function in the standard manner: $[m_1L^2 + m_2(L+\Delta L)^2]\ddot{\vartheta}_a = -[(k_1+k_2+k_a)\ell^2 - m_2 g\Delta L]\vartheta_a$. Then, the differential frequency is obtained,: $\nu_d = 1/T_d = \sqrt{\frac{(k_1+k_2+k_a)\ell^2}{(m_1+m_2)L^2} - \frac{g\Delta L}{2L^2}} \Big/ 2\pi$. ΔL is the critical parameter in the previous equation. ΔL can be adjusted to be either slightly positive or negative, resulting into a lower or higher differential frequency.

where g is the local gravity and ΔL can be either positive or negative.

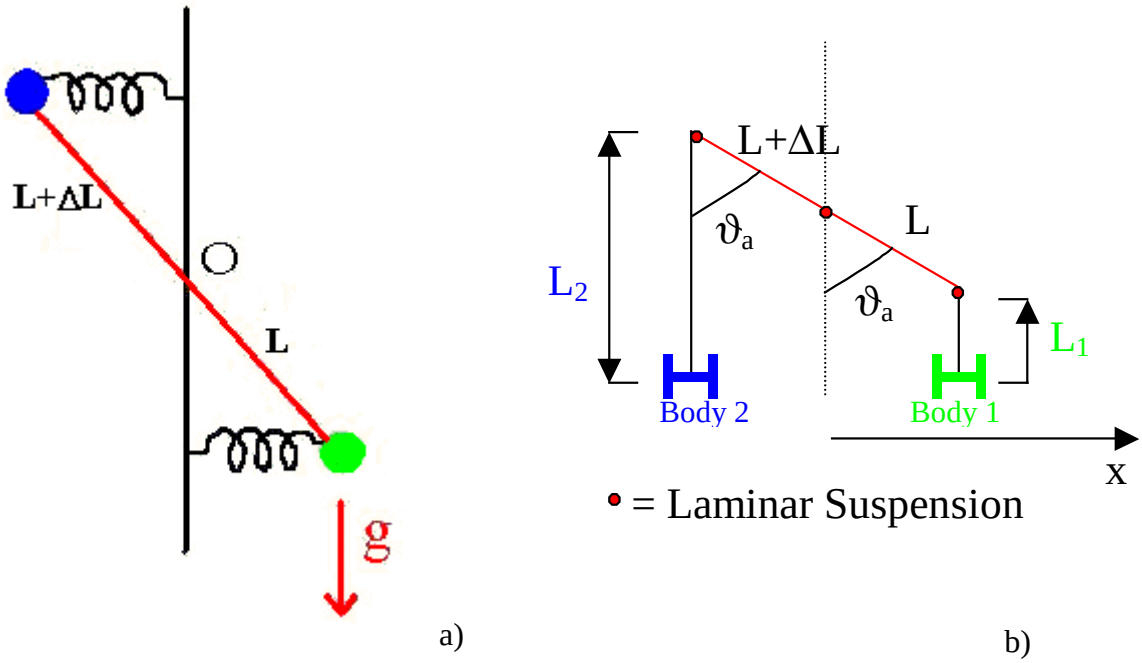

Figure 2.3: Simple dynamical scheme showing how the GGG test bodies are coupled. Part a) Vertical beam balance. Part b) Minimal model of GGG used to evaluate the differential period of oscillation. Three identical laminar suspensions (red points in the sketch) are used to couple the bodies and the balancing arm.

If ΔL<0, gravity acts as a positive spring, thus increasing the stiffness of the coupling, i.e. reducing the differential period. Instead, if ΔL>0, gravity acts as a negative spring and the ratio ΔL/L can be adjusted to reduce the denominator of (2.2) whereby increasing the value of T_d. A differential constant force acting between the two test cylinders in the x-y plane of the laboratory would incline the balance pivoted at its midpoint MP with respect to the vertical, thus giving rise to a relative displacement of the centre of mass of the cylinders in the direction of the force (the coupling arm oscillates and the cylinders' centres of mass move within the horizontal plane in opposition of phase while their symmetry axis remains aligned with the vertical $\hat{z}$). The longer is the period of oscillation, the more sensitive is the system to a differential force. The importance of a weak coupling, hence a long differential period, becomes apparent if we estimate the amount of relative displacement of the centres of mass of the test bodies to be expected in response to a differential force F (see figure 2.4.a):

$$\Delta x_{dif} = x_2 - x_1 = \frac{T_d^2}{4\pi^2}\frac{F}{m} \qquad (2.3)$$

For a given force F, the resulting displacement grows quadratically with the natural period of oscillations of the bodies one with respect to the other. A real instrument can not, in practice, be perfectly differential. If a common force acts on the two test cylinders (see figure 2.4.b), the relative displacement can be written in the form:

$$\Delta x_{com} = x_2 - x_1 = \frac{T_d^2}{4\pi^2}\frac{F\chi_{CMR}}{m} = \Delta x_{dif}\chi_{CMR} \ll \Delta x_{dif} \qquad (2.4)$$

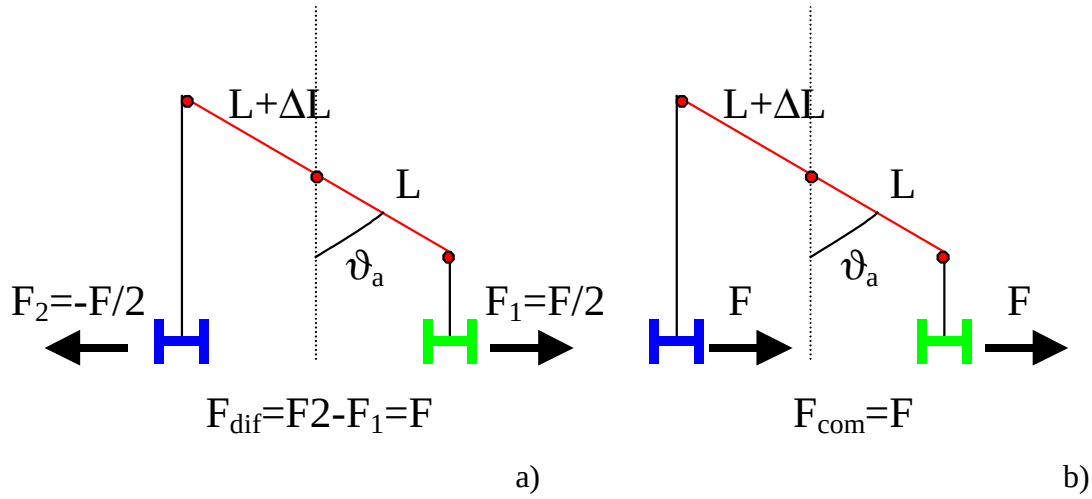

Figure 2.4: Part a) – differential forces; Part b) – common forces.

In equation (2.4) we have introduced the common mode rejection factor χ_{CMR}, which describes the accelerometer's capability to reject common forces as compared to those acting in a differential manner on the test bodies. For the system in figure 2.3.a, the common mode rejection factor is $\chi_{CMR}=\Delta L/2L$. The rejection capability of the real instrument will be evaluated in chapter 4.

In chapter 3 we will evaluate the dynamical behaviour of the GGG instrument set into supercritical rotation and we will show that the differential period (2.2) and the response to differential force (2.3) are not influenced by the rotation; instead, supercritical rotation allows high frequency modulation of the signals, reduction of $1/f$ electrical and mechanical noise. The model in figure 2.3.b is an oversimplification of the real rotor and it allows only a qualitative understanding of the functioning principle of the differential accelerometer. It is not able to predict the right value of the common mode rejection, the existence of natural modes at frequencies higher than the differential one (inverse of the differential period (2.1)) and the dependence of the natural frequencies from the spin speed. These problems will be discussed in detail in chapter 3 and 4 by developing a more complex mathematical model of the spinning rotor.

2.4: THE SIGNAL OF AN EQUIVALENCE PRINCIPLE VIOLATION.

If two test bodies of different composition are suspended on the ground each of them reaches equilibrium when the component on the horizontal plane of the centrifugal force due to the diurnal rotation of the Earth is balanced by the horizontal component of the local gravitational attraction. This is the equilibrium position of an ordinary plumb line, which does not point to the centre of the Earth but it is displaced always along the North-South direction. Therefore, the EP signal (with the Earth as the source mass) is:

$$a_{PE}^{\oplus} = \eta\,\omega_{\oplus}^{2} R_{\oplus} \cos(\lambda_L)\sin(\lambda_L) \qquad (2.5)$$

where λ_L is the latitude of the laboratory, $\vec{\omega}_{\oplus}$ is the diurnal angular velocity of the Earth and $R_{\oplus}$ its radius. The maximum value of (2.5) is at 45° latitude and amounts to $1.7\cdot10^{-2}\eta m/s^2$ (λ_L=45°). Being the displacement fixed in the North-South direction there is no modulation of

the effect. Unfortunately, the GGG accelerometer cannot be used for testing this effect ([31 - 32]). In fact, spinning bodies are subject o gyroscopic effects, whereby they move not in the direction of the applied force but along the component of the external torque perpendicular to the spin axis. In a ground laboratory the gyroscopic effect for a body of mass m, angular momentum $\vec{L}$ and centre of mass suspended with an arm $\vec{l}$ is due to the torque generated by the local gravity and to the angular velocity of the Earth's diurnal rotation around its axis:

$$\left(\frac{d\vec{L}}{dt}\right)_{lab} = \vec{l} \times m\vec{g} - \vec{\omega}_{\oplus} \times \vec{L} = \left(\vec{\Omega}_g - \vec{\omega}_{\oplus}\right) \times \vec{L} \qquad (2.6)$$

where $\Omega_g = -mgl/L$. Gravity makes the body precess around the local vertical (unless the centre of mass lies exactly on the vertical itself), while the non-inertial nature of the laboratory reference frame (because of its diurnal rotation with the Earth) makes it precess around the Earth's rotation vector; the suspensions produce a restoring force towards the vertical. Equilibrium is reached in the North-South direction, the only direction along which the acting torques can balance each other. The test cylinders of GGG undergo different gyroscopic effects, resulting in a net relative displacement in the North-South direction. Its calculation shows a constant displacement at any given spin rate, and a linear increase with it, reaching several microns at a few Hz; if the laminar suspension of the inner test cylinder is substituted by a rigid connection the differential gyroscopic effect increases by about a factor of 10. In both cases it is expected in the same direction as the effect of an EP violation in the gravitational field of the Earth, and much larger. During 2001, numerous measurements have been performed, at various spin frequencies both in clockwise and counter-clockwise rotation.

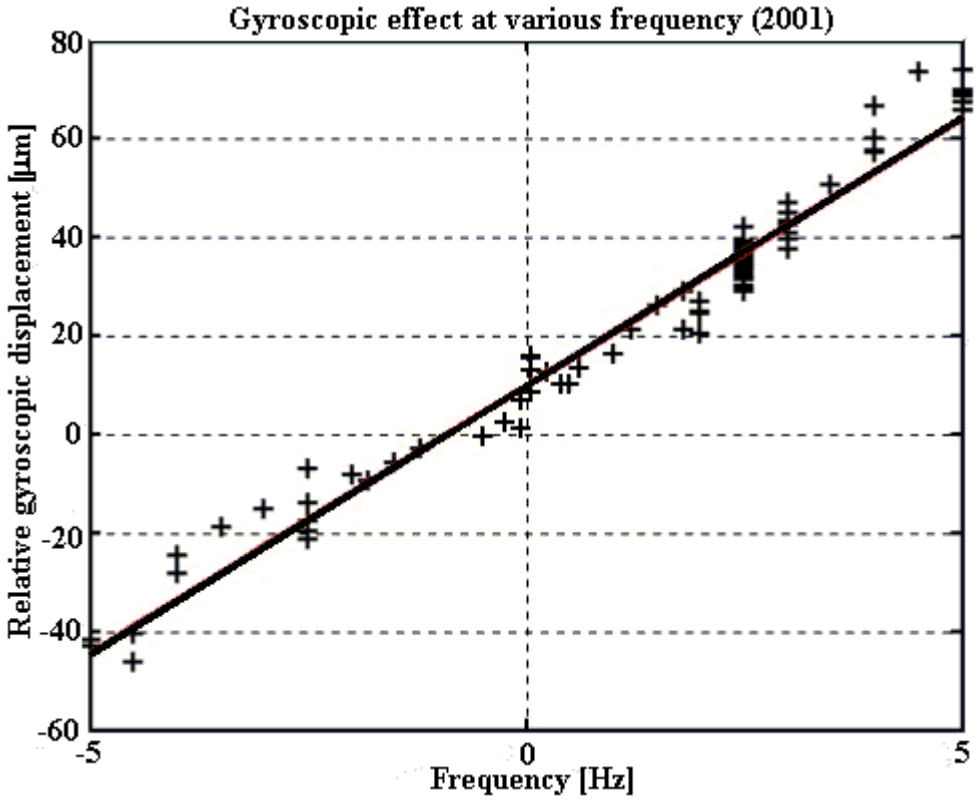

Figure 2.5: Relative displacements (crosses) of the test cylinders, fixed in the horizontal plane of the laboratory, as function of the spin frequency and the sense of rotation, with linear fit to a straight line (clockwise frequencies are indicated as negative, counter-clockwise frequencies as positive). The linear increase with the spin rate and

the change of sign can be ascribed to the gyroscopic effect. The offset at zero spin is due to the inclination of the suspension shaft from the vertical.

Measurements reported in figure 2.5 refer to an apparatus (2001) in which the laminar suspension of the inner test cylinder (at the bottom end of the coupling arm) had been replaced by a solid brass cylinder connecting to the lower half of the coupling arm, suspended from the central laminar suspension and show agreement with the theoretical predictions.
Instead, a relative displacement due to an EP violation in the field of the Sun would show up as an additional vector following the daily motion of the Sun (24-hr period). For this reason the rotating differential accelerometer (GGG) can be used to test the equivalence principle in the field of the Sun, but cannot be used for testing it in the field of the Earth. If one takes the sun as the driving source mass, the equilibrium of the suspended body is between the gravitational attraction from the Sun and the centrifugal force due to the annual motion around it. The resulting signal is, at most:

$$a_{EW}^{\odot} \leq \frac{GM_{\odot}}{R_{\oplus\odot}^{2}} = 0.6 \cdot 10^{-2} \eta \, ms^{-2} \qquad (2.7)$$

where $R_{\oplus\odot}$ is the Earth-Sun distance and $M_{\odot}$ the mass of the Sun. The GGG rotating differential accelerometer can be used to test the equivalence principle in the gravitational field of the Sun to 1 part in 10^{13}. This goal requires detecting low frequency (24-hr) relative displacements of the test cylinders of 10^{-13}m (assuming a differential period of 80s), which in turn requires reducing daily seismic and thermal disturbances.

2.5: THE READ-OUT SYSTEM.

The read-out system (schemes of the electronics are shown in appendix G) reflects the cylindrical symmetry of the apparatus ([11], [32], [38 - 39]). Two capacitance plates CP working as displacements sensors (drawn as vertical yellow lines in between the cylinders in figure 2.1), are located halfway in between the test cylinders in correspondence to the ξ direction (they are fixed in the rotating reference frame (O,ξ,η,z)) with a clear gap of 5mm on either side, and connected to the suspension tube by means of an insulating frame. A similar pair of plates is placed in the η direction. Figure 2.6 shows the 4 plates and their insulating frame. They are part of two capacitance bridges in the ξ and η directions of the plane perpendicular to the symmetry axis (the plane of sensitivity of the instrument): each bridge is formed by four capacitors. 2 capacitors of the bridge are fixed capacitors to which a sinusoidal voltage is applied (see figures 2.7.b and Appendix 8.A). The other two are variable and are formed by a plate and the two test bodies: each capacitor (see figures 2.7.a and Appendix 8.A) is formed by two surfaces, one for each of the two test bodies (grounded), and one plate CP. Any differential displacement of the test masses with respect to the plates causes a loss of balance of the bridge and therefore an output signal.
Any displacement of the test masses is the combination of a common mode displacement Δx_{com} (both mass moves the same) and a differential mode displacement Δx_{dif} (of one body relative to the other), as shown in figure 2.7.b.

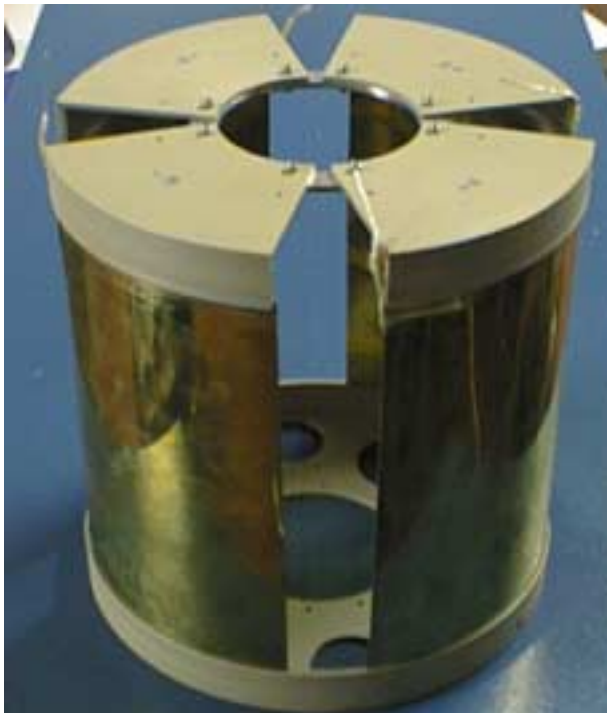

Figure 2.6: The four capacitance plates CP and their insulating frame.

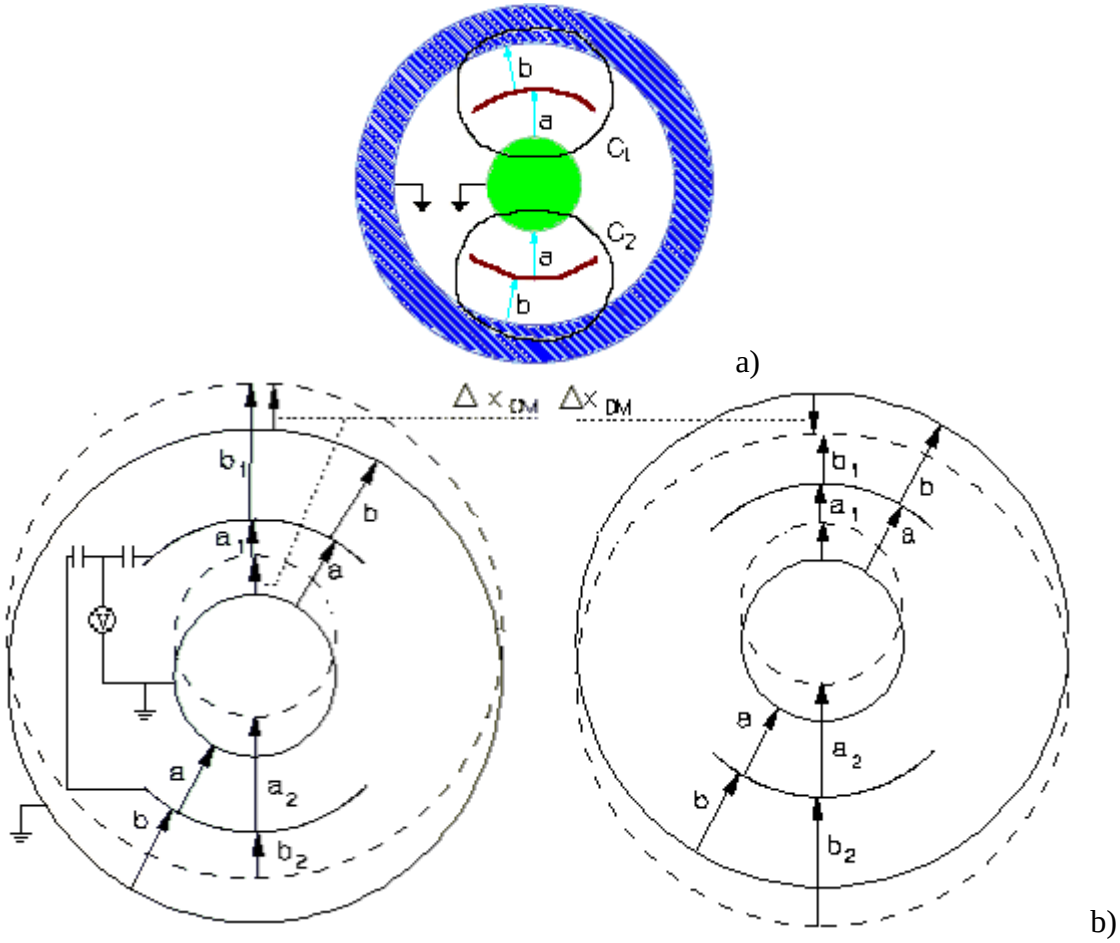

Figure 2.7: Part a) – Schematic drawing of the two capacitance sensor of the bridge of the GG read-out system for detecting relative displacements of the inner and outer test body with respect to one another. Each capacitor is formed by two surfaces, one for each of the two grounded bodies, and one plate, to which a sinusoidal voltage

is applied (1Volt, 500kHz). The other two capacitors of the bridge are fixed capacitors. Any differential displacement of the test masses with respect to the plates causes a loss of balance of the bridge and therefore an output signal. Part b) –The surfaces of the capacitors before a common mode displacement (left) and a differential mode displacement (right).

For the general displacement the total relative change of capacitance will be given by:

$$\frac{C_1 - C_2}{2C_0} \sim \frac{a-b}{a^2}\Delta x_{com} - \frac{1}{a}\Delta x_{dif} \qquad (2.8)$$

where C_0 is the initial value of the capacitances, C_1 and C_2 the values changed due to the displacement. *a* and *b* are defined as in figure 2.7.a; *a* (*b*) is the nominal gap between the inner (outer) mass and one of the 4 capacitance plates. It is apparent from equation (2.8) that the measurement is unaffected by displacements in common mode only if the plates are positioned exactly halfway between the surfaces of the cylinders. Therefore, the bridges need to be mechanically balanced, i.e. the capacitance plates of figure 2.7.a must be positioned at equal distance from the surfaces of the test bodies with sufficient accuracy for all common mode displacements to be smaller than the expected differential signal. If Δx_{EP} is the differential displacement of the expected EP violation signal, it must be:

$$\frac{a - b}{a} \leq \frac{\Delta x_{EP}}{\Delta x_{com}} \qquad (2.9)$$

meaning that in the presence of a displacement in common mode Δx_{com} the relative off-centring of the plates (*a*-*b*)/*a* must not exceed the ratio in equation (2.9). The better the plates are centred, the less sensitive is the read-out to common mode forces, the more suitable it is for EP testing. Any disturbances from parasitic capacitances depend on the geometry of the system and act as DC effects, while the signal is detected at the spin frequency. A voltage signal (1 Volt) of high frequency (500kHz) is applied to the bridge in order to shift the signal of interest to a high frequency band with reduced 1/*f* noise. Since the capacitance bridges rotate with the accelerometer, power and data transfer must be ensured between the rotating and non-rotating frame. For power transfer we use rotating contacts, for data optical transmission. The high frequency bridge measurements are first amplified, demodulated and then converted from analog to digital (now 16 bit, in future 24 bit) to be optically transferred outside the chamber. An annular dish (AD in figure 2.1) is mounted around the upper half of the suspension tube (see figure 2.8), and contains the two capacitance bridge circuits and their preamplifiers. Here is the necessary electronics to demodulate the signal and convert it from analog to digital.

In figure 2.1, at the top of the frame, two optical devices OD are present. Figure 2.9 shows these devices in details. In order to be able to transform the relative displacement as measured by the bridges in the rotating frame (0,ξ,η,z) of the rotor to the non-rotating frame of the laboratory (O,x,y,z), we need to know, in correspondence of each data point, also the phase angle of the rotor. For this purpose a 32-pinhole optical device (OD1) has been mounted, which provides a reference signal for the phase of the rotor and triggers for data acquisition: 31 times per turn, in correspondence of the passage of the diodes under one single hole in the black non-rotating annular dish in figure 2.9, the device generates a voltage signal which triggers data acquisition by means of the annular dish in figure 2.8. This electronic card

combines this signal to the ξ and η channel data into an RS232 format for computer acquisition and send back these data to the circular card in figure 2.9.

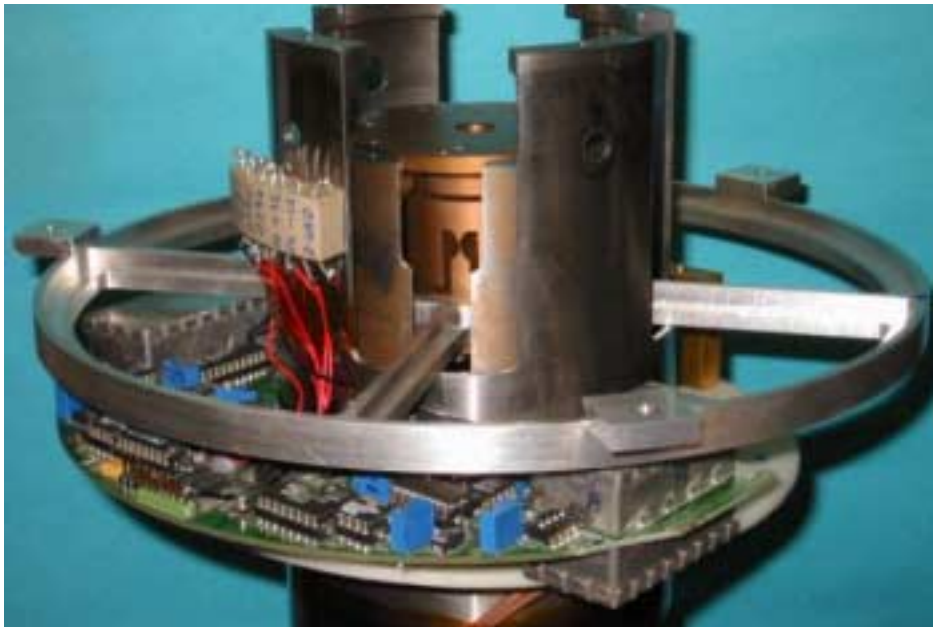

Figure 2.8: Annular dish (AD in figure 2.1) with the read-out electronics: bridges, demodulators, analog to digital converters. It is mounted on the suspension tube ST.

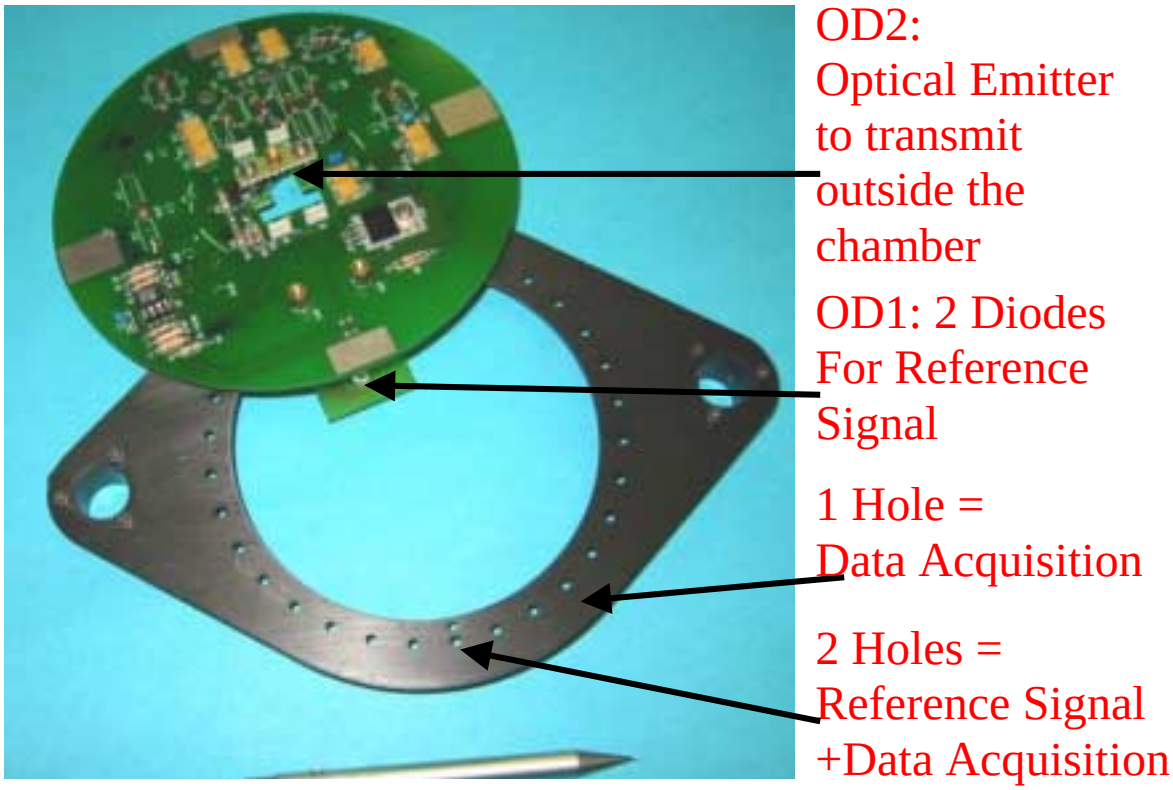

Figure 2.9: A 32- pinhole optical device OD1 provides a reference signal for the phase of the rotor and triggers for data acquisition. The reference signal is combined with the ξ and η channel data into an RS232 format for computer acquisition. Then, a second optical device OD2, shown at the very top of the shaft, transmits the digitally converted signal from the rotor to the non-rotating frame and then outside of the chamber vacuum. The black annular dish with 32 holes is fixed to the non-rotating frame.

Then, a second optical device (OD2), shown at very top of the shaft in figure 2.1, transmits the digitally converted signal from the rotor to the non-rotating frame and then outside the vacuum chamber. Once per turn, when the diodes pass under the coupled holes in the black non-rotating annular dish (figure 2.9), the device OD1 generates two voltage signals: one signal triggers for data acquisition (as said before) and the other one provides a reference signal for the phase. 32 sets of data are acquired per turn. Their format is as follows:

- 1 bit for the reference signal: 1 in correspondence of the coupled holes
  0 in correspondence of a single hole
- time in milliseconds
- ξ channel in the rotating frame (16 bit)
- η channel in the rotating frame (16 bit)
- 1bit for the scale: 1 high gain scale (high sensitivity)
  0 low gain scale (low sensitivity)

The read-out system can operate in a low gain scale (scale 0 with low sensitivity) and in an high gain scale (scale 1, 20 times more sensitive). When the electronics is turned on, data are acquired in the low gain scale 0. In scale 0, the gain is fixed so as the point of saturation of the signal is regulated in correspondence of the maximum allowable displacement between the test masses (i.e. 2 times the gap of 5mm between the surfaces of the test cylinders and the capacitance plates). If the value of the acquired signal remains under a prefixed threshold (300μm) for an entire spin period, then the gain is increased by passing from scale 0 to scale 1. If the value of a single data exceeds a second threshold (500μm) then the gain is reduced by passing from scale 1 to scale 0.
The capacitance bridges are calibrated by displacing the outer test cylinder with respect to the inner one by a known amount and recording the voltage signal read by the capacitance sensors. Displacements are applied in both directions and linearity checks of the calibration curve are performed in both cases. We have obtained a 2% stability of the calibration factor in 100 days. The electric zero of the capacitance bridges is first set at its nominal value, by setting the value of the variable capacitance of the circuit. More accurate checks are performed with the system in rotation, first below and then above the natural frequency of differential oscillations of the test cylinders as discussed in section 2.7.

2.6: WHIRL CONTROL.

Signal modulation performed at high spin rate is much desirable, to reduce $1/f$ mechanical and electrical noises. It is also desirable to soften the mechanical coupling between the test cylinders (leading, as we have just discussed, to larger differential signals). The GGG rotor is actually set into supercritical rotation, at frequencies that are higher than the natural frequencies for differential oscillations of the test cylinders. It is well known ([1 - 3]) that under these conditions spinning bodies are able to self-centre, namely to greatly reduce any original offset between their centres of mass, which inevitably results from construction and mounting errors. These original offsets cannot be reasonably made smaller than 5-10μm. Since relative offsets of this size may result into disturbances masking the EP violation signal, self-centring is an essential concept. On the other hand, in highly supercritical rotation

dissipation of the mechanical suspensions produces unstable whirling motions, whose amplitude increases with time at a rate scaling as the inverse quality factor Q at the spin frequency. For instance, the centres of mass of the GGG test cylinders do develop an orbital motion in the horizontal plane of the laboratory at the natural frequency of differential oscillations around their position of relative equilibrium.

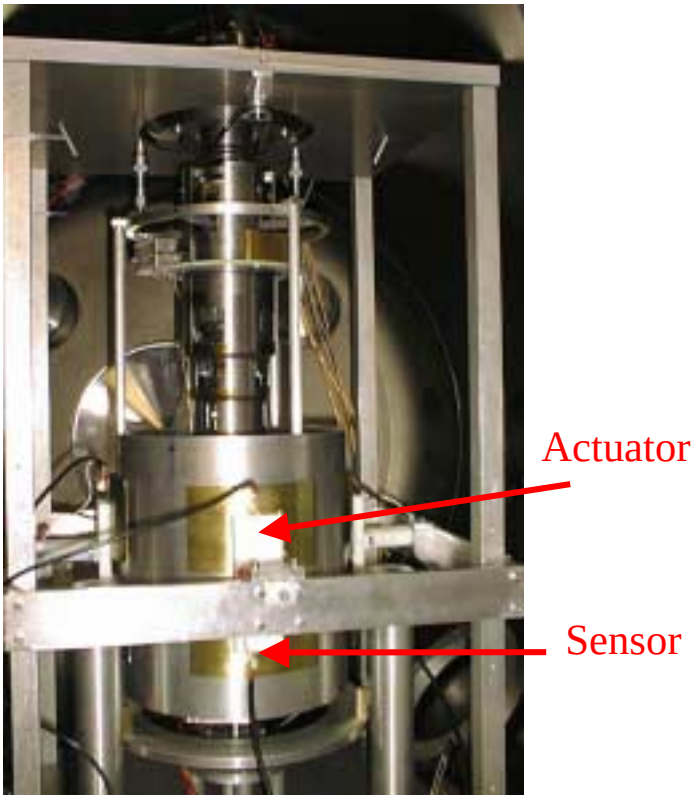

Figure 2.10: The GGG rotor inside the vacuum chamber. 8 capacitance plates are placed near the outside surface of the outer cylinder. They are fixed with the vacuum chamber (i.e. fixed in the non-rotating frame). One half of them is used as sensors, and the other half is used as actuators.

In GGG whirls are controlled actively by means of capacitance sensors/actuators (shown in figure 2.10; schemes of the electronics are shown in appendix G). 8 capacitance plates are placed near the outside surface of the outer mass, fixed with respect to the vacuum chamber (i.e. fixed in the non-rotating frame). One half of them is used as sensors (the two pairs of sensors forming the two halves of two capacitance bridges in the two coordinates of the horizontal plane): measurements of the displacement of the outer cylinder are used to build a damping command proportional to its velocity (see chapter 6 for more details). The electronics of these bridges is essentially the same as that of the bridges of the main sensors except for the fact that here smaller capacitances and less good sensitivity are needed. The other half is used as actuators: high voltage (in the range 0Volt-360Volt) is applied to produce an active force which simulates the non-rotating damping. Finally, a non-rotating passive damper is present under the lowest laminar suspension, and is used for stabilization purposes in passing through the rotor critical speeds. We have implemented two different kinds of passive dampers. Figure 2.11 shows a sketch of the last version of this damper: a needle is fixed with the inner cylinder and its point coincides with the centre of mass of the body. The

passive damper is equipped with a mechanism mounted in the vacuum chamber outside the accelerometer itself that can be activated from outside the chamber in order to move up and down a plane, under the point of the needle. A light and hollow disk is laid on the plane.

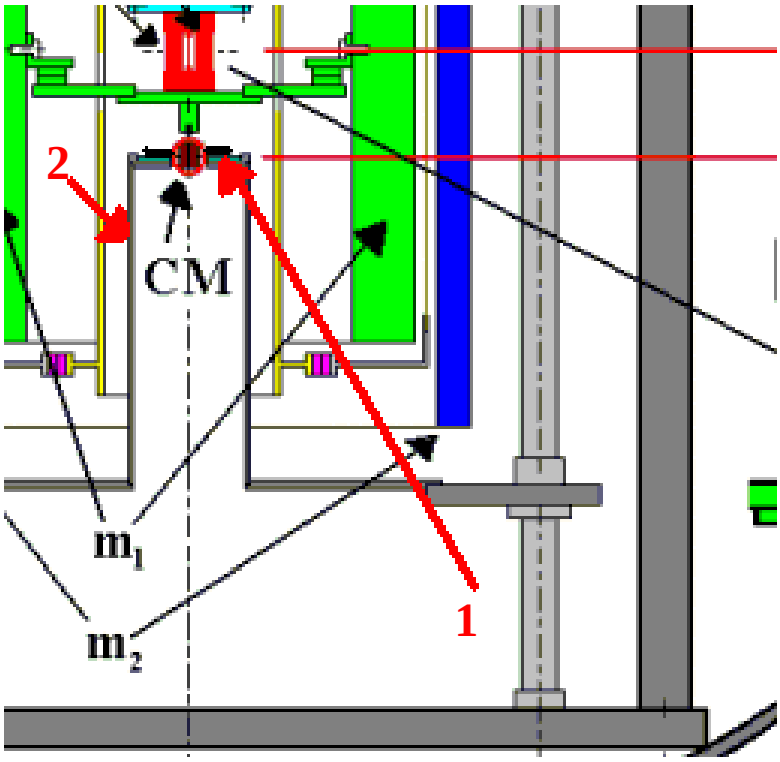

Figure 2.11: Enlargement of figure 2.1. Open circle 1 indicates the very light disk of the passive damper. It is dragged by a needle fixed with the inner mass. The point of the needle coincides with the centre of mass of the inner body. Number 2 indicates the support which can be operated from the outside.

When the plane goes up, the point of the needle enters inside the hole of the disk. If the centre of mass of the inner cylinder moves in the horizontal plane (whirling motion), the point of the needle drags the little disk. Friction between the disk and the plane generates the non-rotating forces. After reaching the final rotation speed, the passive damper can be disconnected and the finer active damper can be employed. The previous version of the damper was less efficient than the new one: it was made of a very light disk with little radial blades immersed in low vapour pressure oil and mounted under the suspension of the inner cylinder.

2.7: ADJUSTMENTS AND SETTINGS.

Various adjustments can be performed for the rotating differential accelerometer to operate as it is designed to [32]. An inclination of the rotating coupling arm, about its midpoint, by a non zero constant angle from the vertical, gives rise to a constant relative displacement of the test cylinders fixed in the rotating frame. It is therefore detected by the (rotating) read-out as a constant offset from zero (in ξ and η), which provides the driving signal for this adjustment. In order to reduce this offset the position of the top suspension (the one of the outer test cylinder; see figure 2.2) can be adjusted so as to be as much as possible in line with the other

two suspensions at the centre and the bottom. This is the coarsest adjustment. Then, on the coupling arm, close to (just below) the central suspension, are mounted two small masses (5g each) that can be displaced across the arm's axis in the ξ and η directions (see figure 2.12; these masses are numbered as 1) in order to reduce the corresponding offsets, and therefore the inclination of the arm. For yet a finer adjustment there are two additional smaller masses (0.5g each), also movable in ξ and η (numbered as 2 in figure 2.12).

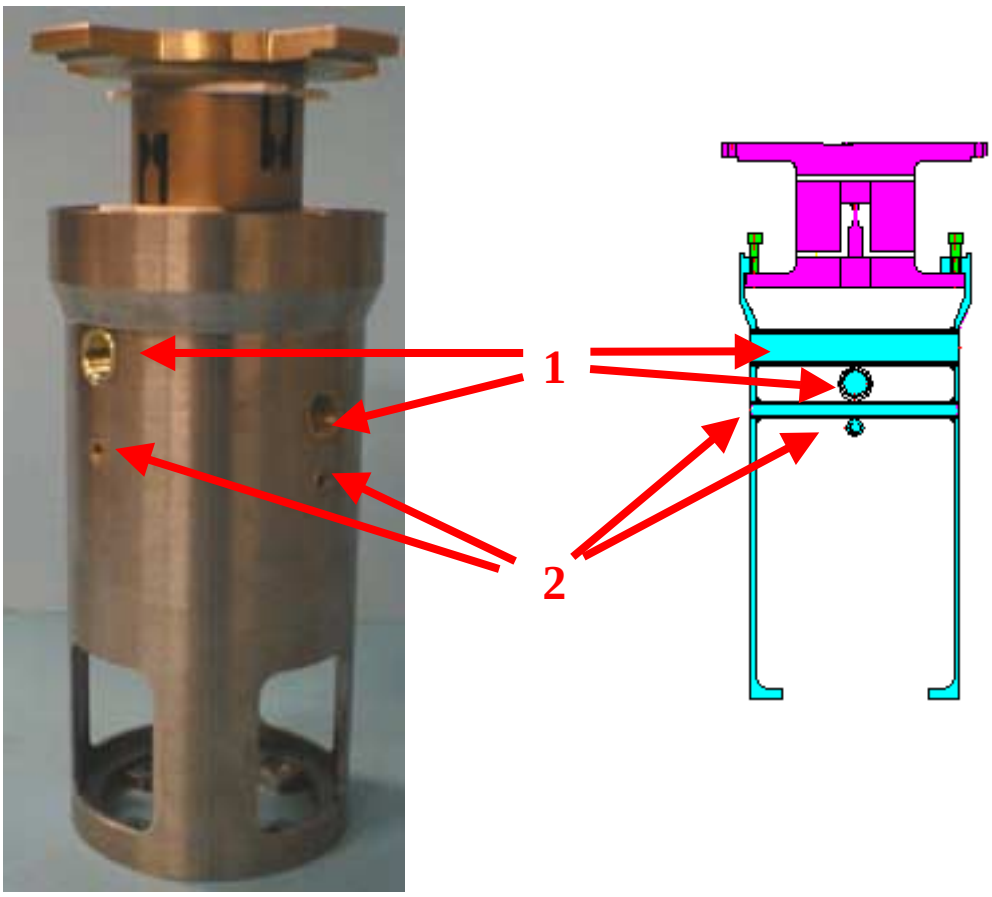

Figure 2.12. The central laminar suspension and one half of the coupling arm. Number 1: two small masses (5g each) can be displaced across the arm's axis in the ξ and η directions in order to reduce its inclination. Number 2: For yet a finer adjustment there are two additional smaller masses (0.5g each).

However, a constant offset in the ξ and η measurements of the relative displacements between the centres of mass of the test cylinders as performed by the rotating capacitance bridges may also be due to the bridge capacitances being out of balance at zero mechanical displacement: which would require the variable capacitances in each bridge to be adjusted, and no change in the inclination of the coupling arm. In order to separate the two effects, and operate the right adjustment, we perform these measurements by spinning the rotor at a frequency first below and then above the natural one for differential oscillations of the test cylinders. If the offsets are due to the inclination of the coupling arm, i.e. to the test cylinders not being suspended along the same axis, it is known that they should decrease when spinning above the natural frequency. Once a non-zero inclination of the coupling arm has been ruled out, we can proceed to reduce the offsets of the measurements by adjusting the variable capacitances. A few iterations of this procedure may be necessary. Electrical offsets can also be recognized by passing from the low gain scale 0 to the high gain scale 1.

Around the lower half of the coupling arm is mounted a small solid ring movable in the vertical direction (not shown in the picture). A change in its vertical position, by changing the mass distribution of the beam balance, will change the natural period of the differential oscillations. Being symmetrical around the arm, the position of the ring affects only the quantity ΔL. From an operational viewpoint, this is the easiest way to change and adjust the differential period of the test cylinders. In the conceptual design of the differential accelerometer it is very important that the suspension tube (the tube ST enclosing the coupling arm, held by a shaft turning inside ball bearings) be aligned with the local vertical. In the case of non zero inclination of the suspension tube from the local vertical, due to the shaft not being mounted perfectly vertical in the laboratory reference frame, there will be a non zero lateral deformation of the central suspension which suspends the beam balance and a consequent relative displacement of the test cylinders. The displacement is fixed in the laboratory (non-rotating) frame along the direction identified by the misalignment of the shaft and is modulated by the rotating capacitance bridges at their spin frequency. The ξ and η measurements are transformed into the x and y relative displacements in the non-rotating frame where the coordinates of the fixed displacement indicate the direction of the suspension tube. They provide the driving signal for this adjustment, which is performed by means of three vertical motorized screws placed at 120° from one another (minimum incremental step: 16nm) which control the inclination of the top plane (the plane with the ball bearings x in figure 2.1) of the frame around the shaft, hence also its verticality.

2.8: LOW FREQUENCY SEISMIC NOISE.

The following section is devoted to the study of the effect of the seismic noise on the experimental apparatus and it is part of the article [40] available in Appendix_Articles: if the terrain where the apparatus is located undergoes low frequency tilts of amplitude α we need to evaluate the effects of such tilts on the experiment and reduce them if necessary ([34], [40]). Let us consider a body of mass m suspended by means of a laminar suspension with elastic constant k and length ℓ (cylindrically isotropic) as in figure 2.13. The tilt angle β at equilibrium is determined by the condition that the restoring force of the suspension equals the horizontal component of the local acceleration of gravity arising because of the tilt. The equilibrium equation is:

$$\beta/\alpha \simeq (k\ell)/(k\ell + mg) \qquad (2.10)$$

where g is the local gravity. If $k\ell/mg \ll 1$, so that terms of order $(k\ell/mg)^2$ or higher can be neglected, we get that tilts are reduced by the factor:

$$\beta/\alpha \simeq k\ell/(mg) \ll 1 \qquad (2.11)$$

Let us now consider the case in which, instead of being subject to a terrain tilt, the system is subject to a horizontal disturbing acceleration with the same (low) frequency as the tilt, and amplitude $a=\alpha g$. In the presence of a suspension providing a stiffness k in the horizontal plane, equilibrium is reached at a different angle γ with the original vertical:

$$\gamma \simeq \frac{a}{g}\left(1 - \frac{k\ell}{mg}\right) \qquad (2.12)$$

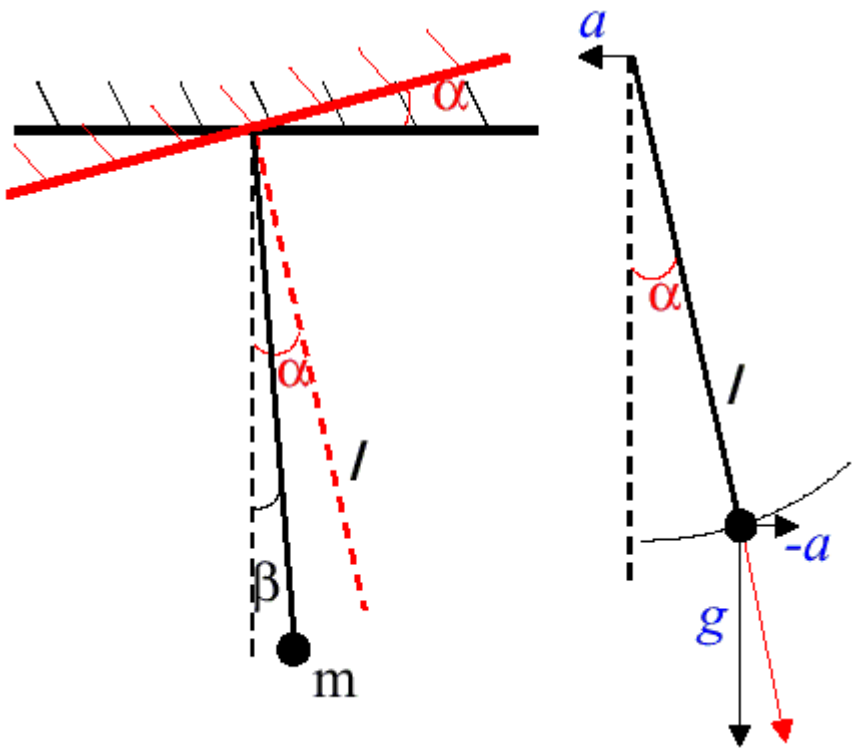

Figure 2.13: Left: if the system is rigid, a terrain tilt will displace it by an angle α. Instead, if the mass m is suspended by means of a laminar cardanic suspension placed at the top of the suspension arm, giving rise to a stiffness k in the horizontal plane the mass will reach equilibrium at a tilt angle β<α.. Right: If the terrain on which the apparatus is located is affected by a horizontal, low frequency, disturbing acceleration of amplitude a the test mass will feel an equal and opposite inertial acceleration which will move it behind to a new position of equilibrium along the direction of the new local vertical (shown by the red line).

In the laboratory, the direction of a new local vertical is given by the vectorial sum $\vec{g}-\vec{a}$ forming an angle $\alpha = a/g$ with the original vertical (defined by the direction of local gravity $\vec{g}$ in absence of the disturbing acceleration). And the deviation from the *new* local vertical is β=α–γ, namely:

$$\beta \simeq \frac{a}{g}\frac{k\ell}{mg} = \alpha\frac{k\ell}{mg} \qquad (2.13)$$

The effect of a suspension with horizontal stiffness k is therefore to make the test mass tilt from the new local vertical only by the same small angle β as in the case of a terrain tilt by the angle $\alpha = a/g$ given by (2.10) (in the same approximation in which terms of the order of $(k\ell/mg)^2$ or higher are neglected).
In terms of the acceleration acting on the test mass (in the horizontal, sensitivity plane), this is

$$a_\perp = g\gamma - a = a\left(k\ell/mg\right) \qquad (2.14)$$

This means a reduction, with respect to the local disturbing acceleration a acting at the top of the system, by the ratio $k\ell/mg \ll 1$, just as in the case of the terrain tilts. We conclude that, because of the equivalence between inertial and gravitational mass which at this level can be assumed to be valid, local terrain tilts cannot be distinguished from horizontal disturbing accelerations. This is true as a matter of principle, and therefore any apparatus measuring tilts will be unable to distinguish them from horizontal accelerations, and vice-versa. The only

way to distinguish horizontal accelerations from tilts for a suspended test mass is by means of an instrument which were also sensitive to *absolute* changes in the direction of the local vertical, not only to relative displacements of the test mass with respect to it. Low frequency tilts in the vicinity of the GGG apparatus have been monitored with the ISA[5] (Italian Space Accelerometer) tiltmeter/accelerometer ([41 - 42]). Daily effects turn out to have an amplitude of about 10^{-6}rad (corresponding to horizontal accelerations of about 10^{-6} g). The resulting effect on the GGG test cylinders is to give rise to relative displacements (in the horizontal plane of the laboratory) at the same frequency and with an amplitude of about $4 \cdot 10^{-7}$ m (the suspension arm relevant for the relative displacements of the test cylinders being about 0.4 m long). The goal of testing the Equivalence Principle to 10^{-13} with GGG requires detecting low frequency (24-hr) relative displacements of the test cylinders of 10^{-13} m, which in turn requires daily seismic disturbances to be reduced below this level. This can be done partly actively and partly passively. Active reduction is done using as sensor a tiltmeter placed inside the vacuum chamber at the top of the GGG frame (not rotating), and as actuators a set of PZTs (also not rotating, at 120° in the horizontal plane around the symmetry axis, providing tilts of the apparatus through vertical displacements). The tiltmeter currently installed can detect tilts of 10^{-9}rad/10^{-10}rad. At the location of the PZTs the arm length with respect to the symmetry axis is about 0.1 m, and therefore the vertical effect of such tilts would be of about 10^{-10}m/10^{-11}m, which they can correct by applying a voltage of the order of a 1mV/0.1mV. If successful, this control would leave a residual relative displacement of the test cylinders of about $4 \cdot 10^{-10}$ m /$4 \cdot 10^{-11}$m. A further reduction by about 4/3 orders of magnitude, down to $4 \cdot 10^{-14}$ m, which would bring the effects of tilts and horizontal disturbances well below the target signal, can be obtained using a passive cardanic suspension. It is worth noticing that in GGG the signal is a relative displacement of the test cylinders around the local vertical (the cylinders are the masses of a *vertical* beam balance, the beam being aligned along the local vertical). As the direction of the local vertical changes because of horizontal seismic accelerations (as in Figure 2), the beam of the balance will follow it, but these absolute displacements are not relevant for the GGG measurements [43].

[5] Kindly granted by Valerio Iafolla, IFSI (CNR), Roma.

CHAPTER 3:

MATHEMATICAL MODEL OF THE GGG SYSTEM.

3.1: INTRODUCTION.

In the present and following chapter, we demonstrate that the original dynamical model of the GGG instrument (set into supercritical rotation), which we have developed, can be used to predict the normal modes of the GGG experimental apparatus (present chapter) and its rejection behaviour (chapter 4). Analytical solutions are obtained under special limits, that fix the theoretical understanding. A simulational environment is set up, obtaining quantitative agreement with the available experimental data [36]. In this chapter we determine the normal modes of the GGG accelerometer in all regimes, from subcritical to supercritical rotation. The mathematical model is solved by means of a user-friendly simulation method. The physical content of the model is also discussed by means of approximated analytical solutions, useful to support the physical intuition. This chapter is organized as follows: after the definition of the generalized coordinates in the rotating reference frame in section 3.2, we introduce the mathematical model of GGG. We then turn in sections 3.3 – 3.8 to the description of the numerical method that we have implemented and present all the results on the determination of the normal modes in section 3.9. Approximated analytical solutions are shown in section 3.10.

3.2: GENERALISED COORDINATES AND THE GGG MATHEMATICAL MODEL.

The GGG rotor is composed of 3 bodies, coupled by means of 3 cardanic suspensions, stiff in the axial direction and very soft in the horizontal plane (2 degrees of freedom for each suspensions), amounting to $c=2\times3=6$ degrees of freedom. Hence, the problem can be studied using only six generalized coordinates[1]. We have chosen as generalized coordinates for each body the following two angles:

ϑ'_a - it is the angle between the coupling arm and the vertical axis z (the axis z of the rotating frame coincides with the axis z of the inertial frame). This angle runs in the interval $[0, \pi]$. It is drawn in figure 3.1.

ϕ'_a - it is the angle from the ξ axis to the projection of the coupling arm on the ξ- η plane of the rotating reference frame (O, ξ,η,z) and runs in the interval $[0, 2\pi]$.

[1] The motion of a rigid body is described by six degrees of freedom. The GGG rotor is composed of 3 bodies, amounting to $c=6\times3=18$ degrees of freedom. The presence of the central suspension prevents the bodies from performing translational motions, thereby introducing $v1=3\times3=9$ constraints. The presence of the motor, forces the three bodies to rotate at a constant angular velocity, introducing $v2=1\times3=3$ new constraints. At the end, the degrees of freedom for the model amounts to $n=c-v1-v2=18-12=6$. Hence the problem can be studied using only six generalized coordinates.

From now on, the label λ=a, 1, 2 will be used to refer to the coupling arm, the inner and the outer mass. ϑ'_1 and ϕ'_1 are related to the inner body and are defined in the same way. ϑ'_2 and ϕ'_2 refer to the outer cylinder.

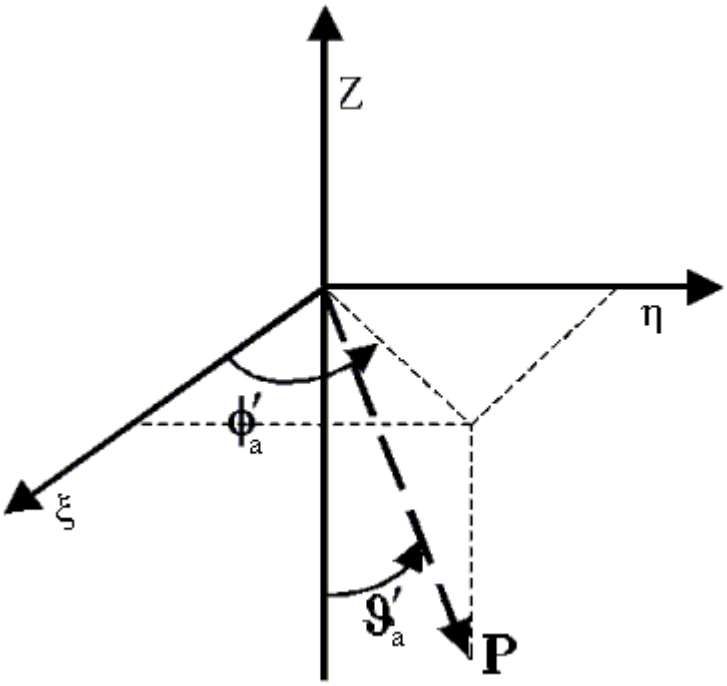

Figure 3.1: Generalized coordinates ϑ' and ϕ' of the point P.

It is important to notice that these angles are defined in a slightly different manner with respect to the usual Euler angles [5 – 6]:

$$\vartheta' = \pi - \vartheta_{\text{Euler}} \tag{3.1}$$

$$\phi' = \phi_{\text{Euler}} + 3\pi/2 \tag{3.2}$$

$$\psi' = \psi_{\text{Euler}} \tag{3.3}$$

The derivatives of the angles are:

$$\dot{\vartheta}' = -\dot{\vartheta}_{\text{Euler}} \tag{3.4}$$

$$\dot{\phi}' = \dot{\phi}_{\text{Euler}} \tag{3.5}$$

$$\dot{\psi}' = \dot{\psi}_{\text{Euler}} \tag{3.6}$$

We thus define the vector $Q' = [q'_1, q'_2, q'_3, q'_4, q'_5, q'_6]^T$ of the generalized coordinates, i.e. $q'_1 = \vartheta'_a; q'_2 = \vartheta'_2; q'_3 = \vartheta'_1; q'_4 = \phi'_a; q'_5 = \phi'_2; q'_6 = \phi'_1$, and the corresponding velocities $\dot{Q}$. After having described our choice for lagrangean coordinates, we are now in a position to outline the minimal model to describe the dynamical behaviour of the real instrument. Figure 3.2 displays a schematic representation of the model in the reference frame (O, ξ,η,z) rotating with the shaft at the angular frequency $\omega_s = 2\pi\nu_s$ around the z axis ($\vec{\omega}_s = \omega_s \hat{z}$). The relevant parts of the instrument depicted in figure 2.1 are sketched in figure 3.2 with the same colours. MO (brown) is the motor. The arm with mass m_a (drawn in cyan) and length 2L++ΔL is suspended at its midpoint MP from the rotating shaft and suspension tube ST (yellow) by means of the central laminar suspension LS (orange) with elastic constant k. The vector $\vec{\varepsilon}$

displaces the suspension point of the coupling arm MP (black cross) from the rotation axis, and take into account possible offsets due to construction and mounting errors. The centre of mass of the coupling arm turns out to be displaced from the suspension point MP by a quantity ΔL/2, that is, if ΔL=0, the arm centre of mass is located in its midpoint.

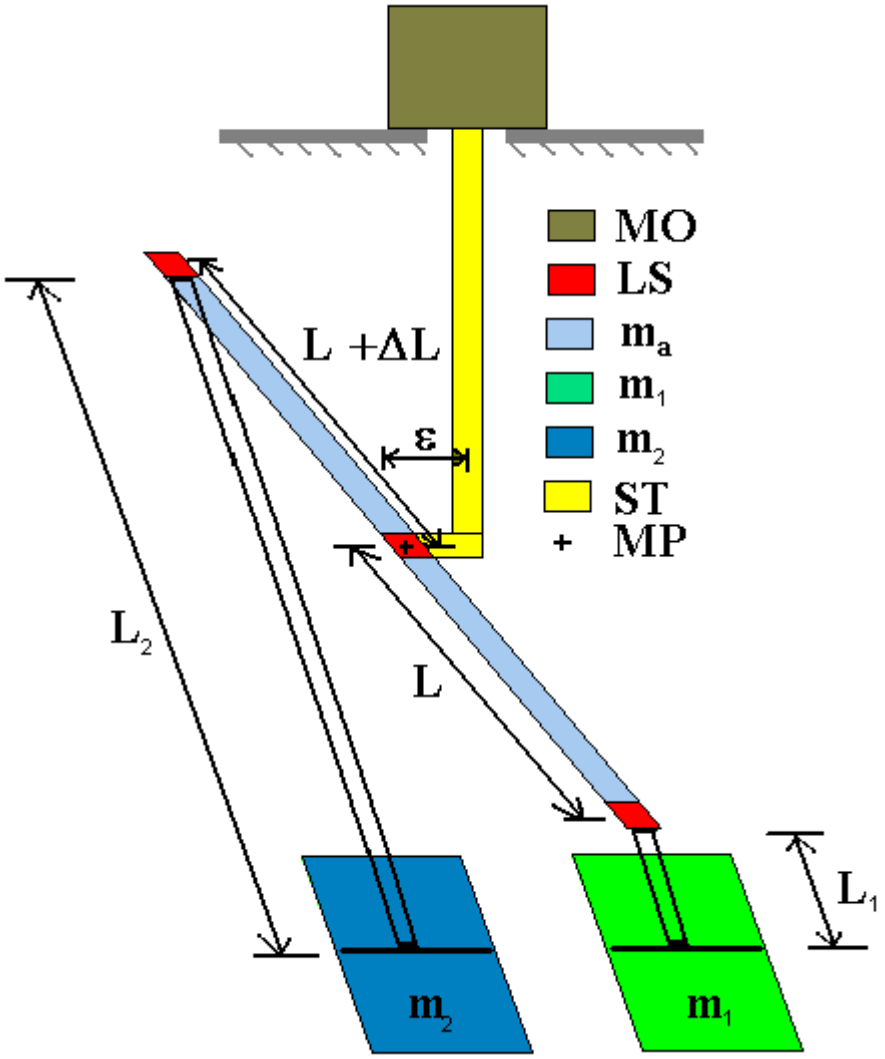

Figure 3.2: Minimal model for the instrument drawn in figure 2.1, as detailed in the text. The various parts are drawn with the colours and the labels corresponding to figure 2.1. The relevant dimensions L_a, L_1 and L_2 of the coupling beams are indicated. The offset $\vec{\varepsilon}$ due to construction and mounting imperfections is also indicated. MO (brown) is the motor. ST (yellow) is the suspension tube. The arm with mass m_a (in cyan) and length 2L+ΔL is suspended at its midpoint MP. Bodies are coupled by means of 3 laminar suspensions LS (red). The two cylinders have mass m_2(blue) and m_1(green).

The outer cylindrical mass m_2 (blue) is suspended from the top of the coupling arm, L_2 being the distance of its centre of mass from the suspension. In a similar manner, the inner mass m_1 (green) is suspended from the bottom of the coupling arm, L_1 being its characteristic distance. ΔL can be adjusted to be either positive or negative, resulting into a shorter or longer differential period. In the model the laminar suspensions have length ℓ, and the central one is different from the other two, so that we assume $k_1=k_2=k$ and define a new parameter Λ such that $k_y=\Lambda k_x$, i.e. the central suspension is non-isotropic. In equations (3.7), (3.8) and (3.9) the unit vectors $\hat{L}_a$, $\hat{L}_1$ and $\hat{L}_2$ (see figure 3.2) are defined.

$$\hat{L}_a = \left[\sin(\vartheta'_a)\cos(\phi'_a),\ \sin(\vartheta'_a)\sin(\phi'_a),\ -\cos(\vartheta'_a)\right]^T \tag{3.7}$$

$$\hat{L}_1 = \left[\sin(\vartheta'_1)\cos(\phi'_1),\ \sin(\vartheta'_1)\sin(\phi'_1),\ -\cos(\vartheta'_1)\right]^T \tag{3.8}$$

$$\hat{L}_2 = \left[\sin(\vartheta'_2)\cos(\phi'_2),\ \sin(\vartheta'_2)\sin(\phi'_2),\ -\cos(\vartheta'_2)\right]^T \tag{3.9}$$

The vectors pointing to the centres of mass of the arm and starting from the origin O is

$$\vec{r}_a = \vec{\varepsilon} - \frac{\Delta L}{2}\hat{L}_a \tag{3.10}$$

The inner cylinder's position vector with respect to the origin O is given by equation:

$$\vec{r}_1 = \vec{\varepsilon} + L\hat{L}_a + L_1\hat{L}_1 \tag{3.11}$$

while the centre of mass of the outer cylinder is:

$$\vec{r}_2 = \vec{\varepsilon} - (2L + \Delta L)\hat{L}_a + L_2\hat{L}_2 \tag{3.12}$$

3.3: THE LAGRANGEAN OF THE SYSTEM IN THE ROTATING REFERENCE FRAME.

Equations (3.A.24) in Appendix 3.A, together with (3.A.25) and (3.A.26) yield the Lagrange function of a rigid body in a rotating reference frame. In equation (3.A.26), U includes the potential energies associated to gravity and to the elastic forces, namely

$$U = U_g + U_k \tag{3.13}$$

where the gravitational potential energy is:

$$U_g = -\sum_{\lambda=a,1,2} m_\lambda \vec{g}\cdot\vec{L}_\lambda \ ^2 \tag{3.14}$$

and the elastic potential energy:

$$U_k = \frac{1}{2}\sum_{\lambda=1,2} k_\lambda \ell^2 \left|\hat{L}_a \times \hat{L}_\lambda\right|^2 + \frac{1}{2}L_a^2\left(k_\xi\left|\hat{L}_a\cdot\hat{\xi}\right|^2 + k_\eta\left|\hat{L}_a\cdot\hat{\eta}\right|^2\right) \tag{3.15}$$

(clearly, $\hat{\xi},\hat{\eta},\hat{z}$ are the unit vectors related to the axes ξ, η and z in the rotating frame). $\vec{v}_\lambda$ (λ=a,1,2) are the total derivatives of the position vector $\vec{r}_\lambda$. For each body λ (λ=a,1,2) equations (3.A.25) and (3.A.26) can be applied performing the substitutions: $\vec{R}\to\vec{r}_\lambda$, $\vec{V}\to\vec{v}_\lambda$, $M\to m_\lambda$, $\vartheta\to\vartheta'_\lambda$, $\phi\to\phi'_\lambda$, $I_\Upsilon\to I_{\Upsilon,\lambda}$ e $I_\Xi\to I_{\Xi,\lambda}$. Collecting all the results as indicated by equation (3.A.24) the total Lagrangean L is obtained.

[2] $\vec{g} = -g\hat{z}$ is the local gravity.

3.4: EQUILIBRIUM POSITIONS AND SECOND-ORDER EXPANSION OF THE LAGRANGEAN.

Normal and successful operation of the GGG rotor is based on small amplitude motions. The Lagrange function of the accelerometer can thus be expanded to second order in $(Q', \dot{Q}')$ around the equilibrium solution $(Q'^0, \dot{Q}'^0 = 0)$[3], to derive linearized equations of motion. To this aim, let us begin with determining the equilibrium position. This is determined from the equations:

$$\left.\frac{\partial U_{total}}{\partial q_i'}\right|_{q_i'^0} = 0 \quad \forall i = 1,...,6 \tag{3.16}$$

We then use the assumption that during motion, the Q' are slightly perturbed from their equilibrium values Q'^0. Hence, it is possible to perform the substitution:

$$\begin{cases} q_i' = q_i + q_i'^0 \\ \dot{q}_i' = \dot{q}_i \end{cases} \quad \forall i = 1,...,6 \tag{3.17}$$

or, equivalently, in terms of the angular coordinates ϑ_λ and ϕ_λ:

$$\begin{aligned} &q_1' = \vartheta_a' = \vartheta_a + \vartheta_a'^0; \quad q_4' = \phi_a' = \phi_a + \phi_a'^0; \\ &q_2' = \vartheta_2' = \vartheta_2 + \vartheta_2'^0; \quad q_5' = \phi_2' = \phi_2 + \phi_2'^0; \\ &q_3' = \vartheta_1' = \vartheta_1 + \vartheta_1'^0; \quad q_6' = \phi_1' = \phi_1 + \phi_1'^0 \end{aligned} \tag{3.18}$$

The new equilibrium position is then:

$$\left\{ q_i^0 = 0 \; ; \; \dot{q}_i^0 = 0 \right. \qquad \forall i = 1,...,6 \,. \tag{3.19}$$

The Lagrange function $L(Q, \dot{Q})$ can now be expanded to second order, namely:

$$L = a_0 + \sum_i b_i \dot{q}_i + \sum_{i<j} a_{ij} q_i q_j + \sum_{i<j} b_{ij} \dot{q}_i \dot{q}_j + \sum_{i,j} c_{ij} q_i \dot{q}_j \tag{3.20}$$

where we remark that now the q_j's are small[4] according to the substitution (3.17) and (3.18), and that the linear terms have cancelled out because of (3.16). The matrix coefficients a_0, b_i, $a_{i,j}$, $b_{i,j}$ and $c_{i,j}$ are known functions of the Q^0 and of the governing parameters of the system, and in general are to be numerically evaluated.

3.5: LINEARIZED EQUATIONS OF MOTION.

The equations of motion in terms of the known a_0, b_i, $a_{i,j}$, $b_{i,j}$ and $c_{i,j}$ coefficients are determined from in the standard manner:

$$\frac{d}{dt}\frac{\partial L}{\partial \dot{q}_i} - \frac{\partial L}{\partial q_i} = F_i \qquad i = 1,2,...,6 \tag{3.21}$$

---

[3] $Q'^{0T} = \left[q_1'^0, \, q_2'^0, \, q_3'^0, \, q_4'^0, \, q_5'^0, \, q_6'^0 \right]$

[4] The new equilibrium position is $(Q^0 = 0, \dot{Q}^0 = 0)$, being $Q^T = \left[q_1, \, q_2, \, q_3, \, q_4, \, q_5, \, q_6 \right]$

where we have introduced the generalized forces:

$$F_i = \sum_{\lambda=a,1,2} \sum_{j=1}^{3} F_{\lambda,j} \cdot \frac{\partial r_{\lambda,j}}{\partial q_i} \tag{3.22}$$

starting from the Cartesian components $F_{\lambda,j}$ of the forces acting on each body. At this level, the generalized forces (3.22) are to be consistently expanded to first order, namely

$$F_i = \sum_j \alpha_{i,j} q_j + \sum_j \beta_{i,j} \dot{q}_j \tag{3.23}$$

Combining equations (3.20) and (3.23) together[5], the equations of motion can be written in a compact matrix form as

$$[M] \cdot \underline{\ddot{Q}} = [S] \cdot \begin{pmatrix} \underline{Q} \\ \underline{\dot{Q}} \end{pmatrix} \tag{3.24}$$

with the obvious notation:

$$\underline{Q} = \begin{bmatrix} q_1 \\ q_2 \\ q_3 \\ q_4 \\ q_5 \\ q_6 \end{bmatrix};\ \underline{\dot{Q}} = \begin{bmatrix} \dot{q}_1 \\ \dot{q}_2 \\ \dot{q}_3 \\ \dot{q}_4 \\ \dot{q}_5 \\ \dot{q}_6 \end{bmatrix};\ \underline{\ddot{Q}} = \begin{bmatrix} \ddot{q}_1 \\ \ddot{q}_2 \\ \ddot{q}_3 \\ \ddot{q}_4 \\ \ddot{q}_5 \\ \ddot{q}_6 \end{bmatrix} \tag{3.25}$$

In equation (3.24) **M** is the "mass"-matrix (6×6) composed by the coefficients:

$$M_{i,j} = 2b_{i,j}\delta_{i,j} + b_{i,j}\left(1 - \delta_{i,j}\right) \tag{3.26}$$

where the factor of 2 on the diagonal elements is a consequence of the restricted j<k sum in the expansion (3.20). S is a 6×12 matrix containing the a_0, b_i, $a_{i,j}$, $b_{i,j}$ and $c_{i,j}$ coefficients:

$$[S] = [A_2] + [\alpha] + [C_2] + [\beta] \tag{3.27}$$

The first matrix in equation (3.27) is:

$$\begin{aligned} [A_2]_{i,j} &= 2a_{i,j}\delta_{i,j} + a_{i,j}(1 - \delta_{i,j}) \qquad j \le 6 \\ &= 0 \qquad\qquad\qquad\qquad\qquad\quad 6 < j \le 12 \end{aligned} \tag{3.28}$$

i.e.

$$[A_2] = \begin{bmatrix} 2a_{1,1} & a_{1,2} & a_{1,3} & a_{1,4} & a_{1,5} & a_{1,6} & 0 & 0 & 0 & 0 & 0 & 0 \\ a_{1,2} & 2a_{2,2} & a_{2,3} & a_{2,4} & a_{2,5} & a_{2,6} & 0 & 0 & 0 & 0 & 0 & 0 \\ a_{1,3} & a_{2,3} & 2a_{3,3} & a_{3,4} & a_{3,5} & a_{3,6} & 0 & 0 & 0 & 0 & 0 & 0 \\ a_{1,4} & a_{2,4} & a_{3,4} & 2a_{4,4} & a_{4,5} & a_{4,6} & 0 & 0 & 0 & 0 & 0 & 0 \\ a_{1,5} & a_{2,5} & a_{3,5} & a_{4,5} & 2a_{5,5} & a_{5,6} & 0 & 0 & 0 & 0 & 0 & 0 \\ a_{1,6} & a_{2,6} & a_{3,6} & a_{4,6} & a_{5,6} & 2a_{6,6} & 0 & 0 & 0 & 0 & 0 & 0 \end{bmatrix} \tag{3.29}$$

---

[5] $\frac{d}{dt}\frac{\partial L}{\partial \dot{q}_i} = 2b_{i,i}\ddot{q}_i + \sum_{j \ne i} b_{ij}\ddot{q}_j + \sum_j c_{ji}\dot{q}_j$; $\frac{\partial L}{\partial q_i} = 2a_{i,i}q_i + \sum_{j \ne i} a_{ij}q_j + \sum_j c_{ij}\dot{q}_j$; $\frac{\partial F_i}{\partial q_j} = \alpha_{i,j}$; $\frac{\partial F_i}{\partial \dot{q}_j} = \beta_{i,j}$

The second matrix is:

$$\begin{aligned}[\alpha]_{i,j} &= \alpha_{i,j} \qquad j \le 6 \\ &= 0 \qquad\quad 6 < j \le 12\end{aligned} \quad {}^{6} \tag{3.30}$$

i.e.

$$[\alpha] = \begin{bmatrix} \alpha_{1,1} & \alpha_{1,2} & \alpha_{1,3} & \alpha_{1,4} & \alpha_{1,5} & \alpha_{1,6} & 0 & 0 & 0 & 0 & 0 & 0 \\ \alpha_{1,2} & \alpha_{2,2} & \alpha_{2,3} & \alpha_{2,4} & \alpha_{2,5} & \alpha_{2,6} & 0 & 0 & 0 & 0 & 0 & 0 \\ \alpha_{1,3} & \alpha_{2,3} & \alpha_{3,3} & \alpha_{3,4} & \alpha_{3,5} & \alpha_{3,6} & 0 & 0 & 0 & 0 & 0 & 0 \\ \alpha_{1,4} & \alpha_{2,4} & \alpha_{3,4} & \alpha_{4,4} & \alpha_{4,5} & \alpha_{4,6} & 0 & 0 & 0 & 0 & 0 & 0 \\ \alpha_{1,5} & \alpha_{2,5} & \alpha_{3,5} & \alpha_{4,5} & \alpha_{5,5} & \alpha_{5,6} & 0 & 0 & 0 & 0 & 0 & 0 \\ \alpha_{1,6} & \alpha_{2,6} & \alpha_{3,6} & \alpha_{4,6} & \alpha_{5,6} & \alpha_{6,6} & 0 & 0 & 0 & 0 & 0 & 0 \end{bmatrix} \tag{3.31}$$

The third matrix in (3.27) is then:

$$\begin{aligned}[C_2]_{i,j} &= 0 \qquad\qquad j \le 6 \\ &= c_{i,j-6} - c_{j-6,i} \qquad 6 < j \le 12\end{aligned} \tag{3.32}$$

i.e.

$$[C_2] = \begin{bmatrix} 0 & 0 & 0 & 0 & 0 & 0 & 0 & c_{1,2}-c_{2,1} & c_{1,3}-c_{3,1} & c_{1,4}-c_{4,1} & c_{1,5}-c_{5,1} & c_{1,6}-c_{6,1} \\ 0 & 0 & 0 & 0 & 0 & 0 & c_{2,1}-c_{1,2} & 0 & c_{2,3}-c_{3,2} & c_{2,4}-c_{4,2} & c_{2,5}-c_{5,2} & c_{2,6}-c_{6,2} \\ 0 & 0 & 0 & 0 & 0 & 0 & c_{3,1}-c_{1,3} & c_{3,2}-c_{2,3} & 0 & c_{3,4}-c_{4,3} & c_{3,5}-c_{5,3} & c_{3,6}-c_{6,3} \\ 0 & 0 & 0 & 0 & 0 & 0 & c_{4,1}-c_{1,4} & c_{4,2}-c_{2,4} & c_{4,3}-c_{3,4} & 0 & c_{4,5}-c_{5,4} & c_{4,6}-c_{6,4} \\ 0 & 0 & 0 & 0 & 0 & 0 & c_{5,1}-c_{1,5} & c_{5,2}-c_{2,5} & c_{5,3}-c_{3,5} & c_{5,4}-c_{4,5} & 0 & c_{5,6}-c_{6,5} \\ 0 & 0 & 0 & 0 & 0 & 0 & c_{6,1}-c_{1,6} & c_{6,2}-c_{2,6} & c_{6,3}-c_{3,6} & c_{6,4}-c_{4,6} & c_{6,5}-c_{5,6} & 0 \end{bmatrix} \tag{3.33}$$

The fourth matrix in (3.27) is:

$$\begin{aligned}[\beta]_{i,j} &= 0 \qquad j \le 6 \\ &= \beta_{i,j-6} \qquad 6 < j \le 12\end{aligned} \quad {}^{7} \tag{3.34}$$

i.e.:

$$[\beta] = \begin{bmatrix} 0 & 0 & 0 & 0 & 0 & 0 & \beta_{1,1} & \beta_{1,2} & \beta_{1,3} & \beta_{1,4} & \beta_{1,5} & \beta_{1,6} \\ 0 & 0 & 0 & 0 & 0 & 0 & \beta_{1,2} & \beta_{2,2} & \beta_{2,3} & \beta_{2,4} & \beta_{2,5} & \beta_{2,6} \\ 0 & 0 & 0 & 0 & 0 & 0 & \beta_{1,3} & \beta_{2,3} & \beta_{3,3} & \beta_{3,4} & \beta_{3,5} & \beta_{3,6} \\ 0 & 0 & 0 & 0 & 0 & 0 & \beta_{1,4} & \beta_{2,4} & \beta_{3,4} & \beta_{4,4} & \beta_{4,5} & \beta_{4,6} \\ 0 & 0 & 0 & 0 & 0 & 0 & \beta_{1,5} & \beta_{2,5} & \beta_{3,5} & \beta_{4,5} & \beta_{5,5} & \beta_{5,6} \\ 0 & 0 & 0 & 0 & 0 & 0 & \beta_{1,6} & \beta_{2,6} & \beta_{3,6} & \beta_{4,6} & \beta_{5,6} & \beta_{6,6} \end{bmatrix} \tag{3.35}$$

---

[6] $\alpha_{i,k} = \alpha_{k,i}$

[7] $\beta_{i,k} = \beta_{k,i}$

3.6: EQUATIONS OF MOTION IN STATE-VARIABLE FORM.

For all practical purposes, it is convenient to turn (3.24) into a more symmetric form involving only first-order time derivatives ([44-47]). To this aim, we define the 12-components state vector $\vec{x}$ as:

$$\vec{x}^{T} = \left[q_1\ \dot{q}_1\ q_2\ \dot{q}_2\ q_3\ \dot{q}_3\ q_4\ \dot{q}_4\ q_5\ \dot{q}_5\ q_6\ \dot{q}_6\right] = \left[\vartheta_a\ \dot{\vartheta}_a\ \phi_a\ \dot{\phi}_a\ \vartheta_2\ \dot{\vartheta}_2\ \phi_2\ \dot{\phi}_2\ \vartheta_1\ \dot{\vartheta}_1\ \phi_1\ \dot{\phi}_1\right] \quad (3.36)$$

i.e.:

$$\begin{cases} x_{2i-1} = q_i \\ x_{2i} = \dot{q}_i \end{cases} \qquad i = 1,...,6 \quad (3.37)$$

Equation (3.24) can be written as:

$$\ddot{\underline{Q}} = \left[M\right]^{-1} \cdot \left[S\right] \cdot \begin{pmatrix} \underline{Q} \\ \dot{\underline{Q}} \end{pmatrix} \quad (3.38)$$

Combining equations (3.37) and (3.38), we obtain[8]:

$$\begin{cases} \dfrac{d}{dt} x_{2i-1} = x_{2i} & \left(i = 1,...,6\right) \\ \dfrac{d}{dt} x_{2i} = \displaystyle\sum_{j=1}^{6} \left(M^{-1}S\right)_{i,j} x_{2j-1} + \sum_{j=1}^{6} \left(M^{-1}S\right)_{i,2j} x_{2j} \end{cases} \quad (3.39)$$

(3.39) is a system of 12 equations involving only first-order time derivatives. These equations can be written in a compact matrix form as:

$$\dot{\vec{x}} = A \cdot \vec{x} \quad (3.40)$$

where A is now the square matrix 12×12 defined from $\mathbf{M}^{-1}$ and S after inserting rows and zeros:

- o i even, k odd $\quad a_{i,k} = \left(M^{-1}S\right)_{i,\frac{k-1}{2}+1}$ (3.41)
- o i even, k even $\quad a_{i,k} = \left(M^{-1}S\right)_{i,\frac{k-2}{2}+7}$ (3.42)
- o i odd $\quad \begin{cases} a_{i,i+1} = 1 \\ a_{i,k\neq i+1} = 0 \end{cases}$ (3.43)

---

[8] Inserting the definition (3.37) in (3.38) we obtain: $\begin{cases} \dfrac{d}{dt} x_{2i-1} = \dfrac{d}{dt} q_i \\ \dfrac{d}{dt} x_{2i} = \dfrac{d}{dt} \dot{q}_i = \left(M^{-1}S\right)_{\text{Line i}} \begin{bmatrix} \underline{Q} \\ \dot{\underline{Q}} \end{bmatrix} \end{cases}$

The relations (3.40), (3.41), (3.42) and (3.43) are central equations, written in a form amenable for numerical evaluation. The eigenvalues of the A matrix correspond to the normal modes of the rotor, and the solution of the set of differential equations (3.40) completely determines the small-amplitude dynamical behaviour of the rotor modelled in figure 3.2.

3.7: ROTATING AND NON-ROTATING DAMPING.

By means of equations (3.21), (3.22) and (3.23) we can in principle impose any known force determining the dynamical behaviour of the rotor. In the following we specialize such a procedure to include dissipative force $\vec{F}_{damp\_R}$ due to rotating and $\vec{F}_{damp\_NR}$ due to non-rotating damping mechanism.
The rotating part of the dissipative force (3.44) is to be ascribed to the dissipations of the laminar suspensions. In supercritical rotation, this acts to destabilize the system, generating whirl motions.

$$\vec{F}_{damp\_R} = -\Gamma_{Ra}\left[\dot{\hat{L}}_a - \left(\dot{\hat{L}}_a \cdot \hat{z}'\right)\cdot \hat{z}'\right] - \sum_{\lambda=1,2} \Gamma_{R\lambda}\left[\dot{\hat{L}}_\lambda - \left(\dot{\hat{L}}_\lambda \cdot \hat{L}_a\right)\cdot \hat{L}_a\right] \qquad (3.44)$$

The non-rotating damping has instead the effect of stabilizing the system in supercritical rotation. In our rotor, it is applied only to one mass: the passive damper acts only on the inner mass while the active damper acts only on the outer one. It can be written as:

$$\vec{F}_{damp\_NR} = -\Gamma_{NR}\left[\vec{v}_i + \vec{\omega}_s \times \vec{L}_i\right] \qquad (3.45)$$

3.8: NUMERICAL SIMULATION OF THE GGG SYSTEM.

The simulational method that we have implemented, rigorously follows the derivation outlined in this chapter. We have found very convenient to use the Matlab environment, with special packages that are the Symbolic Toolbox and Simulink, as it allows us to perform all the needed symbolic calculations and numerical evaluations, together with the data analysis from the experiment ([48 - 49]).
This means that we start from the formal Lagrange function written in equations (3.A.24), (3.A.25), (3.A.26) and (3.13) by means of symbolic vector operations. We thus specify the choice (3.1),(3.2) and (3.3) for the generalized coordinates with respect to the rotating reference frame and define accordingly all the vectors entering the lagrangean function. We then keep carrying on the symbolic computation by linearizing and expanding the Lagrange function as in (3.20), and define the matrices A_2, C_2, α, β and A. Once the system parameters are fixed (see below), the numerical computation takes place, which uses standard packages to find eigenvalues and eigenvectors of the A matrix, that are the nominal frequencies and modes of the spinning rotor. The A matrix is then inserted as input to perform the dynamical simulation within standard transfer-function method used in the Simulink toolbox.
The parameters which govern the GGG physics are the geometrical dimensions of the three bodies, their weight, the mounting error $\vec{\varepsilon}$, the elastic constants, length and anisotropy factor

of the three laminar suspensions, and the quality factor *Q*. To these parameters, which are fixed after construction, we must add the spinning frequency $\nu_s=\omega_s/2\pi$ that can be varied in the course of the experiment by acting on the stepping motor. The balancing of the beams and the differential period of oscillation can also be adjusted as already discussed, by moving small masses along the arm (i.e. by changing ΔL in the model). Of the whole set of parameters, the anisotropy factor Λ of the suspensions and the construction and mounting error ε are not measured from the instrument. $\Lambda$is fixed together with the balancing ΔL so as to reproduce the natural frequencies of the non-spinning instrument. The mounting error ε is taken to be in the range 1μm - 200μm, and it is *a posteriori* checked to have a non-sizable effect on these results. Q values have been taken from measurements (see chapter 5). We have inserted as inputs of the numerical calculation all the above parameters as determined from the real instrument, and listed in tables 3.1 and 3.2, the spinning frequency varying in the range $0\text{Hz} \le \nu_S \ge 5\text{Hz}$.

Body	Mass (kg)	Inner Radius (cm)	Outer Radius (cm)	Height (cm)	L_λ (cm)
Arm	0.3	3.3	3.5	38+ΔL	19
Mass 1	10	8.0	10.9	21.0	4.5
Mass 2	10	12.1	13.1	29.8	42.5+ΔL

Table 3.1: Governing parameters for the numerical calculations: geometrical dimensions of the real bodies.

Suspension	ℓ (cm)	k (dyne/cm)	Λ
Central	0.5	$10^6\ \ell^2 / L_a^2 = 6.9\cdot 10^2$	2.58
Mass 1 – Inner Cylinder	0.5	10^6	1
Mass 2 – Outer Cylinder	0.5	10^6	1

Table 3.2: Governing parameters for the numerical calculations: the laminar suspensions.

3.9: NORMAL MODES AS DERIVED FROM THE NUMERICAL SIMULATION.

We have solved for the eigenvalues ν_n of the matrix A in equations (3.41), (3.42) and (3.43), using the system parameters listed in tables 3.1 and 3.2. We summarize in figure 3.3 our results for ν_n in the non-rotating frame as function of the rotor spinning frequency ν_s. Theoretical data for ν_n vs. ν_s are displayed both in the absence (solid-blue lines) and in the presence (open circles) of damping, and are compared with the available experimental data (red crosses). The Fast Fourier Transform has been used to find the frequency components of the signal acquired by the capacitance bridge of GGG, after conversion in the non-rotating reference frame. The bisecting red line separates the supercritical ($\nu<\nu_s$) from the subcritical ($\nu>\nu_s$) region. Vertical lines bound the instability regions. Positive and negative signs of the frequency refer to the counter-clockwise and clockwise spinning rotor. Figure 3.3 represents the central result of this chapter, and in the following we proceed to provide a detailed

description of its relevant features. These are the comparison against the experiment and the role of damping, the low-frequency behaviour, the scissor shape, the splitting of crossing modes, and the presence of instability regions.

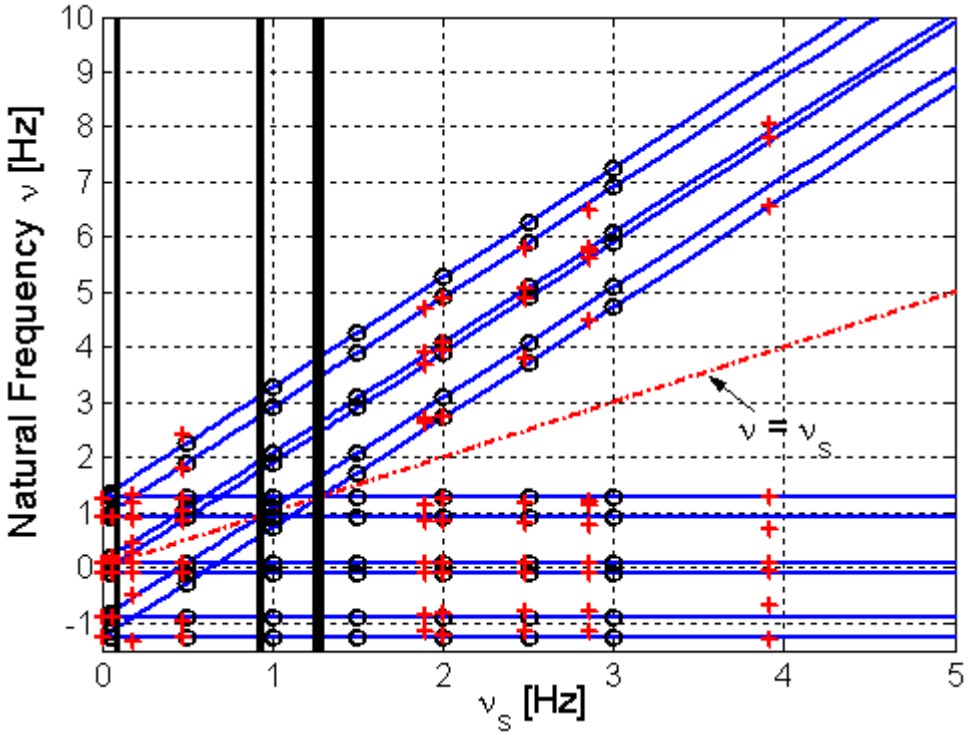

Figure 3.3: Normal modes of the GGG rotor. The frequency ν_n of the normal modes is plotted as a function of the spin frequency. Solid-blue lines: theoretical results without damping, showing no significant difference with the case in the presence of damping (open circles). Red crosses: experimental data. The bisecting red line $\nu=\nu_s$ separates the supercritical ($\nu<\nu_s$) from the subcritical ($\nu>\nu_s$) region. Vertical black lines bound the instability regions.

3.9.A: COMPARISON WITH THE EXPERIMENT.

In the experiment, the rotor is first accelerated to spin at given ν_s by means of the stepping motor. Then, the natural modes are excited by forcing the test bodies into oscillation in the x′ or y′ directions at frequencies close to $\nu_n^0 = \nu_n(\nu_s = 0)$ by means of the actuators. The excitation is performed for a variable amount of time corresponding to several periods of oscillation. The actuators are then switched off, and the bodies' displacements are recorded as functions of time by means of the read out described in chapter 2. Data are acquired in the rotating reference frame. A coordinates transformation is then performed (see chapter 5 for details) to obtain the relative displacement between the two test masses in the non-rotating reference frame. The Fast Fourier Transform (FFT) is used to find the frequency components of the signal. The strong peaks in the FFT of the signal are in correspondence with the natural frequencies of the rotor. In the experimental spectra as well as in the theory, the weights of the modes in the subcritical region $\nu>\nu_s$, are quite small, indicating that the non dispersive modes are preferably excited. For this reason, while the peaks in correspondence with the non-dispersive modes have always been found, the frequencies in correspondence with the

subcritical modes were not always excited. The experimental data, resulting from averaging over several measurements, are represented as red crosses in figure 3.3, while the theoretical prediction is displayed by the solid lines. Excellent agreement is evidently found between the theory and the experiment, which validates the model developed.

3.9.B: THE ROLE OF DAMPING.

We have numerically checked that the very small dissipations present in our system do not significantly shift the natural-mode frequencies. This is seen from figure 3.3 where the results for the rotor with inclusion of damping (open circles) stay on the solid lines, obtained in the absence of damping. As expected, dissipation affects instead the line-shape of the peaks, making them wider than in the absence of damping.

3.9.C: THE LOW-FREQUENCY LIMIT.

At zero spinning frequency (ν_S=0Hz), previous theoretical and experimental results for the non-rotating system have been recovered. In this case, data are acquired in the inertial reference frame. As shown in figure 3.4, zoomed from figure 3.3, the non-spinning rotor is characterized by three normal frequencies for the instrument with ideally isotropic springs, the three bodies oscillating in a vertical plane.

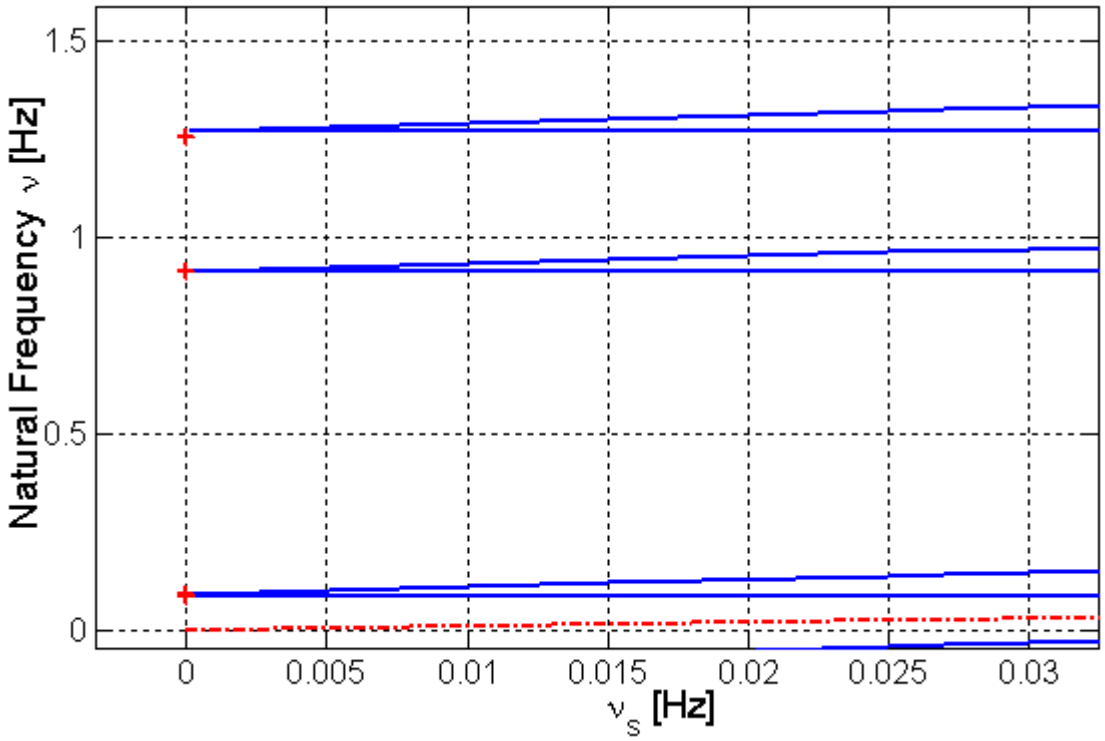

Figure 3.4: Normal modes of the GGG rotor. The low-frequency behaviour is zoomed. Solid-blue lines: theoretical results. Red crosses: experimental data.

The frequency ν_d^0=0.09 Hz corresponds to the differential mode, where the centres of mass of the two test bodies oscillate in opposition of phase; the frequencies ν_{c1}^0=0.91Hz and

ν_{c2}^0=1.26 Hz correspond to common modes, in which the total centre of mass of the two test bodies is displaced from the vertical (i.e. the centres of mass of the two cylinders oscillate in phase). It is important to notice that the frequencies ν_d^0=-0.09 Hz, ν_{c1}^0=-0.91 Hz and ν_{c2}^0=-1.26 Hz are also present[9]. If the springs have non-isotropic behaviour in two orthogonal directions, as in the case of our real cardanic suspensions, each natural frequency is expected to split up ($\nu \to \nu \pm \delta\nu$ where $\delta\nu \simeq 10^{-2} \div 10^{-3}$ Hz). This is zoomed in figure 3.5, where the splitting for the differential mode is evident. Each couple of splitted frequencies has a corresponding couple with negative sign. The total number of frequencies is then 12, 6 with negative sign and 6 with positive sign, corresponding to the eigenvalues of the matrix A (12×12).

3.9.D: NORMAL MODES AS FUNCTIONS OF THE SPIN FREQUENCY.

Figure 3.5 shows that each natural frequency of the non-spinning system is split up into two branches at ν_s>0 Hz, a lower branch remaining approximately constant and an upper branch increasing with $2\nu_s$. This characteristic scissors' shape can be traced back to general properties of spinning bodies (see also chapter 1, sections 1.10 and 1.11).

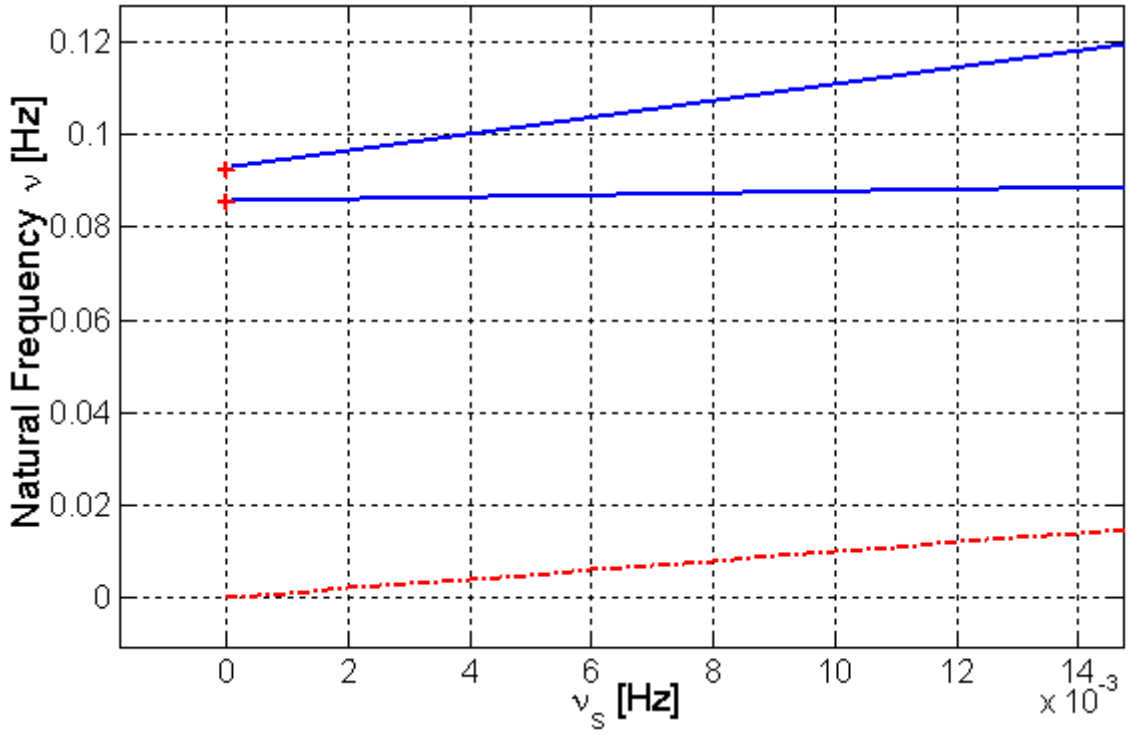

Figure 3.5: Differential mode ν_d^0=0.09Hz of the GGG rotor. The splitting of the mode due to anisotropy of the cardanic suspensions, is evidenced starting from ν_s=0Hz. Solid-blue lines: theoretical results. Red crosses: experimental data.

The two branches may cross at selected frequencies in the regime $\nu_d^0/2 < \nu_s < \nu_{c2}^0/2$. Crossing and anticrossing of degenerate modes is a very general concept, which applies to a variety of physical systems running from classical to quantum mechanics, from single to

[9] From now on, positive frequencies are connected with forward whirl (anti-clockwise), negative frequencies with backward whirl (clockwise).

many-particles physics. We have found in the numerical results all the 15 crossings expected for our system. At the present time, their role is still under investigation.

3.9.E: INSTABILITY REGIONS.

Dynamical instability may occur whenever the values of the natural frequencies are in proximity of the spinning frequency. In such regions, the oscillation amplitude is exponentially growing. This is a well-known characteristic of rotating machines, and in chapter 1 it has been described within the simple model of the so-called Jeffcott rotor. The number of instability regions can be predicted from figure 3.3 after drawing the dotted-dashed line $\nu=\nu_s$. We have found indeed three instability regions, and zoomed the one at lowest frequency in figure 3.6.

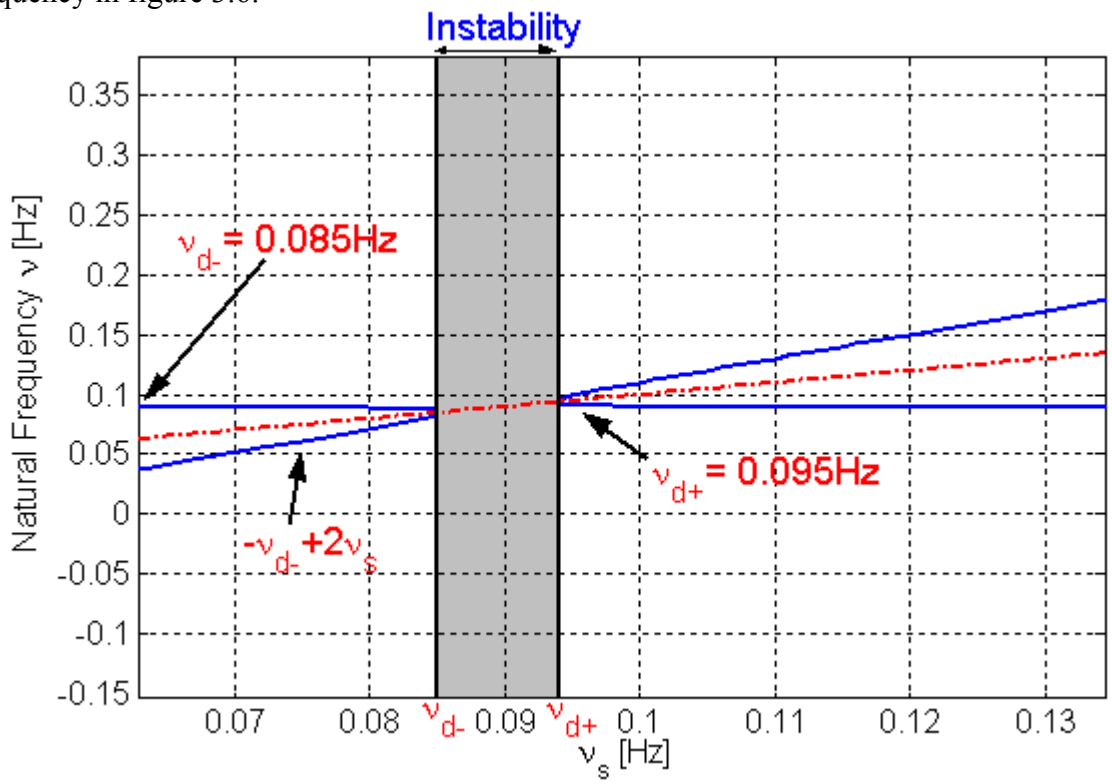

Figure 3.6: Normal modes of the GGG rotor. The lowest-frequency instability region is zoomed from figure 3.3.

We may have a flavour of the unstable behaviour of the system by evaluating the characteristics of the instability region connected with the differential natural frequency ν_d. We have shown that if the springs have non-isotropic behaviour each natural frequency is expected to split up. The differential natural frequency ν_d is split up into $\nu_{d+}=\nu_d+\delta\nu=0.095\text{Hz}$ and $\nu_{d-}=\nu_d-\delta\nu=0.085\text{Hz}$ (red crosses in figure 3.7), where $\delta\nu$ is a small shift in the frequency, typically of order of $10^{-2}\div10^{-3}$ Hz. We have also shown the presence of the frequencies $-\nu_{d+}$ and $-\nu_{d-}$ with negative sign, corresponding to backward whirls. Hence, we have demonstrated that there are branches increasing with $2\nu_s$. We can combine these three properties of the system and find the intersection between the flat branch $\nu(\nu_s)=\nu_{d-}$ with the increasing branch $\nu(\nu_s)=-\nu_{d-}+2\nu_s$. The intersection is found for $\nu_s=\nu_{d-}$, i.e. when the two branches cross the bisecting line $\nu(\nu_s)=\nu_s$. The presence of an

elastic anisotropy of the rotating part of the system causes the occurrence of an instability range that spans from the lowest $\nu_s = \nu_{d-}$ to the highest $\nu_s = \nu_{d+}$ critical speed. The same conclusion has already seen in section 1.11 dealing with the non-isotropic Jeffcott rotor and it is still valid for the common mode natural frequencies. Interestingly enough, this theoretical results shown in figures 3.3 and 3.6 may explain the difficulty that we meet in the experiment while spinning the rotor through the frequency range 0.9→1.3 Hz. In this range indeed, we see from figure 3.3 that two sizable and adjacent instability regions are predicted. The unstable behaviour of the instrument in this frequency range normally requires the use of a passive damper (see chapter 2 for details). In fact, non-rotating damping reduces the instability range between the critical speeds.

3.9.F: GGG FREQUENCY RESPONSE.

In figure 3.7 the FFT of the x component of the relative displacement between the two test bodies for the non-spinning rotor is shown (red curve) in comparison with the theoretical transfer function of the system.

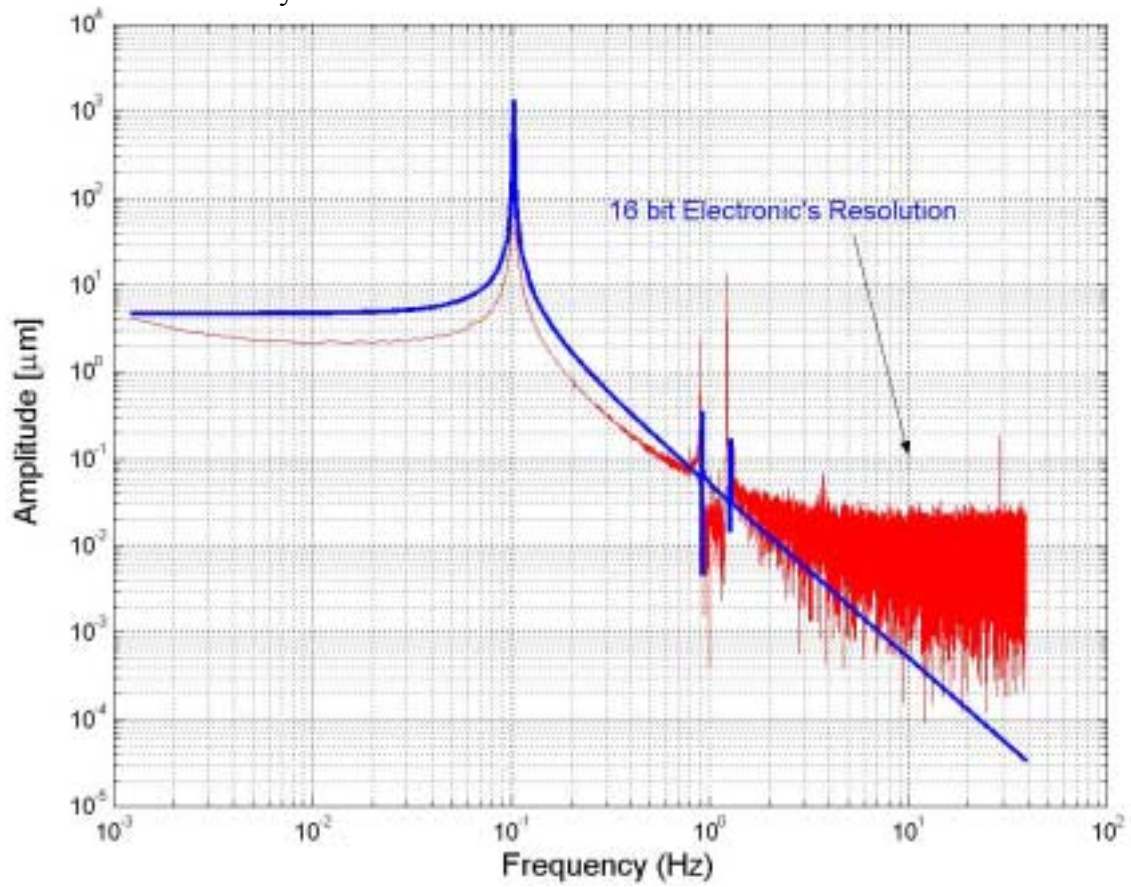

Figure 3.7: Comparison with the experiment. Red curve: FFT of the relative displacement (experimental data) as function of the frequency for the non-spinning rotor. Blue curve: theoretical frequency response of the system as predicted by the mathematical model of GGG. At high frequency (i.e. ν>2Hz), the red curve is almost flat. This is connected with the 16bit electronics' limit of resolution.

Since the rotor was not spinning, only three peaks are visible at frequency ν_d^0=0.1 Hz (it corresponds to the differential mode; when those data have been acquired (September 2001)

the differential period was about 10s, i.e. a little different from the differential period (about 11s in May 2002) in figures 3.3 – 3.6), and at frequencies ν_{c1}^0=0.91Hz and ν_{c2}^0=1.26 Hz. Note that if we had shown the y component of the relative displacement, the figure would have been similar but the peaks would have been at frequencies a little different because of the anisotropy. A good agreement is evidently found between the theory and the experiment.
In figure 3.8 the frequency components of the relative displacement between the test bodies along x direction in the laboratory frame (rotor spinning at ν_s =.05Hz) is shown. Data have been acquired in August 2002. 4 peaks can be recognized: one corresponding to ν_s, two corresponding to the differential frequency splitted up into $\nu_{d+} = \nu_d + \delta\nu$ and $\nu_{d-} = \nu_d - \delta\nu$, and one corresponding to the increasing branch $-\nu_{d-} + 2\nu_s$.

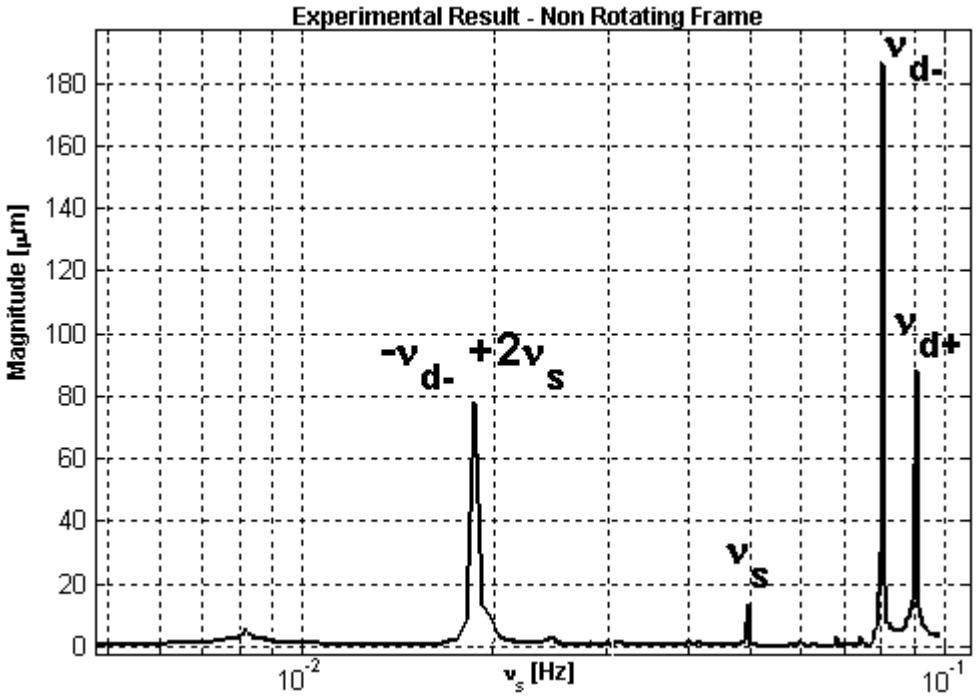

Figure 3.8: Frequency components of the relative displacement. The rotor was spinning at 0.05Hz. 4 peaks can be recognized: one corresponding to the spin frequency ν_s, two corresponding to the differential frequency splitted up into $\nu_{d+} = \nu_d + \delta\nu$ and $\nu_- = \nu_d - \delta\nu$, and one corresponding to the increasing branch $-\nu_{d-} + 2\nu_s$.

3.10: APPROXIMATED FORMULA FOR DERIVING THE NORMAL MODES.

The frequencies $\nu_{d+} = \nu_d + \delta\nu = 0.095\text{Hz}$ and $\nu_{d-} = \nu_d - \delta\nu = 0.085\text{Hz}$ correspond to differential modes of oscillation, where the centres of mass of the two test bodies move in opposition of phase. If the springs have isotropic behaviour in the horizontal plane, the small shift $\delta\nu$ vanishes and $\nu_{d+} = \nu_{d-} = \nu_d$. In section 2.3, for simplicity reasons, we have evaluated an analytical expression of the differential frequency (period) in the very simplified case in which the springs are isotropic and the bodies are neither rotating (i.e. ϕ_a=ϕ_1=ϕ_2 =0) nor subject to any dissipative or other external forces except for gravity. The numerical study of the eigenvalues and eigenvectors of the A matrix in equations (3.35) and (3.36) demonstrates that in the differential mode the coupling arm oscillates and the cylinders' centres of mass

move within the horizontal plane in opposition of phase while their symmetry axis remains aligned with the vertical $\hat{z}$ (i.e. $\vartheta_1=\vartheta_2=0$). The minimal model of the system is drawn in figure 2.3.b.

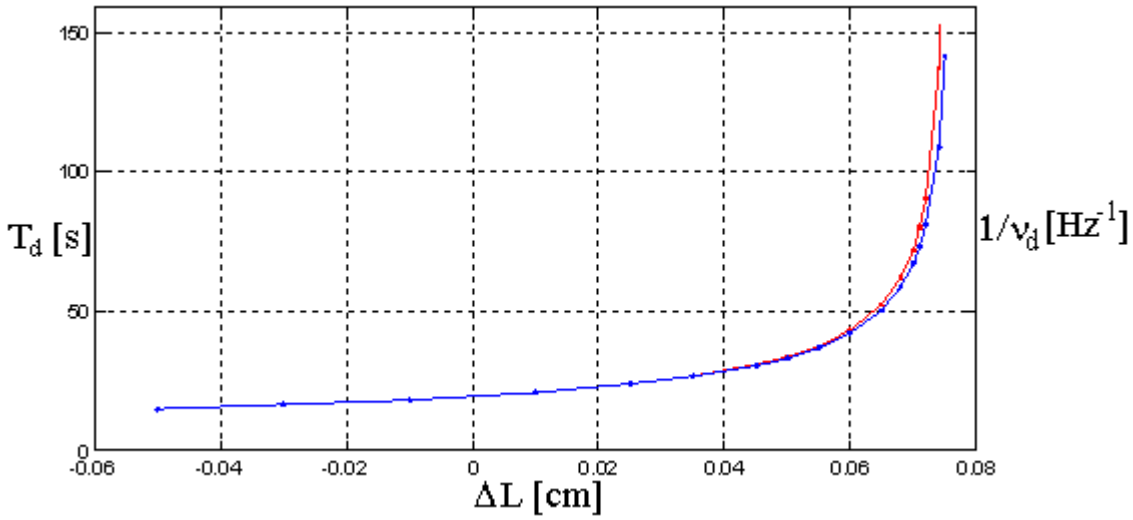

Figure 3.9: Differential period (inverse of the differential frequency ν_d) as a function of ΔL. Excellent agreement is found between the results of numerical simulations (red) and the approximated formula (blue).

Under the reasonable assumption that $\vartheta_1=\vartheta_2=0$ and $\phi_i=0$ the analytical formula of the differential period (2.2) is easily obtained. ΔL can be adjusted to be either slightly positive or negative, resulting into a lower or higher differential frequency, while the value of common mode frequencies is not influenced by it. In figure 3.9 the differential period (inverse of the differential frequency) is shown as a function of ΔL; the approximated value (blue) of the period (2.2) is compared with the results of the numerical simulations (red). We have derived an approximated formula for the natural frequency $\nu_{c1}=0.9$ Hz too. In the common mode ν_{c1}, the coupling arm and the cylinders' centres of mass oscillate in phase (i.e. $\vartheta_1=\vartheta_2=\vartheta_a$). Only the central laminar suspension undergoes deformations. The minimal model of the system is drawn in figure 3.10.

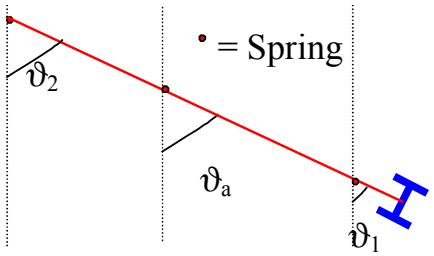

Figure 3.10: Common modeν_{c1}. Minimal model of GGG as detailed in the text.

The natural frequeny is easily obtained after writing the equation of motion[10], namely:

$$\nu_{c1\_app}=\sqrt{\frac{k\ell^2+(m_1+m_2)g(L+L_1)}{\left[I_1+I_2+(m_1+m_2)(L+L_1)^2\right]}}\Big/2\pi \qquad (3.46)$$

[10] They can be written starting from the lagrangean L. The total potential energy U expanded to 2-nd order is: $U=0.5[k\ell^2+(m_1+m_2)g(L+L_1)]\vartheta_a^2$. The kinetic energy is: $T=0.5[(I_1+I_2)+(m_1+m_2)(L+L_1)^2]\dot{\vartheta}_a^2$.

The natural frequency (3.46) corresponding to the parameters listed in tables 3.1 and 3.2 is evaluated to be ν=0.94 Hz in reasonable agreement with the measured value 0.91 Hz. It is important to notice that equation (3.46) depends only on the governing parameters of the system and it is not a function of ΔL.
At last, we derive an approximated formula for the natural frequency ν_{c2}=1.26 Hz. In the common mode ν_{c2} the coupling arm and the outer cylinder oscillate in phase (i.e. $\vartheta_2=\vartheta-\alpha\vartheta_a$). The inner cylinder oscillates in opposition of phase, i.e. $\vartheta_1=-\alpha\vartheta_a$.

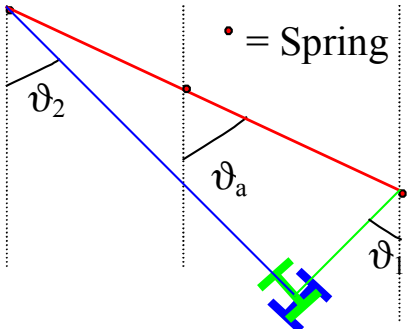

Figure 3.11: Common modeν_{c2}. Minimal model of GGG as detailed in the text.

The α coefficient is determined by imposing that the displacement of the outer cylinder's centre of mass $\sim L_2\vartheta_a(1-\alpha)-L\vartheta_a$ to be equal to the displacement of the inner cylinder's centre of mass $\sim L\vartheta_a-\alpha L_1\vartheta_a$, i.e. $\alpha=L_1/2L$. The natural frequency is obtained in the standard manner:

$$\nu_{c2\_app}=\sqrt{\frac{\left(k_a+\alpha^2k_2+(1+\alpha)^2k_1\right)\ell^2+g\left[m_1L_1\alpha^2+m_2L_2(1-\alpha)^2\right]}{\left[\alpha^2I_1+I_2(1-\alpha)^2+m_1(L-\alpha L_1)^2+m_2(L_2(1-\alpha)-L)^2\right]}}\Big/2\pi \quad (3.47)$$

The natural frequency (3.47) corresponding to the parameters listed in tables 3.1 and 3.2 is evaluated to be ν=1.01 Hz while the measured value is 1.26 Hz. As for ν_{c1}, ν_{c2} (3.47) depends only on the governing parameters of the system and it is not a function of ΔL. Equations (2.2), (3.46) and (3.47) are simple expressions for the natural frequencies of the GGG accelerometer. They are useful in order to understand the dependence of these frequencies from the governing parameters of the apparatus.

3.11: CONCLUDING REMARKS.

We have demonstrated that the linearized model set up in this chapter can quantitatively account for the dynamical response of the GGG rotor, as determined from the experiment (section 3.10). We have shown that a qualitative understanding is also possible by means of helpful analytical solutions of the simplified model under special limits. Along these lines, we have been able to establish a detailed knowledge of the instrument functioning and features, especially in regard to the normal modes in the whole range of spinning frequencies from subcritical to supercritical rotation, and as functions of the governing parameters listed in table 3.1 and 3.2.
To be definite, the following result is of central importance from this chapter. The normal modes of the non-spinning rotor split up into two scissor-like branches as in figure 3.3, once

the instrument is set in rotation. Of the two branches, only the non-dispersive one remains significantly excited, meaning that rotation can be considered coupled from the intrinsic response of the system only in the intermediate range of ν_s. We have also found that damping due to dissipative suspensions is not a concerning issue, and verified the presence of mechanical instability regions, allowing us to predict at which frequencies a stabilizing passive damper has to be used.

CHAPTER 4:

DYNAMICAL RESPONSE OF THE GGG DIFFERENTIAL ACCELEROMETER.

4.1: INTRODUCTION.

The GGG experiment has been described in chapter 2, and its underlying physics has been embodied (in chapter 3) in an effective model that fully accounts for the measured normal modes of the GGG rotor in the whole range of frequencies from subcritical to supercritical rotation.
The solution of the model equations, performed after setting an user-friendly and versatile simulational environment, also demonstrates two good features of GGG, namely that rotation is decoupled from the normal modes of the non spinning instrument, for a wide range of (low and high) frequencies, and that damping does not introduce appreciable shifts of the modes frequencies. In the present chapter, we apply the model to evaluate the rejection capability of the GGG rotor as determined by all the governing system parameters [37].
This study naturally provides an effective tool to optimise the real instrument in response to external disturbances. While we refer to chapters 2 and 3 for all the definitions and descriptive parts of the experiment and of the model, chapter 4 is organized as follows. We complete in section 4.2 the description of the numerical method as already initiated in chapter 3, specializing here to the introduction of external forces. In section 4.3 and 4.4 we define the coefficients of two new matrices, B and C, already introduced in section 4.2.
We show in section 4.5 how the transfer matrix and thus the output are transformed in the non-rotating reference frame. In sections 4.6, 4.7, 4.8 and 4.9 we first define the rejection factor and fix the theoretical understanding by evaluating it in the case of the non spinning rotor in terms of a scaling parameter, and then present the simulational results that validate the analytical solution in the low and high spin frequency regime, and demonstrate the enhanced rejection for intermediate frequencies. We devote section 4.10 to place these results in the realistic range of parameters of the GGG rotor. Sections 4.11 and 4.12 are devoted to the self-centring.

4.2: EXTERNAL FORCES AND COMPUTATION OF THE TRANSFER FUNCTION.

In charter 3 we have introduced only internal forces with the exception of the non-rotating damper. We devote this section to the introduction of external forces: here we describe the problem in the state – variable form, where the external forces determining the rotor dynamical behaviour, expanded to first order in the coordinates x_i and to zero order in the forces, are included on the right hand side of equation (3.40), that becomes:

$$\dot{\vec{x}}=A\cdot\vec{x}+B\cdot\vec{u} \qquad (4.1)$$

where $\vec{u}$ is an input vector[1]. (4.1) is a system of 12 equations involving only first-order time derivatives ([44-49]). The A matrix (see equation (3.41), (3.42) and (3.43)) is said " State Matrix " and it is n × n, while the B matrix is known as "Input Matrix ", and it is n × m ($\vec{u}$ has m components). The definition of the problem is completed after specifying the p components output vector $\vec{y}$, by means of the general expression:

$$\vec{y}=C\cdot\vec{x}+D\cdot\vec{u} \tag{4.2}$$

involving the output p × n matrix C, and the coupling input – output matrix D with dimensions p × m. In our problem D=0, and the $\vec{y}$'s components are the displacements of the masses from their equilibrium positions.
Equations (4.1) and (4.2) are solved in the frequency domain ($\vec{x}(t)\rightarrow X(s),\vec{u}(t)\rightarrow U(s)\ldots$), after Laplace transform to the variable s=jω:

$$\begin{cases} s\,I\,X(s)=AX(s)+BU(s) \\ Y(s)=CX(s) \end{cases} \tag{4.3}$$

(I is the identity matrix). Combining the two equations in (4.3) into one equation, we have direct link between the output vector and the input forces:

$$\begin{cases} X(s)=(sI\text{-}A)^{-1}BU(s) \\ Y(s)=CX(s) \end{cases} \Rightarrow Y(s)=C(sI\text{-}A)^{-1}BU(s) \tag{4.4}$$

Equation (4.4) can be written in a more compact form:

$$Y(s)=H^{Rot}(s)U(s) \tag{4.5}$$

Equation (4.5) defines the p × m transfer matrix H in the rotating frame in terms of the A, B and C matrices:

$$H^{Rot}(s)=C(sI\text{-}A)^{-1}B \tag{4.6}$$

The derivations of B and C for the present problem are reported in sections 4.3 and 4.4. As we need the output $Y^{NR}(s)$ into the laboratory frame, we show in section 4.5 how the transfer matrix is transformed in the non-rotating frame.

4.3: THE C MATRIX.

Starting from equations (3.36) and (3.37), the equilibrium position is defined as:

$$\vec{x}^{0}=\left[\vartheta^{0}\quad 0\quad \vartheta_{2}^{0}\quad 0\quad \vartheta_{1}^{0}\quad 0\quad \phi^{0}\quad 0\quad \phi_{2}^{0}\quad 0\quad \phi_{1}^{0}\quad 0\right]^{T} \tag{4.7}$$

As in chapter 3, the label "a" refers to the suspension arm, the labels "1" and "2" to the inner and outer cylinders respectively. By combining equations (3.10), (3.11) and (3.12) with (4.7),

[1] In this work it is made of the m components of the external forces acting on the rotor.

the vectors pointing to the three bodies' centers of mass in the equilibrium position are readily obtained:

$$\vec{r}_a^{\,0,Rot} = \vec{\varepsilon} - \frac{\Delta L}{2}\begin{bmatrix} \sin(x_1^0)\cos(x_7^0) \\ \sin(x_1^0)\sin(x_7^0) \\ -\cos(x_1^0) \end{bmatrix} \tag{4.8}$$

$$\vec{r}_2^{\,0,Rot} = \vec{\varepsilon} - (L+\Delta L)\begin{bmatrix} \sin(x_1^0)\cos(x_7^0) \\ \sin(x_1^0)\sin(x_7^0) \\ -\cos(x_1^0) \end{bmatrix} + L_2\begin{bmatrix} \sin(x_3^0)\cos(x_9^0) \\ \sin(x_3^0)\sin(x_9^0) \\ -\cos(x_3^0) \end{bmatrix} \tag{4.9}$$

$$\vec{r}_1^{\,0,Rot} = \vec{\varepsilon} + L\begin{bmatrix} \sin(x_1^0)\cos(x_7^0) \\ \sin(x_1^0)\sin(x_7^0) \\ -\cos(x_1^0) \end{bmatrix} + L_1\begin{bmatrix} \sin(x_5^0)\cos(x_{11}^0) \\ \sin(x_5^0)\sin(x_{11}^0) \\ -\cos(x_5^0) \end{bmatrix} \tag{4.10}$$

At a certain time t, the position vectors of the three bodies are given by the following equations:

- coupling arm

$$\begin{aligned} \vec{r}_a^{\,Rot}(t) &= \vec{\varepsilon} - \frac{\Delta L}{2}\begin{bmatrix} \sin(x_1 + x_1^0)\cos(x_7 + x_7^0) \\ \sin(x_1 + x_1^0)\sin(x_7 + x_7^0) \\ -\cos(x_1 + x_1^0) \end{bmatrix} \\ &\sim \vec{\varepsilon} - \frac{\Delta L}{2}\begin{bmatrix} x_1\cos(x_1^0)\cos(x_7^0) - x_7\sin(x_1^0)\sin(x_7^0) + \sin(x_1^0)\cos(x_7^0) \\ x_1\cos(x_1^0)\sin(x_7^0) + x_7\sin(x_1^0)\cos(x_7^0) + \sin(x_1^0)\sin(x_7^0) \\ -\cos(x_1^0) + x_1\sin(x_1^0) \end{bmatrix} \\ &\sim \vec{r}_a^{\,0,Rot} - \frac{\Delta L}{2}\begin{bmatrix} x_1\cos(x_1^0)\cos(x_7^0) - x_7\sin(x_1^0)\sin(x_7^0) \\ x_1\cos(x_1^0)\sin(x_7^0) + x_7\sin(x_1^0)\cos(x_7^0) \\ x_1\sin(x_1^0) \end{bmatrix} \end{aligned} \tag{4.11}$$

- outer cylinder:

$$\begin{aligned} \vec{r}_2^{\,Rot}(t) \sim \vec{r}_2^{\,0,Rot} &- (L+\Delta L)\begin{bmatrix} x_1\cos(x_1^0)\cos(x_7^0) - x_7\sin(x_1^0)\sin(x_7^0) \\ x_1\cos(x_1^0)\sin(x_7^0) + x_7\sin(x_1^0)\cos(x_7^0) \\ x_1\sin(x_1^0) \end{bmatrix} \\ &+ L_2\begin{bmatrix} x_3\cos(x_3^0)\cos(x_9^0) - x_9\sin(x_3^0)\sin(x_9^0) \\ x_3\cos(x_3^0)\sin(x_9^0) + x_9\sin(x_3^0)\cos(x_9^0) \\ x_3\sin(x_3^0) \end{bmatrix} \end{aligned} \tag{4.12}$$

- inner cylinder:

$$\vec{r}_1^{\,Rot}(t) \sim \vec{r}_1^{\,0,Rot} + L\begin{bmatrix} x_1\cos(x_1^0)\cos(x_7^0) - x_7\sin(x_1^0)\sin(x_7^0) \\ x_1\cos(x_1^0)\sin(x_7^0) + x_7\sin(x_1^0)\cos(x_7^0) \\ x_1\sin(x_1^0) \end{bmatrix} + L_2\begin{bmatrix} x_5\cos(x_5^0)\cos(x_{11}^0) - x_{11}\sin(x_5^0)\sin(x_{11}^0) \\ x_5\cos(x_5^0)\sin(x_{11}^0) + x_{11}\sin(x_5^0)\cos(x_{11}^0) \\ x_5\sin(x_5^0) \end{bmatrix} \tag{4.13}$$

The displacements from the equilibrium positions is then:
- outer cylinder

$$\Delta\vec{r}_2^{\,Rot}(t) = \vec{r}_2^{\,Rot}(t) - \vec{r}_2^{\,0,Rot} \tag{4.14}$$

- inner cylinder

$$\Delta\vec{r}_1^{\,Rot}(t) = \vec{r}_1^{\,Rot}(t) - \vec{r}_1^{\,0,Rot} \tag{4.15}$$

Finally, we have the linearized expression of the relative position vector:

$$\Delta\vec{r}^{\,Rot}(t) = \Delta\vec{r}_2^{\,Rot}(t) - \Delta\vec{r}_1^{\,Rot}(t) = -(2L+\Delta L)\begin{bmatrix} x_1\cos(x_1^0)\cos(x_7^0) - x_7\sin(x_1^0)\sin(x_7^0) \\ x_1\cos(x_1^0)\sin(x_7^0) + x_7\sin(x_1^0)\cos(x_7^0) \\ x_1\sin(x_1^0) \end{bmatrix} + L_2\begin{bmatrix} x_3\cos(x_3^0)\cos(x_9^0) - x_9\sin(x_3^0)\sin(x_9^0) \\ x_3\cos(x_3^0)\sin(x_9^0) + x_9\sin(x_3^0)\cos(x_9^0) \\ x_3\sin(x_3^0) \end{bmatrix} - L_1\begin{bmatrix} x_5\cos(x_5^0)\cos(x_{11}^0) - x_{11}\sin(x_5^0)\sin(x_{11}^0) \\ x_5\cos(x_5^0)\sin(x_{11}^0) + x_{11}\sin(x_5^0)\cos(x_{11}^0) \\ x_5\sin(x_5^0) \end{bmatrix} \tag{4.16}$$

In our experiment, equation (4.5) is characterized by 2 outputs (the 2 components of $\vec{y}$), that are the components of the relative displacement $\Delta\vec{r}^{\,Rot}(t)$ (4.16) between the two test cylinders in the sensitivity plane ξ-η as measured in the rotating frame:

$$\vec{y} = \begin{bmatrix} y_1 \\ y_2 \end{bmatrix} = \begin{bmatrix} \Delta r_\xi^{Rot} \\ \Delta r_\eta^{Rot} \end{bmatrix} \tag{4.17}$$

Combining equations (4.2), (4.16) and (4.17), we obtain the coefficients of the C matrix:

$$C_{1,1} = -(2L+\Delta L)\cos(x_1^0)\cos(x_7^0) \tag{4.18.a}$$

$$C_{1,3} = L_2\cos(x_3^0)\cos(x_9^0) \tag{4.18.b}$$

$$C_{1,5} = -L_1\cos(x_5^0)\cos(x_{11}^0) \tag{4.18.c}$$

$$C_{1,7} = (2L+\Delta L)\,x_7\sin(x_1^0)\sin(x_7^0) \tag{4.18.d}$$

$$C_{1,9} = -L_2 x_9\sin(x_3^0)\sin(x_9^0) \tag{4.18.e}$$

$$C_{1,11} = L_1 x_{11} \sin(x_5^0)\sin(x_{11}^0) \tag{4.18.f}$$

$$C_{2,1} = -(2L + \Delta L)\cos(x_1^0)\sin(x_7^0) \tag{4.18.g}$$

$$C_{2,3} = L_2 \cos(x_3^0)\sin(x_9^0) \tag{4.18.h}$$

$$C_{2,5} = -L_1 \cos(x_5^0)\sin(x_{11}^0) \tag{4.18.i}$$

$$C_{2,7} = -(2L + \Delta L)\, x_7 \sin(x_1^0)\cos(x_7^0) \tag{4.18.l}$$

$$C_{2,9} = L_2 x_9 \sin(x_3^0)\cos(x_9^0) \tag{4.18.n}$$

$$C_{2,11} = -L_1 x_{11} \sin(x_5^0)\cos(x_{11}^0) \tag{4.18.o}$$

while all the coefficients not listed above are equal to zero. For all practical purposes, it is convenient to turn (4.18) into a more symmetric form:

$$\begin{cases} C_{1k} = \gamma_k \cos(x_k^0)\cos(x_{k+6}^0) & k \le 6 \\ C_{1k} = \gamma_k \sin(x_{k-6}^0)\sin(x_k^0) & k > 6 \\ C_{2k} = \gamma_k \cos(x_k^0)\sin(x_{k+6}^0) & k \le 6 \\ C_{2k} = -\gamma_k \sin(x_{k-6}^0)\cos(x_k^0) & k > 6 \end{cases} \tag{4.18.p}$$

where $\gamma_1 = -\gamma_7 = -(2L+\Delta L)$, $\gamma_3 = -\gamma_9 = L_2$, $\gamma_5 = -\gamma_{11} = -L_1$ and $\gamma_k = 0$ for even k.

4.4: THE B MATRIX.

In our model, the vector $\vec{u}$ in equation (4.1) is defined as the components of the given external forces $\vec{F}$ applied to the centers of mass of the two test bodies in the sensitivity plane in the rotating reference frame. As a consequence, $\vec{u}$ had to be composed of four components. Under reasonable conditions, instead, the problem can be studied by considering a two components input vector $\vec{u}$ [2].

$$\vec{u} = \begin{bmatrix} u_1 \\ u_2 \end{bmatrix} = \begin{bmatrix} F_\xi^{Rot} \\ F_\eta^{Rot} \end{bmatrix} \tag{4.19}$$

Hence, the B matrix transforms the 2 components $\vec{u}$ vector into its 12 components counterpart $B\vec{u}$. In this section we define the coefficients of the B matrix. To this aim, let us begin with writing equation (3.24) as follows:

$$[M]\cdot \underline{\ddot{Q}} = [S]\cdot \begin{pmatrix} \underline{Q} \\ \underline{\dot{Q}} \end{pmatrix} + \underline{F_g} \tag{4.20}$$

[2] For example, in case of common mode forces, the forces acting on the two bodies are the same, while when acting in a differential manner, they have the same amplitude but opposite sign.

where we have introduced the 6 component vector $\vec{F}_g$ of the generalized forces[3] defined as $\vec{F}_g = \left[B_g \right] \vec{u}$. $[B_g]$ is a 6×2 matrix. In the case of common mode external forces, we may figure out them as acting on both test masses and the coupling arm in the same way. The resulting B_g matrix is then:

$$B_g = \begin{bmatrix} \left(\frac{\partial r_{a,\xi}}{\partial \vartheta_a} \cdot \frac{m_a}{m_1} + \frac{\partial r_{1,\xi}}{\partial \vartheta_a} + \frac{\partial r_{2,\xi}}{\partial \vartheta_a} \right) & \left(\frac{\partial r_{a,\eta}}{\partial \vartheta_a} \cdot \frac{m_a}{m_1} + \frac{\partial r_{1,\eta}}{\partial \vartheta_a} + \frac{\partial r_{2,\eta}}{\partial \vartheta_a} \right) \\ \frac{\partial r_{2,\xi}}{\partial \vartheta_2} & \frac{\partial r_{2,\eta}}{\partial \vartheta_2} \\ \frac{\partial r_{1,\xi}}{\partial \vartheta_1} & \frac{\partial r_{1,\eta}}{\partial \vartheta_1} \\ \left(\frac{\partial r_{a,\xi}}{\partial \phi_a} \cdot \frac{m_a}{m_1} + \frac{\partial r_{2,\xi}}{\partial \phi_a} + \frac{\partial r_{1,\xi}}{\partial \phi_a} \right) & \left(\frac{\partial r_{a,\eta}}{\partial \phi_a} \cdot \frac{m_a}{m_1} + \frac{\partial r_{2,\eta}}{\partial \phi_a} + \frac{\partial r_{1,\eta}}{\partial \phi_a} \right) \\ \frac{\partial r_{2,\xi}}{\partial \phi_2} & \frac{\partial r_{2,\eta}}{\partial \phi_2} \\ \frac{\partial r_{1,\xi}}{\partial \phi_1} & \frac{\partial r_{1,\eta}}{\partial \phi_1} \end{bmatrix} \tag{4.21.a}$$

In equation (4.21.a), the factor m_a/m_1 has been introduced so that the external force produces on the arm the same force as on the inner and outer bodies. In the case of a differential force, we may figure out it having opposite signs when acting on the two test cylinders. The B_g matrix is expressed as:

$$B_g = \begin{bmatrix} \left(\frac{\partial r_{1,\xi}}{\partial \vartheta_a} - \frac{\partial r_{2,\xi}}{\partial \vartheta_a} \right) & \left(\frac{\partial r_{1,\eta}}{\partial \vartheta_a} - \frac{\partial r_{2,\eta}}{\partial \vartheta_a} \right) \\ -\frac{\partial r_{2,\xi}}{\partial \vartheta_2} & -\frac{\partial r_{2,\eta}}{\partial \vartheta_2} \\ \frac{\partial r_{1,\xi}}{\partial \vartheta_1} & \frac{\partial r_{1,\eta}}{\partial \vartheta_1} \\ \left(\frac{\partial r_{1,\xi}}{\partial \phi_a} - \frac{\partial r_{2,\xi}}{\partial \phi_a} \right) & \left(\frac{\partial r_{1,\eta}}{\partial \phi_a} - \frac{\partial r_{2,\eta}}{\partial \phi_a} \right) \\ -\frac{\partial r_{2,\xi}}{\partial \phi_2} & -\frac{\partial r_{2,\eta}}{\partial \phi_2} \\ \frac{\partial r_{1,\xi}}{\partial \phi_1} & \frac{\partial r_{1,\eta}}{\partial \phi_1} \end{bmatrix} \tag{4.21.b}$$

[3] See equations (3.21), (3.22) and (3.23).

The coefficients $b_{i,k}$ of the matrix B are determined starting from the definition of the matrix B_g[4]:

- o i even, $b_{i,1}=\sum_{h=1}^{12}\left(M^{-1}\right)_{i,h}B_{g_{h,1}}$; $b_{i,2}=\sum_{h=1}^{12}\left(M^{-1}\right)_{i,h}B_{g_{h,2}}$ (4.22.a)
- o i odd $b_{i,k}=0$ (4.22.b)

4.5: THE TRANSFER FUNCTION IN THE NON-ROTATING REFERENCE FRAME.

We here show how to transform the transfer function (4.6) into the non-rotating frame. In this section the label NR refers to the vectors in the non-rotating frame while Rot to the same quantities in the rotating reference frame. In our setting, we may write for the two components outputs $\vec{y}^{NR}$ and inputs $\vec{F}^{NR}$ in the non-rotating frame as function of their counterparts in the rotating frame:

$$\begin{bmatrix} y_1^{NR} \\ y_2^{NR} \end{bmatrix}=\begin{bmatrix} \cos(\omega_s t) & -\sin(\omega_s t) \\ \sin(\omega_s t) & \cos(\omega_s t) \end{bmatrix}\cdot\begin{bmatrix} y_1^{Rot} \\ y_2^{Rot} \end{bmatrix} \tag{4.23.a}$$

$$\begin{bmatrix} F_1^{NR} \\ F_2^{NR} \end{bmatrix}=\begin{bmatrix} \cos(\omega_s t) & -\sin(\omega_s t) \\ \sin(\omega_s t) & \cos(\omega_s t) \end{bmatrix}\cdot\begin{bmatrix} u_1^{Rot} \\ u_2^{Rot} \end{bmatrix} \tag{4.23.b}$$

We show in appendix 4.A how the equation (4.5) is transformed in the non-rotating frame. The result[5] is:

$$\begin{bmatrix} y_1^{NR}(s) \\ y_2^{NR}(s) \end{bmatrix}=\begin{bmatrix} \Re e\left\{H_{11}^{Rot}(s-j\omega_s)+jH_{21}^{Rot}(s-j\omega_s)\right\} & \Re e\left\{H_{12}^{Rot}(s-j\omega_s)+jH_{22}^{Rot}(s-j\omega_s)\right\} \\ \Im m\left\{H_{11}^{Rot}(s-j\omega_s)+jH_{21}^{Rot}(s-j\omega_s)\right\} & \Im m\left\{H_{12}^{Rot}(s-j\omega_s)+jH_{22}^{Rot}(s-j\omega_s)\right\} \end{bmatrix}\cdot\begin{bmatrix} F_1^{NR}(s) \\ F_2^{NR}(s) \end{bmatrix} \tag{4.24}$$

We have obtained the transfer function for the non-rotating outputs $Y^{NR}(s)$ in response to the non-rotating forces $F^{NR}(s)$, namely:

$$H^{NR}(s)=\begin{bmatrix} \Re e\left\{H_{11}^{Rot}(s-j\omega_s)+jH_{21}^{Rot}(s-j\omega_s)\right\} & \Re e\left\{H_{12}^{Rot}(s-j\omega_s)+jH_{22}^{Rot}(s-j\omega_s)\right\} \\ \Im m\left\{H_{11}^{Rot}(s-j\omega_s)+jH_{21}^{Rot}(s-j\omega_s)\right\} & \Im m\left\{H_{12}^{Rot}(s-j\omega_s)+jH_{22}^{Rot}(s-j\omega_s)\right\} \end{bmatrix} \tag{4.25}$$

---

[4] Starting from equation (4.20) we find $\ddot{\underline{Q}}=[M]^{-1}\cdot[S]\cdot\begin{pmatrix}\underline{Q}\\ \dot{\underline{Q}}\end{pmatrix}+[M]^{-1}\cdot\underline{F_g}$. Using (3.39), equations (4.22.a), (4.22.b) and (4.22.c) are obtained.

[5] Let us introduce the complex function $K(s)=A(s)/B(s)+jC(s)/D(s)$, where A(s), B(s), C(s) and D(s) are polynomials with real and constant coefficients. We define $\Re e(K(s))=A(s)/B(s)$ and $\Im m(K(s))=C(s)/D(s)$.

Let us now look at the poles and zeros of the rotor response[6]. The rotating transfer function $H_{\alpha\beta}^{Rot}(s)$ can be decomposed as:

$$H_{\alpha\beta}^{Rot}(s)=\frac{\prod_{i}(s-z_i^{\alpha\beta}+j\omega_s)(s-z_i^{\alpha\beta^*}-j\omega_s)}{\prod_{k}(s-p_k^{\alpha\beta}+j\omega_s)(s-p_k^{\alpha\beta^*}-j\omega_s)} \tag{4.26}$$

showing that poles (zeros) in the rotating frame are the combination of a DC component $p_k^{\alpha\beta}$ ($z_i^{\alpha\beta}$) and of a term $\pm j\omega_s$ modulated at the spin frequency. By inspection from equation (4.26), since $H^{Rot}(s)$ coincides with $H^{NR}(s)$ when ω_s=0 rad/s, the DC components of the poles (zeros) in the rotating frame are equal to the poles (zeros) in the non-rotating frame, i.e. $p_k^{\alpha\beta}$ and $z_i^{\alpha\beta}$ are the poles and the zeros of $H^{NR}(s)$. From equation (4.26) we have:

$$H_{\alpha\beta}^{Rot}(s-j\omega_s)=\frac{\prod_{i}(s-z_i^{\alpha\beta})(s-z_i^{\alpha\beta^*}-2j\omega_s)}{\prod_{k}(s-p_k^{\alpha\beta})(s-p_k^{\alpha\beta^*}-2j\omega_s)} \tag{4.27}$$

By inserting equation (4.27) in (4.25), we may write the transfer function $H^{NR}(s)$ in the non-rotating frame as function of the poles $p_k^{\alpha\beta}$ and $z_i^{\alpha\beta}$. By inspection from equation (4.26) it follows that the poles are shifted from $p_k^{\alpha\beta}\pm j\omega_s$ to $p_k^{\alpha\beta}$ and $p_k^{\alpha\beta}+2j\omega_s$, namely at zero and twice the spin frequency. It is important to underline that the 4 functions $H_{\alpha\beta}^{Rot}(s)$ have different zeros $z_i^{\alpha\beta}$ but the poles are the same.

4.6: THE COMMON MODE REJECTION FACTOR.

The rejection function χ describes the rotor's mechanical ability to reject common forces as compared to those acting in a different manner on the test bodies. The smallest χ is, the best is the performance of the instrument. The rejection is a function of frequency, as much as the dynamical response of the system does. We have proceeded to numerically evaluate $\chi(\nu)$ by first determining the transfer function in the rotating frame for the two cases of common and differential forces acting on the test cylinders. The common $H_{com}^{NR}(s)$ and differential $H_{dif}^{NR}(s)$ transfer functions are then calculated in the non-rotating frame, yielding the corresponding relative displacements:

$$\begin{bmatrix}\Delta x_{COM}^{NR}(s)\\ \Delta y_{COM}^{NR}(s)\end{bmatrix}=H_{COM}^{NR}(s-j\omega_s)\cdot\frac{1}{m_1}\cdot\begin{bmatrix}F_X(s)\\ F_Y(s)\end{bmatrix} \tag{4.28}$$

$$\begin{bmatrix}\Delta x_{DIF}^{NR}(s)\\ \Delta y_{DIF}^{NR}(s)\end{bmatrix}=H_{DIF}^{NR}(s-j\omega_s)\cdot\frac{1}{2m_1}\cdot\begin{bmatrix}F_X(s)\\ F_Y(s)\end{bmatrix} \tag{4.29}$$

The factor ½ in (4.29) is introduced to make the values of common and differential forces

[6] The zeros are simply the numerator roots, and the poles, the denominator roots.

equal. With this definition, if $F_{com}= F$ is the force acting in a common manner on the two test masses, the differential forces are $F_{difl}= F/2$ and $F_{dif2}= -F/2=- F_{difl}$, so that $\Delta F= F_{difl}- F_{dif2}=F$. The rejection functions on the x and y directions thus are:

$$\chi_X(s)=\frac{\Delta x_{COM}^{NR}(s)}{\Delta x_{DIF}^{NR}(s)} \tag{4.30}$$

$$\chi_Y(s)=\frac{\Delta y_{COM}^{NR}(s)}{\Delta y_{DIF}^{NR}(s)} \tag{4.31}$$

Since the EP signal in the GGG experiment is modulated at the very low frequency ν_{mod}=11.574μHz of diurnal Earth motion, in the following we focus on the $\chi(s\rightarrow 0)\equiv\chi_0$ behaviour of the rejection function at different values of the spin frequency ν_s.

4.7: ANALYTICAL SOLUTION AT ZERO SPIN.

Before proceeding to the numerical evaluation of $\chi(\nu)$ we show that the ν=0 behaviour can be predicted by carrying out an analytical solution to the equations for the rotor in figure 3.2. Let us now write the right–hand–side of equation (2.3) by inserting the expression (2.2) for the differential period of oscillation. After some simple algebra and defining the total elastic constant $K_t=k+k_1+k_2$ and the total mass $M_t=m_1+m_2+m_a=2m+m_a$ ($m=m_1=m_2$), we obtain:

$$\Delta x_{dif}=\frac{a_{dif}\,M_t L^2}{K_t\ell^2-gM_t\Delta L/2} \tag{4.32}$$

We have to evaluate the relative displacement between the two cylinders due to common forces. These can be obtained from equation (3.16) of chapter 3 in the limit of small angles and null spin frequency, and after adding the terms embodying in the potential energy U the work done by the external force. This procedure leads to the equations[7]:

$$\begin{cases} mgL_1\vartheta_1-k_1\ell^2(\vartheta_a-\vartheta_1)-F_{com}L_1=0 \\ mgL_2\vartheta_2-k_2\ell^2(\vartheta_a-\vartheta_2)-F_{com}L_2=0 \\ \left[K_t\ell^2-M_tg\Delta L/2\right]\vartheta_a-k_1\ell^2\vartheta_1-k_2\ell^2\vartheta_2+M_t\Delta LF_{com}/2m=0 \end{cases} \tag{4.33}$$

From the first and the second equation of the system (4.33) we have:

$$\vartheta_1=\left(\vartheta_a+L_1F_{com}/(k_1\ell^2)\right)\Big/\left(1+mgL_1/(k_1\ell^2)\right) \tag{4.34}$$

$$\vartheta_2=\left(\vartheta_a+L_2F_{com}/(k_2\ell^2)\right)\Big/\left(1+mgL_2/(k_2\ell^2)\right) \tag{4.35}$$

[7] In the limit $\nu\rightarrow$0Hz, the problem has three degrees of freedom. Hence it can be studied using only three generalized coordinates, i.e. the angles ϑ_a, ϑ_1 and ϑ_2.

By substituting (4.34) and (4.35) in the third equation of the system (4.33), the approximated value of the equilibrium angle ϑ_a of the coupling arm is obtained:

$$\vartheta_a \sim -\frac{\frac{1}{2}\frac{M_t \Delta L}{m} - L_1 \frac{k_1 \ell^2}{k_1 \ell^2 + mgL_1} - L_2 \frac{k_2 \ell^2}{k_2 \ell^2 + mgL_2}}{K_t \ell^2 - \frac{1}{2} M_t g \Delta L} F_{com} \tag{4.36}$$

The angles ϑ_1 and ϑ_2 may be evaluated by inserting the expression (4.36) into equations (4.34) and (4.35):

$$\vartheta_1 = \frac{k_1 \ell^2}{k_1 \ell^2 + mgL_1}\left[\frac{mL_1}{k_1 \ell^2} - \frac{M_t \Delta L}{2K_t \ell^2 - M_t g \Delta L}\right]\frac{F_{com}}{m} \sim \frac{L_1}{k_1 \ell^2 + mgL_1} F_{com} \tag{4.37}$$

$$\vartheta_2 \sim \frac{L_2}{k_2 \ell^2 + mgL_2} F_{com} \tag{4.38}$$

In the limit of small angles, the displacement Δx_{com} is:

$$\Delta x_{com} = L_2 \vartheta_2 - L_1 \vartheta_1 - (2L + \Delta L)\vartheta_a \tag{4.39}$$

After substituting (4.36), (4.37) and (4.38) into (4.39) we eventually obtain[8]:

$$\Delta x_{com} \sim \frac{F_{com}}{m} \frac{\left\{(L_2 - L_1)\left(K_t \ell^2 - \frac{1}{2} M_t g \Delta L\right) - (2L + \Delta L)(k_2 + k_1)\ell^2 + \frac{(2L + \Delta L)\Delta L g M_t}{2}\right\}}{\left(K_t \ell^2 - \frac{1}{2} M_t g \Delta L\right) g} \tag{4.40}$$

With the use of the relations $L_2 = 2L + \Delta L + L_1$ and $K_t = k + k_1 + k_2$ and after expanding equation (4.40) in the parameters $K_t \ell^2 - M_t g \Delta L / 2 << 1$ (see tables 3.1 and 3.2), the displacement can be written as:

$$\Delta x_{com} \sim \frac{(2L + \Delta L) k \ell^2}{K_t \ell^2 - M_t g \Delta L / 2} \frac{F_{com}}{mg} \tag{4.41}$$

The inverse rejection factor turns out to be:

$$\frac{1}{\chi_0} = \frac{\Delta x_{dif}}{\Delta x_{com}} = \frac{M_t g L^2}{(2L + \Delta L) k \ell^2} \frac{F_{dif}}{F_{com}} \tag{4.42}$$

---

[8] $$\Delta x_{com} = \left\{\frac{\left[L_2\left(K_t \ell^2 - \frac{1}{2} M_t g \Delta L\right) - (2L + \Delta L) k_2 \ell^2\right]}{\left(K_t \ell^2 - \frac{1}{2} M_t g \Delta L\right)(k_2 \ell^2 + mgL_2)} mL_2 - \frac{L_1\left(K_t \ell^2 - \frac{1}{2} M_t g \Delta L\right) + (2L + \Delta L) k_1 \ell^2}{\left(K_t \ell^2 - \frac{1}{2} M_t g \Delta L\right)(k_1 \ell^2 + mgL_1)} mL_1 + \frac{(2L + \Delta L)\Delta L M_t}{2K_t \ell^2 - M_t g \Delta L}\right\}\frac{F_{com}}{m}$$

The rejection factor (4.43) results from equation (4.42) after setting $F_{dif} = F_{com}$, and neglecting the ratio $\Delta L/L$ and $m_a/m_{1,2}$.

$$\chi_0 \sim \frac{k\ell^2}{mgL} \tag{4.43}$$

With the values listed in table 3.1 the rejection factor is χ_0=1/745.

4.8: LOW AND HIGH SPIN FREQUENCY REGIME.

The relation (4.43) results from a series of approximations (small oscillations, $\Delta L/L<<1$, $m_a/m<<1$ and $k_\lambda \ell^2 / mgL_\lambda << 1$) performed to describe the non-spinning rotor. We devote section 4.8 to numerically evaluate the extent to which equation (4.43) is valid for low (0Hz < ν_S <ν_d/2) and high frequencies (ν_S >ν_{c2}/2), postponing to the next section the discussion of the more complex case of the rotor spinning at intermediate frequencies (ν_d/2< ν_S <ν_{c2}/2).

4.8.A: THE PERIOD OF NATURAL DIFFERENTIAL OSCILLATION.

In order to calculate the dependence of the rejection on the scaling parameter χ_0 (4.43), we proceed to vary the governing parameters one at a time in a way to keep the differential period T_D fixed.

Curve	$K_{x'}$ (dyne/cm)	Λ	ℓ (cm)
a)	10^6	2.58	0.5
b)	10^6	1	0.5
c)	$5\cdot10^5$	1	0.5
d)	$2.5\cdot10^5$	1	0.5
e)	$1.5\cdot10^5$	1	0.5
f)	$5\cdot10^4$	1	0.5
g)	10^6	1	0.15

Table 4.1: Legend corresponding to figure 4.1.

This condition can be fulfilled by varying ΔL[9], as emerges from figure 4.1, where T_D vs. ΔL is displayed under the different experimental conditions listed in table 4.1.

4.8.B: RELATIVE DISPLACEMENT AS FUNCTION OF FREQUENCY OF THE EXTERNAL FORCE.

Once the differential period is fixed, we need to set the observables that are needed to extract the rejection function. We numerically evaluate the relative displacement resulting from the application of a common force acting at frequency ν, for the rotor spinning at frequency ν_s=2.5Hz and report the result in figure 4.2.

[9] The differential period depends on ΔL as shown by equation (2.2). The scaling parameter χ_0 is not a function of ΔL instead, as it will shown in the following sections.

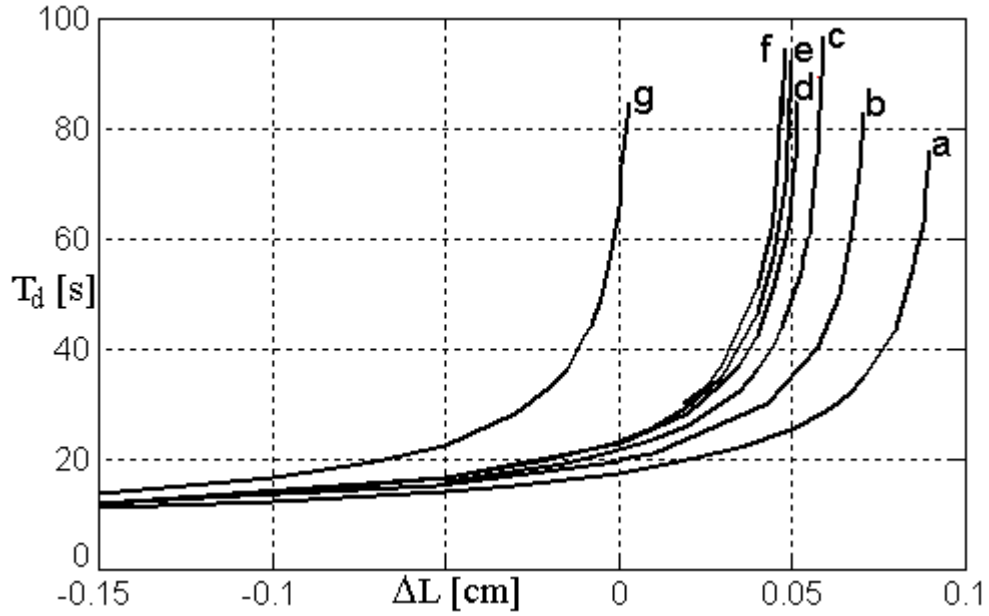

Figure 4.1: Differential Period as a function of the balancing parameter ΔL. Different curves refer to different values of the other system parameters with ν_s=2.5Hz, as in table 4.1.

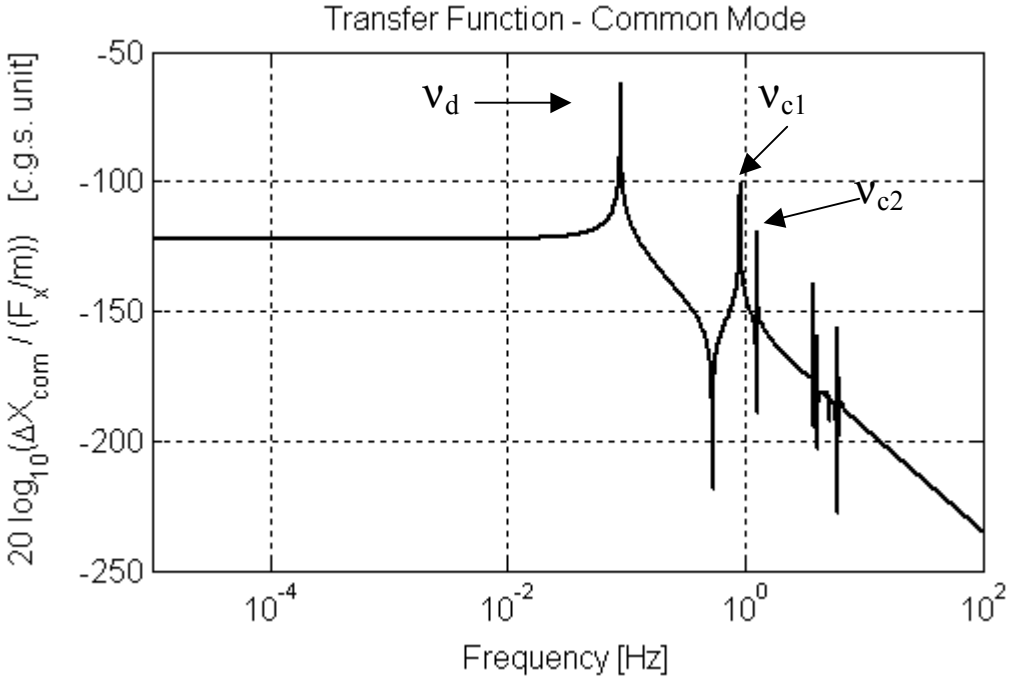

Figure 4.2: Numerically evaluated common mode relative displacement as function of frequency ν in Hz (non-rotating frame). The rotor is spinning at ν_s=2.5 Hz. T_D=12.5s. The other parameters are typical of the instrument and they are listed in tables 3.1 and 3.2. Vertical axis: $20\log_{10}(\Delta x_{com} / (F_{com}/m))$ expressed in c.g.s. units.

In the case of common input forces, the rotor is seen to respond at all its natural frequencies. Figure 4.2 shows peaks at frequencies ν_{poles} corresponding to the differential ν_d^0=0.09 Hz, to the common ν_{c1}^0=0.91 Hz and ν_{c2}^0=1.26 Hz, and to their combinations with $2\nu_s$, namely $2\nu_s \pm \nu_d^0$, $2\nu_s \pm \nu_{c1}^0$ and $2\nu_s \pm \nu_{c2}^0$. Two zeros of the transfer function are also evident, the first located in between ν_d^0 e ν_{c1}^0 and the second in between ν_{c1}^0 and ν_{c2}^0.
The relative displacement resulting from the application of a differential force acting at frequency ν, for the rotor spinning at frequency ν_s=2.5Hz is displayed in figure 4.3. In the

case of differential input forces instead, no zeros are present in the transfer function, and only the mode at frequencies ν_d^0=0.09 Hz is significantly excited while that at $2\nu_s \pm \nu_d^0$ has vanishing weight. The $\nu \to 0$Hz value of the relative displacement turns out to be in perfect agreement with equation (4.32).

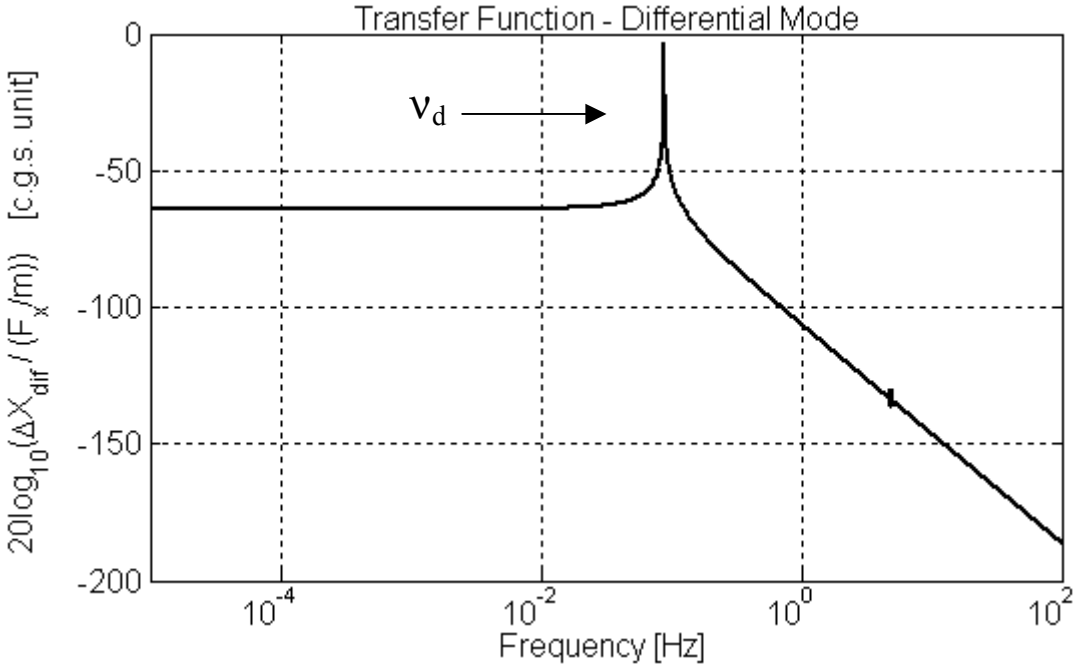

Figure 4.3: Differential mode relative displacement as function of frequency ν in Hz (non-rotating frame). It is numerically evaluated for the rotor spinning at ν_s=2.5 Hz. T_D=12.5s. The other parameters are typical of the instrument and they are listed in tables 3.1 and 3.2. Vertical axis:$20\log_{10}(\Delta x_{dif} /(F_x /m))$ expressed in c.g.s. units.

The inverse rejection factor resulting from equations (4.30) and (4.31) is displayed in figure 4.4 as function of frequency ν in Hz.

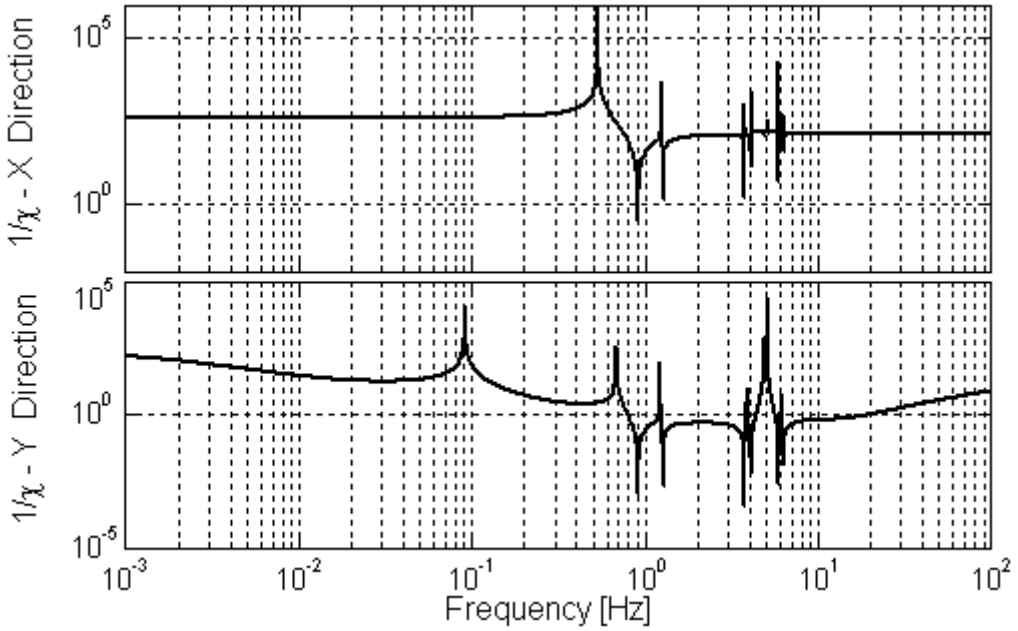

Figure 4.4: Numerically evaluated inverse rejection function $1/\chi(\nu)$ vs. frequency in the x (top) and y (bottom) directions of the non-rotating frame for the rotor spinning at ν_s=2.5Hz. The other system parameters are the same as in figure 4.2 and 4.3.

Even though the external forces (common and differential) have been applied along x direction in the non-rotating frame, finite differential displacements occur also along y, due to the dissipative nature of the suspensions (the quality factor *Q* is finite; on this argument see section 1.7). For this reason, the spectrum along the y direction shows an additional peak at the differential mode frequency. However, the magnitude of both the common and differential y displacements are very small, depressed by a factor *Q* with respect to those along x direction (their ratio remaining of the same order of magnitude as that in the x direction).

4.8.C: COMMON MODE REJECTION OF LOW FREQUENCY FORCES.

We have thus varied one at a time each of the system parameters according to equation (4.77) and keeping T_D fixed. Figure 4.5 displays the behaviour of the static value of $|1/\chi_0| = |1/\chi(\nu = 0\text{Hz})|$ after changing either one of the following quantities: the balancing arm length L, the mass m_λ of the suspended cylinders, the elastic constant k of the central laminar suspension and its length ℓ, and finally the anisotropy Λ.

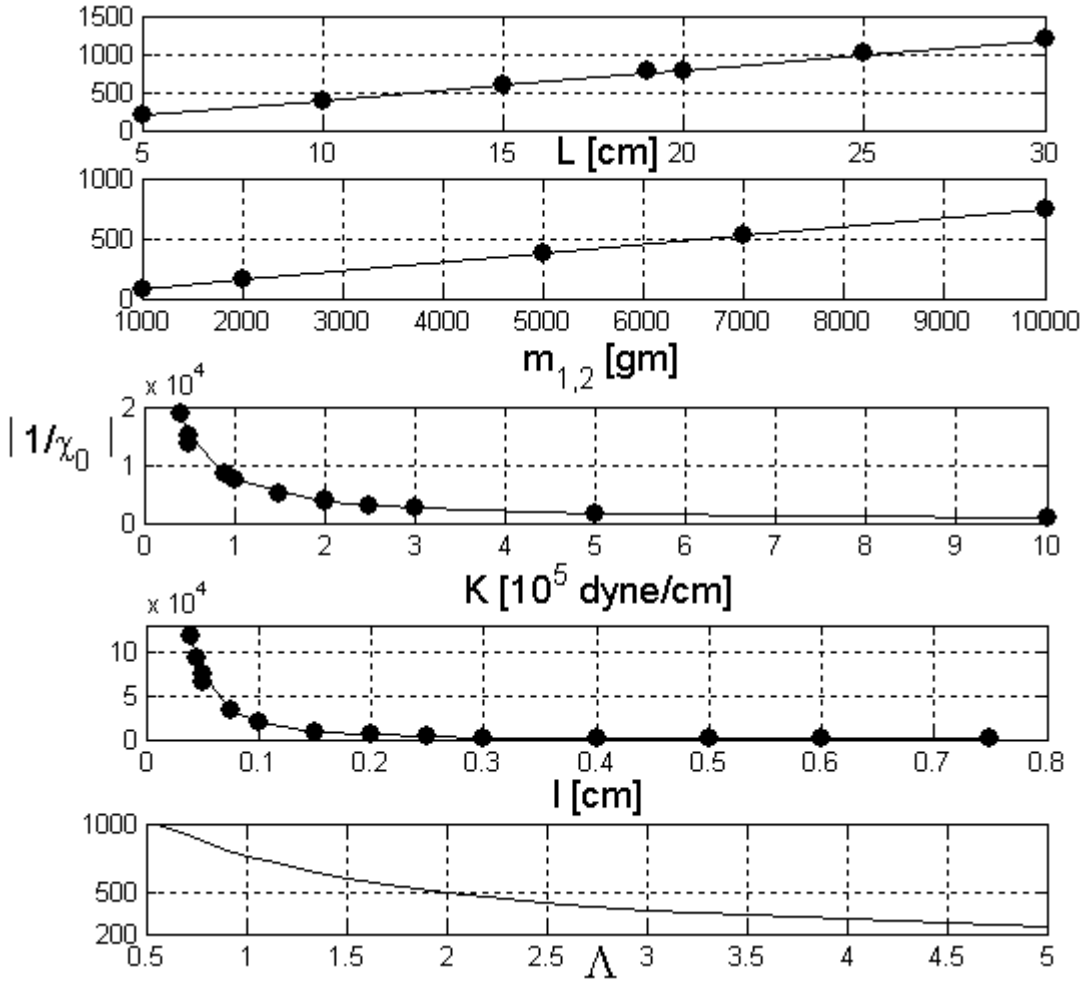

Figure 4.5: Numerically evaluated inverse static rejection $1/\chi_0$ as a function of various system parameters. From top to bottom vs. L, m_λ, k, ℓ and the anisotropy Λ. Solid line: non-spinning rotor. Points: rotor spinning at ν_s=2.5Hz. The parameters are changed one at a time from the values reported in the tables 3.1 and 3.2.

In each panel we report the results for the non-spinning rotor (solid lines from equation (4.43)) and for the rotor spinning at 2.5Hz (points), namely in the low and high frequency region. Negligible differences are seen between the results obtained in the two cases. This means that equation (4.43) represents the rejection factor in regime of low ($0Hz < \nu_S < \nu_d/2$) and high ($\nu_S > \nu_{c2}/2$) spin frequencies. This is explained by noticing that in the low and high spin frequency range the flat and the $2\nu_s$ linear branches of the normal modes are to a very good extent decoupled (see section 3.9), and the linear branch is less excited than the corresponding flat one because of energy reasons. We have verified this statement by performing a spectral analysis of the weights of the linear branch modes in the data available from the experiment. This conclusion is not valid in the intermediate frequency regime, where the flat and linear modes are coupled and both are expected to give a significant contribution, as it will be shown in section 4.9. We can now collect all the results discussed so far to quantify the validity of equation (4.43). The bisecting solid line in figure 4.6 refers to the numerically evaluated $|1/\chi_0|$ in the case of a non-spinning rotor with isotropic central suspension (Λ=1), which coincides with equation (4.43). This result hold also in the case of the non-isotropic rotor spinning at both low and high frequencies. Circles refer to the case of a rotor with isotropic central suspension spinning at very low frequency. For high spin frequencies, the inverse rejection of the non-isotropic spinning rotor is still proportional to the scaling parameter (4.43), through a coefficient that deviates from unity as shown by the triangles in figure 4.6. The amount of the deviation depends on Λ, as displayed in the bottom panel of figure 4.5.

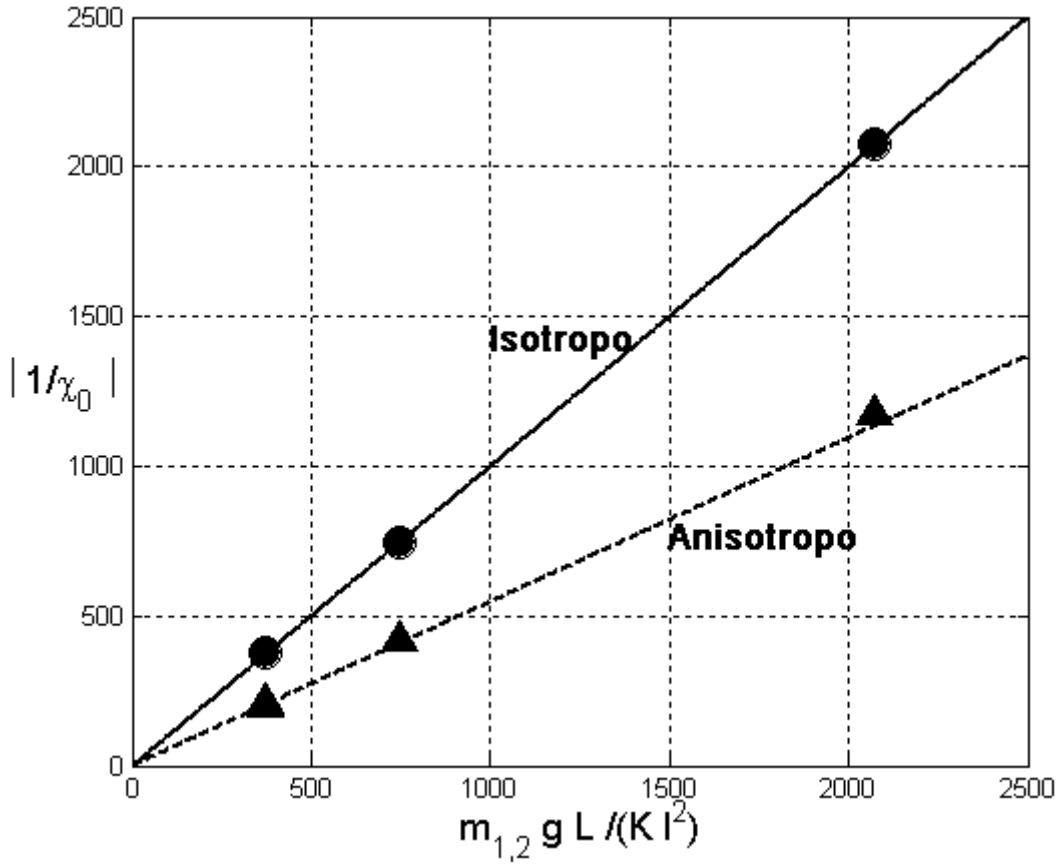

Figure 4.6: Numerically evaluated results for the inverse static rejection $1/\chi_0$ as a function of the scaling parameter $mgL/(k\ell^2)$, showing perfect agreement with (4.43) in the low and high spin frequency regime. Solid

line: isotropic (Λ=1) non-spinning rotor, that is numerically seen to coincide with the case of isotropic spinning rotor at both low and high frequency. Symbols: non-isotropic rotor (Λ=2.58) spinning with low (circles) and high (triangles) frequencies. The dashed line is a guide for the eye. The system parameters in figure 4.3, 4.4 and 4.5 correspond to $mgL/(k\ell^2)=745$.

4.9: INTERMEDIATE SPIN FREQUENCIES REGIME.

We turn now to evaluate the inverse rejection function $1/\chi(\nu)$ for intermediate values of the spin frequency $\nu_d/2< \nu_S <\nu_{c2}/2$. We have repeated the same calculations as those displayed in figure 4.4 in the whole range of increasing spin frequencies ν_S from 0Hz to 5Hz, picking the ν=0Hz value of $1/\chi_0$. The resulting $|1/\chi_0|_{\nu_S}=|1/\chi(\nu=0\text{Hz})|_{\nu_S}$ is reported in figure 4.7, where the best performance of the instrument is predicted at the values $\nu_s \simeq 0.36\text{Hz}>\nu_d^0$ and $\nu_s \simeq 0.6\text{Hz}>\nu_d^0$ for the current set of system parameters. With these parameters, values of $1/\chi_0$ as high as 10^6 are computed.

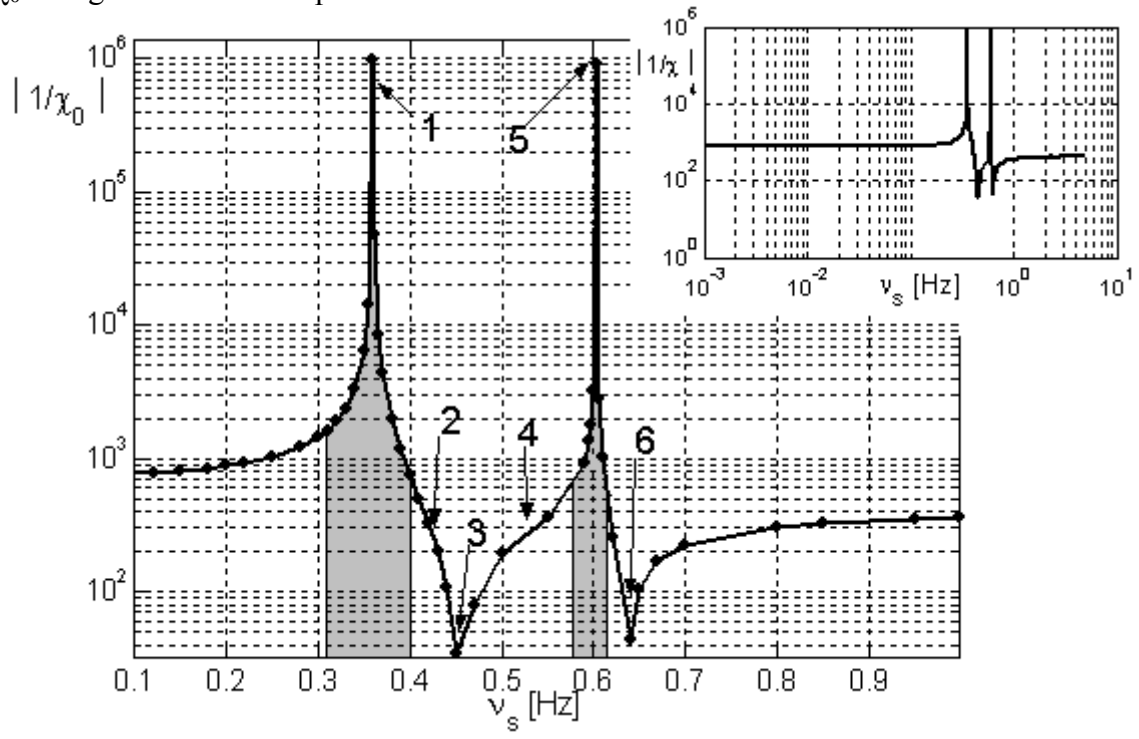

Figure 4.7: The static $|1/\chi_0|_{\nu_S}$ as a function of the spin frequency (numerically evaluated). The system parameters are reported in table 3.1 and 3.2. The numbered arrows indicate crossing points and minima (see text) and correspond to those in figure 4.8.

The difference between the $\nu_s\to 0$ ($|1/\chi_0|\to 745$) and the $\nu_s\to\infty$ ($|1/\chi_0|\to 360$) values of $|1/\chi_0|$ is due to the anisotropy of the central suspension, as already remarked from figure 4.6. We have run the same system of figure 4.7 but with isotropic elastic constants, and have numerically verified that $|1/\chi_0(\nu_s=0\text{Hz})|=|1/\chi_0(\nu_s\to\infty)|=745$, the positions of the peaks being slightly changed according to the corresponding change in the differential period.
The enhanced rejection behaviour at intermediate spin frequencies is related to the dependence of the zeros and of the poles of the transfer matrix on ν_s, as explained below. In section 3.10 (see figure 3.5) we have demonstrated that the poles change with the spin

frequency showing the two branches behaviour, namely two flat branches $\pm|\nu^0_{pole}|$ and two branches increasing with $2\nu_s$, $\nu_{pole}(\nu_s) = \pm|\nu^0_{pole}| + 2\nu_s$. As for the poles of the transfer function, also the values of the zeros change in the same manner, namely $\pm|\nu^0_{zero}|$ and $\nu_{zero}(\nu_s) = \pm|\nu^0_{zero}| + 2\nu_s$.

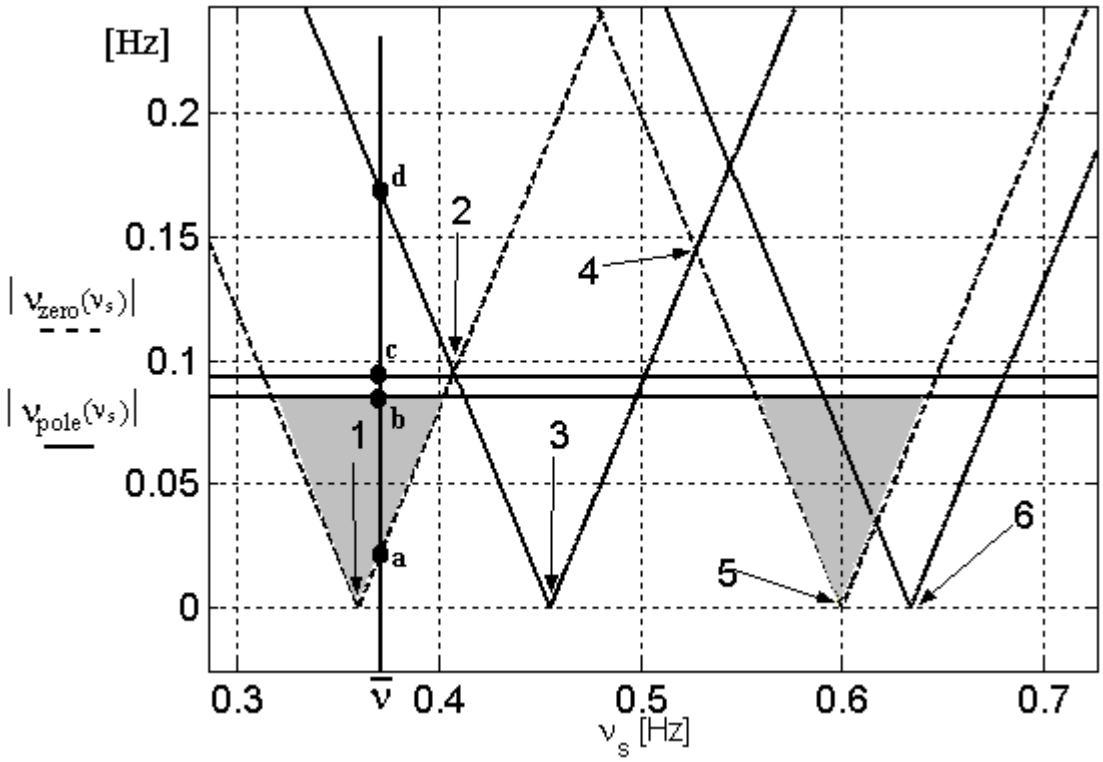

Figure 4.8: Absolute value of the zeros (dashed lines) of the transfer function H(s) vs. the spin frequency. The flat branches correspond to the differential frequencies $|\nu_d \pm \delta\nu|$ splitted by the anisotropy. For ν_s within the shaded areas, the response is dominated by the zeros of the transfer function H(s), and the relative distance due to common mode forces is strongly suppressed.

This is evidenced in figure 4.8 where the absolute values $|\nu_{zero}|$ of the zeros and $|\nu_{pole}|$ of the poles are displayed by dashed and solid lines. The flat branches in figure 4.8, represented by the solid horizontal lines, correspond to the poles at the differential frequencies, that are splitted because of the anisotropy. The zeros branches, represented by dashed lines, are characterized by minima indicated by the points 1 and 5 which correspond to the maxima of the function $|1/\chi_0|_{\nu_s}$ in figure 4.7. As consequence, the best performances against the rejection of common mode external disturbances such as tidal forces and seismic noise are obtained when $\nu_{zero}(\nu_s) = 0\text{Hz}$, i.e. when the following condition is satisfied:

$$\nu_s = |\nu^0_{zero}|/2 \tag{4.44}$$

In general, if $|\nu_{zero}(\nu_s)| < |\nu_d|$ (i.e. when $|\nu_{zero}(\nu_s)| = |-|\nu^0_{zero}| + 2\nu_s| < \nu_d$) the value of the inverse of the rejection factor $|1/\chi_0|_{\nu_s}$ is increased with respect to its value for the non-spinning rotor $1/\chi_0$ (i.e. $|1/\chi_0|_{\nu_s} > |1/\chi_0|$). We see that there are range of spin frequencies for which $|\nu_{zero}(\nu_s)| < |\nu_d|$. This occurs within the shaded region of frequencies indicated in figure 4.8, whose width is easily evaluated to be precisely ν_d[10].

[10] ν_d is also the peak's width (about 10^{-1} Hz ÷ 10^{-2}Hz)

For example, when the system spins at frequency $\nu_s = \bar{\nu}$, its natural frequencies are found by the intersections (a, b, c, d,…) between the vertical red line in figure 4.8 and the branches $|\nu_{zero}(\nu_s)| = |\pm|\nu^0_{zero}| + 2\nu_s|$ and $|\nu_{pole}(\nu_s)| = |\pm|\nu^0{}_{pole}| + 2\nu_s|$. The mode labelled as "a" corresponds to a zero of the transfer function. Instead, "b", "c" and "d" are poles. In this case $|\nu_{zero}(\nu_s)| < |\nu_d|$ (i.e. a<b, c, d), the low frequency rotor response is dominated by the position of the zero labelled as "a", and thus the value of $\Delta x_{com}(\nu \to 0\text{Hz})$ is strongly suppressed. We have found $20\log_{10}(\Delta x_{com}/(F_x/m)) \approx -190$ (c.g.s. unit) at ν_s=0.36Hz. For comparison, we notice that in the case displayed in figures 4.2 and 4.3 we have instead $|\nu_{zero}(\nu_s)| > |\nu_d|$ and a pole dominated response with larger common mode displacements $20\log_{10}(\Delta x_{com}/(F_x/m)) \approx -120$ (c.g.s. unit). The zeros minima are shifted from the minima of the poles branch, that are located at the points 3 and 6. At the points 2 and 4, the zeros branch with $\nu_{zero}(\nu_s) = -|\nu^0_{zero}| + 2\nu_s$ crosses the poles' branch with $\nu_{pole}(\nu_s) = -|\nu^0{}_{pole}| + 2\nu_s$. To make the correspondence clear, we have reported in figure 4.7 the same points 1-5 marked in figure 4.8. We thus see that the peaks of $|1/\chi_0|_{\nu_s}$ correspond to the minima 1 and 5 of the zeros branches, the valleys of $|1/\chi_0|_{\nu_s}$ to the minima 3 and 6 of the poles branches, and finally the saddle points of $|1/\chi_0|_{\nu_s}$ to the crossings 2 and 4 between zeros and poles branches. The fundamental question thus arises how we can move the location of the peaks in figure 4.7 to enhance the rejection behaviour at larger supercritical values of ν_s, as it is needed for best modulation of the signal in the GGG rotor. We face this question in the next section.

4.10: ENHANCED COMMON MODE REJECTION.

We have so far shown that away from the regime of intermediate spin frequencies, the scaling parameter (4.43) precisely describes the rejection behaviour of the GGG rotor, the differential period being adjusted for every set of parameters after varying ΔL. We have then introduced the tuning of the spin frequency in the intermediate regime, as a way to obtain enhanced rejection in a non-trivial manner. We now need one more independent knob to move the rejection function's peaks towards higher spin frequencies, where the GGG rotor is normally operated. One could think of varying the scaling parameter in the intermediate frequency range. However, as shown in figure 4.9, this amounts to move the ν_s/Hz $\to$0 and the ν_s/Hz $\to\infty$ values of $|1/\chi_0|_{\nu_s}$, according to 4.6, while leaving the position of the peaks unaffected. On the other hand, we can still vary the remaining free parameters $L_{1,2}$ while keeping $mgL/(k\ell^2)$ fixed. Figure 4.10 shows that increasing values of L_1 have indeed the effect of increasing the separation between the peaks of $|1/\chi_0|_{\nu_s}$. All the cases displayed in figure 4.10 refer to a realistic rotor. In particular, in the four panels $mgL/(k\ell^2)$=370, with $k=10^5$ dyne/cm, L=19cm, ℓ=1cm, m=10kg and L_1 varying from 2.5 to 15 cm. For the top panel with L_1=15cm, the inverse static rejection function displays a peak at ν_s=1.12Hz, that becomes as high as $|1/\chi_0| = 1.5\cdot10^5$.

4.11: MOMENT OF INERTIA AND SELF-CENTRING OF ROTORS.

In chapter 1 we have studied the dynamical behaviour of the Jeffcott rotor (un-damped (section 1.2), damped (section 1.3), coupled (section 1.7) and non-isotropic (sections 1.10 and

1.11)). In all the models the rotor was assumed to be a point mass. Actually, the moments of inertia of the cylinders in the GGG apparatus can influence its dynamic behaviour, in particular the self-centring mechanism and the equilibrium position in the rotating frame. Hence, before proceeding with the evaluation of the equilibrium position in the GGG rotor, we introduce a simplified model which allows an understanding of the most important phenomena connected to the non-null value of the moment of inertia.

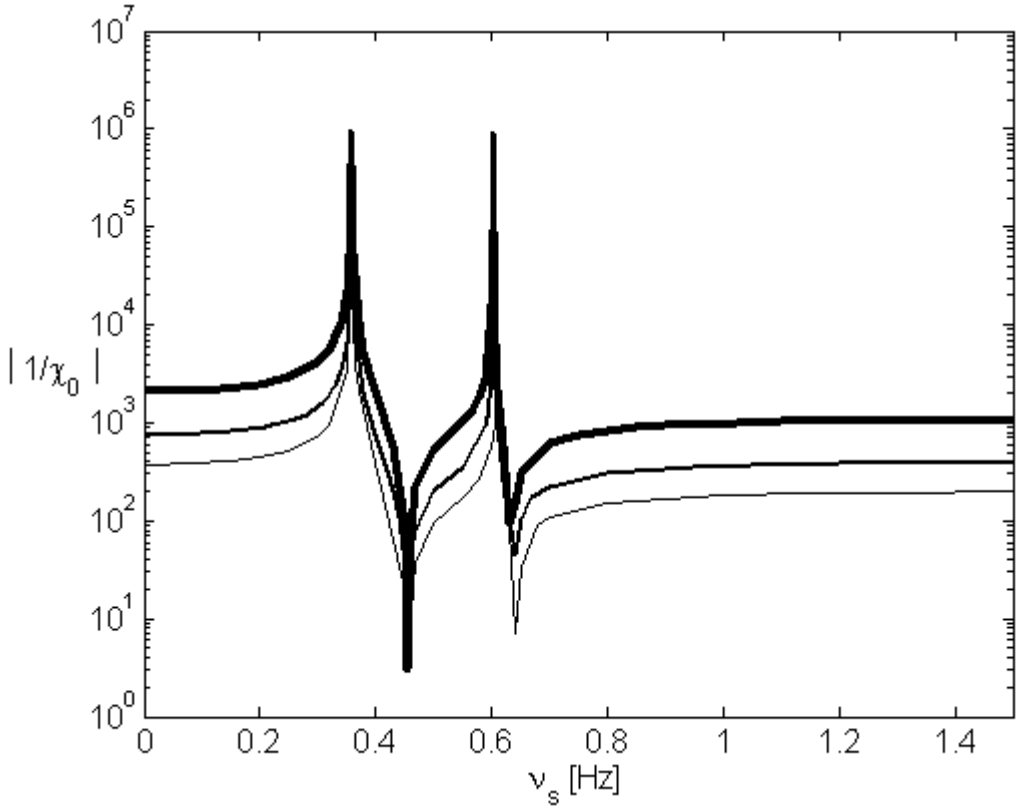

Figure 4.9: Inverse static rejection $|1/\chi_0|_{\nu_S}$ as a function of the spin frequency. Curves with increasing thickness refer to increasing values of the scaling parameter (4.43) $mgL/(k\ell^2)$=370, 745 and 2070, while keeping L_1=4.5cm fixed. Note that variations of the parameter leave the position of the peaks unaffected.

We consider only one spinning cylinder (see figure 4.11) with mass m, moments of inertia I_Ξ and I_Υ ((M,Ξ,Π,ϒ) is the reference system fixed with the body. Its axes coincide with the principal axes of inertia of the cylinder. M is the body's centre of mass. Clearly, it is $I_\Pi=I_\Xi$). We conveniently write all the vectors in the (O,ξ,η,z) rotating reference frame. The centre of mass M of the cylinder is suspended at distance L from the point K by means of a cardanic suspension with non-isotropic elastic constant (k_ξ= k, $k_\eta=\Lambda k$) and length ℓ. There is an offset $\vec{\varepsilon}$ along the ξ direction. We study the dynamical behaviour of this simple rotor in appendix 4.B by following the steps in appendix 3.A [37]. The problem can be studied by using only two generalized coordinates. We have chosen as generalized coordinates the two angles ϑ′ and ϕ′ shown in figure 4.11. ϑ′ is the angle between the KM arm and the vertical axis z and it runs in the interval [0, π]; ϕ′ is the angle from the ξ axis to the projection of the arm KM on the ξ-η plane of the rotating reference frame (O,ξ,η,z) and runs in the interval [0, 2π]. The vector $\vec{r}$ starts from the origin O and points to the centre of mass M of the body. We introduce the effective length $L'^2=L^2+I_\Xi/m-2I_\Upsilon/m$ [11] which takes into account the extended

[11] Only if $L^2+I_\Xi/m>2I_\Upsilon/m$ (as in the case of GGG) L′ can be defined.

nature of the suspended body (L′=L for a point-like mass). After some manipulations (see appendix 4.B), in the limit of small oscillations, the equilibrium angles are obtained:

$$\vartheta_0' = \mp \frac{\varepsilon}{L} \frac{1}{(L'/L)^2 - (\omega_n/\omega_s)^2} \qquad (4.45)$$

(with $\omega_n^2 = g/L + k\ell^2/(mL^2)$ the natural frequency of oscillation for the system in figure 4.11 in the case of a non spinning point-like body, i.e. ω_s=0rad/s, $I_\Xi = I_\Upsilon$=0 kg·m^2) and with $\phi_0' = 0\ (\pi)$ in the case of the upper (lower) sign in equation (4.45), respectively.

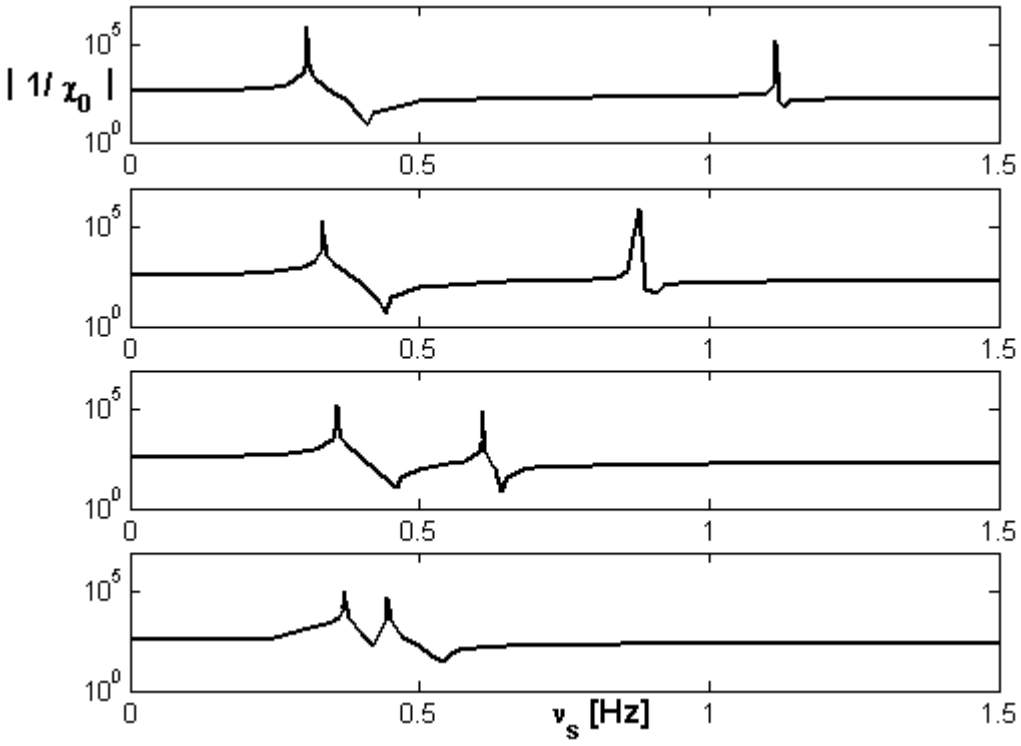

Figure 4.10: Inverse static rejection $|1/\chi_0|_{\nu_s}$ as a function of the spin frequency at different values of L_1 and the scaling parameter (4.43) fixed as 370. From bottom to top: L_1=2.5cm, 4.5cm, 9cm and 15cm. Note the increasing separation between the peaks, leading to enhanced rejection under supercritical rotation, i.e. ν_s=1.12Hz.

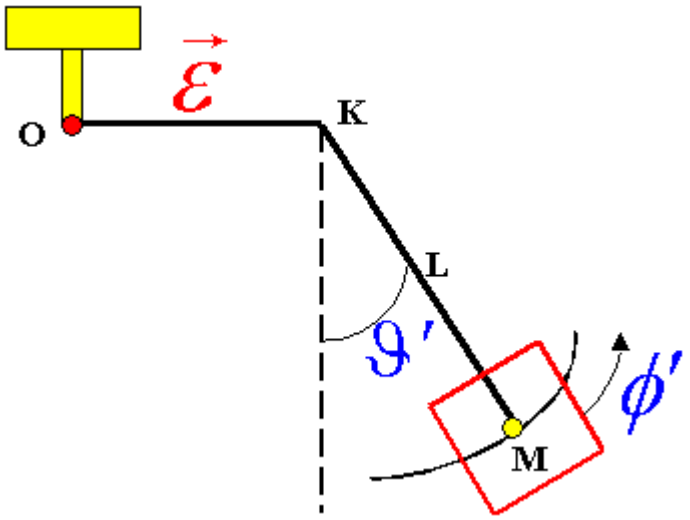

Figure 4.11: Sketch of the rotor. M is the centre of mass of the cylinder. KM is a rigid arm. $\vec{\varepsilon}$ is the eccentricity.

Note that the equilibrium position is in the ξ direction, namely in the direction of the offset ε. The cylinder's centre of mass is eventually located at the distance:

$$\Delta\xi \sim \varepsilon \pm L\vartheta_0 = \varepsilon\left[1 - \frac{\omega_s^2}{\omega_s^2\left(L'^2/L^2\right) - \omega_n^2}\right] \tag{4.46}$$

In the case of an extended body (L′≠L), equation (4.46) can be written as:

$$\Delta\xi = \varepsilon\left\{\frac{\left[\left(\frac{L'}{L}\right)^2 - 1\right]\omega_s^2 - \omega_n^2}{\omega_s^2\left(\frac{L'}{L}\right)^2 - \omega_n^2}\right\} \tag{4.47}$$

The displacement $\Delta\xi(\omega_s)$ has two zeros (only if L′>L) :

$$\omega_s^z = \pm\frac{L}{\sqrt{L'^2 - L^2}}\omega_n \tag{4.48}$$

and two poles:

$$\omega_s^p = \pm L\omega_n / L' \tag{4.49}$$

In the case L′=L (point-like mass), equation (4.46) is equivalent to (1.8). In particular, equation (1.8) shows that, in supercritical rotation ($\omega_s>\omega_n$), the distance Δξ decreases monotonically for increasing values of the spin speed while the system is resonant at frequency $\omega_s=\omega_n$. We can then obtain the constant Δξ=ε value from this equation in the limit of small spin frequencies ($\omega_s<<\omega_n$). In the case L′≠L, the position of the poles (4.49) is shifted with respect to the point-like case ($\omega_s^p = \omega_n$); the shift is dictated by the difference between L and L′. Below the frequency (4.49), the equilibrium is reached at distance Δξ=ε, i.e. the values of Δξ coincide for both cases (i.e L′=L and L′≠L) to the same constant. Above resonance in supercritical rotation, the behaviour of the extended body is remarkably different from that of the point-like mass. The Δξ has a minimum related to the presence of the zeros (4.48) in equation (4.47); the position of this minimum evidently shifts towards higher frequencies as long as L′→L. In the limit $\omega_s>>\omega_n$, equation (4.47) yields

$$\Delta\xi \sim -\varepsilon\frac{\omega_n^2}{\omega_s^2} + \varepsilon\frac{L'^2 - L^2}{L'^2} \sim \varepsilon\frac{L'^2 - L^2}{L'^2} \tag{4.50}$$

that explains how the cylinder's equilibrium position Δξ tends to a constant for increasing values of the spin speed. Instead, in the limit $\omega_s\to\infty$, the point at distance $\tilde{L} = L'^2/L$ from the suspension point has the best self-centring with Δξ=0. We can consider a more complex system with 2 offsets ε and ε_2 as shown in figure 4.12. The presence of the second offset does not affect very much the behaviour of the rotor as can be argued from figure 4.13 where the self-centring capability Δξ is reported as a function of the spin frequency, in the cases of a cylinder and of a point-like mass.

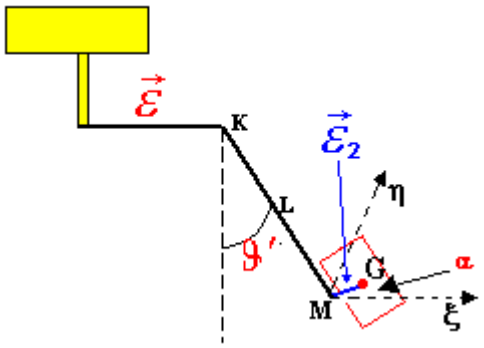

Figure 4.12: Sketch of the rotor. G is the centre of mass of the cylinder. KM is a rigid arm. The distance between M and the centre of mass G is the eccentricity $\vec{\varepsilon}_2 = \overrightarrow{MG}$. The projection of $\vec{\varepsilon}_2$ in the ξ–η plane forms an angle α with $\hat{\xi}$.

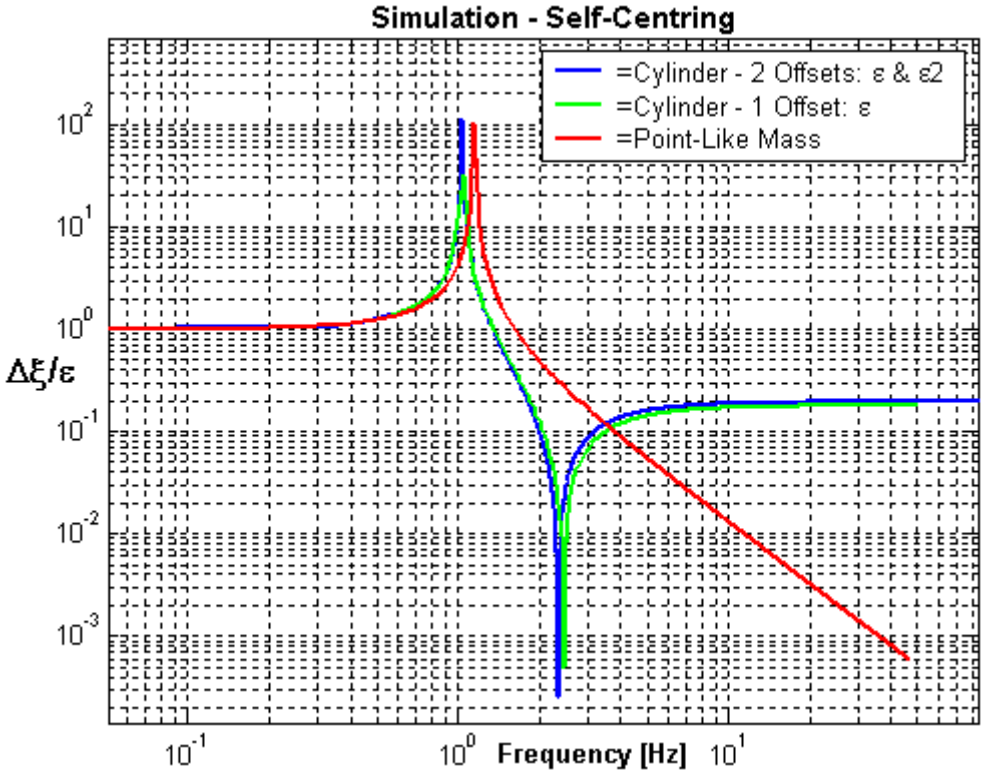

Figure 4.13: Distance $\Delta\xi$ of the centre of mass from the motor axis as a function of the spin frequency, showing agreement with equations (4.46), (4.47) and (4.50). The self-centring case of a point-like mass (only one offset ε) is displayed as the red line. In the limit of small spin frequencies the values of the distance coincide for all the cases to the same constant, then $\Delta\xi$ increases up to a maximum value, that is located at slightly shifted position for the three cases. In supercritical rotation, the behaviour of the cylindrical body is remarkably different from that of the point-like mass. In the limit of high spin frequencies, the cylinder's equilibrium position has a minimum and then tends to a constant value, while for the point-like mass it decreases monotonically.

4.12: SELF-CENTRING IN THE GGG ROTOR.

We have then introduced a second offset $\vec{\varepsilon}_2$ in the mathematical model of the GGG rotor (see figure 4.14). $\vec{\varepsilon}_2$ and $\vec{\varepsilon}$ are not parallel, i.e. $\vec{\varepsilon}_2$ is not aligned with the ξ axis. We have numerically evaluated the equilibrium position for the rotor as a function of the spin speed.

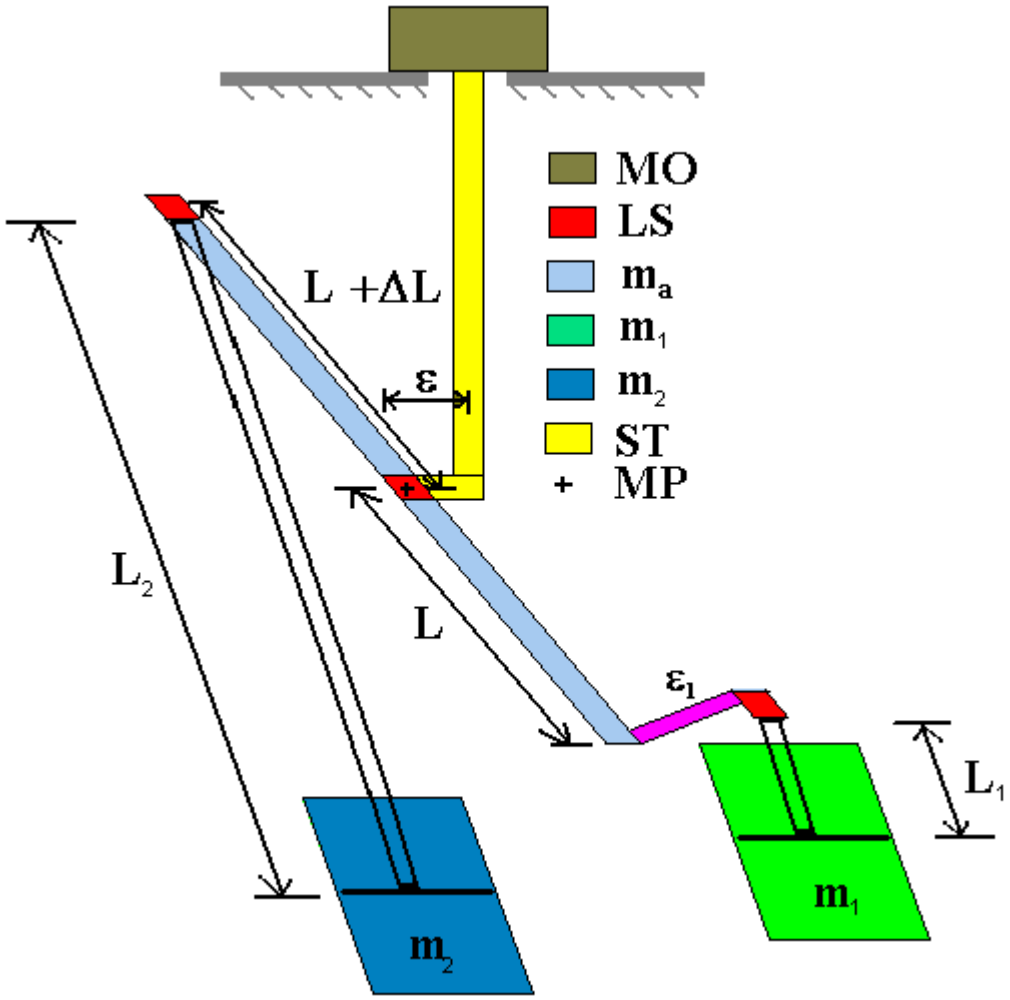

Figure 4.14: Minimal model for the instrument drawn in figure 2.1 in presence of 2 offsets $\vec{\varepsilon}$ and $\vec{\varepsilon}_1$ (in violet). The various parts are drawn with the colours and the labels corresponding to figure 2.1. The relevant dimensions L_a, L_1 and L_2 are indicated. MO is the motor. ST is the suspension tube. The arm with mass m_a and length $2L+\Delta L$ is suspended at its midpoint MP. Bodies are coupled by means of 3 suspensions LS.

Numerical results are plotted in figures (4.15) and (4.16). Figure 4.15 shows the equilibrium position (non-dimensional distance of the centre of mass of the inner cylinder from the spin axis) as a function of the spin speed. Three peaks are present, at frequencies ν_d, ν_{c1} and ν_{c2}. Thus, the same peak/minimum structure as in figure 4.13 occurs for the natural modes of the two hollow cylinders composing the GGG rotor. As a result, the $\Delta\xi$ of the GGG cylinders in the limit of very low and very high spin frequencies has the same cylinder's behaviour displayed in figure 4.13. Figure 4.16 shows the non-dimensional relative distance ($\Delta\xi_{rel}/\varepsilon$) between the test cylinders as a function of the spin speed in correspondence of the equilibrium position shown in figure 4.15. Three peaks are present, at frequencies ν_d, ν_{c1} and ν_{c2}. There are also two zeros at frequencies ν_{zero} (i.e. $\Delta\xi_{rel}/\varepsilon \to 0$ for $\nu_s \to \nu_{zero}$); we have checked that the zeros in the relative distance $\Delta\xi_{rel}/\varepsilon$ are the same as the zeros in the transfer function $\Delta x_{com}/F_{com}$ (see equation (4.28) and figure 4.2). Instead, in section 4.9 (see figures 4.7 and 4.8) we have shown that the best performances against common mode external disturbances are obtained when $\bar{\nu}_s \sim \nu_{zero}/2$, i.e when the condition (4.44) is satisfied. Figure 4.16 shows that the relative distance $\Delta\xi_{rel}$ between the test cylinders for the rotor spinning at frequency

$\bar{\nu}_s \sim \nu_{zero}/2$ is about $7\cdot10^{-1}\varepsilon$, i.e. it is not as good as the level of self-centring required by the target of an EP test at the level of $\eta=10^{-13}$. This problem can be solved by considering that the horizontality of the plane on which the motor is mounted can be regulated by means of 3 high resolution DC actuators (see figure 7.4, sections 2.8 and 7.2 for details on the actuators and their accommodation). If this plane forms an angle ϑ_{ref} with the horizontal plane, the central suspension does not exert a restoring force towards the local vertical; instead, the restoring force is directed towards the non perfectly vertical motor axis. This fact can be used to improve the level of self-centring, hence the performances of the apparatus. The output of the read-out electronics in the rotating frame is the driving signal which can be used to adjust the angle ϑ_{ref} in order to obtain a better level of self-centring at frequency $\bar{\nu}_s \sim \nu_{zero}/2$. Numerical results are shown in figure 4.17 ($\vartheta_{ref}=1.05\cdot10^{-4}$rad). This figure shows the presence of a new zero in correspondence of the spin frequency $\bar{\nu}_s \sim \nu_{zero}/2$. It is very important to note that the position of the original zeros is slightly affected by the correction of the angle ϑ_{ref}. As a consequence, best performances against common mode forces and best levels of self-centring can be obtained at the same spin frequency $\bar{\nu}_s \sim \nu_{zero}/2$.

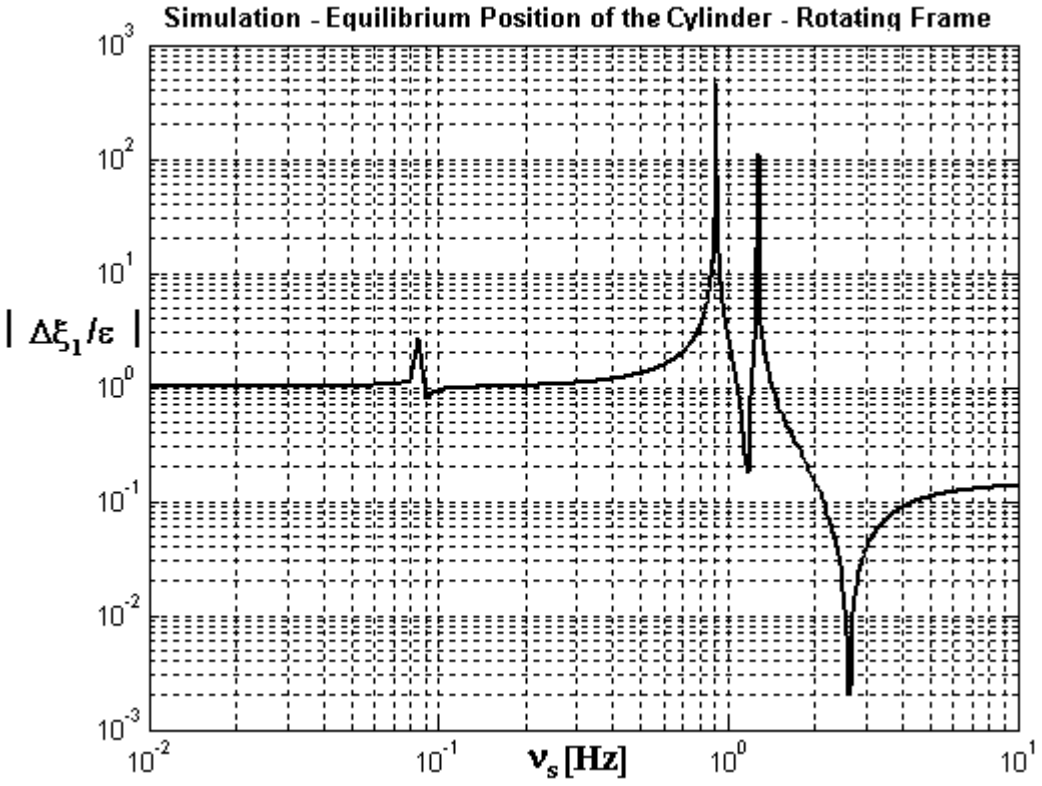

Figure 4.15: Non-dimensional distance of the centre of mass of the inner cylinder from the motor axis as a function of the spin frequency showing agreement with the simple system in figure 4.12.

4.13: CONCLUDING REMARKS.

Figures 4.7, 4.8 and 4.17 represent central results of this chapter, as they show the way to perform a controlled tailoring of the rejection capability of GGG. This can be done by tuning ν_s, L_1 and the governing parameters combined in $mgL/(k\ell^2)$. In the experiment, the most convenient way is to first fix $mgL/(k\ell^2)$ and L_1 in such a way that the values of the zero and

the pole at higher frequencies (for the non spinning system) are increased.

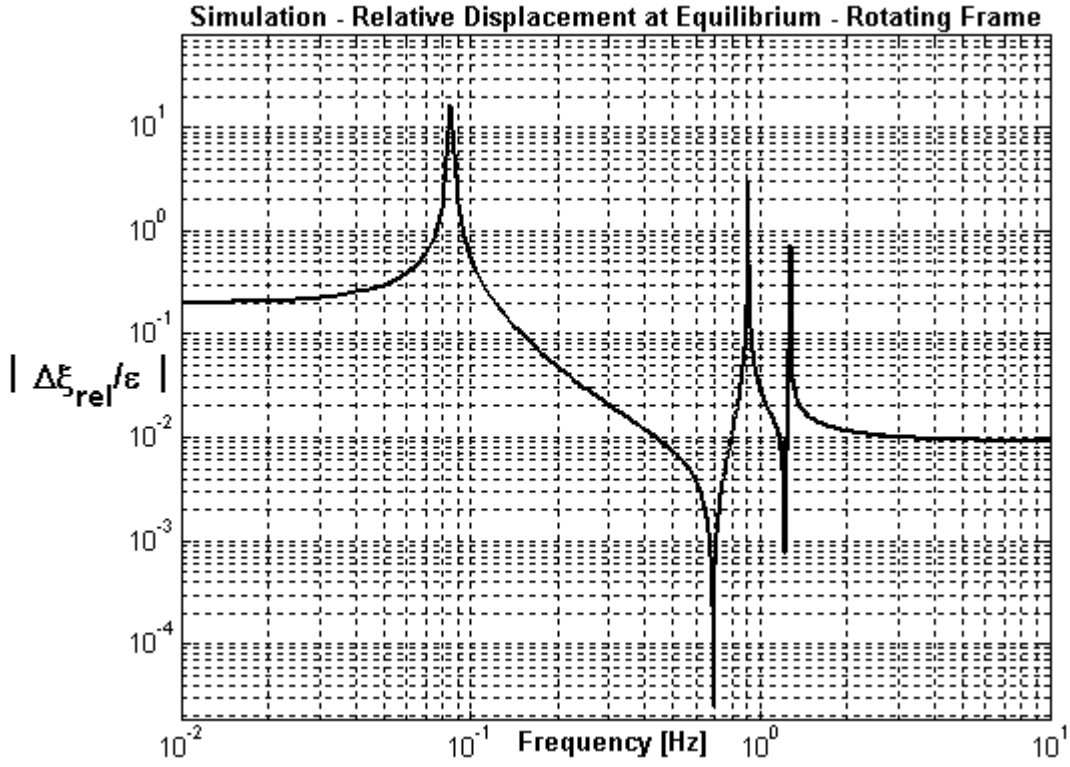

Figure 4.16: Non-dimensional relative displacement between the test cylinders at the equilibrium as a function of the spin speed. 3 peaks are present, at frequencies ν_d, ν_{c1} and ν_{c2}. Two zeros are also present.

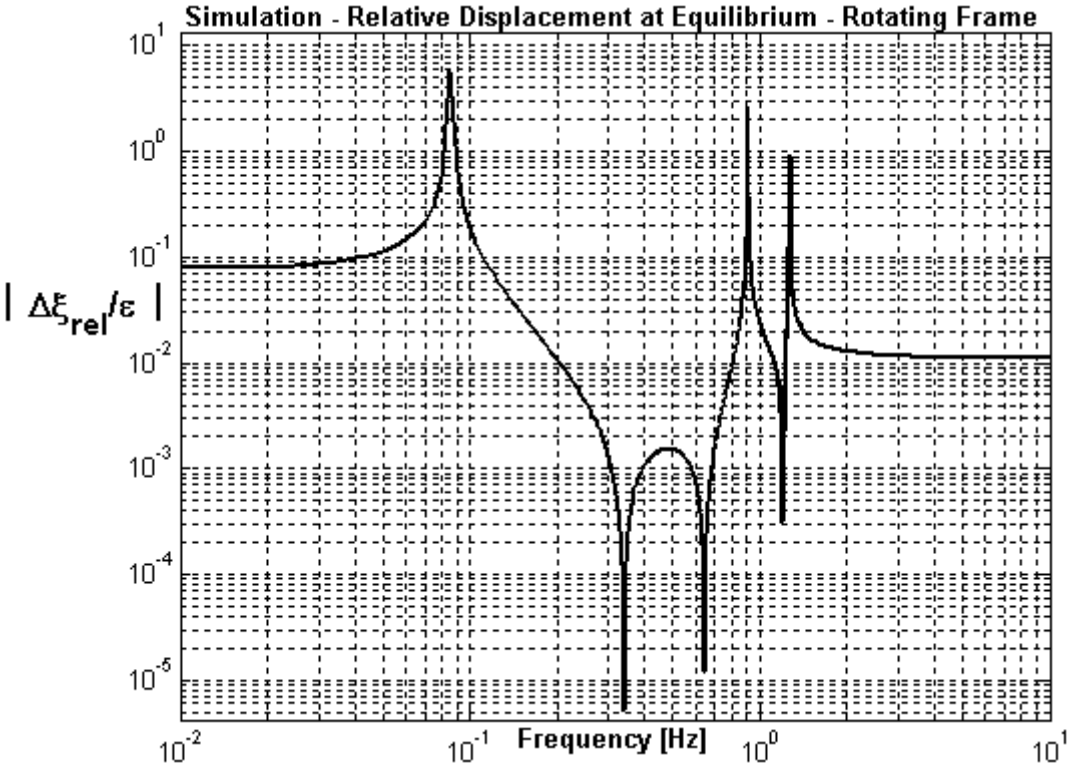

Figure 4.17: Non dimensional relative displacement between the test cylinders at the equilibrium as a function of the spin speed. An additional zero is obtained when $\vartheta_{ref} \neq 0$rad. It is possible to regulate ϑ_{ref} in order to have the zero at frequency $\overline{\nu}_s \sim \nu_{zero}/2$.

We can then tune ν_s to bring the zero below the differential frequency (i.e. $-\left|\nu_{zero}^0\right| + 2\nu_s < \left|\nu_d^0\right|$, see section 4.9) as depicted in figure 4.8. This can be done in a highly controlled way (i.e. when $\overline{\nu}_s \sim \nu_{zero}/2$), allowing to place the system in correspondence to one of the peaks of $\left|1/\chi_0\right|_{\nu_s}$ (see figure 4.7). By regulating the inclination ($\vartheta_{ref} \neq 0$) of the plane on which the motor is mounted it is possible to obtain a level of self-centring as good as we need at the spin frequency $\overline{\nu}_s \sim \nu_{zero}/2$ (see figure 4.17).

CHAPTER 5:

EXPERIMENTAL RESULTS ON WHIRL MOTION AND QUALITY FACTOR.

5.1: INTRODUCTION.

In charter 1, we have seen that supercritical rotors tend to rotate about their centre of mass instead of their geometrical centre (equations (1.10), (1.11), (1.63) and figures 1.3 and 1.14). We have also seen that they develop whirling motions (equations (1.8) and (1.65)); in particular, in presence of rotating damping, forward whirl are unstable (self excited) and their amplitude grows in time with exponential law (figure 1.9, equations (1.21) and (1.23)). Whirl is due to losses in the suspensions (the higher the quality factor, the slower the growth rate) and needs to be damped (1.23), but it can be separated from data to recover the equilibrium position.
In this chapter we report the results obtained during several months of operation (in particular May 2002) of the rotating differential accelerometer. These results concern the growth rate of whirl motion and the quality factor of the system. Measurements are performed in the rotating frame (sections 5.2 and 5.3); after coordinate transformation to the non-rotating reference frame, whirl forward and backward can be extracted and compared with a theoretical model (sections 5.4, 5.5 and 5.6).
Quality factors at the natural frequencies can be measured for the whole system, at zero spin rate, by exciting oscillations at this frequencies and measuring the decay in the oscillation amplitude (sections 5.7, 5.8 and 5.9); these results are also collected in [34] (this article is available in Appendix_Articles).

5.2: THE MEASUREMENT DATA.

The relative displacements of the test cylinders in the ξ and η directions[1] of the plane perpendicular to the spin axis are read by two capacitance bridges, rotating with the system (see section 2.5 for details). From now on, the symbol Φ_ξ will be used to refer to data acquired by the capacitance bridge sensitive along ξ direction in the rotating frame, and Φ_η will be used to refer to data acquired by the bridge sensitive along η direction. 32 data per spin period are acquired by the electronics (for each channel). The sampling frequency is then:

$$\nu_C=32\nu_S \tag{5.1}$$

and the sampling period

$$T_C=1/(32\nu_S) \tag{5.2}$$

[1] Rotating reference frame: (O,ξ,η,z). Inertial Frame= Non-rotating frame: (O,x,y,z).

Suppose that Φ_ξ (n) equals the time sample of the continuous time process Φ_ξ (t) (the relative displacement between the test cylinders along ξ axis as a function of time):

$$\Phi_\xi=[\Phi_\xi(1), \Phi_\xi(2), \Phi_\xi(3),\ldots, \Phi_\xi(n),\ldots] \quad (5.3)$$

where $\Phi_\xi(n)$ is n-th data sampled. In figure 5.1, the signal acquired on 15 May 2002 at 2:29 P.M. is shown (the system was spinning at frequency ν_S=1.9Hz; active and passive dampers were disconnected). This set of data will be analysed in the following sections.

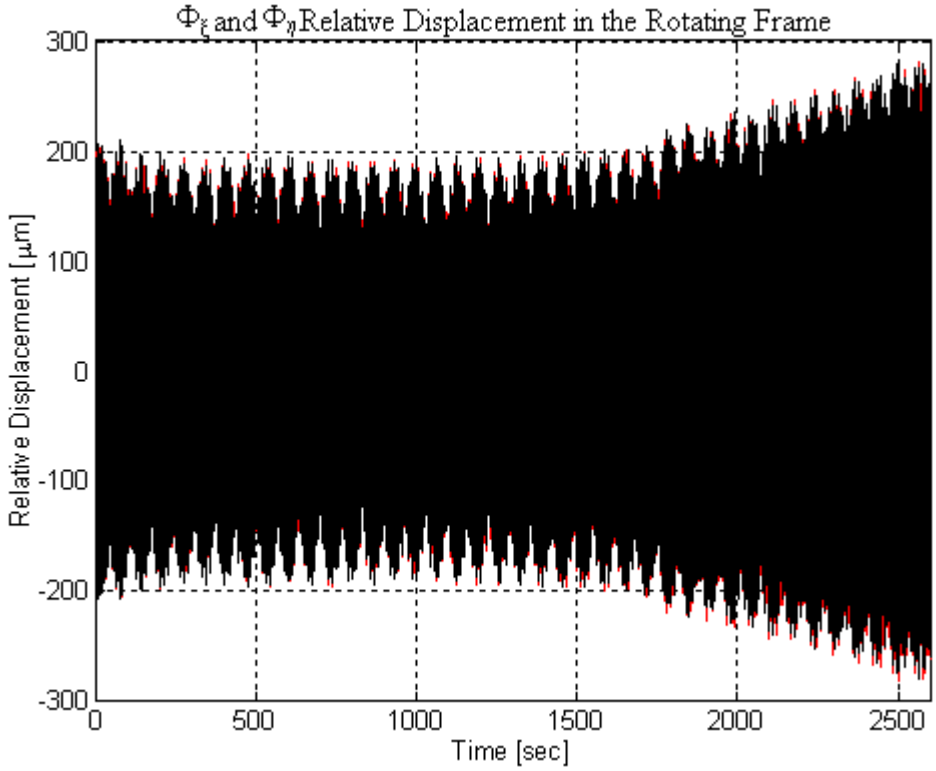

Figure 5.1: The signal acquired on 15 May 2002 (at 2:29 P.M.). Black: Φ_ξ. Red: Φ_η. Spin frequency: ν_S=1.9019Hz.

The process Φ_ξ can be seen as the superimposition of a deterministic signal (which we want to recover) and random noise. By applying the Fourier filter described in appendix 5.A ([50 – 52]), it is transformed into the process R_ξ ($R_\xi(n)$ is a discrete time process sampled at frequency $1/(8T_C)=\nu_C/8$ in the rotating frame; the noise is partly reduced by the Fourier filter). In the same manner, R_η is the signal obtained starting from the process Φ_η acquired by the capacitance bridge sensitive along η direction after applying the same filter. In figure 5.2 the FFT of the reconstructed R_ξ signal, sampled at frequency $\nu_C/8$, is shown as a function of frequency (the FFT of R_η is similar and it is not shown).

5.3: THEORETICAL MODEL OF THE WHIRL.

R_ξ and R_η are discrete time signals representing the relative displacements of the test cylinders along the ξ and η axis of the rotating reference frame. They have been extracted from the original sampled data Φ_ξ and Φ_η, after applying the Fourier filter. By performing a coordinate transformation to the inertial non-rotating reference frame, the discrete time

signals in the laboratory frame are obtained, namely X^e_{nr} and Y^e_{nr} (from now on, the label "e" refers to the experimental data and "t" refers to the expected theoretical signal). In figure 5.3 we show the FFT of the signal X^e_{nr} in the non-rotating (laboratory) reference frame. In this run the residual low frequency noise was about 10^{-7}m and it was due to the electronics noise[2]. In section 1.7 we have shown that the whirling motion is the superimposition of a circular forward whirl (i.e. occurring in the same direction of the spin speed) which is self-excited, and a circular backward whirl motion which is damped (see equation 1.65). In section 1.11, then, we have seen that in the case of a non-isotropic rotor the frequencies of forward and backward whirl are slightly different (1.100).

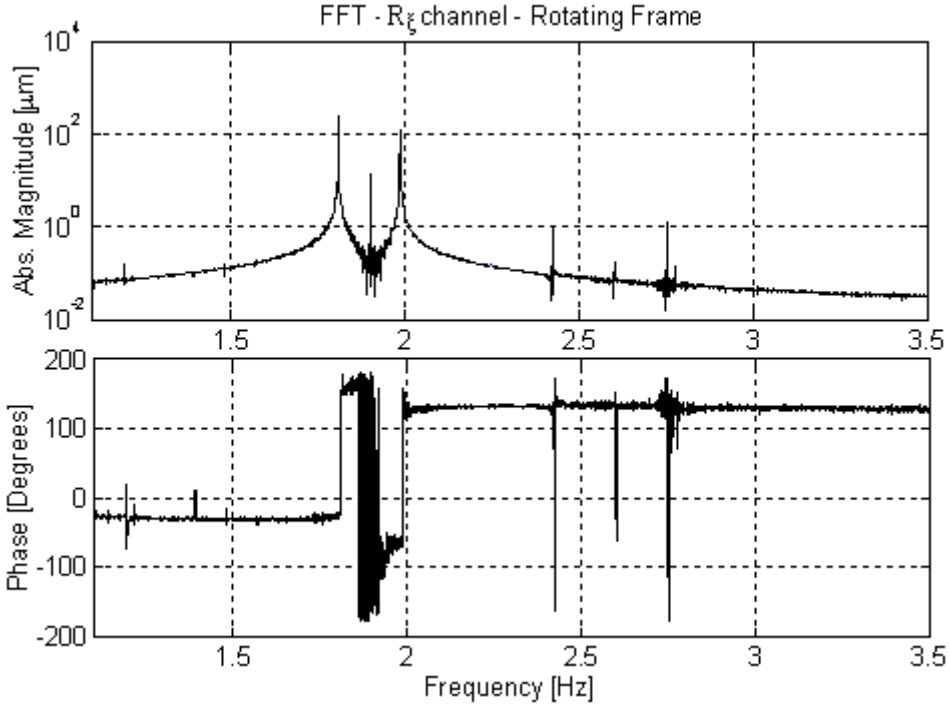

Figure 5.2: FFT of the discrete time signal R_ξ in the rotating reference frame. Top panel: the magnitude of the signal as a function of frequency. In particular, it is possible to recognize three high peaks: the peak at the spin frequency ν_s= 1.9 Hz, the peak corresponding to the forward whirling (at frequency lower than ν_s, about 1.8Hz), and the peak corresponding to the backward whirl (at frequency higher than ν_s, about 2Hz). Bottom panel: the phase of the signal as a function of the frequency.

We thus expect the whirl motion in the non-rotating reference frame to be written in the form:

$$\begin{cases} X^t_{nr} = A_1\cos(\omega_1 t+\varphi_1)e^{-t/\tau_1} + A_2\cos(\omega_2 t+\varphi_2)e^{t/\tau_2} = X^t_{nr1} + X^t_{nr2} \\ Y^t_{nr} = A_1\cos(\omega_1 t+\varphi_1+\pi/2)e^{-t/\tau_1} + A_2\cos(\omega_2 t+\varphi_2-\pi/2)e^{t/\tau_2} \\ \quad = Y^t_{nr1} + Y^t_{nr2} \end{cases} \quad (5.4)$$

[2] The maximum allowable displacement between the test masses is ≈10mm. It is acquired by the electronics described in chapter 2 (16 bit). Hence, there is the correspondence 1bit → $10\text{mm}/2^{15}\approx 3\mu$m. When the read-out is operated in "high gain scale", it is about 20 times more sensitive; unfortunately, this is only a recent improvement of the apparatus, and the measurements reported in this chapter refer to the previous version (less sensitive) of the read-out.

where ω_1 is the angular velocity of the backward whirl with amplitude decreasing in time and ω_2 the angular speed of the self excited, forward whirl. The labels 1 and 2 refer to the backward and forward whirl parameters.

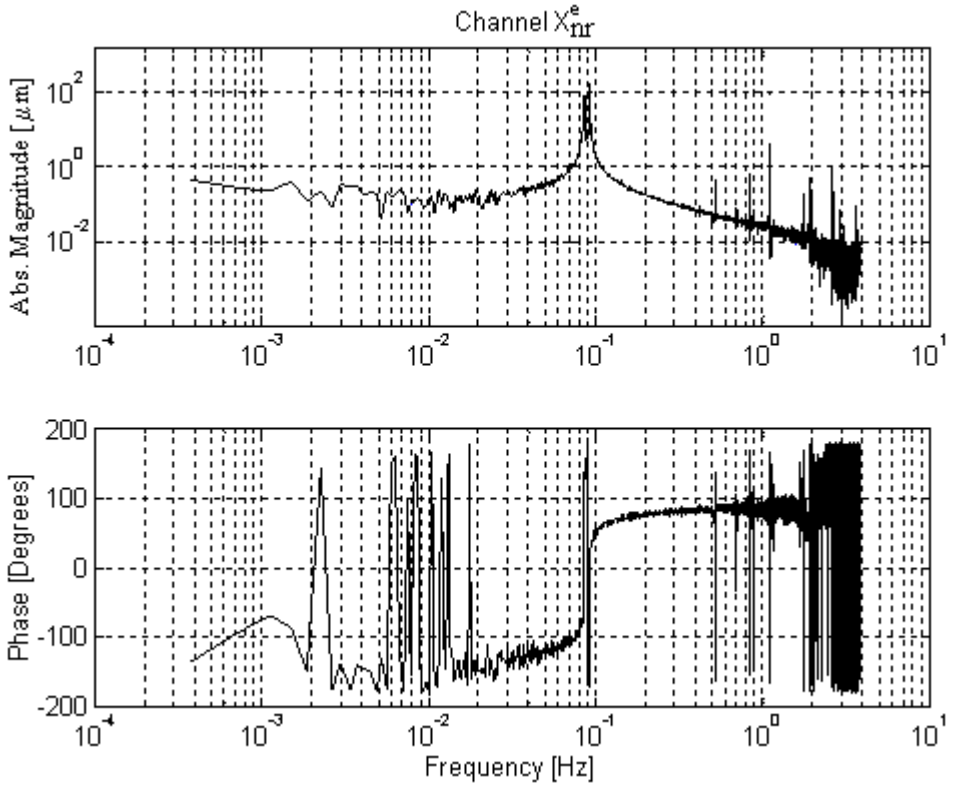

Figure 5.3:FFT of the signal in the laboratory frame (X component). Two peaks are present, at frequencies slightly different, i.e. 0.086Hz and 0.093Hz.

The theoretical signals along x and y axis of the laboratory frame are out of phase from each other by 90°. They are continuous time function of the temporal variable t. By analysing the theoretical signals X^t_{nr} and Y^t_{nr}, we want to develop a procedure to extract the forward and backward whirl motions from data. From (5.4), it follows:

$$\begin{cases} X^t_{nr} = A_1\cos(\omega_1 t+\varphi_1)e^{-t/\tau_1} + A_2\cos(\omega_2 t+\varphi_2)e^{t/\tau_2} = X^t_{nr1} + X^t_{nr2} \\ Y^t_{nr} = -A_1\sin(\omega_1 t+\varphi_1)e^{-t/\tau_1} + A_2\sin(\omega_2 t+\varphi_2)e^{t/\tau_2} = Y^t_{nr1} + Y^t_{nr2} \end{cases} \quad (5.5)$$

Given the signals X^t_{nr1}, X^t_{nr2}, Y^t_{nr1}, Y^t_{nr2} in (5.5), their Fourier transforms $\Im(\omega)$ are:

$$X^t_{nr1} \rightarrow \Im_{X^t_{nr1}}(\omega) = A_1\tau_1 \frac{1+j\omega\tau_1}{\left\{\left[1+\tau_1^2\left(\omega_1^2-\omega^2\right)\right]+2j\omega\tau_1\right\}} \quad (5.6)$$

$$Y^t_{nr1} \rightarrow \Im_{Y^t_{nr1}}(\omega) = -A_1\omega_1\tau_1^2 \frac{1}{\left\{\left[1+\tau_1^2\left(\omega_1^2-\omega^2\right)\right]+2j\omega\tau_1\right\}} \quad (5.7)$$

$$X^t_{nr2} \rightarrow \Im_{X^t_{nr2}}(\omega) = A_2\tau_2 \frac{j\omega\tau_2-1}{\left\{\left[1+\tau_2^2\left(\omega_2^2-\omega^2\right)\right]-2j\omega\tau_2\right\}} \quad (5.8)$$

$$Y^t_{nr2} \rightarrow \Im_{Y^t_{nr2}}(\omega)=A_2\omega_2\tau_2^2\frac{1}{\left\{\left[1+\tau_2^2\left(\omega_2^2-\omega^2\right)\right]-2j\omega\tau_2\right\}} \tag{5.9}$$

Clearly, the Fourier Transform of X^t_{nr} and Y^t_{nr} (5.5) is obtained in the following manner:

$$\Im_{X^t_{nr}}(\omega)=\Im_{X^t_{nr1}}(\omega)+\Im_{X^t_{nr2}}(\omega) \tag{5.10}$$

$$\Im_{Y^t_{nr}}(\omega)=\Im_{Y^t_{nr1}}(\omega)+\Im_{Y^t_{nr2}}(\omega) \tag{5.11}$$

Let us now introduce the functions σ+ and σ–, defined (in the frequency domain) as:

$$\sigma_+(\omega)=\frac{1}{\sqrt{2}}\left(\Im_{X^t_{nr}}(\omega)+j\Im_{Y^t_{nr}}(\omega)\right)\quad \omega<\omega_C/2;\ \omega_C=2\pi\nu_C \tag{5.12.a}$$

$$\sigma_+(\omega)=\frac{1}{\sqrt{2}}\left(\Im_{X^t_{nr}}(\omega)-j\Im_{Y^t_{nr}}(\omega)\right)\quad \omega>\omega_C/2 \tag{5.12.b}$$

$$\sigma_-(\omega)=\frac{1}{\sqrt{2}}\left(\Im_{X^t_{nr}}(\omega)-j\Im_{Y^t_{nr}}(\omega)\right)\quad \omega<\omega_C/2 \tag{5.12.c}$$

$$\sigma_-(\omega)=\frac{1}{\sqrt{2}}\left(\Im_{X^t_{nr}}(\omega)+j\Im_{Y^t_{nr}}(\omega)\right)\quad \omega>\omega_C/2 \tag{5.12.d}$$

In appendix 5.B we demonstrate that the Fourier Transform σ+ contains only the spectral line corresponding to the forward whirling motion (i.e. a peak at frequency ω_2), while the Fourier transform σ- contains only the line corresponding to the backward whirling motion at frequency ω_1. By performing the inverse Fourier transform of σ+, the resulting signal is, in essence, the forward whirling motion. Instead, starting from σ- the backward whirl is obtained.

5.4: BACKWARD AND FORWARD WHIRLS IN THE EXPERIMENT.

Having a suitable physical theory of the line formation, the backward and forward whirling motions can be read off from the experimental data X^e_{nr} and Y^e_{nr}. As said before, they are discrete time signals acquired at the rate of $1/(8T_C)$ samples per second and their discrete Fourier transforms are called $\Im_{Xnr}(k)$[3] and $\Im_{Ynr}(k)$. Note that X^e_{nr} and Y^e_{nr} are 4N components vectors[4]. Hence, their discrete Fourier transforms have 4N spectral components. Note that although the sequences X^e_{nr} and Y^e_{nr} are real, $\Im_{Xnr}(k)$ and $\Im_{Ynr}(k)$ are complex. The first component of the transformed data $\Im_{Xnr}(1)$ ($\Im_{Ynr}(1)$) is the constant contribution proportional to the mean value of X^e_{nr} (Y^e_{nr}) and the $\Im_{Xnr}(2N+1)\in\mathbb{R}$ element corresponds to the Nyquist frequency[5]. The (2N+1+k)-th component corresponds to the complex conjugate

[3] The measurements are performed for N=1400 spin periods, the total integration time is $T_{tot}=32NT_C=2660s>>T_C$. The smaller frequency component which can be identified in the frequency domain is then: $\omega_{min}=2\pi/T_{tot}=2\pi/(32NT_C)=2\pi\cdot 0.000376\text{Hz}$. The Fourier transform $\Im(\omega)$ is computed only at discrete values of ω, namely: $\omega(k)=(k-1)\omega_{min}$ for k=1,2,…,2N.

[4] The original vector X has 32N components while X_{nr} has 32N/8 components.

[5] Nyquist frequency: $\nu_C/2$.

of the (2N+1-k)-th component in the first half of $\Im_{Xnr}(k)$, i.e. $\Im_{Xnr}(2N+1+k)=\left(\Im_{Xnr}(2N+1-k)\right)^{*}$. The whirl frequencies ω_1 and ω_2 are not known "a priori", but they are obtained by searching for the peaks in $\Im_{Xnr}(k)$ and $\Im_{Ynr}(k)$. Their values are listed in tables 5.1 and 5.2.

Multiple of ω_{min} k	Frequency [Hz]	X_{nr} : Magnitude [μm]	X_{nr} : Phase [Degrees]
226	0.085007	18.27	-75.8
227	0.085383	41.27	-73.3
228	0.085759	65.92	158.7
229	0.086135	19.62	127.2
230	0.086511	11.48	134.8

Table 5.1: Frequency components of $\Im_{Xnr}(k)$. Backward whirl occurs at frequency $\omega_1=2\pi\cdot0.085759$rad/sec (i.e. k=228). Magnitude value is intermediate between the initial and final value of the oscillation's amplitude.

Multiple of ω_{min} k	Frequency [Hz]	X_{nr} : Magnitude [μm]	X_{nr} : Phase [Degrees]
246	0.09253	22.05	-151.5
247	0.092906	41.28	-124.4
248	0.093282	124.33	-28.9
249	0.093658	22.24	16.8
250	0.094034	14.15	27.9

Table 5.2: Frequency components of $\Im_{Xnr}(k)$. Forward whirl occurs at frequency $\omega_2=2\pi\cdot0.093282$rad/sec (i.e. k=248).

To proceed further, we have to introduce the new vector $\Psi(k)$, which helps us to construct the vectors $\sigma+(k)$ and $\sigma-(k)$ defined in section 5.3 (equations (5.12.a), (5.12.b), (5.12.c) and (5.12.d)). Its components are obtained from $\Im_{Ynr}(k)$ as follows:

$$\Psi(1)=\Im_{Y_{nr}}(1) \tag{5.13.a}$$

$$\Psi(2:2N)=j\Im_{Y_{nr}}(2:2N) \tag{5.13.b}$$

$$\Psi(2N+1)=\Im_{Y_{nr}}(2N+1) \tag{5.13.c}$$

$$\Psi(2N+2:4N)=-j\Im_{Y_{nr}}(2N+2:4N) \tag{5.13.d}$$

$\Psi(k)$ is a complex vector, and its inverse Fourier transform is real. By combining the definitions (5.12) and (5.13), it readily follows:

$$\sigma_{+}(k)=\left(\Im_{X_{nr}}(k)+\Psi(k)\right)/\sqrt{2} \tag{5.14}$$

$$\sigma_{-}(k)=\left(\Im_{X_{nr}}(k)-\Psi(k)\right)/\sqrt{2} \tag{5.15}$$

In figure 5.4 $\sigma+(k)$ (5.14) is plotted as a function of the frequency $\nu(k)$.

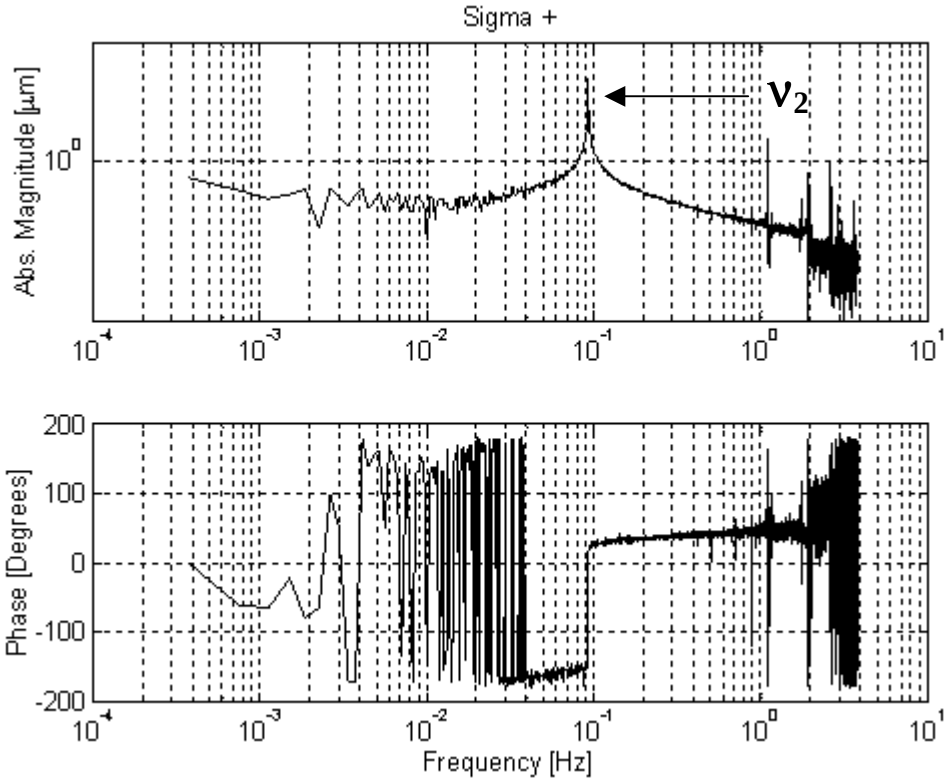

Figure 5.4: σ+ as a function of the frequency. The strong peak at the frequency 0.093Hz (forward whirl) is easily recognized. The peak at the frequency 0.086 Hz has disappeared.

Figure 5.5 shows the σ−(k) function as defined by (5.15).

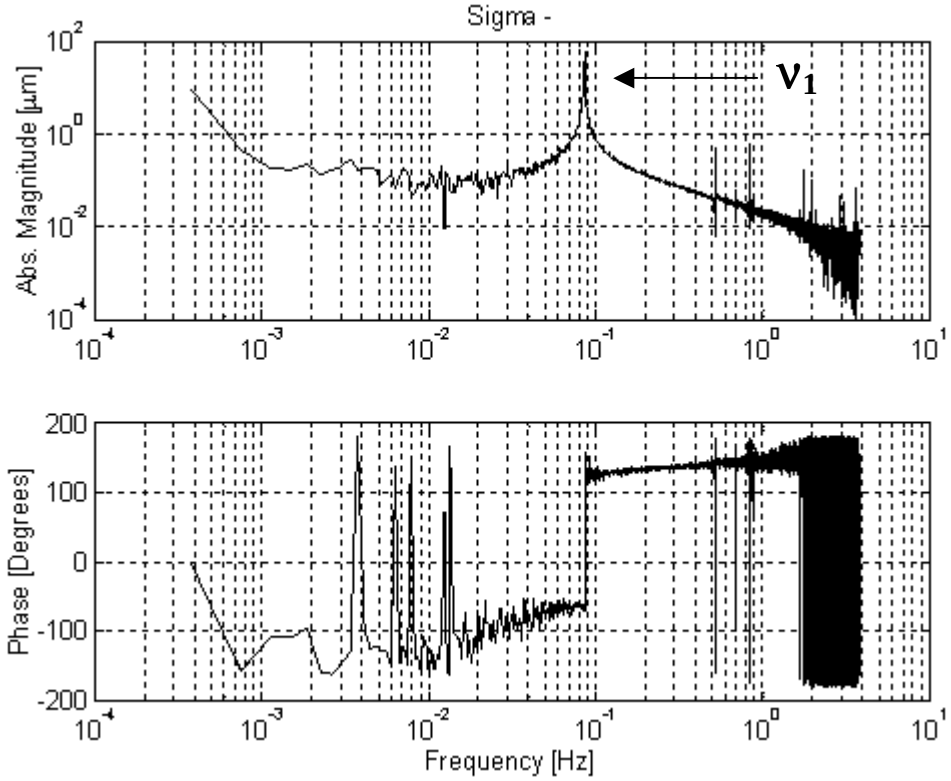

Figure 5.5: σ− as a function of the frequency. The strong peak at the frequency 0.086Hz (backward whirl) is easily recognized. The peak at the frequency 0.093 Hz has disappeared.

As expected (see (5.B.9) and (5.B.16) in appendix 5.B), σ-(k) has only a peak at frequency ω_1 corresponding to a backward whirl and σ+(k) a peak at frequency ω_2 corresponding to a forward whirl. Hence, backward and forward whirls have been separated. The frequency components of σ–(k) and σ+(k) are listed in tables 5.3 and 5.4.

Multiple of ω_{min} k	Frequency [Hz]	σ+: Magnitude [μm]	σ+: Phase [Degrees]
227	0.085383	40.92	-70.8
228	0.085759	64.16	158.0
229	0.086135	19.13	122.4

Table 5.3: Frequency Components of σ+.

Multiple of ω_{min} K	Frequency [Hz]	σ-: Magnitude [μm]	σ-: Phase [Degrees]
247	0.092906	42.40	-122.1
248	0.093282	126.50	-28.9
249	0.093658	22.88	14.1

Table 5.4: Frequency Components of σ–.

By performing the inverse discrete Fourier transform of σ+ (5.14), the forward whirl Wf(t) is obtained as a function of time. In the same manner, the backward whirl Wb(t) is obtained by performing the inverse discrete Fourier transform of σ- (5.15). In figure 5.6, the discrete time function Wf(t) is plotted as a function of time. Its amplitude grows with exponential law.

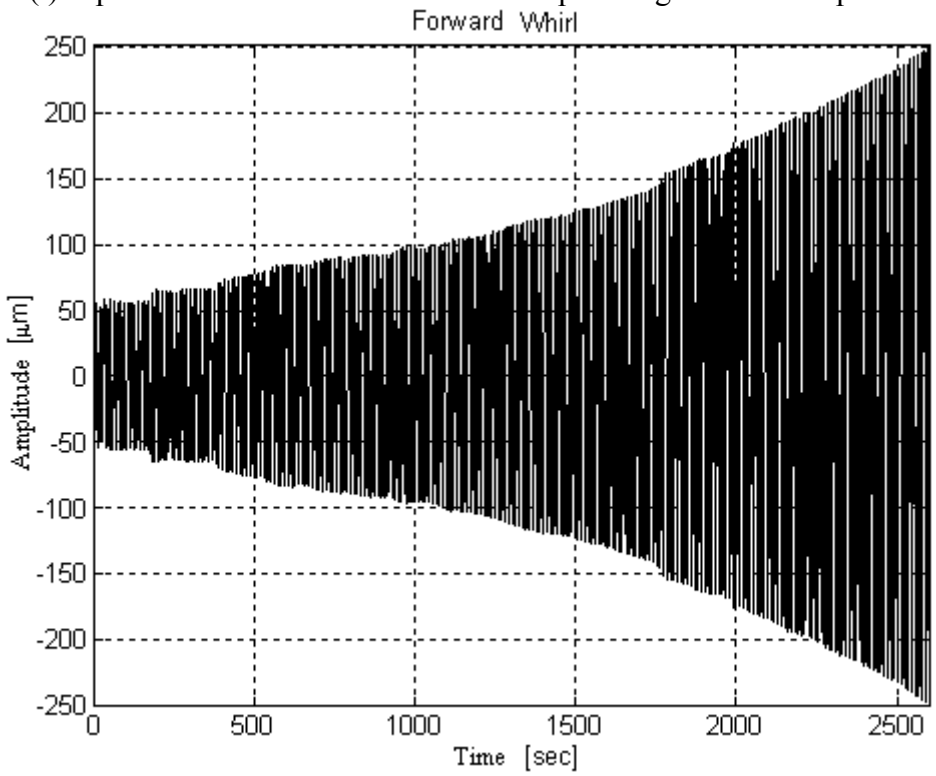

Figure 5.6: The discrete time function Wf(t) is plotted as a function of time. Its amplitude grows in time with exponential law.

In figure 5.7, instead, the discrete signal Wb(t) is plotted.

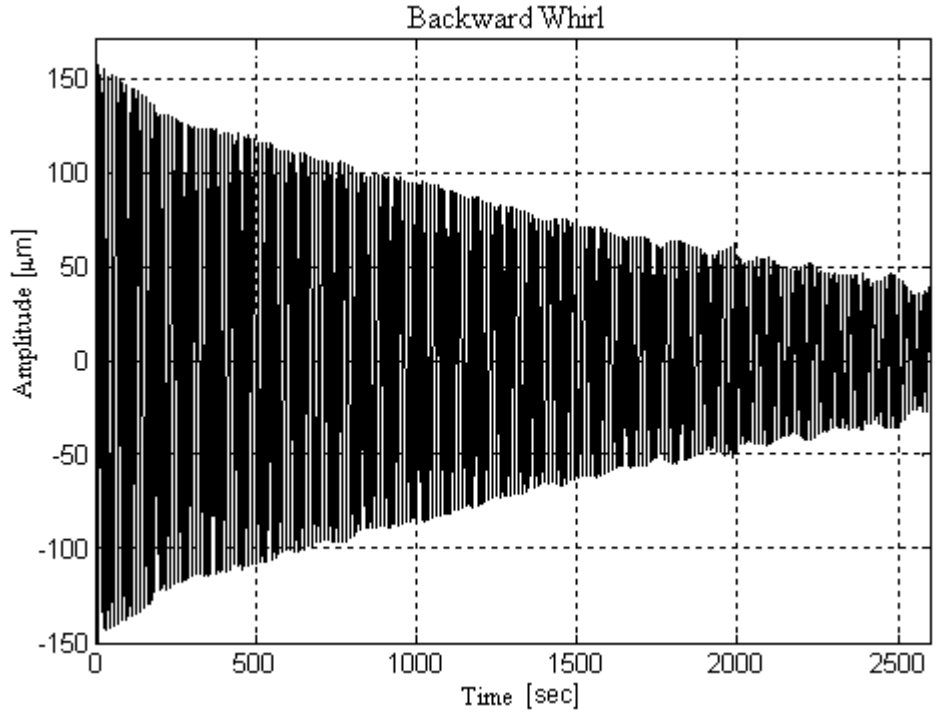

Figure 5.7: The discrete time function Wb(t) is plotted as a function of time. Its amplitude decreases in time with exponential law.

Clearly, this is a backward whirl with decreasing amplitude. The relative displacements of the test cylinders in the horizontal (non-rotating) plane of the laboratory (polar plot Y_{nr}^{e} vs. X_{nr}^{e}) with accelerometer spinning at 1.9Hz (counter-clockwise) is shown in figure 5.8.

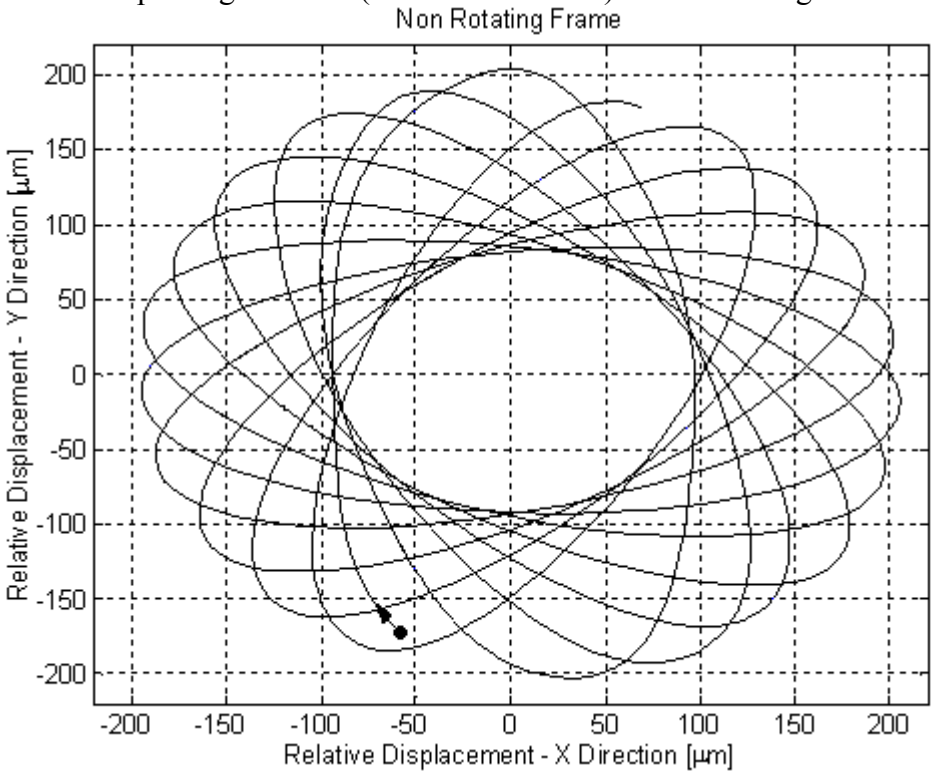

Figure 5.8: The relative displacements of the test cylinders in the horizontal (non-rotating) x-y plane of the laboratory (polar plot X_{nr}^{e} vs. Y_{nr}^{e}) with accelerometer spinning at 1.9Hz (counter-clockwise). The black circle represents the starting point. The cylinders perform essentially a backward whirl motion (clockwise).

The black circle represents the starting point. During the first 150 seconds of the run lasting 2600 seconds, the cylinders perform essentially a backward whirl motion (clockwise, as indicated by the arrow), showing the possibility of backward whirling to be excited by unbalances in presence of a non-isotropic rotor accelerating from 0 Hz to the supercritical range (on the same argument see section 1.10).
It is useful to stress that the backward whirl is stable and its amplitude decreases in time, while the forward one is unstable, with increasing amplitude. As a consequence, at first they combine in a way that the resulting motion is backward, then the forward motion becomes dominant. There is an intermediate interval of time during which the resulting motion is linear[6]. In figure 5.9 the linear motion is depicted in red. After this intermediate interval, the dominant motion is a forward whirl with increasing amplitude (see figure 5.10) while the backward whirl tends to vanish. In the end, the motion is almost circular.

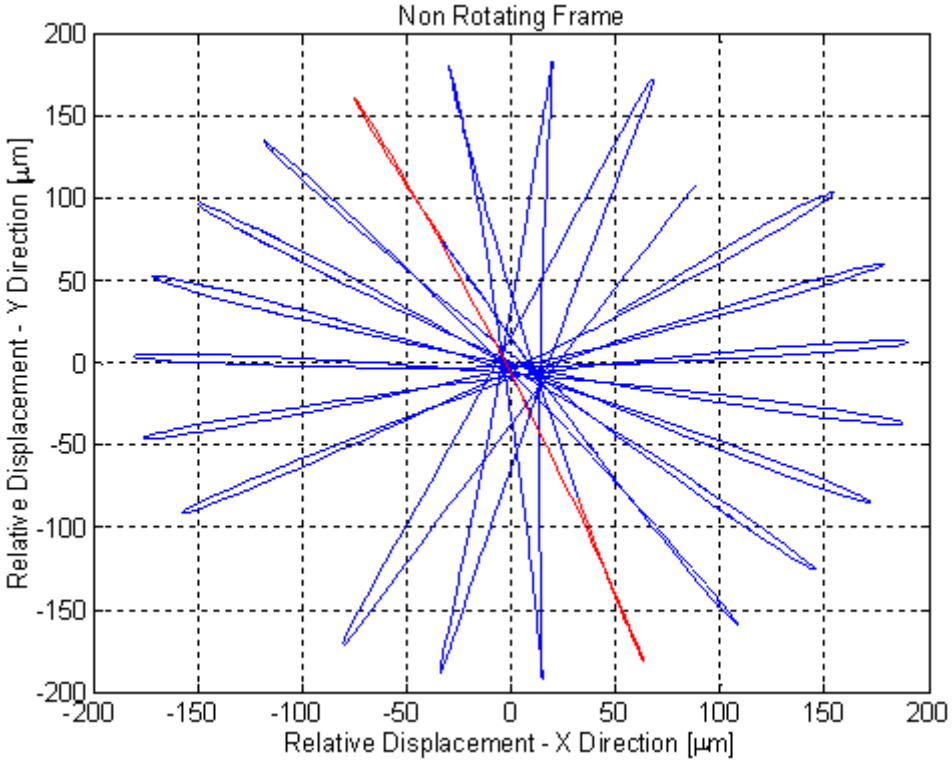

Figure 5.9: Polar plot (in the non-rotating frame) of the relative displacements between the two test cylinders. The intermediate interval of time during which the resulting motion is linear is shown (red).

5.5: BEST FIT OF THE WHIRL MOTION.

The first aim of our analysis amounts to find the time constant of the free forward whirling. The signal Wf(k) (obtained from σ+) has been fitted to the theoretical signal:

$$\text{fit}\_\text{Wf}(t) = A_2 \cos(\omega_2 t + \varphi_2) e^{t/\tau_2} + k_2 \qquad (5.16)$$

We evaluate the parameters A_2, φ_2, τ_2, k_2 by minimizing $\sum_{i=1}^{4N} [\text{Wf}(t(i)) - \text{fit}\_\text{Wf}(t(i))]^2$. In figure 5.11 the forward whirl obtained from the experimental data Wf(t) (blue curve) is compared with the fitting curve (5.16) (red curve).

[6] Linear means that there is an harmonic vibration along one direction.

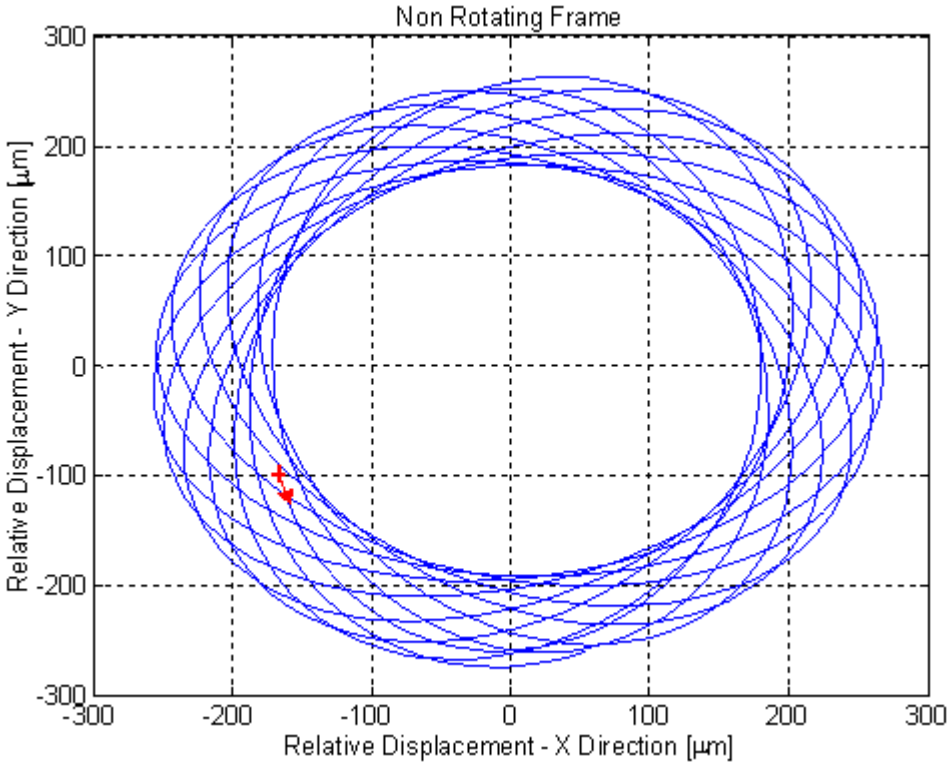

Figure 5.10: Polar plot (non-rotating frame) of the displacements between the 2 test cylinders. At the end, the bodies perform a forward whirling motion (almost circular).

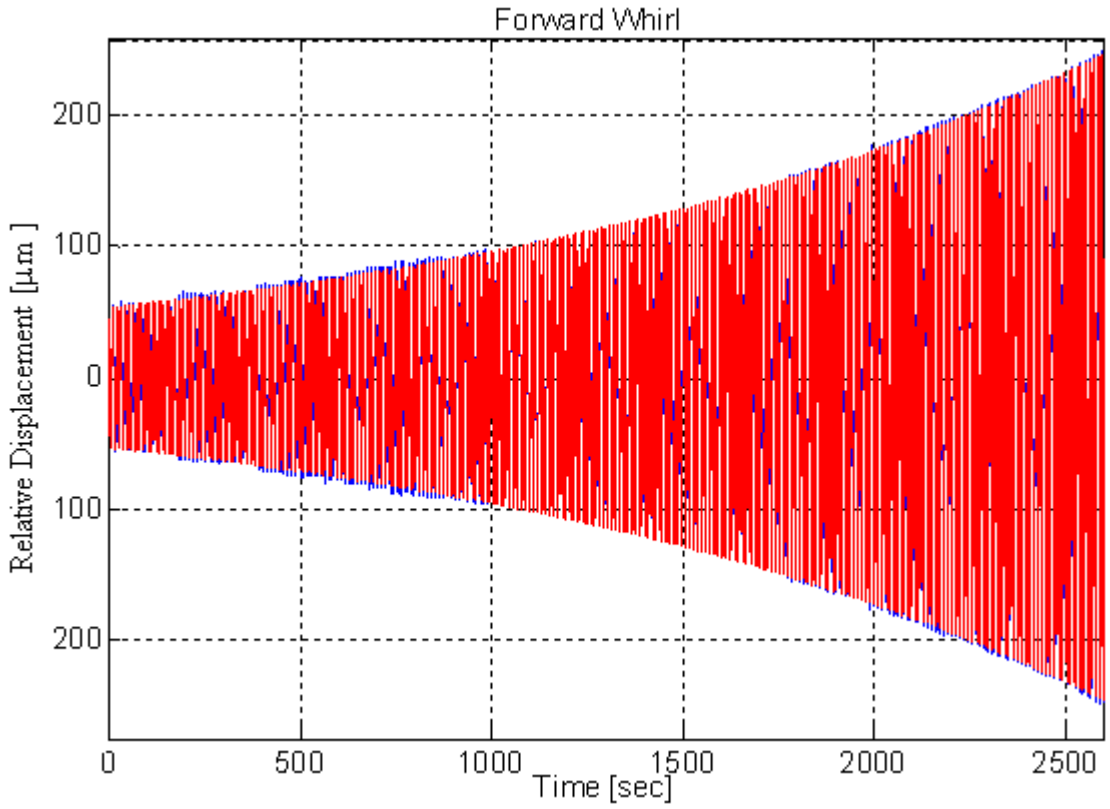

Figure 5.11: Forward whirl Wf(t) (blue) compared with the fitting curve (red).

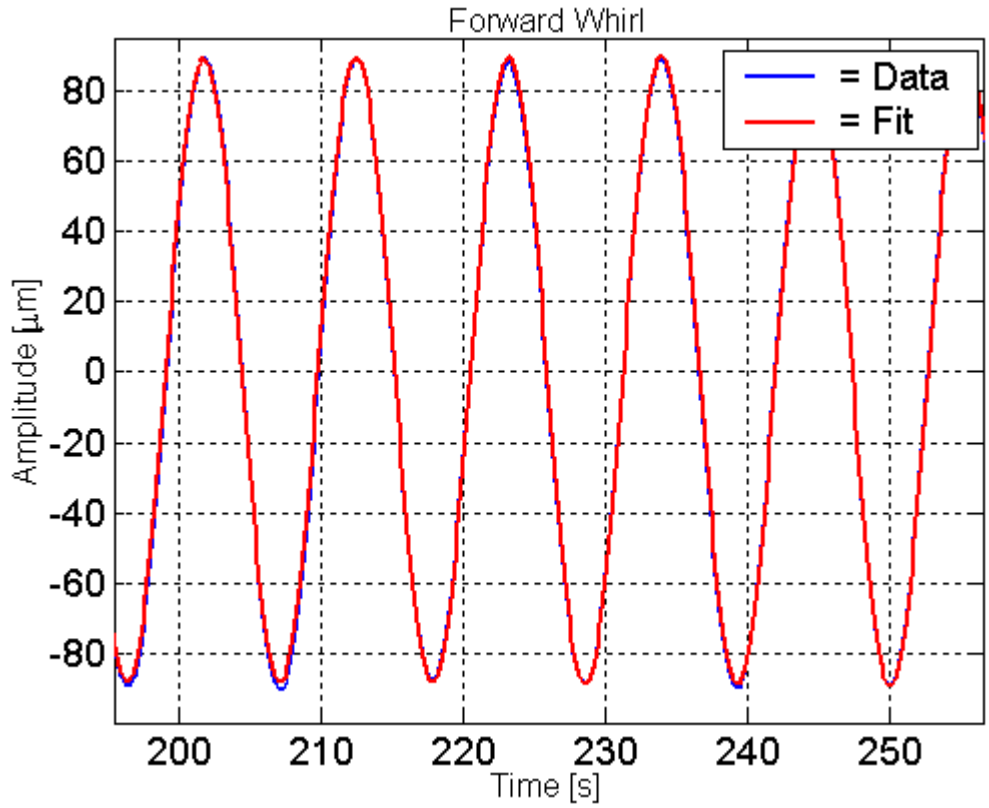

Figure 5.12: Enlargement of figure 5.11 showing in detail a small interval of time. Blue: Experimental data in the non-rotating frame. Red: Fitting curve.

Figure 5.12 is an enlargement of figure 5.11 and shows in detail a small interval of time. In figure 5.13 the discrete Fourier transform $\sigma_+(k)$ (5.14) of Wf(t) (blue) is compared with the FFT of the theoretical signal fit_Wf(t) (red).

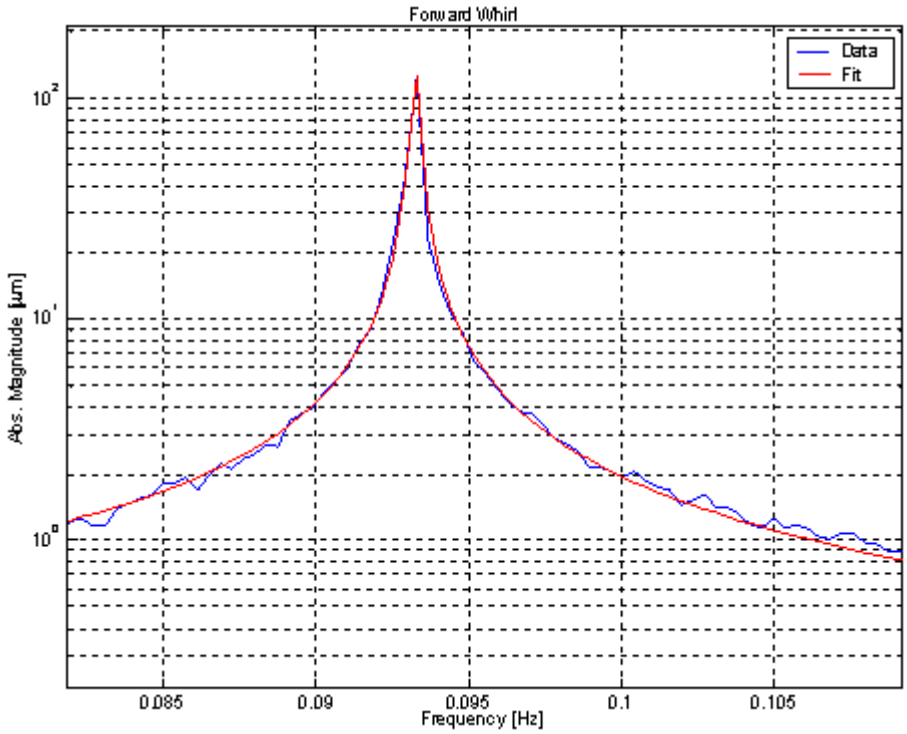

Figure 5.13: Blue curve: σ_+ as a function of frequency. Red curve: FFT of (5.37).

Then, in figure 5.14, the residue is plotted as a function of time.

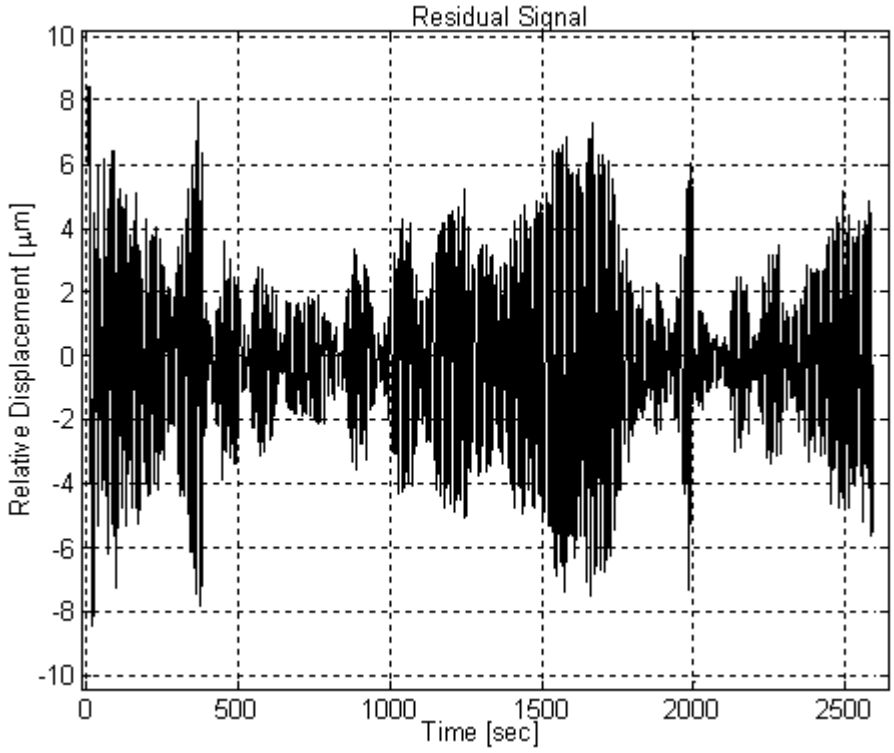

Figure 5.14: The residue Wf(t) - fit_WF(t) is plotted as a function of time.

The backward whirling motion Wb(t) has been fitted in a similar manner. Outputs of the data analysis are the time constants of the forward (τ_2 = 1703.4s) and backward (τ_1 = 1861.9 s) whirling motion. The time constant scales as the quality factor of the system, namely:

$$Q_w = -\omega_w \tau_w / 2 \qquad (5.17)$$

where ω_w is the whirling frequency (i.e. $\omega_w=\omega_1$ or $\omega_w=\omega_2$). By inserting the whirling frequencies ω_1, ω_2 and the outputs of our analysis τ_1 and τ_2 in (5.38), the Q_w values are easily obtained, i.e Q_1=-501 and Q_2=-499.

5.6: GENERAL CONSIDERATIONS ON THE QUALITY FACTOR OF THE GGG SYSTEM.

The results represented in section 5.6 (i.e. Q_1=-501 and Q_2=-499) refer to the apparatus which has been operated in May 2002. These values are lower than we had expected indicating that big losses take place in the system once in supercritical rotation.
In the following sections we will show some results obtained from measurements performed during the last three years (2001-2003) which are related to this problem, showing the dependence of the quality factor Q from the pressure inside the vacuum chamber and from the oscillation amplitude and frequency.
By these Q measurements at different pressures (for free oscillations at zero spin rate) it was possible to establish that residual air in between the test cylinders gives rise to dissipation

only above 10^{-4}mbar. Hence, if the system is operated at sufficiently low pressure, the losses depend on the laminar suspensions only.
We have also checked that the value of *Q* increases with decreasing oscillation amplitude of the non-spinning rotor. In the same way, the quality factor at the natural frequencies has been measured at zero spin rate, by exciting oscillations at these frequencies and measuring the decay in the free oscillation amplitude. We have thus checked that the value of *Q* increases with the frequency (losses are smaller at higher frequency) reaching very high values (about 93000) at 1.4Hz.
Though the measurements for the non-spinning rotor clearly show that it is possible to manufacture high quality cardanic suspensions of rather complex shape, the measurements performed with the spinning rotor have identified an important issue which requires attention. In spite of the high *Q* values measured at zero rate and low pressure (due to the suspensions only), the growth rate of whirl once in supercritical rotation is indeed much faster than expected by high *Q*, indicating that, during rotation, much bigger losses take place in the system beside the ones in the suspensions.
A source of rotating damping (the kind of damping which is known to produce whirl instability) may be due to the rubber O-ring (OR in figure 2.1) used to transmit rotation from the motor (in its offset location) to the rotating suspension tube ST (the O-ring is the unique part of the apparatus which undergoes deformations only when the system rotates and does not contribute to the energy dissipation at zero spin rate). We have performed some tests which confirm our prediction. This problem can be solved by eliminating the O-ring altogether, i.e. by locating the motor on the spin axis. Other possible causes of spurious losses are under investigation in order to obtain the values measured in absence of rotation.

5.7: Q MEASUREMENTS AT ZERO SPIN RATE.

In section 5.3, we have described the procedure developed to extract whirling parameters (in particular the quality factor) from experimental data. This section, instead, is devoted to the description of the procedure for measuring the quality factors at natural frequencies for the system at zero spin rate (free oscillations[7]):

- Pressure inside the vacuum chamber lower than $5 \cdot 10^{-5}$ mbar
- At first, the oscillation amplitude is actively damped.
- Oscillations at the natural frequencies are, then, excited by an external electrical force generated by the plates used for the active control of whirling motions (see section 2.6 and chapter 6). For example, in the case described below, this exciting force was applied along the x direction.
- After having switched off the exciting force, the amplitude decay is measured as a function of time. For these measurements we use the capacitance sensors placed near the outside surface of the outer mass (typically devoted to the active control of whirling motion). In fact, the electronics of the main sensors, which provides best sensitivity to differential oscillations, is essentially insensitive to common mode

[7] From now on, "free oscillations" and "free system" mean "at zero spin rate" , i.e. they refer to the system operated at zero spin rate (ν_S=0Hz).

oscillation. These data are acquired by National Instrument card, mounted onboard a computer.

The quality factors are obtained from the raw data of the capacitance bridges by the procedure described below (for demonstration purposes, we will describe this procedure by applying it to the signal acquired on 9 April 2003 at 16:45). The FFT of the raw signal (displacements along x direction in the non-rotating reference frame) is shown in figure 5.16. The system was operated in a configuration slightly different from the one described in chapters 3 and 4 (with natural frequencies ν_d=0.09 Hz, ν_{c1}=0.91Hz and ν_{c2}=1.26Hz), which was operated during 2002. In particular the length L_1 had been increased in order to obtain an higher common mode frequency ν_{c2}, i.e. 1.4160 Hz and ΔL had been regulated to obtain 20 seconds of differential period. As a consequence, the three natural modes in figure 5.16 have frequencies ν_d=0.0553 Hz, ν_{c1}=0.891Hz and ν_{c2}=1.4160 Hz.

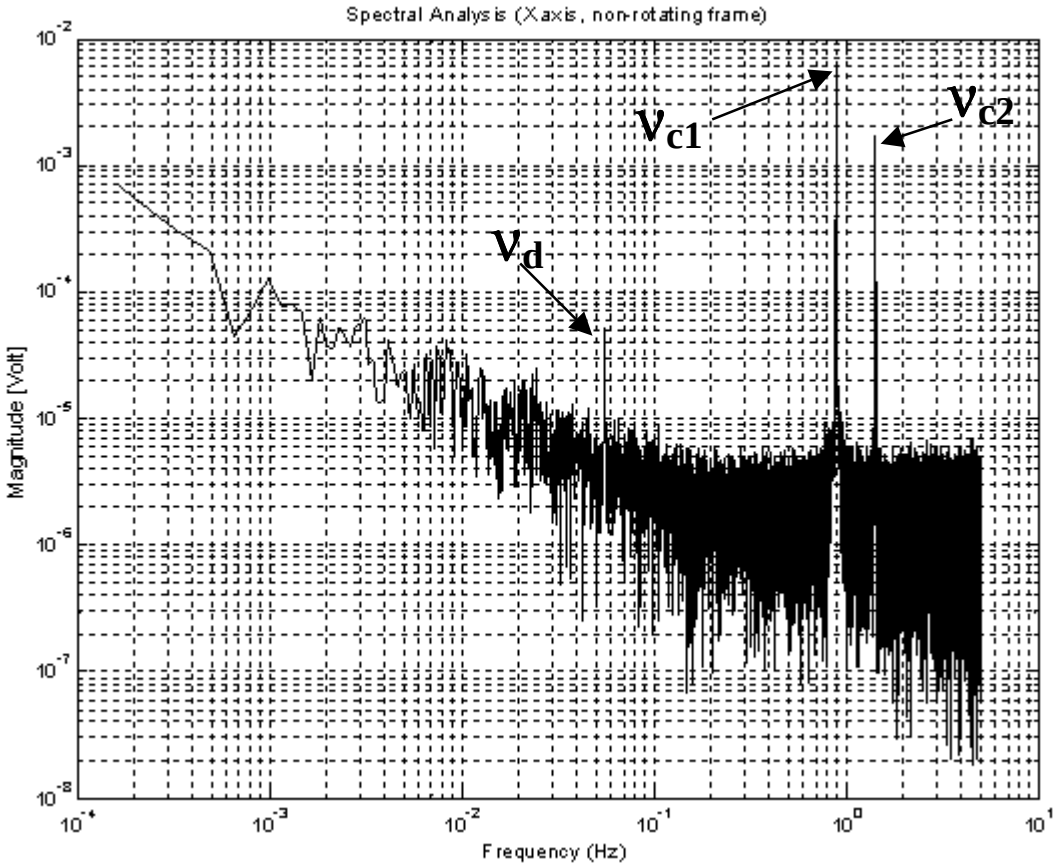

Figure 5.15: FFT of the signal acquired on 9 April 2003 at 16:45. Free oscillations.

We can perform a peak detection on the signal by fitting it to the function (5.18) in the time domain:

$$X(t)=\sum_{i=d,1,2} A_i \exp(-t/\tau_i)\cos(\omega_i t+\varphi_i) \qquad (5.18)$$

Outputs are the parameters to be used for the fit, i.e. the amplitudes, the time constants and the phases. By inserting the time constants in equation (5.17), the resulting quality factors of the GGG accelerometer at the natural frequencies (at zero spin rate) are obtained. The FFT of the

original signal (red), the FFT of the fitting function (blue) and the FFT of the residue (original signal minus the function in (5.18)) are shown in figure 5.16.

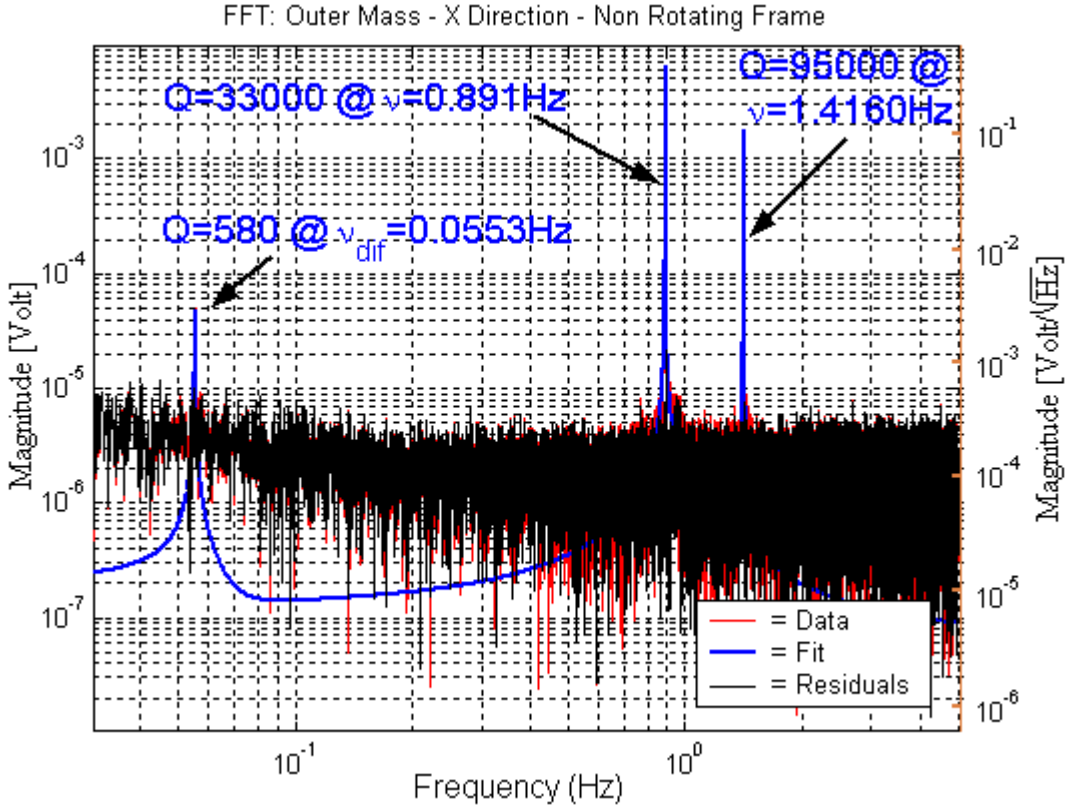

Figure 5.16: The FFT of the original signal (red), the FFT of the fitting function (blue) and the FFT of the residue (original signal minus function (5.18) in black).

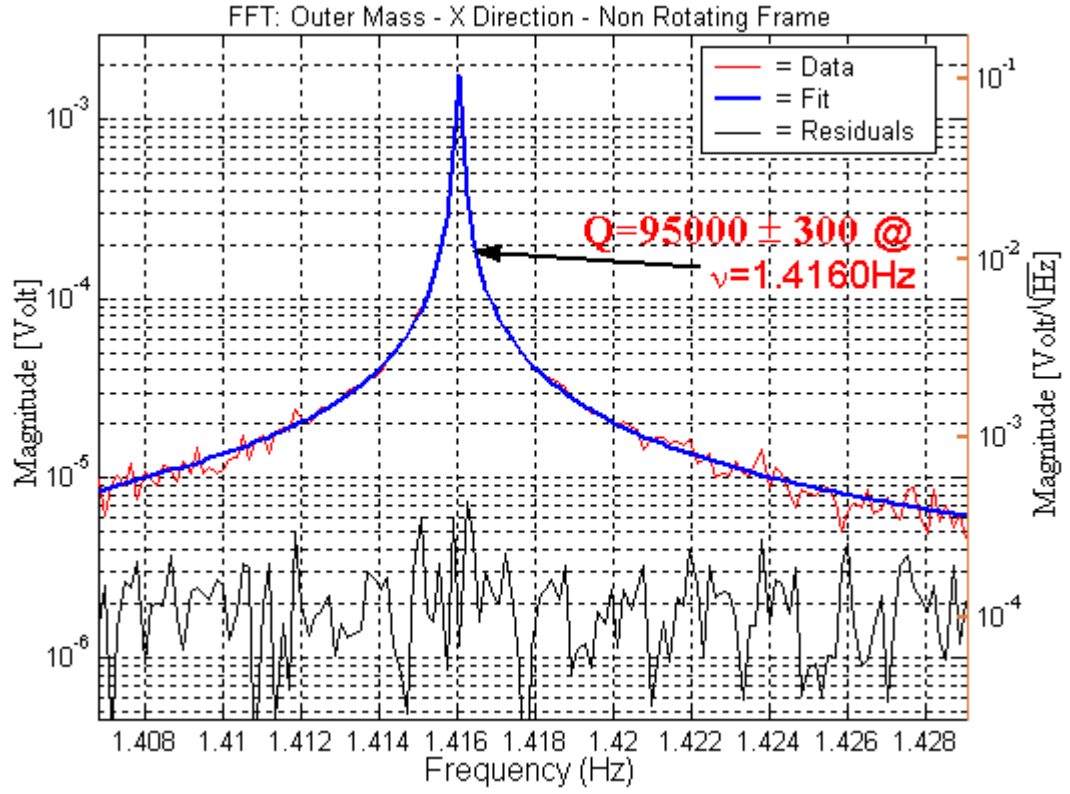

Figure 5.17: Enlargement of figure 5.16. Q measurement at the natural frequency ν_2=1.416Hz.

We have to evaluate the background level of the noise: in figure 5.17 an enlargement of figure 5.16 is plotted; it is possible to see that the value of the residue at the frequency ν_{c2}=1.416Hz is about 10^{-4} Volt/√Hz which is the level of the noise fluctuations in the card used for data acquisition (figure 5.18). Obviously, the *Q* values obtained by fitting experimental data to the function (5.18) are in agreement with the values evaluated by considering the standard definition of the quality factor, i.e. $Q=\omega/\Delta\omega$.

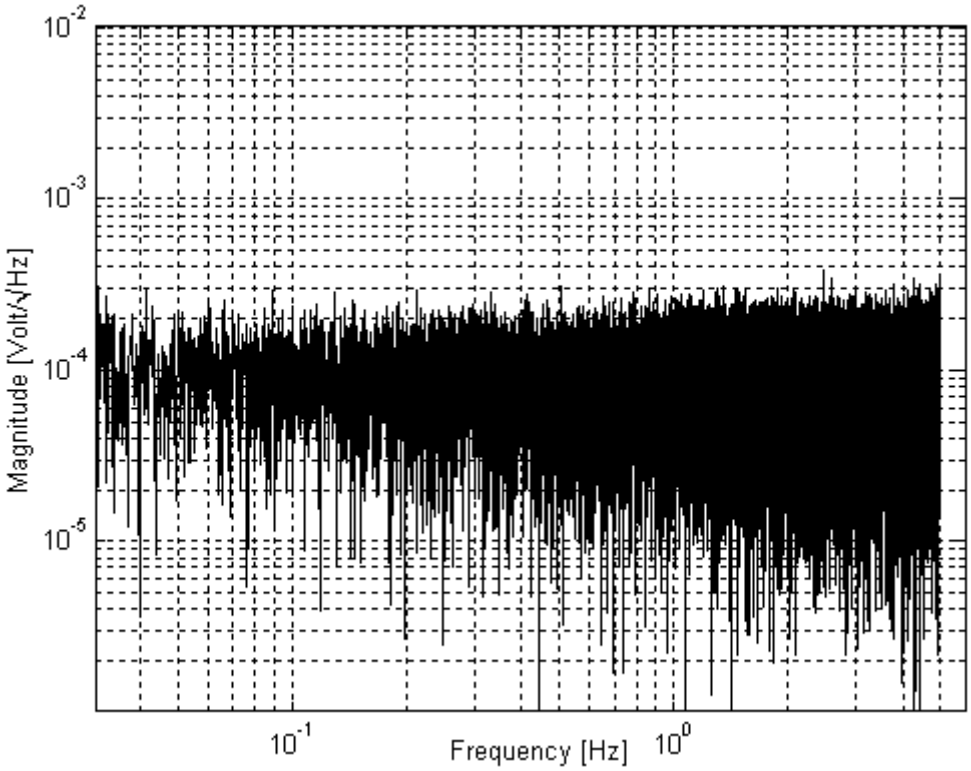

Figure 5.18: Background level of noise in the card used for data acquisition.

The growth rate of whirls is determined by losses in the system (see equation (1.80) in section 1.9), essentially in the mechanical suspensions. We have stressed the fact (see sections 1.5 and 1.7) that in supercritical rotation mechanical suspensions are known to undergo deformation (and therefore to dissipate energy) at the high spin frequency and not at the lower whirling frequency. This fact is confirmed by figure 5.2, where the FFT of the ξ component of the relative displacement between the two test cylinders in the rotating frame is shown as a function of the frequency; 3 high peaks are recognized: the peak at the spin frequency ν_s= 1.9 Hz, the peak corresponding to the forward whirling at about 1.8Hz, and the peak corresponding to the backward whirl at about 2Hz. This means that, in the rotating frame and in highly supercritical rotation, whirling motions grow at the frequencies $\nu_s \pm \nu_w$, hence, energy dissipations occur at these high frequencies. As a consequence, in figure 5.16 the relevant *Q* is that measured at the high frequency ν_{c2}=1.4Hz (93000) and not that measured at the low frequency ν_d=0.05Hz (580).

By performing *Q* measurements at different pressures it was possible to prove that residual air in between the cylinders gives rise to dissipation. Losses due to air friction decrease with pressure until they remain constant and no longer depend on it below 10^{-4} mbar. Figure 5.19 shows the Log_{10}-Log_{10} plot of the $1/Q$ value of the natural differential oscillations (almost 8 s period during 2001), at zero spin rate, as function of the residual air pressure in the chamber

with linear best fits to the two sets of data, above and below 10^{-4}mbar. Each point refers to a separate run. For pressures greater than about 10^{-4}mbar the value of *Q* decreases as pressure increases. For lower pressures the value of Q reaches about 1590 and is then independent by pressure since it is the maximum value allowed by losses in the laminar suspensions. Figure 5.19 indicates that, as long as the system is operated at sufficiently low pressure, losses depend on the laminar suspension only.

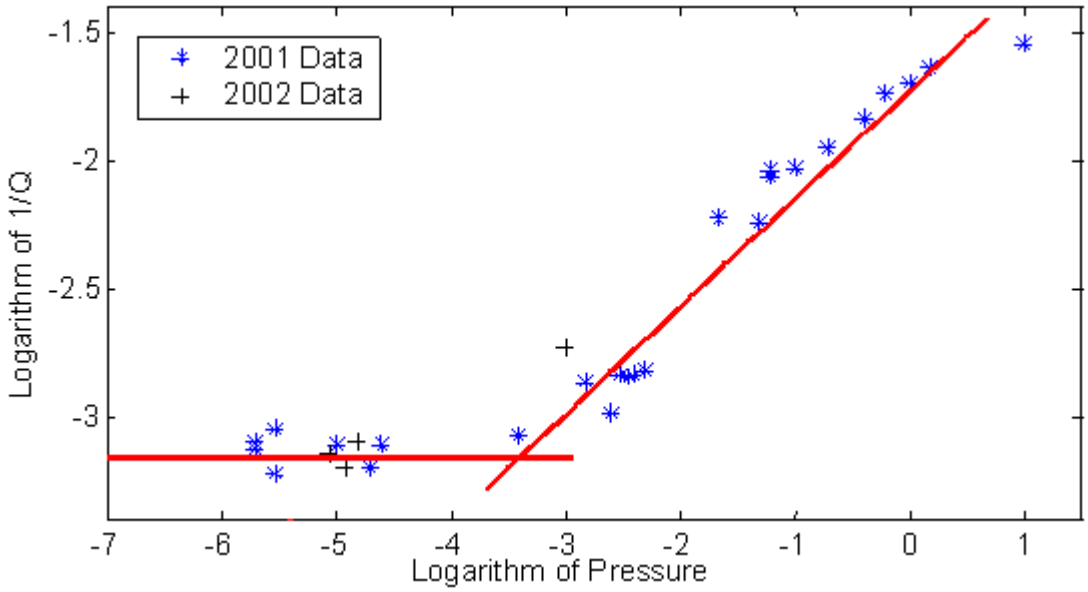

Figure 5.19: Log_{10} plot of 1/Q of the natural differential oscillations (8s period), at zero spin rate, as function of the pressure in the vacuum chamber with linear best fits to the two sets of data, above and below 10^{-4}mbar. Each point refers to a separate run.

Figure 5.20 shows, then, the value of *Q*, at ν_S=0Hz, as a function of the oscillation amplitude.

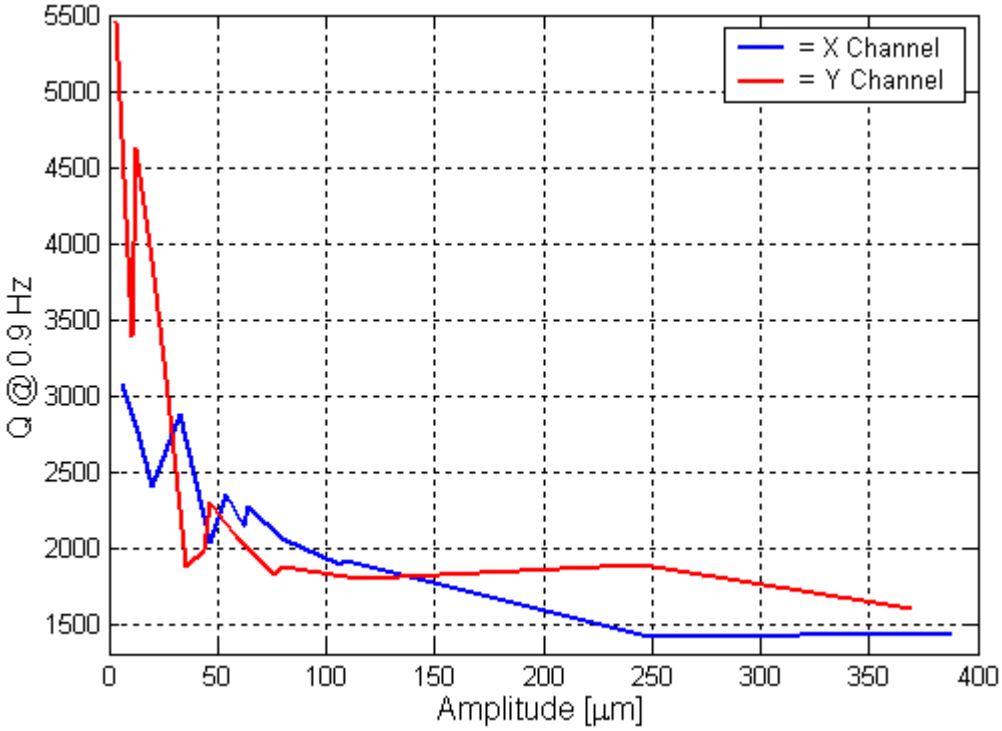

Figure 5.20: Plot of Q as a function of the oscillations amplitude (measured at the start of the run). Each point refers to a separate run. These data have been acquired in September 2002.

For amplitudes greater than about 100μm the value of *Q* is almost constant. For lower amplitudes the value of *Q* increases as initial amplitude decreases.

CHAPTER 6:

ACTIVE LINEAR CONTROL OF THE WHIRL MOTIONS.

6.1: INTRODUCTION.

In supercritical rotors losses at the spin frequency are relevant for the growth of whirl motions that such rotors develop in the non-rotating system ([1 –3], [7 – 8]). For instance, the centres of mass of the GGG test cylinders develop an orbital motion in the horizontal plane (i.e. x-y plane) of the laboratory around their position of relative equilibrium (see (1.65)). Whirl motion grows in amplitude at a rate which depends on the quality factor *Q* of the system at the spin frequency (the time constant scales as *Q*, i.e. $1/\tau_w \propto 1/Q(\nu_s)$) .
The rotating part of the dissipative force $\vec{R}_{Rot}$ is to be ascribed to the deformations of the laminar suspension and, in supercritical rotation, it may act to destabilize the system. Rotating damping $\vec{R}_{Rot}$ has been introduced by means of equations (3.21), (3.22) and (3.23) as a generalized force. It can be expressed as:

$$R_{Rot}(Q,\dot{Q}) = -\Gamma_{Ra}(\dot{\hat{L}}_a - (\dot{\hat{L}}_a \cdot \hat{z}')\hat{z}') - \sum_{\lambda=1,2} \Gamma_{R\lambda}(\dot{\hat{L}}_\lambda - (\dot{\hat{L}}_\lambda \cdot \hat{r}_a(Q))\hat{r}_a(Q)) \quad (6.1)$$

where the velocities $\dot{\hat{L}}_\lambda, \dot{\hat{L}}_a$ coincide with (3.7), (3.8) and (3.9). The non-rotating damping has instead the function of stabilizing the system in supercritical rotations. In our accelerometer, non-rotating damping is introduced in two different ways. A passive damper is used when the rotor is accelerated to pass the resonance frequencies and acts only on the inner mass as discussed in section 2.6. It can be written as

$$R_{NR}(Q,\dot{Q}) = -\Gamma_{NR}(\vec{v}_i(Q,\dot{Q}) + \vec{\omega}_s \times \vec{r}_i(Q)) \quad (6.2)$$

When the rotor spins at its nominal frequency, whirls are controlled actively by means of capacitance sensors/actuators (see figures 2.10 and 6.1; see appendix G for the schemes of the electronics). Control forces act only on the outer test mass and are included in the mathematical model as depicted by equation (4.1).
In sections 6.2 and 6.3, simulations have been performed to study the capabilities of the controller to reduce the whirl motions. The electronics needed for the active control of whirl motions have been partially constructed and tested: experimental results are shown in section 6.4 and have been reported in [34] too (this article is available in Appendix_Articles).

6.2 THE B MATRIX.

This section is devoted to the implementation of the active damping in the mathematical model developed in chapters 3 and 4. We want to write the equations of motion in the state form (4.1).

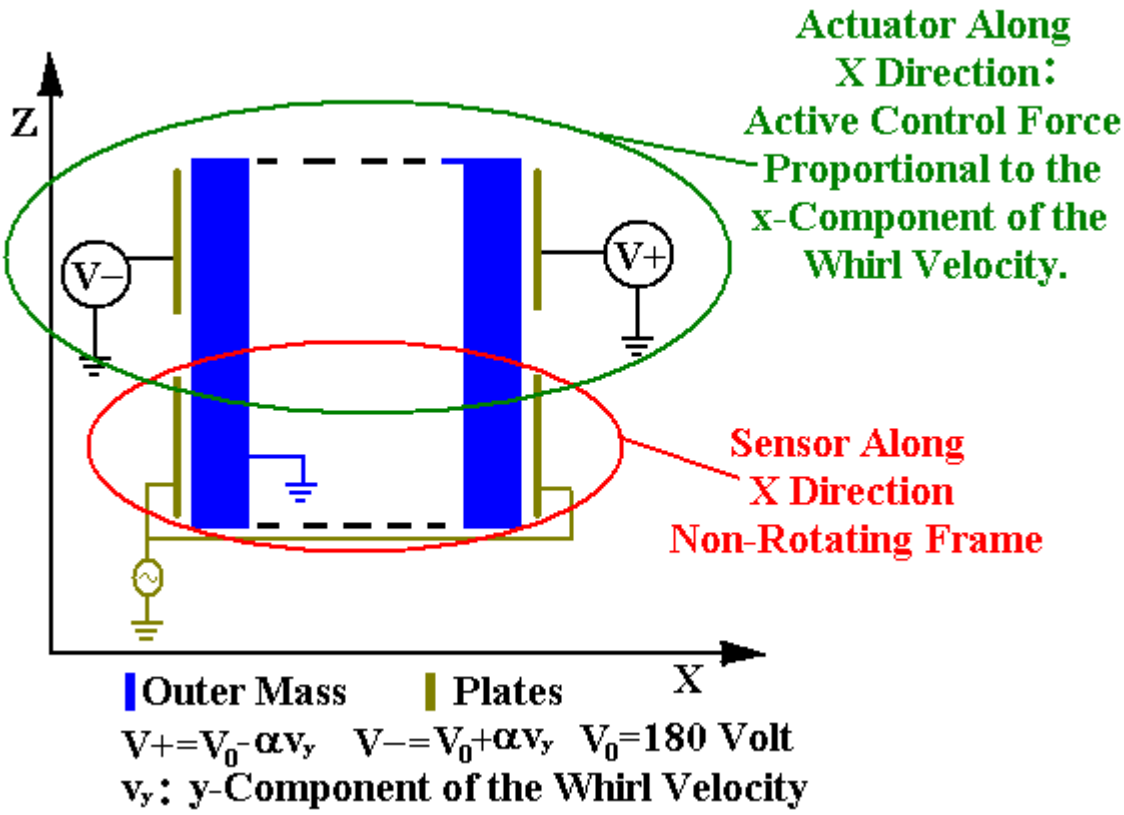

Figure 6.1: Section through the spin axis of the outer test cylinder (blue). 8 capacitance plates are placed near the outside surface of the outer cylinder (only four plates are shown in the picture). They are fixed with the vacuum chamber (i.e. fixed in the non-rotating frame). One half of them is used as sensors: measurements of the displacement of the outer test mass are used to build a damping command proportional to its velocity. The other half is used as actuators: a voltage (in the range 0Volt-360Volt) is applied to produce an active force which simulates the non-rotating damping. The x (y) component of the active force is proportional to the x (y) component of the whirling velocity.

While matrix A is not changed in comparison with chapter 4, matrix B changes according to the different definition of the vector $\vec{u}$. Now, inputs are the components of the control force in the ξ–η plane of the rotating reference frame, i.e.

$$\vec{u}=\begin{bmatrix} u_1 \\ u_2 \end{bmatrix}=\begin{bmatrix} F_{C,\xi}^{Rot} \\ F_{C,\eta}^{Rot} \end{bmatrix} \tag{6.3}$$

Matrix B_g (6×2-components; see equation (4.20)) transforms the 2-components input vector $\vec{u}$ into its 6-components counterpart $\vec{F}_g$ (the label "g" means generalized force), i.e. $\vec{F}_g = [B_g]\vec{u}$. Its components a re given by equation (6.4).

$$Fg_i = \sum_{j=\xi,\eta} \vec{u}_j \cdot \frac{\partial \vec{r}_{2,j}}{\partial q_i} \tag{6.4}$$

Starting from equation (6.4) matrix B_g is easily obtained and it results:

$$B_g = \begin{bmatrix} \dfrac{\partial r_{2,\xi}}{\partial \vartheta_a} & \dfrac{\partial r_{2,\eta}}{\partial \vartheta_a} \\ \dfrac{\partial r_{2,\xi}}{\partial \vartheta_2} & \dfrac{\partial r_{2,\eta}}{\partial \vartheta_2} \\ 0 & 0 \\ \dfrac{\partial r_{2,\xi}}{\partial \phi_a} & \dfrac{\partial r_{2,\eta}}{\partial \phi_a} \\ \dfrac{\partial r_{2,\xi}}{\partial \phi_2} & \dfrac{\partial r_{2,\eta}}{\partial \phi_2} \\ 0 & 0 \end{bmatrix} \tag{6.5}$$

The B matrix is numerically evaluated from matrix B_g by means of equations (4.22.a), (4.22.b) and (4.22.c). The C matrix is changed according to the different definition of the vector $\vec{y}$:

$$\vec{y} = \begin{bmatrix} y_1 \\ y_2 \end{bmatrix} = \begin{bmatrix} \Delta r_{2,\xi}^{Rot} \\ \Delta r_{2,\eta}^{Rot} \end{bmatrix} \tag{6.6}$$

where $\Delta\vec{r}_2^{Rot}(t)$ is defined in equation (4.14). Combining equations (4.2), (4.14) and (6.6), we obtain the coefficients of the new C matrix:

$$C_{1,1} = -(L + \Delta L)\cos(x_1^0)\cos(x_7^0) \tag{6.7.a}$$

$$C_{1,3} = L_2 \cos(x_3^0)\cos(x_9^0) \tag{6.7.b}$$

$$C_{1,7} = (L + \Delta L)\, x_7 \sin(x_1^0)\sin(x_7^0) \tag{6.7.c}$$

$$C_{1,9} = -L_2 x_9 \sin(x_3^0)\sin(x_9^0) \tag{6.7.d}$$

$$C_{2,1} = -(L + \Delta L)\cos(x_1^0)\sin(x_7^0) \tag{6.7.e}$$

$$C_{2,3} = L_2 \cos(x_3^0)\sin(x_9^0) \tag{6.7.f}$$

$$C_{2,7} = -(L + \Delta L)\, x_7 \sin(x_1^0)\cos(x_7^0) \tag{6.7.g}$$

$$C_{2,9} = L_2 x_9 \sin(x_3^0)\cos(x_9^0) \tag{6.7.h}$$

while all the coefficients not listed above are equal to zero ($\vec{x}^0$ indicates the equilibrium position (4.7)).

6.3 WHIRL DAMPING AND SIMULATION OF THE CONTROL SCHEME.

The State-Space block in figure 6.2 implements a system whose behaviour is defined by equations (4.1), where $\vec{x}$ is the state vector, $\vec{u}$ the input vector, and $\vec{y}$ the output vector. The matrix coefficients must have the characteristics illustrated in section 4.1. The block accepts

one input and generates one output. The input vector has 2 components, determined by the number of columns in the B and D matrices. The output vector has 2 components too, representing the displacement of the outer cylinder from the equilibrium position in the ξ–η plane in the rotating reference system.

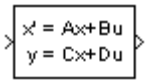

Figure 6.2: The State – Space Block in Simulink.

The stabilization of whirl motion can be implemented by building in a non-rotating frame a damping command proportional to the velocities between the two test bodies. The total block diagram of the damping command is illustrated in figure 6.3.

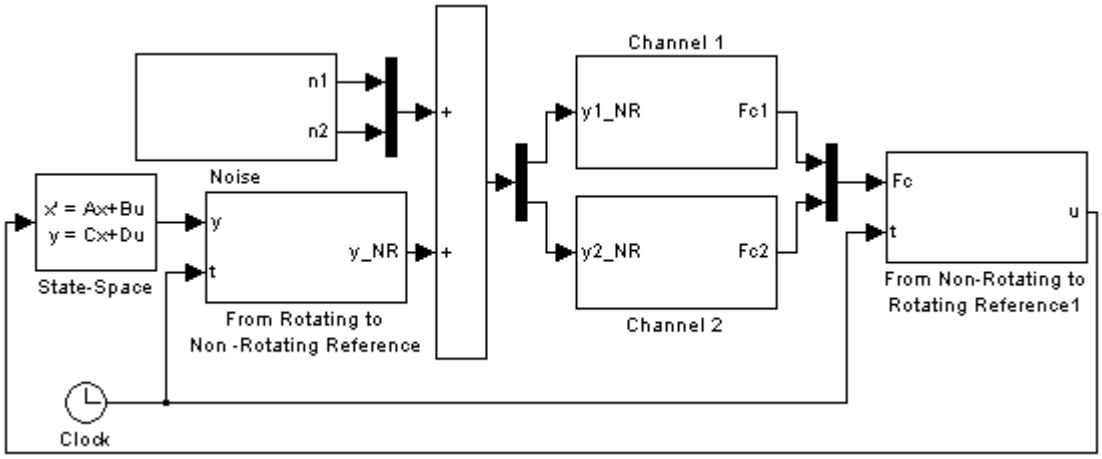

Figure 6.3: Total block diagram of the damping command.

The output vector $\vec{y}$ of the State-Space Block is the input of the Block "From Rotating to Non-Rotating Reference". This block is illustrated in figure 6.4. It transforms the vector $\vec{y}$ into the vector $\vec{y}_{NR}$ whose components are the displacements of the outer cylinder in the laboratory frame. The rotation matrix R is given by equation:

$$R = \begin{bmatrix} \cos(\omega_s t) & -\sin(\omega_s t) \\ \sin(\omega_s t) & \cos(\omega_s t) \end{bmatrix} \tag{6.8}$$

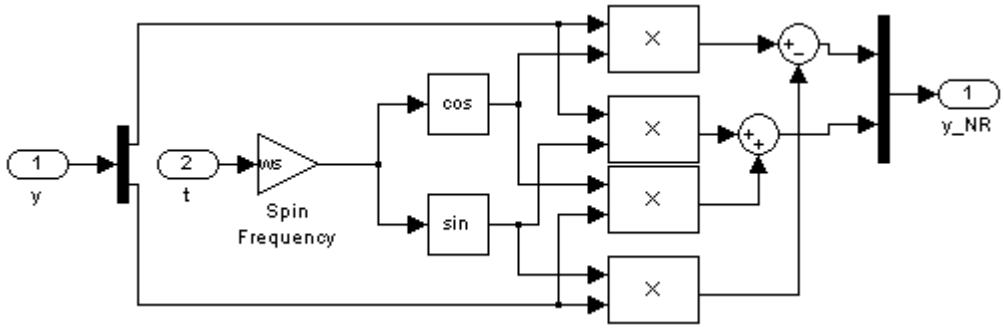

Figure 6.4: "From Rotating to Non-Rotating Reference" block. The output vector $\vec{y}_{NR}$ is a 2 dimensions vector. It represents the displacement of the outer cylinder in the x-y plane in the non-rotating reference system.

In the model we assume using non-perfect sensors, so we introduce reasonable errors in the block "Noise" (see figure 6.5) as follows:
-) RMS of the readout capacitors 10^{-2}μm

-) bias of the readout capacitors 10μm
We have introduced 2 other kinds of "errors" too:
-) constant offset in the rotating frame ε=20μm
-) initial amplitude of the whirl motion >100μm.

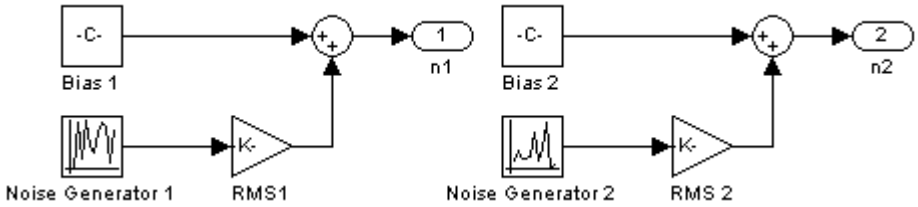

Figure 6.5: "Noise" block. The "Noise Generator" block generates normally distributed random numbers. The sequence produced has a mean of 0 and a variance of 1. Any "Noise Generator" block uses different seed and parameters to produce a different sequence of numbers (in this way, noise n1 affecting the signal of channel x is uncorrelated to the one (n2) of channel y). These numbers are then multiplied by the factor "RMS".

The heart of this block is represented by the "Noise Generator" block. This block generates normally distributed random numbers. The sequence produced has a mean of 0 and a variance of 1. Then, these numbers are multiplied by the factor "RMS" and are added to a fixed bias. Any "noise Generator" block uses different seed and parameters to produce different sequence of numbers. In this way noise n1 affecting the signal x_{NR} is uncorrelated with noise n2 affecting the signal y_{NR}. Noise n1 is added to the first component of vector y_{NR} and generates the signal $y1_{NR}$ which simulates the output of the sensors in the non-rotating frame. In the same way n2 is added to the second component of vector y_{NR} to produce the signal $y2_{NR}$. $y1_{NR}$ is the input of "Channel 1" block which is illustrated in figure 6.6. The displacement is converted in a voltage signal by the "Volt/m" block. A 2-nd order Butterworth band-pass filter pre-forms the signal in order to cut DC components (i.e. frequencies lower than 10^{-2}Hz) and high frequencies (i.e. frequencies higher than 3Hz). 3 different Digital Pass-band Filters select the spectral components of the signal at frequencies ν_d,ν_{c1}, and ν_{c2}.

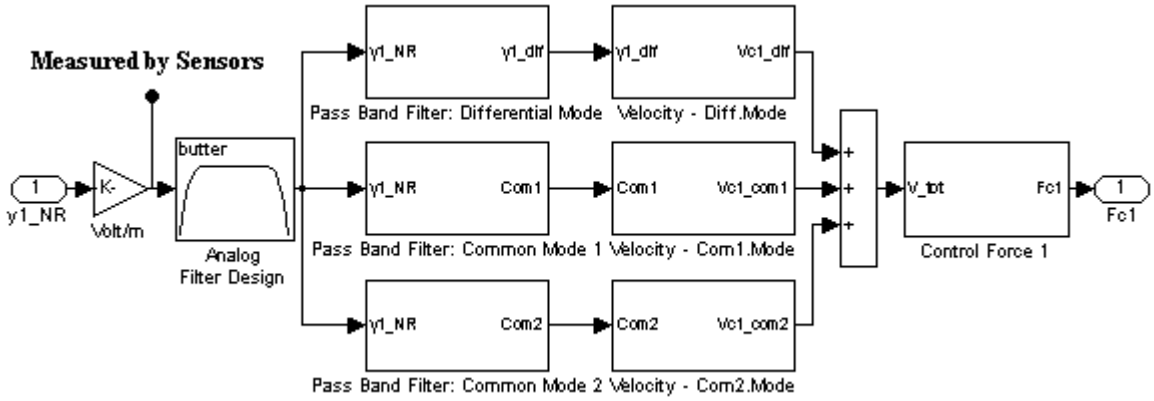

Figure 6.6: "Channel 1" block. The displacement is converted in a voltage signal by the "Volt/m" block; this is the signal measured by the capacitance sensors (red dot). An Analog Pass-band Filter pre-forms the signal in order to cut DC components (i.e. frequencies lower than 10^{-2}Hz) and high frequencies (i.e. frequencies higher than 3Hz). 3 different Digital Pass-band Filters select the spectral components of the signal at frequencies ν_d,ν_{c1}, and ν_{c2}. Then the whirl velocity is calculated and a control force proportional to it is generated.

Figure 6.7 shows the content of "Pass Band Filter: Differential Mode" block[1]. The "Zero-Order Hold" block implements a sample-and-hold function operating at the specified sampling rate (10 Hz). The block accepts one input and generates one output, both of which are scalar. This block provides a mechanism for discretizing the input signal. Its output is a discrete sample time data sequence which is filtered by the "Digital Filter Differential Mode" block.

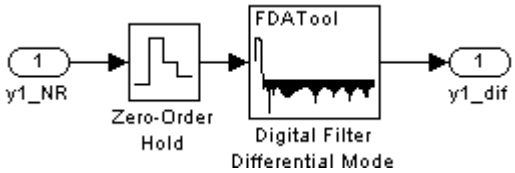

Figure 6.7: "Pass Band Filter: Differential Mode" block. The "Zero-Order Hold" block provides a mechanism for discretizing the input signal. The " Digital Filter Differential Mode" block filters a discrete sample time data sequence.

The "Digital Filter Differential Mode" block returns a band-pass filter with pass-band 0.05 Hz < ν < 0.15 Hz. The "Velocity – Diff. Mode" block is introduced to compute the whirl velocity. Whirl motion can be described by the vector:

$$\vec{r}_w = r_w e^{t/\tau_w}\left(\cos(\omega_w t), \sin(\omega_w t)\right) \tag{6.9}$$

If the quality factor Q is very high (i.e. Q>>1), the time constant τ_w is very long when compared with the whirl period T_w, namely $\tau_w >> T_w$. Whirl velocity is obtained by means of analytical evaluation of the derivative of (6.9):

$$\dot{\vec{r}}_w = r_w e^{t/\tau_w}\left(\cos(\omega_w t)/\tau_w - \omega_w \sin(\omega_w t), \sin(\omega_w t)/\tau_w + \omega_w \cos(\omega_w t)\right) \tag{6.10}$$

Since $\tau_w >> T_w$, $1/\tau_w << \omega_w$ and the first term in (6.10) can be neglected:

$$\dot{\vec{r}}_w \sim r_w \omega_w e^{t/\tau_w}\left(-\sin(\omega_w t), \cos(\omega_w t)\right) \tag{6.11}$$

By observing that $\sin(\omega_w(t - T_w/4)) = -\cos(\omega_w t)$ and $\cos(\omega_w(t - T_w/4)) = \sin(\omega_w t)$, (6.11) can be written as:

$$\dot{\vec{r}}_w \sim -\omega_w \vec{r}_w(t - T_w/4) \tag{6.12}$$

Hence, whirl velocity is obtained by delaying the relative displacement (6.9) by $T_w/4$. This technique is implemented in "Velocity – Diff. Mode" block. Figure 6.8 shows the content of this block.

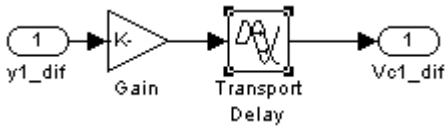

Figure 6.8: "Velocity – Diff. Mode" block. The Transport Delay block delays the input by a specified amount of time. It can be used to simulate a time delay.

The Transport Delay block delays the input by $T_w/4$ and it is used to reconstruct the whirl velocity. Two pairs of capacitance plates faced on the outer test cylinder are used as actuators. If v_x is the x component of whirl velocity (converted in an voltage signal) in the non-rotating reference frame, a voltage $V+=V_0 + \alpha v_x$ (α<0 is a pure gain; V_0=180Volt is a constant voltage

[1] "Pass Band Filter: Common Mode 1" and "Pass Band Filter: Common Mode 2" blocks are equivalent.

applied to the 4 plates) is applied to the plate placed along the x axis in the direction of positive x while a voltage V-=180Volt-αv_x is applied to the plate in the direction of negative x. The resulting force is:

$$F_{Cx} = \frac{1}{2}\varepsilon_0 S\frac{V_+^2}{d^2} - \frac{1}{2}\varepsilon_0 S\frac{V_-^2}{d^2} = \frac{2\varepsilon_0 S}{d^2}V_0\alpha v_x \qquad (6.13)$$

where S is the plate's surface, d the clearance between the plates and the outer surface of the test cylinder and ε_0 the permittivity of vacuum. Equation (6.13) shows that the active control force is proportional to the whirl velocity (but with opposite sign). This control command is implemented in "Control Force" block which is illustrated in figure 6.9. The Saturation block imposes upper and lower bounds on the signal. When the input voltage (V_+ or V_-) is within the range specified by the Lower limit (0 Volt) and Upper limit (+360 Volt) parameters, it passes through unchanged.

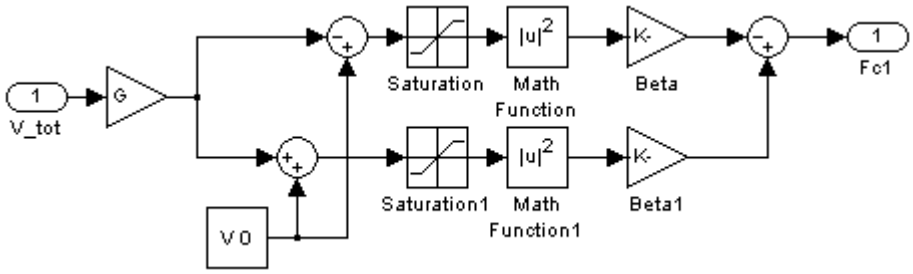

Figure 6.9: "Control Force" block. The output is a force proportional to the whirl velocity (with opposite sign). The Saturation block imposes upper and lower bounds on the voltage. When the input voltage is within the range specified by the Lower limit (0 Volt) and Upper limit (+360 Volt) parameters, it passes through unchanged. When the input voltage is outside these bounds, it is clipped to the upper or lower bound.

When the input voltage is outside these bounds, the voltage is clipped to the upper or lower bound. The "From Non-Rotating to Rotating Reference" block in figure 6.3 is introduced in order to perform a transformation from the non-rotating to the rotating reference frame. In this way, the control force $\vec{F}_c$ (in the laboratory frame) is converted into the vector $\vec{u}$ (equation (6.3)) in the ξ–η plane of the rotating reference frame. This is the feedback control force used as input of the "State – Space" block.

Figures 6.9 and 6.10 show the results of the simulations. Time evolution of the relative distance between the two test bodies is reported in figure 6.9 showing that the amplitude of the oscillation at whirl frequency can be reduced in a few minutes.

Figure 6.11 shows a polar plot of the relative motion of the test cylinders with respect to the equilibrium position. The orbit depicted is a logarithmic spiral with a decreasing radius and indicates that the scheme proposed is effective even in presence of a big initial whirl radius (note that, even if the control forces are proportional to the velocity of the centre of mass of the outer cylinder, the relative displacement between the two test cylinders is also reduced).

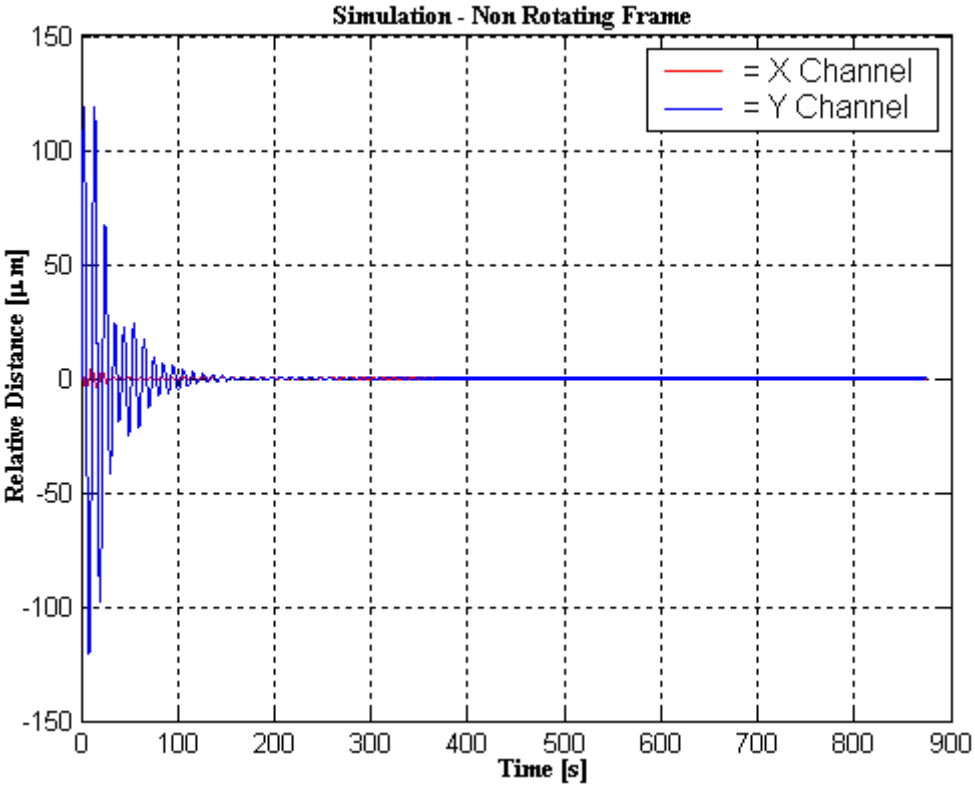

Figure 6.10: Time evolution of the relative distance between the two test bodies.

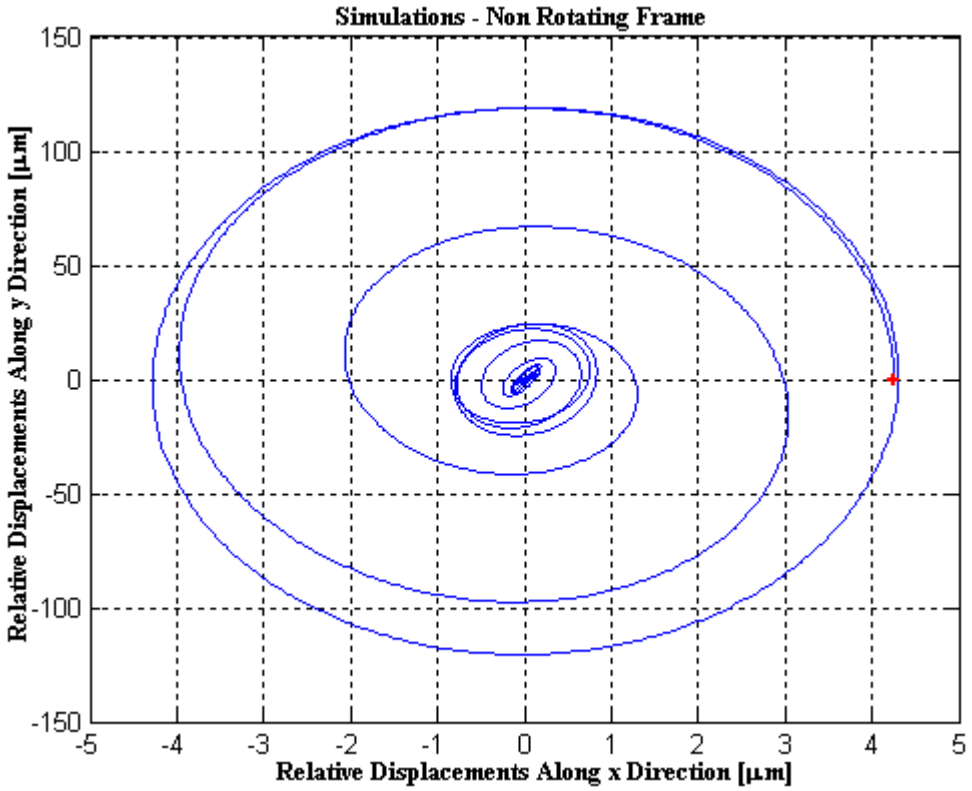

Figure 6.11: Polar plot of the relative distance between the test cylinders. Red cross: starting point.

6.4 EXPERIMENTAL RESULTS.

In this section we report the results obtained during laboratory tests of operation of the rotating differential accelerometer GGG. Pressure in the chamber was low enough to rule out any dissipation due to residual air (see figure 5.21). We have performed runs with the accelerometer spinning at a few Hz and only active damper applied. The control scheme is the one described in section 6.3, with two important differences: since the Digital Filters (see figure 6.7) were not constructed yet, only the analog band-pass filter has been used. It has been regulated in order to cut frequencies lower than 10^{-2}Hz and higher than 0.3Hz. Hence, only differential modes have been actively controlled. Figure 6.12 shows the rapid decay (over a few hundred seconds) of the whirl oscillations' amplitude in the non-rotating frame.

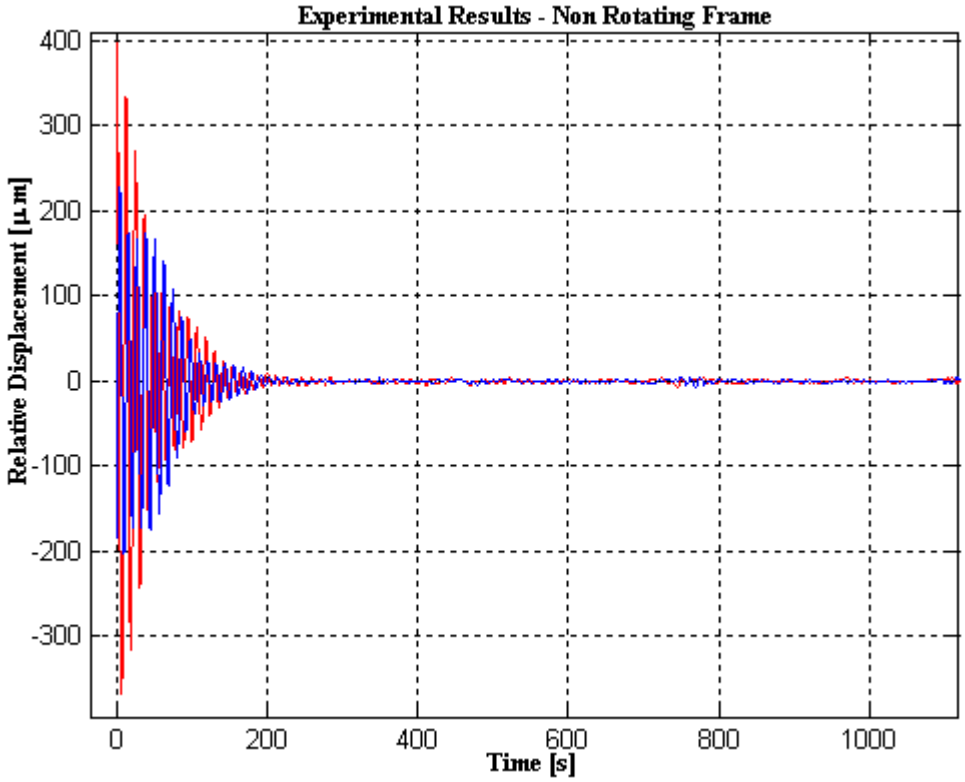

Figure 6.12: The decay of the whirl oscillations' amplitude. Red line refers to the x component of the relative displacement. Blue line to the y component.

A polar plot of this signal is illustrated in figure 6.13. The circle is the starting point, hence the motion is forward, i.e. it occurs in the same direction (anticlockwise) as the spin speed. Thanks to the control applied, oscillation's amplitude rapidly decreases and the rotor is stable in supercritical rotation. The whirl radius has been reduced from a few hundred μm (see figure 6.12) to about 0.1μm (see FFT plot of figures 6.14 and 6.15). Since only differential modes have been actively controlled, small peaks at frequencies corresponding to common modes are still present. Note that the level of 0.1μm of residual forward whirling at 0.08 Hz is connected to the presence of this peaks at higher frequencies. In fact, the upper edge frequency of the analog pass-band filter is 0.3Hz. As a consequence, the attenuation factor of signals at frequency ν_{c1}^{0}=0.9Hz is about 1/10 and the attenuation factor at frequency ν_{c2}^{0}=1.4Hz is about 1/20. If the whirling motions amplitude (at the differential frequency) is higher than about 1μm, the output of the analog pass-band filter can be represented as the

superimposition of a forward whirl (with radius higher than 1μm) plus small perturbations at higher frequencies (for example, the amplitude of the natural mode at frequency ν_{cl}^{0} is reduced by the filter from 2μm to 0.2μm); hence the control force has the right "shape" to reduce forward whirls. When the amplitude (at the differential frequency) becomes small enough (about 0.1μm), the output of the pass-band filter is the superimposition of many terms with almost the same amplitude, and the actuators are not able to reduce the whirling radius further on.

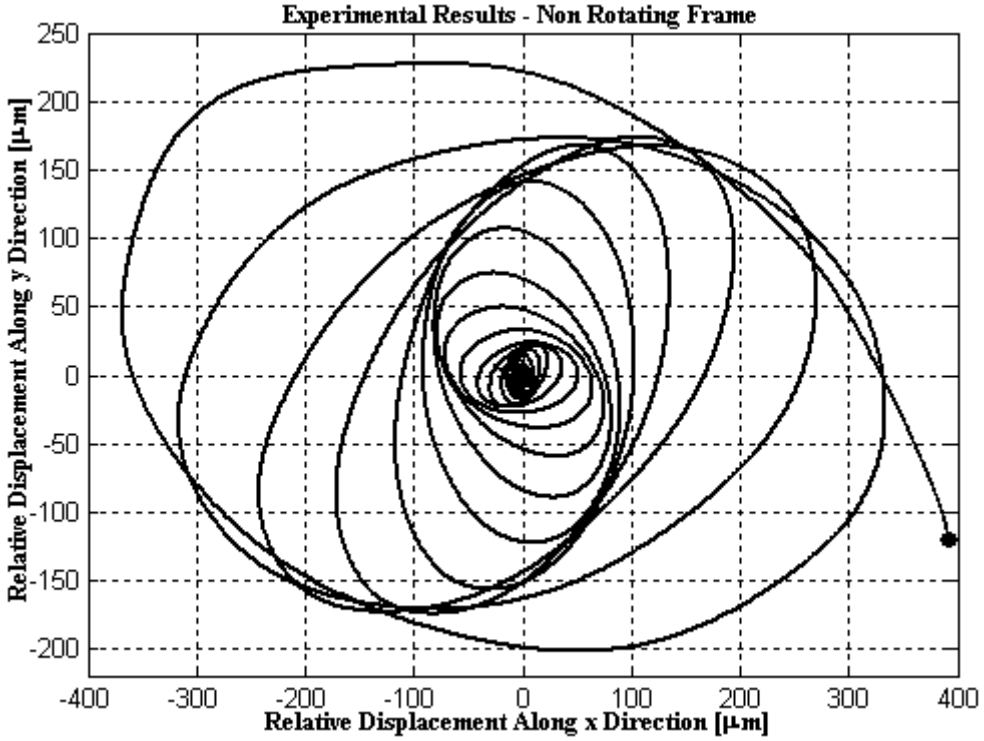

Figure 6.13: Polar plot of forward whirl motion. The circle is the starting point.

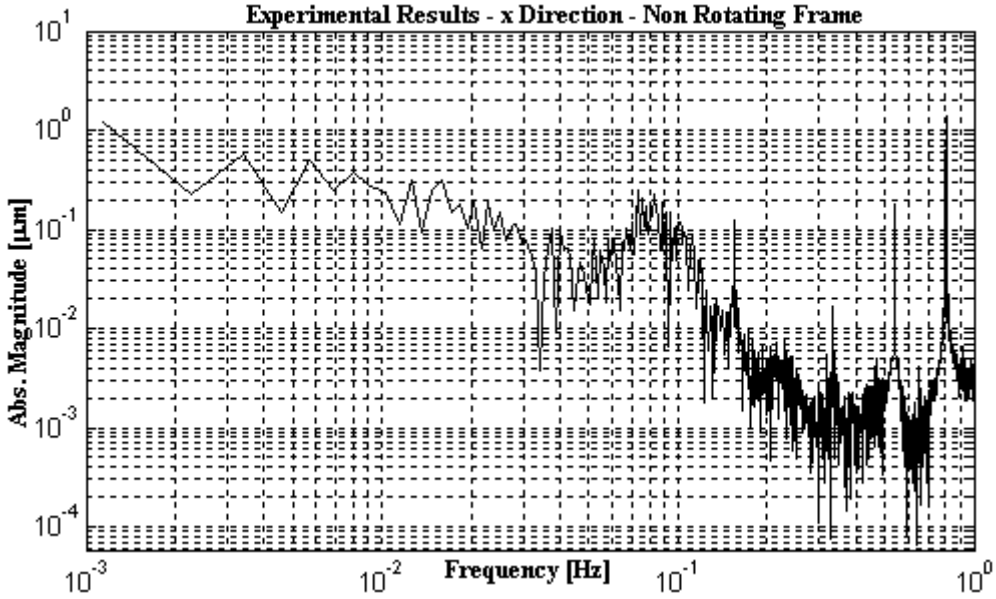

Figure 6.14: FFT of the relative displacement of the test cylinders in x direction of the horizontal plane in the non-rotating system. The relevant whirl at the natural frequency of 0.08Hz has been reduced to about 0.1μm.

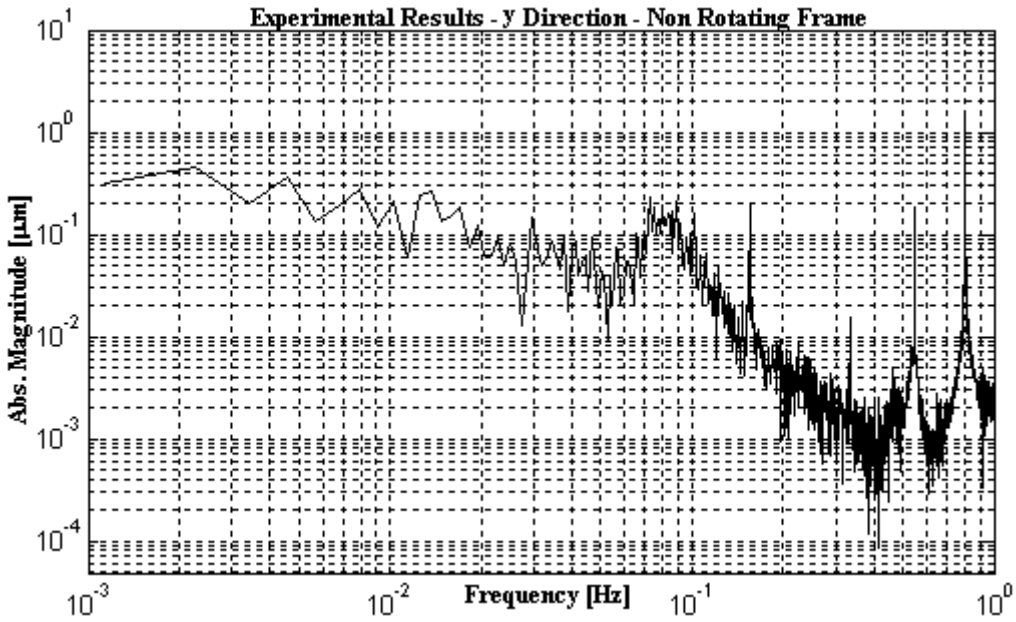

Figure 6.15: FFT of the relative displacement of the test cylinders in y direction of the horizontal plane in the non-rotating reference system. The relevant whirl at the natural frequency of 0.08 Hz has been reduced to about 0.1µm.

Another example of controlled signal is shown in figure 6.16. In this case the starting radius was very big (about 1mm), but the controller was able to reduce it in less than 5 minutes.

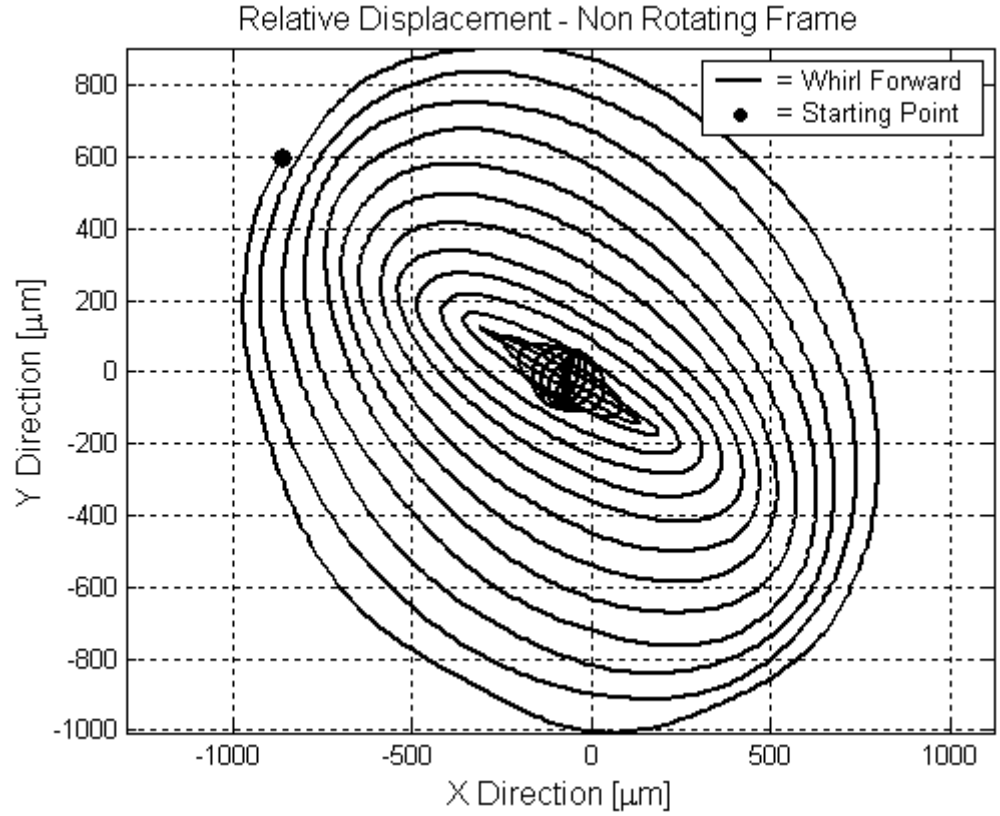

Figure 6.16: Polar plot of forward whirl motion. The circle is the starting point. The whirl motion has been damped even though the initial radius was very large.

In summary, theoretical analyses demonstrate that the whirl control problem of the complete GGG system can be solved. Measurements of the relative displacements of the test cylinders confirm, after coordinate transformation to the non-rotating reference system, a controlled whirl motion at a differential frequency of 0.08Hz at the level of 0.1μm. In order to detect the effect of a low frequency differential force (such as in the case of a 24hr EP violation signal in the field of the Sun), the corresponding displacement between the centers of mass should be separated out from the whirl and also emerge from the residual low frequency noise, mostly seismic noise.

An example of recover of an applied signal at frequency below whirl frequency is shown in figure 6.17, where a signal applied at 0.01Hz in the y direction of the non-rotating reference frame is recovered from the output data though about 100 times smaller than the whirl at about 0.1Hz. This example indicates that recovery is possible even though the applied force produces a displacement much smaller than the whirl radius (not damped), hence, in order to measure an EP violation signal at the level of 10^{-13}m it is not necessary to reduce the whirling radius with the same accuracy.

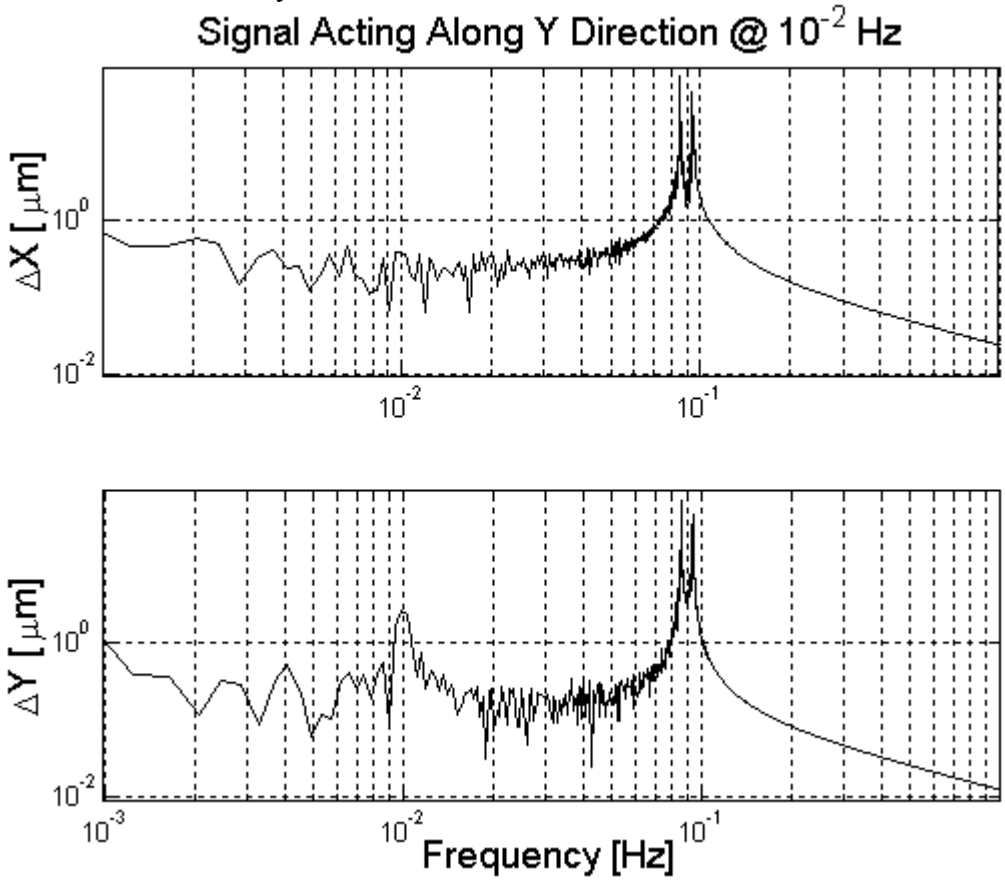

Figure 6.17: A signal applied at 0.01Hz in the Y direction of the non-rotating reference system is recovered from the output data though about 100 times smaller than the whirl at about 0.1 Hz (system spinning at 2Hz).

CHAPTER 7:

ACTIVE REDUCTION OF SEISMIC NOISE.

7.1: MEASURED ENVIRONMENTAL DISTURBANCES.

After a brief overview of the daily tilts measurements performed during about two years, we devote this chapter to the study of an active linear control able to increase the tilt rejection of the accelerometer in the measurement bandwidth. Sections 7.2 is devoted to the study of the open-loop scheme, with no feedback control. The frequency response of the accelerometer is evaluated (numerically and analytically).
Then we consider a common type of feedback which in the process industries is called proportional integral control [44 – 49], which improves steady-state properties. Figure 7.1 shows the variation of the horizontal plane (in direction East – West) in the laboratory measured with an ISA accelerometer (see section 2.8) [41 – 42] during the period February 2001- June 2002.

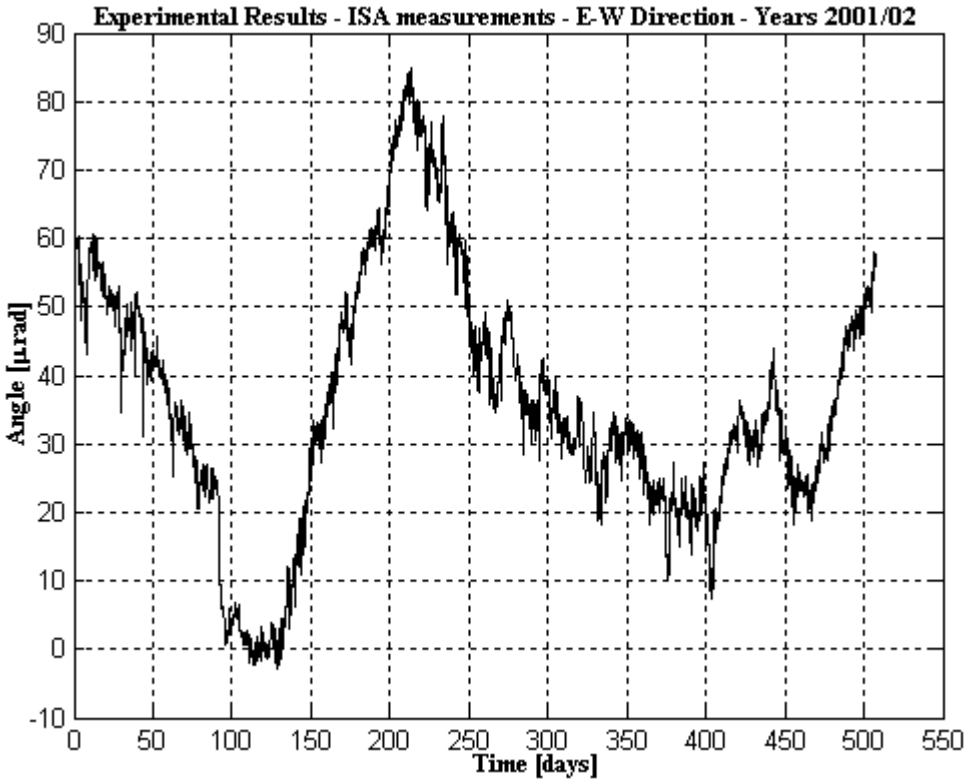

Figure 7.1: Variation of the horizontal plane measured in the laboratory.

Figure 7.2 shows the correspondent temperature variation in the laboratory. The frequency components of the measured tilts is shown in figure 7.3. We have plotted the absolute value of the FFT of the signal in figure 7.1 (divided by the product $T \cdot \nu_C/2$; T is the integration time, ν_C the sampling frequency) to stress the fact that the peak at frequency $1.16 \cdot 10^{-5}$Hz can not be treated as noise and can not be reduced by increasing the integration time.

Above 10^{-8} Hz, the magnitude decreases at the rate of 20 dB/decade, i.e. ϑ_d can be approximated as a function of frequency in the form:

$$\vartheta_d(\nu) = \frac{\alpha}{\nu}\mu\text{rad}\sqrt{\text{Hz}} \qquad (7.1)$$

where $\alpha=5\cdot10^{-3}$. An example of asymptotic behaviour is depicted in figure 7.3. Two peaks are present at frequencies $\nu_{24h}=1.16\cdot10^{-5}$Hz and $\nu_{12h}=2.31\cdot10^{-5}$Hz. The first peak (at the lower frequency) is due to the daily tidal/thermal effects and represents a signal which competes directly with the EP violation signal. The second peak corresponds to 12hr period effects.
We have to construct a control command in order to reduce tilts at low frequencies. The goal is to reduce daily seismic disturbances below the sensitivity of the tiltmeter used as sensor.

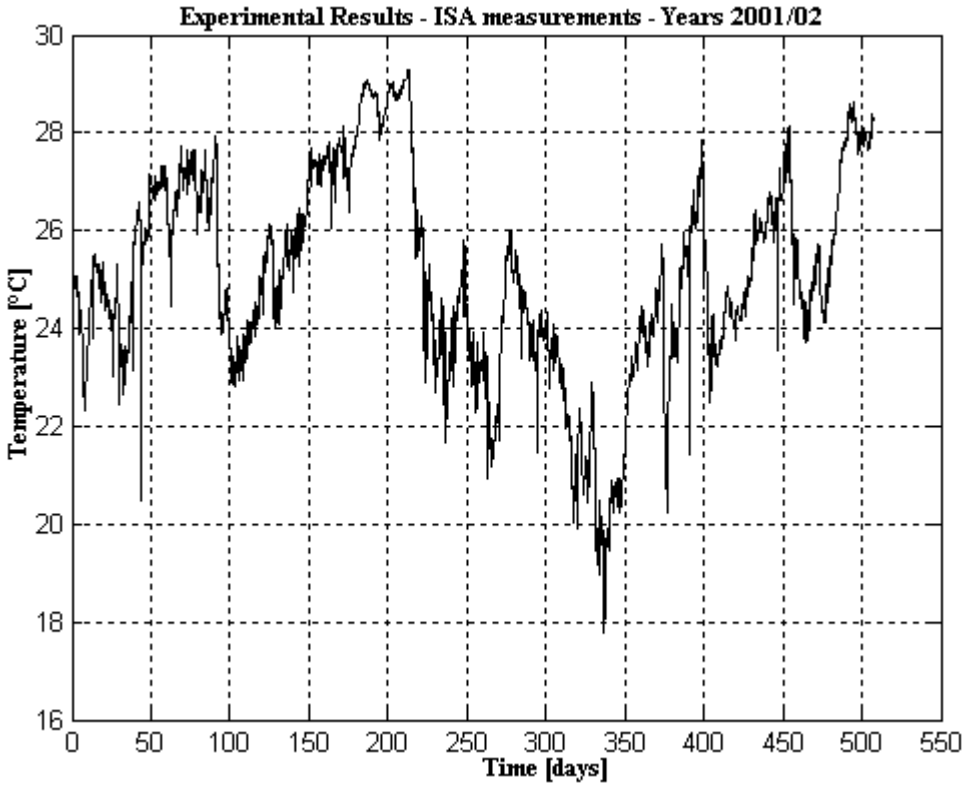

Figure 7.2: Variation of the temperature measured in the laboratory.

The angular variation of the horizontal plane shown in figure 7.1 will be introduced as disturbance; the capabilities of the command will be checked at the end by combining its transfer function with this seismic disturbance.

7.2: OPEN LOOP SCHEME OF THE SYSTEM.

At the start, constant reference angle ϑ_{ref} can be regulated by means of three high resolution DC actuators through vertical displacements (see figure 7.4). These actuators are operated only at the start. ϑ[1] is the angular deviation (tilt) of the horizontal plane from the initial

[1] The procedure described in this chapter can be applied to control tilts acting in one direction (x or y). Hence, we need two independent control circuits (see Appendix 8.A) to control tilt in both directions.

position ϑ_{ref} and it is due to seismic disturbances ϑ_d acting on the vacuum chamber. Low frequency tilts ϑ can be monitored with a tiltmeter placed inside the vacuum chamber on the horizontal plane on the top of the apparatus. The tiltmeter installed can detect tilts less than $2\cdot10^{-10}$ rad in one day of integration time[2]. Active reduction at this level of accuracy will be done using as actuators three PZTs (see section 2.8).

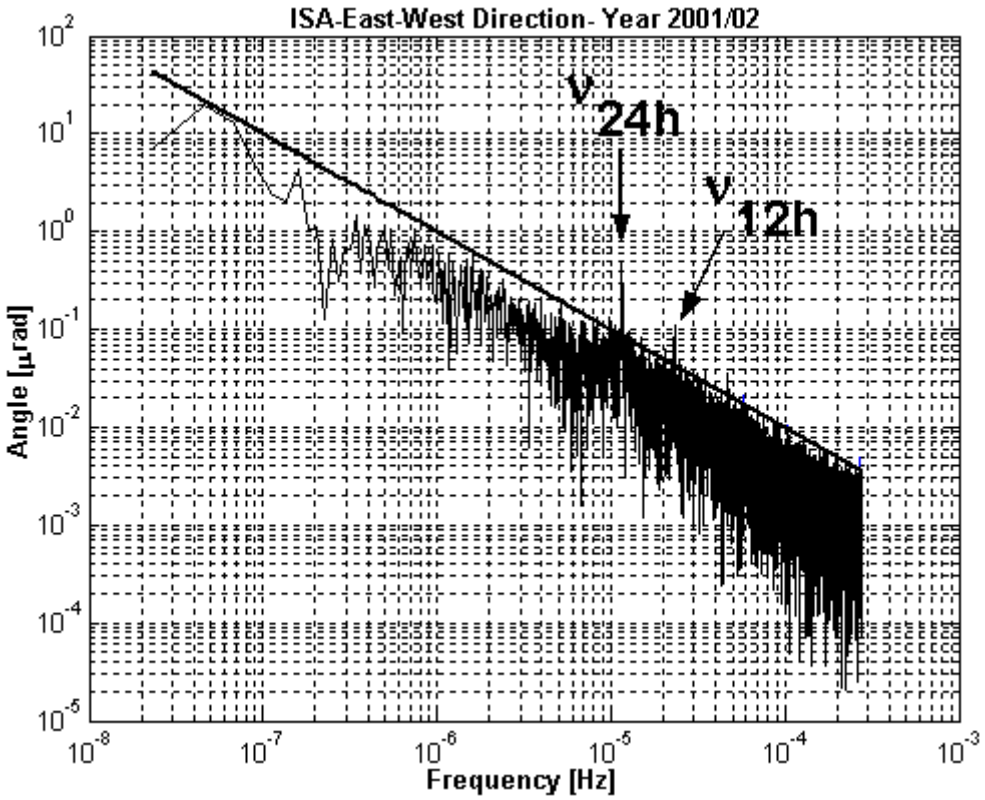

Figure 7.3: Frequency components of the measured tilt angle. Two strong peaks are present at frequencies $\nu_{24h}=1.16\cdot10^{-5}$Hz and $\nu_{12h}=2.31\cdot10^{-5}$Hz. The first peak (at the lower frequency) is due to the daily tidal/thermal effects. The second peak corresponds to 12hr period effects. The slope of the asymptotic line is 20 dB/decade.

Instead, in case of the open-loop scheme (no active control) the angular deviation ϑ follows the disturbances ϑ_d (ϑ_d is shown in figure 7.1) and the transfer function of the open-loop system is simply H=1. Figure 7.5 shows open-loop block diagram.
We are interested in evaluating the relative distance between the test bodies due to the angular deviation ϑ in the case of open-loop scheme: seismic disturbance ϑ_d shown in figures 7.1 and 7.3 is the input, the subsequent relative distance between the test cylinders is the output. The DC gain of the system has been measured to be about:

$$K_{\omega=0} = 1.2\cdot10^{-1}\,\mu m/\mu rad \qquad (7.2)$$

and the maximum relative displacement at the frequency of the EP signal is:

$$\Delta x = 6\cdot10^{-2}\,\mu m \quad @ \quad \omega_{24h} = 2\pi/86400 \quad rad/sec \qquad (7.3)$$

The frequency response of the accelerometer to seismic disturbances can also be numerically evaluated by introducing the measured noise (figures 7.1 and 7.3) as an input in the mathematical model developed in Matlab/Simulink.

[2] For example, daily tides produce tilts of 10^{-8}rad.

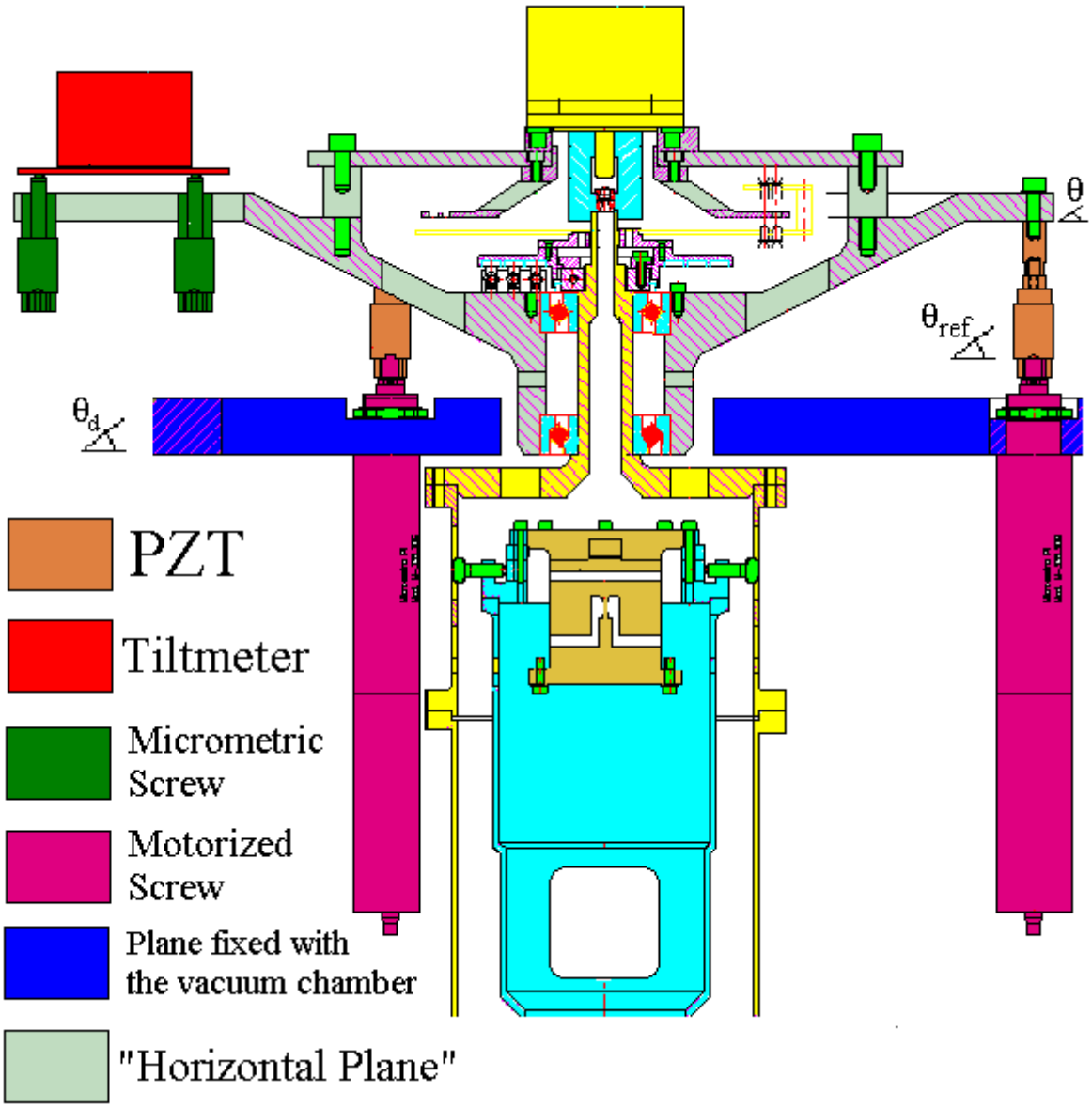

Figure 7.4: Constant reference angle ϑ_{ref} with respect to the frame (in blue) can be regulated by means of three high resolution DC actuators ("motorized screw" in violet) through vertical displacements. These actuators are operated only at the start. ϑ is the angular deviation of the" horizontal plane" (in grey) from the initial position ϑ_{ref} and it is due to seismic disturbances ϑ_d acting on the vacuum chamber (blue). Low frequency tilts ϑ can be monitored with a tiltmeter (in red) placed on the horizontal plane on the top of the apparatus. It is aligned with the horizontal plane by means of micrometric screws (green). Low frequency tilts ϑ can be actively controlled by means of 3 PZTs (in brown). In figure the new design of the rotor with the motor located on the spin axis is shown.

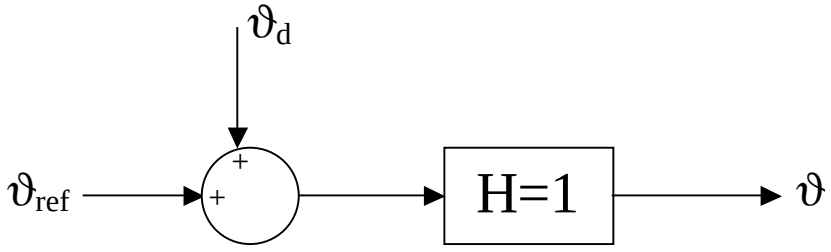

Figure7.5: Open-loop block diagram.

An analytical expression for the steady state value of the output (7.2) can also be carried out for the non-spinning rotor. We have to evaluate the relative displacement between the two cylinders due to a constant angle $\bar{\vartheta}$. This result can be obtained from equations (7.4) in the limit of small angles and null spin frequency; U is the sum of the elastic and gravitational potential energy (see (3.13), (3.14) and (3.15)).

$$\frac{\partial U}{\partial q_i} = 0 \quad ; \quad q_i = \vartheta_a, \vartheta_1, \vartheta_2 \tag{7.4}$$

(labels a, 1 and 2 refer to the coupling arm, inner and outer test cylinder; the three generalized coordinates are defined as in chapter 3). This procedure leads to the equations:

$$\vartheta_a \cong \frac{k\ell^2\bar{\vartheta}}{3k\ell^2 - mg\Delta L - \frac{\left(k\ell^2\right)^2}{k\ell^2 + mgL_1} - \frac{\left(k\ell^2\right)^2}{k\ell^2 + mgL_2}} = 3\cdot 10^{-1}\bar{\vartheta} \tag{7.5}$$

$$\vartheta_1 = k\ell^2\bar{\vartheta} \Big/ \left(k\ell^2 + mgL_1\right) \cong \bar{\vartheta}/160 \tag{7.6}$$

$$\vartheta_2 = k\ell^2\bar{\vartheta} \Big/ \left(k\ell^2 + mgL_2\right) \cong \bar{\vartheta}/1600 \tag{7.7}$$

ϑ_1 and ϑ_2 are about 2-3 orders of magnitude smaller than ϑ_a and can be neglected, i.e. we can assume $\vartheta_1=\vartheta_2=0$. In essence, the symmetry axis of the two test cylinders remain approximately aligned with the vertical z. The relative displacement between the two test bodies is determined only by the equilibrium angle ϑ_a, namely $\Delta x = (2L + \Delta L)\vartheta_a \cong 12\text{cm}\cdot\bar{\vartheta}$. Starting from this result, equation (7.2) is readily obtained. Note that the angles (7.5), (7.6) and (7.7) do not depend on the mechanical balancing of the apparatus, hence steady state values of these angles do not depend on the differential natural period (2.2).

7.3: PROPORTIONAL-INTEGRAL CONTROL OF SEISMIC NOISE.

Feedback can be used to stabilize systems and provide disturbances rejection. Integral control, when combined with proportional control, improves the system behaviour at low frequencies. The feedback diagram studied to control seismic disturbances is depicted in figure 7.6. Low frequency tilts ϑ are monitored with a tiltmeter T(s). The output of the tiltmeter is combined with the reference angle ϑ_{ref} and amplified by the integrators I(s), then the resulting signal is applied as input to the PZTs.

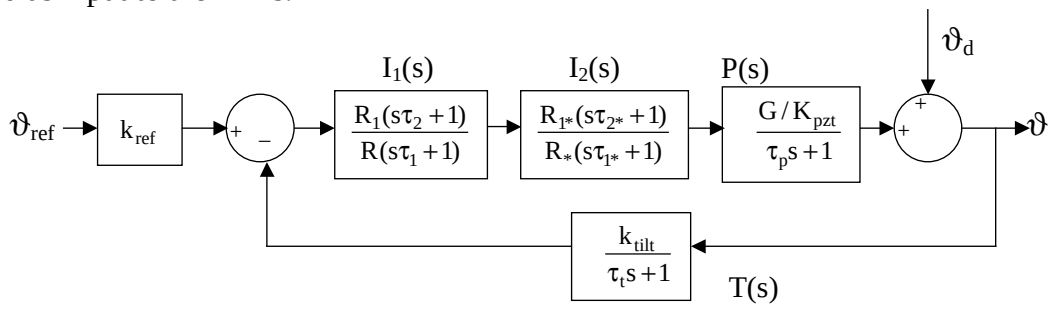

Figure 7.6: Closed-loop control block diagram. Low frequency tilts ϑ can be monitored with a tiltmeter. Its output is amplified by the integrators I(s), then the resulting signal is applied as input to the PZTs.

A typical example of integrator is shown in figure 7.7.

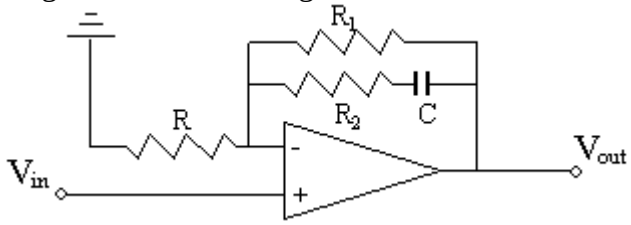

Figure 7.7: Sketch of the Integrator.

The first integrator unit has the transfer function $I_1(s) = (R_1/R)(s\tau_2+1)/(s\tau_1+1)$ with $\tau_1=R_1C$ and $\tau_2=R_2C$ (R_1=200MΩ, R_2=150kΩ, R=200kΩ and C=1600nF). The gain below the break point $\nu_1=1/(2\pi\tau_1)$ is $G_1=R_1/R$ while the gain above the second break point $\nu_2=1/(2\pi\tau_2)$ is $G_2=R_2/R$. The slope of the curve $I_1(j\omega)$ in the region between the two frequencies ν_1 and ν_2 is –20dB/decade. The second integrator unit has the transfer function $I_2(s) = (R_{1*}/R_*)(s\tau_{2*}+1)/(s\tau_{1*}+1)$ with $\tau_{1*}=R_{1*}C_*$ and $\tau_{2*}=R_{2*}C_*$ (R_{1*}=200MΩ, R_{2*}=221kΩ, R_*=221kΩ and C_*=20μF). The frequency response ($|I(j\omega)| = |I_1(j\omega)\cdot I_2(j\omega)|$) of the two integrators used for the active control is shown in figure 7.8.

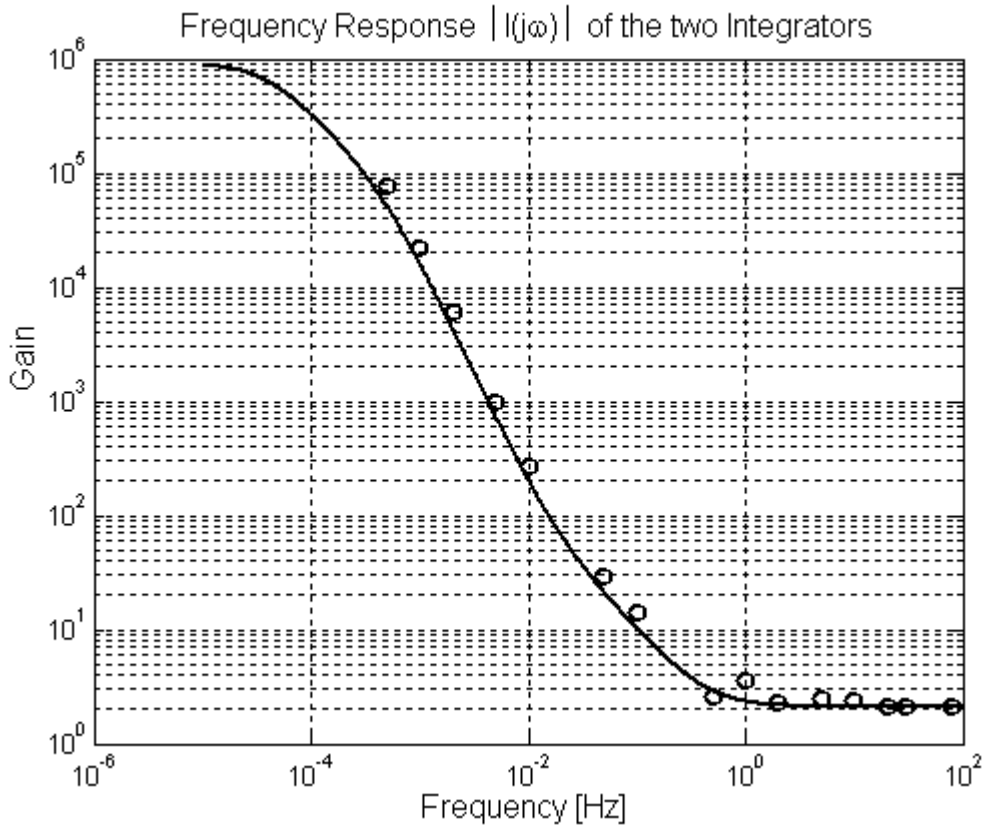

Figure 7.8: Frequency Response of the integrator $|I(j\omega)|$. Solid line: theoretical response. Circles: measurement data.

The nominal transfer function T(s) of the sensor (tiltmeter) has a first order pole $1/\tau_t$ and gain k_{tilt}. The pole is related to the presence of a low-pass filter inside the tiltmeter (nominal time constant τ_t =0.05seconds). Electronics converts angles into a voltage signal in the range from –10V to +10 V. The DC gain has been experimentally checked and it results:

$$K_{tilt} = 4\cdot 10^4 \, V/rad \qquad (7.8)$$

Low voltage PZTs are used as actuators. PZTs may be represented by the P(s) block. Input voltage is multiplied by the gain factor G=10 by an amplifier module. The frequency response of the PZTs may be schematised by introducing the term $1/(\tau_p s+1)$. Below the break point $1/\tau_p \approx 2\pi\cdot 10^3$Hz the magnitude curve is expected approximately constant (=1), while above the break point the curve's slope is expected -20 dB per decade. $1/K_{pzt}$ converts the input voltage signal into an angle:

$$\left(K_{pzt}\right)^{-1} = 8\cdot 10^{-7}\,\mathrm{rad/V} \qquad (7.9)$$

Note that the maximum angular variation which can be compensated is $\pm 4\cdot 10^{-5}$rad[3]. The block $k_{ref}=5\cdot 10^4$V/rad is introduced to convert the reference DC angle ϑ_{ref} into a voltage.
After some manipulations, the block diagram in figure 7.6 may be converted into a system without a component in the feedback path, usually referred to as a unity feedback system (see figure 7.9).

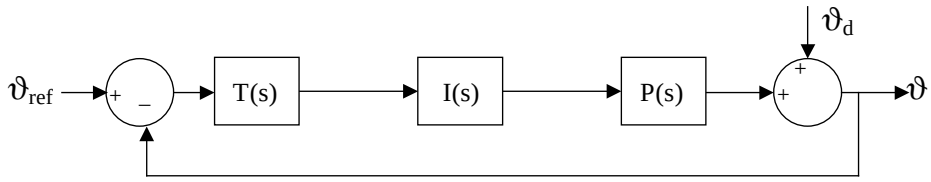

Figure 7.9: Unity feedback system.

We define TP(s)=T(s)·P(s) the total transfer function of the system piezo + tiltmeter. It is expected to be:

$$TP^{theoretical}(s) = G\frac{K_{tilt}}{K_{pzt}}\frac{1}{1+\tau_t s} \qquad (7.10)$$

We have experimentally checked the frequency response of the system piezo+tiltmeter and compared the results with the theoretical function (7.10). These results are shown in figure 7.10: measurements data are represented by dots; the red curve is obtained from equation (7.10). Figure 7.10 clearly shows that the frequency response of the system is not well approximated by the nominal function (7.10). Instead, the blue curve is obtained from the fitting function (7.11):

$$TP^{exp}(s) = K_{TP}\frac{1-\tau_{TP}s}{\left(1+\tau_{TP}s\right)^2} \qquad (7.11)$$

where $K_{TP}=0.1$ and $\tau_{TP}=0.2$ seconds.

7.3.A: THE TRANSFER FUNCTIONS.

In figure 7.3 we have shown the FFT of the seismic disturbances measured in the laboratory during the period February 2001- June 2002. The peak at frequency $\nu_{24h}=1.16\cdot 10^{-5}$Hz has amplitude:

$$\vartheta_{pk}^{24h} \sim 5\cdot 10^{-7}\,\mathrm{rad} \qquad (7.12)$$

[3] Each amplifier output voltage can be set in the range 0V to 100V. A DC-offset potentiometer adds a DC bias +50V to the input.

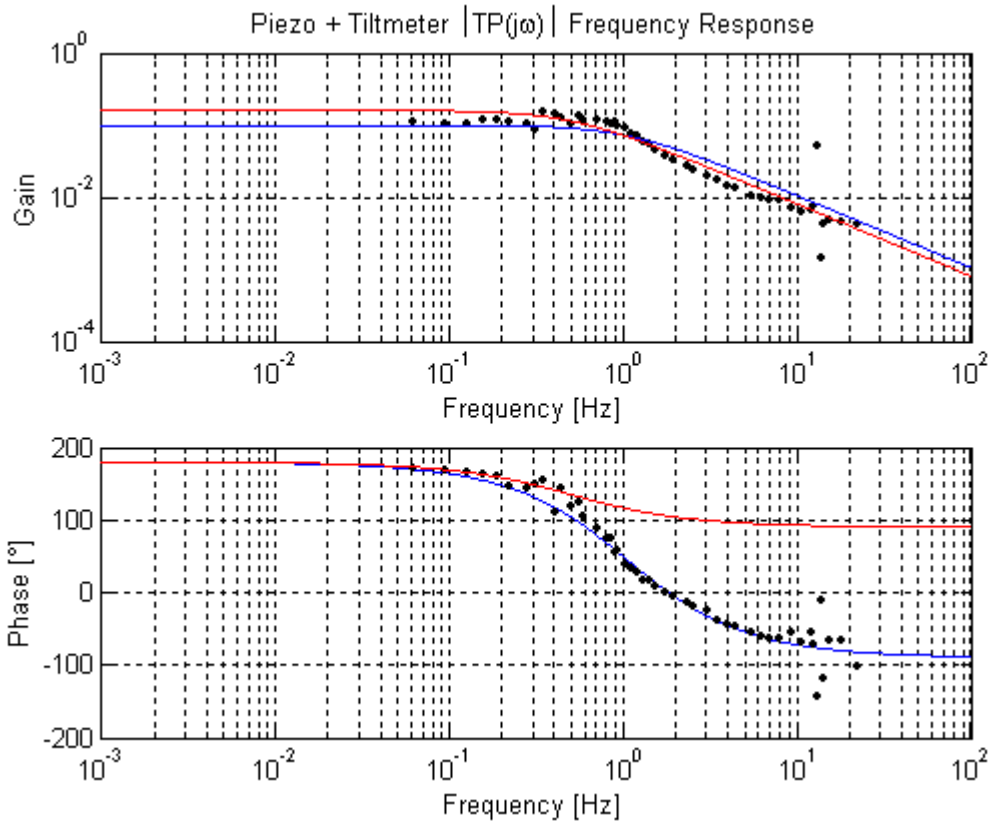

Figure 7.10: Frequency response of the system piezo+tiltmeter.

In 10 days of integration time, seismic noise at frequency ν_{24h} =1.16·10^{-5}Hz can be evaluated from equation (7.1) and turns out to be:

$$\vartheta_{noise}^{24h} \sim 6 \cdot 10^{-7}\,\text{rad} \tag{7.13}$$

Seismic disturbances at frequency ν_{24h} are then:

$$\vartheta_{d}^{24h} = \sqrt{\left(\vartheta_{pk}^{24h}\right)^2 + \left(\vartheta_{noise}^{24h}\right)^2} \sim 8 \cdot 10^{-7}\,\text{rad} \tag{7.14}$$

The electrical noise affecting the sensor (tiltmeter) has been measured to be smaller than:

$$V_{noise\_tilt} \leq 3 \cdot 10^{-3} \frac{V}{\sqrt{Hz}}\,^{4} \tag{7.15}$$

or, equivalently:

$$\vartheta_{noise\_tilt} = K_{tilt} \cdot V_{noise\_tilt} \leq 1.5 \cdot 10^{-7} \frac{rad}{\sqrt{Hz}} \tag{7.16}$$

In 10 days of integration time, the equivalent angle ϑ_{n}^{24h} at frequency ν_{24h} due to the electrical noise can be easily obtained from (7.16):

$$\vartheta_{n}^{24h} \sim 2 \cdot 10^{-10}\,\text{rad} \tag{7.17}$$

[4] 3·10^{-3}V/√Hz is the result from the superimposition of the electrical noise of the tiltmeter and the electrical noise of the data acquisition card. This measurement was largely dominated by the second noise source.

The transfer function from the input disturbance ϑ_d and the output signal ϑ is given by the following equation:

$$H_{\vartheta}(s)=\frac{\vartheta(s)}{\vartheta(s)}=\frac{1}{1+I(s)\cdot TP^{exp}(s)} \tag{7.18}$$

The noise reduction factor at low frequency may be easily obtained by substituting s=0 in (7.18):

$$\left|H_{\vartheta}(\omega\to 0)\right|=\frac{1}{1+K_{TP}\cdot\frac{R_1}{R}\cdot\frac{R_1^*}{R^*}}\sim\frac{1}{K_{TP}\cdot G_1\cdot G_2}\sim 10^{-5} \tag{7.19}$$

As a consequence low frequency disturbances can be reduced by a factor of 10^5. The feedback control performances are conditioned by the presence of the electrical noise. The transfer function from the electrical noise V_{noise_tilt} and the output ϑ is given by equation (7.20):

$$H_{Vn}(s)=\frac{\vartheta(s)}{V_{noise\_tilt}(s)}=\frac{TP(s)\cdot I(s)/K_{TP}}{1+TP(s)\cdot I(s)} \tag{7.20}$$

It can be readily evaluated by observing the block diagram in figure 7.11.

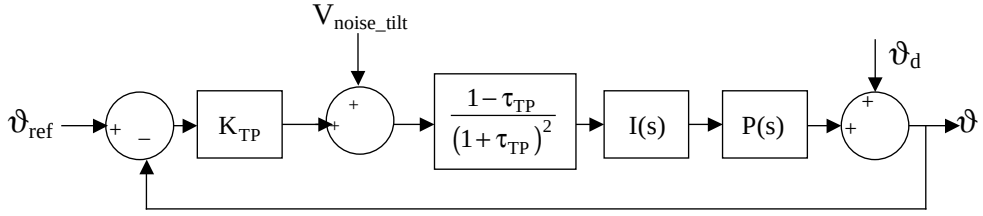

Figure 7.11: Block diagram + electrical noise of the tiltmeter.

Since the electrical noise V_{noise_tilt} can be converted into an equivalent angle $\vartheta_n=K_{tilt}\cdot V_{noise\_tilt}$, the transfer function from ϑ_n and the output ϑ is readily obtained:

$$H_n(s)=\frac{\vartheta(s)}{\vartheta_n(s)}=\frac{K_{tilt}}{K_{TP}}\frac{TP(s)\cdot I(s)}{1+TP(s)\cdot I(s)} \tag{7.21}$$

Even in presence of very large capacitances and resistances (for example R_1=1GΩ, C=10μF), the break-point frequency $\nu_1=1/(2\pi\tau_1)$ is higher than ν_{24h}; having in mind to evaluate the daily effect of the electrical noise, we are particularly interested in the DC gain of the closed-loop system, i.e.:

$$\left|H_n(\omega\to 0)\right|=K_{tilt}/K_{TP}\sim 1 \tag{7.22}$$

From (7.22), it follows that low frequency electrical noise can not be attenuated by the feedback control; as a consequence the minimal goal of the active control is to reduce daily seismic disturbances ϑ_d^{24h} at the level of $\vartheta_n^{24h}=1.5\cdot 10^{-10}$ rad (10 days of integration time).

7.3.B: PRELIMINARY EXPERIMENTAL RESULTS.

A preliminary prototype of the two integrators in figure 7.6 have been realised and tested. Their frequency response has been shown in figure 7.8 (dots). The overall circuit is shown in

Appendix 8.A. The output of the tiltmeter can be acquired on a card on the PC. It is previously filtered and amplified in order to obtain a better signal to noise ratio (see the box "ACQUISITION" in the scheme in Appendix 8.A). The mean value of the output of the tiltmeter can be adjusted (see the box "ADJ. OFFSET") by adding a constant voltage offset. This is equivalent to change the reference angle ϑ_{ref}. Since the voltage offset can be regulated with great accuracy, this control permits finer adjustments of the horizontality than the motorized screws. The PSD of the results is plotted (blue coloured) in figure 7.12. Measurement data have been collected for a total time of 85 hours. The peak-value[5] of the residual signal is also plotted in the same figure.

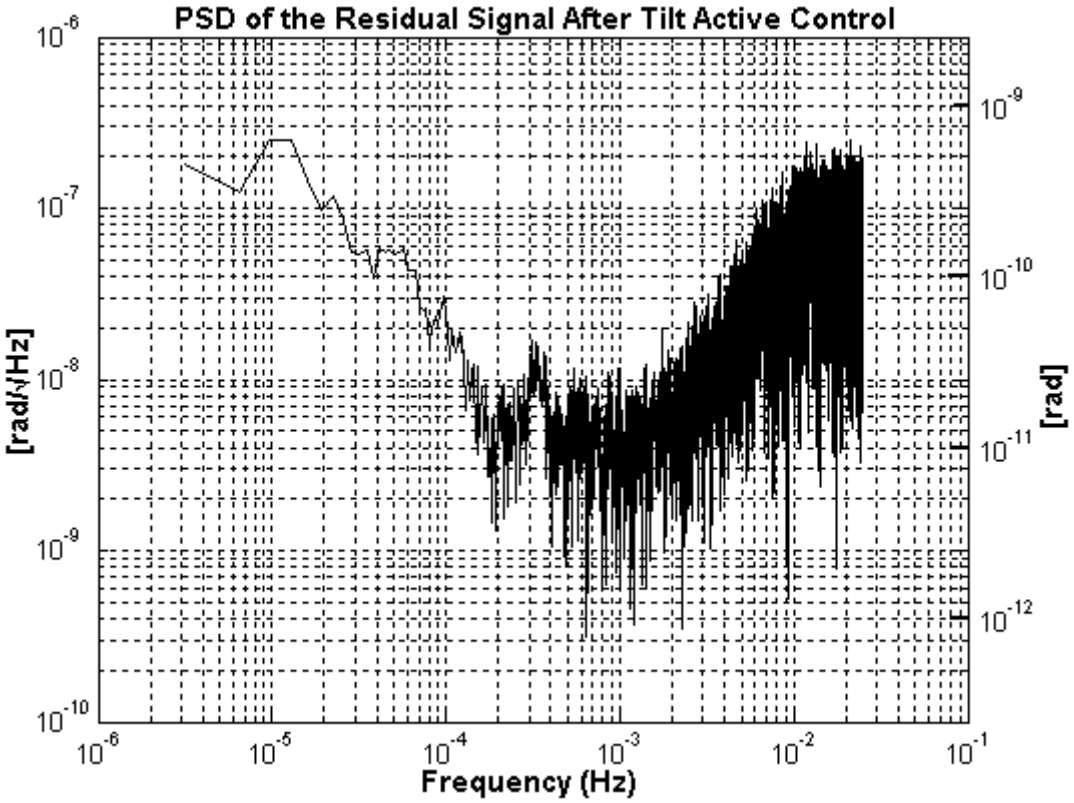

Figure 7.12: PSD of the residual signal after tilt active control. Measurement data have been collected for a total time of 85 hours.

[5] For the convertion between the PSD amplitude and peak value, the following simple formulae can be used: $\vartheta_{pk}(\nu)[\text{rad}] = \vartheta_{noise}(\nu) \cdot \sqrt{2} \Big/ \sqrt{T_{int}}\,[\text{rad}/\sqrt{\text{Hz}}]$ where T_{int} is the integration time.

.

CHAPTER 8:

THE GGG EXPERIMENT- CONCLUDING REMARKS AND PERSPECTIVES.

Experimental tests of the Equivalence Principle are of seminal relevance as probes of General Relativity and have been aimed at obtaining increasing levels of accuracy ever since the landmark experiment by Eötvös [16], which has verified the EP with an accuracy $\eta \approx 10^{-9}$ with a torsion balance. This result has been improved to about 10^{-12} by Dicke et al. [17] and by Braginsky and Panov [18]. After more than 30 years, current ground experiments have improved the Braginsky results by less than one order of magnitude, as obtained by Adelberger and co-workers [19], comparing the accelerations towards the Sun of two samples with an average composition similar to those respectively of the Earth and the Moon ($\Delta a_{\odot} / a_{\odot} \simeq 9.3 \times 10^{-13}$).

In a recent work by Damour, Piazza and Veneziano [23], a violation have been predicted near the 10^{-13} level. This work is based on string theory and the existence of the dilaton ϕ, the scalar partner of the spin 2 graviton. A version of the cosmological dilaton-fixing and decoupling mechanism is studied in their work. In particular, they investigate the ϕ dependence of the various coupling functions in the effective low-energy action. If a special value ϕ_m (which extremizes all the coupling functions) of ϕ exists, the dilaton ϕ naturally runs towards ϕ_m and approximately decouples from matter. The residual dilaton couplings lead to equivalence-principle violations.

The goal of $\eta = 10^{-13}$ is in principle accessible in the Galileo Galilei on the Ground experiment ([33 – 37], [40]) and requires to detect relative displacements (24hr period) of the test cylinders of 10^{-13}m. In the previous chapters we have described the general aspects of the GGG experiment developing a mathematical model of the apparatus and showing the more relevant experimental results obtained so far.

We have developed a mathematical model of the GGG accelerometer that embodies all the relevant physics (chapters 3 and 4) and we have demonstrated that the normal modes of the instrument can be predicted with great accuracy in good agreement with experimental results [36]. In figure 3.3 normal modes of the GGG rotor (both theoretical predictions and experimental results) are shown as a function of the spin speed.

Three natural frequencies play a relevant role in the dynamics of the system: the frequencies ν_{c1}^0 (typical value 0.91Hz) and ν_{c2}^0 (typically =1.25/1.4 Hz) correspond to common modes (see section 3.9.c), in which the centres of mass of the two cylinders oscillate in phase.

The frequency ν_d^0 corresponds to the differential mode, where the centres of mass of the two test bodies oscillate in opposition of phase, one with respect to the other. Tuning of the natural frequency ν_d^0 (i.e. of the differential period $T_d = 1/\nu_d^0$) is made possible in the experiment after changing the mass distribution of the beam balance. The apparatus has been operated with natural period T_d in the range from 5s to 20s. The longer is the differential period the more

.

sensitive is the accelerometer to effects acting in a different manner on the two test bodies (see (2.3)). Hence, we have planned to increase this period to reach the value of 80s.

In chapter 4 we have also evaluated the rotor's mechanical ability to reject common forces as compared to those acting in a differential manner on the test bodies and we have shown how the features of the real instrument can be tailored for best performance in rejecting external disturbances such as tidal forces [37]. The static rejection function is characterized by two distinct behaviours, depending on the regime of spin frequencies at which the rotor is operated. For low and high values of ν_s, the dependence of the rejection function is quantitatively condensed in equation (4.43). In the case of intermediate values of ν_s (i.e. for values of the spin frequency higher than the differential frequency of the rotor and lower than its second common mode frequency), peaks emerge in $|1/\chi_0|\nu_S$ (see figures 4.7 and 4.8), whose positions are affected by the parameters of the system (L, L_1, k, $k_{1,2}$, m, ℓ) and by the offsets. We can then tune ν_s (i.e. $\overline{\nu}_s \sim \nu_{zero}/2$) to place the system in correspondence to one of the peaks of $|1/\chi_0|\nu_S$ obtaining values as high as 10^6. It is also possible to regulate the inclination (see figure 4.17) of the plane on which the motor is mounted to obtain a level of self-centring as good as it is required by the target of an EP test at the level of $\eta=10^{-13}$. Hence, figures (4.7), (4.8) and (4.17) suggest to operate at intermediate frequencies where extremely good performances of the apparatus can be obtained. Note that intermediate frequencies are sufficiently high in order to obtain good frequency modulation of the signal, reduction of 1/*f* noise (at the present time this noise is lower than the resolution of the 16-bit electronics) and high *Q* values (see below about the *Q* measurements).

In chapter 5 we have shown some experimental results concerning whirling motions and *Q* measurements. Whirling motions have been compared with a theoretical model showing that in highly supercritical rotation mechanical suspensions undergo deformations at the spin frequency (see figure 5.2), hence the time constant of the growth is proportional to the quality factor at this frequency ([10], [12 – 13]).

After some coordinates transformation, we have separated backward and forward whirling motions (see figures 5.6 and 5.7) showing that backward whirls are stable, with amplitude decreasing in time with exponential law, while forward whirls are unstable with increasing amplitude.

In chapter 5, we have also shown that it is possible to manufacture high quality cardanic suspensions of rather complex shape (*Q*=33000 @ 0.9Hz, *Q*=93000 @ 1.4Hz; see section 5.8) but we have also shown that, in spite of the high *Q* values measured at zero spin speed (due to the suspension only), the growth rate of whirl in supercritical rotation is much faster than expected, indicating that, during rotation, much bigger losses take place in the system beside the ones in the suspensions.

The cause of these spurious losses is under investigation in order to obtain very long time constants and a whirl growth so slow that data taking can be performed between successive damping, thus avoiding any disturbance at all from active damping forces.

A source of rotating damping may be due to the O-ring (OR in figure 2.1) used to transmit rotation from the motor (in its offset location) to the rotating suspension tube ST (see figure 2.1). In the new generation of the rotor (which is under construction) we will eliminate the O-ring altogether by locating the motor on the spin axis.

.

Our theoretical understanding of the experimental apparatus has been applied in order to actively reduce whirling growth in supercritical rotation (chapter 6). The whirl radius at a differential frequency of 0.08Hz has been reduced from about 1mm to about 0.1 μm (see figure from 6.13 to 6.17). The next goal is to obtain a better active stabilization of whirl motions at all the natural frequencies by improving the electronics needed for the whirling motion control. In particular we are constructing new digital filters and the electronics for controlling whirling motions acting at common mode frequencies ν_{c1}^0 and ν_{c2}^0. In fact, as argued in section 6.4, the level of 0.1μm of residual forward whirling at 0.08 Hz is connected to the presence of this peaks at higher frequencies.

We have reasons to think that the residual low frequency noise (below 10^{-2}Hz) is connected to the vacuum chamber closing system, to its pump and to the 16-bit electronics used for data acquisition. We have substituted the old closing system of the chamber and found a new accommodation for the pump; we have also applied movable feet to the chamber to regulate its horizontality.

By comparison with the target of the GGG experiment in testing the equivalence principle, the observed residual 0.1 μm separation between the centres of mass of the test cylinders corresponds to a violation at the level of $\eta<10^{-7}$. This means that the GGG rotating differential accelerometer can be used to test the equivalence principle in the gravitational field of the Sun to 1 part in 10^{13} only if its sensitivity will be improved by a factor 10^6 (with the introduction of new electronics for data acquisition and operating with an high differential period of oscillation) and if daily seismic disturbances will be reduced by seven orders of magnitude with respect to daily tilts measured so far (see figures 7.1 and 7.3).

The short-term goal of the experiment is to obtain an active reduction (3/4 orders of magnitude) of low frequency seismic noise (see section 2.8 and chapter 7) [40]. We have performed measurements of the seismic disturbances during two years and we have studied the problem in order to define the control laws required for the active compensation of the tilts. We are now evaluating the characteristics of the electronics needed to perform this active control. Preliminary experimental results have shown that it is possible to correct tilts at the level of $7\cdot10^{-10}$rad.

The next long-term goal requires the introduction of a passive cardanic suspension to suspend the whole apparatus (as discussed in section 2.8; the advantage of working in a suspended laboratory in order to reduce vibrational disturbances is outlined in chapter 10 where the PGB laboratory is illustrated [53]) and the construction of new 24-bit electronics.

A space version of the fast rotating GGG differential accelerometer presented here, to be used within the GG mission ([10 - 11], [26 – 27]), will be described in the following chapter. The GGG accelerometer has been constructed to have the same features as the one proposed for flight, essentially weak coupling, high frequency supercritical rotation and differential capacitance read-out. It is a full-scale prototype devoted to testing the main features of the proposed space instrument, in spite of the fact that the local acceleration of gravity is about eight orders of magnitude bigger than the largest disturbances the accelerometer would be subject to in space.

The space version would take advantage of the stronger driving signal (8.4 m/s^2 from the Earth at 520km altitude in GG, instead of 0.006 m/s^2 from the Sun in GGG). It would also allow much weaker suspensions due to the absence of weight, and consequent higher

.

sensitivity (which depends on the differential period squared) by a factor of about 450. It can be argued that another factor of about 200 can be gained due to the absence of motor and motor/bearings noise, and thanks to the much higher symmetry of the space accelerometer (no 1-g preferential direction, hence much better rejection of common mode forces and consequent higher sensitivity to differential forces). Overall this amounts to about 8 orders of magnitude gain, thus making a 10^{-17} test in space a goal worth pursuing. In point of fact, the error budget of the space experiment, as developed within mission studies so far, has turned out to be compatible with this goal. The improvement over current best ground results would be of 5 orders of magnitude.

CHAPTER 9:

THE GG SPACE EXPERIMENT.

9.1: INTRODUCTION.

"Galileo Galilei – GG" is a proposed experiment in low orbit around the Earth aiming to test the Equivalence Principle (EP) to the level of 1 part in 10^{17} at room temperature from its most direct consequence, the Universality of Free Fall (UFF), whereby all bodies fall with the same acceleration regardless of their mass and composition ([10 - 11], [26 - 29]).
A space mission can reach a sensitivity many orders of magnitude higher than within a ground experiment: test bodies in low Earth orbit are subject to a driving signal by about 3 orders of magnitude stronger than on torsion balances on the ground. Another main advantage of space is weightlessness: the gravitational attraction of the Earth is largely compensated by the centrifugal force due to the orbital motion of the spacecraft so the main 1g local acceleration of gravity is absent.
Three space experiments, aiming to test the equivalence principle, are under investigation by space agencies: μSCOPE ([24 - 25]) with the goal $\eta = 10^{-15}$, "GALILEO GALILEI" (GG) ([10 - 11], [26 - 29]) with the goal $\eta = 10^{-17}$ and STEP ([30 - 31]), with the goal $\eta = 10^{-18}$. In all these experiments, the test bodies are weakly coupled, concentric, co-axial, hollow cylinders of different composition.
A unique feature of GG, which is pivotal to achieve high accuracy at room temperature, is fast rotation in supercritical regime around the symmetry axis of the test cylinders, with very weak coupling in the plane perpendicular to it. Another unique feature of GG is the possibility to fly 2 concentric pairs of test cylinders, the outer pair being made of the same material for detection of spurious effects. GG was originally designed for an equatorial orbit, but the much lower launching cost for higher inclinations has made it worth redesigning the experiment for a sun-synchronous orbit.
The GG accelerometer is designed to have the same features as the ground experiment GGG, essentially: weak coupling, high frequency supercritical rotation and differential read-out. It has been extensively described in [11].
We devote this chapter to describe the general aspects of the GG experiment (sections 9.2, 9.3 and 9.4). A mathematical model of the apparatus has been developed in [11] and it will be described in sections 9.5-9.11. In [11] the complete GG system has been simulated using DCAP (Dynamics and Control Analysis Package) software developed by ALENIA SPAZIO under ESA contract. Here the dynamic model has been set up with Simulink software. Thanks to some simplifications with respect [11], equations of motion become more manageable and full analytical solutions have been obtained in sections 9.5 and 9.6. The harmonic analysis described in sections 9.9 is a little different from the analysis in [11]: a smaller number of calculations is sufficient to reconstruct the whirl velocity starting from the measurement data of the rotating capacitance bridges.
The following sections 9.1, 9.2 and 9.4 are parts of the article [28] available in Appendix_Articles.

9.2: THE GG EXPERIMENT CONCEPT.

In GG two test masses of different composition are arranged to form a differential accelerometer. The test bodies are concentric, co-axial, hollow cylinders[1] weakly coupled like in a beam balance, with the beam directed along the symmetry axis, so as to be sensitive to differential accelerations acting between the bodies in the x,y plane perpendicular to it (the weaker the coupling, the higher the sensitivity). Coupling and balancing allow common mode effects to be rejected. Two capacitance bridges in between the test cylinders read their relative displacements (caused by differential accelerations) in the plane of sensitivity. The better the mechanical balance of the bridge capacitance plates halfway in between the test cylinders, the more insensitive is the read-out to common mode effects. Thus, the differential nature of the accelerometer is ensured both by the suspension and by the read-out.
High frequency modulation of the expected signal – for the reduction of $1/f$ electronic and mechanical noise – is obtained by spinning the accelerometer around the symmetry axis; a cylindrical spacecraft encloses, in a nested configuration, a cylindrical cage with the test cylinders inside, and is stabilized by rotation around the symmetry axis.

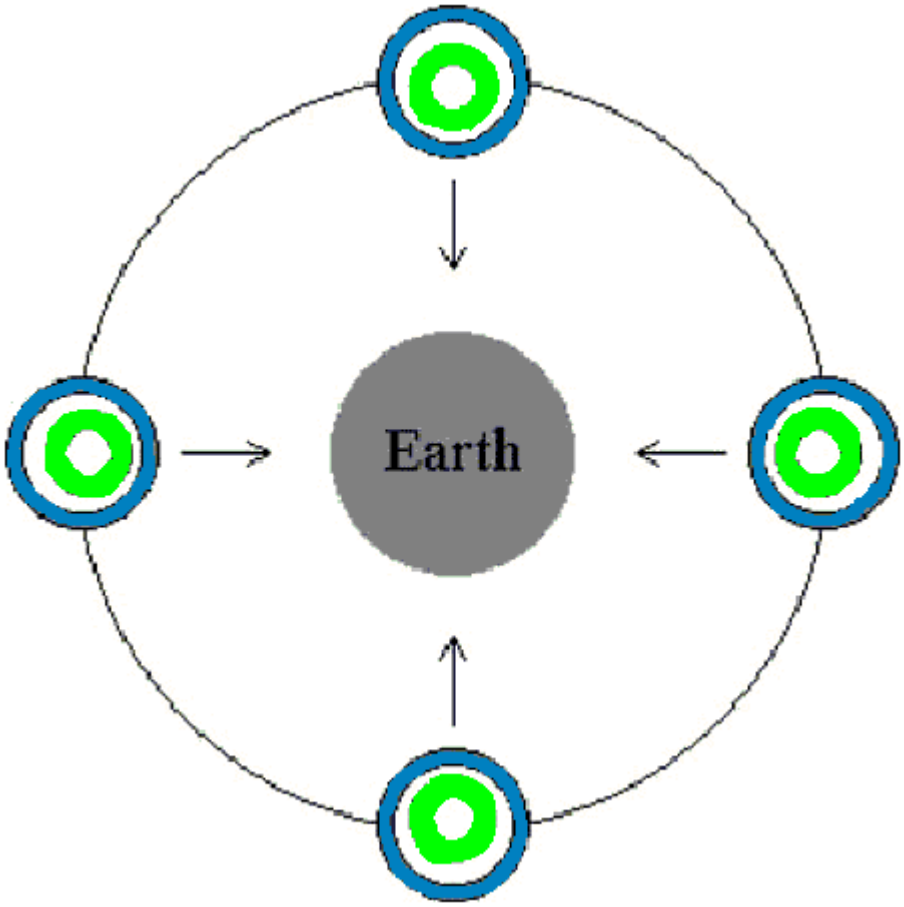

Figure 9.1: Section across the spin/symmetry axis of the GG outer and inner test cylinders (of different composition) as they orbit around the Earth. The centres of mass of the test cylinders are shown to be displaced

[1] From now on, simply cylinder.

towards the centre of the Earth as in the case of a violation of the equivalence principle in the field of the Earth (indicated by the arrows). The signal is at the orbital frequency.

Once the spacecraft has been given the required rate of rotation at the beginning of the mission (2Hz with respect to the centre of the Earth), no motor is needed in space. Hence, the space experiment is not affected by noise from the motor, contrary to what happens with rotating apparata in ground based laboratories where the motor and its noise are a serious matter of concern.

As shown in figure 9.1, an EP violation in the field of the Earth would generate a signal of constant amplitude (for zero orbital eccentricity) whose direction always points to the centre of the Earth, hence changing orientation with the orbital period of the satellite. The read-out, also rotating with the system, will therefore modulate an EP violation signal at its spin frequency with respect to the Earth. The expected signal benefits from the spacecraft orbiting the Earth at low altitude. Having selected 520 km for GG, an orbit inclination of 97.5° ensures that the spacecraft follows the annual motion of the Sun (sun-synchronous orbit) and makes it possible to use a high altitude, low cost launcher for orbit injection. By maintaining the spin/symmetry axis of the spacecraft within about ten degrees from the orbit normal, there is almost no degradation of the signal in the sensitivity plane of the accelerometer.

Figure 9.2 shows a section through the spin/symmetry axis of the system. There are four test cylinders (weighing 10 kg each), one inside the other, all centred at the same point (nominally, the centre of mass of the spacecraft) forming two differential accelerometers: the inner one for EP testing (cylinders made of different materials; they are shown in green and blue, respectively) and the outer one for zero check (cylinders of the same composition; both shown in brown). In each accelerometer the two test cylinders are coupled to form a beam balance by being suspended at their top and bottom from the two ends of a coupling arm made of two concentric tubes (each tube suspends one test cylinder at each end, which makes it asymmetric top/down; however, the two of them together form a symmetric coupling). All four tubes are suspended at their midpoints from the same suspension shaft (the longest vertical tube in the figure). In all cases the suspensions are ∪-shape thin strips (shown in red), to be curved out of a solid piece of CuBe. At each connection there are three of them, at 120° from one another. They are sensitive to differential acceleration in a plane perpendicular to the symmetry axis which is also the axis of rotation (see figure 9.3), so as to provide frequency modulation of the expected signal. There are capacitance plates (connected to the suspension shaft; shown as yellow lines in figure 9.2) for the read-out of differential displacements in between each pair of test cylinders (shown as yellow lines in section).

In order to provide an intermediate stage of isolation between the spacecraft and the test cylinders the accelerometers of figure 9.2 are not suspended directly from the spacecraft, but instead from the so called PGB-"Pico Gravity Box" laboratory (see appendix 9.A for details): a cylindrical structure which is mechanically suspended from the spacecraft along its symmetry axis (see figure 9.4) so as to provide weak coupling in the plane perpendicular to the axis while being stiffer along it (a prototype of the PGB laboratory has been studied to reduce vibrational noise on board the International Space Station –see appendix 9.B for details).

In GG the four cylinders are suspended mechanically and centred at the centre of mass of the spacecraft in order to reduce common mode tidal effects and improve the reliability of the zero check. However, whatever the nature of the suspensions, there will always be a non-zero

offset vector $\vec{\varepsilon}$ from the spin axis (in the reference frame fixed with the system) due to construction and mounting errors.

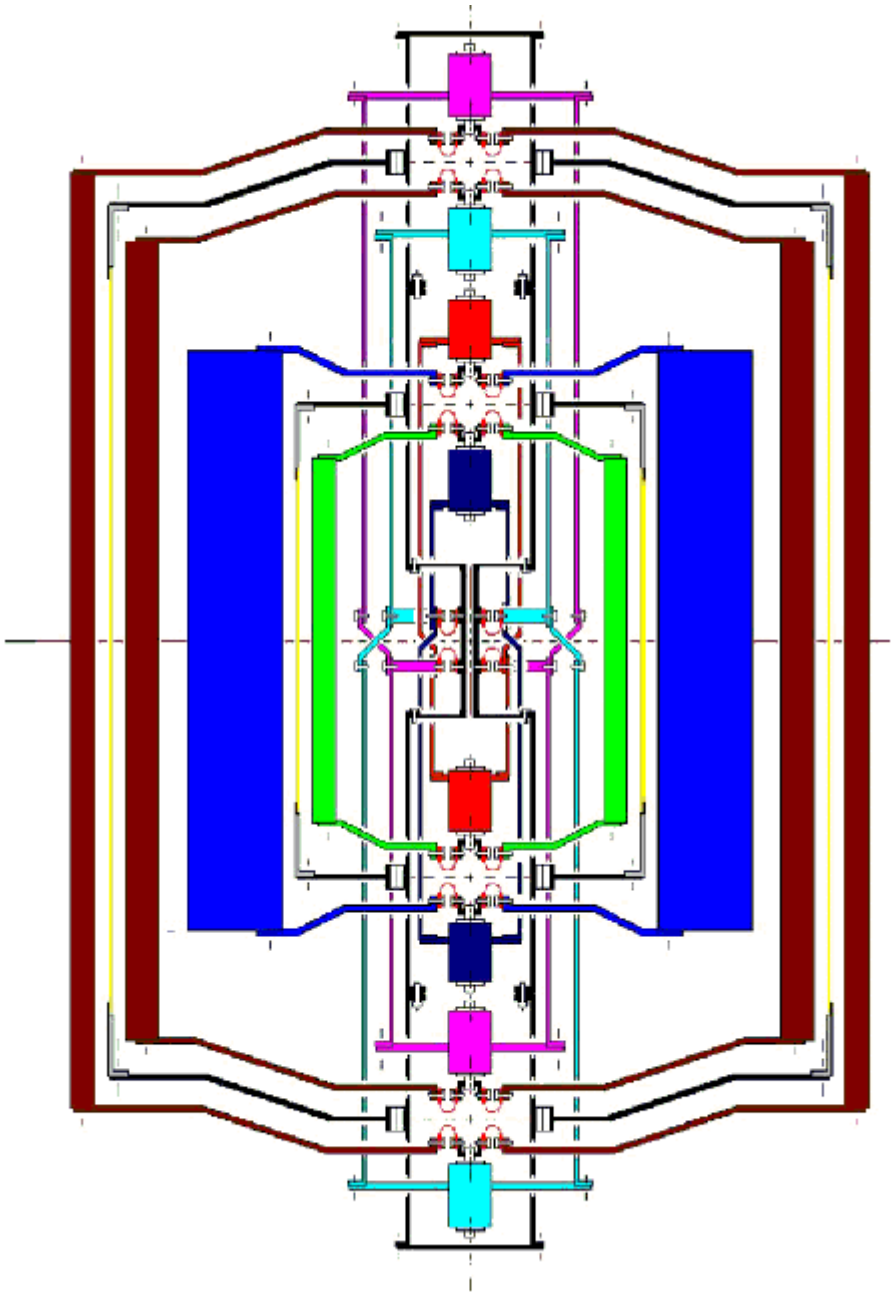

Figure 9.2: Section through the symmetry axis of the system. There are four test cylinders (green, blue and brown), one inside the other, all centred at the same point forming two differential accelerometers. In each accelerometer the two test cylinders are coupled to form a beam balance by being suspended at their top and bottom from the two ends of a coupling arm made of two concentric tubes (each tube suspends one test cylinder at each end, which makes it asymmetric top/down; however, the two of them together form a symmetric coupling). All four tubes are suspended at their midpoints from the same suspension shaft (the longest vertical black tube in the figure). In all cases the suspensions are ∪-shape thin strips (shown in red). At each connection there are three of them, at 120° from one another.

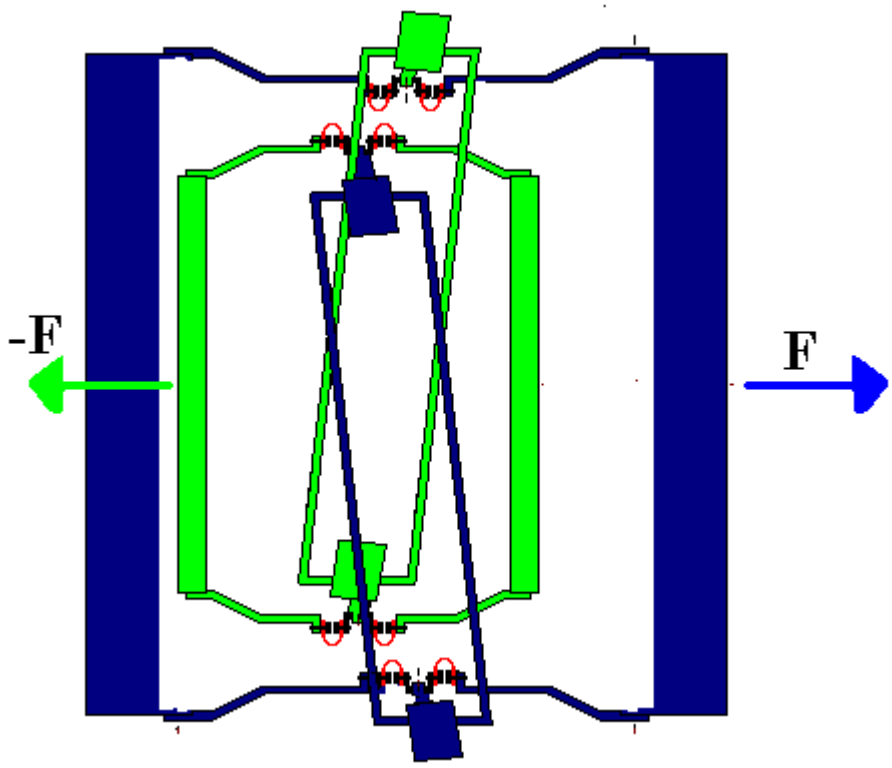

Figure 9.3: Relative displacement due to a force acting in a differential manner on two couplet test masses.

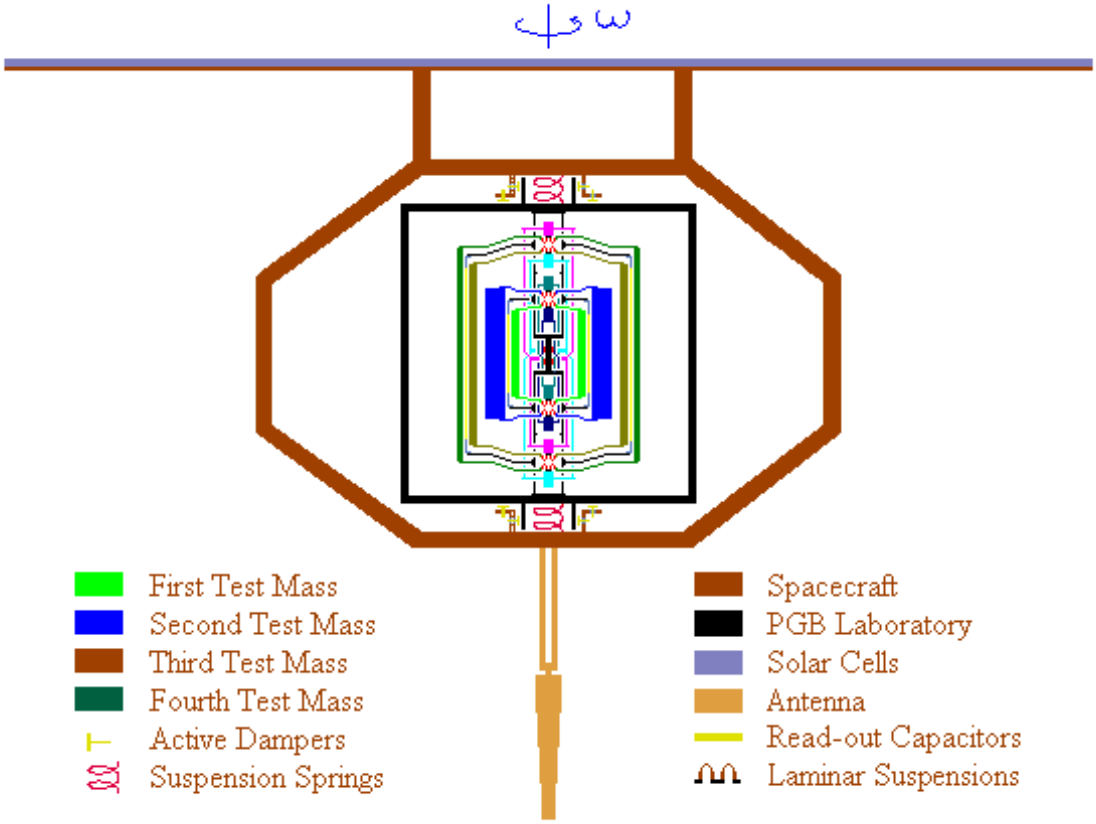

Figure 9.4: The GG spacecraft as it has been designed for flight in high inclination, sun-synchronous orbit. This figure shows a section along the spin/symmetry axis. It is possible to see the PGB laboratory and the

accelerometers inside the spacecraft. The section and the legend give details on the main parts of the spacecraft and the experimental apparatus. The total mass is 280 kg, the orbit is almost circular, has an altitude of 520km and an inclination of 97.5°.

The equilibrium position vector of the centre of mass of the suspended body, for given angular spin frequency ω_S, is given by the equation:

$$\vec{r}_{eq} = \frac{1}{1-\left(\omega_s/\omega_n\right)^2}\vec{\varepsilon} \tag{9.1}$$

where ω_n is the natural frequency of the suspended mass. In space, thanks to the absence of weight, the suspension can be extremely weak, so that the condition $\omega_S >> \omega_n$ can be easily satisfied. From (9.1), it follows that in this case equilibrium will take place closer than $\vec{\varepsilon}$ to the spin axis, namely:

$$\vec{r}_{eq} \simeq -\frac{\omega^2}{\omega_s^2}\vec{\varepsilon} \tag{9.2}$$

Equation (9.2) shows that extremely good auto-centring will be achieved (the equilibrium position vector, like the original offset vector, is fixed with the rotor).
The only disadvantage of rotation at frequencies above the natural one is the onset of whirl motions, at the natural frequencies of the system, around the equilibrium position. Whirl is due to losses in the suspensions (the smaller the losses, the slower the growth rate of whirl) and needs to be damped to prevent instability (see chapter 9), but it can be separated to recover the equilibrium position thanks to the fact that the whirl frequencies of the system are known.
The read-out consists of two pairs of capacitance plates located halfway in between the test cylinders and forming two capacitance bridges in two orthogonal direction in the plane perpendicular to the spin/symmetry axis (for more details, see section 2.5 where the read-out in the GGG experiment is described).
The GG accelerometer is designed to have the same features as the ground experiment GGG, essentially: weak coupling, high frequency supercritical rotation and differential read-out. It has been extensively described in [11].

9.3: THE SPACECRAFT AND THE ORBIT.

The GG spacecraft is designed around the accelerometers and it is meant to provide the rotation of the system around its symmetry axis (see figure 9.4). It is therefore an axis-symmetric spacecraft passively stabilized by rotation around its axis of maximum moment of inertia. At 520 km altitude, a sun–synchronous orbit requires an inclination of 97.5° over the equator. The orbit is almost circular. The sensitive plane of the accelerometers should lie in the plane of the expected signal, that is in the orbital plane. The spin/symmetry axis should therefore be normal to the orbit plane. However, while the spin axis is almost unaffected by external torques and therefore remains fixed in space, regression of the nodes of an inclined orbit due to the flattening of the Earth makes the orbit normal precess around the axis

perpendicular to the equator (with a 1 year period in the case of a sun-synchronous orbit). As a result, a spin axis originally aligned with the orbit normal would no longer be so as time goes by. However, it can be shown [54] that if the spin axis stays within about ±10° from the orbit normal, the expected signal is only very slightly diminished (along only one component) with respect to its maximum value. Therefore, the GG spacecraft is equipped with cold gas thrusters to be used to realign its spin axis along the orbit normal every about 20 days of data taking. For the spacecraft to maintain its cylindrical symmetry and its centre of mass not to be affected by attitude manoeuvres, two tanks have been designed, both of toroidal shape, to be located one above and one below the centre of mass. During attitude manoeuvres all the masses suspended inside the spacecraft are locked using inch-worms placed around their central coupling arm.

Since the spin/symmetry axis of the spacecraft is maintained near the axis perpendicular to the sun-synchronous orbit, solar cells for power generation are located on the surface of a dish facing the sun. This dish serves also the purpose of shielding the spacecraft body (a compact, 1m size structure in the shape of a spinning top enclosing the accelerometers) from sunlight, so as to reduce the effects of thermal disturbances on the experiment. The largest disturbing acceleration experienced by the accelerometers is due to the effect of residual air drag acting on the spacecraft and not on test masses suspended inside it, thus resulting in an inertial acceleration opposite to the acceleration by air drag on the spacecraft. Moreover, the largest and most dangerous air drag effect is due to its along track component, which has the same orbital frequency as the signal and differs from it only in phase (the signal is in the radial satellite-centre of the Earth direction).

The inertial acceleration resulting from air drag – and in general from non gravitational forces acting on the spacecraft – are in principle the same on the test bodies in each accelerometer. They are known as common mode effects and should not produce any differential signal to compete with the target differential signal of an equivalence principle violation. However, this would be so only in the ideal case that the suspensions of the test cylinders in the accelerometers were perfectly identical and the capacitance bridges of the read-out were perfectly balanced, i.e. under condition of perfect common mode rejection. In the GG space experiment the strategy chosen is for air drag to be partially compensated by the spacecraft drag free control system, and partially rejected by the accelerometers themselves. In this way, the burden of reducing to an acceptable level this very large effect is shared between the spacecraft and the experimental apparatus, each of them being given a reasonable task.

Common mode rejection relies on the coupled suspension of the test cylinders and the capacitance differential read-out in between them, and on well established in-flight balancing procedures. Drag compensation requires the spacecraft to be equipped with thrusters and an appropriate control system to force the spacecraft itself to follow the motion of an undisturbed test mass inside it. Since drag compensation must be active during data taking, the are severe limitation on the disturbances it produces which make ordinary impulsive thrusters not suitable. Finely tuneable proportional thrusters based on field emission electric propulsion (FEEP) appear to be the best choice, also because of their high specific impulse and consequent need of only a negligible mass of propellant. The test mass which drives the drag-free control system is the PGB, whose motion relative to the spacecraft in the plane perpendicular to the symmetry axis is read by two capacitance bridges. In terms of frequency, drag must be compensated in a narrow frequency range around the orbital one, in order reduce

its component along track. For this purpose, a control based on a notch filter has been tested in numerical simulations of the GG system and found to be effective [11]. The PGB can provide the required driving signal to the drag control system because the orbital frequency around which drag must be compensated is below its natural frequency above which disturbances acting on the spacecraft are attenuated.

The transfer function of the PGB (see figure 9.5 – it is derived in appendix 9.A) shows that effects at the orbital frequency are unaffected by the PGB suspension. They are sensed by the capacitance read-out in between the PGB and the spacecraft through the relative displacements they produce between the two, and these measurements serve as input to the drag free control. Note that the expected signal too is at the orbital frequency (see figure 9.1), hence, it is not attenuated. Instead, the figure shows that disturbances at the spin frequency of the spacecraft (in the non rotating frame) are significantly reduced. Such disturbances are due primarily to the FEEP thrusters used for drag compensation, because in order to compensate for the effect of drag at the orbital frequency of the spacecraft around the Earth while spinning with the spacecraft itself, they must fire at the spin frequency relative to the centre of the Earth (2Hz). Since this is also the modulation frequency of the expected signal, its attenuation by the PGB by about 5 orders of magnitude (40dB per decade at frequencies above the natural one) is a considerable advantage for the experiment.

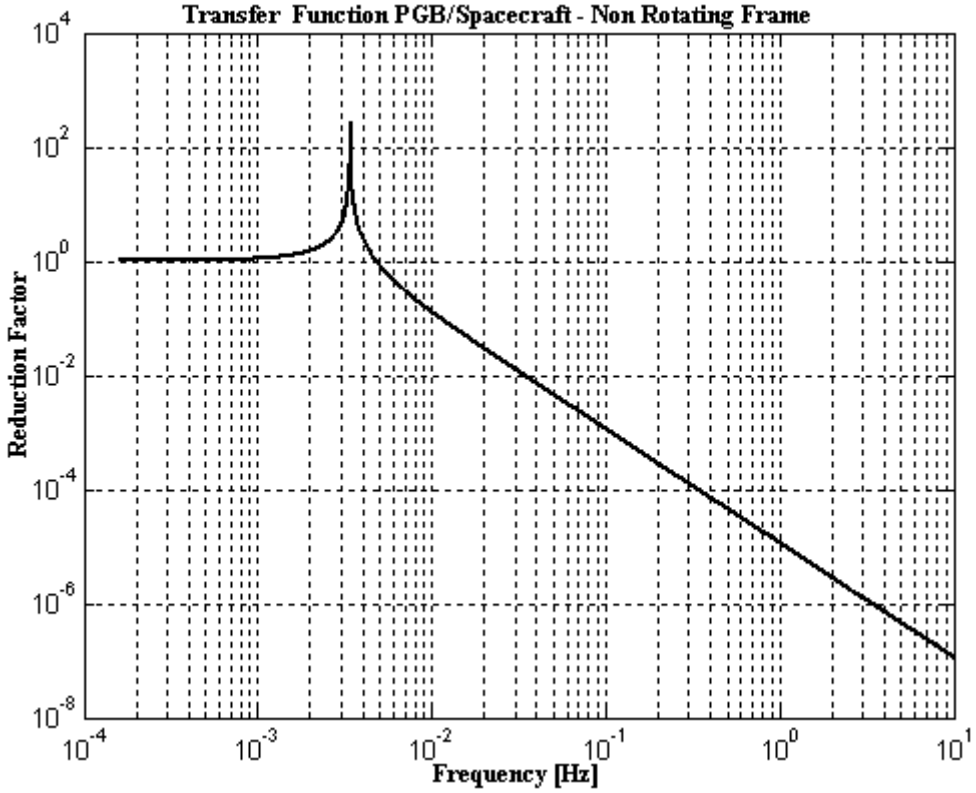

Figure 9.5: Transfer function of the PGB laboratory (enclosing the accelerometers), suspended inside the spacecraft. The frequency of the natural oscillations in the plane perpendicular to spin /symmetry axis is 1/360Hz. The transfer function is shown in the non rotating reference frame: any effect at frequencies below the natural one (the threshold frequency) is essentially unaffected, while above the threshold, disturbances are attenuated (the higher the frequency, the better the attenuation). In this case the value of the quality factor is 90.

9.4: REQUIREMENTS AND ERROR BUDGET.

In order to be sensitive to differential effects in the plane perpendicular to the spin/symmetry axis, the test cylinders of each accelerometer (see figure 9.2) are weakly coupled to one another. With the suspensions as designed, the natural differential period is 540 seconds. Instead, all suspensions are stiff along the axis as well as in response to force acting on both masses in the accelerometer (common mode effects). These mechanical features have been chosen for best sensitivity to differential forces in the plane, while minimizing the effects of common mode forces in the same plane as well as those of all disturbances along the axes. In particular, the goal of testing the EP to 1 part in 10^{17} in the gravitational field of the Earth requires to detect the effect of a differential acceleration of $a_{EP} \approx 8.4 \times 10^{-17} ms^{-2}$ (pointing to the centre of the Earth), which amounts to a relative displacement between the test cylinders of the inner accelerometer of 0.6 pm. The main requirements which need to be fulfilled in order to reach the mission goal are concerned with: mechanical balance of the test cylinders; drag compensation; mechanical balance of the capacitance bridges; temperature variations (in space and time); damping of whirl motions and quality factor at the spin frequency.

Each accelerometer is conceptually a beam balance with the beam along the symmetry axis. Ideally, it should be insensitive to common mode forces in the plane of sensitivity perpendicular to it. Perfect rejection is obviously impossible, and we require that all common mode forces in the plane are rejected by a factor $\chi_{CMR}=1/10^5$. Much better rejection than this is achieved with ordinary balances on the ground where the common mode force (local gravity) is many orders of magnitude stronger than the largest common mode force (due to residual air drag) acting on the GG test cylinders. The balancing procedure relies on the capacitance bridges in between the test cylinders as sensors and the inch-worms on the accelerometer's coupling arms (see figure 9.2) as actuators. Once balancing is completed, the inch-worms can be switched off so as not to disturb the measurements. For the residual effect of air drag at the orbital frequency and in the plane of sensitivity we require a compensation factor of $1/10^4$, using the capacitance bridges between PGB and spacecraft as sensors and FEEP thrusters as actuators. As a result of both compensation and rejection, the residual differential effect of air drag on the test masses of the accelerometers is 10^9 times smaller than its original value, which for the GG spacecraft and orbit is $a_{drag} \leq 2 \times 10^{-7} ms^{-2}$ (worst case).

This means that the disturbance due to air drag is larger than the signal by a factor 2.4 at most, and can anyway be distinguished from it because of the large phase difference between the two. The amount of drag effect remaining after compensation by FEEP thrusters gives a common mode effect on the test masses of the accelerometers, which – if the capacitance plates of the read-out are not perfectly balanced in between the test cylinders (i.e., the gaps on the two sides are not equal) – results in a spurious differential signal. For it to be a few times smaller than the target signal the unbalance must be (with a 5 mm gap) of a few μm, which is not a stringent requirement. We also require drag compensation by a factor 1/400 along the spin/symmetry axis (at the orbital frequency) in order to reduce the separation between the centres of mass of the test cylinders along this axis.

All mechanical balancing will be affected by temperature variations. Since there are about 20 days available for data taking between two successive attitude manoeuvres, we require that temperature variations be small enough not to destroy the balancing of the system for that span of time. Temperature time variations must be such that $\dot{T} < 0.1 K / day$, the requirement

being set by the mechanical balance of the capacitance bridges, which are affected by the differential thermal expansion of the test masses and bridge frame. Variations of the suspensions stiffness with the temperature are not relevant. Along the z′ spin/symmetry axis it must be $\Delta T<\Delta z'<4K/m$, and the requirement is set by the mechanical balance of the test cylinders since it is affected by the expansion/contraction of the coupling arms. Passive thermal isolation is sufficient to avoid temperature variations larger than these, and no active thermal control is needed. Temperature constraints are not very demanding in GG because its rapid rotation averages out azimuthal temperature variations and makes the radiometer effect negligible; much more demanding constraints need to be satisfied in case of slow rotation of the test cylinders [55 - 56]. During eclipses, when the satellite happens to go in and out of the Earth's shadow, different heating of the outer shell of the spacecraft as compared to the internal apparatus (which is thermally isolated) would produce a differential rotation rate due to changes in the moment of inertia and conservation of angular momentum. This is avoided by means of a small mass compensation system based on a photo-diode sensor to detect the phase lag between the outer and the inner part of the spacecraft, and inch-worms actuators to displace little masses and compensate moment of inertia changes; the masses required are of a few grams because changes of moment of inertia caused by temperature variations are very small. Whirl motions of all suspended bodies are damped by means of capacitance sensors/actuators. In the non rotating frame whirls have the frequencies of natural oscillations (slow), while the sensors/actuators spin fast with the whole system (2Hz). The spacecraft is equipped with Earth elevation sensors to measure its state of rotation in order to perform the coordinate transformation between the rotating and non rotating frame which is needed for an accurate reconstruction and damping of the whirl motion [11]. The growth rate of whirls is determined by losses in the system, essentially in the mechanical suspensions as they undergo deformations at the frequency of spin. The time constant of the growth is $T_w Q_S/\pi$, where Q_S is the quality factor at the frequency of spin and T_w the natural period of the whirl. The force required to damp the whirl is a fraction Q_S of the mechanical coupling force (see section 1.8). In GG the requirement is Q_S=20000 at 2Hz, which laboratory test have shown to be achievable (see chapter 5). With a Q of at least 20000, whirl growth is so slow that data taking can be performed between successive damping, thus avoiding any disturbance at all from damping forces. In order to reconstruct the position of relative equilibrium of the test cylinders in the non rotating reference frame, as affected by a low frequency differential force (like an EP violation at the orbital frequency around the Earth) whirl motion at the natural frequency of oscillation can be separated out. Tests with the laboratory prototype demonstrate that a low frequency differential effect can be detected even in the presence of a much larger whirl (see section 6.4).

The error budget of the space experiment is performed keeping in mind that both the frequency and phase of the expected signal are well known: once the high frequency signal modulation due to the spin rate of the spacecraft has been eliminated by coordinate transformation to the non rotating system, the signal must appear as a differential displacement at the orbital frequency, and always pointing to the Earth.

The most dangerous perturbing effects are therefore those which are close to the signal both in frequency and phase. There are two such effects: the Earth monopole coupling to higher mass moments of the test bodies and the radiometer effect. The first is due to the fact that the test bodies are not monopoles; they have non zero higher mass moments, and the monopole

mass moment of the Earth will couple differently to them giving rise to a differential force. Being due to the Earth, which is also the source mass of a possible violation of equivalence, this effect cannot in any way be distinguished from the signal. For a given spacecraft altitude and a given target in EP testing, the dominant mass moment of the test cylinders (quadrupole) must be small enough for this effect to be below the signal. The values required (about 0.01) are realistic to obtain by test mass machining. The radiometer effect is caused by the residual gas pressure in the presence of temperature gradients across the test masses generated by the infrared radiation from the Earth. In GG temperature gradients are averaged out by the fast rotation and the radiometer effect is negligible even at room temperature [55-56].
At the same frequency as the signal but, with a phase difference of about 90 degrees, we have the inertial force caused by residual air drag acting on the outer surface of the spacecraft along its orbit. With the requirements given above for drag compensation and common mode rejection, the residual differential acceleration due to air drag is 2-3 times larger than the signal (worst case) and can be separated from it thanks to the large phase difference. At twice the orbital frequency there is the tidal effect due to a non zero separation between the centres of mass of the test cylinders along the spin/symmetry axis whenever it is not exactly aligned with the orbit normal [11]. With a compensation of non gravitational forces (mostly solar radiation pressure) along the spin axis by 1/400, and with a common mode rejection in that direction of 1/50 (by suspensions machining only) this tidal effect is almost one order of magnitude smaller than the signal. At the natural frequency of differential oscillation of the test masses (1/540s) there is a residual whirl motion of their centres of mass which gives rise to a tidal effect from the Earth at the whirl frequency. However, it can be proven that it does not affect the position of relative equilibrium around which whirl motion takes place [54]. it causes a small deformation of the whirl orbit which circulates with the motion of the spacecraft around the Earth, does not accumulate in time and does not prevent recovery of the equilibrium position by separation of the whirl motion. Similarly, the whirl orbit is also affected by resonant drag effects due to air granularities along the spacecraft orbit around the Earth. In this case too the equilibrium position is not affected, the deformation of the whirl orbit circulates with the orbital period, it does not accumulate with time and can be separated out. There is a modest drag compensation requirement along the spin axis because a centre of mass separation along it will generate (in the presence of a tilt angle with respect to the orbit normal) a tidal effect in the sensitive plane whose frequency is close to that of the signal. Mechanical suspensions allow the test masses to be electrically grounded, thus avoiding the need to measure the amount of accumulated charge and to discharge the masses, which inevitably disturbs the measurements. Residual so-called patch effects are known to be small and slowly moving. Moreover, their presence can be checked by changing sign to an applied known electric potential corresponding to the resolution achieved: since the force is proportional to the square of the potential, the resulting effect must be the same to rule out patch effect potential at that level. Requirements on magnetic impurities and magnetic susceptibility for the test masses can be met. Rotation of the whole system together makes many effects coming from local (fixed) disturbances, (such as local mass anomalies or parasitic capacitances) to become DC signals, and therefore not an issue. Finally, thermal noise, is compatible with the goal of the experiment thanks to the high frequency of spin, to the high Q of the system and the large mass of the test cylinders (10kg test bodies compensate for working at 300K rather than at a few K but with masses of 100g).

9.5: THE MATHEMATICAL MODEL.

This section describes the four-body dynamic model set up with Simulink software for the complete GG experiment, including the spacecraft, the PGB laboratory and the two test masses. Both the mathematical model describing the behaviour of the system and the controller scheme implementing the whirling stabilisation loops are outlined in detail. Whirling motions need to be damped both on the ground and in space, but in space they can only be actively damped with capacitance sensors/actuators which are fixed in the rotating frame of the whole system. In GGG, instead, active damping has been performed in the non rotating frame. A full 3D simulation including conical and cylindrical modes is reported in [11]: from numerical evaluations emerges that conical motions are very slow and are stable once the test bodies are stabilized by the active control of their whirl motions; hence, for simplicity reasons, we assume for the present that the rotations are perfectly controlled. Thanks to this simplification, equations of motion become more manageable (the rotational variables vanish from them) and full analytical solutions may be obtained hollowing us an understanding of the most important phenomena typical of coupled rotors. Let us now introduce the rotating reference frame $S_R(O;\xi,\eta,z)$ with the origin O and the z axis coinciding with that of the inertial frame $S_I(O;x,y,z)$. Axes ξ and η rotate in the x-y plane with angular velocity ω_s. The origin O coincides, at the initial time, with the centre of mass of the whole system spacecraft/PGB/test masses. The system is composed of 4 hollow bodies one inside the other, connected by means of weak springs. The spacecraft bus is represented by the label s and has mass m_s (in blue in figure 9.6); the position vector $\vec{r}_s$ points to the spacecraft centre of mass CM_S. The spacecraft is connected to the PGB by means of a coupling spring with elastic constant k. $\vec{\varepsilon}$ is the vector locating the suspension point of the spring with respect to CM_S. The spacecraft is rotating around the z axis, which is perpendicular to the x-y plane. The rotation is counter-clockwise. The PGB laboratory is represented by the label p (with mass m_p). $\vec{r}_p$ is the PGB centre of mass position vector with respect to the origin O. The PGB is connected to the test masses (with mass m_i) by means of isotropic springs with elastic constant k_i (i=1 for the inner mass, i=2 for the outer one; we assume $k_1=k_2$). The restoring force of the suspensions k_i is not applied to the centre of mass CM_i of the i-th test body; $\vec{\varepsilon}_i$ is the vector locating the suspension point of the spring with respect CM_i. $\vec{r}_i$ is the position vector of the i-th test body. We consider dissipative mechanical suspensions; c_R and c_{Ri} are the coefficients of rotating damping for the suspensions k and k_i respectively. In the inertial reference frame $S_I(O;x,y,z)$, the equations of motions are:

$$
\begin{cases}
m_s\ddot{\vec{r}}_s = -k\left(\vec{r}_s - \vec{r}_p + \vec{\varepsilon}\right) - c_R\left[\dot{\vec{r}}_s - \dot{\vec{r}}_p - \vec{\omega}_s \times \left(\vec{r}_s - \vec{r}_p\right)\right] + \vec{F}_{ext} \\
m_p\ddot{\vec{r}}_p = -k\left(\vec{r}_p - \vec{r}_s - \vec{\varepsilon}\right) - c_R\left[\dot{\vec{r}}_p - \dot{\vec{r}}_s - \vec{\omega}_s \times \left(\vec{r}_p - \vec{r}_s\right)\right] - k_1\left(\vec{r}_p - \vec{r}_1 - \vec{\varepsilon}_1\right) + \\
-c_{R1}\left[\dot{\vec{r}}_p - \dot{\vec{r}}_1 - \vec{\omega}_s \times \left(\vec{r}_p - \vec{r}_1\right)\right] - k_2\left(\vec{r}_2 - \vec{r}_p + \vec{\varepsilon}_2\right) - c_{R2}\left[\dot{\vec{r}}_2 - \dot{\vec{r}}_p - \vec{\omega}_s \times \left(\vec{r}_2 - \vec{r}_p\right)\right] \\
m_1\ddot{\vec{r}}_1 = -k_1\left(\vec{r}_1 - \vec{r}_p + \vec{\varepsilon}_1\right) - c_{R1}\left[\dot{\vec{r}}_1 - \dot{\vec{r}}_p - \vec{\omega}_s \times \left(\vec{r}_1 - \vec{r}_p\right)\right] \\
m_2\ddot{\vec{r}}_2 = -k_2\left(\vec{r}_2 - \vec{r}_p + \vec{\varepsilon}_2\right) - c_{R2}\left[\dot{\vec{r}}_2 - \dot{\vec{r}}_p - \vec{\omega}_s \times \left(\vec{r}_2 - \vec{r}_p\right)\right]
\end{cases}
\tag{9.3}
$$

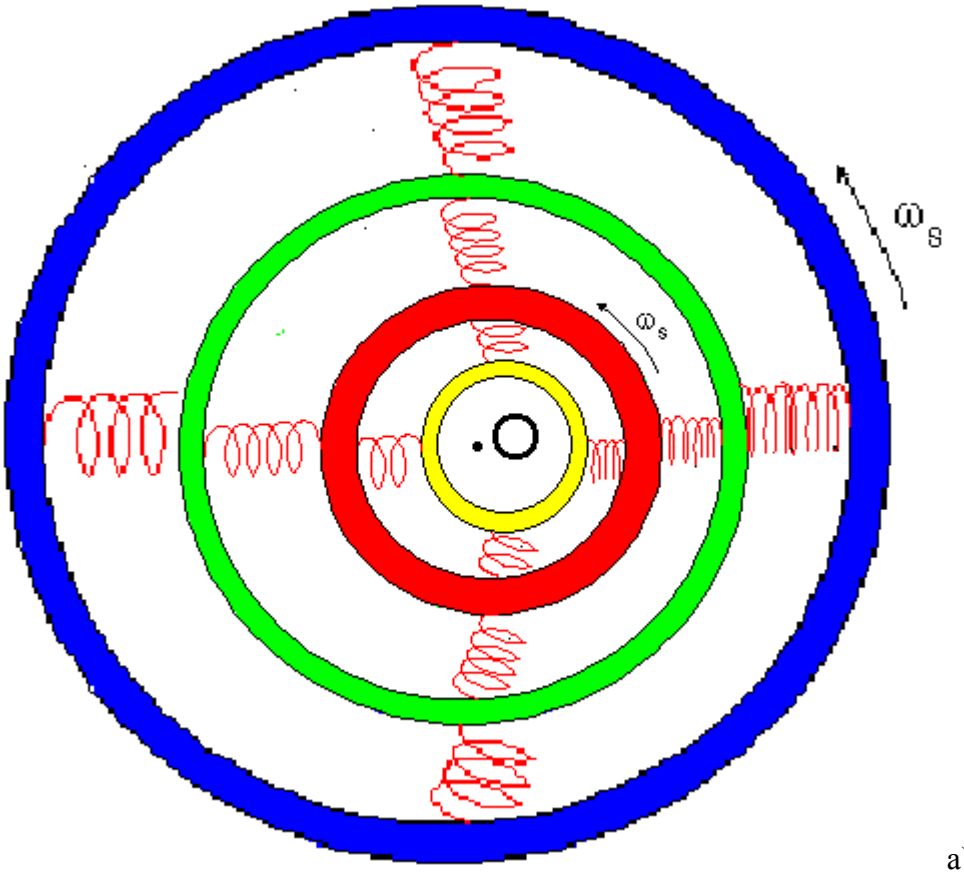

a)

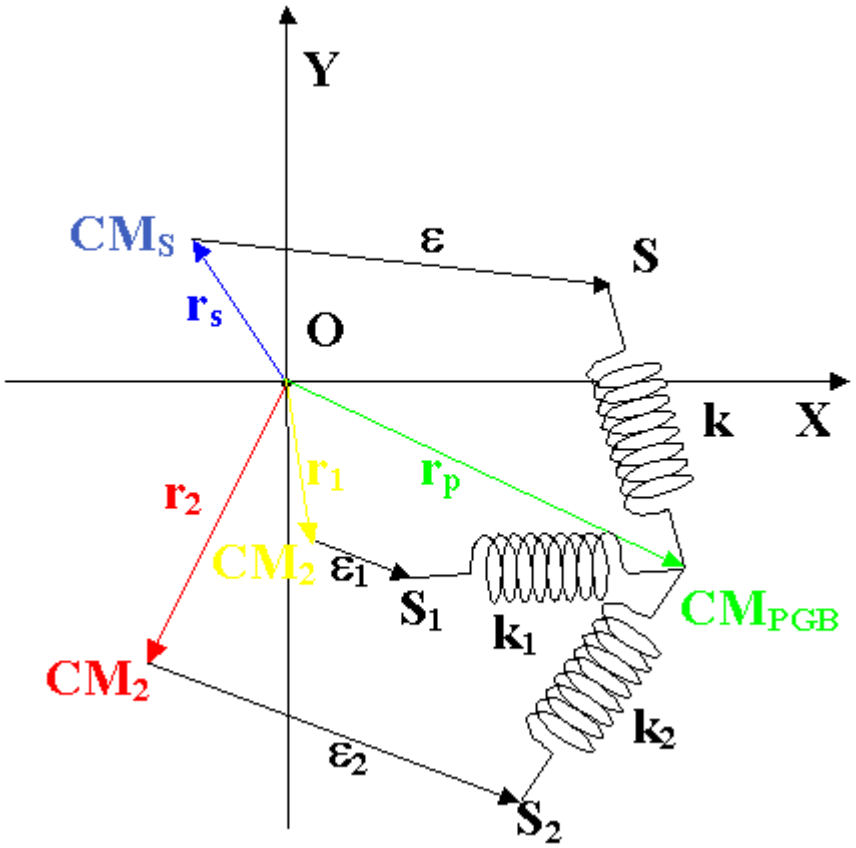

b)

Figure 9.6: Mathematical model of the GG system. Blue: spacecraft. Green: PGB. Red: Outer mass 2. Yellow: Inner mass 1.

By introducing the mean vector $\vec{r}_t = (\vec{r}_1 + \vec{r}_2)/2$ and the mean eccentricity $\vec{\varepsilon}_t = (\vec{\varepsilon}_1 + \vec{\varepsilon}_2)/2$, and adding the fourth equation to the third one, the new equation (9.4) is readily obtained:

$$m_t \ddot{\vec{r}}_t = -k_t\left(\vec{r}_t - \vec{r}_p + \vec{\varepsilon}_t\right) - c_{Rt}\left[\dot{\vec{r}}_t - \dot{\vec{r}}_p - \vec{\omega}_s \times \left(\vec{r}_t - \vec{r}_p\right)\right] \tag{9.4}$$

with $m_t=m_1+m_2$, $k_t=k_1+k_2$ and $c_{Rt}=c_{r1}+c_{R2}$. In a similar manner, the second equation changes into:

$$\begin{aligned} m_p \ddot{\vec{r}}_p = -k\left(\vec{r}_p - \vec{r}_s - \vec{\varepsilon}\right) - c_R\left[\dot{\vec{r}}_p - \dot{\vec{r}}_s - \vec{\omega}_s \times \left(\vec{r}_p - \vec{r}_s\right)\right] - k_t\left(\vec{r}_p - \vec{r}_t - \vec{\varepsilon}_t\right) + \\ - c_{Rt}\left[\dot{\vec{r}}_p - \dot{\vec{r}}_t - \vec{\omega}_s \times \left(\vec{r}_p - \vec{r}_t\right)\right] \end{aligned} \tag{9.5}$$

From now on, we consider the new system composed by the spacecraft, the PGB and the equivalent test mass m_t (obtained by the two masses m_1 and m_2), suspended to the PGB by means of a spring of elastic constant k_t and damping coefficient c_{Rt}. In the non rotating frame the new 3-body mathematical model (obtained by combining equations (9.4), (9.5) and the first one of the system (9.3)) is full equivalent from the standpoint of the translational modes of the system (9.3):

$$\begin{cases} m_s \ddot{\vec{r}}_s = -k\left(\vec{r}_s - \vec{r}_p + \vec{\varepsilon}\right) - c_R\left[\dot{\vec{r}}_s - \dot{\vec{r}}_p - \vec{\omega}_s \times \left(\vec{r}_s - \vec{r}_p\right)\right] + \vec{F}_{ext} \\ m_p \ddot{\vec{r}}_p = -k\left(\vec{r}_p - \vec{r}_s - \vec{\varepsilon}\right) - c_R\left[\dot{\vec{r}}_p - \dot{\vec{r}}_s - \vec{\omega}_s \times \left(\vec{r}_p - \vec{r}_s\right)\right] - k_t\left(\vec{r}_p - \vec{r}_t - \vec{\varepsilon}_t\right) + \\ \qquad - c_{Rt}\left[\dot{\vec{r}}_p - \dot{\vec{r}}_t - \vec{\omega}_s \times \left(\vec{r}_p - \vec{r}_t\right)\right] \\ m_t \ddot{\vec{r}}_t = -k_t\left(\vec{r}_t - \vec{r}_p + \vec{\varepsilon}_t\right) - c_{Rt}\left[\dot{\vec{r}}_t - \dot{\vec{r}}_p - \vec{\omega}_s \times \left(\vec{r}_t - \vec{r}_p\right)\right] \end{cases} \tag{9.6}$$

Let us now define the relative positions $\Delta\vec{r} = \vec{r}_p - \vec{r}_s$ and $\Delta\vec{r}_t = \vec{r}_t - \vec{r}_p$ and the reduced mass $m_r=m_sm_p/(m_s+m_p)$ (for the system spacecraft/PGB) and $m_{rt}=m_tm_p/(m_t+m_p)$ (for the system PGB/test mass m_t). We can also define the new quantities $m_{r1}=m_s(m_t+m_p)/M_{tot}$, $m_{r2}=m_t(m_s+m_p)/M_{tot}$ and the total mass $M_{tot}=m_s+m_p+m_t$. Starting from (9.6), after some algebraic manipulation, we can write the equations for the relative motions of the 3 bodies:

$$\begin{cases} \Delta\ddot{\vec{r}} = -\dfrac{k}{m_r}\left(\Delta\vec{r} - \vec{\varepsilon}\right) - \dfrac{c_R}{m_r}\left[\Delta\dot{\vec{r}} - \vec{\omega}_s \times \Delta\vec{r}\right] - \dfrac{\vec{F}_{ext}}{m_r} + \dfrac{k_t}{m_p}\left(\Delta\vec{r}_t + \vec{\varepsilon}_t\right) + \dfrac{c_{Rt}}{m_p}\left[\Delta\dot{\vec{r}}_t - \vec{\omega}_s \times \Delta\vec{r}_t\right] \\ \Delta\ddot{\vec{r}}_t = -\dfrac{k_t}{m_{rt}}\left(\Delta\vec{r}_t + \vec{\varepsilon}_t\right) - \dfrac{c_{Rt}}{m_{rt}}\left[\Delta\dot{\vec{r}}_t - \vec{\omega}_s \times \Delta\vec{r}_t\right] + \dfrac{k}{m_p}\left(\Delta\vec{r} - \vec{\varepsilon}\right) + \dfrac{c_R}{m_p}\left[\Delta\dot{\vec{r}} - \vec{\omega}_s \times \Delta\vec{r}\right] \end{cases} \tag{9.7}$$

In the following section, the general solution of the system (9.7) can be obtained by combining the solution of the homogeneous system with the particular integral evaluated in presence of an external force and in presence of the unbalances $\vec{\varepsilon}$ and $\vec{\varepsilon}_t$.

9.6: GENERAL SOLUTION OF THE EQUATIONS OF MOTION.

We can now complete the mathematical model specializing here to the introduction of an external force $\vec{F}_{ext}$ (constant or slowly variable) acting on the spacecraft[2]. By introducing the quality factors $Q = k/(C_R\omega_s)$, $Q_t = k_t/(C_{Rt}\omega_s)$ and the frequencies $\omega_{n1}^2 = k/m_{r1}$, $\omega_{n2}^2 = k/m_{r2}$, the equilibrium position in presence of the force $\vec{F}_{ext}$ is:

$$\begin{cases} \Delta\vec{r}^{F} = -\dfrac{1}{\omega_{n1}^2\left(1+1/Q^2\right)}\dfrac{1}{m_s}\left[\vec{F}_{ext} + \dfrac{1}{Q}\hat{z}\times\vec{F}_{ext}\right] \\ \Delta\vec{r}_t^{F} = -\dfrac{1}{\omega_{n2}^2\left(1+1/Q_t^2\right)}\dfrac{1}{m_p+m_s}\left[\vec{F}_{ext} + \dfrac{1}{Q_t}\hat{z}\times\vec{F}_{ext}\right] \end{cases} \tag{9.8}$$

Note that, even though the external force is applied along the x direction, finite differential displacements occurs along the y direction, due to the rotation and to the dissipative nature of

---

[2] By imposing $\Delta\ddot{\vec{r}} = 0, \Delta\ddot{\vec{r}}_t = 0, \Delta\dot{\vec{r}} = 0, \Delta\dot{\vec{r}}_t = 0$ in (9.7), the equilibrium position in presence of a constant force $\vec{F}_{ext}$ is the solution of the following system:

$$\begin{cases} 0 = -\dfrac{k}{m_r}(\Delta\vec{r}) + \dfrac{c_R}{m_r}[\vec{\omega}_s\times\Delta\vec{r}] - \dfrac{\vec{F}_{ext}}{m_r} + \dfrac{k}{m_p}(\Delta\vec{r}_t) - \dfrac{c_{Rt}}{m_p}[\vec{\omega}_s\times\Delta\vec{r}_t] \\ 0 = -\dfrac{k_t}{m_{rt}}(\Delta\vec{r}_t) + \dfrac{c_{Rt}}{m_{rt}}[\vec{\omega}_s\times\Delta\vec{r}_t] + \dfrac{k}{m_p}(\Delta\vec{r}) - \dfrac{c_R}{m_p}[\vec{\omega}_s\times\Delta\vec{r}] \end{cases}$$

Using complex notation $\Delta z' = \Delta r_x + j\Delta r_y$, $\Delta z_t' = \Delta r_{tx} + j\Delta r_{ty}$ and $F'_{ext} = F_{ext,x} + jF_{ext,y}$ the dynamics in the inertial reference frame can be written as:

$$\begin{cases} \left(-k/m_r + j\omega_s c_R/m_r\right)\Delta z' + \left(k_t/m_p - j\omega_s c_{Rt}/m_p\right)\Delta z_t' = F'_{ext}/m_r \\ \left(k/m_p - j\omega_s c_R/m_p\right)\Delta z' + \left(-k_t/m_{rt} + j\omega_s c_{Rt}/m_{rt}\right)\Delta z_t' = 0 \end{cases}$$

Then, the equilibrium position is easily obtained:

$$\begin{cases} \Delta z' = -\dfrac{F'_{ext}}{m_s}\dfrac{1 + jc_R\omega_s/k}{\left(k + c_R^2\omega_s^2/k\right)}\dfrac{m_p^2 m_r}{\left(m_p^2 - m_r m_t\right)} \\ \Delta z_t' = -F'_{ext}\dfrac{1 + jc_{Rt}\omega_s/k_t}{\left(k_t + c_R^2\omega_s^2/k_t\right)}\dfrac{m_t}{M_{tot}} \end{cases}$$

In terms of the vectors $\Delta\vec{r}$, $\Delta\vec{r}_t$, the equilibrium position can be written as:

$$\begin{cases} \Delta\vec{r} = -\dfrac{1}{\left(k + c_R^2\omega_s^2/k\right)}\dfrac{m_p + m_t}{M_{tot}}\left[\vec{F}_{ext} + \dfrac{C_R}{k}\vec{\omega}_s\times\vec{F}_{ext}\right] \\ \Delta\vec{r}_t = -\dfrac{1}{\left(k_t + c_{Rt}^2\omega_s^2/k_t\right)}\dfrac{m_t}{M_{tot}}\left[\vec{F}_{ext} + \dfrac{C_{Rt}}{k_t}\vec{\omega}_s\times\vec{F}_{ext}\right] \end{cases}$$

Note that the vector $\Delta\vec{r}_t$ describing the displacement of the equilibrium position for the system test mass/PGB depends only on the spring coupling between these two bodies (i.e. it depends on k_t and C_{Rt}). In a similar manner the vector $\Delta\vec{r}$ depends on k and C_R.

the suspensions (the quality factor Q is finite. Compare equations (9.8) and (1.68)). However, the magnitude of the displacement along the y direction ("orthogonal") is depressed by a factor $1/Q<<1$ with respect to that along x. Hence, the two degrees of freedom are coupled from the energy dissipation only if Q has a finite value. We have assumed the presence of two static (in the rotating frame) unbalances $\vec{\varepsilon}$ and $\vec{\varepsilon}_t$.
Starting from the equations (9.7) and introducing the natural frequencies of oscillation $\omega_n^2 = k/m_r$ and $\omega_{nt}^2 = k_t/m_{rt}$, we can now write the particular integrals due to the unbalances for the systems spacecraft/PGB and PGB/ test mass, respectively:[3]

[3] Using complex notation, the system (9.7) becomes :

$$\begin{cases} \Delta\ddot{z}' = -\frac{k}{m_r}\Delta z' - \frac{c_R}{m_r}\Delta\dot{z}' + j\omega_s\frac{c_R}{m_r}\Delta z' + \frac{k_t}{m_p}\Delta z_t' + \frac{c_{Rt}}{m_p}\Delta\dot{z}_t' - j\omega_s\frac{c_{Rt}}{m_p}\Delta z_t' + u \\ \Delta\ddot{z}_t' = -\frac{k_t}{m_{rt}}\Delta z_t' - \frac{c_{Rt}}{m_{rt}}\Delta\dot{z}_t' + j\omega_s\frac{c_{Rt}}{m_{rt}}\Delta z' + \frac{k}{m_p}\Delta z' + \frac{c_R}{m_p}\Delta\dot{z}' - j\omega_s\frac{c_R}{m_p}\Delta z' + u_t \end{cases}$$

where

$$u(t) = \left(\frac{k}{m_r}\varepsilon_x + \frac{k_t}{m_p}\varepsilon_{tx}\right) + j\left(\frac{k}{m_r}\varepsilon_y + \frac{k_t}{m_p}\varepsilon_{ty}\right),\ u_t(t) = \left(-\frac{k}{m_p}\varepsilon_x - \frac{k_t}{m_{rt}}\varepsilon_{tx}\right) + j\left(-\frac{k}{m_p}\varepsilon_y - \frac{k_t}{m_{rt}}\varepsilon_{ty}\right).$$

In the frequency domain (after introducing the Laplace variable s), the previous system turns into:

$$\begin{cases} \left[s^2 + \frac{k}{m_r} + \frac{c_R}{m_r}s - j\omega_s\frac{c_R}{m_r}\right]\Delta z' = \left[\frac{k_t}{m_p} + \frac{c_{Rt}}{m_p}s - j\omega_s\frac{c_{Rt}}{m_p}\right]\Delta z_t' + u \\ \left[s^2 + \frac{k_t}{m_{rt}} + \frac{c_{Rt}}{m_{rt}}s - j\omega_s\frac{c_{Rt}}{m_{rt}}\right]\Delta z_t' = \left[\frac{k}{m_p} + \frac{c_R}{m_p}s - j\omega_s\frac{c_R}{m_p}\right]\Delta z' + u_t \end{cases}$$

This system can be simplified in the following manner:

$$\begin{cases} a(s)\Delta z' = b_t(s)\Delta z_t' + u(s) \\ a_t(s)\Delta z_t' = b(s)\Delta z' + u_t(s) \end{cases}$$

where $a(s)$, $b(s)$, $a_t(s)$ and $b_t(s)$ are obtained by comparing the 2 systems of equations. We have:

$$\frac{b_t(s)}{a_t(s)} = \left(\frac{k_t}{m_p} + \frac{c_{Rt}}{m_p}s - j\omega_s\frac{c_{Rt}}{m_p}\right)\Big/\left(s^2 + \frac{k_t}{m_{rt}} + \frac{c_{Rt}}{m_{rt}}s - j\omega_s\frac{c_{Rt}}{m_{rt}}\right)$$

Then, $\Delta z'$ can be written in terms of the inputs u and u_t:

$$\Delta z' = \left(a_t(s)u(s) + b_t(s)u_t(s)\right)\Big/\left(a(s)a_t(s) - b(s)b_t(s)\right)$$

By imposing $s=j\omega_s$ and noticing that

$$\left|\frac{b_t(j\omega_s)}{a_t(j\omega_s)}\right| = \left|k_t\Big/\left(-\omega_s^2 + \frac{k_t}{m_{rt}}\right)m_p\right| = \left|\frac{m_{rt}}{m_p}\frac{\omega_{nt}^2}{\omega_{nt}^2 - \omega_s^2}\right| \ll 1$$

we finally obtain:

$$\Delta z'(j\omega_s) \simeq \frac{a_t(j\omega_s)}{a(j\omega_s)a_t(j\omega_s) - b(j\omega_s)b_t(j\omega_s)}u(j\omega_s) = \frac{\left(k_t/m_{rt} - \omega_s^2\right)}{\left(k_t/m_{rt} - \omega_s^2\right)\left(k/m_r - \omega_s^2\right) - kk_t/m_p^2}u(j\omega_s)$$

In the limit $\omega_s>>\omega_n$, ω_{nt} the previous relation can be simplified as:

$$\Delta z'(j\omega_s) \simeq u(j\omega_s)\Big/\left(\omega_n^2 - \omega_s^2\right)$$

$$\begin{cases} \Delta\vec{r}^{\,\varepsilon}(t) = \left(m_p\omega_n^2\vec{\varepsilon}(t) + m_{rt}\omega_{nt}^2\vec{\varepsilon}_t(t)\right)\Big/\left[m_p\left(\omega_n^2 - \omega_s^2\right)\right] \\ \Delta\vec{r}_t^{\,\varepsilon}(t) = -\left(m_r\omega_n^2\vec{\varepsilon}(t) + m_p\omega_{nt}^2\vec{\varepsilon}_t(t)\right)\Big/\left[m_p\left(\omega_{nt}^2 - \omega_s^2\right)\right] \end{cases} \tag{9.9}$$

Before evaluating the solution of the homogeneous system, it is better to write equations (9.7) in a matrix form:

$$\begin{cases} \Delta\ddot{\vec{r}} + C_{NR}\Delta\dot{\vec{r}} + K_{NR}\Delta\vec{r} + C'_{NR,t}\Delta\dot{\vec{r}}_t + K'_{NR,t}\Delta\vec{r}_t = 0 \\ \Delta\ddot{\vec{r}}_t + C_{NR,t}\Delta\dot{\vec{r}}_t + K_{NR,t}\Delta\vec{r}_t + C'_{NR}\Delta\dot{\vec{r}} + K'_{NR}\Delta\vec{r} = 0 \end{cases} \tag{9.10}$$

where we have introduced the matrices:

$$C_{NR} = \begin{bmatrix} c_R/m_r & 0 \\ 0 & c_R/m_r \end{bmatrix} \tag{9.11.a}$$

$$K_{NR} = \begin{bmatrix} k/m_r & c_R\omega_s/m_r \\ -c_R\omega_s/m_r & k/m_r \end{bmatrix} \tag{9. 11.b}$$

$$C'_{NR,t} = \begin{bmatrix} -c_{Rt}/m_p & 0 \\ 0 & -c_{Rt}/m_p \end{bmatrix} \tag{9. 11.c}$$

$$K'_{NR,t} = \begin{bmatrix} -k_t/m_p & -c_{Rt}\omega_s/m_p \\ c_{Rt}\omega_s/m_p & -k_t/m_p \end{bmatrix} \tag{9. 11.d}$$

$$C'_{NR} = -\frac{m_r}{m_p}C_{NR} = \begin{bmatrix} -c_R/m_p & 0 \\ 0 & -c_R/m_p \end{bmatrix} \tag{9. 11.e}$$

$$K'_{NR} = -\frac{m_r}{m_p}K_{NR} = \begin{bmatrix} -k/m_p & -c_R\omega_s/m_p \\ c_R\omega_s/m_p & -k/m_p \end{bmatrix} \tag{9. 11.f}$$

$$C_{NR,t} = -\frac{m_p}{m_{rt}}C'_{NR,t} = \begin{bmatrix} c_{Rt}/m_{rt} & 0 \\ 0 & c_{Rt}/m_{rt} \end{bmatrix} \tag{9. 11.g}$$

$$K_{NR,t} = -\frac{m_p}{m_{rt}}K'_{NR,t} = \begin{bmatrix} k_t/m_{rt} & c_{Rt}\omega_s/m_{rt} \\ -c_{Rt}\omega_s/m_{rt} & k_t/m_{rt} \end{bmatrix} \tag{9. 11.h}$$

The λ and λ_t eigenvalues of the problem are obtained (see appendix 9.C) by solving the characteristic equation associated to the homogeneous system:

The expression for $\Delta z'_t$ as a function of the spin frequency is obtained in a similar manner:

$\Delta z'_t(j\omega_s) \simeq u_t(j\omega_s)\Big/\left(\omega_{nt}^2 - \omega_s^2\right)$

By performing the inverse Laplace transform, the last two equations can be written in the time domain. The solutions (9.9) and (9.10) are easily obtained.

$$\det\left(\begin{bmatrix} \lambda^2 I + C_{NR}\lambda + K_{NR} & C'_{NR,t}\lambda_t + K'_{NR,t} \\ C'_{NR}\lambda + K'_{NR} & \lambda_t^2 I + C_{NR,t}\lambda_t + K_{NR,t} \end{bmatrix}\right) = 0 \tag{9.12}$$

It is clear that when the time history is written in the form

$$\begin{cases} \Delta\vec{r}^{\,W}(t) = \sum_i \Delta\vec{r}_i^{\,0} e^{\Re e(j\lambda_i)t} e^{j\Im m(j\lambda_i)t} \\ \Delta\vec{r}_t^{\,W}(t) = \sum_i \Delta\vec{r}_{ti}^{\,0} e^{\Re e(j\lambda_{ti})t} e^{j\Im m(j\lambda_{ti})t} \end{cases} \tag{9.13}$$

the system is stable if the real parts of all complex eigenvalues $s=j\lambda$ and $s_t=j\lambda_t$ are negative. In appendix 9.C we show that the system has four eigenvalues with positive real parts, hence the system is unstable. By combining the solutions (9.8), (9.9) and (9.13) the general integral of the system (9.7) is readily obtained:

$$\begin{cases} \Delta\vec{r}(t) = \Delta\vec{r}^{\,F}(t) + \Delta\vec{r}^{\,\varepsilon}(t) + \Delta\vec{r}^{\,W}(t) \\ \Delta\vec{r}_t(t) = \Delta\vec{r}_t^{\,F}(t) + \Delta\vec{r}_t^{\,\varepsilon}(t) + \Delta\vec{r}_t^{\,W}(t) \end{cases} \tag{9.14}$$

9.7: DYNAMICAL EVOLUTION IN THE ROTATING FRAME.

The relative displacement between the spacecraft and the PGB in the rotating frame $S_R(O;\xi,\eta,z)$ is $\Delta\vec{\rho}=[\xi\ \eta]$ while the relative displacement between the PGB and the test mass (TM) is $\Delta\vec{\rho}_t=[\xi_t\ \eta_t]$. Vectors $\vec{\varepsilon}^{\,R}, \vec{\varepsilon}_t^{\,R}$ and $\vec{F}_{ext}^{\,R}$ are the eccentricities and the external force[4], respectively. In the space experiment everything is co-rotating with the spacecraft, so we need to recast equations (9.7) and (9.10) in the rotating frame[5]:

$$\begin{cases} \Delta\ddot{\vec{\rho}} - \omega_s^2\Delta\vec{\rho} + 2\vec{\omega}_s\times\Delta\dot{\vec{\rho}} = -\dfrac{k}{m_r}\left(\Delta\vec{\rho} - \vec{\varepsilon}^{\,R}\right) - \dfrac{c_R}{m_r}\Delta\dot{\vec{\rho}} - \dfrac{\vec{F}_{ext}^{\,R}}{m_s} + \dfrac{k_t}{m_p}\left(\Delta\vec{\rho}_t + \vec{\varepsilon}_t^{\,R}\right) + \dfrac{c_{Rt}}{m_p}\Delta\dot{\vec{\rho}}_t \\ \Delta\ddot{\vec{\rho}}_t - \omega_s^2\Delta\vec{\rho}_t + 2\vec{\omega}_s\times\Delta\dot{\vec{\rho}}_t = -\dfrac{k_t}{m_{rt}}\left(\Delta\vec{\rho}_t + \vec{\varepsilon}_t^{\,R}\right) - \dfrac{c_{Rt}}{m_{rt}}\Delta\dot{\vec{\rho}}_t + \dfrac{k}{m_p}\left(\Delta\vec{\rho} - \vec{\varepsilon}\right) + \dfrac{c_R}{m_p}\Delta\dot{\vec{\rho}} \end{cases} \tag{9.15}$$

or in a more compact form:

$$\begin{cases} \Delta\ddot{\vec{\rho}} + C_R\Delta\dot{\vec{\rho}} + K_R\Delta\vec{\rho} + C'_{Rt}\Delta\dot{\vec{\rho}}_t + K'_{Rt}\Delta\vec{\rho}_t = \vec{F} \\ \Delta\ddot{\vec{\rho}}_t + C'_R\Delta\dot{\vec{\rho}} + K'_R\Delta\vec{\rho} + C_{Rt}\Delta\dot{\vec{\rho}}_t + K_{Rt}\Delta\vec{\rho}_t = \vec{F}_t \end{cases} \tag{9.16}$$

where the matrices are defined as:

$$C_R = \begin{bmatrix} c_R/m_r & -2\omega_s \\ 2\omega_s & c_R/m_r \end{bmatrix} \tag{9.17.a}$$

---

[4] For the purposes of the present analysis the orbital motion of the satellite can be neglected; the orbiting reference system is therefore approximated by an inertial reference frame.

[5] Equations (9.15) are obtained from (9.7) by replacing the vectors $\Delta\vec{r}\to\Delta\vec{\rho}$, $\Delta\dot{\vec{r}}\to\Delta\dot{\vec{\rho}}+\vec{\omega}_s\times\Delta\vec{\rho}$ and $\Delta\ddot{\vec{r}}\to\Delta\ddot{\vec{\rho}}-\omega_s^2\Delta\vec{\rho}+2\vec{\omega}_s\times\Delta\dot{\vec{\rho}}+\cancel{\dot{\vec{\omega}}_s\times\Delta\vec{\rho}}$.

$$K_R = \begin{bmatrix} k/m_r - \omega_s^2 & 0 \\ 0 & k/m_r - \omega_s^2 \end{bmatrix} \quad (9.17.b)$$

$$C'_{R,t} = \begin{bmatrix} -c_{Rt}/m_p & 0 \\ 0 & -c_{Rt}/m_p \end{bmatrix} \quad (9.17.c)$$

$$K'_{R,t} = \begin{bmatrix} -k_t/m_p & 0 \\ 0 & -k_t/m_p \end{bmatrix} \quad (9.17.d)$$

$$C'_R = \begin{bmatrix} -c_R/m_p & 0 \\ 0 & -c_R/m_p \end{bmatrix} \quad (9.17.e)$$

$$K'_R = \begin{bmatrix} -k/m_p & 0 \\ 0 & -k/m_p \end{bmatrix} \quad (9.17.f)$$

$$C_{R,t} = \begin{bmatrix} c_{Rt}/m_{rt} & -2\omega_s \\ 2\omega_s & c_{Rt}/m_{rt} \end{bmatrix} \quad (9.17.g)$$

$$K_{R,t} = \begin{bmatrix} k_t/m_{rt} - \omega_s^2 & 0 \\ 0 & k_t/m_{rt} - \omega_s^2 \end{bmatrix} \quad (9.17.h)$$

$$\vec{F} = -\vec{F}_{ext}^{R}/m_s + k/m_r\vec{\varepsilon}^{R} + k_t/m_p\,\vec{\varepsilon}_t^{R} \quad (9.17.i)$$

$$\vec{F}_t = -k/m_p\vec{\varepsilon}^{R} - k_t/m_{rt}\vec{\varepsilon}_t^{R} \quad (9.17.l)$$

In appendix 9.C, section 9.C.2, we give a detailed description of the state-space block diagram whose behaviour is defined by equations (9.16). Samples from a 24000 seconds simulation of the system are shown in the following figures. Figure 9.7 shows a polar plot in the x-y plane (non rotating frame) of the relative motion of the PGB with respect to the spacecraft ($\Delta\vec{r}(t)$ in blue) and the relative motion of the test mass TM with respect to the PGB ($\Delta\vec{r}_t(t)$ in red). Due to the losses, the whirl instability ($\Delta\vec{r}^{W}(t)$ and $\Delta\vec{r}_t^{W}(t)$) builds up in either case around the ideal equilibrium circle caused by the residual air drag force $\vec{F}_{ext}$ ($\Delta\vec{r}^{F}(t)$ and $\Delta\vec{r}_t^{F}(t)$). The constant displacement along the x direction is caused by the DC term of air drag. $\Delta\vec{r}^{\varepsilon}(t)$ and $\Delta\vec{r}_t^{\varepsilon}(t)$ are to small to be displaced in figure 9.7. In figure 9.8, the whirl radiuses are shown as a function of time. They grow in time because the system is unstable. Note that we have used a value $Q_{PGB/TM}$=500 for the quality factor of the suspension connecting the TM to the PGB to save CPU time.

9.8: NON ROTATING DAMPING AND WHIRLING STABILISATION.

The simplest way to stabilize the system it is adding some non rotating damping (i.e. damping between non rotating parts of the system), which is mathematically expressed by the terms containing the coefficient c_{NR} (see equation (1.13)).

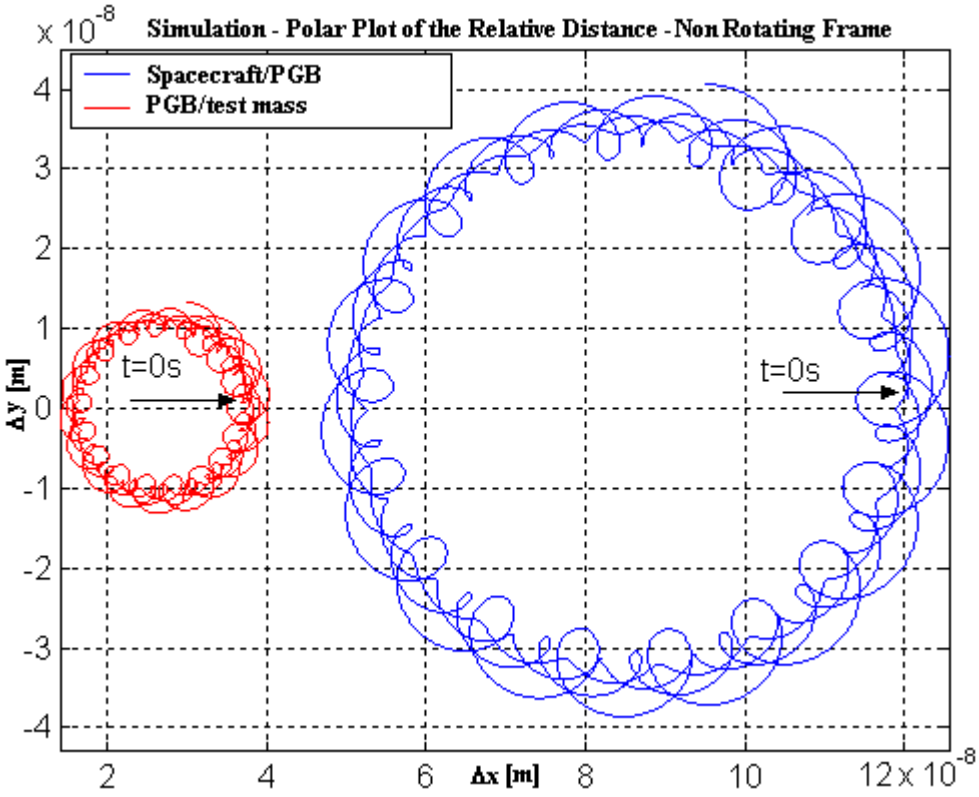

Figure 9.7: Polar plot in the x-y plane of the non rotating frame showing the relative motion of the PGB with respect to the spacecraft ($\Delta\vec{r}(t)$ in blue) and the relative motion of the test mass TM with respect to the PGB ($\Delta\vec{r}_t(t)$ in red). Due to the losses the whirl instability builds up in either case around the ideal equilibrium circle caused by the residual air drag force. The constant displacement along the x direction is caused by the DC term of air drag.

The damping force is proportional to the relative velocity between the bodies in the inertial reference frame. In the rotating frame, the damping forces can be written as

$$-c_{NR}\Delta\dot{\vec{\rho}} - c_{NR}\,\vec{\omega}_s \times \Delta\vec{\rho} \tag{9.18}$$

and

$$-c_{NRt}\Delta\dot{\vec{\rho}}_t - c_{NRt}\,\vec{\omega}_s \times \Delta\vec{\rho}_t \tag{9.19}$$

By inserting (9.18) and (9.19) in (9.16), the matrices (9.17) change as follows:

$$C_R = \begin{bmatrix} (c_R + c_{NR})/m_r & -2\omega_s \\ 2\omega_s & (c_R + c_{NR})/m_r \end{bmatrix} \tag{9.20.a}$$

$$K_R = \begin{bmatrix} k/m_r - \omega_s^2 & -c_{NR}\omega_s/m_r \\ c_{NR}\omega_s/m_r & k/m_r - \omega_s^2 \end{bmatrix} \tag{9.20.b}$$

$$C'_{R,t} = \begin{bmatrix} -(c_{Rt} + c_{NRt})/m_p & 0 \\ 0 & -(c_{Rt} + c_{NRt})/m_p \end{bmatrix} \tag{9.20.c}$$

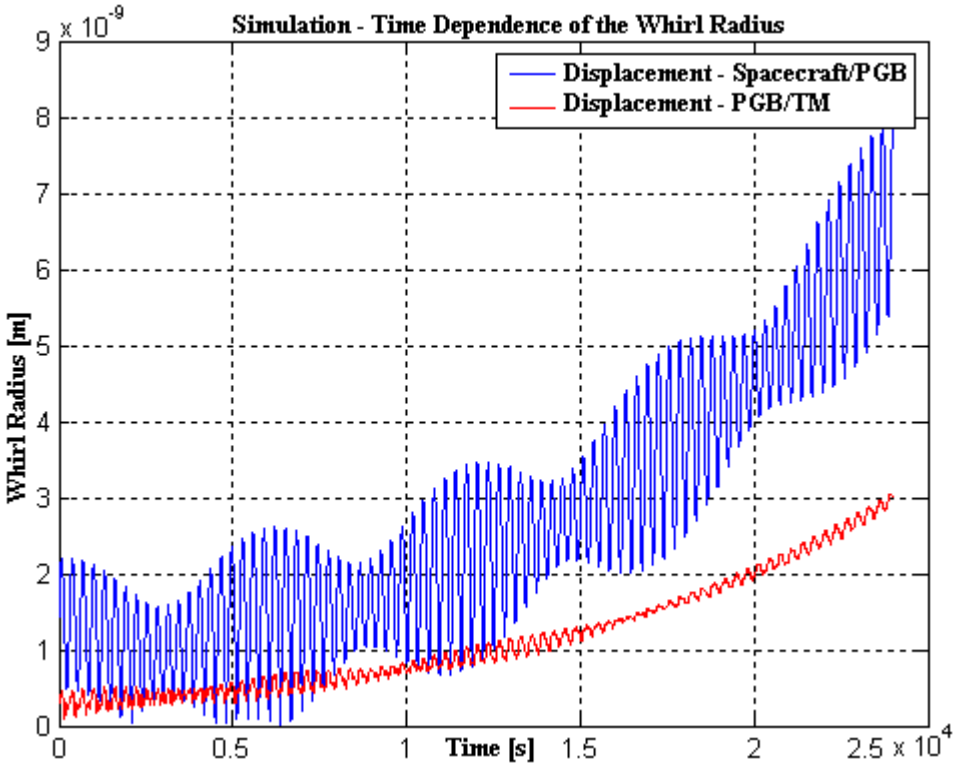

Figure 9.8: Whirl radius as a function of time.

$$K'_{R,t} = \begin{bmatrix} -k_t/m_p & c_{NRt}\omega_s/m_p \\ -c_{NRt}\omega_s/m_p & -k_t/m_p \end{bmatrix} \tag{9.20.d}$$

$$C'_R = \begin{bmatrix} -(c_R + c_{NR})/m_p & 0 \\ 0 & -(c_R + c_{NR})/m_p \end{bmatrix} \tag{9.20.e}$$

$$K'_R = \begin{bmatrix} -k/m_p & c_{nr}\omega_s/m_p \\ -c_{nr}\omega_s/m_p & -k/m_p \end{bmatrix} \tag{9.20.f}$$

$$C_{R,t} = \begin{bmatrix} (c_{Rt} + c_{NRt})/m_{rt} & -2\omega_s \\ 2\omega_s & (c_{Rt} + c_{NRt})/m_{rt} \end{bmatrix} \tag{9.20.g}$$

$$K_{R,t} = \begin{bmatrix} k_t/m_{rt} - \omega_s^2 & -c_{NRt}\omega_s/m_{rt} \\ c_{NRt}\omega_s/m_{rt} & k_t/m_{rt} - \omega_s^2 \end{bmatrix} \tag{9.20.h}$$

The system behaviour in presence of non rotating damping has been simulated in appendix 9.C, section 9.C.3. Results are shown in the following figures. The system was not in equilibrium at the start of the simulation. Figure 9.9 shows a polar plot in the x-y plane (non rotating frame) of the relative motion of the PGB with respect to the spacecraft ($\Delta\vec{r}(t)$ in blue) and the relative motion of the test mass TM with respect to the PGB ($\Delta\vec{r}_t(t)$ in red). The whirl motions start to be damped, but still need some time. After the first orbit, the whirl motions are damped and the bodies are already very close their zero whirl orbits (corresponding to the ideal equilibrium circles caused by the residual air drag force $\vec{F}_{ext}$).

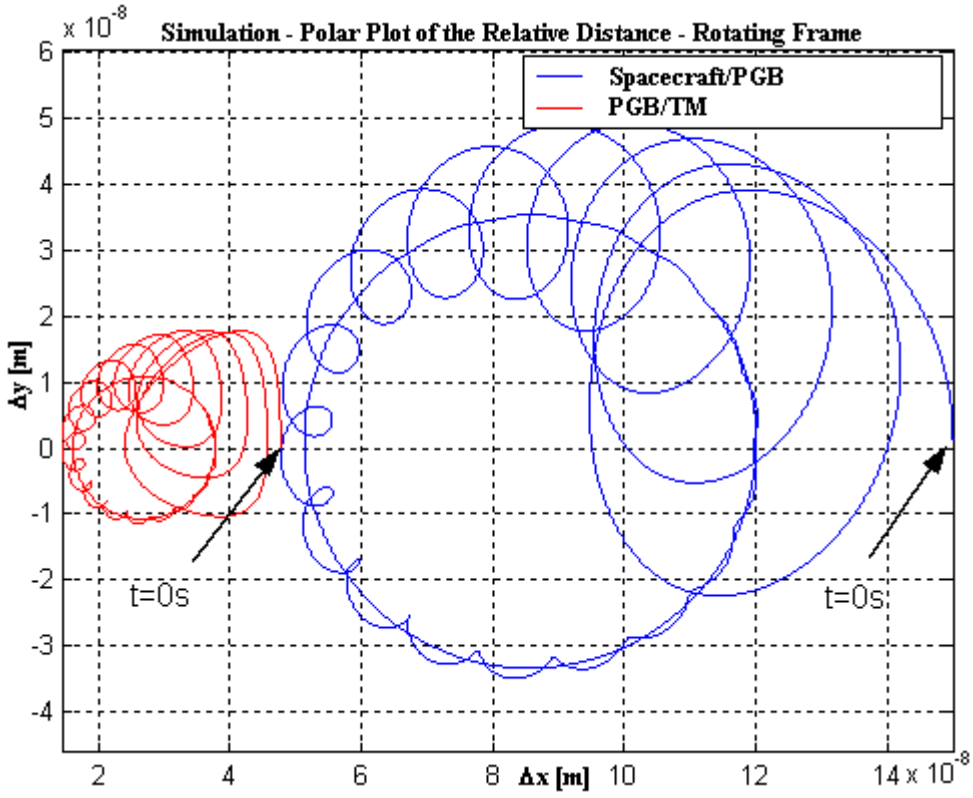

Figure 9.9: Polar plot in the x-y plane of the non rotating frame showing the relative motion of the PGB with respect to the spacecraft ($\Delta\vec{r}(t)$ in blue) and the relative motion of the test mass TM with respect to the PGB ($\Delta\vec{r}_t(t)$ in red).

In figure 9.10, the values of the whirl radiuses are shown for the same time interval as in figure 9.9. They decrease in time and reduce to a few Angstrom after 7000-8000 seconds only. In the two figures there are three types of oscillations: one is at the orbital period, due to the component of the drag at this frequency, another is at the whirl period of the spacecraft/PGB system (controlled), and the one with the shortest oscillation period is the controlled whirl motion of the TM with respect to the PGB. Note that we have used a value for the non rotating damping coefficient about 10 times lager than the minimum value required for stability (see equation (1.23)). This allows us to damp the system more rapidly, hence saving CPU time.

9.9: RECONSTRUCTION OF THE WHIRL MOTION.

Since in the GG experiment all the apparatus rotates around the spin axis of the satellite, there is not any source of non rotating damping; hence it is necessary to build in the rotating frame a damping command proportional to the relative velocity between the bodies in the inertial reference frame to damp whirling motions and prevent the occurrence of instability.
If $\Delta\vec{\rho}$ ($\Delta\vec{\rho}_t$) is the relative displacement between the spacecraft and the PGB (between the PGB and the TM) in the rotating frame $S_R(O;\xi,\eta,z)$, the damping force is given by equation (9.18) and (9.19). The main drawback of a continuous approach is that the whirl motion builds up with long time constants, hence the rate of change of the relative amplitude is

dominated by the measurement noise. Furthermore, the relative velocity must be built from the difference of two relative displacements of the bodies measured at different times. A modified approach based on signal filtering has therefore been introduced. In the following sections we will describe this approach and apply the control law to damp whirl motions in the four-body GG system.

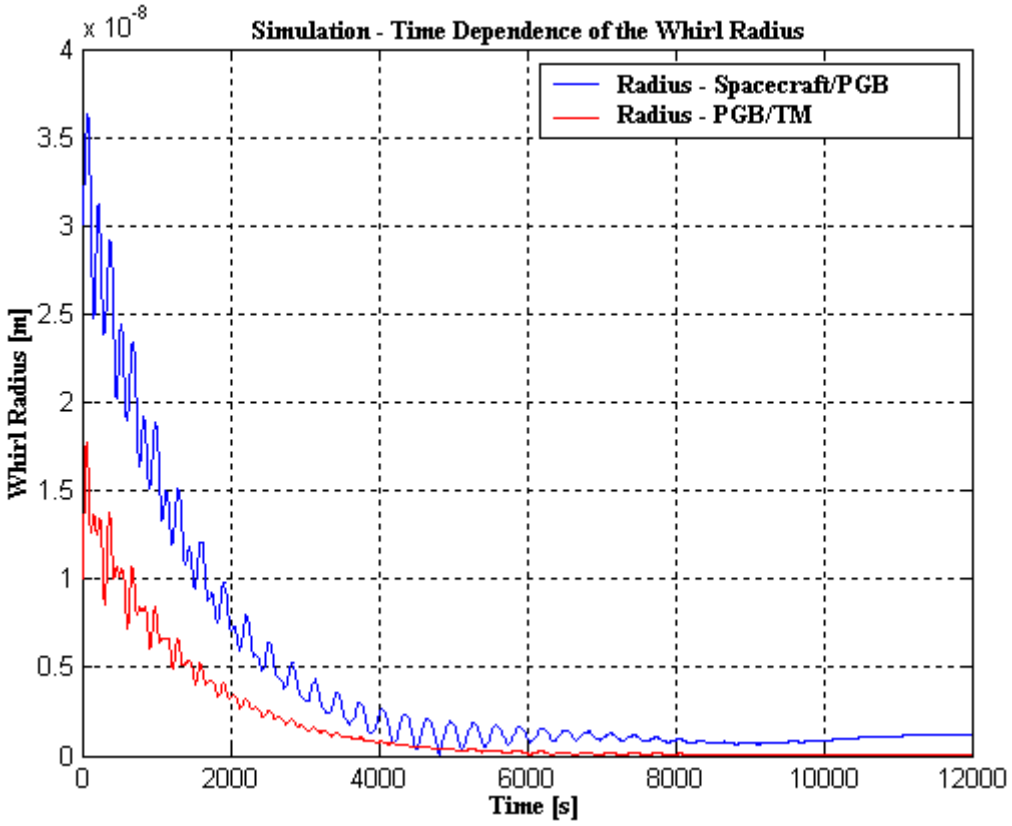

Figure 9.10: Whirl radiuses as a function of time. They reduce to a few Angstrom after 7000 – 8000 seconds only.

The read-out of GG consists of two pairs of capacitance plates located halfway in between the PGB and the TM and other two pairs located halfway in between the spacecraft and the PGB. These plates form bridges in two orthogonal directions in the plane perpendicular to the spin/symmetry axis (for more details, see section 2.5 where the read-out in the GGG experiment is described). The bridges are sensitive to relative displacements in that plane.
We assume using non perfect sensors and then we introduce realist errors as follows: a bias of the read-out capacitors and white noise, generated as normally distributed random numbers with mean of 0 and a standard deviation of σ. Furthermore, the spin rate is measured by the ESS (Sun Elevation Sensor). These sensors can provide a measurement accuracy of $\Delta\omega_s/\omega_s=10^{-4}$ [11]. The nominal value of the spin frequency is 2Hz. Let us see the solution of the equation of motion (relative displacement of the bodies) in the rotating reference frame; in absence of non rotating damping the relative displacement of the PGB with respect to the spacecraft is $\Delta\vec{\rho}$ ($\Delta\vec{\rho}_t$ the relative displacement of the TM with respect to the PGB). $\Delta\vec{\rho}$ ($\Delta\vec{\rho}_t$) can be seen as the superimposition of three vectors: the first term is a fixed vector in the rotating reference frame which depends on the initial offset of the mounting point of the spring (see equation (9.9) showing the same vector as seen in the inertial reference frame); the second term is a vector co-rotating with the drag force (see equation (9.8) in the inertial

frame). In the simulation, we assume a drag defined by a DC component plus a term at orbital frequency in the inertial reference frame (see appendix 9.C for details, see also [11]), so the corresponding term of the relative displacement (in the rotating frame) has ω_s and $\omega_s-\omega_{orb}$ angular frequencies[6]. The third term, describing the growing spiral of the whirl motion, has $\omega_s-\omega_w$ angular frequencies with ω_w the natural frequencies of the system corresponding to unstable modes.

9.9.A RECONSTRUCTION OF THE RELATIVE DISPLACEMENT.

The first step of our analysis is to obtain the relative displacements $\Delta\vec{r}$ and $\Delta\vec{r}_t$ starting from their counterparts in the rotating frame. $\Delta\vec{\rho}_e$ ($\Delta\vec{\rho}_{te}$) is the total measurement error of the sensors while $\Delta\tilde{\rho}=\Delta\vec{\rho}+\Delta\vec{\rho}_e$ ($\Delta\tilde{\rho}_t=\Delta\vec{\rho}_t+\Delta\vec{\rho}_{te}$) is the measured signal. From now on, we consider only $\Delta\tilde{\rho}=\Delta\vec{\rho}+\Delta\vec{\rho}_e$, having in mind the fact that the same approach is suitable for $\Delta\tilde{\rho}_t=\Delta\vec{\rho}_t+\Delta\vec{\rho}_{te}$. If $\Delta\vec{\rho}_e=0$, $\Delta\tilde{\rho}=\Delta\vec{\rho}$ and the relative displacement in the inertial frame is easily obtained:

$$\Delta\vec{r}=R^{-1}\Delta\vec{\rho}=\begin{pmatrix}\cos(\omega_s t) & -\sin(\omega_s t)\\ \sin(\omega_s t) & \cos(\omega_s t)\end{pmatrix}\Delta\vec{\rho} \qquad (9.21)$$

Since $\Delta\vec{\rho}_e\neq 0$, this approach is not applicable because the relative displacement $\Delta\vec{r}$ in the inertial frame will be dominated by the sensor noise. The idea is of analysing the harmonic component at T_s of the measured signal $\Delta\tilde{\rho}$ in order to reconstruct the modulating signal amplitude and phase. Note that in this way any bias is removed (it is a constant additional term to $\Delta\vec{\rho}$) and the random noise is attenuated. The relative displacement signal $\Delta\tilde{\rho}$ is sampled within every spin period T_s with N points; the sampling period is then $T_c=T_s/N$. The fundamental harmonic at 2Hz can be obtained from Fourier integral (first Fourier filter) as:

$$\Delta\tilde{\rho}_\xi^{2Hz}=B_\xi\cos(\omega_s t)+C_\xi\sin(\omega_s t)=A_\xi\cos(\omega_s t+\varphi_\xi) \qquad (9.22.a)$$

$$\Delta\tilde{\rho}_\eta^{2Hz}=B_\eta\cos(\omega_s t)+C_\eta\sin(\omega_s t)=A_\eta\cos(\omega_s t+\varphi_\eta) \qquad (9.22.b)$$

Let us assume that at t=0s the x and y axis coincide with the ξ and η axis, respectively. By starting from the harmonic components (9.22.a) and (9.22.b) in the rotating frame, it is possible to extract the signal at low frequency in the inertial frame, namely:

$$\Delta\tilde{r}_x=A_\xi\cos(\varphi_\xi)=B_\xi \qquad (9.23.a)$$

$$\Delta\tilde{r}_y=A_\eta\sin(\varphi_\eta)=B_\eta \qquad (9.23.b)$$

as it can be argued from figure 9.11. Given N points in the i-th spin period, they are sampled at time:

$$t_{i,k}=kT_s/N+iT_s \qquad k=0,1,\ldots,N-1 \qquad (9.24)$$

with $t_{i,N}=t_{i+1,0}$.

[6] ω_{orb} is the orbital angular frequency.

If $\Delta\tilde{\rho}$ is a continuous time process, the coefficients in equations (9.22) and (9.23) may be obtained by evaluating the following integrals:

$$B_\gamma(t) = \frac{2}{T_s}\int_0^t \Delta\tilde{\rho}_\gamma(t)\cos(\omega_s t)dt \tag{9.25}$$

$$C_\gamma(t) = \frac{2}{T_s}\int_0^t \Delta\tilde{\rho}_\gamma(t)\sin(\omega_s t)dt \tag{9.26}$$

(the label γ refers to the ξ,η components). In particular, the coefficients $B_{\xi,i}(t)$ and $C_{\xi,i}(t)$ corresponding with the i-th spin period are:

$$B_{\xi,i} = \frac{2}{T_s}\int_{(i-1)T_s}^{iT_s} \Delta\tilde{\rho}_\xi(t)\cos(\omega_s t)dt \tag{9.27}$$

$$= \frac{2}{T_s}\left[\int_0^{iT_s} \Delta\tilde{\rho}_\xi(t)\cos(\omega_s t)dt - \int_0^{(i-1)T_s} \Delta\tilde{\rho}_\xi(t)\cos(\omega_s t)dt\right] = B_\xi(iT_s) - B_\xi((i-1)T_s)$$

$$C_{\xi,i} = C_\xi(iT_s) - C_\xi((i-1)T_s) \tag{9.28}$$

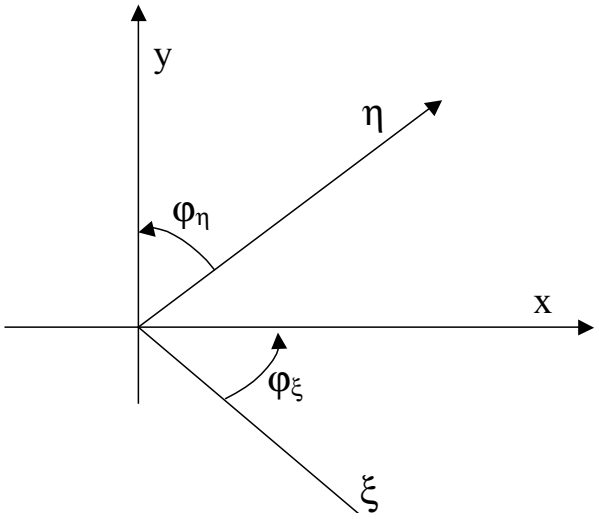

Figure 9.11: Phases of the signal.

Since we work only with discrete data, numerical computation of the Fourier coefficients (9.27) and (9.28) can be performed in the following manner:

$$B_{\xi,i} = \frac{2}{T_s}\sum_{k=0}^{N-1} \Delta\tilde{\rho}_\xi(t_{i,k})\cos(\omega_s t_{i,k}) \tag{9.29}$$

Having evaluated the coefficients $B_{\xi i}$ and $B_{\eta i}$ in the i-th spin period, by using the relations (9.23.a) and (9.23.b) we are able to write the relative displacement vector in the inertial reference frame $\Delta\tilde{r}$. Note that this vector can also be obtained by evaluating the coefficients $C_{\xi,i}$ and $C_{\eta,i}$ (from $\Delta\tilde{\rho}$ with a delay of $T_s/4$):

$$\Delta\tilde{r}_x = -C_\eta(t \to t + T_s/4) \tag{9.30.a}$$

$$\Delta\tilde{r}_y = C_\xi(t \to t + T_s/4) \qquad (9.30.b)$$

We have two independent measurements ((9.23) and (9.30)) of the components of the relative displacement in the inertial frame obtained from the measurements performed by the bridges sensitive along the ξ and η directions. Since sensor errors are not correlated, a better evaluation of the relative displacement $\Delta\tilde{r}$ is obtained by combining the relations (9.23) and (9.24), namely:

$$\Delta\tilde{r}_x = \left[B_\xi - C_\eta(t \to t + T_s/4)\right]/2 \qquad (9.31.a)$$

$$\Delta\tilde{r}_y = \left[B_\eta + C_\xi(t \to t + T_s/4)\right]/2 \qquad (9.31.b)$$

For details about the simulation of the Fourier filter see appendix 9.C, section 9.C.4. Figure 9.12 shows results of the simulation.

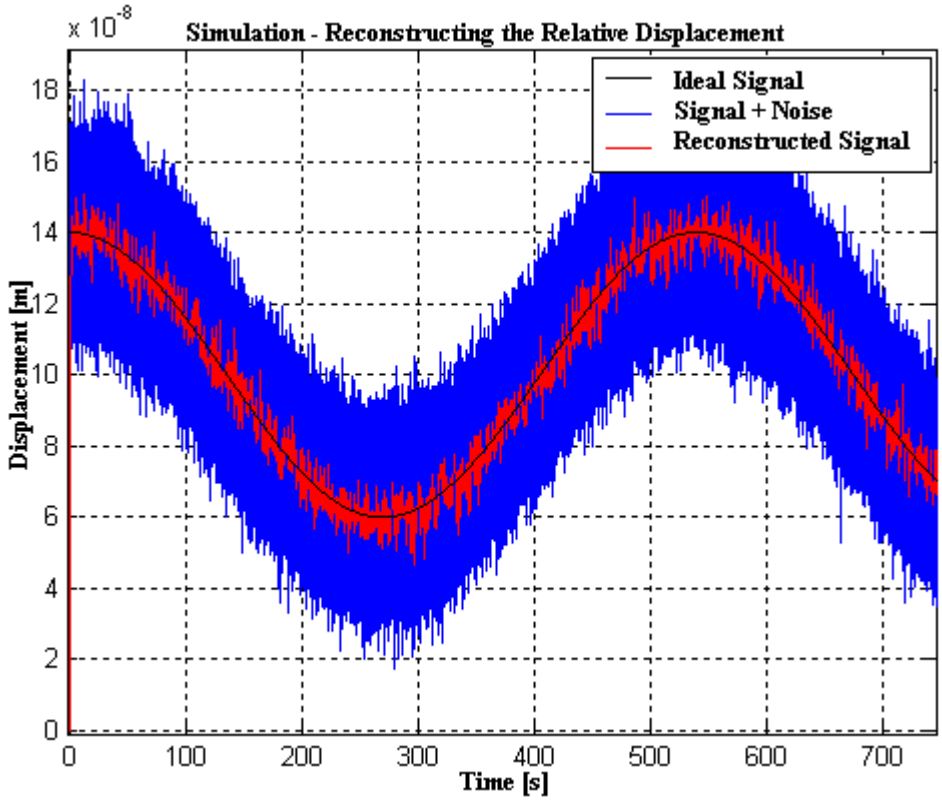

Figure 9.12: Actual relative displacement spacecraft/PGB in the inertial reference frame (along x direction) as predicted with Simulink is drawn in black. It is compared with the relative displacement (9.21) drawn in blue and with the relative displacement reconstructed by the first Fourier filter (9.31) from measurements of the rotating sensors. The improvement due to the filter is apparent.

Actual relative displacement spacecraft/PGB in the inertial reference frame as predicted with Simulink is drawn in black. It is compared with the relative displacement (9.21) drawn in blue and with the relative displacement reconstructed by the first Fourier filter from measurements of the rotating sensors. The improvement due to the filter is apparent. Note that the relative displacement will be delayed by one spin period, since one T_s is needed to sample the starting data.

9.9.B: RECONSTRUCTION OF THE RELATIVE VELOCITY.

From the difference between the corresponding values of the relative displacement in two spin periods[7], the velocity of the modulating signal in the inertial frame is then reconstructed:

$$\Delta\tilde{v}_i = \left(\Delta\tilde{r}_i - \Delta\tilde{r}_{i-1}\right)/T_s \tag{9.32}$$

The reconstructed velocity is driven by the noise. The solution is to perform a second Fourier harmonic analysis at the whirl period T_w[8]. The formulas for the second Fourier filter are the same of the first Fourier filter (9.22), after substituting T_s with T_w and $\Delta\tilde{\rho}$ with $\Delta\tilde{v}$, namely:

$$\Delta v_x^w(t) = B_x\cos(\omega_w t) + C_x\sin(\omega_w t) \tag{9.33.a}$$

$$\Delta v_y^w(t) = B_y\cos(\omega_w t) + C_y\sin(\omega_w t) \tag{9.33.b}$$

An example of this double-filter approach is shown in figure 9.13 (details about the simulation are available in appendix 9.C, section 9.C.4).

9.10: THE CONTROL FORCE.

The velocity (9.33) has been reconstructed after the double Fourier filter. Let us introduce its phase φ_v in the inertial reference frame (see figure 9.14), i.e. $\Delta\tilde{v}_x = |\Delta\tilde{v}|\cos(\varphi_v)$ and $\Delta\tilde{v}_y = |\Delta\tilde{v}|\sin(\varphi_v)$. The continuous compensation requires a stabilization force in the form of a sinusoidal signal and proportional to the relative velocity in the inertial frame:

$$F_x^c = -c_{nr}|\Delta\tilde{v}|\cos(\varphi_v) \tag{9.34.a}$$

$$F_y^c = -c_{nr}|\Delta\tilde{v}|\sin(\varphi_v) \tag{9.34.b}$$

Since the active plates are fixed in the rotating frame, the force (9.34) has to be written in this frame:

$$F_\xi^c = -c_{nr}|\Delta\tilde{v}|\cos(\omega_s t - \varphi_v) \tag{9.35.a}$$

$$F_\eta^c = c_{nr}|\Delta\tilde{v}|\sin(\omega_s t - \varphi_v) \tag{9.35.b}$$

The attracting force can be applied in the form of a step pulse. See table 9.1 for the waveform's parameters. In [11] a non rotating damping in pulsed mode has been developed.

---

[7] $\Delta\tilde{r}_i$ can be used with $\Delta\tilde{r}_{i-n}$ at the step t_i-nT_s to determine the velocity, i.e. $\Delta\tilde{v}_i = \left(\Delta\tilde{r}_i - \Delta\tilde{r}_{i-n}\right)/nT_s$. Using an interval of n spin periods, the noise is well attenuated, but the phase shift is encreased.

[8] Let us consider an unstable forward whirling mode at frequency ω_w. The time constant is then $2Q/\omega_w$ (see equations (5.4), (1.65)), i.e. it is Q/π times larger than the whirl period. By using a Q=90 for the spacecraft/PGB system and its natural period 296s, the signal doubles in 28.6 T_w. Hence, there is enough time to measure the relative displacement and perform the second Fourier harmonic analysis at the whirl period. Note that Q=90 is the lowest quality factor of the GG system; hence this is the fastest growing instability and therefore the most dangerous and difficult to control.

The attracting force is applied in the form of sinusoidal pulses, with two pulses in one turn, one for each actuator.

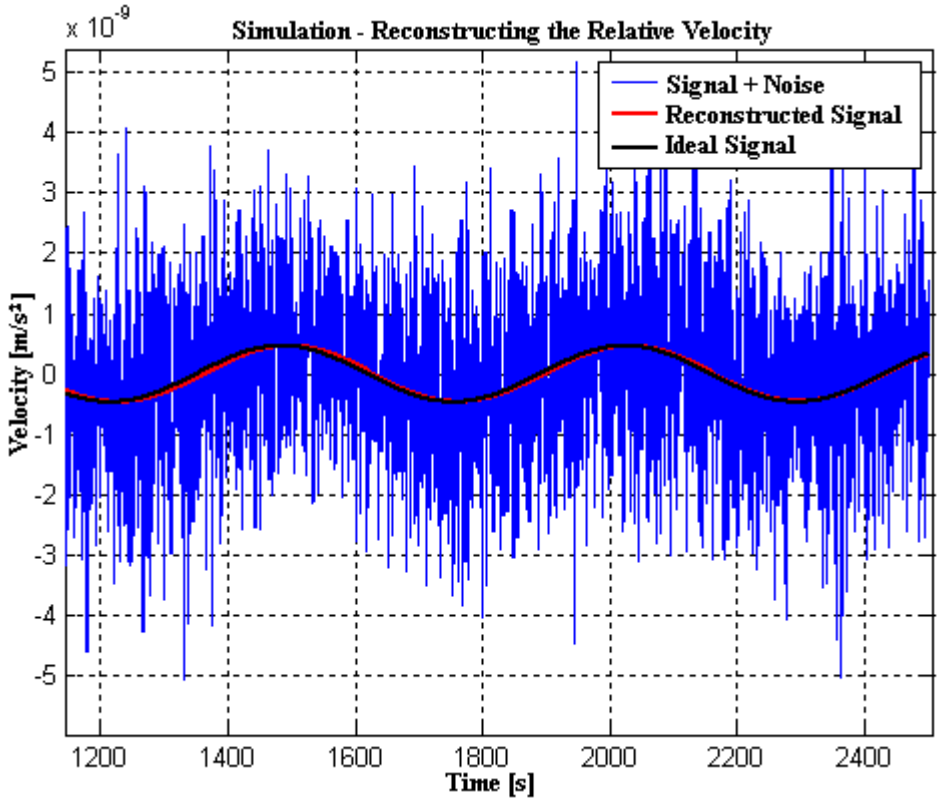

Figure 9.13: Actual relative velocity spacecraft/PGB in the inertial reference frame (along x direction) as predicted with Simulink is drawn in black. It is compared with the relative velocity (9.32) drawn in blue and with the relative displacement reconstructed by the second Fourier filter (9.33) from measurements of the rotating sensors. The improvement due to the filter is apparent.

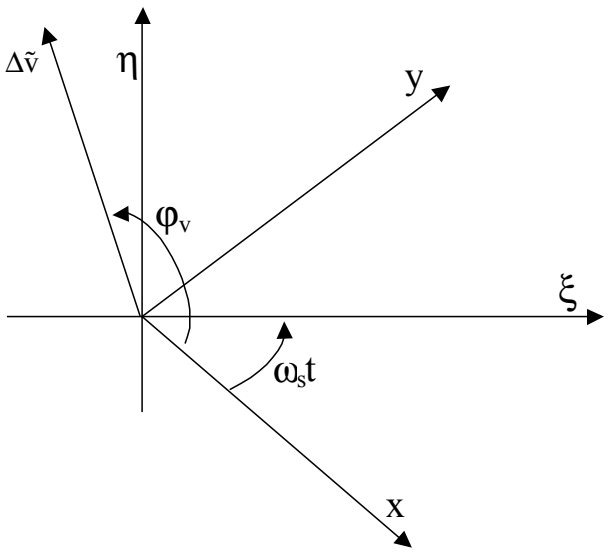

Figure 9.14: Relative velocity in the inertial and rotating frames.

Pulse Width	Force's Components
$-3\pi/4 \le \omega_s t - \varphi_v \le -\pi/4$	$F_\xi^c = 0\ ;\ F_\eta^c = -c_{nr}\left\|\Delta\tilde{v}\right\|$
$-\pi/4 \le \omega_s t - \varphi_v \le \pi/4$	$F_\xi^c = -c_{nr}\left\|\Delta\tilde{v}\right\|\ ;\ F_\eta^c = 0$
$\pi/4 \le \omega_s t - \varphi_v \le 3\pi/4$	$F_\xi^c = 0\ ;\ F_\eta^c = c_{nr}\left\|\Delta\tilde{v}\right\|$
$3\pi/4 \le \omega_s t - \varphi_v \le 5\pi/4$	$F_\xi^c = c_{nr}\left\|\Delta\tilde{v}\right\|\ ;\ F_\eta^c = 0$

Table 9.1: Step pulsed force.

The pulses must be sized $2c_{NR}\left|\Delta\tilde{v}\right|$ in order to provide the equivalent stabilization of the continuous command. See table 9.2 for the waveform's parameters of this damping force. In figure 9.15, the continuous compensation force (9.35.a) is shown compared with the pulsed force (both step pulse and sinusoidal pulse).

Pulse Width	Force's Components
$-3\pi/4 \le \omega_s t - \varphi_v \le -\pi/4$	$F_\xi^c = 0\ ;\ F_\eta^c = 2c_{nr}\left\|\Delta\tilde{v}\right\|\cos\left[2\left(\omega_s t - \varphi_v\right)\right]$
$-\pi/4 \le \omega_s t - \varphi_v \le \pi/4$	$F_\xi^c = -2c_{nr}\left\|\Delta\tilde{v}\right\|\cos\left[2\left(\omega_s t - \varphi_v\right)\right]\ ;\ F_\eta^c = 0$
$\pi/4 \le \omega_s t - \varphi_v \le 3\pi/4$	$F_\xi^c = 0\ ;\ F_\eta^c = -2c_{nr}\left\|\Delta\tilde{v}\right\|\cos\left[2\left(\omega_s t - \varphi_v\right)\right]$
$3\pi/4 \le \omega_s t - \varphi_v \le 5\pi/4$	$F_\xi^c = 2c_{nr}\left\|\Delta\tilde{v}\right\|\cos\left[2\left(\omega_s t - \varphi_v\right)\right];\ F_\eta^c = 0$

Table 9.2: Sinusoidal pulsed force.

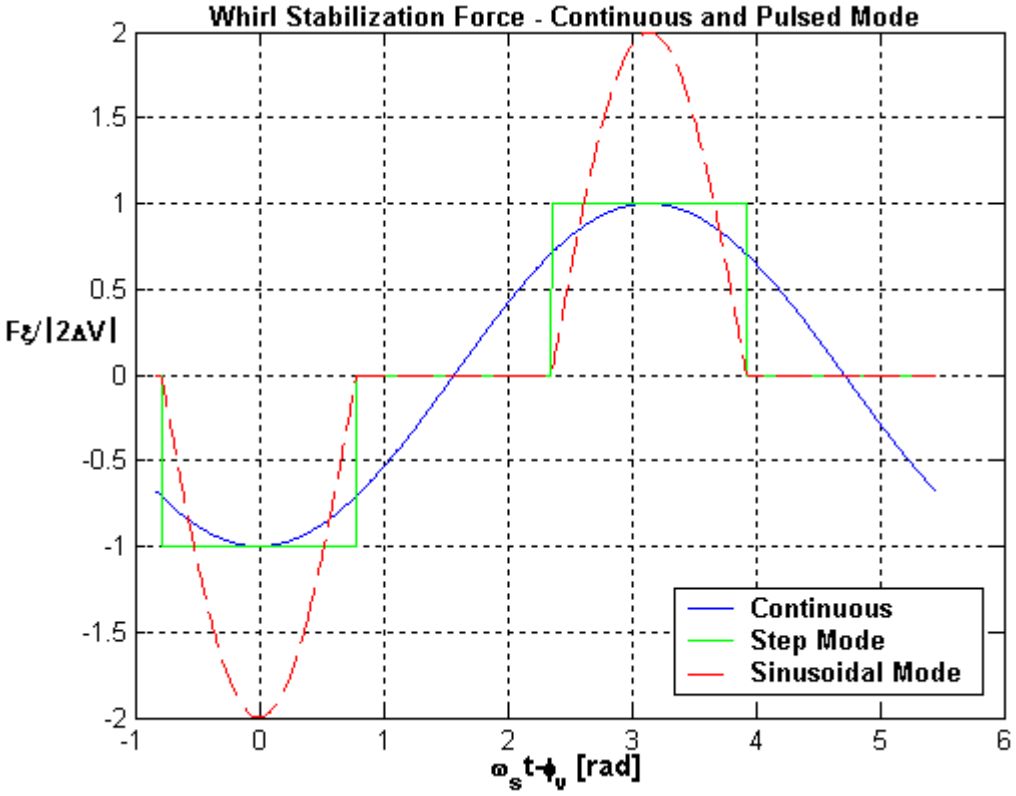

Figure 9.15: Comparison between continuous and pulsed stabilization commands.

9.11: RESULTS OF THE NUMERICAL SIMULATIONS AND CONCLUSIONS.

In this section we apply the control laws in order to damp whirl motions. The total block diagram implemented in Simulink is shown in figure 9.17; it is described in appendix 9.C. The values for the coefficients of non rotating damping (c_{NR} and c_{NRt}) are 15 times larger than the minimum value required for stability; this allows us to save CPU time. The sampling period is fixed to 0.025 seconds, i.e. N=20 samples per spin period. The relative velocity $\Delta\tilde{v}_i = (\Delta\tilde{r}_i - \Delta\tilde{r}_{i-n})/nT_s$ (9.32) has been evaluated by assuming n=10.
The errors included were: errors on sensors, RMS=10^{-2}μm, bias=10μm, angular bias=1°, RMS of the ESS= $10^{-4}\omega_s$. The main drag component has been set to $5\cdot10^{-9}$N (after drag free control). It converts to a signal at frequency ω_s in the rotating reference frame. A second component of the drag acts at frequency ω_s-ω_{orb} in the rotating frame and has amplitude $2\cdot10^{-9}$N. Results are summarized in the following figures. All plots are shown in the non rotating frame.
Figure 9.16 shows the components of the whirling motion along x direction in the inertial reference frame. The pulsed command described in section 9.9 (see table 9.2) reduce the whirl radius to about one Angstrom after 5000 seconds and stabilize the system. The inset shows the residual signal after whirling compensation.

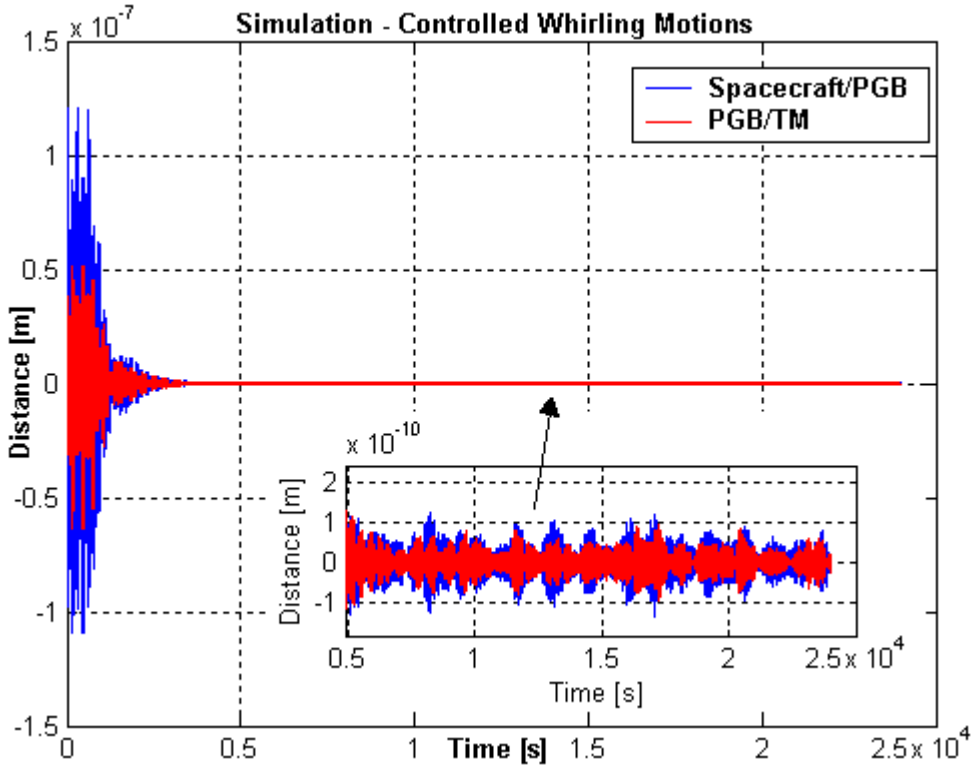

Figure 9.16:Components along x axis of the whirling motions. The whirl radius reduces to about one Angstrom after 5000 seconds.

In figure 9.18 we plot the active force of control along ξ direction as a function of time. This chapter demonstrates that the whirl control problem of the GG system can be solved in realistic conditions.

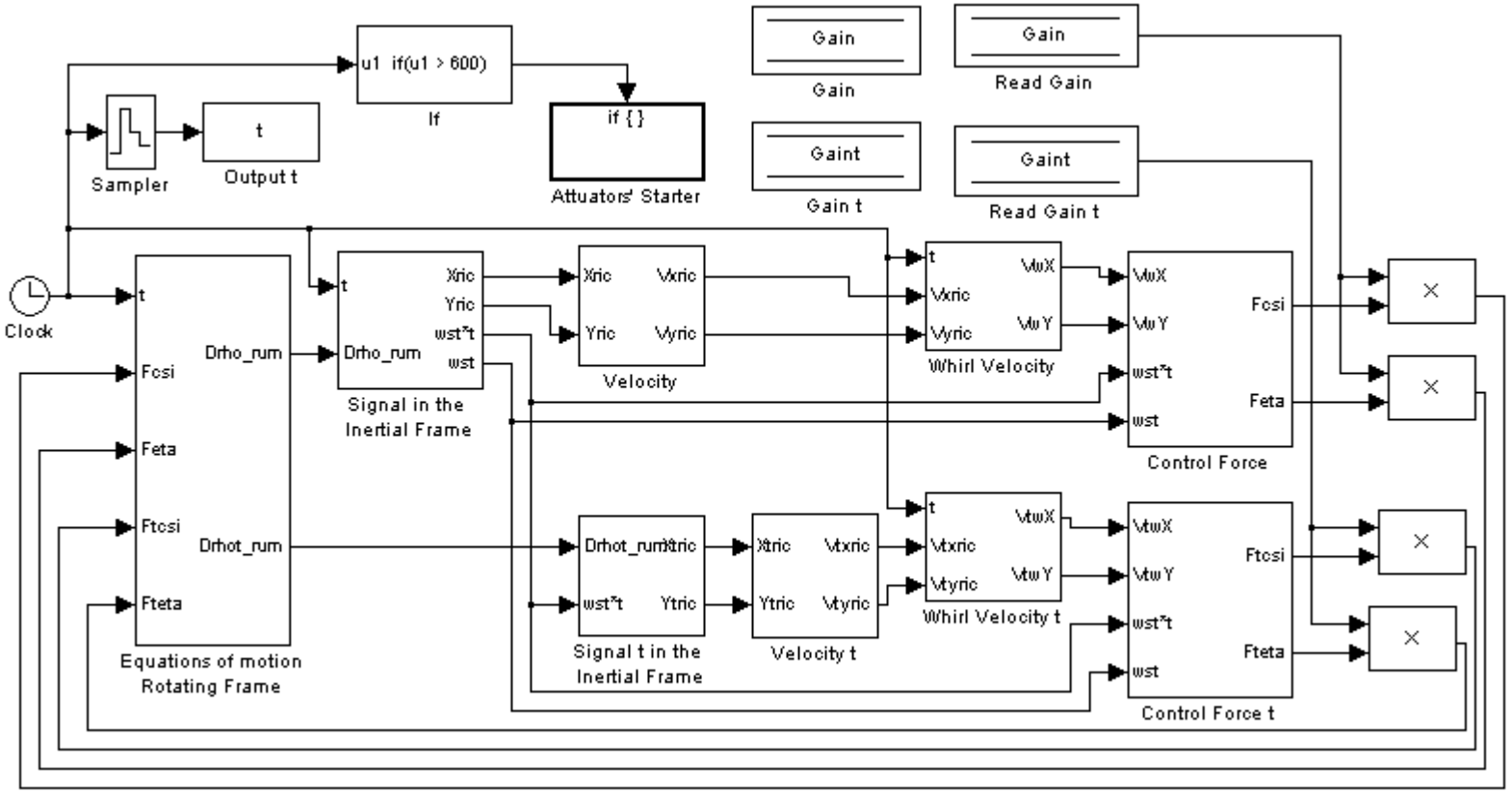

Figure 9.17: Block diagram implemented in Simulink.

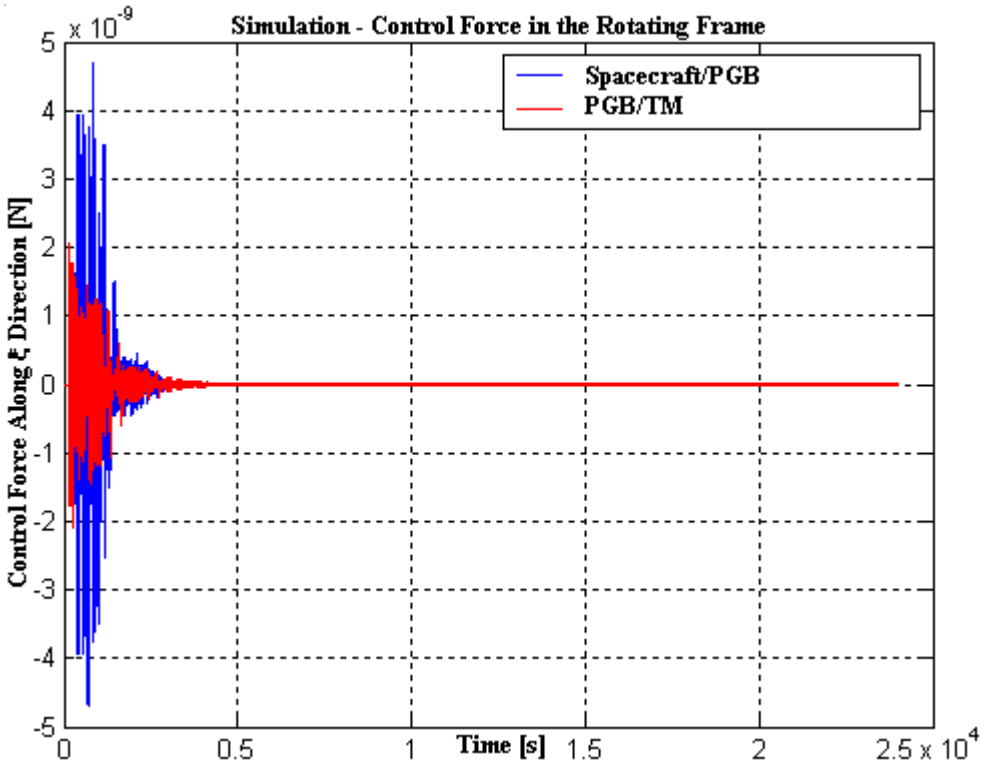

Figure 9.18: Active force of the control along the ξ direction in the rotating reference frame.

9.12: TIDAL EFFECTS ON THE GG TEST MASSES.

Experiments to test the equivalence principle (EP) in low Earth orbit require to detect the effects of an extremely small non-classical differential acceleration between test masses of different composition. In all proposed experiments the test masses are concentric coaxial cylinders, so as to reduce classical tidal effects which are differential too. Perfect centring being impossible, tidal effects need to be carefully investigated as they impose severe constraints on the basic features of the experiment design. The analysis in [54] shows that with free flying (uncoupled) test masses an EP violation signal could be detected if the initial conditions of the masses were finely adjusted for them to remain at a fixed distance relative to each other while orbiting around the Earth. However, such an experiment is severely limited by non-gravitational effects. If the test cylinders are weakly coupled in 2D in the plane perpendicular to their symmetry axis (close to the orbit plane), while rapidly spinning around it, a position of relative equilibrium is provided by physical laws which makes tidal effects widely separated from the signal. Weak coupling in 1D along the symmetry axis (to lie and slowly rotate in the orbit plane) is viable but less advantageous.

The following sections 9.12.a, 9.12.b, 9.12.c and 9.12.d are parts of the article [54] available in Appendix_Article. In section 9.12.a we demonstrate that one way to separate the EP violation signal from the tide is to couple the test masses in the orbit plane, e.g., with a mechanical spring, thus introducing a natural frequency of differential oscillation of the test masses with respect to one another. In this case, while the EP signal is still detected at the orbital frequency, tides are at the natural differential

frequency, and at this frequency plus or minus twice the orbital frequency. This is the case of the proposed "Galileo Galilei-GG" space experiment, where the natural differential frequency is about a factor 10 away from the orbital frequency, which makes it easy to separate tidal effects from the signal. The need for all EP experiments in space to spin the spacecraft in order to provide a frequency modulation of the signal is discussed in section 9.12.b. In section 9.12.c the GG experiment is analysed under realistic conditions, including the rotation of the system in super-critical regime, to demonstrate that indeed an EP violation signal would not be masked by tidal effects.

9.12.A: EP VIOLATION SIGNAL AND TIDAL EFFECTS FOR TEST MASSES COUPLED IN THE ORBIT PLANE.

We now show that if two test bodies are coupled in the orbit plane, tidal effects and EP violation signal appear at different frequencies, which makes it possible to separate them out. Let us consider a spacecraft orbiting the Earth with radius r and Keplerian angular velocity $\omega_{orb} = \sqrt{GM/r^3}$.

Let the test masses m_1 and m_2 be separated by Δr ($\Delta r << r$) in their initial orbital distance, and be coupled to each other with a positive stiffness k (the coupling may be of different nature, e.g., mechanical, electrostatic or magnetic) in the orbit plane. The suspension is assumed to be rigid (in reality it is only much stiffer) along the orbit normal. We investigate their motion in the reference frame of the orbiting satellite. The frame is centred on the centre of mass of the Earth, with the x′ axis in the Earth-to-satellite direction, the z axis perpendicular to the orbit plane and the y′ axis to complete the Cartesian system.

In this frame we call $\vec{r}_1$ and $\vec{r}_2$ the test masses position vectors with respect to the centre of mass of the spacecraft, and $\vec{\rho}_1 = \vec{r} + \vec{r}_1$, $\vec{\rho}_2 = \vec{r} + \vec{r}_2$ their position vectors with respect to the centre of mass of the Earth. The bodies have the same inertial mass but different composition. In addition it is assumed that there is a violation of the equivalence principle to the level η, namely: $m_1^i = m_2^i = m$, $m_1^g = m$ and $m_2^g = m(1+\eta)$. The Lagrange function is:

$$L = \frac{1}{2}m\left[\dot{r}_{1x}^2 + \dot{r}_{1y}^2 + \dot{r}_{2x}^2 + \dot{r}_{2y}^2 + 3\omega_{orb}^2\left(r_{1x}^2 + r_{2x}^2\right) + \omega_{orb}\left(r_{1x}\dot{r}_{1y} - r_{1y}\dot{r}_{1x} + r_{2x}\dot{r}_{2y} - r_{2y}\dot{r}_{2x}\right)\right]$$
$$-\frac{1}{2}k\left(r_{1x}^2 + r_{1y}^2 + r_{2x}^2 + r_{2y}^2 - 2r_{1x}r_{2x} - 2r_{1y}r_{2y}\right) - m\omega_{0rb}^2 R\eta r_{2x} + \frac{1}{2}m\omega_{0rb}^2\eta\left(2r_{2x}^2 - r_{2y}^2\right) \tag{9.36}$$

Tidal effects can be singled out by putting η =0 in (9.36) (i.e., no EP violation), and then deriving the equations of motion of the test masses in their relative coordinates X= r_{2x}-r_{1x} and Y=r_{2y}-r_{2x}:

$$\begin{cases} \ddot{X} - 2\omega_{orb}\dot{Y} + \left(\omega_n^2 - 3\omega_{orb}^2\right)X = 0 \\ \ddot{Y} + 2\omega_{orb}\dot{X} + \omega_n^2 Y = 0 \end{cases} \tag{9.37}$$

The angular frequency $\omega_n = \sqrt{2k/m}$ appearing in (9.37) is the natural frequency of oscillation of the test masses relative to one another in the orbit plane due to the

coupling stiffness k: the weaker the coupling stiffness, the more sensitive the test bodies are to differential forces, such as those due to tides or EP violation. In space, thanks to weightlessness, the coupling can be very weak, much weaker than on the ground where suspensions must be stiff enough to withstand local gravity. Hence, the natural differential frequency can be much lower in space than in the laboratory. Yet, it is always much larger than the orbital frequency, which in all proposed space experiments is about $1.7\cdot10^{-4}$ Hz (typical orbital periods in low Earth orbit are 6000s). By combining equation (9.37) into one single equation of higher order, we obtain

$$\dddot{X}+\left(\omega_{orb}^2+2\omega_n^2\right)\ddot{X}+\omega_n^2\left(\omega_n^2-3\omega_{orb}^2\right)X=0 \tag{9.38}$$

whose eigenvalues are:

$$\Lambda_{1,2,3,4}=\pm i\sqrt{\omega_n^2+\omega_{orb}^2/2\mp 2\omega_{orb}\omega_n\sqrt{1+\omega_{orb}^2/(16\omega_n^2)}} \tag{9.40}$$

These eigenvalues give the angular frequencies of tidal effects in the reference frame of the satellite which orbits around the Earth at ω_{orb}. For the EP experiments in space it is $\omega_n>>\omega_{orb}$, and these frequencies become:

$$\Lambda_{1,2,3,4}=\pm i\left(\omega_n\pm\omega_{orb}\right) \tag{9.41}$$

If seen in the inertial reference frame (centred on the centre of mass of the Earth and fixed in space), tidal effect would therefore appear at frequencies:

$$\nu_n,\nu_n\pm 2\nu_{orb} \tag{9.42}$$

($\nu=\omega/2\pi$). Hence, the effect of coupling the test masses in the orbit plane is to shift the tidal signal from the orbital frequency ν_{orb} to the (typically much larger) natural differential frequency ν_n introduced by the coupling. What about the effect of coupling on an EP violation signal?

In order to answer this question we consider $\eta\neq0$ in the Lagrange function (9.36) and find that in this case there exists a position of relative equilibrium of the test masses in the Earth-to-satellite direction (the x axis of the orbiting reference frame). The coordinates of the test masses at equilibrium are:

$$\begin{cases} r_{1x}^0=\dfrac{\omega_n^2R\eta}{6\left(\omega_n^2-3\omega_{orb}^2\right)+2\eta\left(\omega_n^2-6\omega_{orb}^2\right)} \\ r_{2x}^0=r_{1x}^0\left(1-6\dfrac{\omega_{orb}^2}{\omega_n^2}\right) \\ r_{1y}^0=r_{2y}^0=r_{1x}^0\left(\dfrac{\omega_n^2}{\omega_n^2+2\eta\omega_{orb}^2}\right) \end{cases} \tag{9.43}$$

Since the equilibrium position (18) due to an EP violation η is fixed in the orbit plane of the reference frame of the orbiting satellite, it is apparent that in the inertial reference system the EP violation signal has the main component at the orbital frequency (as in

the case of uncoupled test masses), while tides are now close to the natural differential frequency due to coupling. Since the orbital frequency is several times lower than the natural one, we conclude that—thanks to coupling in the orbit plane—an EP violation signal can be well separated from classical tidal effects.

9.12.B: TIDAL EFFECTS IN SUPERCRITICAL ROTATION.

For high accuracy EP tests in space the spacecraft should also rotate, so as to modulate the signal at its rotation frequency relative to the Earth (the synodic frequency). EP tests require weak suspensions and large rotation rates: weak suspensions increase the sensitivity of the test masses to applied forces; fast rotation provides high frequency modulation and reduced "1/*f*" noise. Conceptually, the problem is that of a rotating oscillator made of a body of mass m whose centre of mass is suspended with stiffness k from a point located a vector $\vec{\varepsilon}$ away from the rotation axis. $\vec{\varepsilon}$ is the inevitable offset due to construction and mounting errors, and is fixed with the rotor. Two frequencies are relevant for equilibrium: the spin frequency ω_s and the natural frequency ω_n. Equilibrium is achieved at a position $\vec{r}_{eq}$ where the centrifugal force is balanced by the restoring force of the suspension; for highly supercritical rotation the self-centring (see equation (9.2)) occurs since the original offset is reduced by the large factor ω_n^2/ω_s^2. The same line of reasoning holds for two rotating coupled masses, whose relative position at equilibrium is as in (9.1), ω_n now being the frequency of differential oscillations. This is the case of the GG experiment design, for which tidal effects and EP violation signal are analysed in detail in sections 9.11.c and 9.11.d. Note that, since the offset vector $\vec{\varepsilon}$ is fixed with the rotor, the position vector of relative equilibrium is also fixed with the rotor, and therefore the corresponding tidal effect is (in the rotating reference frame) at twice the spin frequency, just as lunisolar tides on the surface of the Earth have periodicities of 12 h (solar tide) and 12 h 25 min (lunar tide).

9.12.C: THE GG EXPERIMENT: EP VIOLATION SIGNAL, WHIRL MOTION AND TIDAL EFFECTS IN THE SENSITIVE PLANE.

We have numerically integrated equations of motion for the GG satellite in presence of an EP violation signal. Note that: ν_s=2.000175 Hz is the spin frequency of the satellite around its symmetry axis with respect to a star fixed reference frame; $\nu_{orb}=1.75\cdot10^{-4}$ Hz is the orbital frequency around the Earth and $\nu_{prec}=\Omega_{prec}/2\pi=3.17\cdot10^{-8}$ Hz is the frequency of precession of the normal to the orbit around the normal to the equator (too small to be detected in 20 days of integration time). For demonstration purposes the numerical integration is carried out with a very large whirl radius $r_w=2.5\cdot10^{-4}$m and assuming a very high level of violation $\eta=10^{-11}$. Instead, the natural differential period of the coupling (also the whirl period) is T_w =540 s as in GG, the quality factor is *Q*=20000 as originally assumed in GG (though better values have been measured), and $\varepsilon=10^{-6}$ m. Since at this point we are interested only in frequencies much faster than the precession frequency, the numerical integration time span is short and precession is not

included. The resulting FFT of the relative acceleration between the test bodies is shown in figure 9.19 where all four expected peaks are visible: whirl motion appears at ν_w=0.00185 Hz, tidal effect at ν_w, ν_w-2ν_{orb}=0.0015 Hz and ν_w+2ν_{orb}=0.0022 Hz and EP signal at $\nu_{orb}=1.75\cdot10^{-4}$ Hz (EP signal has a peak at ν_s too due to the offset).

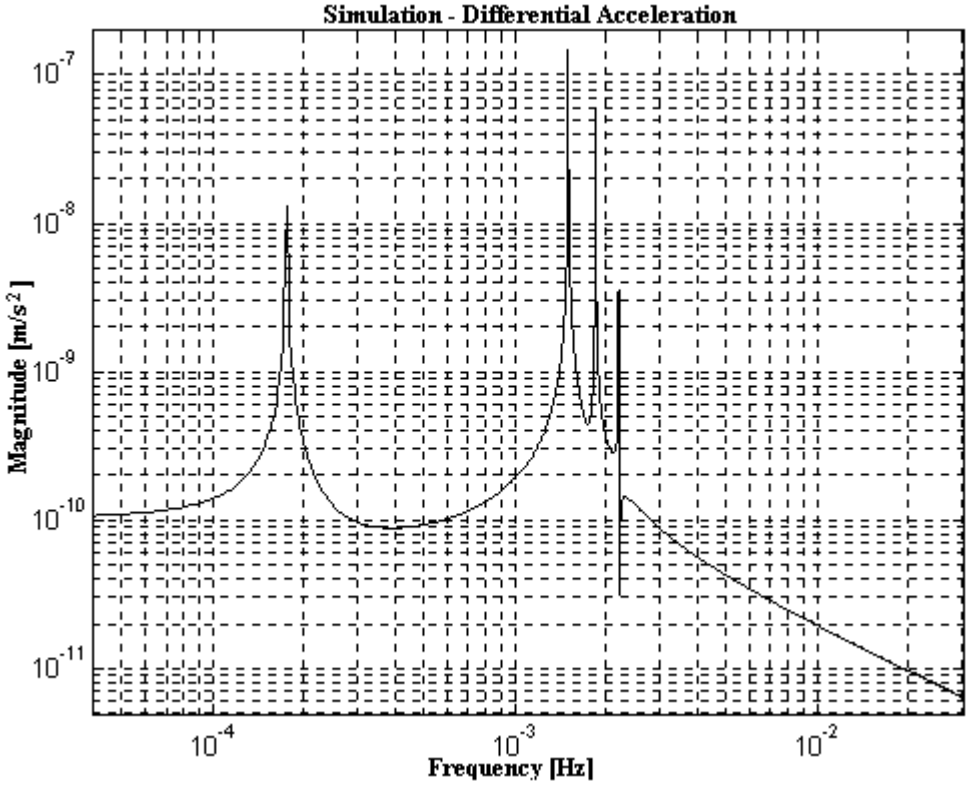

Figure 9.19: FFT of the differential acceleration where all 4 expected peaks are visible.

We now derive the same results by analytical methods, taking into account also precession. We use a simplified model and write the equations of motion in the inertial reference frame (x,y,z) centred on the centre of the Earth, the x-axis along the nodal line of the satellite's orbit at initial time, the y-axis perpendicular to it in the orbit plane at initial time and the z-axis along the spin axis, coinciding with the orbit normal at initial time.

Let (s_1,s_2,s_3) be a reference frame fixed with the satellite, where s_3 is in the direction of the spin axis (coinciding with the orbit normal z at initial time), s_1 is along the nodal line at initial time (same as x-axis) and (s_1,s_2) is therefore the sensitive plane of the instrument. In the reference system identified by the equatorial plane of the Earth and by its rotation axis it is: s_3=(0,-sinI,cosI), s_1=(1,0,0) and s_2=(0,sinI,cosI) where I=97.5° is the inclination of the orbit. The unit position vector of the satellite at time t is:

$$\hat{r}=\cos\left(\omega_{orb}t+\varphi\right)\begin{pmatrix}\cos\left(\Omega_{prec}t\right)\\ \sin\left(\Omega_{prec}t\right)\\ 0\end{pmatrix}+\sin\left(\omega_{orb}t+\varphi\right)\begin{pmatrix}-\cos(I)\sin\left(\Omega_{prec}t\right)\\ \cos(I)\cos\left(\Omega_{prec}t\right)\\ \sin(I)\end{pmatrix} \qquad (9.44)$$

while whirl motion of the two test bodies is described by the vector:

$$\vec{p}=r_w e^{\frac{\omega_w t}{2Q}}\begin{pmatrix}\cos(\omega_w t)\\ \sin(\omega_w t)\cos(I)\\ \sin(\omega_w t)\sin(I)\end{pmatrix} \tag{9.45}$$

Then, the tidal (differential) acceleration between the test bodies is:

$$\vec{a}=3\frac{GM}{r^3}r_w e^{\frac{\omega_w t}{2Q}}\left\{\sin(\omega_w t)\left[(\hat{r}\times\hat{s}_3)\cdot\hat{s}_1\right]\hat{r}+\cos(\omega_w t)(\hat{r}\cdot\hat{s}_1)\hat{r}+\vec{p}\right\} \tag{9.46}$$

and its components in the sensitive plane are:

$$a_{s_1}=\vec{a}\cdot\hat{s}_1=\frac{GM}{r^3}\left\{3r_w e^{\frac{\omega_w t}{2Q}}\left[\sin(\omega_w t)\left[(\hat{r}\times\hat{s}_3)\cdot\hat{s}_1\right]+\cos(\omega_w t)(\hat{r}\cdot\hat{s}_1)\right](\hat{r}\cdot\hat{s}_1)-\vec{p}\cdot\hat{s}_1\right\} \tag{9.47.a}$$

$$a_{s_2}=\vec{a}\cdot\hat{s}_2=\frac{GM}{r^3}\left\{3r_w e^{\frac{\omega_w t}{2Q}}\left[\sin(\omega_w t)\left[(\hat{r}\times\hat{s}_3)\cdot\hat{s}_1\right]+\cos(\omega_w t)(\hat{r}\cdot\hat{s}_1)\right](\hat{r}\cdot\hat{s}_2)-\vec{p}\cdot\hat{s}_2\right\} \tag{9.47.b}$$

Using (9.44) in (9.47.a) and (9.47.b) we can list all the frequencies at which the whirl-related tides take place. Acceleration a_{s1} can be seen as the sum of the nine signals listed in table 9.3. The same holds for a_{s2}. The table shows that tides between the test masses occur at angular frequencies ν_w, $\nu_w\pm2\nu_{orb}$, $\nu_w\pm2\nu_{prec}$, $\nu_w\pm2\nu_{orb}\pm2\nu_{prec}$, $\nu_w\pm2\nu_{orb}\pm\nu_{prec}$. In the case of GG, however, ν_{prec} is too tiny to be detected. Thus, the relevant frequencies of the tides in GG are ν_w, $\nu_w\pm2\nu_{orb}$ in agreement with the numerical simulation. We conclude this analysis by showing in figure 9.20 the time evolution of the EP violation signal component $a_{s1}=-GM_\oplus\eta(\vec{r}\cdot\hat{s}_1)/r^2$ as compared to the same component of the tidal effect, giving the corresponding FFT analysis in figure 9.21. It is apparent that the wide separation in frequency allows an EP violation signal to be recovered even if it is much smaller than tidal effects.

Component	Frequency
$GM_\oplus 3r_w e^{\omega_w t/(2Q)}\cos(\omega_w t)\cos^2(\omega_{orb}t)\cos^2(\Omega_{prec}t)/r^3$	ω_w, $\omega_w\pm2\omega_{orb}$, $\omega_w\pm2\Omega_p$, $\omega_w\pm2\omega_{orb}\pm2\Omega_p$
$GM_\oplus(3/2)r_w e^{\omega_w t/(2Q)}\sin^2(I)\sin(\omega_w t)\sin(2\omega_{orb}t)\cos(\Omega_{prec}t)/r^3$	$\omega_w\pm2\omega_{orb}\pm\Omega_p$
$-GM_\oplus r_w e^{\omega_w t/(2Q)}\cos(\omega_w t)/r^3$	ω_w
$GM_\oplus 3r_w\sin^2(I)\cos(I)e^{\omega_w t/(2Q)}\sin(\omega_w t)\sin^2(\omega_{orb}t)\sin(\Omega_{prec}t)/r^3$	$\omega_w\pm\Omega_p$, $\omega_w\pm2\omega_{orb}\pm2\Omega_p$
$GM_\oplus(3/2)r_w\cos(I)e^{\omega_w t/(2Q)}\sin(\omega_w t)\cos^2(\omega_{orb}t)\sin(2\Omega_{prec}t)/r^3$	$\omega_w\pm2\Omega_p$, $\omega_w\pm2\omega_{orb}\pm2\Omega_p$
$-GM_\oplus(3/2)r_w\cos(I)e^{\omega_w t/(2Q)}\cos(\omega_w t)\sin(2\omega_{orb}t)\sin(2\Omega_{prec}t)/r^3$	$\omega_w\pm2\omega_{orb}\pm2\Omega_p$
$GM_\oplus(3/2)r_w\cos^2(I)e^{\omega_w t/(2Q)}\sin(\omega_w t)\sin(2\omega_{orb}t)\cos(2\Omega_{prec}t)/r^3$	ω_w, $\omega_w\pm2\omega_{orb}$, $\omega_w\pm2\Omega_p$, $\omega_w\pm2\omega_{orb}\pm2\Omega_p$
$GM_\oplus(3/2)r_w\cos^2(I)e^{\omega_w t/(2Q)}\cos(\omega_w t)\sin^2(\omega_{orb}t)\sin^2(\Omega_{prec}t)/r^3$	$\omega_w\pm2\omega_{orb}\pm2\Omega_p$
$GM_\oplus(3/2)r_w\cos^3(I)e^{\omega_w t/(2Q)}\sin(\omega_w t)\sin^2(\omega_{orb}t)\sin(2\Omega_{prec}t)/r^3$	$\omega_w\pm2\Omega_p$, $\omega_w\pm2\omega_{orb}\pm2\Omega_p$

Table 9.3: Tidal acceleration components in the sensitive plane of the GG system.

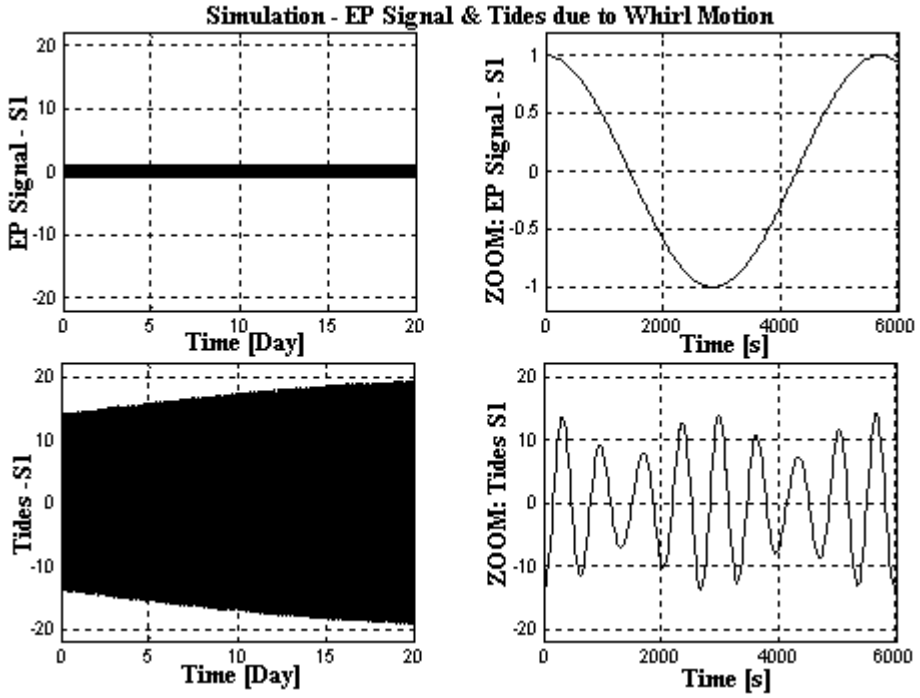

Figure 9.20: Time evolution of the EP violation signal (above) and of the tidal signal (below) along the s_1 direction in the sensitive plane. All signals are given in units of $\eta GM_{\oplus}/r^2 = 1$.

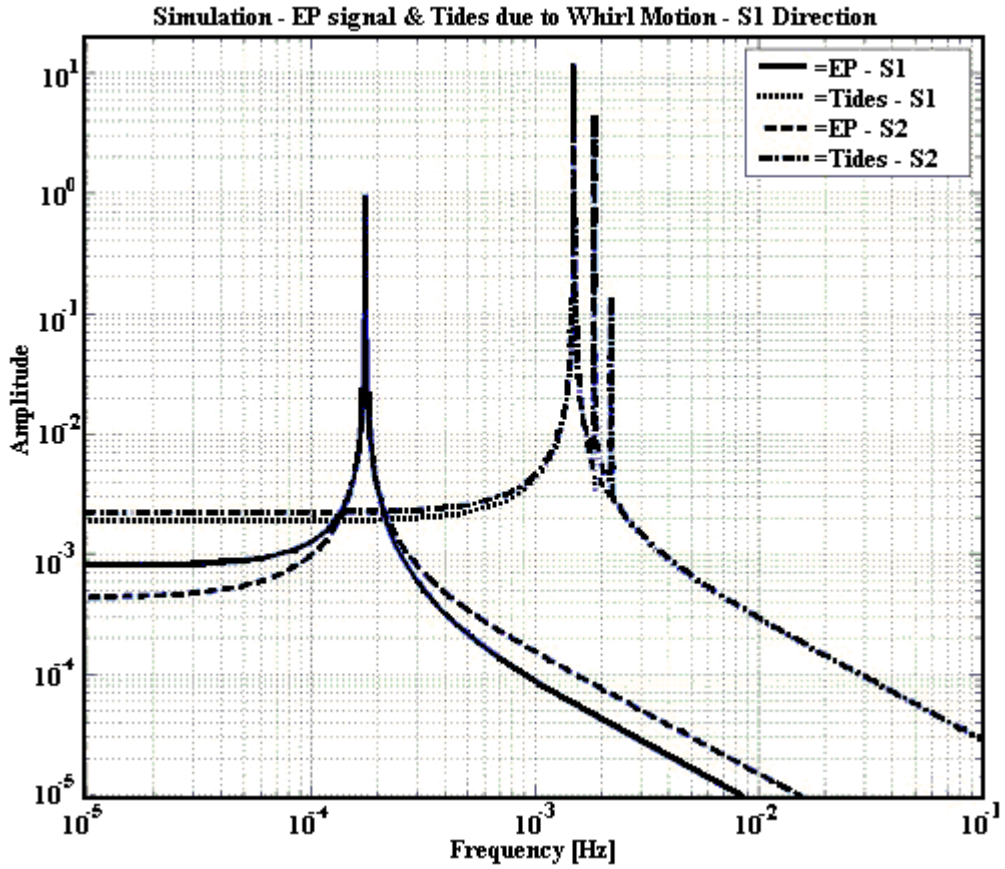

Figure 9.21: FFT analysis of the data shown in figure 9.20. The amplitudes of the tidal peaks are about 20 times larger than the EP signal. Nevertheless, the differences between the orbital and the whirl frequency allows us to recover the EP signal from the analysis. All signals are given in units of $\eta GM_{\oplus}/r^2 = 1$.

9.12.D: THE GG EXPERIMENT: TIDES DUE TO RELATIVE DISPLACEMENTS ALONG THE SPIN AXIS.

Even if the GG system is stiff along the spin/symmetry axis z, perturbations acting along this direction are present (e.g., due to solar radiation pressure or to coupling of the Earth's monopole with higher mass moments of the test bodies) which may produce a displacement between the centres of mass of the test cylinders. Unless the spin axis remains all time exactly perpendicular to the orbit plane (which is not the case in GG), a centre of mass separation along its direction will give a tidal signal also in the sensitive plane. We use the same analytical procedure as in section 9.11.d to describe the resulting tidal signal. The tidal acceleration $\vec{a}$ corresponding to the relative separation vector (0,0,Δz) with respect to the satellite centre-of-mass, can be written as

$$\vec{a} = -\frac{1}{2}\frac{GM_{\oplus}}{\left(R_{\oplus}+h\right)^3}\Delta z\,\hat{s}_3 + \frac{3}{2}\frac{GM_{\oplus}}{\left(R_{\oplus}+h\right)^3}\Delta z\,\hat{r}\left(\hat{r}\cdot\hat{s}_3\right) \tag{9.48}$$

In the reference frame (s_1 s_2), we have

$$\begin{aligned} a_{s1} &= \frac{3}{2}\frac{GM_{\oplus}}{\left(R_{\oplus}+h\right)^3}\Delta z\, r_x\left(r_y\sin(I) - r_z\cos(I)\right) \\ a_{s2} &= \frac{3}{2}\frac{GM_{\oplus}}{\left(R_{\oplus}+h\right)^3}\Delta z\left[\frac{1}{2}\left(r_y^2 - r_z^2\right)\sin(2I) - r_y r_z\cos(2I)\right] \end{aligned} \tag{9.49}$$

The corresponding FFT analysis is reported in figure 9.22.

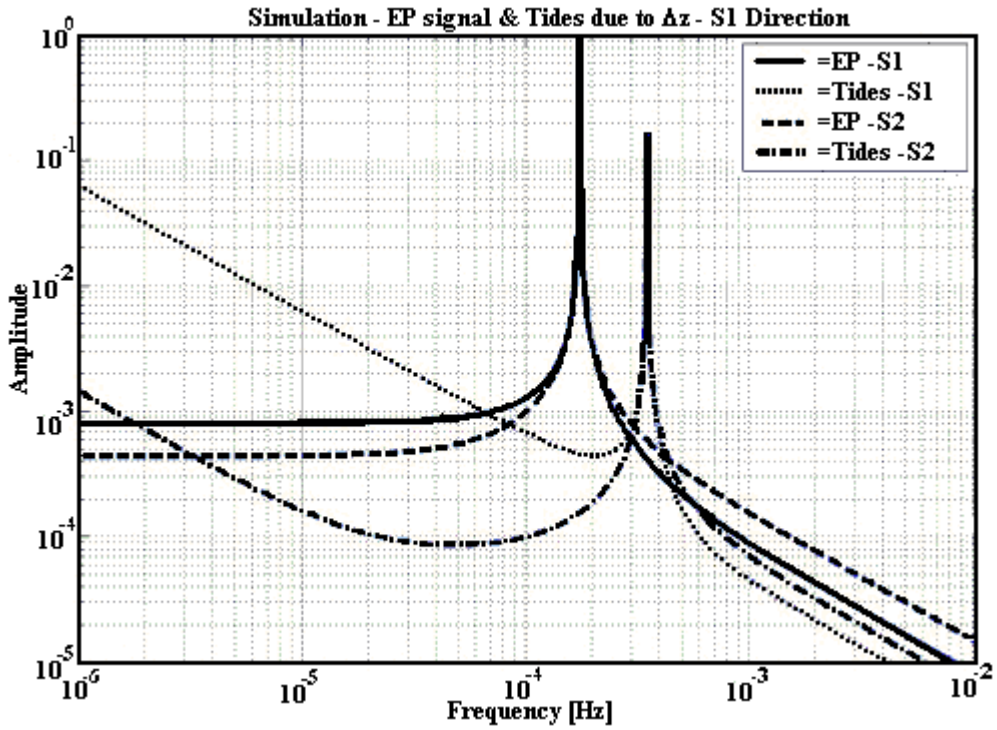

Figure 9.22: FFT analysis for a centre of mass separation along the z axis; tidal effects appear in the sensitive plane at frequency $2\nu_{orb}$, while the EP signal is still at ν_{orb}.

In this case, tidal effects are detected at frequency $2\nu_{orb}$, while the EP signal is still at ν_{orb}. The peak at $2\nu_{orb}$ in figure 9.22 actually does not resolve the contributions at $2\nu_{orb} \pm \nu_{prec}$ and $2\nu_{orb} \pm 2\nu_{prec}$. We end this section noticing that, although the frequency analysis of tidal effects is useful in order to understand the physical nature of these subtle perturbations, in the actual GG experiment the measurement data provided by the capacitance bridges, rotating with the test cylinders and the whole spacecraft at a nominal frequency of 2 Hz, are transformed (using the reference signal provided by the Earth elevation sensor onboard the spacecraft) into an Earth pointing, non-rotating reference frame centred in the centre of mass of the spacecraft. In this frame an EP violation signal appears as a constant offset (for zero orbital eccentricity) in the satellite-to-Earth direction while tidal disturbances appear at a frequency close to the natural differential frequency of the test cylinders, and therefore average out to zero.

APPENDIX 3.A:

THE LAGRANGEAN OF A ROTOR.

In an inertial reference frame S_0, the Lagrangean L of a rigid body is expressed by equation (A.1), where $\vec{v}_0$ is the velocity of the mass element dm and U is the potential energy of the body.

$$L_0 = \frac{1}{2}\int \vec{v}_0^2 dm - U \qquad (3.A.1)$$

If we consider a reference frame S_1 moving with respect to S_0 with velocity $V_1(t)$, we have that:

$$\vec{v}_0 = \vec{v}_1 + \vec{V}_1(t) \qquad (3.A.2)$$

$\vec{v}_1$ being the velocity of the body in the new reference frame S_1. Combining equations (A.1) and (A.2) together, the Lagrange function can thus be written as:

$$L_1 = \frac{1}{2}\int (\vec{v}_1 + \vec{V}_1(t))^2 dm - U = \frac{1}{2}\int \vec{v}_1^2 dm + \int \vec{v}_1 \cdot \vec{V}_1(t) dm + \cancel{\frac{1}{2}\int \vec{V}_1^2 dm} - U \qquad (3.A.3)$$

After noticing that $V_1(t)^2$ is the total derivative of a time dependent function, we can neglect the corresponding term in the lagrangean L_1. For the same reason we can write

$$\int \vec{v}_1 \cdot \vec{V}_1(t) dm = \vec{V}_1(t) \cdot \int \frac{d\vec{r}_1}{dt} dm = \cancel{\frac{d\int \vec{r}_1 \cdot \vec{V}_1(t) dm}{dt}} - \int \vec{r}_1 \cdot \frac{d\vec{V}_1}{dt} dm \qquad (3.A.4)$$

By defining the acceleration

$$W(t) = \frac{dV_1}{dt} \qquad (3.A.5)$$

we finally obtain the Lagrange function in the reference frame S_1:

$$L_1 = \frac{1}{2}\int \vec{v}_1^2 dm - \int \vec{r}_1 \cdot \frac{d\vec{V}_1}{dt} dm - U = \frac{1}{2}\int \vec{v}_1^2 dm - \int \vec{r}_1 \cdot \vec{W}(t) dm - U \qquad (3.A.6)$$

We introduce another reference system S with the origin coinciding with that of the preceding frame, which rotates in the horizontal plane with angular velocity $\vec{\omega}_s$. The velocity $\vec{v}$ in S is easily related to the velocity in S_1[1]:

$$\vec{v}_1 = \vec{v} + (\vec{\omega}_s \times \vec{r}) \qquad (3.A.7)$$

Combining equations (3.A.6) and (3.A.7) we derive the operational expression for the Lagrange function of a rigid body in a rotating reference frame:

[1] $\vec{r}$ is the position vector of the mass element dm in S.

$$L = \frac{1}{2}\int \vec{v}^2 dm + \int \vec{v}\times(\vec{\omega}_s\times\vec{r})dm + \frac{1}{2}\int (\vec{\omega}_s\times\vec{r})^2 dm - \int \vec{r}\cdot\vec{W}(t)dm - U \qquad (3.A.8)$$

Since the rotor GGG does not perform translational motions, the lagrangean of interest follows from equation (3.A.8) by imposing $\vec{W} = 0$.

$$L = \underbrace{\frac{1}{2}\int \vec{v}^2 dm}_{T_{kinetic}} + \underbrace{\int \vec{v}\times(\vec{\omega}_s\times\vec{r})dm}_{V_{Coriolis}} + \underbrace{\frac{1}{2}\int (\vec{\omega}_s\times\vec{r})^2 dm}_{U_{Centrifugal}} - U \qquad (3.A.9)$$

[2]

Starting from equation (3.A.9) it is possible to derive equations of motion of a rigid body in a non-inertial reference frame rotating with angular velocity $\vec{\omega}_s$. As a matter of fact, bodies can rotate around themselves, so equation (3.A.9) must be extended in order to take into account their rotational kinetic energy. We call $\vec{R}$ the centre of mass G position vector with respect to the origin O of the rotating frame (ξ,η,z). In this frame, $\vec{\rho}$ is the position vector of the element dm with respect to the centre of mass of the body. $\vec{r}=\vec{R}+\vec{\rho}$ is the total vector pointing to dm. $\vec{V}$ is the velocity of the centre of mass.

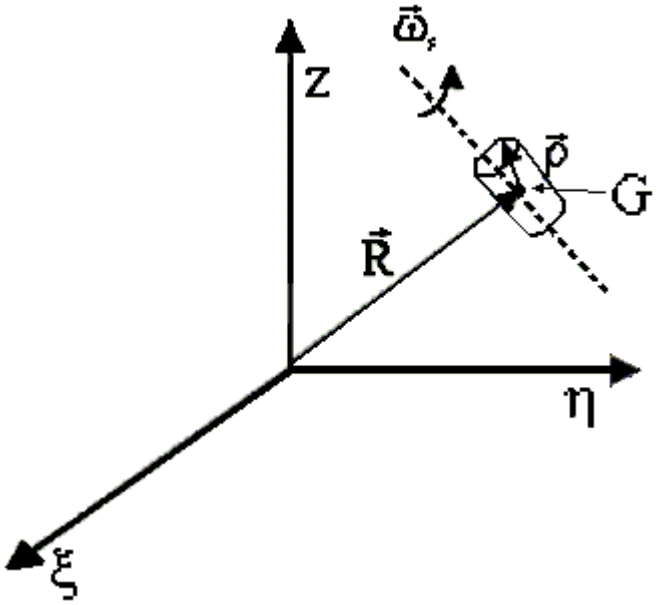

Figure 3.A.1 : The location of one body with respect to the rotating reference frame (ξ,η,z).

The coordinates (Ξ,Π,ϒ) are defined with reference to the body-fixed frame with the origin in the centre of mass of the body and axes coincident with its principal axes of inertia as drawn in figure 3.A.2. We can conveniently write all the vectors in the frame (O,ξ,η,z) in terms of their components in the frame (G,Ξ,Π,ϒ) by means of a rotation[3]. In the body-fixed frame (G, Ξ,Π,ϒ), $\vec{\Omega}_{\Xi,\Pi,\Upsilon}$ is the angular velocity along the principal axes of inertia. $\vec{\Omega}$ is the same

[2] Potential energy (named as U) contains only position vectors. Instead, the term $V_{Coriolis}$ from the Coriolis Force contains also the velocities.

[3] The rotation matrix is: $\begin{pmatrix} \sin\phi & \cos\vartheta\cos\phi & -\sin\vartheta\cos\phi \\ -\cos\phi & \cos\vartheta\sin\phi & -\sin\vartheta\sin\phi \\ 0 & \sin\vartheta & \cos\vartheta \end{pmatrix}$.

angular velocity written in the rotating frame (O,ξ,η,z). The velocity of the element dm in the rotating frame is given by the following equation:

$$\vec{v}=\vec{V}+\left(\vec{\Omega}\times\vec{\rho}\right) \tag{3.A.10}$$

The angles ϑ and ϕ are the generalized coordinate; they are drawn in figure 3.A.3. In terms of those angles the angular velocity in the body-fixed frame becomes:

$$\vec{\Omega}_{\Xi,\Pi,\Upsilon}=\begin{bmatrix}\dot{\vartheta}\\ \dot{\phi}\sin(\vartheta)\\ \omega_s\end{bmatrix} \tag{3.A.11}$$

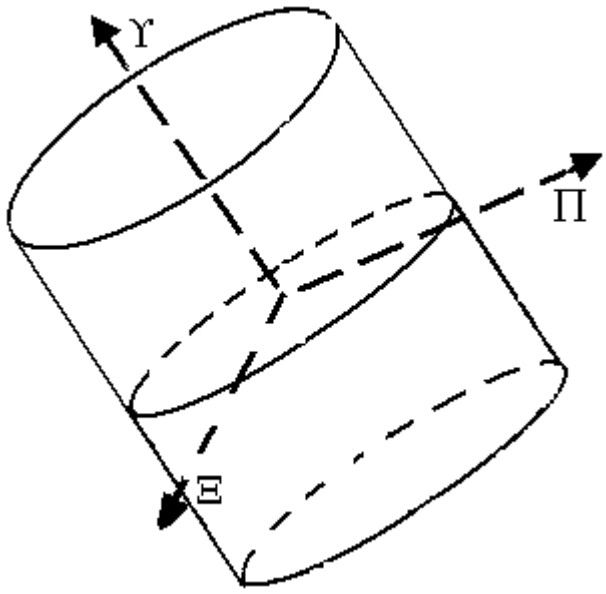

Figure 3.A.2: The reference system fixed with the body. The (Ξ,Π,Υ) axes coincide with principal axes of inertia.

Starting from the lagrangean in equation (3.A.9) the kinetic energy can be written as:

$$T_{\text{kinetic}}=\frac{1}{2}\int\vec{v}^2\,dm \tag{3.A.12}$$

Replacing equation (3.A.10) in the integral (3.A.12) we obtain:

$$T_{\text{kinetic}}=\frac{1}{2}\int\left[\vec{V}+\left(\vec{\Omega}\times\vec{\rho}\right)\right]^2 dm=\frac{1}{2}\int\left[\vec{V}^2+\left(\vec{\Omega}\times\vec{\rho}\right)^2+2\vec{V}\cdot\left(\vec{\Omega}\times\vec{\rho}\right)\right]dm \tag{3.A.13}$$

It is convenient to evacuate the integrals appearing in equation (3.A.13). It is easy to find the following results:

$$\frac{1}{2}\int\vec{V}^2 dm=\frac{1}{2}\vec{V}^2\int dm=\frac{1}{2}M\vec{V}^2 \tag{3.A.14.a}$$

$$\int\vec{V}\cdot\left(\vec{\Omega}\times\vec{\rho}\right)dm=\vec{V}\cdot\int\left(\vec{\Omega}\times\vec{\rho}\right)dm=\left(\vec{V}\times\vec{\Omega}\right)\cdot\int\vec{\rho}\;dm=0^{4} \tag{3.A.14.b}$$

[4] This result follows from the definition of centre of mass, i.e. $\int\vec{\rho}\;dm=0$.

$$\frac{1}{2}\int\left(\vec{\Omega}\times\vec{\rho}\right)^2 dm = \frac{1}{2}\sum_{\beta} I_{\beta,\beta}\Omega_{\beta}^2 \quad [5] \qquad (3.A.14.c)$$

Thanks to equations (3.A.14) the kinetic energy can be written as the sum of a term related to the motion of the centre of mass and one related to the rotations around it:

$$T_{kinetic} = \frac{1}{2}M\vec{V}^2 + \frac{1}{2}\sum_{\beta} I_{\beta,\beta}\Omega_{\beta}^2 = \frac{1}{2}M\vec{V}^2 + \frac{1}{2}I_{\Xi}\left(\dot{\phi}^2\sin^2(\vartheta) + \dot{\vartheta}^2\right) \qquad (3.A.15)$$

The term $V_{Coriolis}$ related to the Coriolis force is:

$$V_{Coriolis} = \int \vec{v}\times(\vec{\omega}_s\times\vec{r})dm = \int\left[\vec{V}+\left(\vec{\Omega}\times\vec{\rho}\right)\right]\cdot\left[\vec{\omega}_s\times\left(\vec{R}+\vec{\rho}\right)\right]dm \qquad (3.A.16)$$

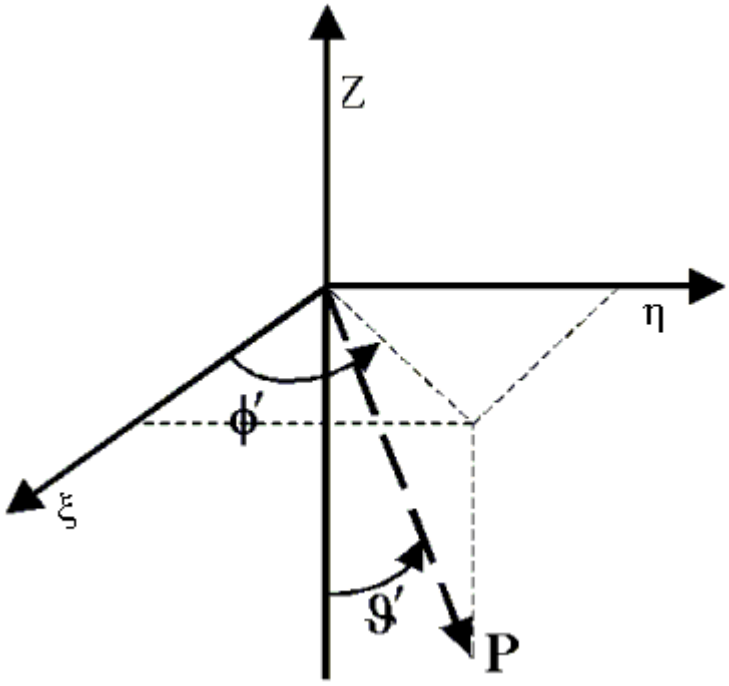

Figure 3.A.3: Generalized coordinates ϑ and ϕ of the point P.

Exploiting the properties of the scalar product equations (3.A.17) are found.

$$\int\vec{V}\cdot\left(\vec{\omega}_s\times\vec{R}\right)dm = \vec{V}\cdot\left(\vec{\omega}_s\times\vec{R}\right)\int dm = M\vec{V}\cdot\left(\vec{\omega}_s\times\vec{R}\right) \qquad (3.A.17.a)$$

$$\int\vec{V}\cdot\left(\vec{\omega}_s\times\vec{\rho}\right)dm = \vec{V}\cdot\int\left(\vec{\omega}_s\times\vec{\rho}\right)dm = 0 \quad [6] \qquad (3.A.17.b)$$

$$\int\left(\vec{\Omega}\times\vec{\rho}\right)\cdot\left(\vec{\omega}_s\times\vec{R}\right)dm = \left(\vec{\omega}_s\times\vec{R}\right)\cdot\int\left(\vec{\Omega}\times\vec{\rho}\right)dm = 0 \quad [7] \qquad (3.A.17.c)$$

$$\int\left(\vec{\Omega}\times\vec{\rho}\right)\cdot\left(\vec{\omega}_s\times\vec{\rho}\right)dm = I_{\Xi}\omega_s\dot{\phi}\sin^2(\vartheta) + I_{\Upsilon}\omega_s^2\cos(\vartheta) \qquad (3.A.17.d)$$

---

[5] $I_{\beta,\beta}$ is the tensor of inertia of the body. In particular, it is $I_{1,1}=I_{2,2}=I_{\Xi}$ and $I_{3,3}=I_{\Upsilon}$ for a cylindrical body.

[6] It follows from the definition of centre of mass: $\int\rho_{\xi}\,dm = \int\rho_{\eta}\,dm = \int\rho_{\zeta}\,dm = 0$

[7] See note 4.

Replacing (3.A.17.a) and (3.A.17.d) in (3.A.16) we finally obtain:

$$V_{Coriolis} = \underbrace{M\vec{V}\cdot\left(\vec{\omega}_s\times\vec{R}\right)+I_\Xi\omega_s\dot{\phi}\sin^2(\vartheta)}_{T_{Coriolis}}\underbrace{+I_\Upsilon\omega_s^2\cos(\vartheta)}_{U_{Coriolis}} \tag{3.A.18}$$

In (3.A.18) $V_{Coriolis}$ has been split up into a potential energy containing only the angle ϑ

$$U_{Coriolis} = I_\Upsilon\omega_s^2\cos(\vartheta) \tag{3.A.19}$$

and a "kinetic" energy containing also the velocities:

$$T_{Coriolis} = M\vec{V}\cdot\left(\vec{\omega}_s\times\vec{R}\right)+I_\Xi\omega_s\dot{\phi}\sin^2(\vartheta) \tag{3.A.20}$$

The centrifugal part $U_{centrifugal}$ has been named as a potential energy:

$$U_{centrifugal}=\frac{1}{2}\int(\vec{\omega}_s\times\vec{r})^2dm=\frac{1}{2}\int\left[\vec{\omega}_s\times\left(\vec{R}+\vec{\rho}\right)\right]^2dm \tag{3.A.21}$$

The integral appearing in (3.A.21) can be conveniently written as the sum of the following terms:

$$\int\left(\vec{\omega}_s\times\vec{R}\right)^2dm = M\left(\vec{\omega}_s\times\vec{R}\right)^2 \tag{3.A.22.a}$$

$$\int\left(\vec{\omega}_s\times\vec{\rho}\right)^2dm=\left[I_\Xi\sin^2(\vartheta)+I_\Upsilon\cos^2(\vartheta)\right]\omega_s^2 \tag{3.A.22.b}$$

$$\int\left(\vec{\omega}_s\times\vec{R}\right)\cdot\left(\vec{\omega}_s\times\vec{\rho}\right)dm=\left(\vec{\omega}_s\times\vec{R}\right)\cdot\int\left(\vec{\omega}_s\times\vec{\rho}\right)dm = 0\,^{8} \tag{3.A.22.c}$$

Substituting (3.A.22.a) and (3.A.22.b) in equation (3.A.21) the final expression for the centrifugal energy is obtained:

$$U_{centrifugal}=\frac{1}{2}M\left(\vec{\omega}_s\times\vec{R}\right)^2+\frac{1}{2}\left[I_\Xi\sin^2(\vartheta)+I_\Upsilon\cos^2(\vartheta)\right]\omega_s^2 \tag{3.A.23}$$

Collecting all these results, one ends up with the final form (3.A.24) for the Lagrange function:

$$L = T_{total} - U_{total} \tag{3.A.24}$$

where we have defined the total kinetic energy

$$T_{total}(\vartheta,\dot{\vartheta},\phi,\dot{\phi}) = T_{cinetical} + T_{Coriolis} = \frac{1}{2}M\vec{V}^2(\vartheta,\dot{\vartheta},\phi,\dot{\phi}) \tag{3.A.25}$$

$$+M\vec{V}(\vartheta,\dot{\vartheta},\phi,\dot{\phi})\cdot\left(\vec{\omega}_s\times\vec{R}(\vartheta,\phi)\right)+I_\Xi\omega_s\dot{\phi}\sin^2(\vartheta)+\frac{1}{2}I_\Upsilon\left(\dot{\phi}^2\sin^2(\vartheta)+\dot{\vartheta}^2\right)$$

and the total potential energy

[8] See note 4.

$$U_{\text{total}}(\vartheta,\phi) = U - U_{\text{centrifugal}} - U_{\text{Coriolis}} = U(\vartheta,\phi) - M\left(\vec{\omega}_s \times \vec{R}(\vartheta,\phi)\right)^2 \\ -\frac{1}{2}\left[I_\Xi \sin^2(\vartheta) + I_\Upsilon \cos^2(\vartheta) \right]\omega_s^2 - I_\Upsilon \omega_s^2 \cos(\vartheta) \tag{3.A.26}$$

APPENDIX 4.A:

TRANSFER FUNCTION IN THE NON-ROTATING FRAME.

In this section the label NR refers to the vectors in the non rotating frame while Rot to the same quantities in the rotating reference frame. $\vec{y}$ is the outputs vector (see equation (4.2)) and $\vec{u}$ the inputs one. Let us introduce the complex variables

$$Z^{Rot}(t) = y_1^{Rot}(t) + jy_2^{Rot}(t) \quad (4.A.1)$$

$$F^{NR}(t) = F_1^{NR}(t) + jF_2^{NR}(t) \quad (4.A.2)$$

Combining equation (B.1) with (4.23.a) and equation (4.A2) with (4.23.b), we obtain:

$$Z^{NR}(t) = y_1^{NR}(t) + jy_2^{NR}(t) = e^{j\omega_s t}\left(y_1^{Rot}(t) + jy_2^{Rot}(t)\right) = e^{j\omega_s t}Z^{Rot}(t) \quad (4.A3)$$

$$W^{Rot}(t) = u_1^{Rot}(t) + ju_2^{Rot}(t) = e^{-j\omega_s t}\left(F_1^{NR}(t) + jF_2^{NR}(t)\right) = e^{-j\omega_s t}F^{NR}(t) \quad (4.A4)$$

In the frequency domain, equations (4.A3) and (4.A4) can be written in the form:

$$Z^{NR}(s) = y_1^{Rot}(s - j\omega_s) + jy_2^{Rot}(s - j\omega_s) = Z^{Rot}(s - j\omega_s) \quad (4.A.5)$$

or else

$$Z^{NR}(s) = y_1^{NR}(s) + jy_2^{NR}(s) \quad (4.A.6)$$

Combining equations (4.A.5) and (4.A.6) we have:

$$y_1^{NR}(s) = \Re e\left[Z^{Rot}(s - j\omega_s)\right] \quad (4.A.7)$$

$$y_2^{NR}(s) = \Im m\left[Z^{Rot}(s - j\omega_s)\right]^1 \quad (4.A.8)$$

In a similar manner, we also have

$$w(s) = u_1^{Rot}(s) + ju_2^{Rot}(s) = F_1^{NR}(s + j\omega_s) + jF_2^{NR}(s + j\omega_s) = F^{NR}(s + j\omega_s) \quad (4.A.9)$$

with:

$$u_1^{Rot}(s) = \Re e\left[F^{NR}(s + j\omega_s)\right] \quad (4.A.10)$$

$$u_2^{Rot}(s) = \Im m\left[F^{NR}(s + j\omega_s)\right] \quad (4.A.11)$$

In section 4.2 we have evaluated the expression (4.5) for $y_i^{Rot}(s)$ in the rotating reference

[1] Let us introduce the complex function $K(s) = A(s)/B(s) + jC(s)/D(s)$, where A(s), B(s), C(s) and D(s) are polynomials with real and constant coefficients. We define $\Re e(K(s)) = A(s)/B(s)$ and $\Im m(K(s)) = C(s)/D(s)$.

frame as function of the s variable. We now evaluate them in s-$j\omega_s$; from (4.5), we have:

$$\begin{aligned} y_1^{Rot}(s-j\omega_s) &= H_{11}^{Rot}(s-j\omega_s)u_1(s-j\omega_s) + H_{12}^{Rot}(s-j\omega_s)u_2(s-j\omega_s) \\ &= H_{11}^{Rot}(s-j\omega_s)\Re e(F^{NR}(s)) + H_{12}^{Rot}(s-j\omega_s)\Im m(F^{NR}(s)) \\ &= H_{11}^{Rot}(s-j\omega_s)F_1^{NR}(s) + H_{12}^{Rot}(s-j\omega_s)F_2^{NR}(s) \end{aligned} \quad (4.A.12)$$

It is important to underline that $F_1(s)$ and $F_2(s)$ are "real" function in the sense of note 1 at the bottom of the previous page. In a similar manner, we have:

$$\begin{aligned} y_2^{Rot}(s-j\omega_s) &= H_{21}^{Rot}(s-j\omega_s)u_1(s-j\omega_s) + H_{22}^{Rot}(s-j\omega_s)u_2(s-j\omega_s) \\ &= H_{21}^{Rot}(s-j\omega_s)\Re e(F^{NR}(s)) + H_{22}^{Rot}(s-j\omega_s)\Im m(F^{NR}(s)) \\ &= H_{21}^{Rot}(s-j\omega_s)F_1^{NR}(s) + H_{22}^{Rot}(s-j\omega_s)F_2^{NR}(s) \end{aligned} \quad (4.A.13)$$

We collect the expressions (4.A.12) and (4.A.13) in a single equation:

$$\begin{bmatrix} y_1^{Rot}(s-j\omega_s) \\ y_2^{Rot}(s-j\omega_s) \end{bmatrix} = \begin{bmatrix} H_{11}^{Rot}(s-j\omega_s) & H_{12}^{Rot}(s-j\omega_s) \\ H_{21}^{Rot}(s-j\omega_s) & H_{22}^{Rot}(s-j\omega_s) \end{bmatrix} \cdot \begin{bmatrix} F_1^{NR}(s) \\ F_2^{NR}(s) \end{bmatrix} = H^{Rot}(s-j\omega_s) \cdot \begin{bmatrix} F_1^{NR}(s) \\ F_2^{NR}(s) \end{bmatrix} \quad (4.A.14)$$

Inserting the expressions (4.A.12) and (4.A.13) for $y_1^{Rot}(s-j\omega_s)$ and $y_2^{Rot}(s-j\omega_s)$ in (4.A.7) and (4.A.8), after some simple algebra, we obtain:

$$\begin{aligned} &y_1^{NR}(s) = \Re e\left(Z^{Rot}(s-j\omega_s)\right) = \Re e\left(y_1^{Rot}(s-j\omega_s) + jy_2^{Rot}(s-j\omega_s)\right) = \\ &\Re e\left\{H_{11}^{Rot}(s-j\omega_s)F_1^{NR}(s) + H_{12}^{Rot}(s-j\omega_s)F_2^{NR}(s) + j\left[H_{21}^{Rot}(s-j\omega_s)F_1^{NR}(s) + H_{22}^{Rot}(s-j\omega_s)F_2^{NR}(s)\right]\right\} \end{aligned} \quad (4.A.15)$$

$$\begin{aligned} &y_2^{NR}(s) = \Im m\left(Z^{Rot}(s-j\omega_s)\right) = \Im m\left(y_1^{Rot}(s-j\omega_s) + jy_2^{Rot}(s-j\omega_s)\right) = \\ &\Im m\left\{H_{11}^{Rot}(s-j\omega_s)F_1^{NR}(s) + H_{12}^{Rot}(s-j\omega_s)F_2^{NR}(s) + j\left[H_{21}^{Rot}(s-j\omega_s)F_1^{NR}(s) + H_{22}^{Rot}(s-j\omega_s)F_2^{NR}(s)\right]\right\} \end{aligned} \quad (4.A.16)$$

We may write equations (4.A.15) and (4.A.16) in a more manageable manner:

$$\begin{aligned} y_1^{NR}(s) &= \Re e\left[H_{11}^{Rot}(s-j\omega_s) + jH_{21}^{Rot}(s-j\omega_s)\right]F_1^{NR}(s) \\ &+ \Re e\left[H_{12}^{Rot}(s-j\omega_s) + jH_{22}^{Rot}(s-j\omega_s)\right]F_2^{NR}(s) \end{aligned} \quad (4.A.17)$$

$$\begin{aligned} y_2^{NR}(s) &= \Im m\left[H_{11}^{Rot}(s-j\omega_s) + jH_{21}^{Rot}(s-j\omega_s)\right]F_1^{NR}(s) \\ &+ \Im m\left[H_{12}^{Rot}(s-j\omega_s) + jH_{22}^{Rot}(s-j\omega_s)\right]F_2^{NR}(s) \end{aligned} \quad (4.A.18)$$

or, in a compact matrix form:

$$\begin{bmatrix} y_1^{NR}(s) \\ y_2^{NR}(s) \end{bmatrix} = \begin{bmatrix} \Re e\left\{H_{11}^{Rot}(s-j\omega_s) + jH_{21}^{Rot}(s-j\omega_s)\right\} & \Re e\left\{H_{12}^{Rot}(s-j\omega_s) + jH_{22}^{Rot}(s-j\omega_s)\right\} \\ \Im m\left\{H_{11}^{Rot}(s-j\omega_s) + jH_{21}^{Rot}(s-j\omega_s)\right\} & \Im m\left\{H_{12}^{Rot}(s-j\omega_s) + jH_{22}^{Rot}(s-j\omega_s)\right\} \end{bmatrix} \cdot \begin{bmatrix} F_1^{NR}(s) \\ F_2^{NR}(s) \end{bmatrix} \quad (4.A.19)$$

which is the transfer function for the non rotating outputs $Y^{NR}(s)$ in response to the non rotating forces $F^{NR}(s)$.

APPENDIX 4.B:

SELF-CENTRING.

We may study the dynamical behaviour of the simple rotor in figure 4.11 by following the steps in appendix 3.A. Equations (3.A.24) in appendix 3.A, together with equations (3.A.25) and (3.A.26) yield the Lagrange function of a rigid body in a rotating reference frame (O,ξ,η,z). O is the origin of the rotating reference frame; the $\hat{z}$ axis coincides with that of the inertial frame. Axes $\hat{\xi}$ and $\hat{\eta}$ rotate in the x-y plane with angular velocity ω_s. The position vector of the centre of mass is $\vec{r}=[\xi,\eta,z]$. We conveniently write all the vectors in the (O,ξ,η,z) reference frame in terms of their components in the (O,x,y,z) frame by means of the rotation:

$$\begin{cases} X=\xi\cos(\omega_s t)-\eta\sin(\omega_s t) \\ Y=\xi\sin(\omega_s t)+\eta\cos(\omega_s t) \\ Z=z \end{cases} \qquad (4.B.1)$$

The problem can be studied using only two generalized coordinates[1]. We have chosen as generalized coordinates the two angles ϑ' and ϕ' shown in figure 4.11. ϑ' is the angle between the KM arm and the vertical axis z and it runs in the interval [0, π].; ϕ' is the angle from the ξ axis to the projection of the arm KM on the ξ-η plane of the rotating reference frame (O, ξ,η,z) and runs in the interval [0, 2π]. The vector $\vec{r}$ starting from the origin O and pointing to the centre of mass M of the body has components:

$$\begin{cases} \xi=\varepsilon+L\sin(\vartheta')\cos(\phi') \\ \eta=\varepsilon+L\sin(\vartheta')\sin(\phi') \\ z=-L\cos(\vartheta') \end{cases} \qquad (4.B.2)$$

It is possible to write the Lagrangean of the system following the procedure described in appendix 3.A. In particular equations (3.A.15), (3.A.18) and (3.A.23) become:

$$T(\vartheta',\dot{\vartheta}',\phi',\dot{\phi}')=\frac{1}{2}\left(mL^2+I_\Xi\right)\left(\dot{\phi}'^2\sin^2(\vartheta')+\dot{\vartheta}'^2\right) \qquad (4.B.3)$$

$$V_{cc}(\vartheta',\dot{\vartheta}',\phi',\dot{\phi}')=m\omega_s\left\{L^2\dot{\phi}'\sin^2(\vartheta')+\varepsilon L\left[\cos(\vartheta')\sin(\phi')\dot{\vartheta}'+\sin(\vartheta')\cos(\phi')\dot{\phi}'\right]\right\} + I_\Xi\omega_s\dot{\phi}'\sin^2(\vartheta')+I_\Upsilon\omega_s^2\cos(\vartheta') \qquad (4.B.4)$$

$$V_c(\vartheta',\dot{\vartheta}',\phi',\dot{\phi}')=\frac{1}{2}m\omega_s^2L\left[L\sin^2(\vartheta')+2\varepsilon\sin(\vartheta')\cos(\phi')\right]+\frac{1}{2}\left(I_\Xi-I_\Upsilon\right)\omega_s^2\sin^2(\vartheta') \qquad (4.B.5)$$

[1] The motion of a rigid body is described by six degrees of freedom. The presence of the central suspension prevents the bodies from performing translational motions, thereby introducing v1=3 constraints. The presence of the motor, forces the body to rotate at a constant angular velocity, introducing v2=1 new constraints. At the end, the degrees of freedom for the model amounts to n=c-v1-v2=6-4=2. Hence the problem can be studied using only two generalized coordinates.

where I_Ξ and I_Υ are the moment of inertia along the principal axis of the body with cylindrical symmetry. Then, the sum of the elastic and gravitational energy is given by:

$$U(\vartheta',\dot{\vartheta}',\phi',\dot{\phi}')=-mgL\cos(\vartheta')+\frac{1}{2}k\ell^2\sin^2(\vartheta')\left(\cos^2(\phi')+\Lambda\sin^2(\phi')\right) \qquad (4.B.6)$$

(we have considered non-isotropic suspensions with $k_\eta=\Lambda k_\xi=\Lambda k$). The equilibrium position is determined from the equations:

$$\begin{cases} -\partial\left(V_c-V\right)/\partial\vartheta'\big|_{\vartheta_0',\phi_0'}=0 \\ -\partial\left(V_c-V\right)/\partial\phi'\big|_{\vartheta_0',\phi_0'}=0 \end{cases} \qquad (4.B.7)$$

These equations may be written in terms of the generalized coordinates as it follows:

$$\begin{cases} \frac{1}{2}m\omega_s^2L\left(L\sin(2\vartheta')+2\varepsilon\cos(\vartheta')\cos(\phi')\right)-mgL\sin(\vartheta')-\frac{1}{2}k\ell^2\sin(2\vartheta')\cos^2(\phi') \\ -\frac{1}{2}\Lambda k\ell^2\sin(2\vartheta')\sin^2(\phi')+\frac{1}{2}\left(I_\Xi-I_\Upsilon\right)\omega_s^2\sin(2\vartheta')-I_\Upsilon\omega_s^2\sin(\vartheta')=0 \\ -\frac{1}{2}m\omega_s^2L\left(2\varepsilon\sin(\vartheta')\sin(\phi')\right)+\frac{1}{2}k(1-\Lambda)\ell^2\sin^2(\vartheta')\sin(2\phi')=0 \end{cases} \qquad (4.B.8)$$

In the limit of small angel ϑ' is found :

$$\vartheta_0'=\mp\frac{m\omega_s^2L\varepsilon}{\omega_s^2\left(mL^2+I_\Xi-2I_\Upsilon\right)-mL^2\left(\frac{g}{L}+\frac{k\ell^2}{mL^2}\right)};\ \phi_0'=0,\pi \qquad (4.B.9)$$

Let us now introduce the natural frequency for the non spinning point-like rotor (the system in figure 4.11 when M is a point-like mass):

$$\omega_n=\sqrt{\frac{g}{L}+\frac{k\ell^2}{mL^2}}\,. \qquad (4.B.10)$$

The effective length $L'^2=L^2+\left(I_\Xi-2I_\Upsilon\right)/m$ takes into account the extended nature of the suspended body ($L'=L$ for a point-like mass)[2]. By introducing ω_n and L' in the expression for ϑ_0', equation (4.B.9) becomes:

$$\vartheta_0'=\mp\frac{\omega_s^2L\varepsilon}{\omega_s^2L'^2-L^2\omega_n^2}=\mp\frac{\varepsilon}{L}\frac{\omega_s^2}{\omega_s^2\left(L'^2/L^2\right)-\omega_n^2} \qquad (4.B.11)$$

[2] Only if $L^2+I_\Xi/m>2I_\Upsilon/m$ (as in the case of GGG) L' can be defined.

APPENDIX 5.A:

DATA ANALYSIS IN THE ROTATING FRAME - FOURIER FILTER.

Starting from the vector Φ_ξ (5.3), we introduce the 8 vectors of data $\Phi_\xi 1$, $\Phi_\xi 2$,...; $\Phi_\xi 8$ (i.e. $\Phi_\xi j$ with j=1,2,...,8) defined as follows:

$\Phi_\xi 1=[\Phi_\xi(1), \Phi_\xi(1+8=9), \Phi_\xi(1+2\cdot 8=17),\ldots, \Phi_\xi(1+n\cdot 8),...]$ (5.A.1.a)

$\Phi_\xi 2=[\Phi_\xi(2), \Phi_\xi(2+8=10), \Phi_\xi(2+2\cdot 8=18),\ldots, \Phi_\xi(2+n\cdot 8),...]$ (5.A.1.b)

$\Phi_\xi 3=[\Phi_\xi(3), \Phi_\xi(3+8=11), \Phi_\xi(3+2\cdot 8=19),\ldots, \Phi_\xi(3+n\cdot 8),...]$ (5.A.1.c)

$\Phi_\xi 4=[\Phi_\xi(4), \Phi_\xi(4+8=12), \Phi_\xi(4+2\cdot 8=20),\ldots, \Phi_\xi(4+n\cdot 8),...]$ (5.A.1.d)

$\Phi_\xi 5=[\Phi_\xi(5), \Phi_\xi(5+8=13), \Phi_\xi(5+2\cdot 8=21),\ldots, \Phi_\xi(5+n\cdot 8),...]$ (5.A.1.e)

$\Phi_\xi 6=[\Phi_\xi(6), \Phi_\xi(6+8=14), \Phi_\xi(6+2\cdot 8=22),\ldots, \Phi_\xi(6+n\cdot 8),...]$ (5.A.1.f)

$\Phi_\xi 7=[\Phi_\xi(7), \Phi_\xi(7+8=15), \Phi_\xi(7+2\cdot 8=23),\ldots, \Phi_\xi(7+n\cdot 8),...]$ (5.A.1.g)

$\Phi_\xi 8=[\Phi_\xi(8), \Phi_\xi(8+8=16), \Phi_\xi(8+2\cdot 8=24),\ldots, \Phi_\xi(8+n\cdot 8),...]$ (5.A.1.h)

$\Phi_\xi j(n)$ equals the time sample of the continuous process $\Phi_\xi(t)$, but the time constant is now $8T_C$:

$\Phi_\xi j=[\Phi_\xi(j), \Phi_\xi(j+8),\ldots, \Phi_\xi(j+n\cdot 8),...]$ (5.A.1.i)

If $\Phi_\xi(1)$ is sampled at the time $t=t_0$, the k-th element of Φ_ξ is sampled at the time:

$t(k) = t_0+(k-1)T_C$ (5.A.2)

Instead, the k-th element of the vector $\Phi_\xi j$ is sampled at the time:

$tj(k) = t_0+(j-1)T_C+8(k-1)T_C = t_0+(j+8k-9)T_C$ (5.A.3)

If the measurements are performed for N>>1 spin periods, the total integration time is:

$T_{tot}=32NT_C>>T_C$ (5.A.4)

while the total integration time for the sampled signal $\Phi_\xi j$ is:

$Tj_{tot}=t(32N-(8-j))-t_0$ (5.A.5)

By combining equations (5.A.4) and (5.A.5), it follows:

$Tj_{tot}=t(32N-(8-j))-t_0= t_0+T_{tot}-(8-j)T_C-t_0= T_{tot}-(8-j)T_C \approx T_{tot}$ (5.A.6)

Equation (5.A.6) shows that the temporal duration of $\Phi_\xi j$ is the same as that of Φ_ξ, even though $\Phi_\xi j$ is a 4N components vector of sampled data while Φ_ξ a 32N components vector. Let us now introduce the Fourier transform of the function f(t):

$$\hat{f}(\omega) = \Im_f(\omega) = \int f(t) e^{-j\omega t} dt \quad (5.A.7)$$

The Fourier transform, in essence, decomposes a function into sinusoids of different frequency which sum to the original waveform. It is often useful to think of functions and their transforms as occupying two domains. They are referred to as the time and frequency

domains respectively. Operations performed in one domain have corresponding operations in the other. A band-limited signal is a signal, f(t), which has no spectral components beyond a frequency ω_B Hz; that is, $\hat{f}(\omega) = 0$ for $|\omega| > 2\omega_B$. The sampling theorem states that this real signal can be reconstructed without error from samples taken uniformly at a rate higher than $2\omega_B$ samples per second. This minimum sampling frequency, $\nu_N = 2\omega_B$ Hz, is called the Nyquist frequency.

Because a computer works only with discrete data, numerical computation of the Fourier transform of f(t) requires discrete sample values of it. In addition, a computer can compute the transform $\hat{f}(\omega)$ only at discrete values of ω, that is, it can only provide discrete samples of the transform. The Fast Fourier Transform (FFT) is a discrete algorithm developed by Tukey and Cooley which can be used to compute transforms and inverse transforms of appropriately-sampled data.

Starting from the definition (5.A.8), it is possible to define the FFT of a N-components vector. The element of the vector are the samples of the continuous time process f(t), taken uniformly at a rate of ν_c samples per second (sampling period: $t_C=1/\nu_c$):

$$\hat{f}(\omega) = \sum_{m=1}^{N} f\left((m-1)t_C + t_0\right) e^{-j\omega\left((m-1)t_C+t_0\right)} \qquad (5.A.9)$$

Let us introduce the shifted function g(t), i.e. $g(t)=f(t+T_A)$. The time shifting property states that the Fourier transform of a shifted function is just the transform of the un-shifted function multiplied by an exponential factor having a linear phase:

$$\hat{g}(\omega) = e^{j\omega t_A}\hat{f}(\omega) \qquad (5.A.10)$$

$$\hat{g}(\omega) = e^{j\omega T_A}\sum_{m=1}^{N} f\left((m-1)t_C + t_0\right) e^{-j\omega\left((m-1)t_C+t_0\right)} \qquad (5.A.11)$$

We can now apply the FFT algorithm to a deterministic signal S(t), not affected by any kind of noise. The discrete time signal S1 is obtained starting from S(t) in the same manner as $\Phi_\xi 1$ is obtained from Φ_ξ (t) (see equation (5.A.1.a)); the signal S2 is obtained in the same manner as $\Phi_\xi 2$ (5.A.2.b). Hence S2 is shifted by $T_A=T_C$ (see (5.2)) with respect to S1 and they are sampled with sampling period $t_C=8T_C$. By considering equations (5.A.9) and (5.A.11), it follows:

$$\hat{S}1(\omega) = \sum_{m} S\left(8(m-1)T_C + t_0\right) e^{-j\omega\left(8(m-1)T_C+t_0\right)} \qquad (5.A.12)$$

$$\hat{S}2(\omega) = e^{j\omega T_C}\hat{S}1(\omega) \qquad (5.A.13)$$

In a similar manner we can extract the sub-vector Ss from S; Ss is shifted by $T_A=(s-1)T_C$ with respect to S1 and sampled with sampling period $t_C=8T_C$. Then, it follows:

$$\hat{S}s(\omega) = e^{j\omega(s-1)T_C}\hat{S}1(\omega) \qquad (5.A.14)$$

From equation (5.A.4) it follows that the smaller frequency component which can be identified in the frequency domain is:

$$\omega_{min} = \frac{2\pi}{T_{tot}} = \frac{2\pi}{32NT_C} \qquad (5.A.15)$$

Then, transform $\hat{S}s(\omega)$ is computed only at discrete values of ω, namely:

$$\omega(k) = (k-1)\omega_{min} \quad k = 1, 2, ..., 2N \tag{5.A.16}$$

In particular, the k-th frequency components are:

$$\hat{S}1(k) = \sum_m S\left(8(m-1)T_C + t_0\right) e^{-j\frac{2\pi}{32NT_C}(k-1)\left(8(m-1)T_C + t_0\right)} \tag{5.A.17.a}$$

and:

$$\hat{S}s(k) = e^{j\frac{2\pi}{32N}(k-1)(s-1)}\hat{S}1(k) \tag{5.A.17.b}$$

We can now apply these concepts to our problem. The real signal $\Phi_\xi(t)$ acquired by the capacitance bridge is a noisy signal, i.e. it can be seen as the superimposition of an ideal deterministic signal S(t) and some random noise n(t). The vectors n1, n2,…,ns are obtained from the noise in the same manner as S1, S2,…,Ss are obtained from S(t), but they are not correlated. Equation (5.A.17.b) can be now written in a more general manner, namely:

$$\hat{\Phi}s(k) = \hat{S}s(k) + \hat{n}s(k) = e^{j\frac{2\pi}{32N}(k-1)(s-1)}\hat{S}1(k) + \hat{n}s(k) \tag{5.A.18}$$

We can define the reconstructed signal as:

$$\hat{R}_\xi(k) = \frac{\sum_{s=1}^{8} e^{-j\frac{2\pi}{32N}(k-1)(s-1)}\hat{\Phi}s(k)}{8} \tag{5.A.19}$$

By combining equations (5.A.18) and (5.A.19), we obtain:

$$\hat{R}_\xi(k) = \frac{8\hat{S}1(k)}{8} + \frac{\sum_{s=1}^{8} e^{-j\frac{2\pi}{32N}(k-1)(s-1)}\hat{n}s(k)}{8} = \hat{S}1(k) + \hat{\tilde{n}}(k) \tag{5.A.20}$$

Clearly, if S(n) is sampled at frequency $1/(8T_C)$ it coincide with S1(n) ($\hat{S}(\omega) = \hat{S}1(\omega)$) and then:

$$\hat{R}_\xi(k) = \hat{S}1(k) + \hat{\tilde{n}}(k) = \hat{S}(k) + \hat{\tilde{n}}(k) \tag{5.A.21}$$

By performing the inverse Fourier transform, the reconstructed signal in the time domain is obtained, i.e R_ξ. R_ξ is a discrete time process sampled at frequency $1/(8T_C)$; its k-th component can be written as $R_\xi(k) = S(k) + \tilde{n}(k)$ (see equation (5.A.21)), i.e. it is the superimposition of the ideal deterministic signal S and the noise $\tilde{n}$, sampled at frequency $\nu_C/8$. It is important to notice that the reconstructed signal $R_\xi(k)$ is closer to the ideal deterministic signal S than the original signal $\Phi_\xi(k)$ was, since the noise has been partly reduced by the Fourier filter:

$$\left|\hat{\tilde{n}}(k)\right| \sim \frac{\left|\hat{n}(k)\right|}{\sqrt{8}} \tag{5.A.22}$$

$R_\eta(k)$ is the reconstructed signal obtained starting from the signal Φ_η acquired by the capacitance bridge sensitive along η direction. Note that it is not possible to extract more than m=8 sub-vectors from Φ_ξ because the corresponding sampling frequency ν_C/m would not be in order to properly reconstruct the signal.

APPENDIX 5.B:

THE σ+ AND σ– FUNCTIONS.

In order to show that the Fourier Transform of the signal σ+ contains only the spectral line corresponding to the forward whirling (i.e. a peak at frequency ω_2), while the Fourier transform of σ- contains only the line corresponding to the backward whirling at frequency ω_1, we evaluate the values of their tails in correspondence of the whirling motion frequencies:

$$\sigma_+(\omega=\omega_1)=\frac{1}{\sqrt{2}}\left\{\Im_{X_{nr}}(\omega=\omega_1)+j\Im_{Y_{nr}}(\omega=\omega_1)\right\}=\sigma_{+1}(\omega=\omega_1)+\sigma_{+2}(\omega=\omega_1) \quad (5.B.1)$$

$$\sigma_-(\omega=\omega_1)=\frac{1}{\sqrt{2}}\left\{\Im_{X_{nr}}(\omega=\omega_1)-j\Im_{Y_{nr}}(\omega=\omega_1)\right\}=\sigma_{-1}(\omega=\omega_1)+\sigma_{-2}(\omega=\omega_1) \quad (5.B.2)$$

where:

$$\sigma_{+1}(\omega=\omega_1)=\frac{1}{\sqrt{2}}\left\{\Im_{X_{nr1}}(\omega=\omega_1)+j\Im_{Y_{nr1}}(\omega=\omega_1)\right\} \quad (5.B.3)$$

$$\sigma_{-1}(\omega=\omega_1)=\frac{1}{\sqrt{2}}\left\{\Im_{X_{nr1}}(\omega=\omega_1)-j\Im_{Y_{nr1}}(\omega=\omega_1)\right\} \quad (5.B.4)$$

$$\sigma_{+2}(\omega=\omega_1)=\frac{1}{\sqrt{2}}\left\{\Im_{X_{nr2}}(\omega=\omega_1)+j\Im_{Y_{nr2}}(\omega=\omega_1)\right\} \quad (5.B.5)$$

$$\sigma_{-2}(\omega=\omega_1)=\frac{1}{\sqrt{2}}\left\{\Im_{X_{nr2}}(\omega=\omega_1)-j\Im_{Y_{nr2}}(\omega=\omega_1)\right\} \quad (5.B.6)$$

We may now write (5.B.3) expressly in terms of the whirling parameters (amplitudes, frequencies and time constants):

$$\left|\sigma_{+1}(\omega=\omega_1)\right|=\frac{1}{\sqrt{2}}\left\{A_1\tau_1\frac{1}{\sqrt{1+4\omega_1^2\tau_1^2}}\right\} \quad (5.B.7)$$

Since $\omega_1\tau_1=2Q$ and Q>>1, the previous equality can be simplified in the form:

$$\left|\sigma_{+1}(\omega=\omega_1)\right|=\frac{1}{\sqrt{2}}\left\{A_1\tau_1\frac{1}{\sqrt{1+16Q^2}}\right\}\sim\frac{1}{\sqrt{2}}\frac{A_1\tau_1}{4Q} \quad (5.B.8)$$

In the same manner it follows:

$$\left|\sigma_{-1}(\omega=\omega_1)\right|=\frac{1}{\sqrt{2}}A_1\tau_1 \quad (5.B.9)$$

$$\left|\sigma_{+2}\left(\omega=\omega_1\right)\right|=\frac{1}{\sqrt{2}}\left\{A_2\tau_2\frac{\sqrt{1+(\omega_1+\omega_2)^2\tau_2^2}}{\sqrt{\left\{\left[1+\tau_2^2\left(\omega_2^2-\omega_1^2\right)\right]^2+4\omega_1^2\tau_2^2\right\}}}\right\} \tag{5.B.10}$$

Let us now introduce the non dimensional parameter $\alpha\sim 0.1$, so that $\omega_1=\omega_2(1-\alpha)$ and $\omega_1^2=\omega_2^2(1-2\alpha)$. By introducing it in (5.B.10), we have:

$$\left|\sigma_{+2}\left(\omega=\omega_1\right)\right|\sim\frac{1}{\sqrt{2}}\left\{A_2\tau_2\frac{\sqrt{1+4\omega_2^2\tau_2^2}}{\sqrt{\left\{\left[1+\tau_2^2\left(2\alpha\omega_2^2\right)\right]^2+4\omega_2^2(1-2\alpha)\tau_2^2\right\}}}\right\} \tag{5.B.11}$$

$$\sim\frac{1}{\sqrt{2}}A_2\tau_2\frac{\sqrt{1+16Q^2}}{\sqrt{\left[1+64\alpha^2Q^4+16(1-\alpha)Q^2\right]}}$$

In the limit Q>>1, we have $(4\alpha^2Q^2)>>1$ and then $64\alpha^2Q^4=16(4\alpha^2Q^2)Q^2>>16Q^2$:

$$\left|\sigma_{+2}\left(\omega=\omega_1\right)\right|\sim\frac{1}{\sqrt{2}}A_2\tau_2\frac{\sqrt{1+16Q^2}}{\sqrt{1+64\alpha^2Q^4}}\sim\frac{1}{\sqrt{2}}A_2\tau_2\frac{4Q}{8\alpha Q^2} \tag{5.B.12}$$

Finally, the magnitude of σ_{+2} is evaluated in correspondence of the frequency ω_1:

$$\left|\sigma_{+2}\left(\omega=\omega_1\right)\right|\sim\frac{1}{\sqrt{2}}A_2\tau_2\frac{1}{2\alpha Q} \tag{5.B.13}$$

Following the same procedure, the ω_1-component of $\sigma_{-2}(\omega)$ obtained:

$$\left|\sigma_{-2}\left(\omega=\omega_1\right)\right|\sim\frac{1}{\sqrt{2}}\left\{A_2\tau_2\frac{\sqrt{1+(\alpha\omega_2)^2\tau_2^2}}{\sqrt{\left\{\left[1+\tau_2^2\left(\omega_2^2-\omega_1^2\right)\right]^2+4\omega_1^2\tau_2^2\right\}}}\right\}\sim\frac{1}{\sqrt{2}}A_2\tau_2\frac{2\alpha Q}{8\alpha Q^2} \tag{5.B.14}$$

and then:

$$\left|\sigma_{-2}\left(\omega=\omega_1\right)\right|\sim\frac{1}{\sqrt{2}}A_2\tau_2\frac{1}{4Q} \tag{5.B.15}$$

We also evaluate the magnitude of σ+ and σ- at the frequency ω_2 (whirl forward); the results are listed below:

$$\left|\sigma_{+2}\left(\omega=\omega_2\right)\right|\sim\frac{1}{\sqrt{2}}A_2\tau_2 \tag{5.B.16}$$

$$\left|\sigma_{-2}\left(\omega=\omega_2\right)\right|\sim\frac{1}{\sqrt{2}}A_2\tau_2\frac{1}{4Q} \tag{5.B.17}$$

$$\left|\sigma_{+1}\left(\omega=\omega_2\right)\right| \sim \frac{1}{\sqrt{2}} A_1 \tau_1 \frac{1}{2\alpha Q} \tag{5.B.18}$$

$$\left|\sigma_{-1}\left(\omega=\omega_1\right)\right| \sim \frac{1}{\sqrt{2}} A_1 \tau_1 \frac{1}{4Q} \tag{5.B.19}$$

The amplitudes of (5.B.9) and (5.B.16) are at least two orders of magnitude larger than the amplitudes of the other terms (depressed by a factor 1/Q). We thus have that only the peak at frequency ω_2 (5.B.16) is present in σ+, while the spectral component at frequency ω_1 is negligible. Instead, σ- has only a peak at frequency ω_1 (5.B.9).

APPENDIX 8.A:

THE GGG ELECTRONIC CIRCUITS.

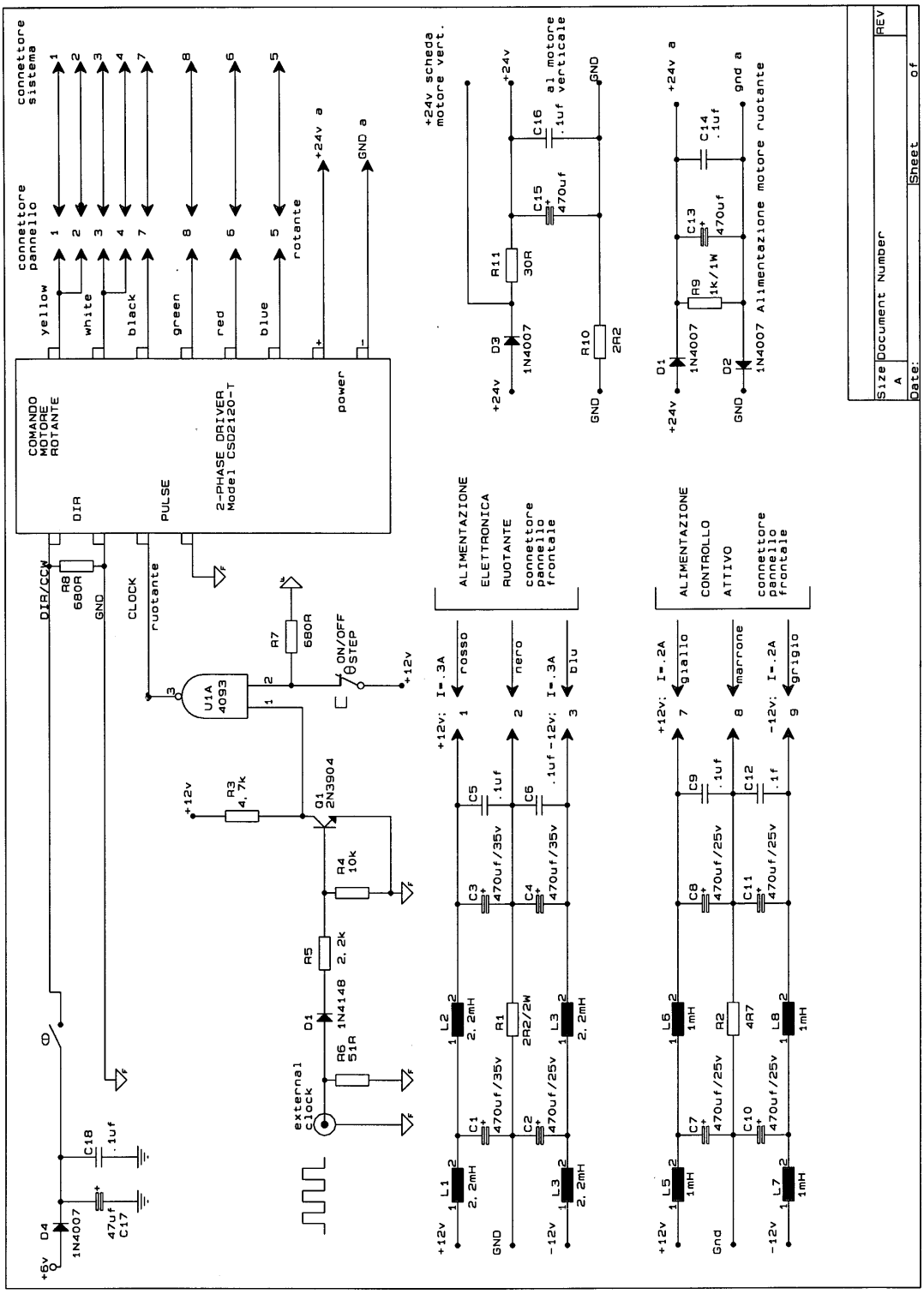

Scheme A: Power Supply and Motor Driver.

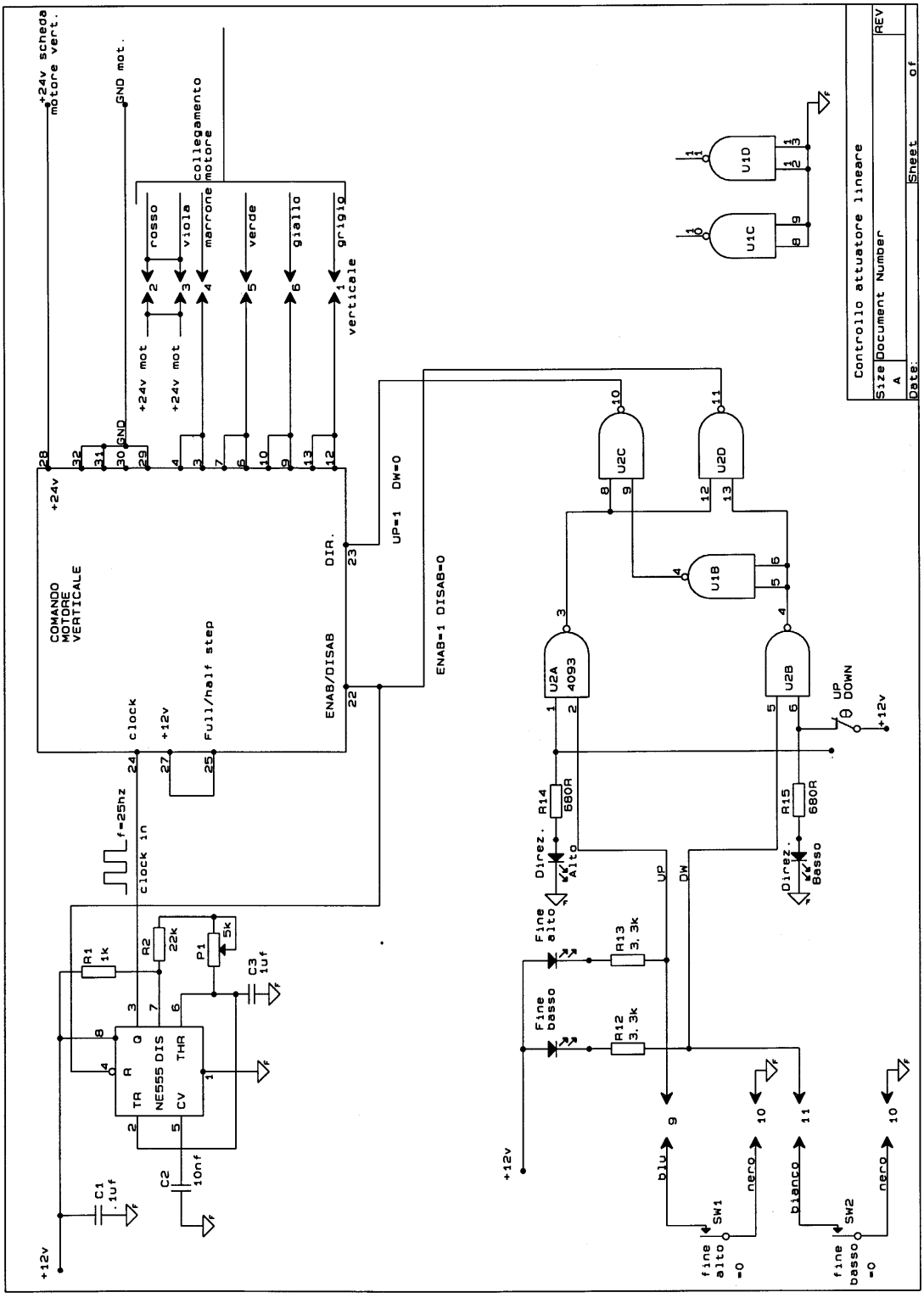

Scheme B: Passive damper driver.

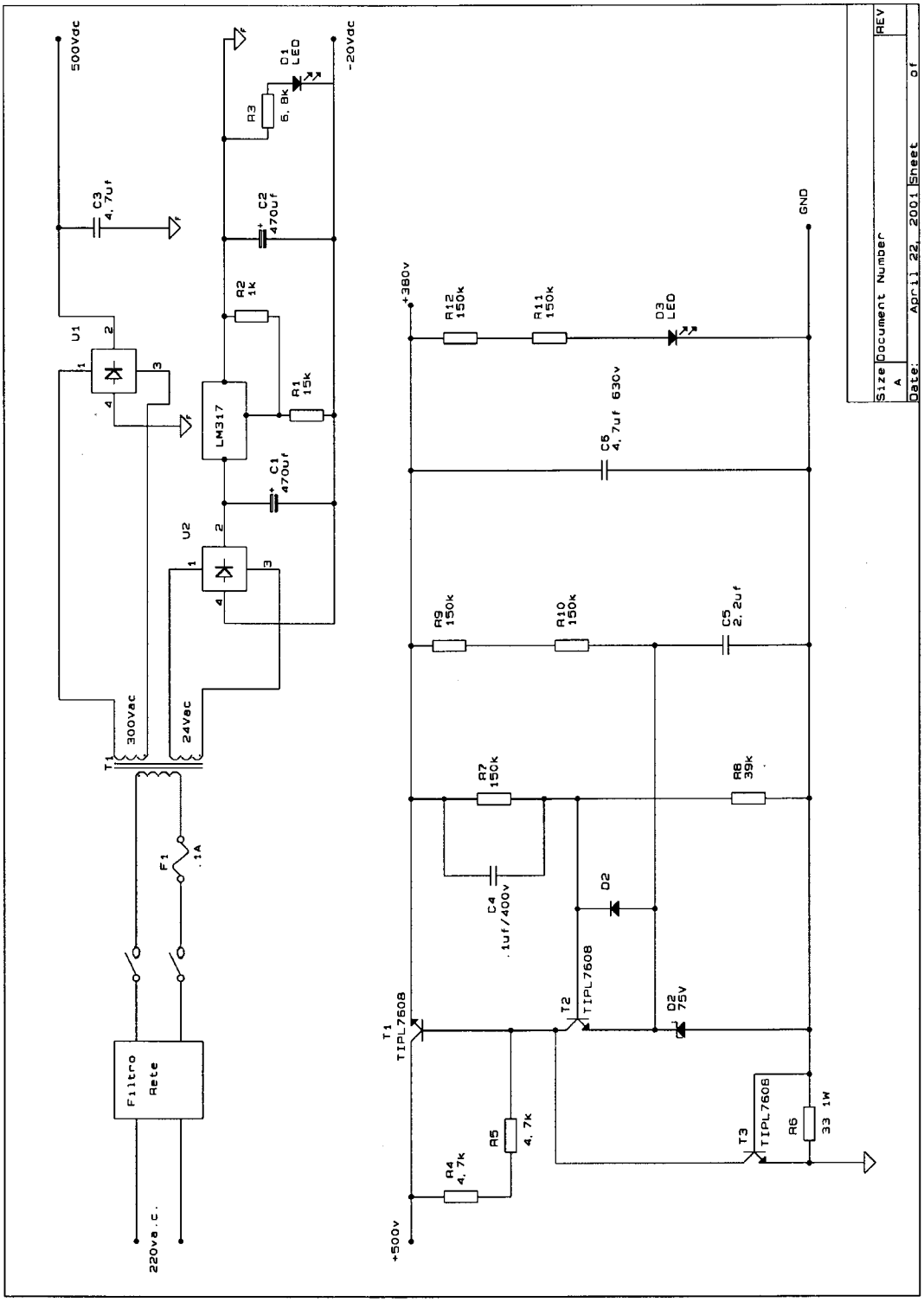

Scheme C: Active control of whirls. High Voltage Power Supply.

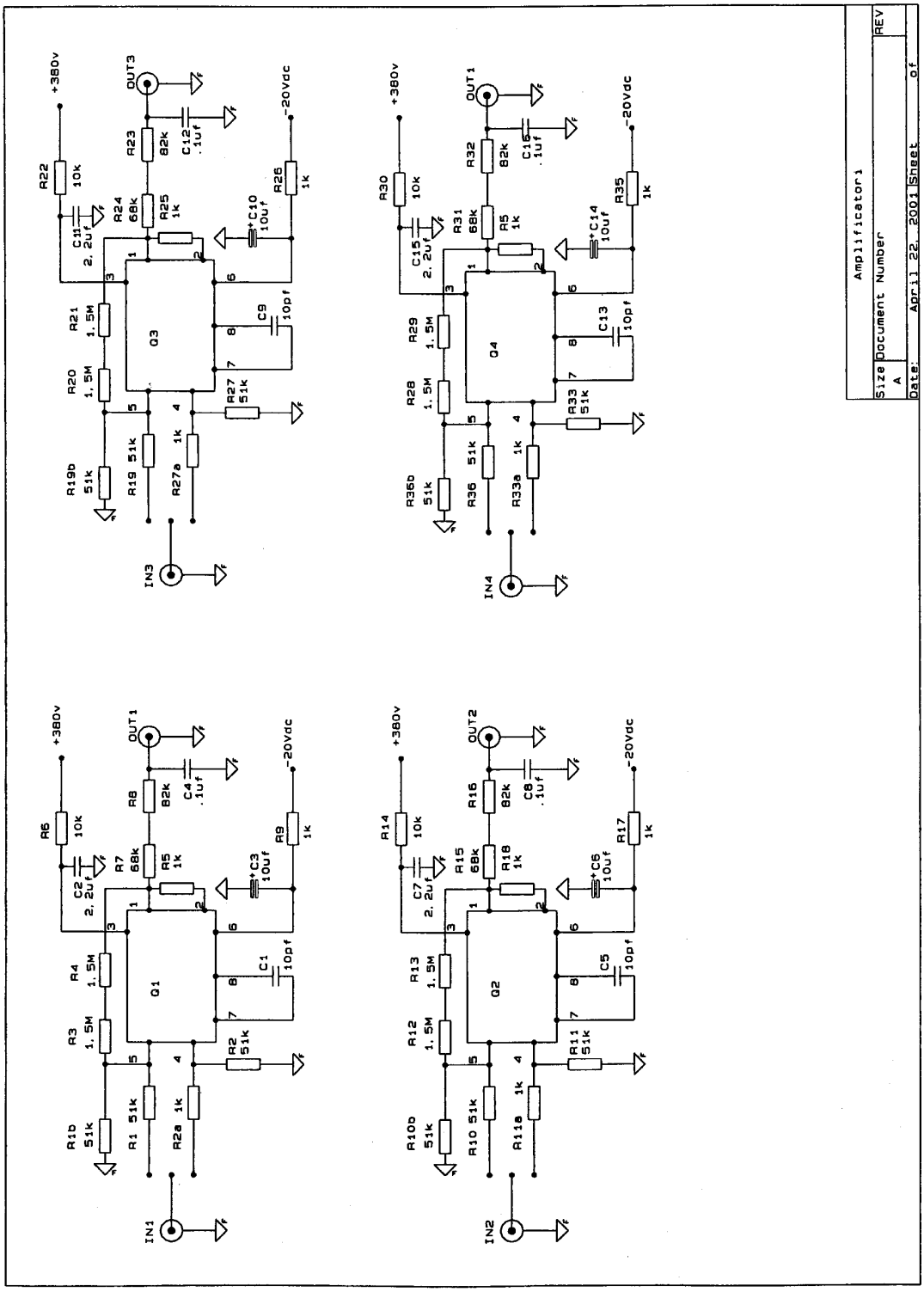

Scheme D: Active control of whirls. Amplifiers.

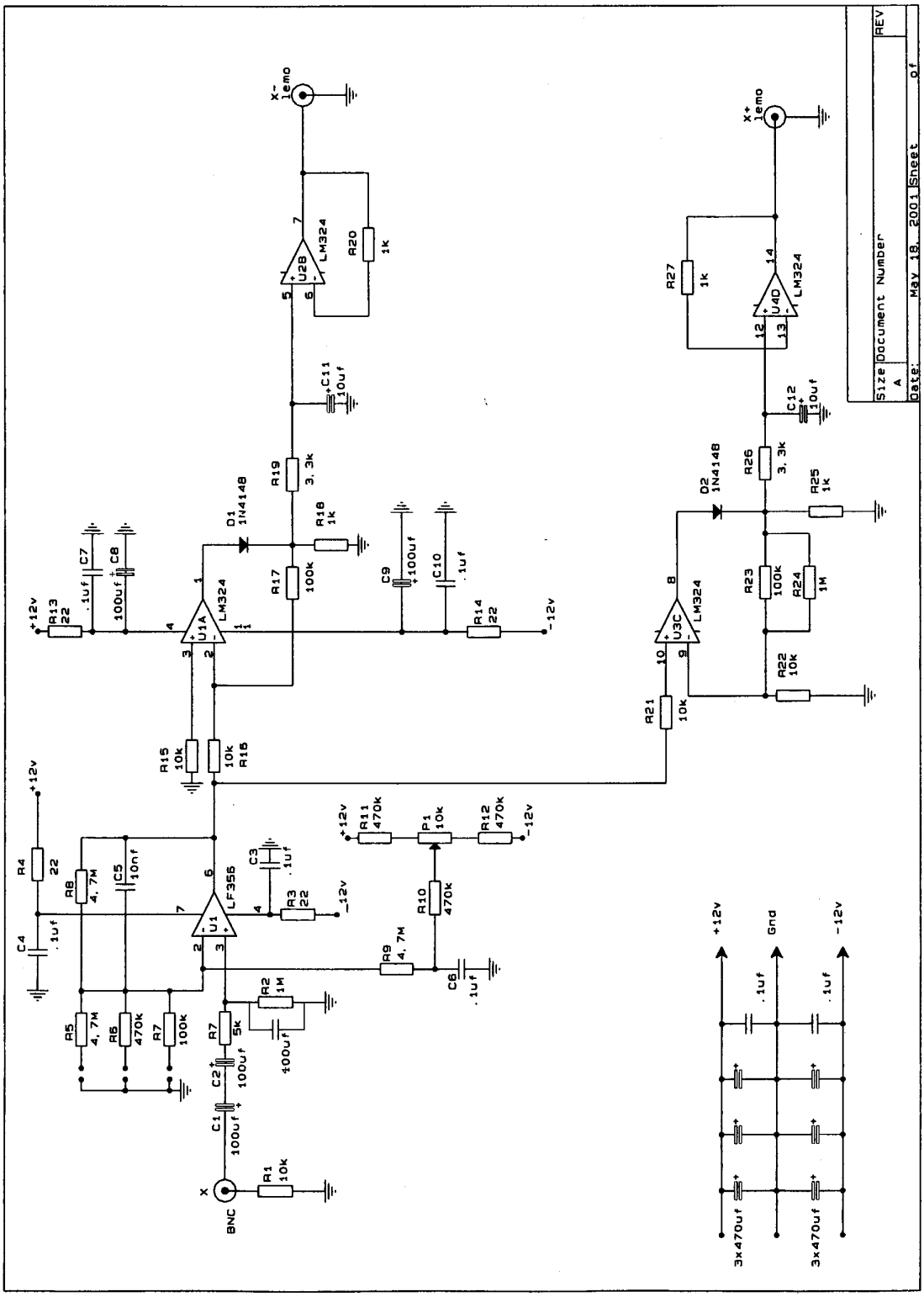

Scheme E: Active control of whirls. X→X+, X-

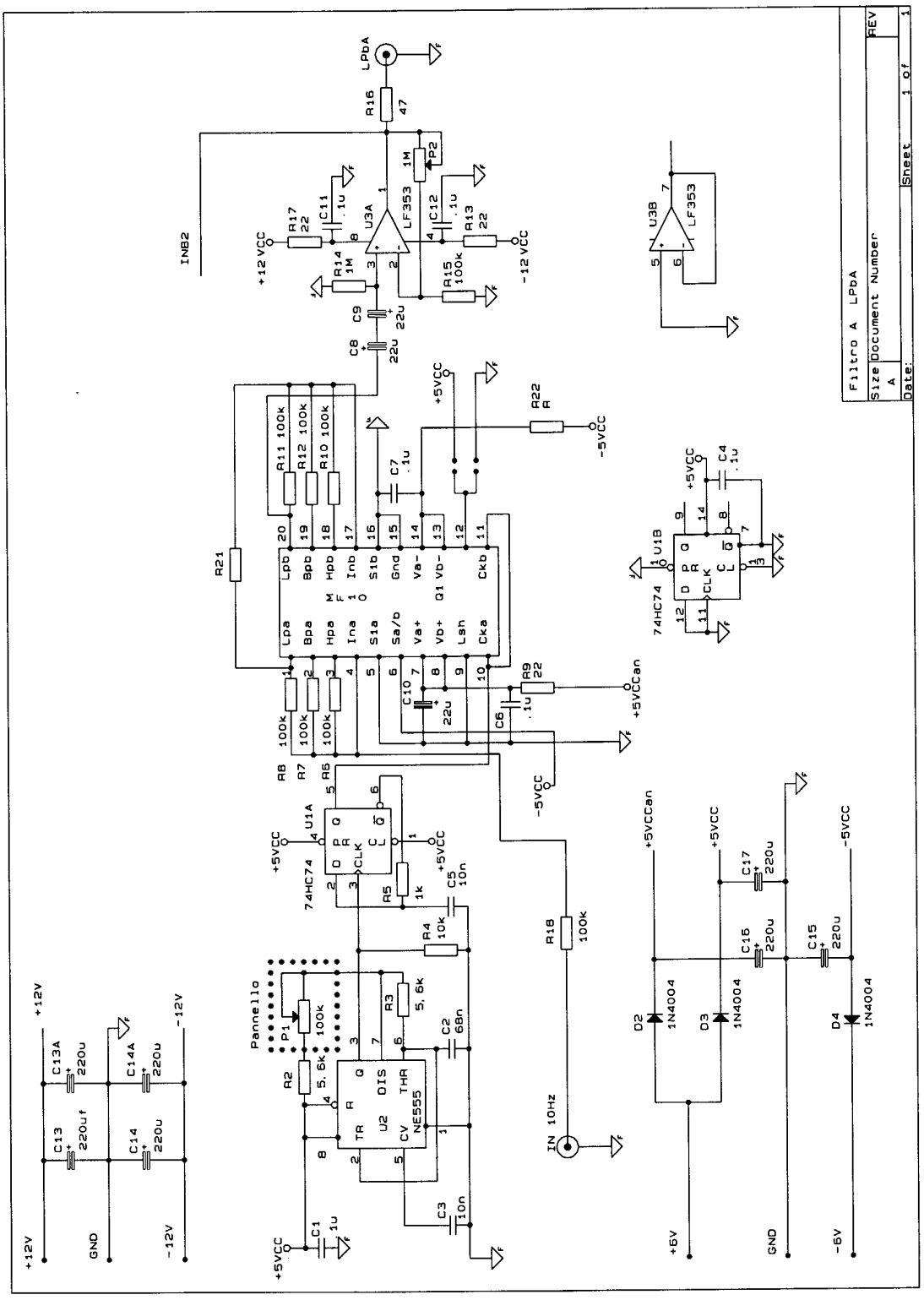

Scheme F: Active control of whirls. Digital Filter.

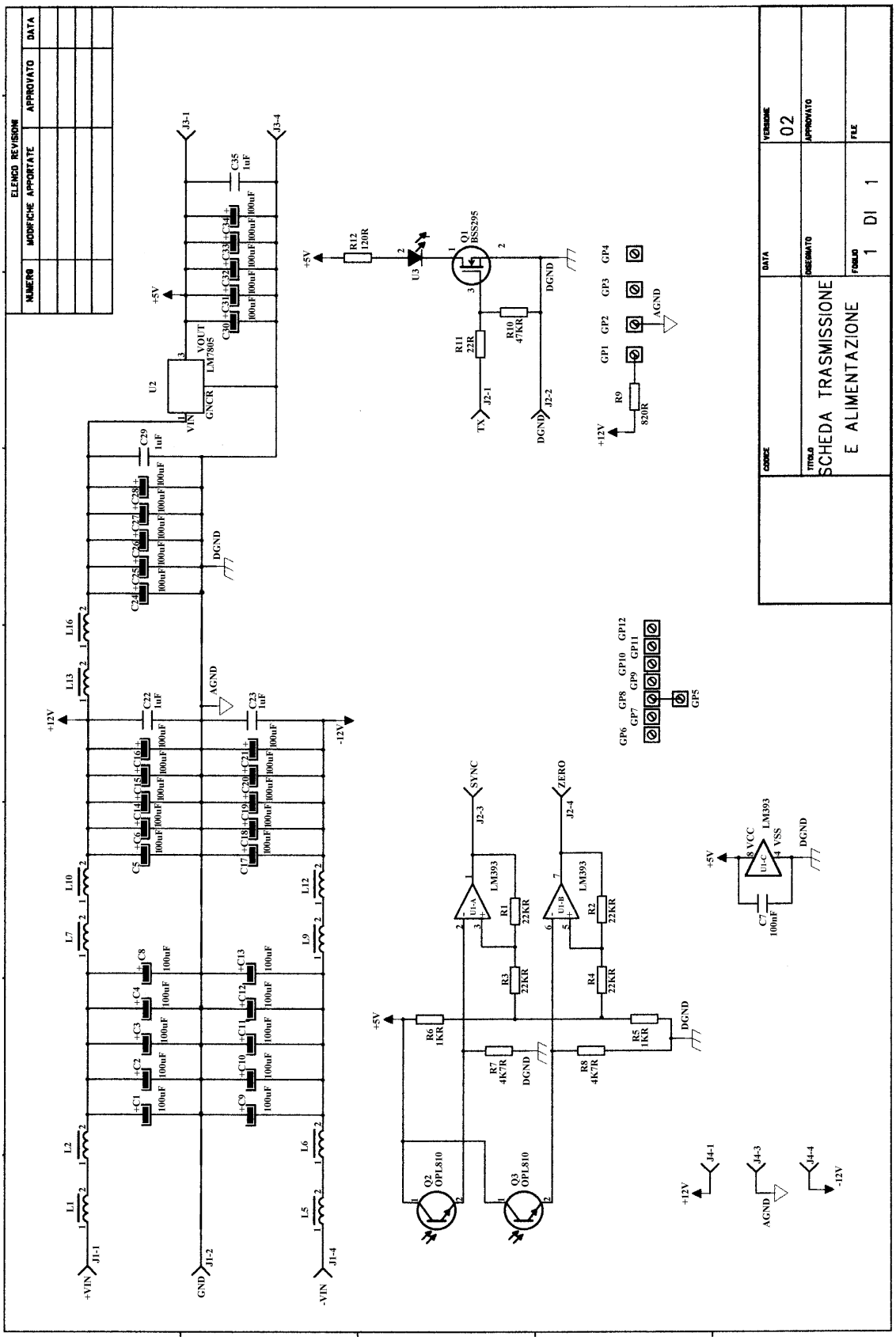

Scheme G: Rotating Electronics. Power supply, synchronism and IR transmission.

Scheme H: Rotating Electronics. Synchronism and reference signal.

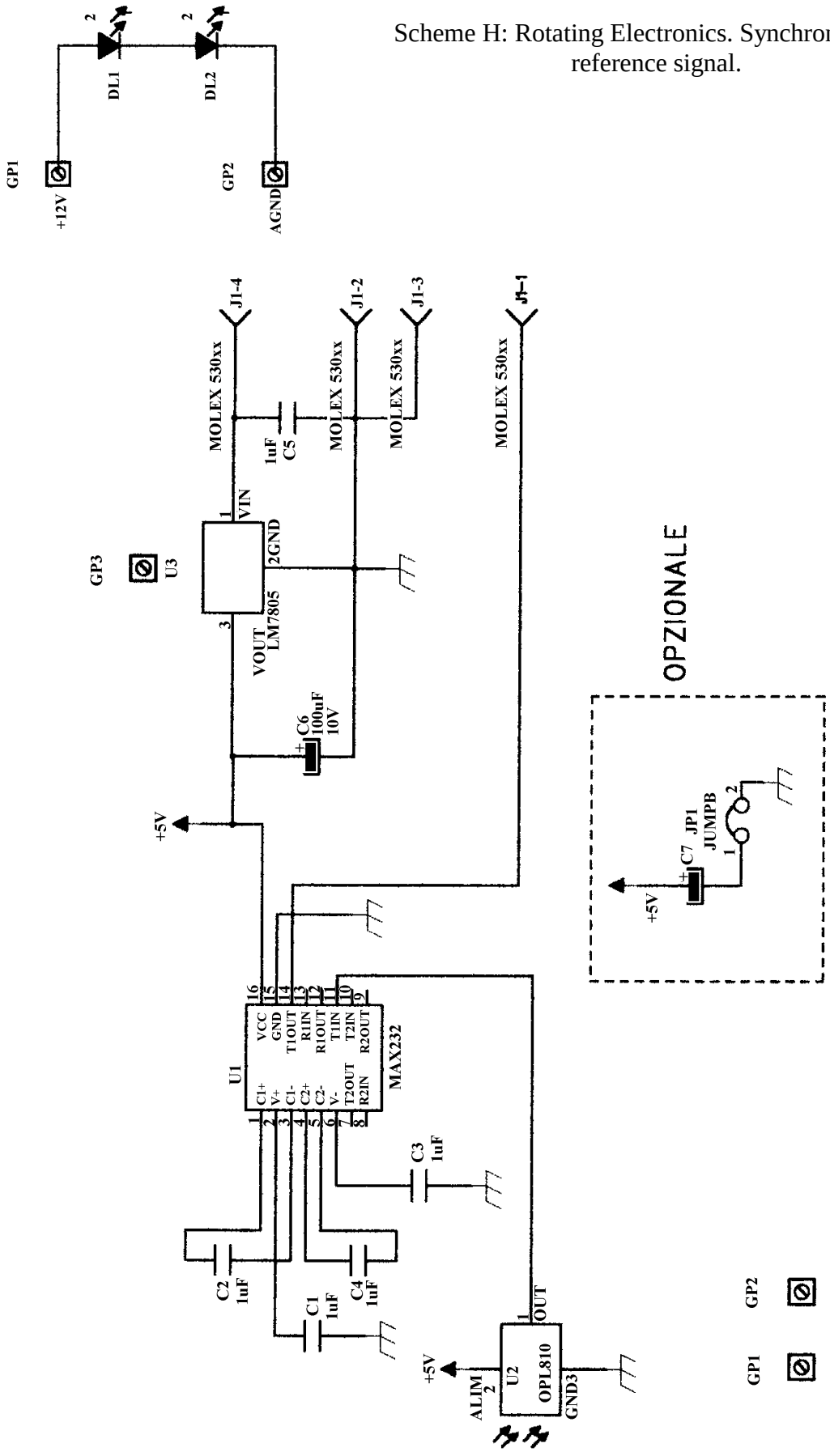

Scheme I: Rotating Electronics. Optical receiver and data transfer to the PC.

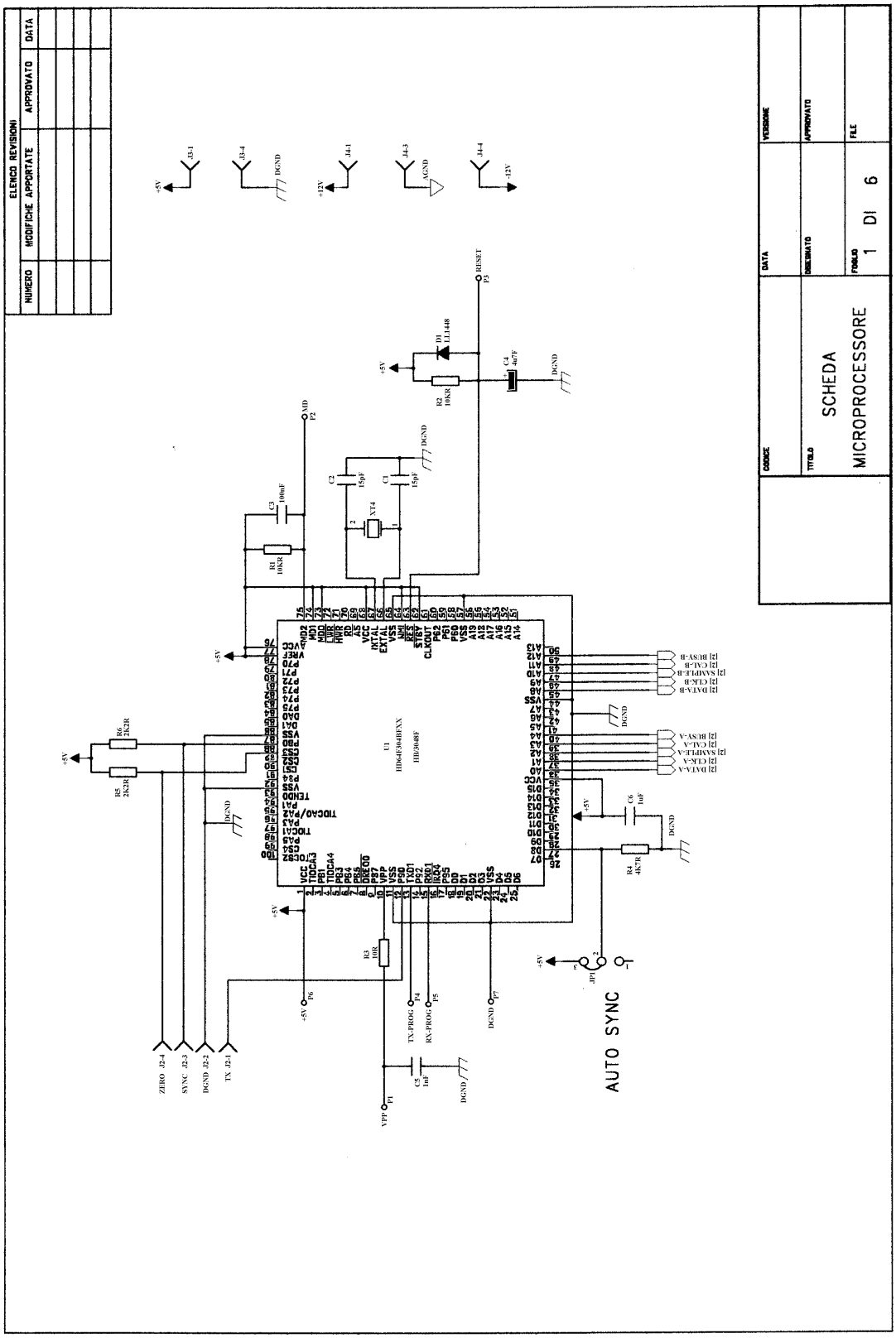

Scheme J: Rotating Electronics. Microprocessor.

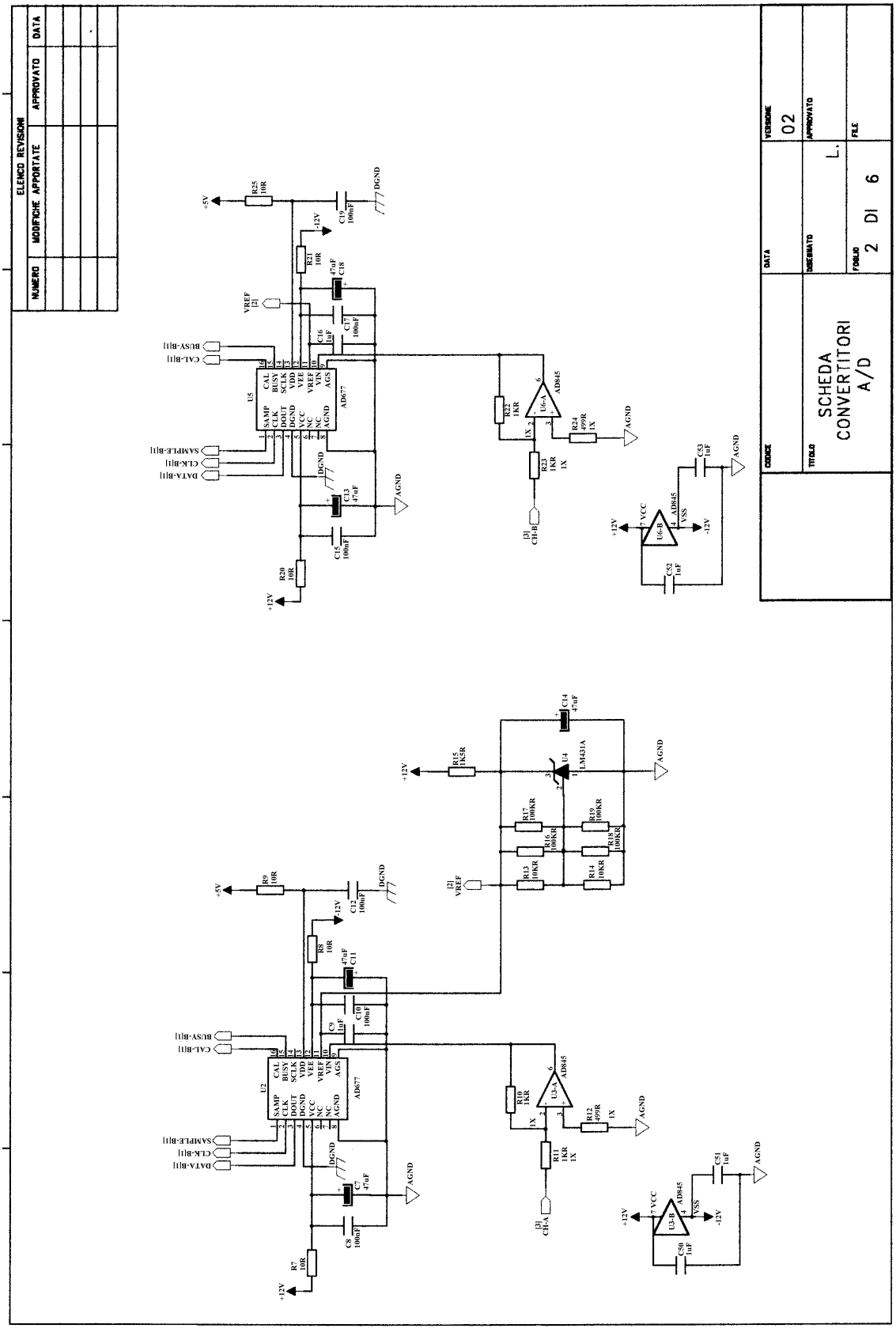

Scheme K: Rotating Electronics. A/D Converter.

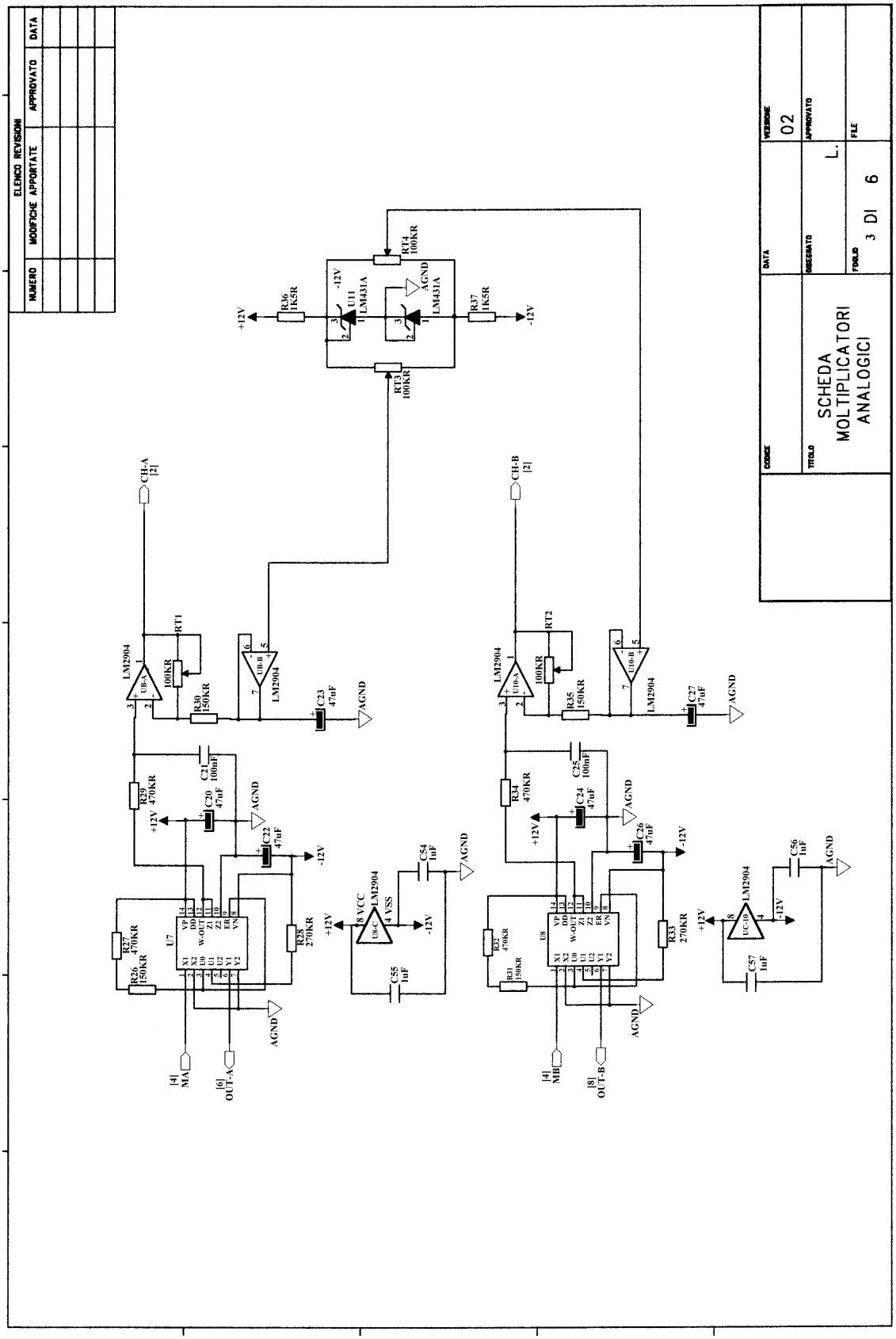

Scheme L: Rotating Electronics. Demodulators and analog amplifiers.

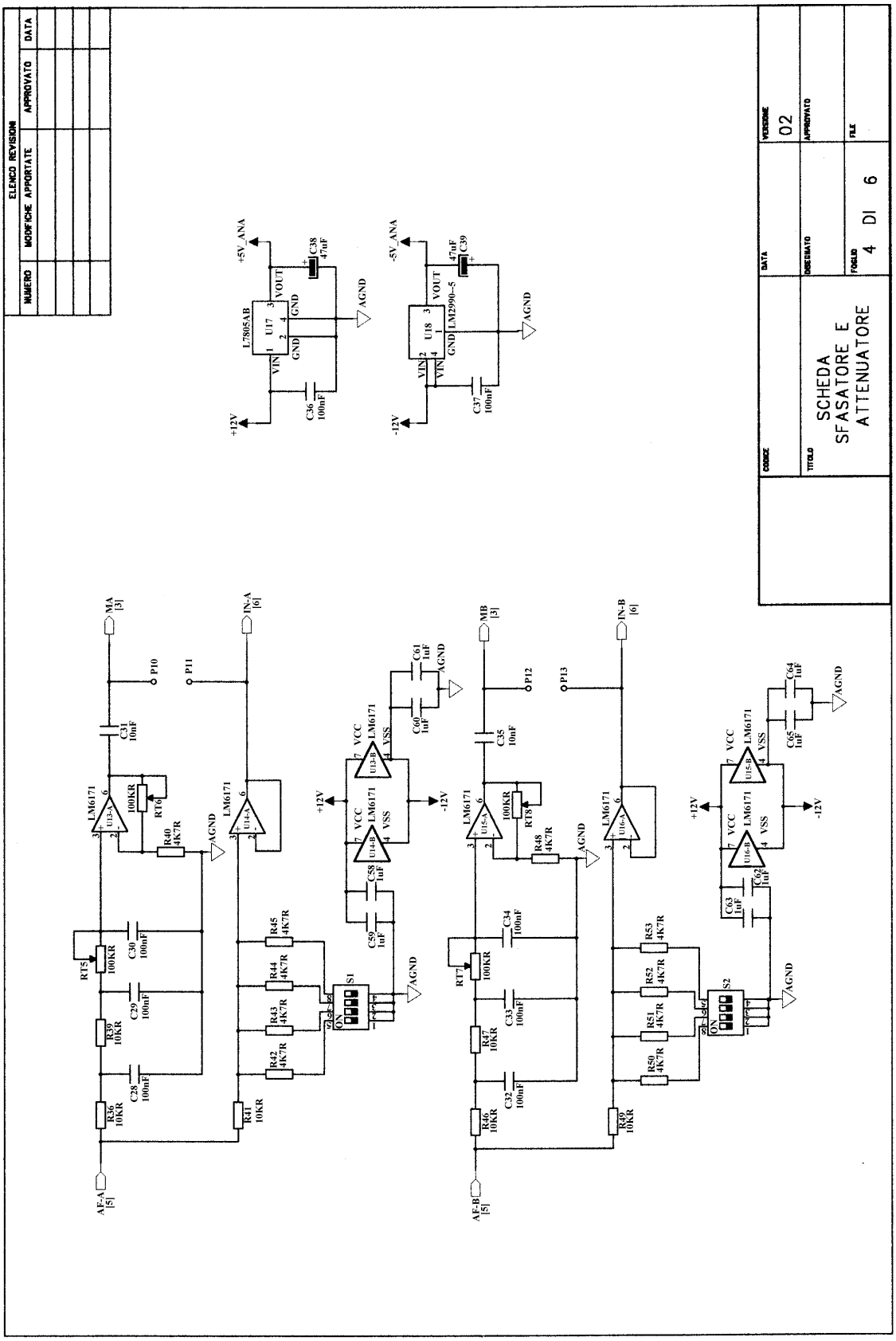

Scheme M: Rotating Electronics. Phase shifters.

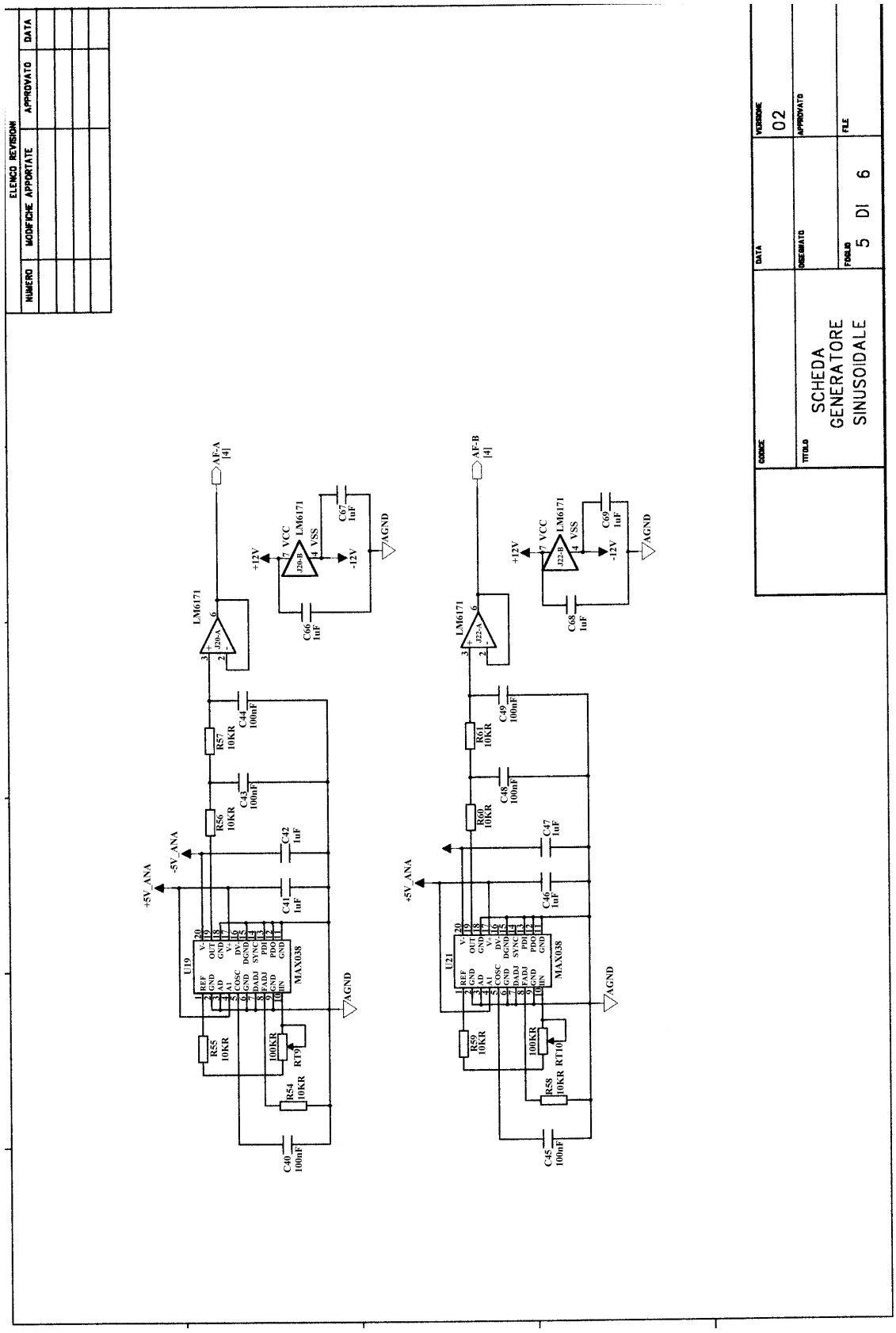

Scheme N: Rotating Electronics. Sine wave generators.

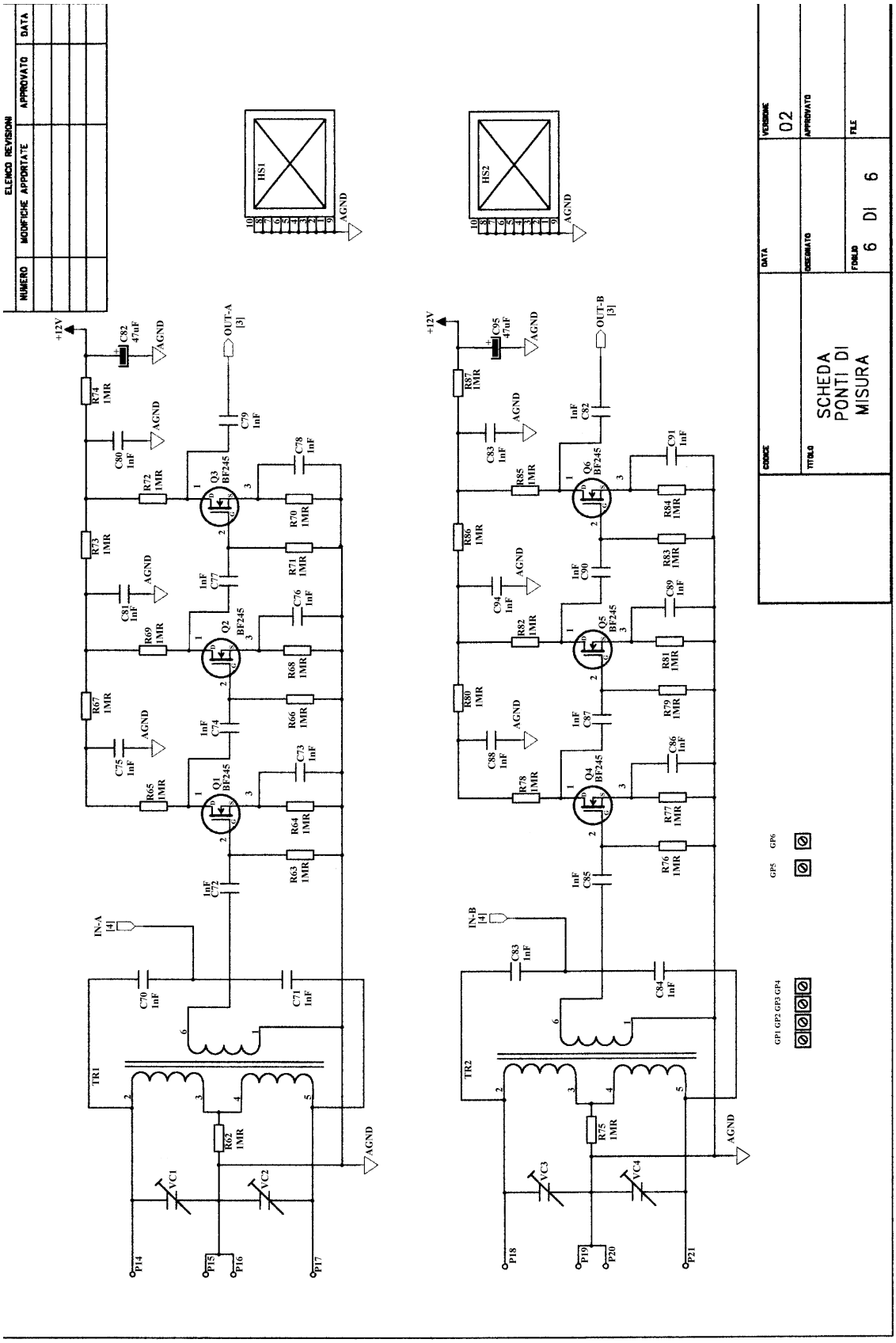

Scheme O: Rotating Electronics. The capacitance bridge sensors and 3-stages preamplifiers with low noise.

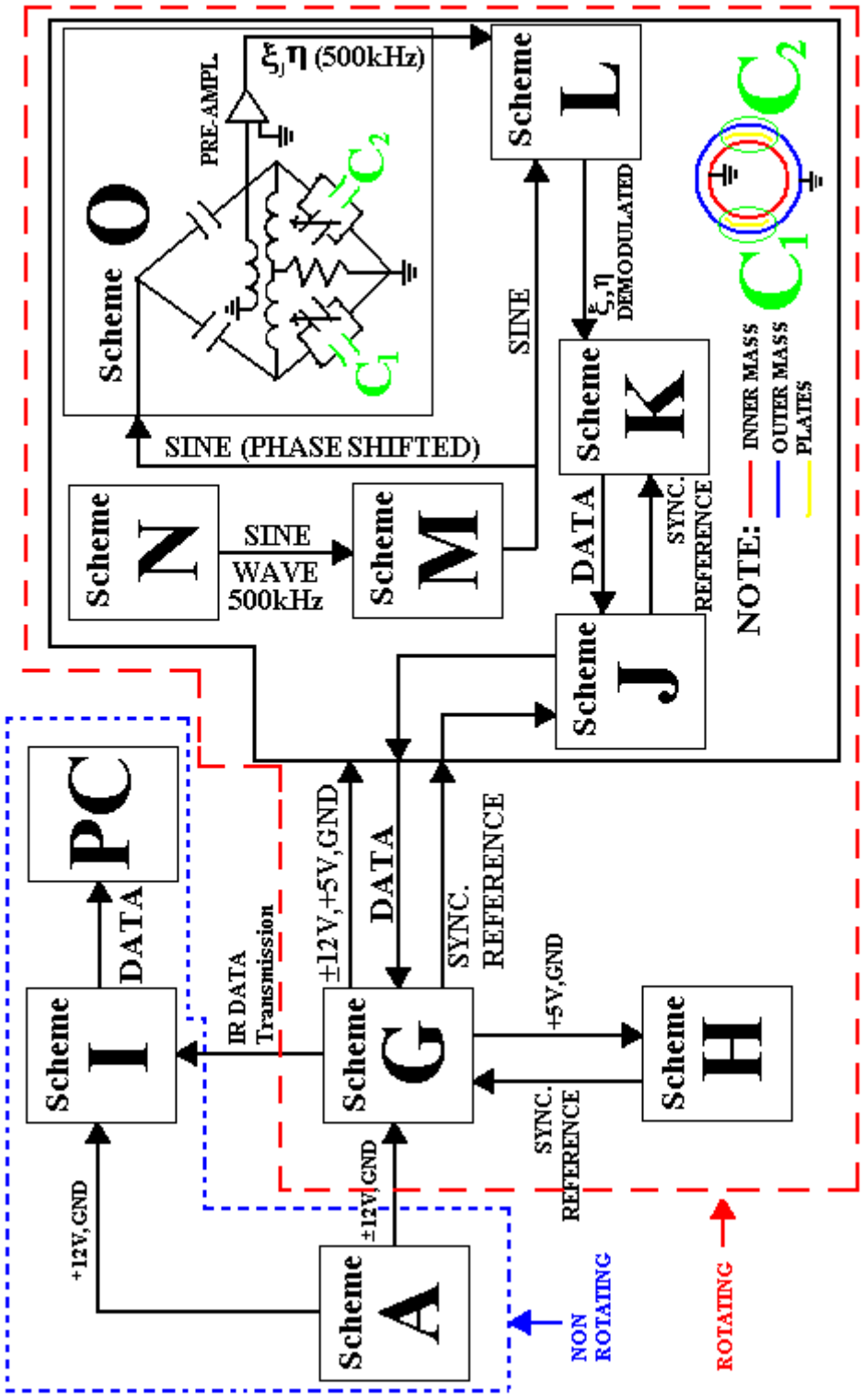

Rotating electronics for data acquisition. Block diagram.
Data (ξ and η components of the relative displacements between the test masses) are measured in the rotating frame.

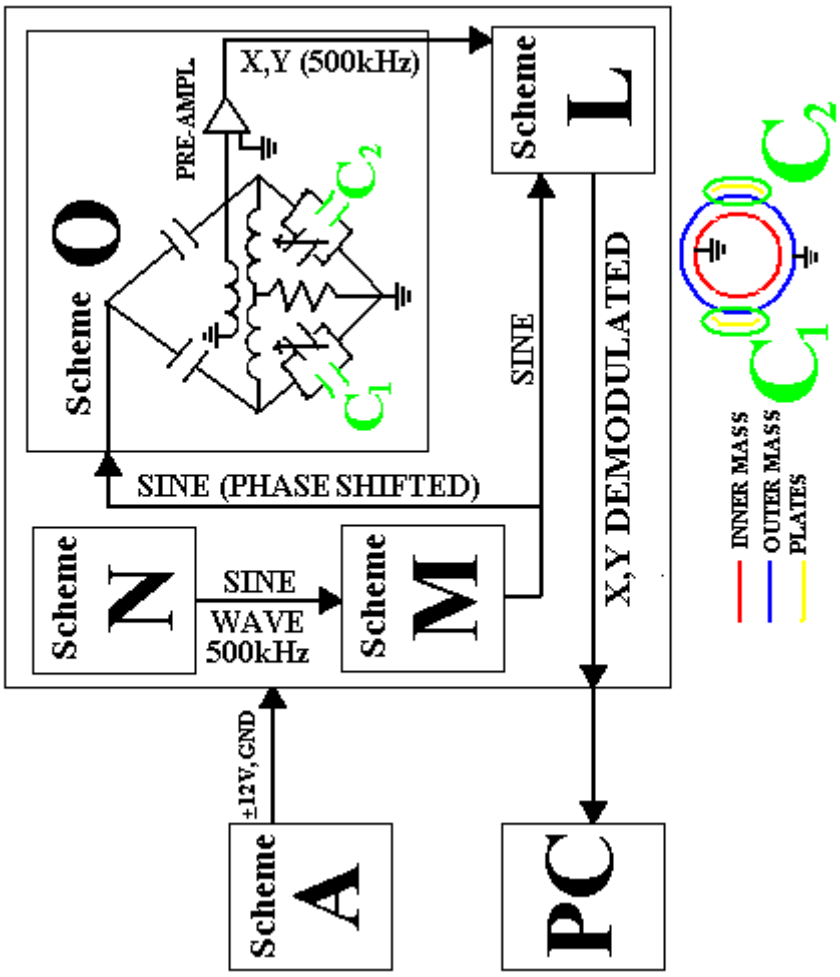

Active control of whirls. Block diagram of the sensors.
Data (x and y of the outer mass with respect to the vacuum chamber) are measured in the laboratory reference frame.

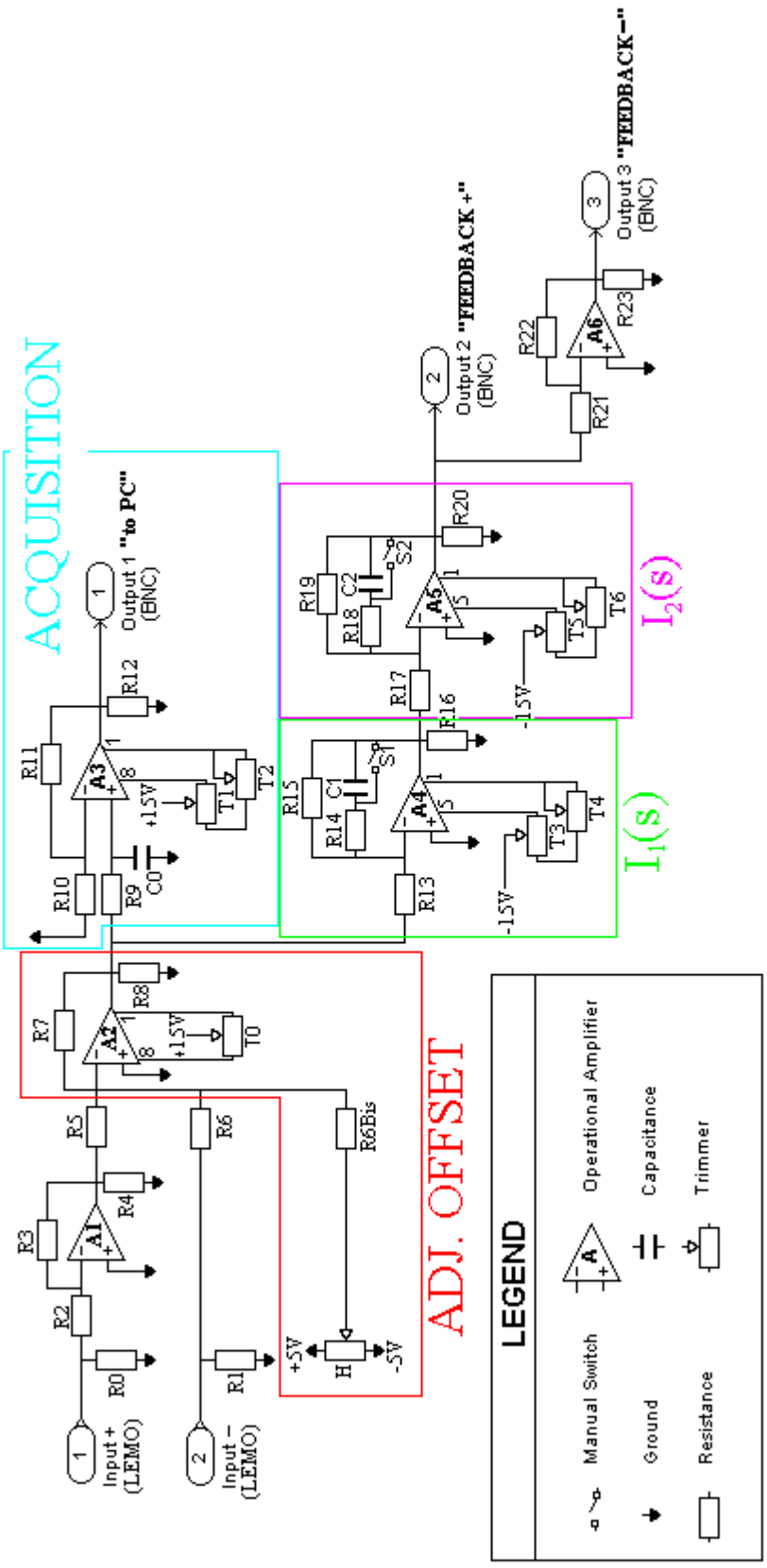

Scheme P: Tilt Active Control.

APPENDIX 9.A:

THE PGB PASSIVE NOISE ATTENUATOR IN THE GG SPACE EXPERIMENT.

Consider a spacecraft of cylindrical symmetry whose symmetry axis is also the axis of maximum moment of inertia. The PGB is a cylindrical structure which is mechanically suspended from the spacecraft along its symmetry axis (see figure 9.4) so as to provide weak coupling in the plane perpendicular to the axis while being more stiff along it (as in the case of the test cylinders); its axis of maximum moment of inertia coincides (within manufacture and mounting errors) with the symmetry axis of the spacecraft. Since we refer here to the GG experiment we consider only the motion of the spacecraft/PGB system in the plane perpendicular to spin axis, which is the plane of the expected signal (we know [11] that tilting torques and motions along the z-axis are negligible). In the inertial frame whose origin O coincides, at the initial time, with the centre of mass of the whole system spacecraft/PGB the equations of motion are:

$$\begin{cases} m_s \ddot{\vec{r}}_s = -k\left(\vec{r}_s - \vec{r}_p\right) - c_R\left[\dot{\vec{r}}_s - \dot{\vec{r}}_p - \vec{\omega}_s \times \left(\vec{r}_s - \vec{r}_p\right)\right] - c_{NR}\left(\dot{\vec{r}}_s - \dot{\vec{r}}_p\right) + \vec{F}_{ext} \\ m_p \ddot{\vec{r}}_p = k\left(\vec{r}_s - \vec{r}_p\right) + c_R\left[\dot{\vec{r}}_s - \dot{\vec{r}}_p - \vec{\omega}_s \times \left(\vec{r}_s - \vec{r}_p\right)\right] + c_{NR}\left(\dot{\vec{r}}_s - \dot{\vec{r}}_p\right) \end{cases} \quad (9.A.1)$$

where m_s is the mass of the spacecraft and m_p the mass of the PGB. $\vec{\omega}_s$ is the spin speed of the system. $\vec{F}_{ext}$ is a non gravitational external force acting on the spacecraft. $\vec{r}_s$ is the position vector of the centre of mass of the spacecraft (with components x_s and y_s); $\vec{r}_p$ is the position vector of the centre of mass of the PGB (with components x_p and y_p). c_R and c_{NR} are the rotating and non rotating damping coefficients, k the elastic constant of the suspensions. $\omega_{ns}^2 = k/m_s$ and $\omega_{np}^2 = k/m_p$ are the natural frequencies of the spacecraft and PGB. From now on, the labels s and p refer to the spacecraft and PGB respectively. Let us now consider the state vector X (with components x_i (i=1…8)) defined as it follows:

$$X^T = [x_s \ \dot{x}_s \ y_s \ \dot{y}_s \ x_p \ \dot{x}_p \ y_p \ \dot{y}_p]^T \quad (9.A.2)$$

It is well known that a linear dynamic system may be represented by its differential equations in state variable form; the matrices for the state variable form are

$$A = \begin{bmatrix} 0 & 1 & 0 & 0 & 0 & 0 & 0 & 0 \\ -\omega_{ns}^2 & -\frac{c_R + c_{NR}}{m_s} & -\frac{c_R \omega_s}{m_s} & 0 & \omega_{ns}^2 & \frac{c_R + c_{NR}}{m_s} & \frac{c_R \omega_s}{m_s} & 0 \\ 0 & 0 & 0 & 1 & 0 & 0 & 0 & 0 \\ \frac{c_R \omega_s}{m_s} & 0 & -\omega_{ns}^2 & -\frac{c_R + c_{NR}}{m_s} & -\frac{c_R \omega_s}{m_s} & 0 & \omega_{ns}^2 & \frac{c_R + c_{NR}}{m_s} \\ 0 & 0 & 0 & 0 & 0 & 1 & 0 & 0 \\ \omega_{np}^2 & \frac{c_R + c_{NR}}{m_p} & \frac{c_R \omega_s}{m_p} & 0 & -\omega_{np}^2 & -\frac{c_R + c_{NR}}{m_p} & -\frac{c_R \omega_s}{m_p} & 0 \\ 0 & 0 & 0 & 0 & 0 & 0 & 0 & 1 \\ -\frac{c_R \omega_s}{m_p} & 0 & \omega_{np}^2 & \frac{c_R + c_{NR}}{m_p} & \frac{c_R \omega_s}{m_p} & 0 & -\omega_{np}^2 & -\frac{c_R + c_{NR}}{m_p} \end{bmatrix} \quad (9.A.3)$$

and B, whose components are null except for $B_{2,1}=B_{4,2}=1/m_s$. The inputs of the system are the components of the external force, namely $u=[u_x \quad u_y]^T=[F_{ext}^x \quad F_{ext}^y]^T$. The outputs of the system are the four components of the projection of the position vectors in the plane perpendicular to the spin axis and they are expressed in a matrix form as:

$$Y=\left[y_1 \quad y_2 \quad y_3 \quad y_4\right]^T=\left[C\cdot X\right]^T \tag{9.A.4}$$

where the C matrix is defined as:

$$C=\begin{bmatrix}1&0&0&0&0&0&0&0\\0&0&1&0&0&0&0&0\\0&0&0&0&1&0&0&0\\0&0&0&0&0&0&1&0\end{bmatrix} \tag{10:5}$$

The second order differential equations (9.A.1) may be written in the form:

$$\dot{X}=A\cdot X+B\cdot u \tag{9.A.6}$$

By combining equations (9.A.4) and (9.A.6) and introducing the Laplace transform ($s=j\omega$ is the complex variable), it follows:

$$Y(s)=C\cdot\left(sI-A\right)^{-1}\cdot B \;\; u(s)=H(s)\,u(s) \tag{9.A.7}$$

H(s) is a matrix of transfer functions which connects the system's outputs to its inputs:

$$H(s)=\begin{bmatrix}\Im_{1,x}&\Im_{1,y}\\\Im_{2,x}&\Im_{2,y}\\\Im_{3,x}&\Im_{3,y}\\\Im_{4,x}&\Im_{4,y}\end{bmatrix} \tag{9.A.8}$$

Note that $\Im_{i,x}$ is the transfer function from the x component of the external force F_{ext}^x to the i-th component of the output vector (9.A.4); in the same manner, $\Im_{i,y}$ is the transfer function from the y component of the force and the same component of the output vector. If the system has an isotropic behaviour, the components of the transfer matrix (9.A.8) are not independent; the following equalities are readily obtained:

$$\begin{cases}\Im_{1,x}=\Im_{2,y}\\\Im_{3,x}=\Im_{4,y}\\\Im_{1,y}=-\Im_{2,x}\\\Im_{3,y}=-\Im_{4,x}\end{cases} \tag{9.A.9}$$

The first two equalities in (9.A.9) mean that the x components of the position vectors in presence of a force F^x acting along the x direction coincide with the y components of the positions vectors in presence of a force F^y acting along the y direction. The last two equalities in (9.A.9) mean that, even though the external force have been applied along a direction, finite differential displacements occurs along the other direction, due to the dissipative nature of the suspensions (see equations (1.68) and (9.12)).

The 8 transfer functions in (9.A.8) are shown in figure9.A.1 as functions of the frequency. They are listed below as functions of the governing parameters of the problem.

$$\Im_{1,x}=\frac{\left[k-m_p\omega^2+j\omega(c_R+c_{NR})\right]\left\{m_pm_s\omega^2-\left[k+j\omega(c_R+c_{NR})\right](m_s+m_p)\right\}-c_R^2\omega_s^2(m_s+m_p)}{\left\{\left\{m_pm_s\omega^2-\left[k+j\omega(c_R+c_{NR})\right](m_s+m_p)\right\}^2+c_R^2\omega_s^2(m_s+m_p)\right\}\omega^2}$$

$$\Im_{2,x}=\frac{c_R\omega_sm_p^2\omega^2}{\left\{\left\{m_pm_s\omega^2-\left[k+j\omega(c_R+c_{NR})\right](m_s+m_p)\right\}^2+c_R^2\omega_s^2(m_s+m_p)\right\}\omega^2}$$

$$\Im_{3,x}=\frac{\left[k+j\omega(c_R+c_{NR})\right]\left\{m_pm_s\omega^2-\left[k+j\omega(c_R+c_{NR})\right](m_s+m_p)\right\}-c_R^2\omega_s^2(m_s+m_p)}{\left\{\left\{m_pm_s\omega^2-\left[k+j\omega(c_R+c_{NR})\right](m_s+m_p)\right\}^2+c_R^2\omega_s^2(m_s+m_p)\right\}\omega^2}$$

$$\Im_{4,x}=\frac{-c_R\omega_sm_pm_s\omega^2}{\left\{\left\{m_pm_s\omega^2-\left[k+j\omega(c_R+c_{NR})\right](m_s+m_p)\right\}^2+c_R^2\omega_s^2(m_s+m_p)\right\}\omega^2}$$

$$\Im_{1,y}=\frac{-c_R\omega_sm_p^2\omega^2}{\left\{\left\{m_pm_s\omega^2-\left[k+j\omega(c_R+c_{NR})\right](m_s+m_p)\right\}^2+c_R^2\omega_s^2(m_s+m_p)\right\}\omega^2}$$

$$\Im_{2,y}=\frac{\left[k-m_p\omega^2+j\omega(c_R+c_{NR})\right]\left\{m_pm_s\omega^2-\left[k+j\omega(c_R+c_{NR})\right](m_s+m_p)\right\}-c_R^2\omega_s^2(m_s+m_p)}{\left\{\left\{m_pm_s\omega^2-\left[k+j\omega(c_R+c_{NR})\right](m_s+m_p)\right\}^2+c_R^2\omega_s^2(m_s+m_p)\right\}\omega^2}$$

$$\Im_{3,y}=\frac{c_R\omega_sm_pm_s\omega^2}{\left\{\left\{m_pm_s\omega^2-\left[k+j\omega(c_R+c_{NR})\right](m_s+m_p)\right\}^2+c_R^2\omega_s^2(m_s+m_p)\right\}\omega^2}$$

$$\Im_{4,y}=\frac{\left[k+j\omega(c_R+c_{NR})\right]\left\{m_pm_s\omega^2-\left[k+j\omega(c_R+c_{NR})\right](m_s+m_p)\right\}-c_R^2\omega_s^2(m_s+m_p)}{\left\{\left\{m_pm_s\omega^2-\left[k+j\omega(c_R+c_{NR})\right](m_s+m_p)\right\}^2+c_R^2\omega_s^2(m_s+m_p)\right\}\omega^2}$$

Let us now define the noise reduction factor as the ratio between the amplitude of disturbing vibration at the PGB level and the amplitude of vibration at the spacecraft level:

$$\Im=\frac{\sqrt{\left|x_p(j\omega)\right|^2+\left|y_p(j\omega)\right|^2}}{\sqrt{\left|x_s(j\omega)\right|^2+\left|y_s(j\omega)\right|^2}} \qquad (9.A.10)$$

The function (9.A.10) is defined in the inertial reference frame and it is plotted on the vertical axis in figure 9.A.2 as a function of frequency. The lower this ratio, the lower the platform noise of the experiment, since the experiment is carried out inside the PGB. We consider the case of Q=90. It is apparent that the system is transparent ($\Im(\omega\to 0)=1$) to frequencies lower than the natural frequency of the system, such as the orbital one, while it

provides good attenuation close to the spinning frequency (40dB/decade in the limit $\omega_s \to \infty$). The system is resonant at frequency ω_{np}.

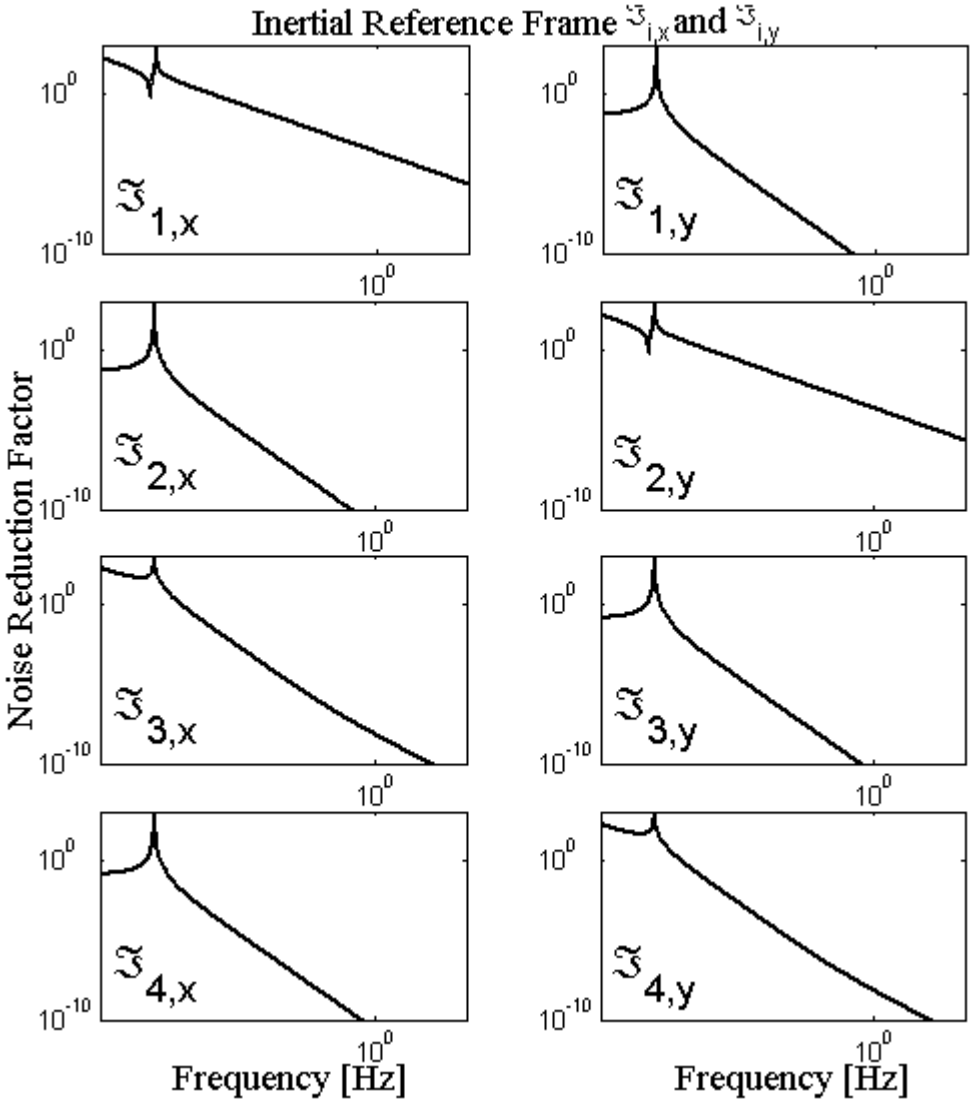

Figure 9.A.1: Transfer functions $\Im_{i,x}$ and $\Im_{i,y}$ of the spacecraft-PGB system in the inertial reference frame for the case of supercritical rotation at 2Hz.

We here show how to transform the noise reduction factor into the rotating frame. In our setting, we may write the two components outputs x^N, y^N in the rotating frame as function of their counterparts in the non rotating frame by means of rotation matrix:

$$R = \begin{pmatrix} \cos(\omega_s t) & \sin(\omega_s t) \\ -\sin(\omega_s t) & \cos(\omega_s t) \end{pmatrix} \tag{9.A.11}$$

It is known that the sine and the cosine may be written as the sum of two complex exponentials:

$$\cos(\omega_s t) = \left(e^{j\omega_s t} + e^{-j\omega_s t} \right) \Big/ 2 \tag{9.A.12.a}$$

$$\sin(\omega_s t) = \left(e^{j\omega_s t} - e^{-j\omega_s t}\right)\Big/ 2j \qquad (9.A.12.b)$$

Let us take a function f(t) and its Laplace transform L(f(t))=F(s).

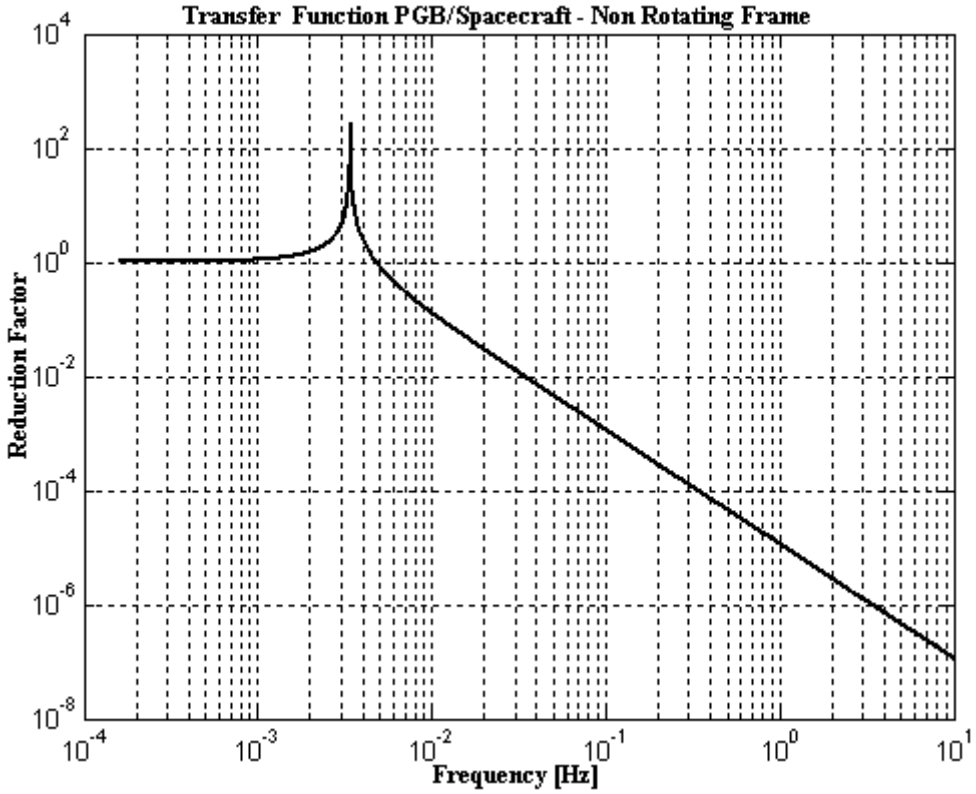

Figure 9.A.2:Noise reduction factor of the GG spacecraft/PGB system as seen in the non rotating reference frame.

The phase shifting property states that the Laplace transform of a function multiplied by an exponential factor is just the transform of the original function shifted of a phase:

$$L(e^{j\alpha t} f(t)) = F(s - j\alpha) \qquad (9.A.13)$$

By combining equations (9.A.11),(9.A.12.a),(9.A.12.b) and (9.A.13) it is possible to write for the Laplace transform of the components of the position vectors in the rotating frame as function of their counterparts in the non rotating frame. After some simple algebra, we obtain:

$$\begin{aligned} x^R_{s,p}(j\omega) &= \left\{x_{s,p}(j\omega - j\omega_s) + x_{s,p}(j\omega + j\omega_s) - j\left[y_{s,p}(j\omega - j\omega_s) - y_{s,p}(j\omega + j\omega_s)\right]\right\}\Big/ 2 \\ y^R_{s,p}(j\omega) &= \left\{j\left[x_{s,p}(j\omega - j\omega_s) - x_{s,p}(j\omega + j\omega_s)\right] + y_{s,p}(j\omega - j\omega_s) + y_{s,p}(j\omega + j\omega_s)\right\}\Big/ 2 \end{aligned} \qquad (9.A.14)$$

Hence, the noise reduction factor in the rotating frame is easily obtained:

$$\Im^R = \frac{\sqrt{\left|x^R_p(j\omega)\right|^2 + \left|y^R_p(j\omega)\right|^2}}{\sqrt{\left|x^R_s(j\omega)\right|^2 + \left|y^R_s(j\omega)\right|^2}} \qquad (9.A.15)$$

In figure 9.A.3 it is plotted as a function of frequency. Perturbations which are seen at 2Hz by the non rotating observer (and attenuated), have frequencies 0Hz and 4Hz for the rotating one, and in fact he too finds that they are attenuated. Instead, perturbations at low frequencies in the non rotating reference frame (lower than the natural one) are seen at about the spin frequency in the rotating frame. Hence, the value of the noise reduction factor is 1 at the spinning frequency, i.e. the system is transparent to 2Hz effects. When viewed in the rotating frame, the peak at the natural frequency in figure 9.A.2 is splitted up into two peaks at frequencies $\omega=\omega_s-\omega_{np}$ and $\omega=\omega_s+\omega_{np}$. In summary, the weak mechanical suspensions of the PGB, which can be used only thanks to the weightlessness, provide an effective, passive means of isolation from the high frequency vibrations around the spin modulation frequency.

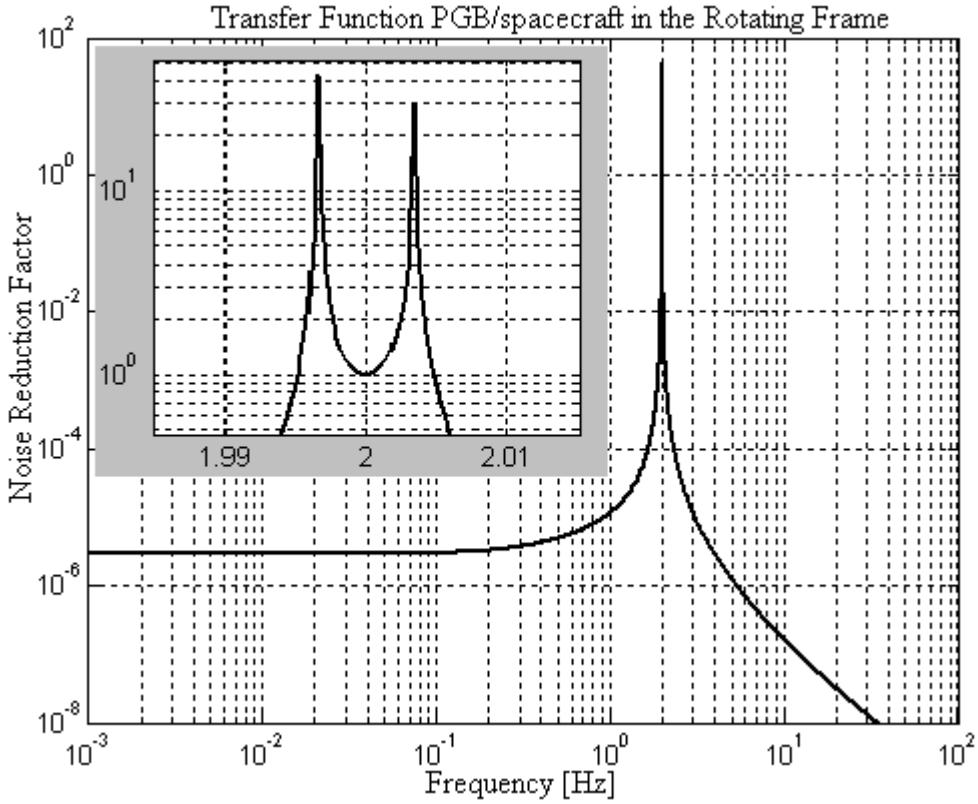

Figure 9.A.3: Noise reduction factor of the GG spacecraft/PGB system as seen in the rotating reference frame. Inset: enlargement around the spin frequency (2Hz). Two peaks are visible at frequencies $\omega=\omega_s-\omega_{np}$ and $\omega = \omega_s + \omega_{np}$.

APPENDIX 9.B:

A PGB-LIKE PASSIVE/ACTIVE NOISE ATTENUATOR ON THE SPACE STATION.

The ISS is a perfect environment to realize experiments which require absence of weight; many activities of the applied sciences are potentially destined to take great advantage from the availability of space structures such as it. However, in some cases the absence of weight is not sufficient and a low level of vibrational noise is required (official data obtained by NASA show an expected noise as large as 10^3 μg). The PGB laboratory is a passive/active vibration isolation system studied to reduce those kind of disturbances [53]. In essence, it is connected to the ISS by means of mechanical suspensions. Weightlessness allows us to use very soft suspensions and hence to have a low threshold frequency of the system and a good attenuation of vibration noise above it. Below and close to this frequency it is possible to use capacitance sensors/actuators in order to reduce noise actively.

Vibration noise is a serious issue for the ISS as far as its use for micro-gravity science and applications is concerned. Many activities typical of the applied sciences (like material and fluid sciences) can take advantage from the availability of the ISS only provided that residual disturbances on board the ISS are significantly reduced.

This is the goal of the PGB: it is a facility for vibration isolation onboard of flying structures which can be easily adjusted (in future) to the needs of the experimentalists.

For a detailed description of the PGB project (transportation to/from the ISS; in-orbit accommodation; locking/unlocking mechanism; interfaces; passive vibration isolation; active vibration isolation; electronic unit; thermal analysis; data acquisition) see [53]. In this chapter we will only study the problem of passive/active control of the system and its thermal stability.

The PGB is a small laboratory (its side is 25 cm) suspended to the ISS by means of two helical springs. It may be accommodated in the volume of a double Middeck Locker box (MDL) in the Express Rack of the US laboratory (figure 9.B1).

We have planned to use two ISA (Italian Space Accelerometer) accelerometers, one rigidly connected to the ISS and one inside the PGB. In this way it is possible to measure the level of the vibrational noise on the ISS and compare it with residual noise in the suspended laboratory. The ISA accelerometer can work in a range of frequency from 10^{-4}Hz to 10Hz reaching the sensitivity of 10^{-11}g/√Hz at a frequency of about 3Hz. The total mass of the system PGB + inner accelerometer is about 40 kg.

Passive noise attenuators rely on the fact that when the suspension point is forced at a frequency ω much larger than the natural frequency ω_o of a pendulum, the oscillation amplitude of the suspended body is reduced by a factor $(\omega_o/\omega)^2$ with respect to that of the suspension point. A noise attenuator should work in all 6 degrees of freedom, because both rotational and translational noise is transmitted by the ISS to the suspended laboratory. Since the torsion elastic constant of a helical spring is very small if compared with its translation elastic constant, the rotational noise is reduced much more effectively than translational noise (see figure 9.B.2). As a result, a passive attenuator must be essentially designed with regard to reduction of translational noise.

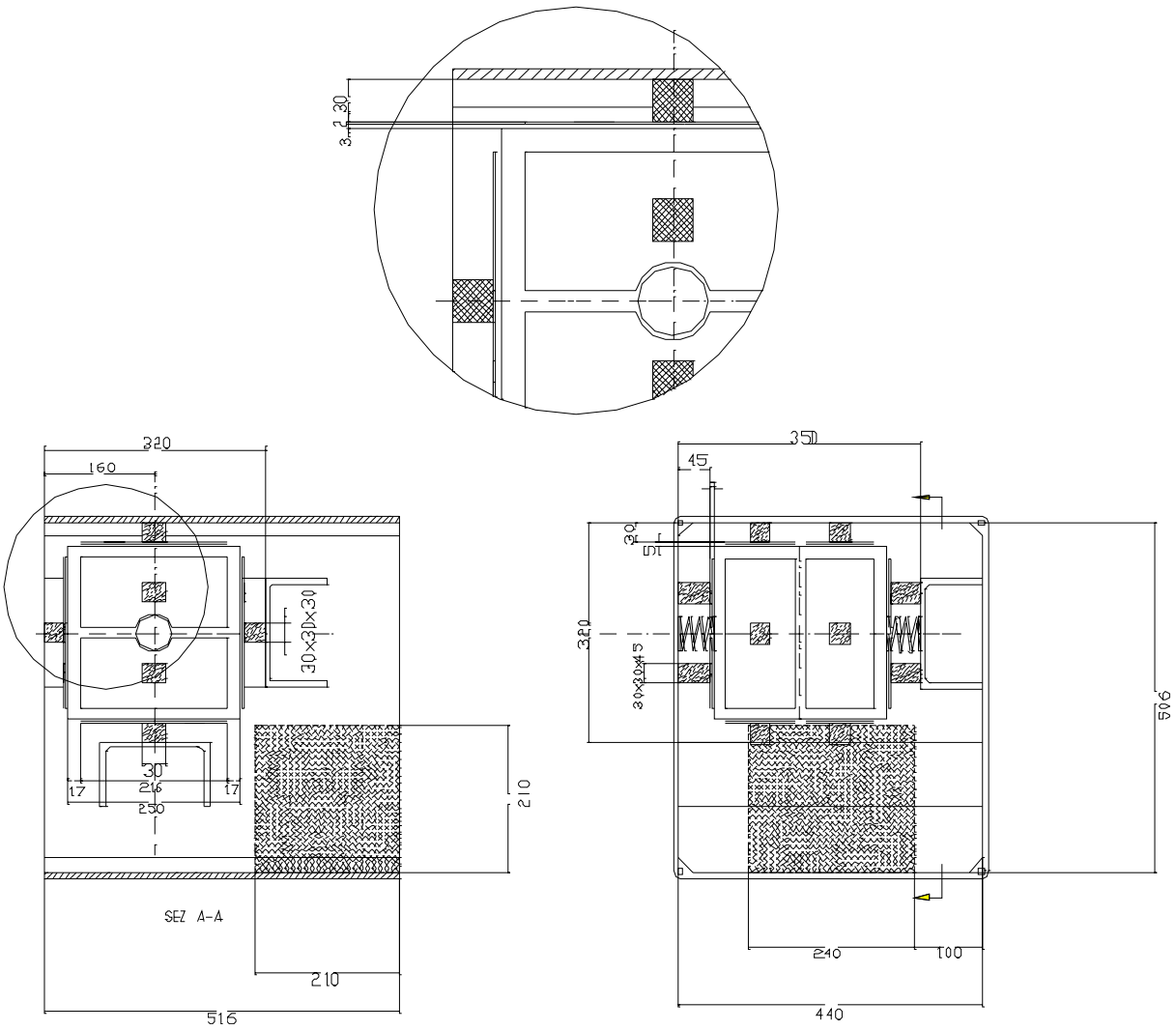

Figure 9.B.1: PGB accommodated in a double Middeck Locker box. We can see the external container, the PGB with the springs and two capacitance plates for each face of the laboratory. The dark square represents the external ISA accelerometer fixed to the rack.

Capacitance plates, rigidly connected to the ISS, located in between the PGB laboratory and the containing rack, form capacitance bridges capable to sense both small displacements and rotations of the PGB. Capacitance plates can also be used as actuators. The clearance between the fixed plates and the PGB surfaces has been designed to be 3-5 mm so that it is possible to produce forces of $2\text{-}4 \cdot 10^{-3}$N assuming 300V maximum voltage.

9.B.1: The Mechanical Suspensions.

Absence of weight in space allows very soft suspensions ([57 – 60]) to be used even for suspending a large mass, thus ensuring a low mechanical threshold frequency of the passive attenuator. By means of the mechanical spring it is also possible an electrical grounding of the PGB box (avoiding electrostatic disturbances) and data/power transmission from/to the any instrument/experiment inside the PGB (in this case, the ISA accelerometer).

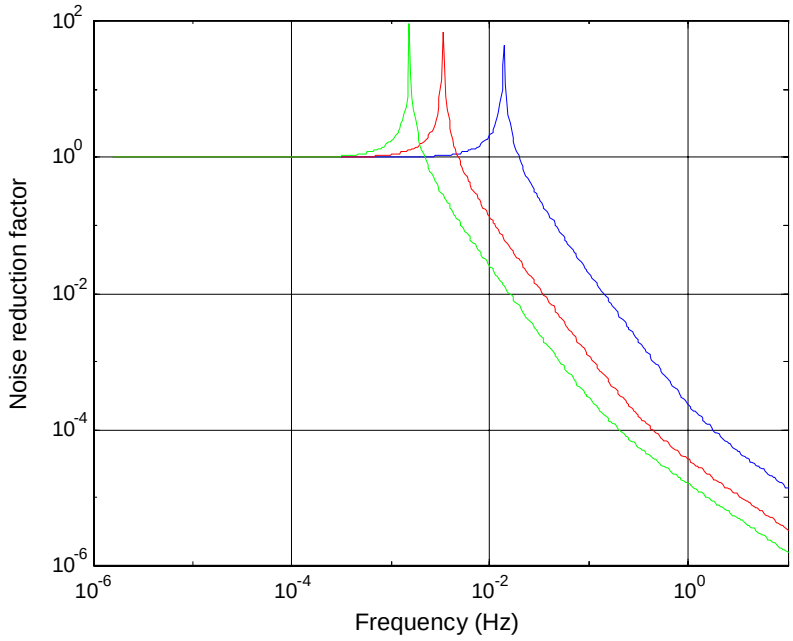

Figure 9.B.2: The transfer function for both rotational and translational noise. Blue line is the translational transfer function; red line is the torsional transfer function for rotations around the symmetry axis of the spring; green line is the flectional transfer function for rotations around an axis normal to the symmetry axis of the spring. They have been evaluated for a system consisting of a box of side 25 cm and mass 40 kg, suspended by a steel helical spring of quality factor Q=100, coil diameter D=4.5cm, wire diameter d=0.021cm, number of coils n=3.25. It is apparent that rotational noise is reduced much more effectively than translational noise.

This is easily made by suspending the PGB laboratory with two helical springs, acting on opposite faces of the box, each one made of four wires: one steel wire, which provides the stiffens and 3 Cu wires for the required electrical connections. This kind of springs have been proposed because they can easily satisfy the needs of the attenuator. One such spring has been manufactured as a prototype spring for the proposed GG experiment (see figure 9.B.3).

Figure 9.B.3: One suspension spring made of 1 steel wire and 3 Cu wires.

A configuration a little different from the one shown in figure 9.B.3 can be studied in order to supply the electric power. For PGB power line is requested at least an equivalent section of AWG32 (0.18–0.2 mm of diameter against 0.12 mm of diameter for the Cu wire in the prototype made for the GG experiment). That can be reached by manufacturing a spring with 3 Cu wires with different diameters (i.e. one steel wire for the stiffness, one Cu wire of 0.18–0.20 mm of diameter for conduction and stiffness too, two thin Cu wires only for conduction) or by splitting power on 2–3 AWG36 lines (0.12 mm of diameter, the same of the

prototype) obtaining a spring with one steel wire for the stiffness and 4–5 thin Cu wires for conduction. Some possible designs are listed below. Q=90 is the value measured in the laboratory for the quality factor of the spring shown in figure 9.B.3 (all wires insulated and grouped together to form a single wire). A value of Q higher than this (i.e. a lower dissipation) can be obtained by manufacturing a spring with separate wires (not grouped together) insulated only at the clamping; in this way, parts were deformations occur are not insulated and therefore give rise to smaller losses.

Because of the many variables involved, a large number of springs can be designed that can satisfy a given set of equations for stress and deflection. We introduce the following parameters (see figure 9.B.4) which characterize the helical spring: D= mean coil diameter, d= wire diameter, L= free length, n= total number of coils, ν= Poisson's ratio, E= modulus of elasticity of the spring material (Young's modulus), G= E/2(1+ν) (modulus of shear), F= working load ($4\cdot10^{-4}$N), τ= design stress at working load F, f= total deflection, p= coil pitch (distance between adjacent spring coils). These factors are related in some fundamental spring equations and are hereafter considered.

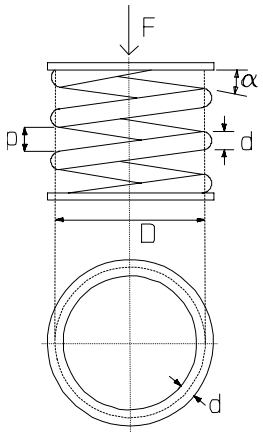

Figure 9.B.4: Sketch of one helical spring .

- Elastic constant.

We can expand the spring's constants as functions of its geometry and the spring's material characteristics. Doing so we find the formulas summarised below. So the linear spring constant in axial direction (see figure 9.B.4.a) is:

$$k_a(N/m) = \frac{Gd^4}{8(n-2)D^3} = \frac{Ed^4}{16(n-2)(1+\nu_P)D^3} \qquad (9.B.1)$$

Assuming Hooke's law, the total deflection of the spring with a working load F is:

$$f_a(cm) = \frac{8\ (n-2)\ D^3F}{Gd^4} \qquad (9.B.2)$$

The linear spring constant for a force applied in the plane of the coil (i.e. normal to the spring's axis; see figure 9.B.4.b) is:

$$k_t(N/m) = \frac{8E\ J_t}{\pi nD^3} = \frac{Ed^4}{8nD^3} \qquad (9.B.3)$$

where we have introduced: $J_t = \pi d^4/64$. We can also distinguish two different kinds of rotation; for rotations around the spring's axis (see figure 9.B.4.c) the constant is:

$$k_{torr}(N \cdot mm/deg) = \frac{Ed^4}{2375(n-2)D} \tag{9.B.4}$$

while for rotations in the plane containing the axis and a diameter of the helical spring figure 9.B.4.d), we have:

$$k_{fl}(N \cdot mm/rad) = 1\Big/\pi n \frac{D}{2}\left(\frac{1}{GJ_p} + \frac{1}{EJ_t}\right) \tag{9.B.5}$$

where $J_p = \pi d^4/32$.

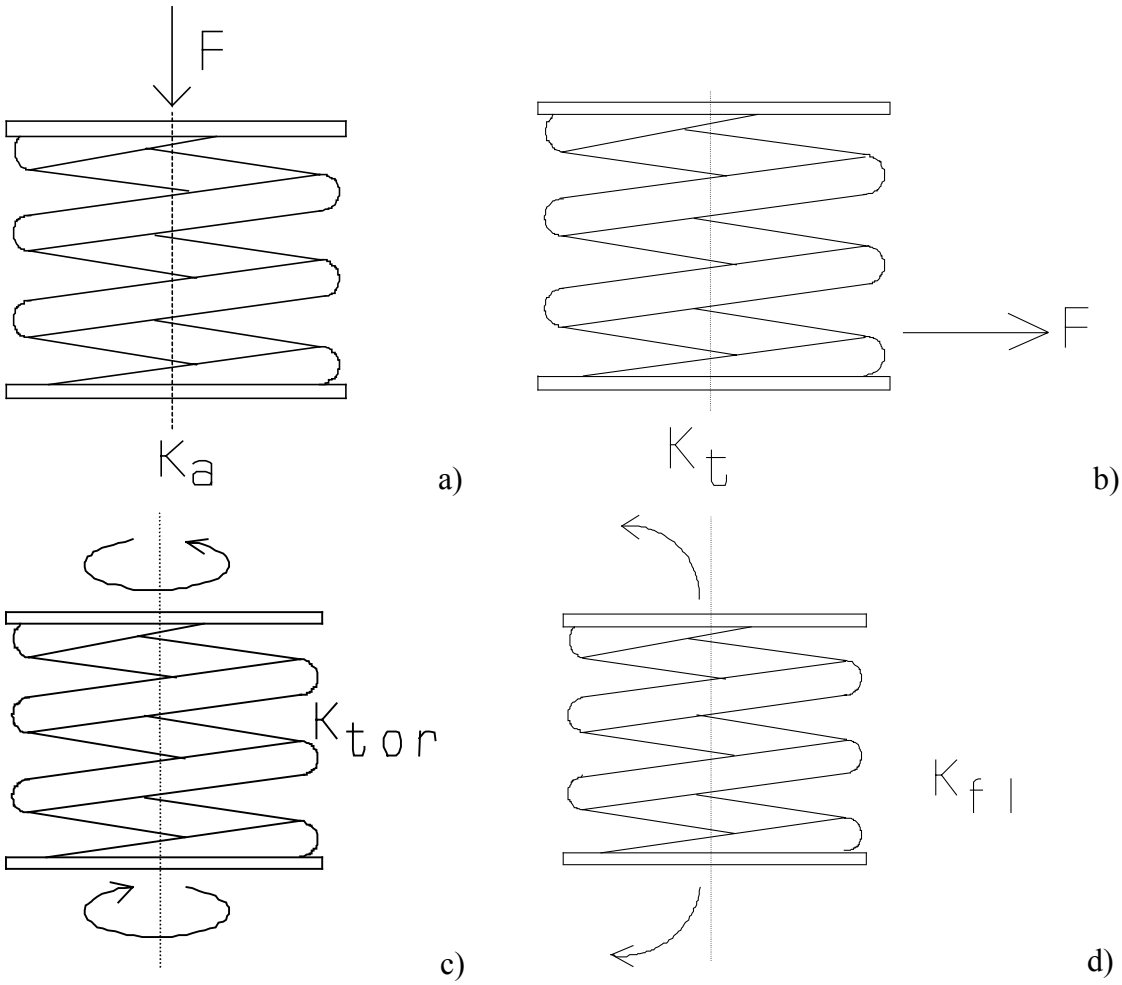

Figure 9.B.5: Sketch of the elastic constants for the helical spring.

- Spring geometry.

The distance between adjacent spring coils (coil pitch) is:

$$p = (L - 2d)/n \sim L/n \tag{9.B.6}$$

The rise angle (α in figure 9.B.4) of the spring coils is:

$$\vartheta = \arctan\left(p/(\pi D)\right) \tag{9.B.7}$$

The free length of the spring is:

$$L \sim n\pi D \tan(\vartheta) \tag{9.B.8}$$

The length of the wire needed to make the spring is:

$$L_w = \pi D\left[2 + (n-2)/\cos(\vartheta)\right] \tag{9.B.9}$$

and its mass is:

$$m \sim \pi^2 n d^2 D\rho/4 \tag{9.B.10}$$

- Failure Criteria and Risk Factors.

If the working load F is much smaller than the critical one, the spring works in safe conditions. The maximum load P for a helical spring is equal to:

$$P = \frac{k_{fl}\ L\left(\frac{2\pi}{L}\right)^2}{1 + \frac{k_{fl}}{k_{tor}}\left(\frac{2\pi}{L}\right)^2} \tag{9.B.11}$$

The condition F<P must be satisfied. Compression spring buckling refers to when the spring deforms in a non-axial direction. This is a very dangerous condition. As a result, it is important to design the spring in such a way that this risk is minimized. One way to check for buckling is to compute the deflection height ratio f/L as a function of the ratio D/L and see if it exceeds the maximum allowable value plotted in figure 9.B.6. The black cross represents the value for the helical spring to be used for suspending the PGB. This value is well below the limit curves depicted in figure 9.B.6.

The maximum shear stress occurs on the inner surface of the coils and it is equal to:

$$\tau = \frac{8\ F\ D}{\pi\ d^3}\left(1 - \frac{3d^2}{16\ D^2} + \frac{3+\nu_P}{2\ (1+\nu_P)}\tan^2(\vartheta)\right) \tag{9.B.12}$$

The Soderberg Criterion provides a way to calculate a failure limit. The spring will fail if the following condition is satisfied:

$$\frac{\tau_{max}}{2} > -\left(\frac{\sigma_{fatigue}}{\sigma_{yield}}\right)\frac{\tau_{max}}{2} + \sigma_{fatigue} \tag{9.B.13}$$

where $\sigma_{fatigue}$ and σ_{yield} are tabulated (see table 9.B.1). We can also plot the stress state of our spring in the Soderberg diagram (figure 9.B.7). For our choices the stress state is always below the limit line.

When springs are used in a mechanism, their dynamic behaviours must be analysed. The first natural frequency of a helical spring is found to be:

$$\nu_S = \frac{1}{2}\sqrt{\frac{k_a}{m_{spring}}} = \frac{d}{9D^2 n}\sqrt{\frac{G}{\rho}} \tag{9.B.14}$$

We need this frequency to be higher than the working frequency 3Hz.

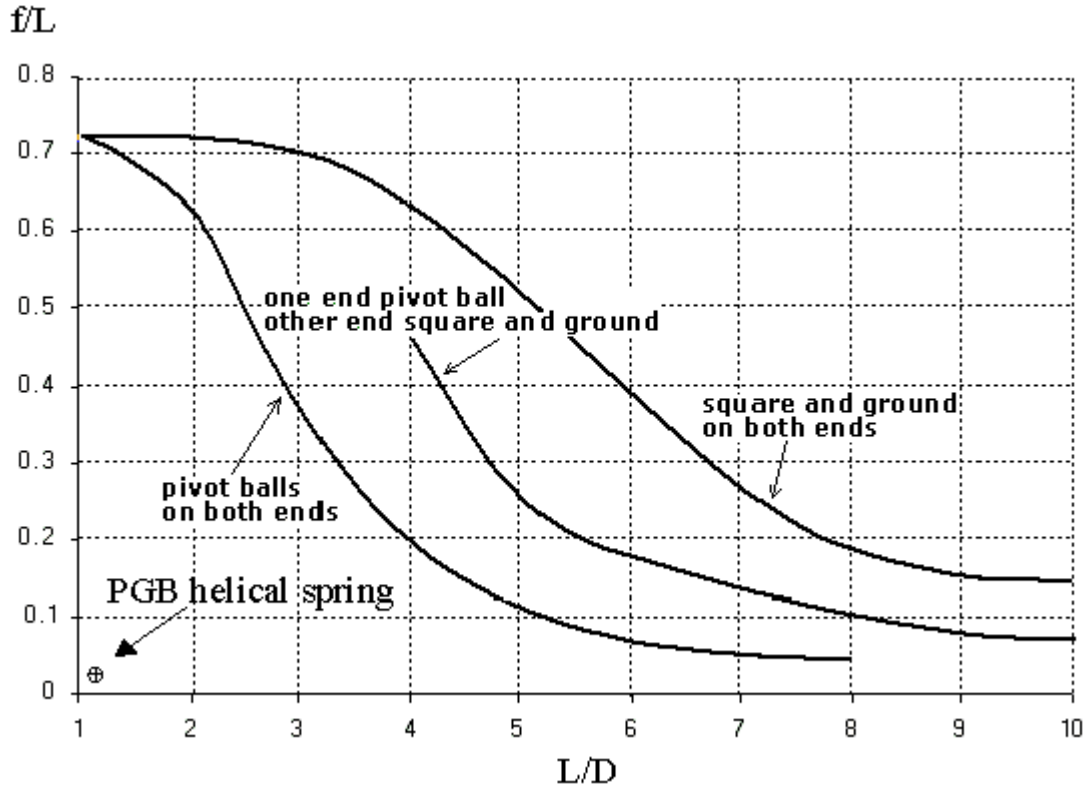

Figure 9.B.6: Check for compression spring buckling.

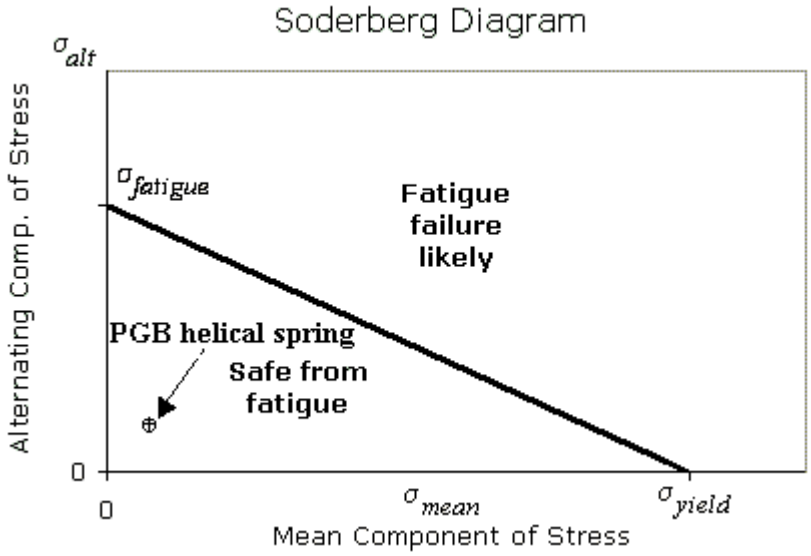

Figure 9.B.7: Soderberg Diagram.

Category	Copper	Steel
Class		Stainless Steel
Type		Austenitic standard
Common Names		Chromium-Nickel steel
Composition	Cu	Cr(17-19%), Ni(8-10%), Mn(2%), Si(1%), C, P, S(<1%)
Density	8.96 g/cm^3 (T=25°C)	8 g/cm^3 (T=25°C)
Poisson's Ratio	0.36	0.27-0.3 (T=25°C)
Elastic Modulus	101 GPa	193 GPa
Tensile Strength		515 MPa
Yield Strength		205 MPa
Thermal Expansion	$1.65 \cdot 10^{-5}$/°K (T=298°K)	$1.72 \cdot 10^{-5}$/°C (T=0-100°C)
Thermal Conductivity	401 W/(m·K)	16.2 W/(m·K)
Specific Heat	385 J/(kg·K)	500 J/(kg·K)
Electric Resistivity	$1.67 \cdot 10^{-8}$ Ω·m (T=293°K)	$720 \cdot 10^{-9}$ Ω·m (T=25°C)

Table 9.B.1: Stainless Steel and Copper Properties.

- Guidelines for Spring Choice.

From equations (9.B.1) and (9.B.3) it is clear that k_a can be equal to k_t only if n=3.25 (n = 3 1/4). This choice is quite unusual since the number of active coils is very small (i.e. n-2 = 1.25). If we want a large number of active coils in the spring (for example ten active coils), from (9.B.1) and (9.B.3) we find that k_a will be about $0.5k_t$. This difference is not a problem from the point of view of the control laws. Once the material has been selected, 3 free parameters (n,d,D) can be varied in order to satisfy a set of conditions. Note that if each spring is made of 4–6 wires, the total elastic constant is evaluated as $k^{Total}=k^{Steel}+\Sigma k^{Cu}$.

9.B.2: Goal and Requirements of the Active Control.

The control equations have been written for the active control required [53]. Numerical simulations of the entire system have been carried out, including both passive and active control, so as to obtain the transfer function to be expected. The transfer function was constrained by the fact that the level of residual vibration noise inside the suspended PGB must be well suited for the characteristics of the ISA accelerometer used to measure it, so as

to be able to make the most sensitive measurement possible. It is necessary that the residual noise achieved is in accordance with the best sensitivity of the instrument located inside the PGB (i.e. the residual noise should not exceed 10^{-11} g/√Hz at about 3 Hz) and that the clearance is compatible with the design of capacitive actuators (an error of ± 5 mm would provide a maximum force of 3 mN assuming a 350 V maximum voltage). Official input data (simulated) have been obtained by NASA representatives on the level of vibration noise expected on board the ISS (see figure 9.B.8). These data refer to vibration noise at high frequencies (from 0.01 Hz till 300 Hz); they also give constraints on the expected quasi stationary noise (at low frequencies), particularly at the orbital frequency.

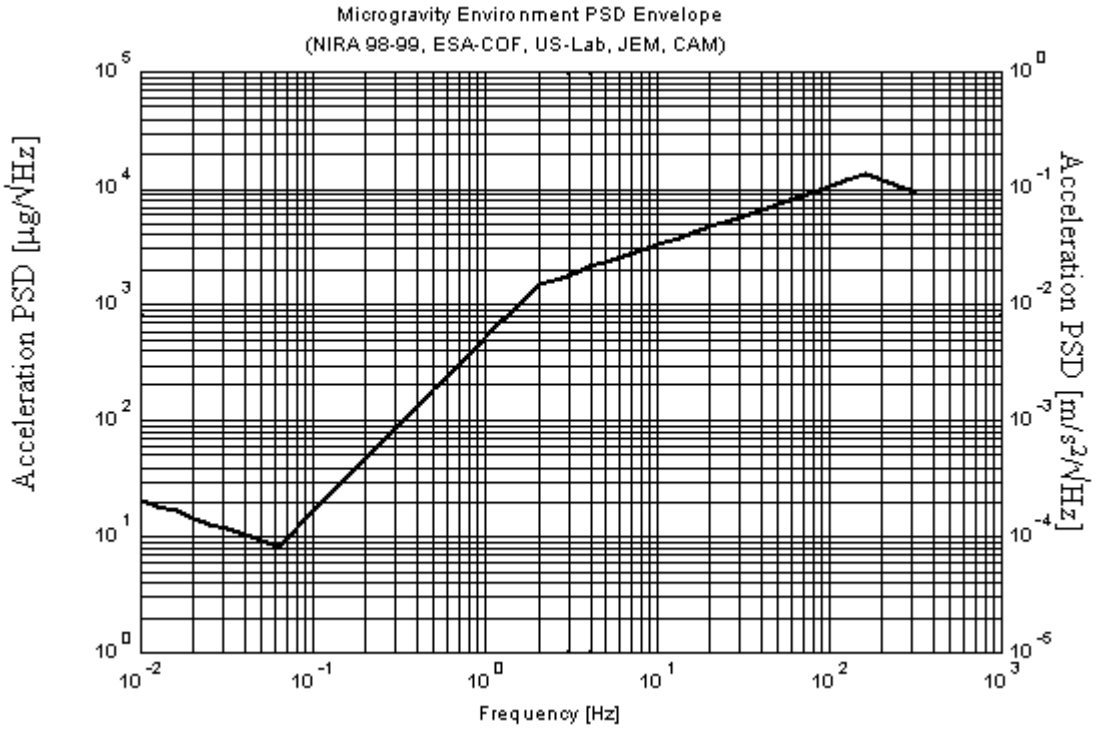

Figure 9.B.8: PSD (Power Spectral Density) of simulated disturbances on the ISS.

Considering the expected environmental disturbance on the ISS, the former of the specified requirements corresponds to impose a rejection margin of at least 130 dB, while the passive system attenuation at this point is 90 dB. Therefore the active control must be able to increase the rejection by at least 40 dB in the measurement bandwidth.

The two-body system is presented in figure 9.B.9. Let us assume that ISS and PGB are described by $(x_1, \dot{x}_1, \ddot{x}_1)$, $(x_2, \dot{x}_2, \ddot{x}_2)$ and that F_C and F_D are the control and the disturbance forces. The equations of motion for the 2 bodies are:

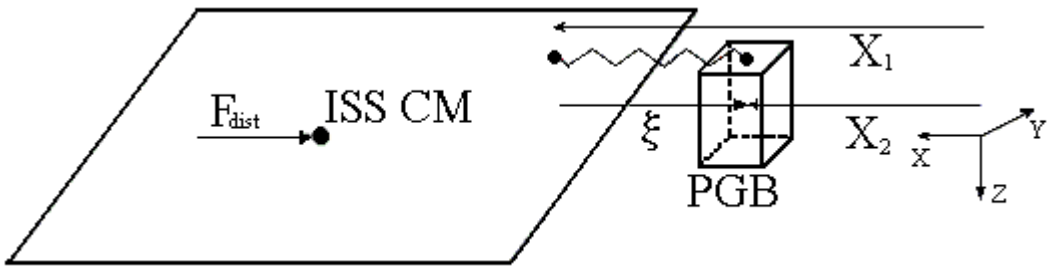

Figure 9.B.9: Two-body representation of the ISS – PGB system.

The equations of motion for the 2 bodies are:

$$\begin{cases} m_1\ddot{x}_1 = k\xi + \beta\dot{\xi} + F_D + F_C \\ m_2\ddot{x}_2 = -k\xi - \beta\dot{\xi} - F_C \end{cases} \Rightarrow \mu\ddot{\xi} = -k\xi - \beta\dot{\xi} - F_C - \mu F_D / m_1 \qquad (9.B.14)$$

with $\xi = x_2 - x_1$ the relative displacement, $\mu = m_1 m_2 /(m_1 + m_2)$ the reduced mass of the system, k the spring stiffness, $\beta = \sqrt{k\mu}/Q$ the damping coefficient and Q the overall mechanical quality factor (including the internal spring damping and external viscous damping acting on the PGB). All the simulations refer to the following values of m_1, m_2, k, Q: m_1 = 300000 Kg - m_2 = 60 Kg - k = 0.3 N/m - Q = 100.
In figure 9.B.10 the control block diagram is shown. The control force is the superimposition of the position control force (output of $[H_{POS}]$=[N/m]) and the acceleration control force (output of $[H_{ACC}]$=[Kg]):

$$F_C = H_{POS}(s)\xi + H_{ACC}(s)\ddot{x} \qquad (9.B.15)$$

In the frequency domain, the relative displacement is:

$$\hat{\xi} = -\frac{\hat{a}_d}{s^2 + \frac{m_2}{\mu}\left[\frac{\mu G + H_{POS}}{m_2 + H_{ACC}}\right]} \qquad (9.B.16)$$

while the absolute accelerations of ISS and PGB are:

$$\begin{cases} \hat{\ddot{x}}_1 = \frac{\mu}{m_1} G\hat{\xi} + \hat{a}_d + \frac{\hat{F}_C}{m_1} \\ \hat{\ddot{x}}_2 = \left(\frac{\mu G + H_{POS}}{m_2 + H_{ACC}}\right)\frac{\hat{a}_d}{s^2 + \frac{m_2}{\mu}\left(\frac{\mu G + H_{POS}}{m_2 + H_{ACC}}\right)} \end{cases} \qquad (9.B.17)$$

with $G = (k + \beta s)/\mu$. $\hat{\xi}$ and $\hat{\ddot{x}}_2$ are the relevant variables from the point of view of the PGB/control performance, while the value of $\hat{F}_C$ has to be within the capacitor capability of generating force.

9.B.3: Derivation of the Transfer Function.

The block diagram of the actively controlled system can be sketched as in figure 9.B.11, where a_{dist} is the acceleration of environmental applied on the ISS and then on the external box of the PGB; a_{PGB} is the acceleration of the PGB in an inertial reference frame; a_{con} is the control acceleration; x_{REF} is the elongation of the idle spring.
$H_a(s)$ is the acceleration filter. It must be able to augment the rejection permitted by the passive system at the frequency of about 3 Hz. H_p is the position filter. Its aim is to maintain the elongation of the spring below a threshold corresponding to the admitted clearance (i.e. ξ-x_{REF} must be lower than the admitted clearance between the internal and the external boxes).

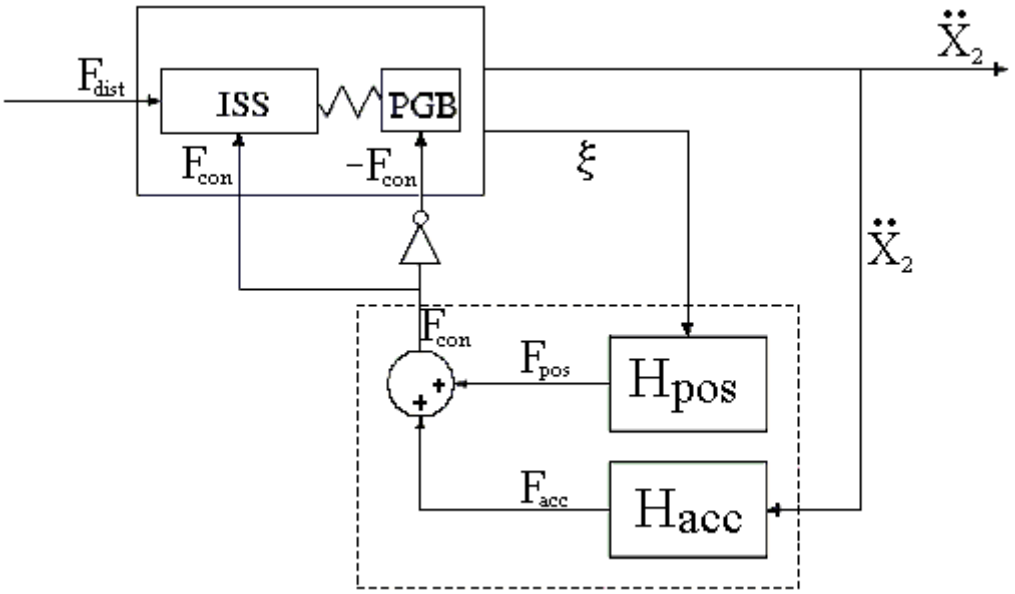

Figure 9.B.10: Block diagram.

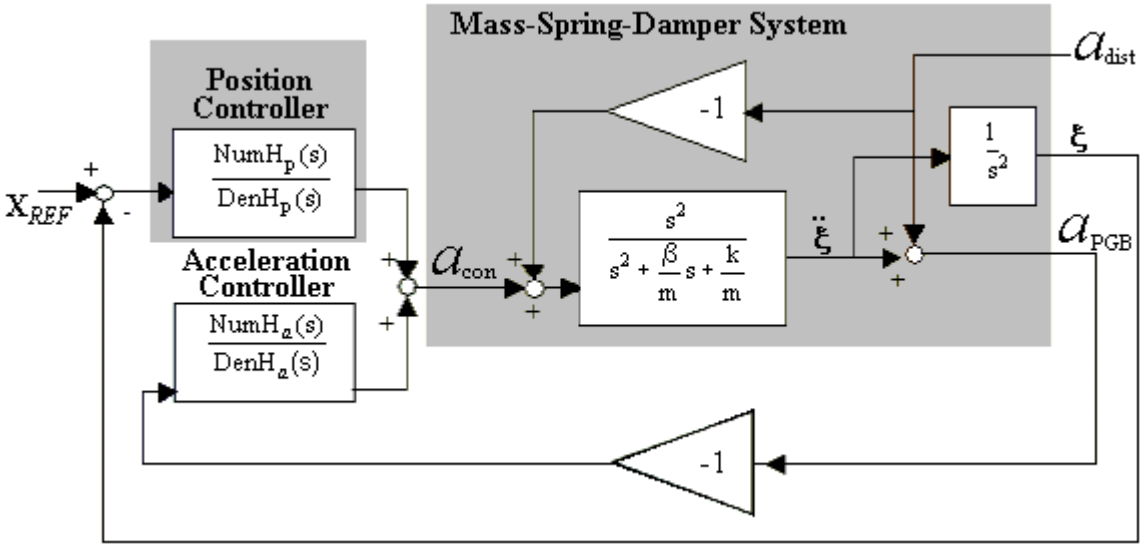

Figure 9.B.11: Block diagram of the controlled system.

The transfer function of the closed loop system from disturbance acceleration and reference spring length to the PGB acceleration is:

$$\hat{a}_{PGB} = \frac{\mathrm{DenH_a}(s)\left(\mathrm{NumH_p}(s)+\left(\frac{\beta}{m}s+\frac{k}{m}\right)\mathrm{DenH_p}(s)\right)\hat{a}_{dist}+\mathrm{DenH_a}(s)\ \mathrm{NumH_p}(s)\ \hat{x}_{REF}}{s^2\left(\mathrm{NumH_a}(s)+\mathrm{DenH_a}(s)\right)\ \mathrm{DenH_p}+\mathrm{DenH_a}(s)\left(\mathrm{NumH_p}(s)+\left(\frac{\beta}{m}s+\frac{k}{m}\right)\mathrm{DenH_p}(s)\right)} \tag{9.B.18}$$

The transfer function of the closed loop system from disturbance acceleration and reference spring length to the elongation is:

$$\hat{\xi} = \frac{-\mathrm{DenH_p}(s)\ \left(\mathrm{NumH_a}(s)+\ \mathrm{DenH_a}(s)\right)\hat{a}_{dist}+\mathrm{DenH_a}(s)\ \mathrm{NumH_p}(s)\ \hat{x}_{REF}}{\left(s^2\left(\mathrm{NumH_a}(s)+\mathrm{DenH_a}(s)\right)+\left(\frac{\beta}{m}s+\frac{k}{m}\right)\mathrm{DenH_a}(s)\right)\mathrm{DenH_p}(s)+\mathrm{DenH_a}(s)\ \mathrm{NumH_p}(s)} \tag{9.B.19}$$

As there isn't a reference profile for the spring elongation the attenuation of the external disturbance and the response in terms of distance between inner and external boxes can be studied considering only the first part of the reported transfer functions (9.B.18) and (9.B.19) depending on $\hat{a}_{\text{dist}}$.

- Acceleration Filter Design.

The simplest acceleration regulator that can be designed is formed by three terms. An high-pass filter, a phase-lead filter introduced for stability reasons and a low-pass filter (see table 9.B.2). Applying that filter the system response is the one represented by the dashed red line, "**a**" in figure 9.B.12. A part for the removal of the resonance peak, its benefit is large in the band between 10^{-3} and 10^{-1} Hz, while at 1 Hz the attenuation w.r.t. the passive system (black continue line) is negligible. Moreover this filter reduces the frequency of the slope start by 2 decades that implies an amplification of the peak-to-peak spring elongation in the order of several centimetres. The response "**b**" (dotted-dashed green line) is obtained from "**a**" moving at higher frequency the frequency of the slope start. This is obtained by a proper modification of acceleration and position filters. The problem is that the maximum clearance is more or less the same permitted by the passive system itself so the effect of the active control reduces in practice to delete the resonance peak and the attenuation is too low to justify introduction of active control. The evident result of this first analysis is that the filter shape must be modified to guarantee a slope of the system response of at least 60 dB/dec. This has been obtained in "**c**" (dotted blue line). The draw-back of this filter is that it maintains a large gain (40 dB) up to frequencies of at least 1 Hz so the cross-over frequency is very high. Theoretically speaking, as the gain reduces by 20 dB/dec, gaining 40 dB up to 2-3 Hz (corresponding to the measurement frequency) the cross-over frequency would be 200-300 Hz, thus the controller should require a sampling rate of at least 400-600 Hz. To guarantee feasibility, the acceleration filter must be made more complex. The solution envisaged in "**d**" (dashed violet line) corresponds to an acceleration filter where the low-pass includes a 4^{th} order lag-lead filter. The gain reduces with a slope of 80 dB/dec between 2 and 7 Hz, then a triple zero modify the slope to 20 dB/dec and the resulting cross-over frequency is between 10 and 20 Hz which permits a control loop at a frequency lower than 100 Hz. The maximum attenuation is between 2 and 3 Hz and corresponds to about 130 dB.

Filter	Order, frequency [Hz]
"High-Pass" - Numerator	1, ω=0
"High-Pass" - Denominator	1, $\omega=1\cdot10^{-4}$
"Phase-Lead" – Numerator	2, $\omega=1\cdot10^{-3}$
"Phase-Lead" - Denominator	2, $\omega=1\cdot10^{-4}$
"Low-Pass" – Numerator	3, ω= 7
"Low-Pass"- Denominator	4, ω= 2.5
"Gain"	85.9

Table 9.B.2:Parameters used in the acceleration filter.

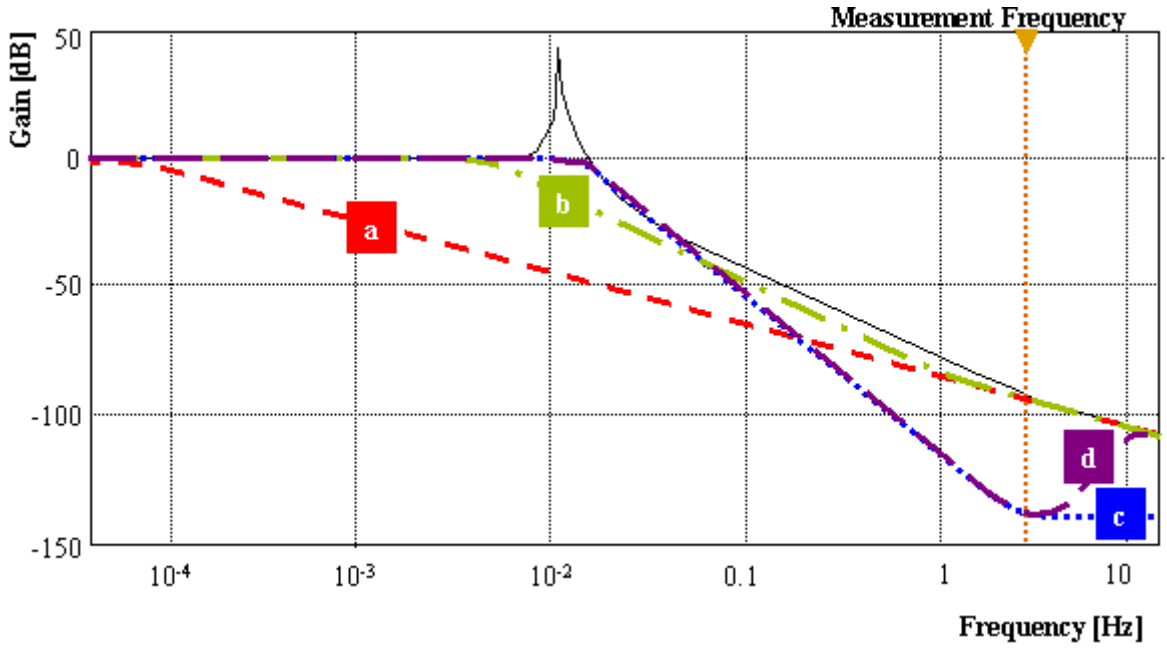

Figure 9.B.12: System response with different filters.

More complex and higher order the acceleration filter is, more complex also the position filter becomes. This is a consequence of the interactions between the two filters (position and acceleration) that have antagonist aims.

- Position Filter Design.

The aim of the position filter is to maintain the elongation of the spring below a threshold corresponding to the admitted clearance. To approach the filter design the equation (9.B.19) can be made equal to a specification equation like:

$$x_{spec} = \frac{-1}{s^2 + (\omega_1 + \omega_2)s + \omega_1\omega_2} a_{dist} \qquad (9.B.20)$$

The frequencies ω_1 and ω_2 have been chosen so that the low frequency gain in (9.B.20) maintain the clearance under 5 mm taking into account a disturbance of 10^{-5} m/s^2 and that the transfer function shape remains similar to the one of the passive system, a part the resonance peak. In this manner the following equations (9.B:21) descends for the numerator and denominator of the position filter:

$$NumH_p(s) = \left(NumH_a(s) + DenH_a(s)\right)\left[(\omega_1 + \omega_2)\ s + \omega_1\omega_2\right] - \left(\frac{\beta}{m}s + \frac{k}{m}\right)DenH_a(s) \qquad (9.B.21.a)$$

$$DenH_p(s) = DenH_a(s)\ \left(\beta s/k + 1\right) \qquad (9.B.21.b)$$

Note that the term $1+\beta s/k$ has been introduced to guarantee that the denominator of the transfer function has a degree equal to the degree of numerator. The resulting shape has been rearranged to guarantee stability and feasibility in terms of sampling frequency. The parameters of the position filter for the cases "**b**", "**c**" and "**d**" are illustrated in the table 9.B.3.

Filter	Order, frequency [Hz]
"Lead-Lag" – Numerator	1, $\omega=5\cdot10^{-5}$
"Lead-Lag" – Denominator	2, $\omega=1\cdot10^{-4}$
"Phase-Lead" – Numerator	2, $\omega=1\cdot10^{-3}$
"Phase-Lead" - Denominator	2, $\omega=3\cdot10^{-2}$
"Gain"	0.226

Table 9.B.3: Parameters used in the position filter.

- Frequency Response.

Figure 9.B.13 shows the expected frequency response of the PGB for acceleration control. Figure 9.B.14 shows its phase as a function of frequency. In figure 9.B.15, instead, the transfer function of the closed loop system from disturbance acceleration to the elongation is shown as a function of frequency. The solid line is referred to passive isolation only while the dashed one is evaluated in the presence of active control "**d**" too. Figure 9.B.16 shows the expected vibration acceleration (RMS) on the PGB. The residual noise at about 3 Hz is at the level of 10^{-10}m/s^2 (i.e.10^{-11} g/√Hz), which is the goal. It is obtained by combining the result plotted in figure 9.B.13 with the expected noise on the ISS shown in figure 9.B.8.

9.B.4: Thermal Analysis.

The ISA accelerometers need thermal stability of the environment in order to minimize thermal noise. This environment is the MDL which includes the PGB. It is necessary to thermally insulate the accelerometer from its environment both radiatively and conductively.
We need to study the main mechanism of heat transmission ([61 – 63]). Let us take two parallel surfaces S with temperatures T and T+ΔT. Vacuum between the two surfaces does ensure radiative transfer of heat according to:

$$Q_{rad} \sim 2\sigma\varepsilon_T S T^3 \Delta T \qquad (9.B.22)$$

where σ is the Stefan-Boltzmann constant and ε_T the emissivity of the material.
The radiative coupling between the mobile structure (PGB) and the MDL can be minimized by means of an aluminised kapton tape on all the surfaces of the fixed structure, which guarantees a very low thermal emissivity.
The conductive coupling between the ISS and the PGB is well reduced by the thin springs. If the helical spring used to suspend the PGB has total length L, wire diameter d and is made of a material with thermal conductivity λ_T, heat conduction from the two ends of the spring at temperatures T and T+ΔT is expressed by the relation (9.B.23).

$$Q_{cond} \sim 4\pi d^2 \lambda_T / L \qquad (9.B.23)$$

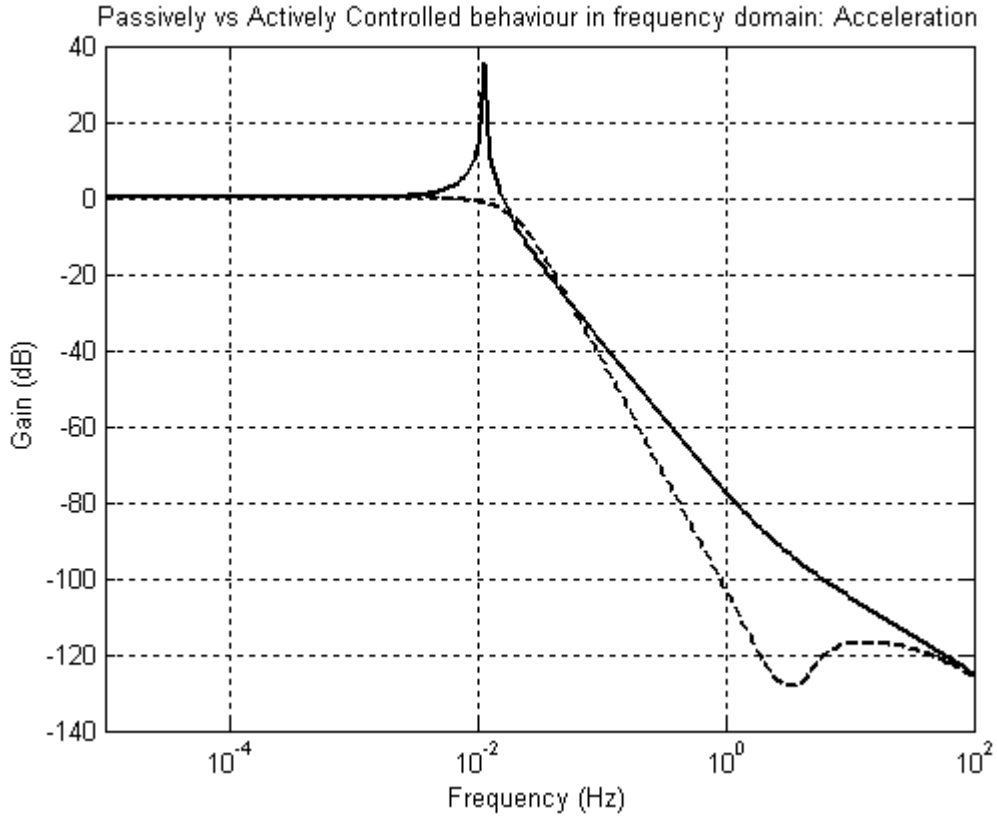

Figure 9.B.13: Transfer function PGB acceleration/disturbance of the actively controlled system. Solid line: passive isolation only. Dashed line: active control "**d**".

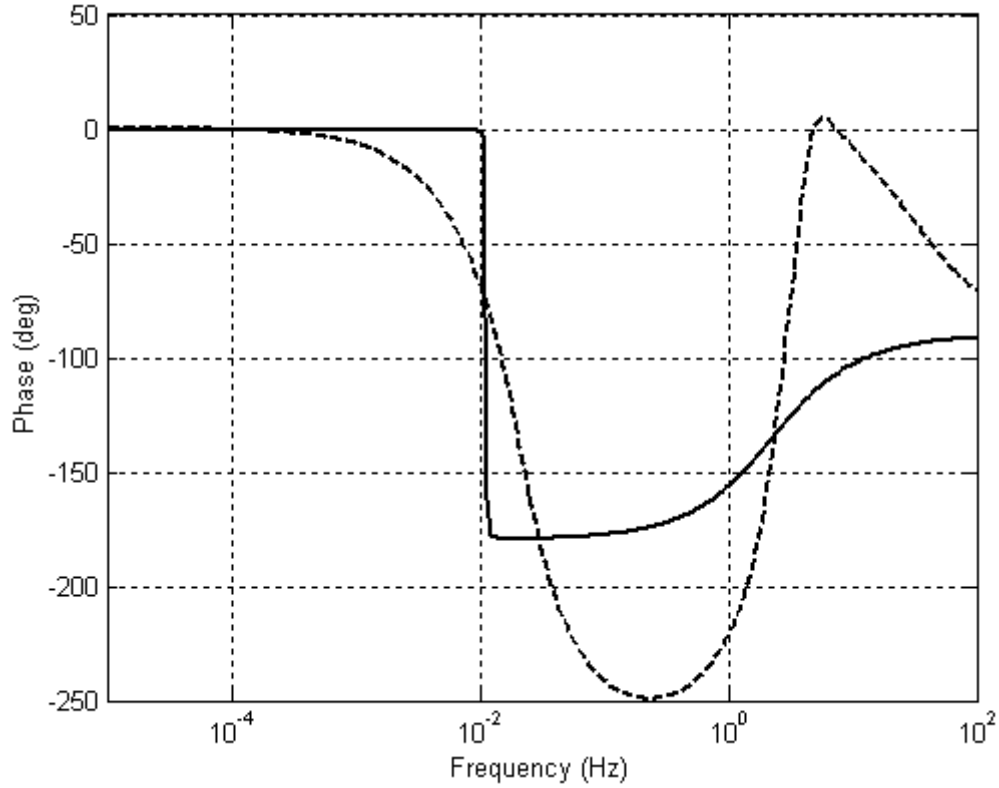

Figure 9.B.14: Phase as a function of frequency. Solid line: passive isolation only. Dashed line: active control "**d**".

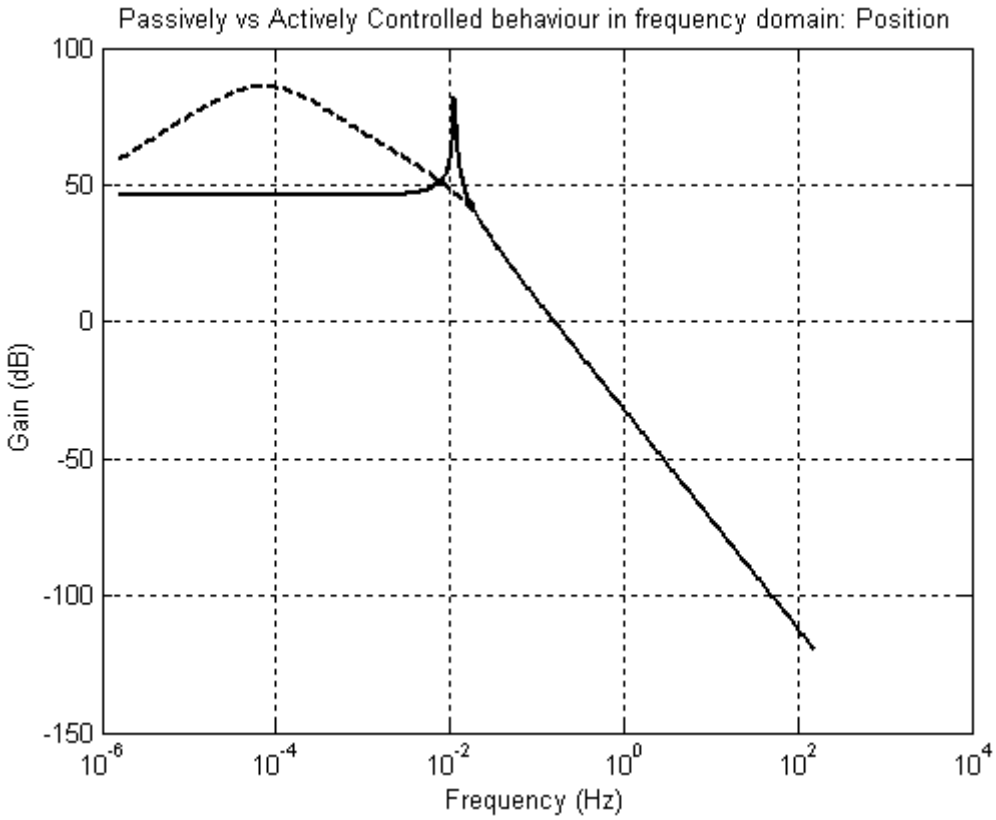

Figure 9.B.15: Transfer function PGB displacement/disturbance of the actively controlled system. Solid line: passive isolation only. Dashed line: active control "**d**".

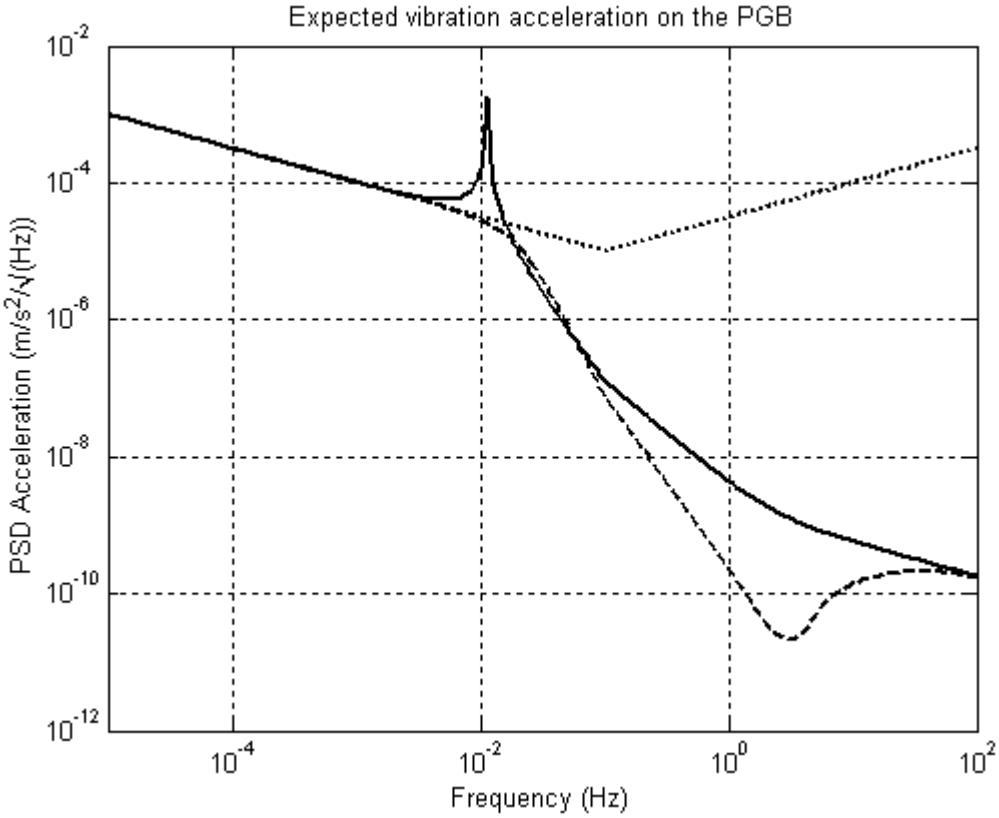

Figure 9.B.16: Log / Log plot of the expected vibration acceleration (RMS) on the PGB. The solid line is

referred to passive isolation only while the dashed one is evaluated in the presence of active control "d" too. The dotted line is the PSD of simulated disturbances on the ISS.

The residual gas in the MDL can contribute to the thermal coupling between the ISS and the PGB. Being p the pressure of the residual gas, the heat transferred per second is:

$$Q_{gas} \sim c_T a_0 p S \Delta T \qquad (9.B:24)$$

We have to take into account the power dissipated by Joule's effect. If ρ_E is the electrical resistivity of the wire of the spring and *i* the electrical current, energy dissipated as heat is:

$$Q_E \sim \rho_E L i^2 / d^2 \qquad (9.B.25)$$

It is easy to show that the temperature variations due to the heat transfer mechanisms (9.B.22), (9.B.23), (9.B.24) and (9.B.25) are negligible if compared with the variation of the air temperature of the cooling system. In this case the expected variation is of 11.1K.
Here we report the results of a preliminary analysis of disturbances due to thermal variations assuming passive thermal isolation only. We analyse how heat passes firstly through the external environment (MDL) and secondly through the Pico Gravity Box. Let us consider both the internal surface of the MDL and the internal surface of the PGB covered by a Multi Layer Insulator composed by ten layers at least. The system can be modelled by a block–diagram with two subsystems (see figure 9.B.17). MDL represents the rack of the international space station containing the PGB. We are interested in temperature fluctuation at the level of the ISA accelerometer located inside the PGB.

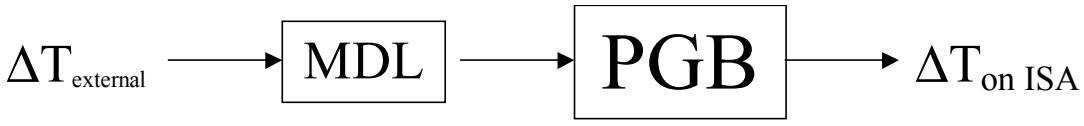

Figure 9.B.17: Thermal Block diagram .

The mass and thermal capacity of a system will reduce thermal variations at frequencies higher than a threshold frequency depending on the timescale of its thermal inertia τ_T. First hand knowledge of the apparatus is required in order to establish how long is this timescale.
The resulting attenuation factor at a frequency ν is $T(\nu) = \Delta T_{ext}(\nu) \Big/ \sqrt{1 + (2\pi\nu\tau)}$. At the first block corresponds a thermal transfer function (TTF) which is constant at low frequencies (i.e. frequencies lower than the critical one; we assume a critical frequency of about 10^{-4}Hz ($\tau_1 \approx 10^4$s), which is not an optimistic assumption) and which decreases at a rate of 20 db per decade at frequencies higher than the critical one.
At the second block corresponds the thermal transfer function of the PGB. In this case the transfer function is similar to the previous one, but the critical frequency is about 10^{-3}Hz (we have assumed a higher frequency because the mass of the body is smaller than the mass of the Container). Instead of this model we could consider a third subsystem in order to take into account the external box (a few kilograms) of ISA. With this choice we would obtain a better rejection at high frequencies, but also the 2-stage model shown in figure 9.B.17 is found to be enough to guarantee a residual thermal noise lower than the vibrational noise expected from active and passive attenuation.

We obtain the total transfer function (for the full system of figure 9.B.17) by multiplying the TTFs of each block. At high frequencies it decreases at the rate of 40 db per decade (see figure 9.B.18).
Now, we must evaluate how temperature variations affect the accelerometer, starting from the experimental evidence that ISA's sensitivity to temperature is of about $5\cdot10^{-7}$ g/√Hz per degree of temperature variation, at all frequencies. As a consequence, in the presence of a temperature variation $\Delta T(\nu)$, the accelerometer will measure an acceleration:

$$a_{\Delta T}(\nu) = 5\cdot10^{-7}\Delta T(\nu)\frac{g/K}{\sqrt{Hz}} \qquad (9.B.26)$$

This noise must be lower than the residual vibrational noise obtained thanks to passive and active attenuation assuming no temperature perturbation. The red line in figure 9.B.19 refers to a single stage system (PGB only) and a temperature fluctuation $\Delta T(\nu)=1K/\sqrt{Hz}$. Green and magenta lines refer to a double stage system (MDL + PGB; see figure 9.B.17) and temperature variations of $\Delta T(\nu)=1K/\sqrt{Hz}$ and $\Delta T(\nu)=11K/\sqrt{Hz}$ respectively at the level of the external surface of the MDL.

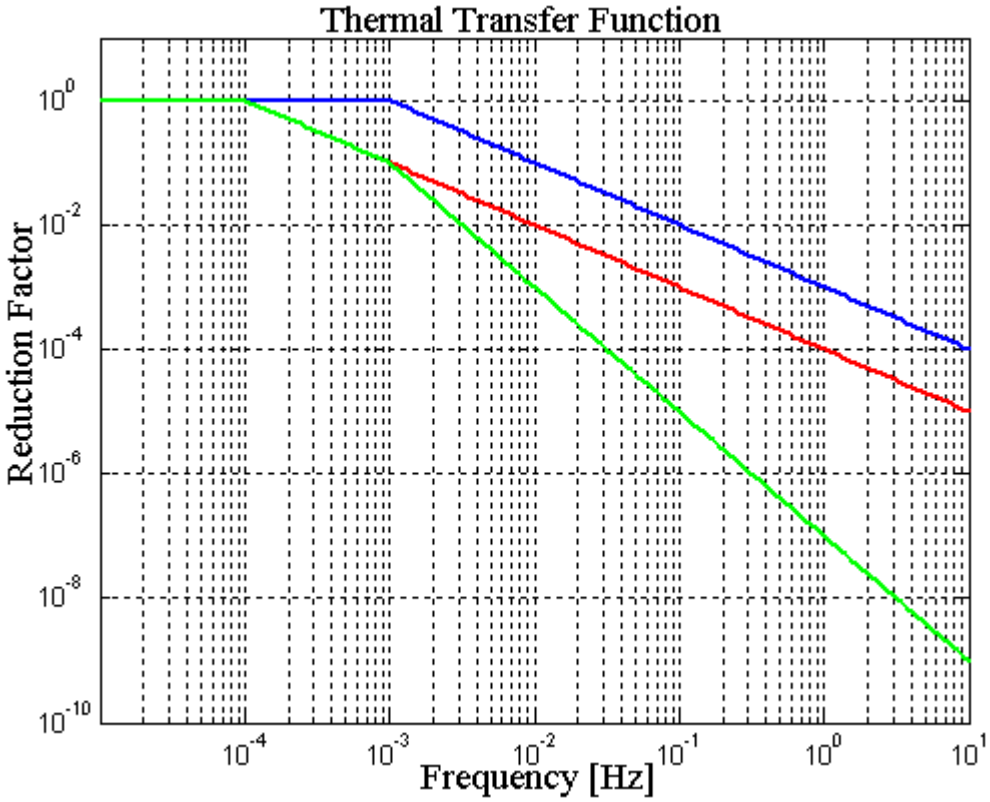

Figure 9.B.18: Thermal transfer functions. Red is the MDL's TTF, blue is the PGB's TTF and green is the total TTF.

Temperature gradients and residual gas pressure around the PGB will give rise to the radiometer effect. The radiometer acceleration is given by:

$$a(\nu) = \frac{p}{2m}\frac{V}{T}\frac{\Delta T(\nu)}{L} \qquad (9.B.27)$$

where p is the pressure of the residual gas, T its temperature, m the mass of the PGB, V its volume and L the length of its side.

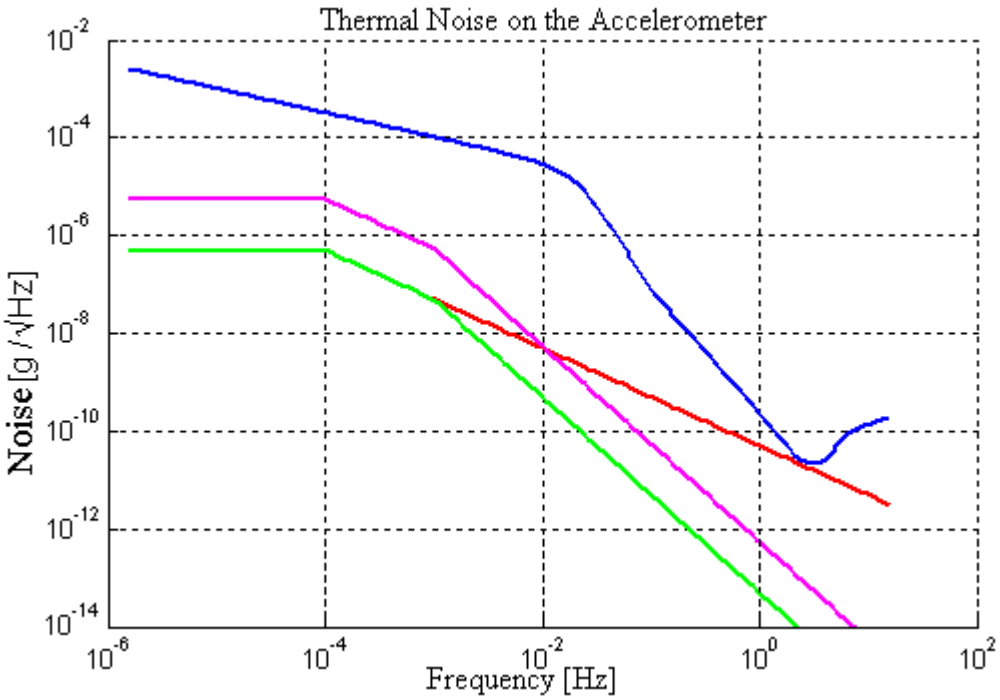

Figure 9.B.19: The blue line represents the level of vibrational noise expected inside the PGB after passive and active attenuation, assuming no temperature perturbation; the other three lines represent the level of disturbances that would be measured by the ISA instrument (inside the suspended PGB) because of the temperature fluctuation $\Delta T(\nu)$: the red line refers to a single stage system (PGB only) and a temperature fluctuation $\Delta T(\nu)=1K/\sqrt{Hz}$ at all frequencies; green and magenta lines refer to a double stage system (MDL + PGB; see figure 10.20) and temperature variations of $\Delta T(\nu)=1K/\sqrt{Hz}$ and $\Delta T(\nu)=11K/\sqrt{Hz}$ respectively (at the level of the external surface of the MDL).

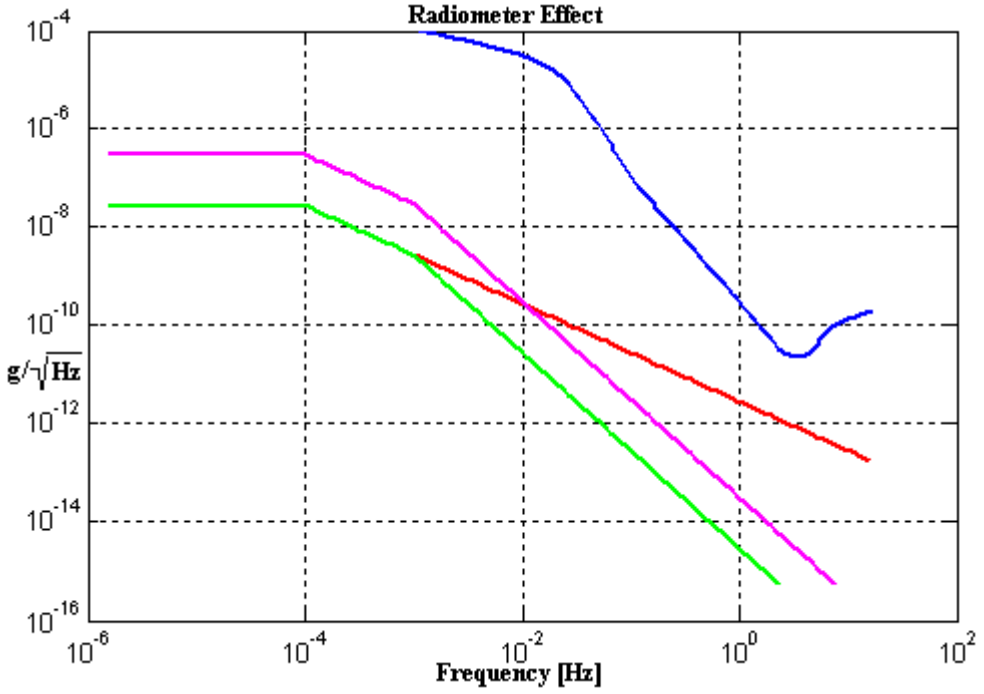

Figure 9.B:20: The blue line represents the level of vibrational noise expected inside the PGB after passive and active attenuation, assuming no temperature perturbation; the other three lines represent the level of disturbances measured by the ISA instrument inside the PGB because of the radiometer effect: the red line refers to a single

stage system (PGB only) and temperature gradients $\Delta T(\nu)=1K/\sqrt{Hz}$; green and magenta lines refer to a double stage system (MDL + PGB; see figure 10.20) and temperature gradients of $\Delta T(\nu)=1K/\sqrt{Hz}$ and $\Delta T(\nu)=11K/\sqrt{Hz}$ across the PGB respectively. In all cases the residual gas pressure is that inside the MDL, i.e. about 10-3 mbar.

In the MDL the residual pressure is quite low ($p\cong 10^{-3}$mbar) and the temperature is about 300K. The radiometer effect resulting from (9.B.27) is plotted (expressed in $g/\sqrt{Hz}$) in figure 9.B.20 as a function of frequency. It is compared to the residual vibrational noise inside the suspended PGB (resulting from active and passive isolation as reported in section 9.B.3), showing that the radiometer effect is not a matter of concern.
The previous analyses appear to indicate that temperature induced disturbances can be kept below the expected level of noise reduction to be provided by the PGB passive/active vibration isolation system without implementing active thermal control of the ISA accelerometer.

APPENDIX 9.C:

NUMERICAL SIMULATION OF THE GG DYNAMICAL SYSTEM.

9.C.1: EIGENVALUES OF THE GG ROTOR IN THE INERTIAL FRAME.

By following the steps in chapter 3, section 3.6, it is convenient to turn (9.10) into a form involving only first-order time derivatives. To this aim, we define the 8-components state vector $\tilde{x}$ as:

$$\tilde{x} = \left[\Delta\vec{r} \quad \Delta\vec{r}_t \quad \Delta\dot{\vec{r}} \quad \Delta\dot{\vec{r}}_t \right]^T \tag{9.C.1}$$

Equations (9.10) may be now written in a compact form:

$$\dot{\tilde{x}} = \tilde{A}\tilde{x} \tag{9.C.2}$$

where $\tilde{A}$ (8×8) is the following square matrix:

$$\tilde{A} = \begin{bmatrix} O(4\times4) & I(4\times4) \\ -K_{NR} & -K'_{NR,t} & -C_{NR} & -C'_{NR,t} \\ -K'_{NR} & -K_{NR,t} & -C'_{NR} & -C_{NR,t} \end{bmatrix} = \begin{bmatrix} O & I \\ -K & -C \end{bmatrix} \tag{9.C.3}$$

O(4×4) is the null matrix; I(4×4) is the identity matrix. K is the matrix of the elastic constants. C is the matrix of the damping coefficients. By introducing the Laplace variable s and the identity matrix $I_{8\times8}$, the characteristic equation may be written as:

$$\det(sI_{8\times8} - \tilde{A}) = \det\left(\begin{bmatrix} sI & -I \\ K & C+sI \end{bmatrix}\right) = \det\left(\begin{bmatrix} sI & -I \\ K & D \end{bmatrix}\right) = 0 \tag{9.C.4}$$

Because $\tilde{A}$ is (8×8), the characteristic polynomial is:

$$p(s) = s^8 + p_7 s^7 + p_6 s^6 + p_5 s^5 + p_4 s^4 + p_3 s^3 + p_2 s^2 + p_1 s^1 + p_0 \tag{9.C.5}$$

The 9 coefficients of the characteristic polynomial are listed in table 9.C.1 as a function of the system parameters. There are several methods of obtaining information about the roots of the polynomial (9.C.5) without solving for them. We may apply the Routh's stability criterion ([44 – 49]) to make certain statements about the stability of the system. To determine the Routh array, we arrange the coefficients of (9.C.5) in two rows, starting with the first and second coefficients and followed by the even numbered and odd numbered coefficients:

$$\begin{array}{lccccc} s^8: & \underline{1} & p_6 & p_4 & p_4 & p_0 \\ s^7: & \underline{p_7} & p_5 & p_3 & p_1 & 0 \end{array}$$

Then we add the third and the fourth rows as follows:

$$b_1 - \frac{\det\begin{bmatrix} 1 & p_6 \\ p_7 & p_5 \end{bmatrix}}{p_7};\ b_2 - \frac{\det\begin{bmatrix} 1 & p_4 \\ p_7 & p_3 \end{bmatrix}}{p_7};\ b_3 - \frac{\det\begin{bmatrix} 1 & p_2 \\ p_7 & p_1 \end{bmatrix}}{p_7};\ b_4 - \frac{\det\begin{bmatrix} 1 & p_0 \\ p_7 & 0 \end{bmatrix}}{p_7} \tag{9.C.6.a}$$

$$c_1 - \frac{\det\begin{bmatrix} p_7 & p_5 \\ b_1 & b_2 \end{bmatrix}}{b_1};\ c_2 - \frac{\det\begin{bmatrix} p_7 & p_3 \\ b_1 & b_3 \end{bmatrix}}{b_1};\ c_3 - \frac{\det\begin{bmatrix} p_7 & p_1 \\ b_1 & b_4 \end{bmatrix}}{b_1} \qquad (9.C.6.b)$$

Coefficient of the characteristic polynomial	Approximated Coefficient[1]
$P_8=1$	$P_8=1$
$p_7 = 2\frac{\omega_n^2}{\omega_s Q}\left(1+\frac{\omega_{nt}^2}{\omega_n^2}\frac{Q}{Q_t}\right)$	$p_7 \simeq 2\frac{\omega_n^2}{\omega_s Q}\quad (p_7 \sim 0)$
$p_6 = \frac{\omega_n^2}{\omega_s Q}\left[2\frac{\omega_{nt}^2}{Q_t}\left(1-\frac{m_r m_{rt}}{m_p^2}\right)+\frac{\omega_n^2}{Q}\left(1+\frac{\omega_{nt}^2}{\omega_n^2}\frac{Q}{Q_t}\right)^2\right]+2\left(\omega_n^2+\omega_{nt}^2\right)$	$p_6 \simeq 2\left(\omega_n^2+\omega_{nt}^2\right)$
$p_5 = 2\frac{\omega_n^4\omega_{nt}^4}{\omega_s^3}\frac{1}{Q^2Q_t}\left(1-\frac{m_r m_{rt}}{m_p^2}\right)\left(1+\frac{\omega_{nt}^2}{\omega_n^2}\frac{Q}{Q_t}\right)+4\frac{\omega_n^2\omega_{nt}^2}{\omega_s}\frac{1}{Q}\left(1-\frac{1}{2}\frac{m_r m_{rt}}{m_p^2}+\frac{1}{2}\frac{\omega_{nt}^2}{\omega_n^2}\frac{Q}{Q_t}\right)$ $+2\frac{\omega_n^4}{\omega_s}\frac{1}{Q}\left(1+2\left(1-\frac{1}{2}\frac{m_r m_{rt}}{m_p^2}\right)\frac{\omega_{nt}^2}{\omega_n^2}\frac{Q}{Q_t}\right)$	$p_5 \simeq 2\frac{\omega_n^2}{\omega_s}\frac{1}{Q}\left[2\omega_{nt}^2\left(1-\frac{1}{2}\frac{m_r m_{rt}}{m_p^2}\right)+\omega_n^2\right]$ $(p_5 \sim 0)$
$p_4 = \frac{\omega_n^4\omega_{nt}^4}{\omega_s^4Q^2Q_t}\left(1-\frac{m_r m_{rt}}{m_p^2}\right)^2+2\frac{\omega_n^4\omega_{nt}^2}{\omega_s^2Q}\left(1-\frac{m_r m_{rt}}{m_p^2}\right)\left(1+2\frac{\omega_{nt}^2}{\omega_n^2}\frac{Q}{Q_t}\right)\left(\frac{1}{Q}+\frac{2}{Q_t}\right)$ $+4\omega_n^2\omega_{nt}^2\left(1+\frac{1}{2}\frac{m_r m_{rt}}{m_p^2 Q Q_t}-\frac{1}{2}\frac{m_r m_{rt}}{m_p^2}\right)+\omega_n^4\left(1+\frac{1}{Q^2}\right)+\omega_{nt}^4\left(1+\frac{1}{Q_t^2}\right)$	$p_4 \simeq 4\omega_n^2\omega_{nt}^2\left(1-\frac{1}{2}\frac{m_r m_{rt}}{m_p^2}\right)+\omega_n^4+\omega_{nt}^4$
$p_3 = -2\frac{\omega_n^4\omega_{nt}^4}{\omega_s^3 Q Q_t}\left(1-\frac{m_r m_{rt}}{m_p^2}\right)^2\left(\frac{1}{Q}+\frac{1}{Q_t}\right)$ $+2\frac{\omega_n^2\omega_{nt}^2}{\omega_s Q}\left(1-\frac{m_r m_{rt}}{m_p^2}\right)\left[2\omega_n^2\left(1+\frac{\omega_{nt}^2}{\omega_n^2}\frac{Q}{Q_t}\right)+\frac{\omega_n^2}{Q_t}\left(1+\frac{1}{Q^2}\right)+\frac{\omega_{nt}^2}{Q_t}\left(1+\frac{1}{Q_t^2}\right)\right]$	$p_3 \simeq 4\frac{\omega_n^4\omega_{nt}^2}{\omega_s Q}\left(1-\frac{m_r m_{rt}}{m_p^2}\right)$
$p_2 = \frac{\omega_n^4\omega_{nt}^4}{\omega_s^2 Q Q_t}\left(1-\frac{m_r m_{rt}}{m_p^2}\right)^2\left[4+\frac{Q}{Q_t}\left(1+\frac{1}{Q^2}\right)+\frac{Q_t}{Q}\left(1+\frac{1}{Q_t^2}\right)\right]$ $+2\omega_n^2\omega_{nt}^2\left(1-\frac{m_r m_{rt}}{m_p^2}\right)\left[\omega_n^2\left(1+\frac{1}{Q^2}\right)+\omega_{nt}^2\left(1+\frac{1}{Q_t^2}\right)\right]$	$p_2 \simeq 2\omega_n^2\omega_{nt}^2\left(1-\frac{m_r m_{rt}}{m_p^2}\right)\left[\omega_n^2+\omega_{nt}^2\right]$
$p_1 = 2\frac{\omega_n^4\omega_{nt}^4}{\omega_s}\left(1-\frac{m_r m_{rt}}{m_p^2}\right)^2\left[\frac{1}{Q_t}\left(1+\frac{1}{Q^2}\right)+\frac{1}{Q}\left(1+\frac{1}{Q_t^2}\right)\right]$	$p_1 = 2\frac{\omega_n^4\omega_{nt}^4}{\omega_s Q}\left(1-\frac{m_r m_{rt}}{m_p^2}\right)^2$
$p_0 = \det(K) = \omega_n^4\omega_{nt}^4\left(1+\frac{1}{Q^2}\right)\left(1+\frac{1}{Q_t^2}\right)\left(1-\frac{m_r m_{rt}}{m_p^2}\right)^2$	$p_0 \simeq \omega_n^4\omega_{nt}^4\left(1-\frac{m_r m_{rt}}{m_p^2}\right)^2$

Table 9.C.1: Coefficients of the characteristic polynomial.

[1] The coefficients are evaluated in the limit $\frac{1}{\omega_s} << \frac{1}{\omega_n}, \frac{1}{\omega_{nt}}$ and $\frac{1}{Q_t} << \frac{1}{Q} << 1$.

We then complete the Routh's array:

$$
\begin{array}{lccccc}
s^8: & \underline{1} & p_6 & p_4 & p_2 & p_0 \\
s^7: & \underline{p_7} & p_5 & p_3 & p_1 & 0 \\
s^6: & \underline{b_1} & b_2 & b_3 & b_4 & 0 \\
s^5: & \underline{c_1} & c_2 & c_3 & 0 & 0 \\
s^4: & \underline{d_1} & d_2 & d_3 & 0 & 0 \\
s^3: & \underline{0 \to \varepsilon} & e_2 & 0 & 0 & 0 \\
s^2: & \underline{f_1} & f_2 & 0 & 0 & 0 \\
s^1: & \underline{g_1} & 0 & 0 & 0 & 0 \\
s^0: & \underline{f_2} & 0 & 0 & 0 & 0
\end{array}
$$

Note that the elements of the successive rows are formed from the two previous rows using determinants, with the two elements in the first column and other elements from successive columns. The first element in the 6-th row is zero, then we can replace it with a small positive constant $\varepsilon>0$. The subsequent rows are determined with the procedure described above and the stability criterion is applied in the limit $\varepsilon\to 0$. If all the coefficients in the first column are positive, then all the roots of the characteristic equation (9.C.4) have real part negative and the system is stable. If they are not all positive, then the number of sign changes in the first column equals the number of roots with positive real part. For example, if the n-th coefficient is positive, the (n-1)-th is negative and the (n-2)-th is positive, then there are two sign changes, hence two roots with positive real part. The coefficients in the first column are listed in table 9.2 together with the sign changes.

Coefficient in the first column	Sign Changes
$1>0$	NO
$p_7 \simeq 2\omega_n^2 / (\omega_s Q) > 0$	NO
$b_1 \simeq \omega_n^2 + \omega_{nt}^2 m_r m_{rt} / m_p^2 > 0$	NO
$c_1 \simeq -2\dfrac{\omega_n^2 \omega_{nt}^4}{\omega_s Q}\left(1-\dfrac{m_r m_{rt}}{m_p^2}\right)^2 \Bigg/ \left(\omega_n^2 + \dfrac{m_r m_{rt}}{m_p^2}\omega_{nt}^2\right) < 0$	YES
$d_1 \simeq \omega_{nt}^2\left[\omega_n^2 + \omega_{nt}^2 + \omega_n^2\left(1 - m_r m_{rt}/m_p^2\right)\right] > 0$	YES
$0\to\varepsilon>0$	NO
$f_1 \simeq -2\left(1 - m_r m_{rt}/m_p^2\right)^2 \omega_n^4 \omega_{nt}^8 / (\omega_s Q) < 0$	YES
$g_1 \simeq 2\dfrac{\omega_n^4 \omega_{nt}^6}{\omega_s Q}\left(1-\dfrac{m_r m_{rt}}{m_p^2}\right)^2 \Bigg/ \left(\omega_n^2 + \omega_{nt}^2 + \omega_n^2\left(1-\dfrac{m_r m_{rt}}{m_p^2}\right)\right) > 0$	YES
$f_2 \simeq \omega_n^4 \omega_{nt}^4 \left(1-\dfrac{m_r m_{rt}}{m_p^2}\right)^2 > 0$	NO

Table 9.C.2: Coefficients in the first column of the Routh's array and the sign changes in that column.

Since there are four sign changes, we conclude that there are four roots of (9.C.4) with positive real part, hence the system is unstable. This conclusion is valid in the limit $\omega_s >> \omega_n$, $\omega_s >> \omega_{nt}$ and $Q_t >> Q >> 1$. Note that the eigenvalues of equation (9.12) differ from the eigenvalues of equation (9.C.4) for a factor j (imaginary unit).

9.C.2: SIMULATION OF THE WHIRLING MOTION IN THE ROTATING FRAME.

In section 9.6 we have written the equations of motion in the rotating reference frame. Before proceeding to implement these equations in Simulink, we need to recast equations (9.15) in a more manageable form:

$$\begin{cases} \Delta\ddot{\vec{\rho}} = \left|\text{to\_PGB/TM}\right\rangle + \left\{\omega_s^2 \Delta\vec{\rho}\right\}_{\text{Centrifugal}} + \left\{2\omega_s \begin{bmatrix} \Delta\dot{\rho}_\eta \\ -\Delta\dot{\rho}_\xi \end{bmatrix}\right\}_{\text{Coriolis}} \\ \qquad\qquad + \left\{-F_{ext}^R / m_s\right\}_{\text{Fext}} + \left|\text{from\_PGB/TM}\right\rangle \\ \Delta\ddot{\vec{\rho}}_t = \left|\text{to\_s/c\_PGB}\right\rangle + \left\{\omega_s^2 \Delta\vec{\rho}_t\right\}_{\text{Centrifugal}} + \left\{2\omega_s \begin{bmatrix} \Delta\dot{\rho}_{t\eta} \\ -\Delta\dot{\rho}_{t\xi} \end{bmatrix}\right\}_{\text{Coriolis}} \\ \qquad\qquad + \left|\text{from\_s/c\_PGB}\right\rangle \end{cases} \tag{9.C.7}$$

where we have introduced the following quantities:

$$\left|\text{to\_PGB\_TM}\right\rangle = -\frac{k}{m_r}\left(\Delta\vec{\rho} - \vec{\varepsilon}^R\right) - \frac{c_R}{m_r}\Delta\dot{\vec{\rho}} \tag{9.C.8.a}$$

$$\left|\text{from\_PGB\_TM}\right\rangle = k_t / m_p \left(\Delta\vec{\rho}_t + \vec{\varepsilon}_t^R\right) + c_{Rt} / m_p \, \Delta\dot{\vec{\rho}}_t \tag{9.C.8.b}$$

$$\left|\text{to\_s/c\_PGB}\right\rangle = -\frac{m_p}{m_{rt}}\left|\text{from\_PGB\_TM}\right\rangle \tag{9.C.8.c}$$

$$\left|\text{from\_s/c\_PGB}\right\rangle = -\frac{m_p}{m_r}\left|\text{to\_PGB\_TM}\right\rangle \tag{9.C.8.d}$$

The total block diagram implemented to simulate the whirling motion is illustrated in figure 9.C.1.

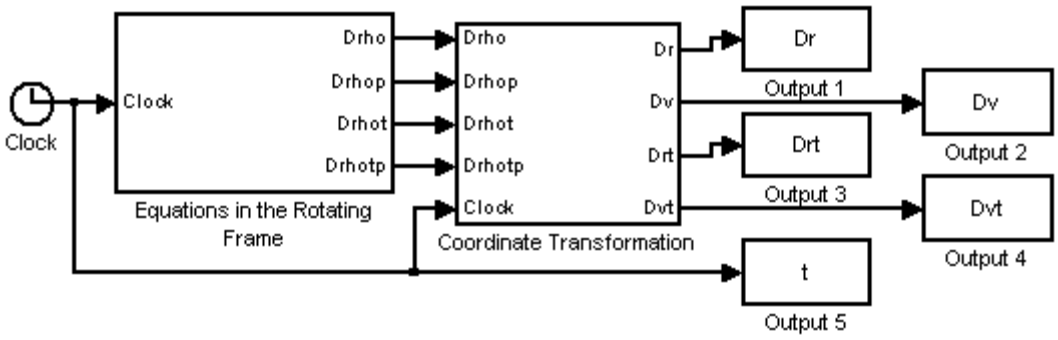

Figure 9.C.1: Total block diagram describing the behaviour of the system.

The block "Equations in the Rotating Frame" implements equations (9.C.7) in the rotating frame. It is illustrated in figure 9.5. It has one input, the temporal variable t, and 4 outputs, the vectors $\Delta\vec{r}, \Delta\dot{\vec{r}}, \Delta\vec{r}_t, \Delta\dot{\vec{r}}_t$. They are the inputs of the block "Coordinate Transformation". This block (not illustrated) transforms a vector in the rotating frame into its counterpart in the non rotating frame.

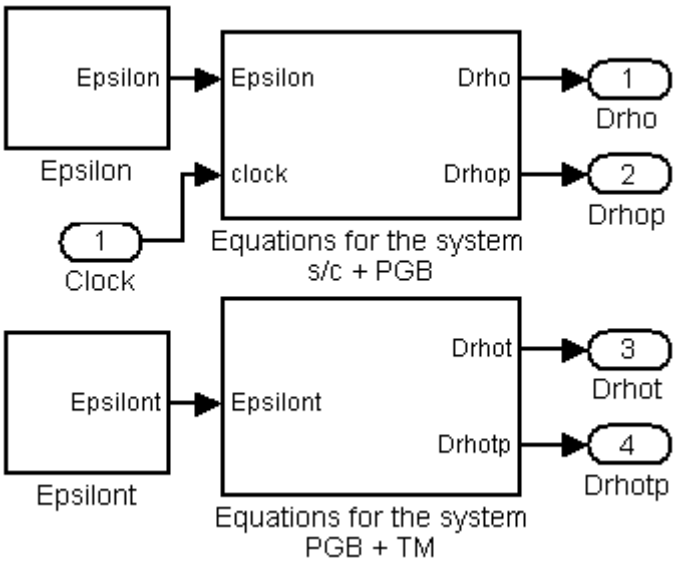

Figure 9.C.2: Block "Equations in the Rotating Frame".

The block "Equations in the Rotating Frame" is illustrated in figure 9.C.2. The two blocks "Epsilon" and "Epsilont" define the eccentricities $\vec{\varepsilon}^R, \vec{\varepsilon}_t^R$. The block "Equations for the system s/c + PGB" implements the first equation of (9.C.7) and it is illustrated in figure 9.C.3, while "Equations for the system PGB +TM" implements the second equation of (9.C.7).

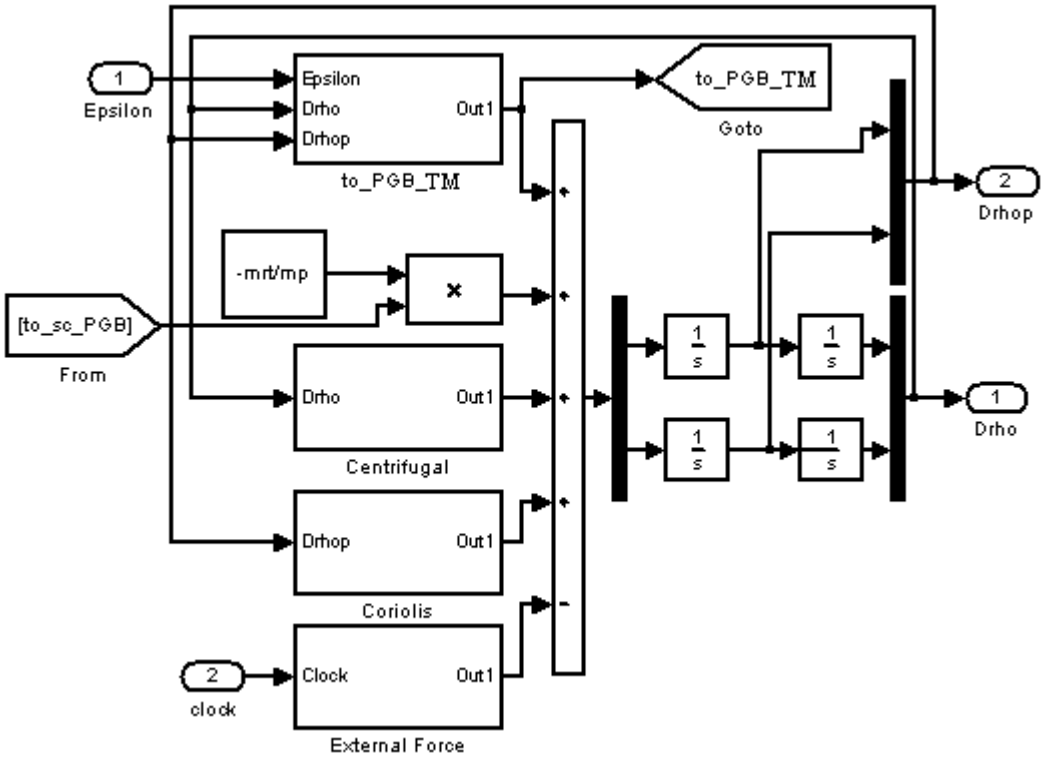

Figure 9.C.3: Block "Equations for the system s/c + PGB".

The block in figure 9.C.3 receive signals from the clock, from the block "epsilon" and from the block "to_sc_PGB". The Sum block adds 5 vectors, i.e. the accelerations in the right side of the first equation in (9.C.7) which are generated in the blocks with the same name (illustrated below). The two components of $\Delta\ddot{\vec{r}}$ are integrated (double integration) in the "Integrator" block 1/s to obtain $\Delta\dot{\vec{r}}$ (first integration) and $\Delta\vec{r}$ (second integration).
The block "External Force" is equivalent to the term $\{-F_{ext}^{R}/m_s\}_{Fext}$ in (9.C.7) and it is shown in figure 9.C.4. The external force is defined in the following way. The referring orbit is a 520 km circular orbit, with angular velocity ω_{orb}. For the purposes of the present analysis the orbital motion of the satellite can be neglected. The orbiting reference system is therefore approximated by an inertial reference frame. The main drag component has been set to $5\cdot10^{-9}$N (after drag free control). It converts to a signal at frequency ω_s in the rotating reference frame. A second component of the drag acts at frequency ω_s-ω_{orb} in the rotating frame and has amplitude $2\cdot10^{-9}$N.
Figure 9.C.5 shows the block "Coriolis", which is equivalent to $\left\{2\omega_s\left[\Delta\dot{\rho}_\eta\,,\ -\Delta\dot{\rho}_\xi\right]\right\}$ in (9.C.7).

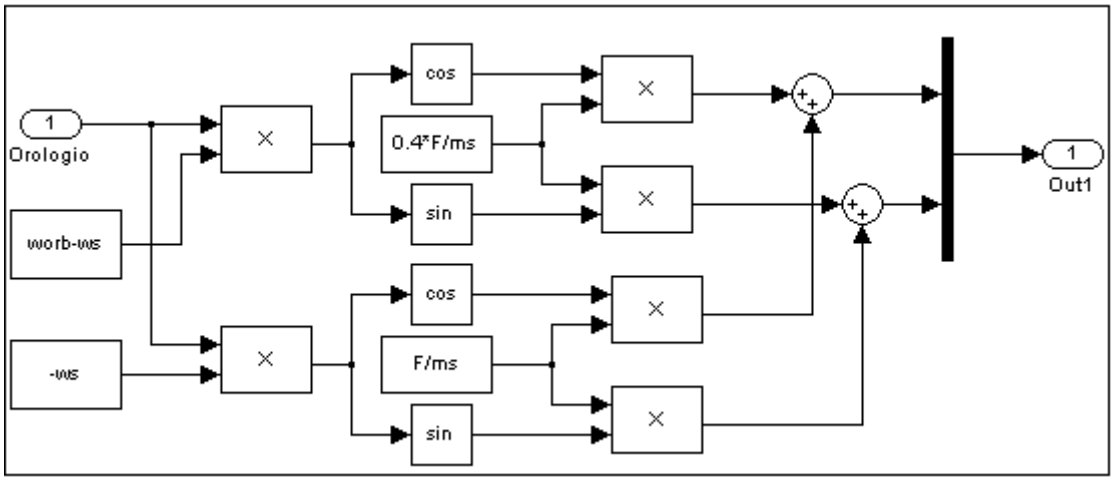

Figure 9.C.4:Block "External Force".

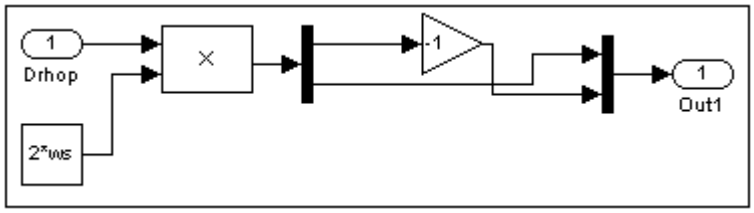

Figure 9.C.5: Block "Coriolis".

The block "Centrifugal" in figure 9.C.6 is equivalent to the term $\left\{\omega_s^2\Delta\vec{\rho}\right\}$.

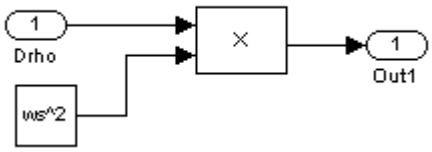

Figure 9.C.6: Block "Centrifugal".

The block $|\text{to\_PGB\_TM}\rangle$ is defined by equation (9.C.8.a) and is shown in figure 9.C.7.

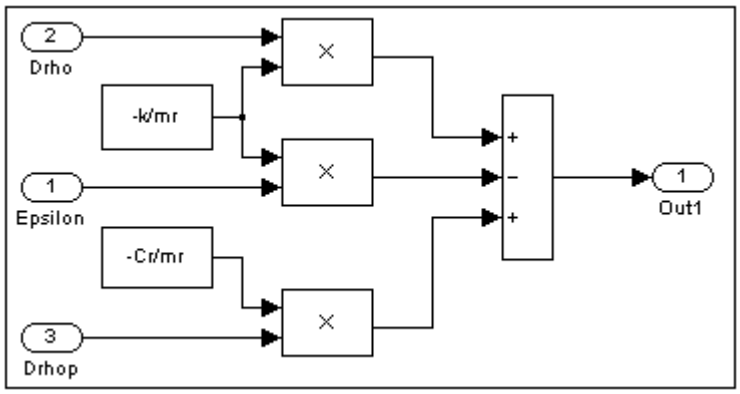

Figure 9.C.7: Block "to_PGB_TM".

The values of the governing parameters in the GG experiment are listed in table 9.C.3.

Parameter	Numerical Value
m_s – Spacecraft's mass	122.071 kg
m_p – PGB's mass	43.647 kg
m_t – test cylinder's mass	20 kg
k, k_t – Elastic constant	0.02 N m^{-1}
Q – Quality factor - PGB/spacecraft	90
Q_t – Quality factor – PGB/test mass	500
ω_s – Spin angular velocity	12.57 rad/s (2Hz)
ε, ε_t - Eccentricity	10^{-7} m
c_R – rotating damping – PGB/spacecraft	1.77 10^{-5} kg s^{-1}
c_{Rt} – rotating damping – PGB/test mass	3.18 10^{-6} kg s^{-1}
T_{orb} – Orbital period	5700 s

Table 9.C.3: Nominal values of the parameters in the GG experiment.

9.C.3: SIMULATION OF THE WHIRLING STABILIZATION – IDEAL CASE.

The damping forces in the rotating frame (9.18) and (9.19) are added to the system (9.C.7) by introducing the blocks "Control_1" and "Control_2", namely:

$$\begin{cases} \Delta\ddot{\vec{\rho}} = \left|\text{to\_PGB/TM}\right\rangle + \left\{\omega_s^2 \Delta\vec{\rho}\right\}_{\text{Centrifugal}} + \left\{2\omega_s \begin{bmatrix} \Delta\dot{\rho}_\eta \\ -\Delta\dot{\rho}_\xi \end{bmatrix}\right\}_{\text{Coriolis}} + \left\{-F_{ext}^R / m_s\right\}_{\text{Fext}} \\ \qquad + \left|\text{from\_PGB/TM}\right\rangle - \left|\text{Control\_1}\right\rangle + \frac{m_{rt}}{m_p}\left|\text{Control\_2}\right\rangle \\ \Delta\ddot{\vec{\rho}}_t = \left|\text{to\_s/c\_PGB}\right\rangle + \left\{\omega_s^2 \Delta\vec{\rho}_t\right\}_{\text{Centrifugal}} + \left\{2\omega_s \begin{bmatrix} \Delta\dot{\rho}_{t\eta} \\ -\Delta\dot{\rho}_{t\xi} \end{bmatrix}\right\}_{\text{Coriolis}} \\ \qquad + \left|\text{from\_s/c\_PGB}\right\rangle - \left|\text{Control\_2}\right\rangle + \frac{m_r}{m_p}\left|\text{Control\_1}\right\rangle \end{cases} \qquad (9.C.9)$$

with:

$$\left|\text{Control}\_1\right\rangle = \frac{c_{nr}}{m_r}\left(\Delta\dot{\vec{\rho}} + \omega_s\begin{bmatrix}-\Delta\rho_\eta \\ \Delta\rho_\xi\end{bmatrix}\right) \tag{9.C.10.a}$$

$$\left|\text{Control}\_2\right\rangle = \frac{c_{nrt}}{m_{rt}}\left(\Delta\dot{\vec{\rho}}_t + \omega_s\begin{bmatrix}-\Delta\rho_{t\eta} \\ \Delta\rho_{t\xi}\end{bmatrix}\right) \tag{9.C.10.b}$$

The non rotating damping coefficients c_{nr} and c_{nrt} used in the simulation are γ and γ_t times larger than the minimum value required for stabilizing a Jeffcott rotor (see equation (1.23)):

$$c_{nr} = \gamma c_{nr}^0 = \gamma k/(\omega_n Q) \tag{9.C.11.a}$$

$$c_{nrt} = \gamma_t c_{nrt}^0 = \gamma_t k_t/(\omega_{nt} Q_t) \tag{9.C.11.b}$$

The block "Equations for the system s/c + PGB" implements the first equation in (9.C.9) and it is illustrated in figure 9.C.8 This block differs from the block in figure 9.C.3 for the presence of non rotating damping forces (9.C.10.a) and (9.C.10.b).

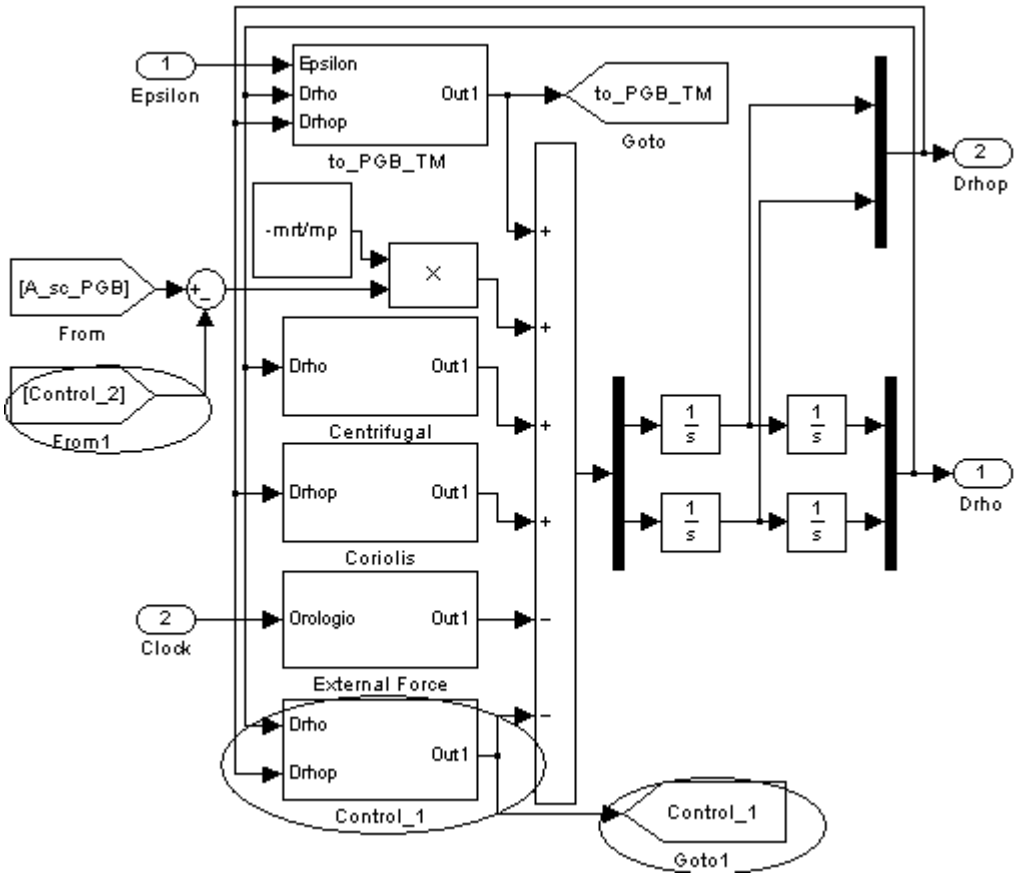

Figure 9.C.8: Block "Equations for the system s/c + PGB" in presence of non rotating damping.

The term $\left|\text{Control}\_1\right\rangle = c_{nr}\left(\Delta\dot{\vec{\rho}} + \omega_s\begin{bmatrix}-\Delta\rho_\eta & \Delta\rho_\xi\end{bmatrix}^T\right)/m_r$ is shown in figure 9.C.9.

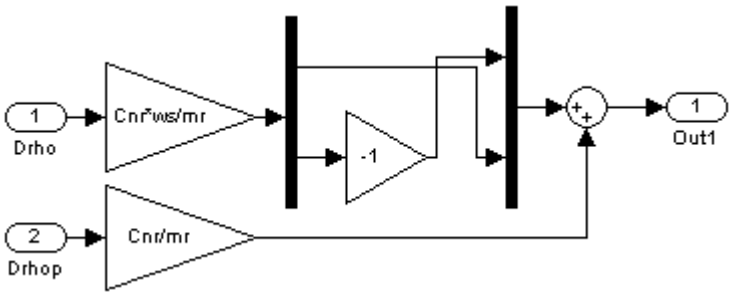

Figure 9.C.9: Block "Control_1".

9.C.4: SIMULATION OF THE WHIRL CONTROL WITH REALIST ERRORS.

The total block diagram implemented in this section is shown in figure 9.15. Figure 9.10 shows the content of the block "Equation of Motion Rotating Frame". Inputs are the components of the control feedback force and the temporal variable t. Its outputs are the vectors $\Delta\tilde{\rho} = \Delta\vec{\rho} + \Delta\vec{\rho}_e$ and $\Delta\tilde{\rho}_t = \Delta\vec{\rho}_t + \Delta\vec{\rho}_{te}$ (errors are added in the two blocks "Drho+Noise" and "Drhot+Noise": a bias of the read-out capacitors and white noise, generated as normally distributed random numbers with mean of 0 and a standard deviation of σ). The block "Equations in the Rotating Frame" is similar to the block in figure 9.C.2.

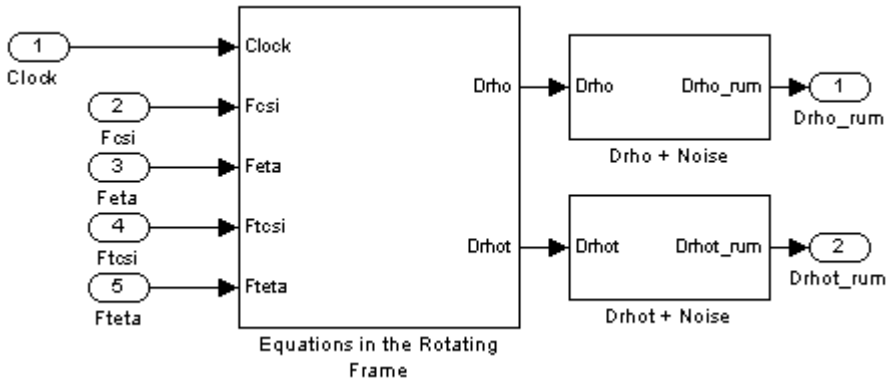

Figure 9.C.10: Block "Equation of Motion - Rotating Frame".

Equation (9.29) is implemented in the block "B(t)" included in "Signal in the Inertial Frame". "B(t)" is illustrated in figure 9.C.11. The "Zero-Order Hold" block implements a sample-and-hold function operating at the specified sampling rate. This block provides a mechanism for discretizing one signal. The block "Integrator" integrates the signal in input. The block can reset its state to the specified initial condition based on an external signal produced by the "Pulse Generator" block (this block produces a pulse with period Ts).

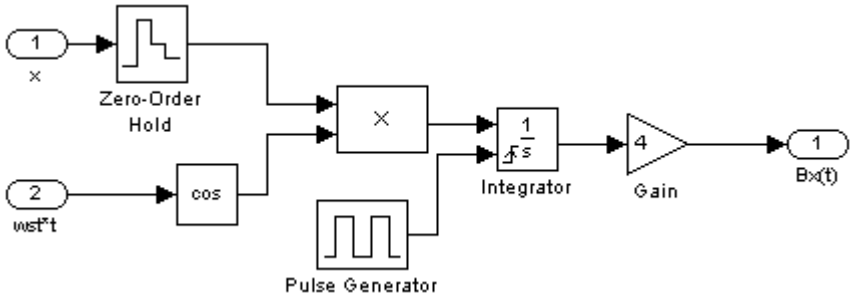

Figure 9.C.11: Block B(t).

wst is the noisy spin angular velocity measured by the ESS. It is generated in the block "Frequency from ESS" shown in figure 9.C.12 inside the block "C(t)" (not shown). Note that white noise is added to the actual value of the spin frequency in order to simulate the sensor noise affecting the ESS. The block "Mean" returns a mean value of the input elements. The block can reset its state to a specified initial condition based on an external signal produced by the "Pulse Generator" block. Vectors (9.31.a) and (9.31.b) are the outputs of the block "Signal in the Inertial Frame".

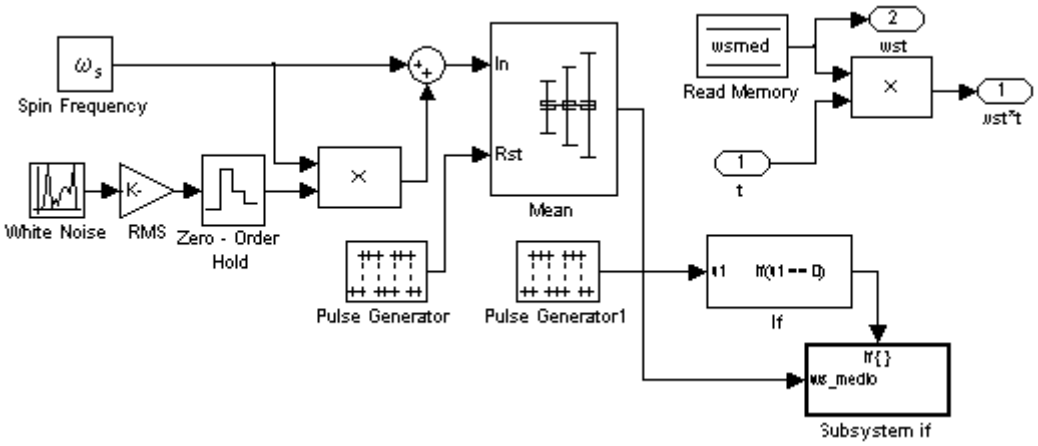

Figure 9.C.12: Block "Frequency from ESS".

From the difference between the corresponding values of the relative displacement in two successive spin periods, the velocity of the modulating signal in the inertial frame is then reconstructed (see equation (9.32) and figure 9.C.13).

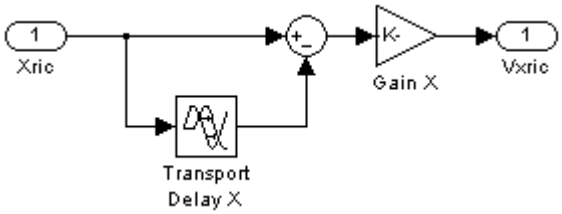

Figure 9.C.13:Block "Velocity".

A second Fourier harmonic analysis at the whirl period T_w is performed in the block "Whirl Velocity" (not described here) to obtain vectors (9.33.a) and (9.33.b). The control command is generated in the form of a pulsed force obtained starting from the reconstructed velocities (9.33.a) and (9.33.b). This operation is performed in the block "Control Force". After changing reference frame (to write the whirl velocities in the rotating frame where the actuators are located), the velocities are sent to the block "Pulsed Control" which generates the control forces. The hearts of this element are the two blocks "V2csi" and "V2eta", where the pulse command at frequency $2\omega_s$ is produced. Input of "V2csi" (see figures 9.C.15 and 9.C.16) is the component of the whirl velocity along the ξ axis in the rotating reference frame. It is sent with positive sign to the block "Positive" and with negative sign to "Negative". These two blocks "Positive" and "Negative" propagate their input only if it is positive (which is true only for one block each time), otherwise the output is null.

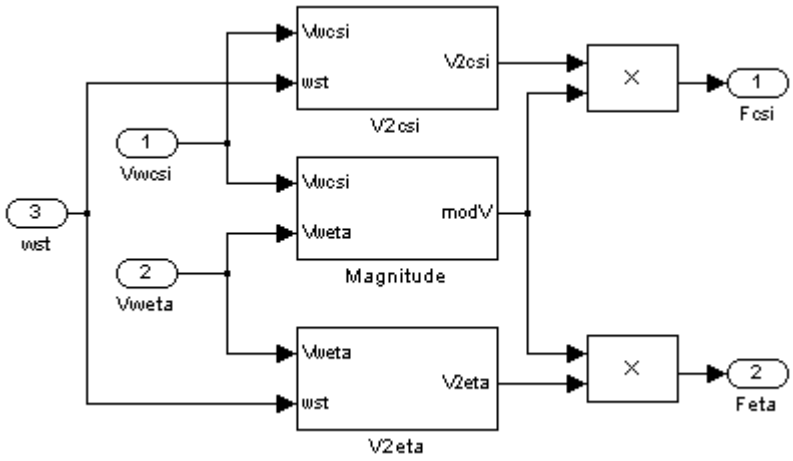

Figure 9.C.14: Block "Pulsed Control".

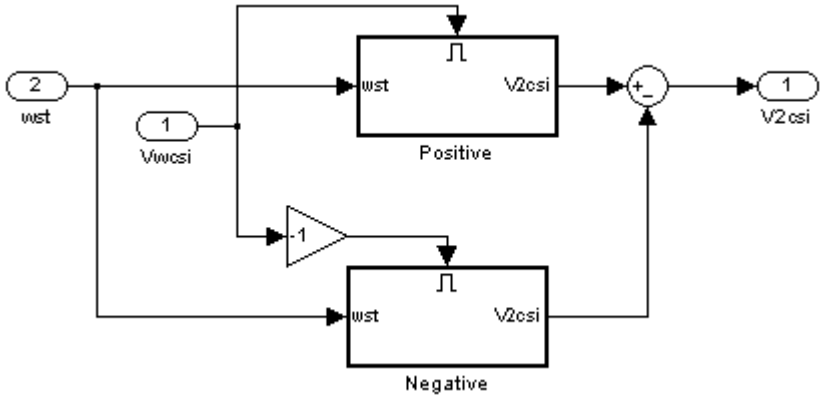

Figure F:15: Block "V2csi".

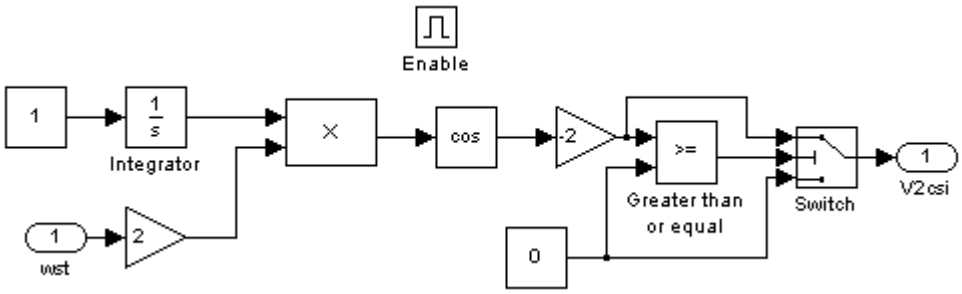

Figure 9.C.16: Block "Positive".

Available online at www.sciencedirect.com
SCIENCE DIRECT®
Physics Letters A 318 (2003) 213–222
PHYSICS LETTERS A
www.elsevier.com/locate/pla

"Galileo Galilei (GG) on the Ground-GGG": experimental results and perspectives

G.L. Comandi [a,b], A.M. Nobili [a,b,*], D. Bramanti [a], R. Toncelli [a,b], E. Polacco [b], M.L. Chiofalo [a,b]

[a] *Space Mechanics Group, Department of Mathematics, University of Pisa, Via F. Buonarroti, I-56127 Pisa, Italy*
[b] *INFN, Sezione di Pisa, Via F. Buonarroti, I-56127 Pisa, Italy*

Received 12 June 2003; accepted 28 July 2003

Communicated by V.M. Agranovich

Abstract

The GGG differential accelerometer is made of concentric coaxial test cylinders weakly coupled in the horizontal plane and spinning in supercritical regime around their symmetry axis. GGG is built as a full scale ground based prototype for the proposed "Galileo Galilei-GG" space experiment aiming to test the equivalence principle (EP) to 10^{-17} at room temperature. We report measured Q values of 95000 at 1.4 Hz, and expect even better ones at typical spin frequencies of a few Hz. An EP violation signal in the field of the Sun would appear as a low frequency displacement in the horizontal plane of the laboratory, and it can be separated out from a much larger whirl motion of the test masses at their natural differential frequency. So far we have managed to reduce the amplitude of this whirl to about 0.1 μm. We discuss how to improve these results in view of the very high accuracy GG experiment in space, and/or to reach a 10^{-13} sensitivity in the lab which would allow us to either confirm or rule out recent predictions of violation to this level.

Keywords: Equivalence principle; Quality factor measurements; Rotordynamics

1. Introduction

A fast rotating differential accelerometer made of weakly coupled concentric and self centering test cylinders, has been designed to be flown inside the small "Galileo Galilei"-GG satellite with the purpose of testing the equivalence principle (EP) to 1 part in 10^{17} at room temperature, see [1,2] and references therein. EP experiments in low Earth orbit take advantage of the stronger signal (by 3 orders of magnitude) for orbiting test masses, and the absence of weight (allowing the test masses to be very weakly suspended and coupled). Two other proposed missions, STEP [3] and μSCOPE [4], also aim to test the equivalence principle in space. The goals are 10^{-15} for μSCOPE and 10^{-17}–10^{-18} for STEP (by running the experiment at very low temperature). Both the STEP and μSCOPE accelerometers are sensitive only along the symmetry axis of the test cylinders and are designed to modulate the signal by rotation around an axis in the plane per-

* Corresponding author.
E-mail address: nobili@dm.unipi.it (A.M. Nobili).

0375-9601/$ – see front matter
doi:10.1016/j.physleta.2003.07.021

pendicular to it. Instead, the GG accelerometer spins around the symmetry axis (which appears to be the natural choice) and is sensitive in the plane perpendicular to it. In addition to preserving the 2D dimension of a possible EP violation signal in the orbital plane of the satellite, and to make fast rotation possible, a 2D accelerometer allows a full scale 1-g version of the instrument to be designed and tested in the laboratory. Indeed, if the spin/symmetry axis is used to suspend the accelerometer against local gravity, its plane of sensitivity lies in the horizontal plane where it could detect the signal of a possible violation of the equivalence principle. The "GG on the Ground"-GGG accelerometer is a full scale prototype of the one proposed for flight with GG (see [5] for details). We report the experimental measurements which confirm the main novel features of the GGG accelerometer as predicted from the theoretical analysis of its dynamical behavior, and the measured quality factors which demonstrate that the accelerometer is suitable for high accuracy EP tests. We also report the current sensitivity of the instrument and discuss how to improve it to demonstrate the feasibility of the GG experiment in space to 10^{-17} and to perform a ground test to 10^{-13}. The latter test would improve the present best results [6,7] by one order of magnitude, enough to either confirm or rule out recent violation predictions based on string theory [8].

2. Design and main features of the GGG differential accelerometer

Experimental tests of the equivalence principle are tests of the most direct experimental consequence of the "Principle", namely the universality of free fall (UFF) by which in a gravitational field all bodies fall exactly the same independently of their mass or composition. UFF experiments require two test bodies of different composition in the gravitational field of a source mass (e.g., the Earth or the Sun). The bodies must be arranged to form a differential accelerometer and to accommodate a read-out system in between them to sense the effects of differential forces. In the GG accelerometer design for space the differential nature of the instrument is obtained in two ways. First, by arranging the test bodies (concentric, coaxial, hollow cylinders) like in a beam balance with the beam along the spin/symmetry axis of the cylinders and very weak coupling in the plane perpendicular to it (the plane of sensitivity). Second, by means of a capacitance read-out which is sensitive primarily to differential displacements of the centers of mass of the test cylinders relative to one another (it may sense common mode displacements too, but only to second order).

Both these features are retained in GGG at 1-g. Like in space, the design is that of a beam balance with the beam along the local vertical, which is also the spin/symmetry axis of the test bodies. These are concentric, coaxial hollow cylinders with the same 10 kg mass as in space. Appropriate cardanic suspensions are used such that they can withstand gravity along the vertical while also weakly coupling the test cylinders in the horizontal plane, for best sensitivity to differential forces. The coupling vertical beam is enclosed inside the rotation shaft by means of 3 such suspensions: the central one to suspend the whole system, the top and down ones for the outer and inner test cylinder respectively (see Fig. 1). The relative displacements between the centers of mass of the test cylinders are detected by a differential capacitance read-out in all similar to the one designed for flight. As in the design for space, the system spins in supercritical regime, i.e., at frequencies (of a few Hz) higher than its natural frequencies which allows self centering and reduced mechanical and electronic noise. The main difference with respect to the experiment in space is the need of a motor and of bearings (which are well-known sources of noise) to provide the rotation of the system. To the contrary, in space, once the whole satellite has been spun to the required rate, this is maintained by conservation of angular momentum and no motor or bearings are needed. Another important difference is that on the ground the spin/symmetry axis of the accelerometer is also the direction of local gravity, a force which exceeds any other force acting on the system by far hence imposing a top/down asymmetry in the accelerometer design, as it is apparent by comparing the GGG accelerometer shown in Fig. 1 with the GG accelerometer shown in Fig. 2 of Ref. [1].

The theoretical analysis of the GGG dynamical system allows us to predict its natural frequencies of oscillation in the plane of sensitivity of the instrument (the horizontal plane), to be compared with their

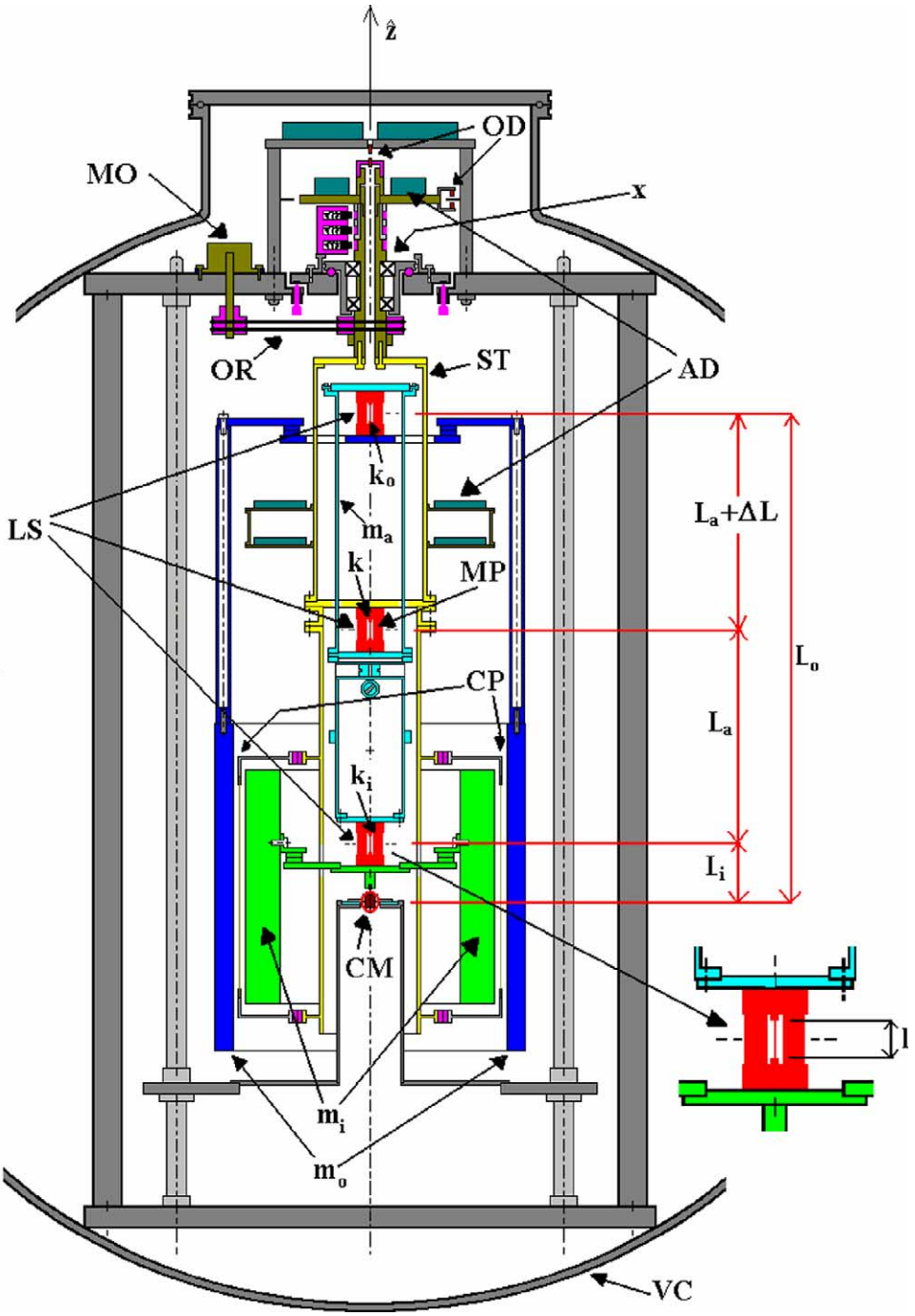

Fig. 1. Section through the spin axis of the GGG differential accelerometer inside the vacuum chamber. (Figure is in colour on the web.) VC: vacuum chamber; MO: motor (drawn in brown); x: ball bearings; OR: O-rings; AD: annular dishes with the read-out electronics; CP: capacitance plates; OD: optical device; m_i: inner test mass (green); m_o: outer test mass (blue); LS: laminar suspensions (orange); m_a: coupling arm (cyan); ST: suspension tube (yellow). The open circle indicates the position of the bodies center-of-mass CM. The drawing is to scale and the inner diameter of the vacuum chamber is 1 m. Also: $L_o = 38$ cm; $L_a = 19$ cm; $L_i = 4.5$ cm; $\Delta L \cong 0$ cm; $l = 0.5$ cm.

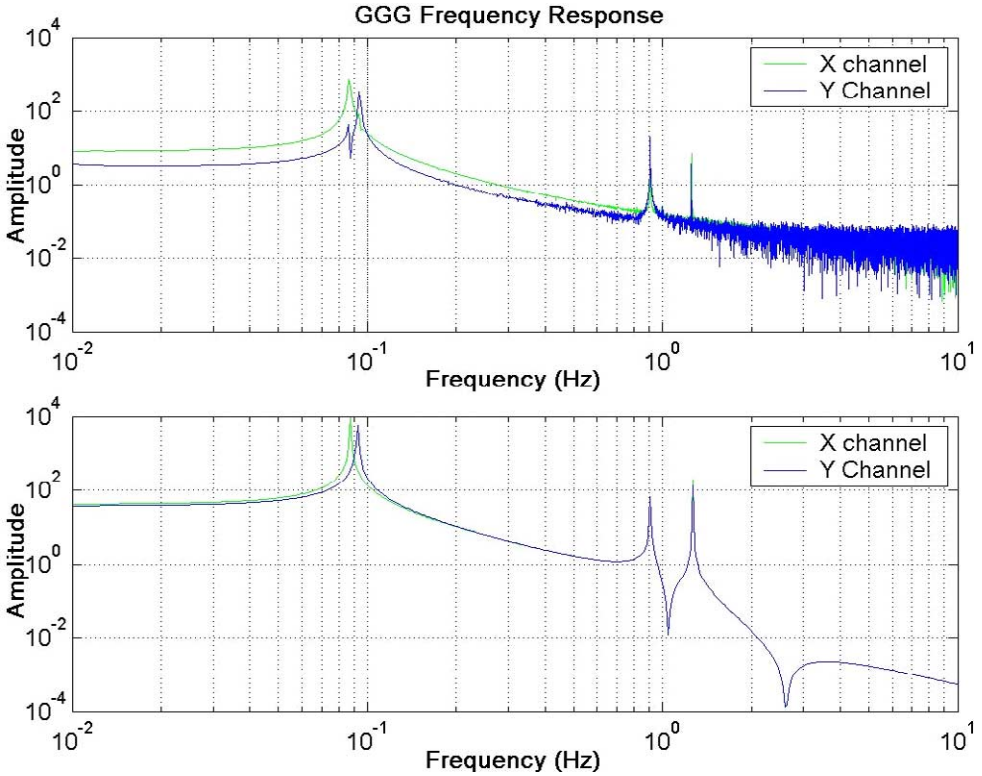

Fig. 2. Natural frequencies of the GGG system in the X and Y directions of the horizontal plane (the plane of sensitivity of the instrument) as theoretically predicted (lower plot) and measured (upper plot). (Figure is in colour on the web.) The measurements are performed at zero spin rate. The lowest frequency (just below 0.1 Hz) is the frequency of the differential oscillations of the test cylinders one with respect to the other. The difference in the X and Y directions is due to manufacturing differences of the cardanic suspension strips in the two directions.

measured values. The sensitivity of the instrument to the effect of differential forces (such as the effect of an EP violation) increases with the natural frequency of differential oscillation of the test cylinders one with respect to the other to power -2, and this frequency can be reduced by using the force of gravity to provide a negative spring.

In Fig. 2 this frequency is just below 0.1 Hz, but it can be further reduced. The figure shows the comparison between the theoretical and the predicted values of the 3 natural frequencies at zero spin rate in the X and Y directions of the horizontal/sensitivity plane, indicating that the values of these frequencies are known beforehand. Once in rotation, the values of the natural frequencies slightly change depending on the spin rate, and these changes can also be predicted theoretically. Fig. 3 shows that all measured values of the natural frequencies lie on the predicted lines. For each spin rate, the supercritical regime lies below the 45° resonance line. In this regime, due to inevitable losses in the system, at the slightly changed values of the natural frequencies the system develops whirl motions (see Section 3). More details on the simulation program that we have developed in order to predict the dynamical behavior of the GGG system (and possibly improve its sensitivity by appropriate changes in the design) are given in [9,10].

3. Quality factor, whirl control and sensitivity

In order to reduce thermal noise and to improve sensitivity, an accelerometer devoted to testing the equivalence principle should have quality factors Q (inverse of loss factors in the system) of values as high as possible. An important advantage of rotation

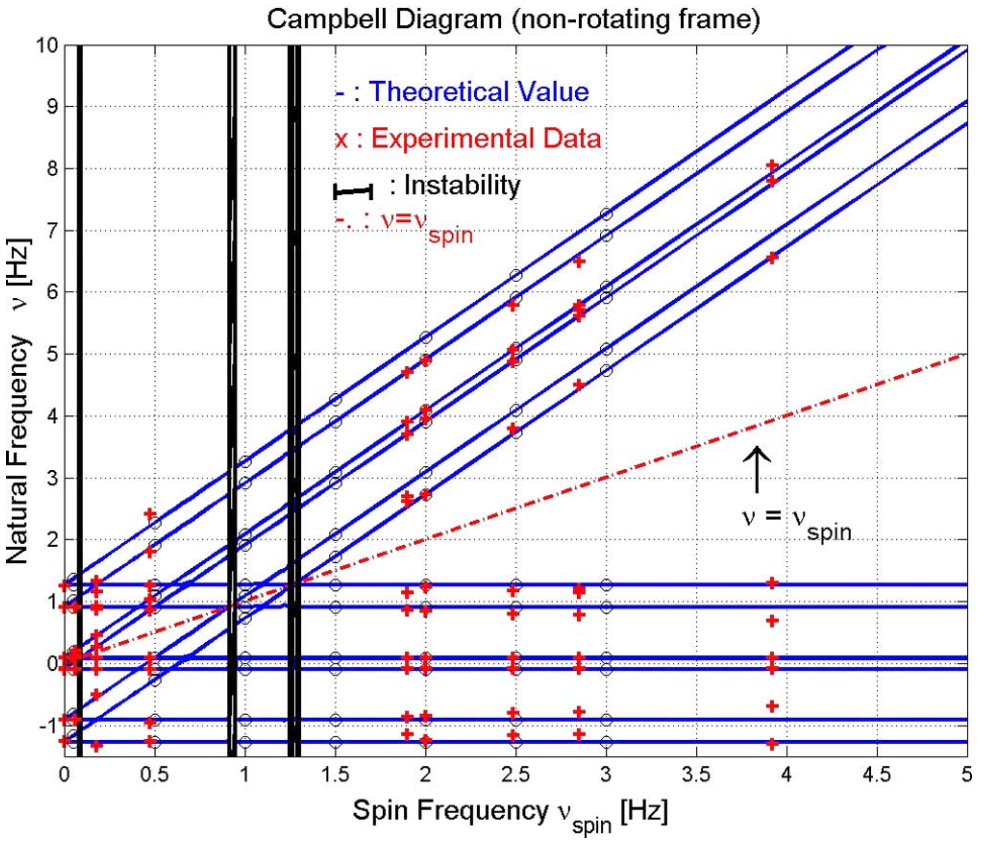

Fig. 3. So-called "Campbell diagram" for the GGG rotor. It gives the natural frequencies of the system (in the non-rotating reference frame of the laboratory) as function of the spin rate of the rotor. (Figure is in colour on the web.) The blue (solid) lines have been predicted within our simulation program of the system (circles on these lines are computed including also a realistic dissipation, i.e., losses in the system, to show that dissipation does not affect the natural frequencies); the red crosses are the measured values, and they clearly confirm the predicted ones. The supercritical regime is easily identified below the red dashed line at 45° inclination (see [9] for details).

.

in supercritical regime (spin frequency higher than the natural ones) comes from the well-known fact that in this regime the suspensions are deformed at the spin frequency of the system, not at their natural ones; hence, losses occur at this frequency (which is the highest in the system), and they are known to decrease with frequency. We can therefore design the system so as to have a very weak coupling of the test cylinders, hence, a very low natural frequency for differential oscillations of their centers of mass one with respect to the other (for best sensitivity to differential forces), and yet obtain a high quality factor by spinning at high frequency. Moreover, since rotation provides the modulation of the signal, high spin rate also means high modulation frequency and reduced "$1/f$" noise. It is therefore apparent that the supercritical regime is extremely well suited for accelerometers aiming to test the equivalence principle.

Quality factors at the natural frequencies can be measured, for the whole system, at zero spin rate, by exciting oscillations at these frequencies and measuring the decay in the oscillation amplitude. Fig. 4 reports measurements performed in 2002 at the 0.9 Hz natural frequency, yielding value of 16450. In 2003, with improved suspensions, we have obtained, at about the same frequency a higher Q value (33000), as shown in Fig. 5. The same figure shows measured Q values at the other 2 natural frequencies (1.4 Hz and 0.08 Hz). As expected, the Q value increases with the frequency (losses are smaller at higher frequencies),

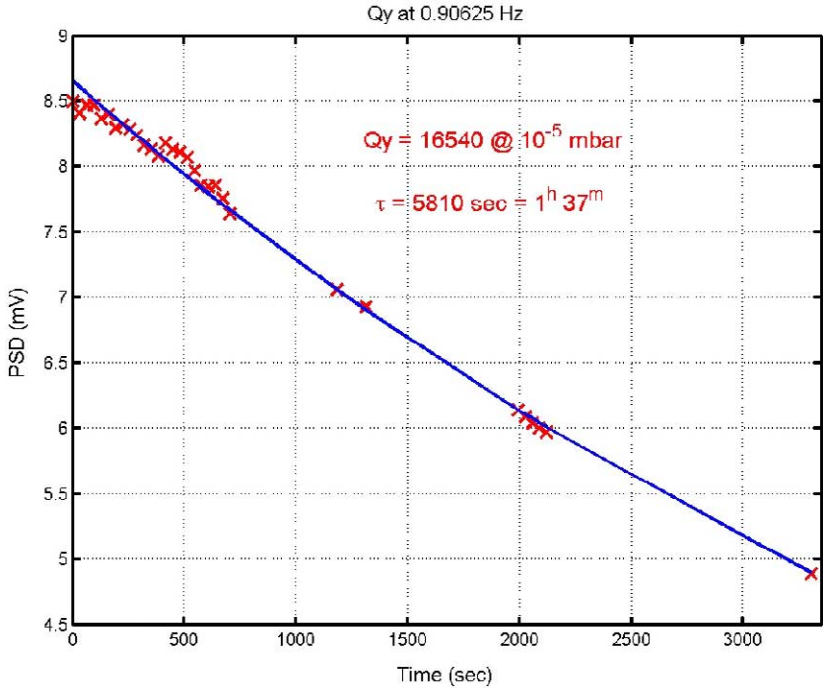

Fig. 4. Measurement of the quality factor of the GGG system at its natural frequency of 0.9 Hz. (Figure is in colour on the web.) The system (at zero spin) is excited at this frequency and the decay in oscillation amplitude is measured. The decay turns out to be compatible with a Q value of 16450. The run refers to the GGG system set up as in the year 2002.

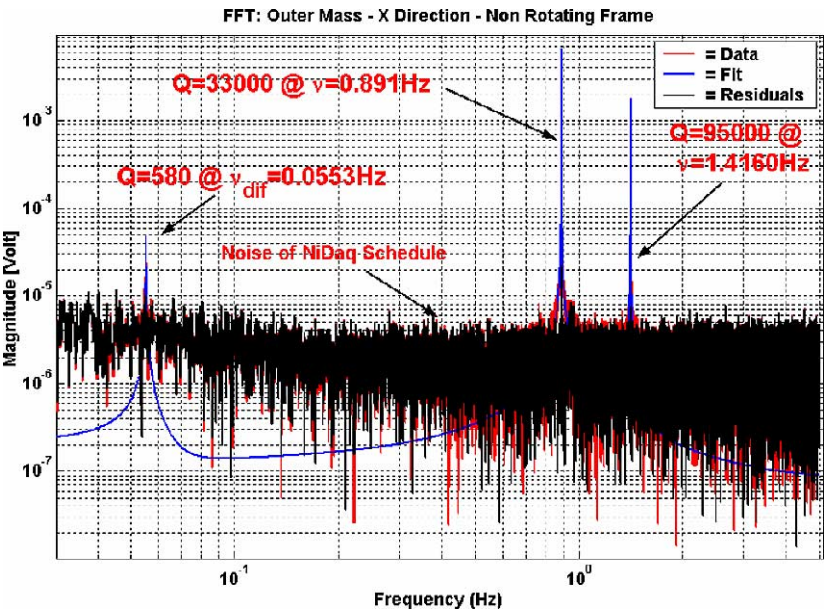

Fig. 5. Resulting quality factors of the GGG accelerometer at the natural frequencies (at zero spin) as obtained by measuring the oscillation decay of the system. (Figure is in colour on the web.) The blue curve is the FFT of the fitted output data. The runs refer to an improved system set up (with improved cardanic suspensions) of June 2003. Note the higher Q value at about 0.9 Hz as compared to the value reported in Fig. 4.

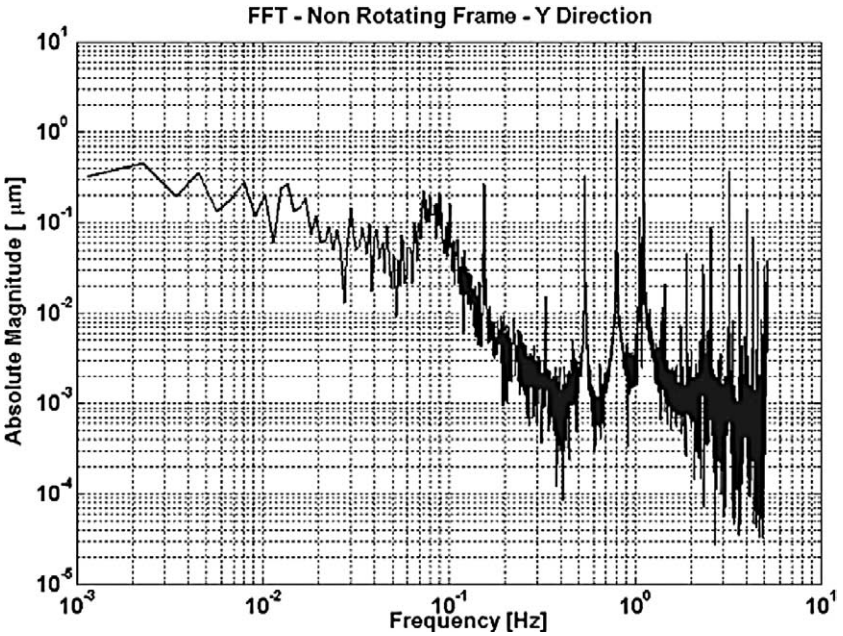

Fig. 6. FFT of the relative displacements of the test cylinders in the Y direction of the horizontal plane in the non-rotating reference system. The relevant whirl at the natural frequency of 0.08 Hz has been reduced to about 0.1 μm. The effect of a differential force at lower frequency must be separated out and emerge from the low frequency residual noise (see Fig. 7).

reaching the value of 95000 at 1.4 Hz. Since the spin rate is 2 Hz and above, we expect that the relevant Q in supercritical regime will be even better (higher) than this value. With cardanic suspensions of rather complex shape (see Fig. 1), which are therefore not easy to manufacture, the measured Q is indeed higher than we had expected. It is worth noting that the GG space mission studies have been carried out assuming, for the mission target of testing the equivalence principle to 10^{-17}, a Q value of 20000 (see [1] and references therein). The ground measurements reported in Fig. 5 indicate that such an assumption is in fact rather conservative.

In supercritical rotors losses at the spin frequency are also relevant for the growth rate of whirl motions that such rotors are known to develop, once in supercritical rotation, at their natural frequencies in the non-rotating system. For instance, the centers of mass of the GGG test cylinders do develop an orbital motion in the horizontal plane of the laboratory at the natural frequency of differential oscillations around their position of relative equilibrium, which is determined by external differential forces (see simulation, Fig. 3 of Ref. [1] for the case in space). Such a whirl motion grows in amplitude at a rate which depends on the Q of the system at the spin frequency: the higher the Q at this frequency, the slower the growth rate of the whirl. More precisely, rotordynamics predicts that whirl grows with a (negative) Q equal and opposite to the Q of the system at its spin frequency. In GGG whirls are controlled actively by means of capacitance sensors/actuators with a control scheme which is proportional to the tangential whirl velocity. Measurements of the relative displacements of the test cylinders show, after coordinate transformation to the non-rotating reference system, a controlled whirl motion at a differential frequency of 0.08 Hz: the whirl radius has been reduced from a few hundred μm to about 0.1 μm (see the FFT plot of Fig. 6 at this whirl frequency). In order to detect the effect of a low frequency differential force (such as in the case of a 24 hr EP violation signal in the field of the Sun), the corresponding displacement between the centers of mass should be separated out from the whirl and also emerge from the residual low frequency noise, mostly seismic noise. An example of recovery of an

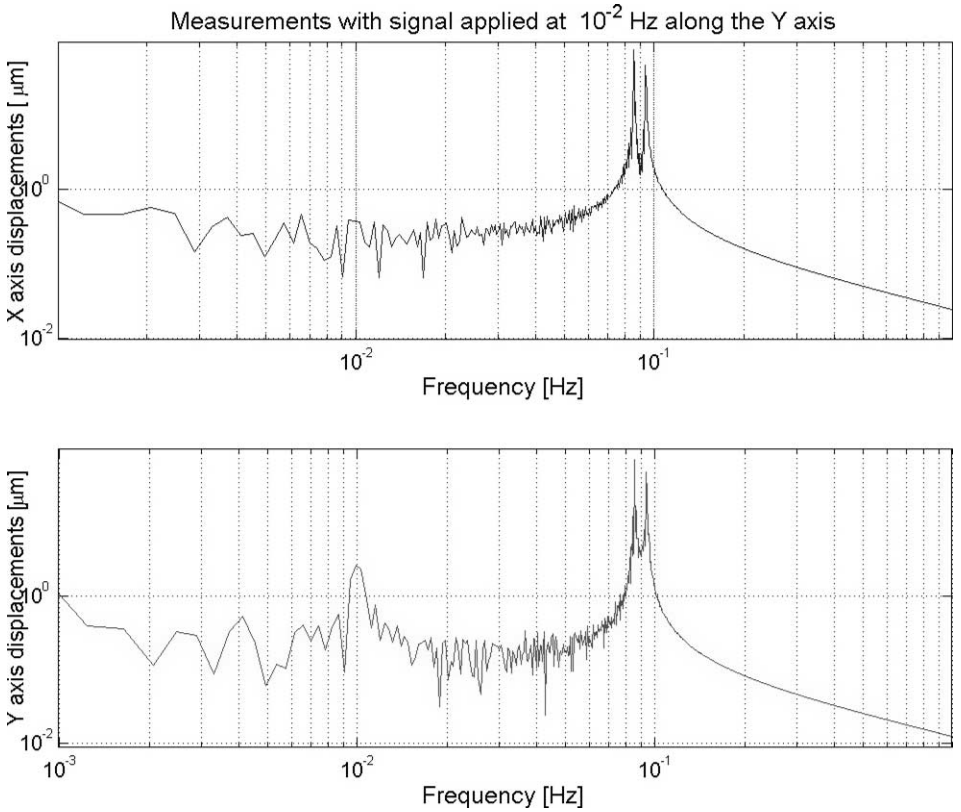

Fig. 7. A signal applied at 0.01 Hz in the Y direction of the non-rotating reference system is recovered from the output data though about 100 times smaller than the whirl (more than 100 µm in amplitude during this run) at about 0.1 Hz (system spinning at 2 Hz). Since it is also 10 times larger than the noise, an applied signal even several hundred times smaller than the whirl could be recovered.

applied signal at frequency below whirl frequency is shown in Fig. 7, and indicates that recovery is possible even though the applied force produces a displacement much smaller than the whirl radius. However, this was possible in the run of Fig. 7 where the residual low frequency noise was also much smaller than the whirl. In Fig. 6 (which reports more recent measurements) the whirl radius is smaller than in Fig. 7 by about 3 orders of magnitude, but residual low frequency noise is not correspondingly smaller. In fact we have reasons to think that this is local noise due to the vacuum chamber opening/closing system, which can be fixed.

Though the measurements reported in Fig. 6 clearly show the potentiality of the GGG novel design for detecting the effect of very small low frequency differential forces in the horizontal plane, they have also identified an important issue which requires immediate attention. In spite of the high Q values measured at zero spin rate (due to the suspensions only), the growth rate of whirl once in supercritical rotation is indeed much faster than expected by high Q, indicating that, during rotation, much bigger losses take place in the system beside the ones in the suspensions. A source of "*rotating damping*" (the kind of damping which is known in rotordynamics to produce whirl instability) may be due to the rubber O-ring used to transmit rotation from the motor (in its offset location) to the rotating suspension shaft/tube (see Fig. 1). This problem can be solved by eliminating the O-ring altogether, i.e., by locating the motor on the spin axis with care to have a hollow shaft for optical transmission of digitised data from the read-out to the computer outside the vacuum chamber. Other possible causes of spurious losses are under investigation in order to obtain the Q values measured in absence of rotation.

4. Conclusions

A space version of the fast rotating GGG differential accelerometer presented here, to be used within the GG mission ([1] and references therein) in low Earth orbit, would take advantage of the stronger driving signal (8.4 $\mathrm{m\,s^{-2}}$ from the Earth at 520 km altitude in GG, instead of 0.006 $\mathrm{m\,s^{-2}}$ from the Sun in GGG). It would also allow much weaker suspensions due to absence of weight, and consequent higher sensitivity (which depends on the differential period squared) by a factor of about 450. It can be argued that another factor of about 200 can be gained due to the absence of motor and motor/bearings noise, and thanks to the much higher symmetry of the space accelerometer (no 1-g preferential direction, hence much better rejection of common mode forces and consequent higher sensitivity to differential forces). Overall this amounts to about 8 orders of magnitude gain, thus making a 10^{-17} test in space a goal worth pursuing. In point of fact, the error budget of the GG space experiment, as developed within mission studies so far, has turned out to be compatible with this goal [1]. The improvement over current best ground results [6,7] would be of 5 orders of magnitude.

Very recently, predictions of violation have been reported [8] at levels close to the current best results, so that even a slight improvement on those experiments on the ground (to reach the 10^{-13} level) would be able to either confirm or rule out these predictions. The GGG rotating differential accelerometer can be used to test the equivalence principle in the gravitational field of the Sun to 1 part in 10^{13}. In GGG this goal requires to detect low frequency (24 hr) relative displacements of the test cylinders of 10^{-13} m, which in turn requires to reduce daily seismic disturbances by 7 orders of magnitude with respect to daily tilts measured so far. This can be done partly actively and partly passively. Active reduction is done using as sensor a tiltmeter placed inside the vacuum chamber at the top of the GGG frame (not rotating), and as actuators a set of PZTs (also not rotating, at 120° in the horizontal plane around the symmetry axis, providing tilts of the apparatus through vertical displacements). 3 orders of magnitude reduction can be obtained in this way. A further reduction by about 4 orders of magnitude, down to 4×10^{-14} m, which would bring the effects of tilts and horizontal disturbances well below the target signal, can be obtained using a passive cardanic suspension and the lever effect (see [11] for details). As discussed in [11], the main reason why such a significant reduction of seismic noise at very low frequency is possible is in the very nature of the GGG differential accelerometer. Since the test cylinders are arranged as in a vertical beam balance, the observable of interest in GGG are the relative displacements of the test cylinders relative to it, not the absolute location of the beam which indeed undergoes much larger displacements by following the local vertical in its seismic disturbed motion. This is not the case in VIRGO-like apparata used to detect gravitational waves with interferometric techniques. The suspended test masses being the mirrors of the interferometric system, their absolute displacements (unless one could make it possible that both mirrors undergo exactly the same displacements) must fulfill a rather stringent requirement coming from the need that locking is preserved (see [12]).

Acknowledgements

Starting mid 2003 the GGG experiment is under funding by INFN. The GG space mission has been funded for Phase A Study and Advanced Phase A study by ASI. The Italian space industry Laben has provided support for the GGG prototype in its laboratories in Florence till June 2003.

References

[1] A.M. Nobili, et al., “GALILEO GALILEI-GG”: design, requirements, error budget and significance of the ground prototype, Phys. Lett. A 318 (2003) 172, this issue.
[2] A. Anselmi, G. Catastini, Design of the GG satellite, Phys. Lett. A 318 (2003) 205, this issue.
[3] STEP Satellite Test of the Equivalence Principle, 1996, report on the phase A study, ESA-SCI(96)5 STEP website: http://einstein.stanford.edu/STEP.
[4] Microscope website: http://www.cnes.fr/activites/connaissance/physique/microsatellite/1sommaire_microsatellite.htm and http://www.onera.fr/dmph-en/accelerometre.
[5] A.M. Nobili, et al., New Astronomy 8 (2003) 371.
[6] Y. Su, et al., Phys. Rev. D 50 (1994) 3614.
[7] S. Baeßler, et al., Phys. Rev. Lett. 83 (1999) 3585.
[8] T. Damour, F. Piazza, G. Veneziano, Phys. Rev. D 66 (2002) 046007.
[9] G.L. Comandi, et al., Dynamical Response of the Galileo Galilei Rotor for a Ground Test of the Equivalence Principle:

Theory, Simulation and Experiment. Part I: The Normal Modes (2003), submitted for publication.
[10] G.L. Comandi, et al., Dynamical Response of the Galileo Galilei Rotor for a Ground Test of the Equivalence Principle: Theory, Simulation and Experiment. Part II: The Rejection Behavior (2003), submitted for publication.
[11] A.M. Nobili, et al., The fast rotating "GGG" differential accelerometer for testing the equivalence principle: current state and analysis of seismic disturbances, in: Proceedings of "Gravitational waves and experimental gravity", Rencontres de Moriond 2003, in press.
[12] V. Dattilo, et al., The VIRGO suspensions: design and recent performance measurements, in press.

Available online at www.sciencedirect.com
SCIENCE DIRECT®
Physics Letters A 318 (2003) 251–269
PHYSICS LETTERS A
www.elsevier.com/locate/pla

Tidal effects in space experiments to test the equivalence principle: implications on the experiment design

G.L. Comandi [a], A.M. Nobili [a,b,*], R. Toncelli [a,b], M.L. Chiofalo [a,b]

[a] *Space Mechanics Group, Department of Mathematics, University of Pisa, Via F. Buonarroti, I-56127 Pisa, Italy*
[b] *INFN, Sezione di Pisa, Via F. Buonarroti, I-56127 Pisa, Italy*

Received 10 June 2003; accepted 30 July 2003

Communicated by V.M. Agranovich

Abstract

Experiments to test the equivalence principle (EP) in low Earth orbit require to detect the effects of an extremely small non-classical differential acceleration between test masses of different composition. In all proposed experiments the test masses are concentric coaxial cylinders, so as to reduce classical tidal effects which are differential too. Perfect centring being impossible, tidal effects need to be carefully investigated as they impose severe constraints on the basic features of the experiment design. The present analysis shows that with free flying (uncoupled) test masses an EP violation signal could be detected if the initial conditions of the masses were finely adjusted for them to remain at a fixed distance relative to each other while orbiting around the Earth. However, such an experiment is severely limited by non-gravitational effects. If the test cylinders are weakly coupled in 2D in the plane perpendicular to their symmetry axis (close to the orbit plane), while rapidly spinning around it, a position of relative equilibrium is provided by physical laws which makes tidal effects widely separated from the signal. Weak coupling in 1D along the symmetry axis (to lie and slowly rotate in the orbit plane) is viable but less advantageous.

Keywords: Equivalence principle; Tidal effects; Rotordynamics

1. Introduction

The equivalence principle (EP) is tested through its most direct consequence, the universality of free fall (UFF), whereby in a gravitational field all bodies fall the same regardless of their mass or composition. UFF experiments therefore require two test masses in the gravitational field of a source body plus a read-out system to detect the effects of tiny, non-classical differential forces acting between the two. If the experiment is carried out with the test masses enclosed by a spacecraft orbiting the Earth at low altitude the driving signal is much stronger than it is for suspended bodies on the surface of the Earth. However, unless the centers of mass of the orbiting bodies are perfectly coincident, classical (differential) tidal effects arise which might compete with a non-classical EP

* Corresponding author.
E-mail address: nobili@dm.unipi.it (A.M. Nobili).

0375-9601/$ – see front matter
doi:10.1016/j.physleta.2003.07.020

violation signal. This is why in all proposed EP experiments in space the test masses are "concentric" coaxial cylinders [1–3]. However, since perfect centering is impossible to achieve, the signature and amplitude of tidal effects must be carefully assessed, as they might compete directly with the target signal of a putative EP violation. For the space missions under study the goals are to perform an EP test to: 10^{-15} with μSCOPE [3], 10^{-17} with "Galileo Galilei" (GG) [1], 10^{-18} with STEP [2].

We proceed by investigating, using analytical as well as numerical methods, different model cases of increasing complexity. We start in Section 2 with the case of free flying (uncoupled) test masses, showing that tidal effects and EP violation signal have the same frequencies. For the relative displacement of an EP violation to be detected with certainty the initial conditions of the bodies should be adjusted so that they orbit the Earth with the same mean angular velocity while remaining fixed relative to each other. Non-gravitational effects due to electric charging of the test masses make it very hard to realize this configuration.

In Section 3 we demonstrate that one way to separate the EP violation signal from the tide is to couple the test masses in the orbit plane, e.g., with a mechanical spring, thus introducing a natural frequency of differential oscillation of the test masses with respect to one another. In this case, while the EP signal is still detected at the orbital frequency, tides are at the natural differential frequency, and at this frequency plus or minus twice the orbital frequency. This is the case of the proposed "Galileo Galilei-GG" space experiment, where the natural differential frequency is about a factor 10 away from the orbital frequency, which makes it easy to separate tidal effects from the signal. The need for all EP experiments in space to spin the spacecraft in order to provide a frequency modulation of the signal is discussed in Section 4. In Section 5 the GG experiment is analysed under realistic conditions, including the rotation of the system in super-critical regime, to demonstrate that indeed an EP violation signal would not be masked by tidal effects. While the well-known self-centring property of super-critical rotors is exploited in GG, this is not possible in the STEP and μSCOPE experiments discussed in Section 6 because the test bodies are constrained to 1D motion. Being in sub-critical regime, they would then be too much off-centred at equilibrium, which makes it necessary to actively force their centres of mass as close as possible to each other. The masses are actively maintained in their fixed position and the force required to do that is the observable from which a possible signal of violation should be extracted. In this case tidal effects are at twice the orbital/EP-violation-signal frequency (i.e., they are separated by a factor 2), and they are larger than the signal because of the difficulties of active centring. Overall this design is less elegant and advantageous than the GG design, the main issue being that the masses do not rotate around their symmetry axis.

2. EP violation signal and tidal effects on free-flying test masses in low Earth orbit

If two test masses of different composition, falling in the gravitational field of the Earth with an acceleration a and the same initial conditions, experience a non-classical differential acceleration Δa it means that there is an EP violation to the level $\eta = \Delta a/a$. However, exactly the same differential acceleration might be due to a difference Δr in the orbital distance r of the two bodies at initial time such that $\Delta r/r \simeq \Delta a/a$, with no EP violation. We demonstrate this fact by analyzing the case of an initial separation Δr and no violation (case (i)), and then the case with a violation to the level η and zero initial separation (case (ii)). We investigate also an ideal experiment configuration such that, having reached appropriate initial conditions, the test masses remain fixed with respect to each other while freely orbiting the Earth. Then, by measuring their fixed relative displacement it should be possible to tell if there is an EP violation or not. Non-gravitational effects appear to be a major limitation to achieving and maintaining such fixed configuration.

2.1. Test masses separated by Δr; no EP violation (case (i))

In absence of EP violation inertial and gravitational mass are the same. Body 1, with mass $m_1^i = m_1^g \ll M_\oplus$, starts its motion around the Earth at an orbital distance $r_1(0) = r$ and with the corresponding Keplerian velocity

$v_1(0) = \sqrt{GM_\oplus/r}$ perpendicular to its position vector, whereas body 2, with mass $m_2^i = m_2^g \ll M_\oplus$, is released at $r_2(0) = r + \Delta r$ with $\vec{v}_2(0) = \vec{v}_1(0)$. Therefore, while body 1 performs a circular orbit with constant angular velocity (mean motion) $n_1 = n_1(0) = \sqrt{GM_\oplus/r^3}$, body 2 moves along an elliptic orbit with major semiaxis a and eccentricity e satisfying the relationship:

$$a(1-e) = r + \Delta r. \tag{1}$$

Referring to Appendix A for details, we obtain

$$\Delta n \equiv n_2 - n_1 \simeq -n_1 \cdot \frac{3\Delta r}{r} \tag{2}$$

for the relative mean motion of the two bodies. Since the orbital periods $P_1 = 2\pi/n_1$ and $P_2 = 2\pi/n_2$ are slightly different, the bodies' separation in longitude around the Earth will grow with time.

We have computed the time-evolution of the relative positions $X \equiv x_1 - x_2$ and $Y \equiv y_1 - y_2$ of the two bodies, by numerically integrating the equations of motion

$$m_\alpha^i \ddot{x}_\alpha = -\frac{GM_\oplus m_\alpha^g x_\alpha}{(x_\alpha^2 + y_\alpha^2)^{3/2}}, \qquad m_\alpha^i \ddot{y}_\alpha = -\frac{GM_\oplus m_\alpha^g y_\alpha}{(x_\alpha^2 + y_\alpha^2)^{3/2}} \tag{3}$$

with $m_\alpha^i = m_\alpha^g$ and $\alpha = 1, 2$. The orbit of body 2 relative to body 1 is shown in Fig. 1. It is a spiral, and the relative distance grows with time at the orbital frequency.

2.2. Test masses with the same initial conditions but with an EP violation η (case (ii))

Body 1 and body 2 start their motion with identical initial conditions, namely, at distance $r_1(0) = r_2(0) = r$ with initial velocity $v_1(0) = v_2(0) = \sqrt{GM_\oplus/r}$ along the tangential direction. In this case though, there is an EP violation η such that:

$$m_2^g = m_2^i(1+\eta). \tag{4}$$

Thus, while the equations of motion for body 1 is the same as (3), those for body 2 are modified into

$$m_2^i \ddot{x}_2 = -\frac{Gm_2^i(1+\eta)x_2}{(x_2^2 + y_2^2)^{3/2}}, \qquad m_2^i \ddot{y}_2 = -\frac{Gm_2^i(1+\eta)y_2}{(x_2^2 + y_2^2)^{3/2}}. \tag{5}$$

As a result, to first order in η the Keplerian elements a and e of orbit 2 and the difference Δn in mean motion are (see Appendix B):

$$e \simeq -\eta, \qquad a \simeq r(1-\eta), \qquad \Delta n \simeq 2\eta. \tag{6}$$

Again, since the orbital periods of the two bodies are slightly different, the motion of body 2 relative to body 1 is a spiral, but in this case it starts from the origin. By comparing the expressions for Δn in (6) and in (2), it turns out that under the condition:

$$\eta = -\frac{3}{2}\frac{\Delta r}{r} \tag{7}$$

the relative orbit resulting from the classical tidal effect of case (i) and the one with an EP violation of case (ii) grow at the same rate. This is shown in Fig. 2, while Fig. 3 shows that the dominant frequency in the relative displacement of the test cylinders is the orbital one, both in the classical case with tides and in the non-classical case with an EP violation (with relation (7) between Δr and η).

Case (i) represents a space-fixed-like configuration. We now consider the case in which the two bodies have the same initial angular velocity $n_1 = n_2 = \sqrt{GM_\oplus/r^3}$ but they are released at different altitudes (Earth-pointing-like

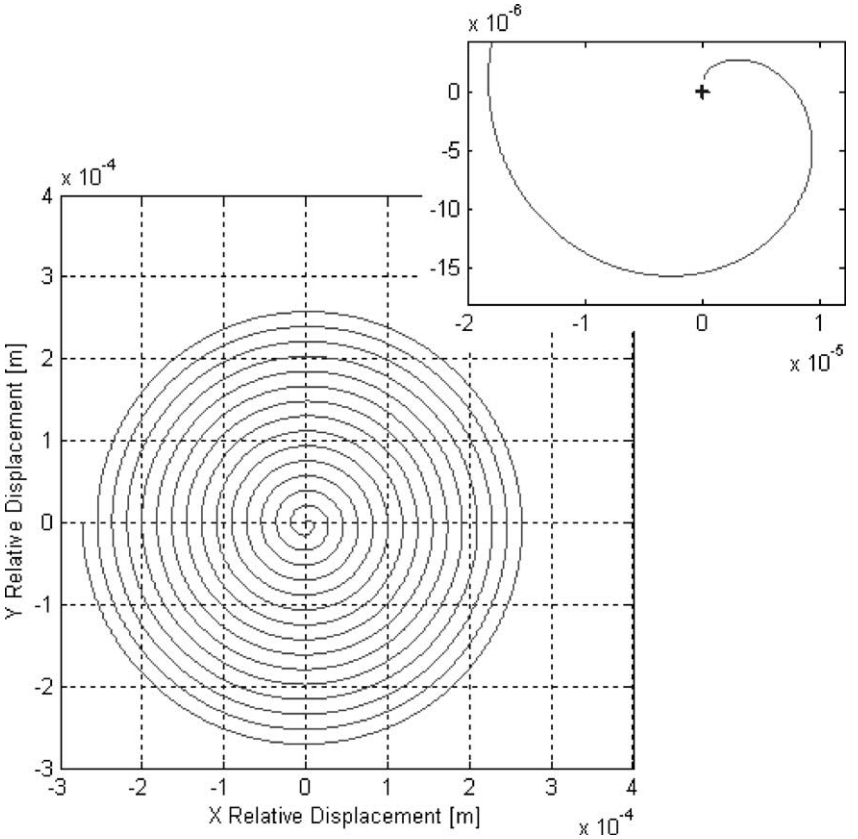

Fig. 1. Case (i): test bodies with initial separation Δr and no EP violation. Orbit of body 2 relative to body 1 for 15 orbital periods having taken $\Delta r = 1 \times 10^{-6}$ m and $r = R_{\oplus} + h$ with $h = 500$ km. Inset: close-up of the relative motion in the first half period.

configuration). The initial conditions for body 1 being the same, for body 2 we take:

$$r_2(0) = r + \Delta r, \qquad v_2(0) = n_1(r + \Delta r). \tag{8}$$

The difference in mean motions in this case is (see Appendix C for details):

$$\Delta n \simeq -n_1 \cdot \frac{6\Delta r}{r}. \tag{9}$$

The motion of body 2 relative to body 1 in the Earth-pointing case is quite similar to that of the space-fixed configuration, the only difference being that the relative distance grows twice as fast. Again, the initial separation Δr mimics an EP violation if

$$\eta = -3\frac{\Delta r}{r}. \tag{10}$$

Expression (10) differs from (7) by the same factor of 2. In any case, the value Δr of the release error of the test masses which would result in a classical effect as large as the targets of the proposed missions is of the order of a nanometer for the least ambitious goal of μSCOPE, and even smaller (to the level of a few tens of picometers or just several picometers in GG and STEP). Release errors as small as these are impossible to achieve. The uncertainty with which initial conditions (and the orbital elements) can be determined would set the limiting sensitivity in EP testing with these experiments. The same conclusion is reported in [4,5]. How is it possible, then, that lunar

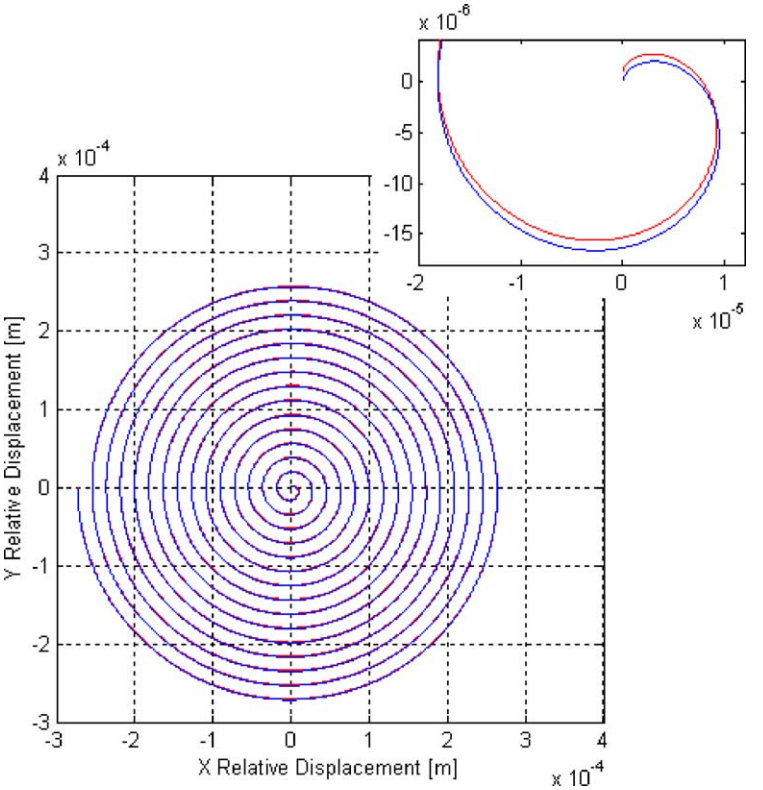

Fig. 2. (Figure is in colour on the web.) Blue curve: orbit of body 2 relative to body 1 for $\eta = 2.1 \times 10^{-13}$ after $15P_1$ of integration time (case (ii): identical initial conditions in the presence of an EP violation). The classical orbit of case (i) with $\Delta r = -2r\eta/3 = 10^{-6}$ m is shown as a red curve for comparison. The value of r is the same as in Fig. 1.

laser ranging (LLR) data can be used to search for EP violations in the Earth–Moon–Sun system of free masses by checking whether the Earth and the Moon fall the same in the gravitational field of the Sun? LLR tests of the equivalence principle have been able to reach $\eta_{\mathrm{LLR}} \simeq 10^{-13}$ [6] because at this level, at the 1 AU orbital distance of the Earth–Moon system from the Sun, Δr must of the order of a few mm, which is just in the present capabilities of current lunar laser tracking technology.

2.3. An ideal EP experiment with free falling test masses

In order to avoid the spiral motion of Figs. 1 and 2, it is possible in principle to adjust the initial conditions of the test bodies so that their relative position vector remains fixed with respect to the centre of the Earth while orbiting around it (i.e., the test bodies must have the same orbital angular velocity). Then, by measuring their separation distance it would be possible to tell whether there is an EP violation or not: if there is a non-zero separation vector $\Delta\vec{r}$ pointing to the center of the Earth, and in addition the masses remain fixed with respect to each other (no motion along track), this means that there is an EP violation to the level $\eta \simeq \Delta r/r$ (provided that the motion is dominated by gravity). The experiment requires: first to be able to reach the initial conditions which make the test masses orbit the Earth in a fixed configuration; then to measure their relative displacement; and finally to make sure that there is no relative motion along track due to gravitation. The first step appears to be the most difficult one because of the electrostatic effects caused by the well-known phenomenon of electric charging of the test masses (note also that charging changes with time in an unpredictable way). As for checking that there is no relative motion along

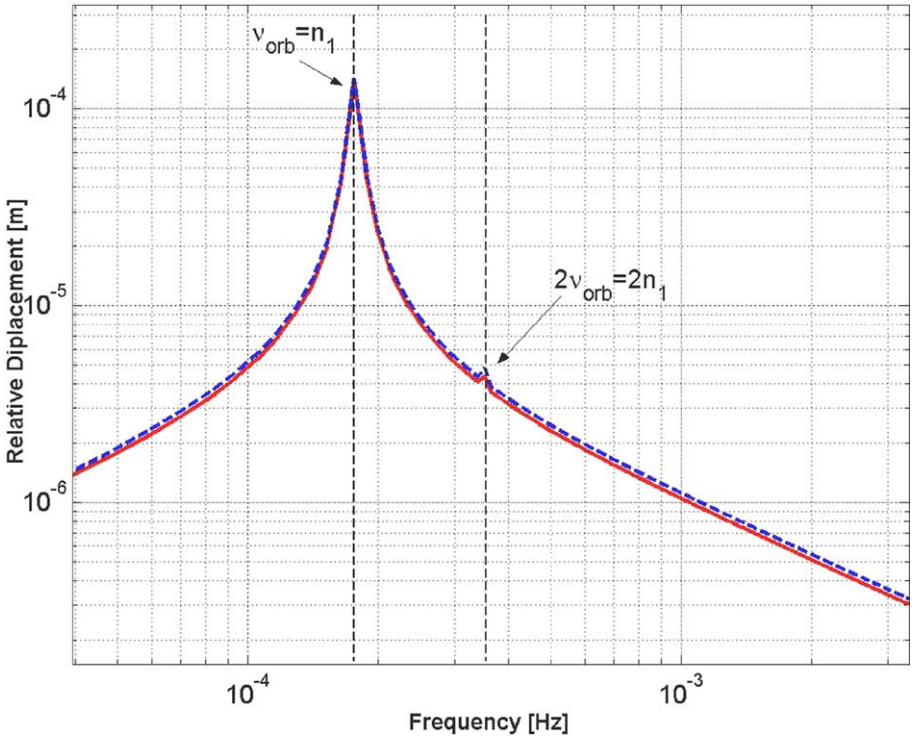

Fig. 3. FFT of the signals in the inertial reference frame. Solid curve: the orbit corresponding to case (ii) of two bodies starting with identical initial conditions in the presence of an EP violation. The orbit corresponding to case (i) with $\Delta r = -2r\eta/3 = 10^{-6}$ m is shown as a dashed curve for comparison. In the inertial reference frame, the tidal effect end EP signal would be detected at $\nu_{\rm orb}$ and $2\nu_{\rm orb}$. The main contribution is at the orbital frequency.

track, this might be difficult because of the competing effect of residual air drag along the orbit of the satellite, whose effect is a linear displacement growing quadratically with time. If the test masses are free flying air drag on the spacecraft gives rise to the same inertial acceleration on both test masses (common mode); however, a residual differential displacement is detected by the read out if the common mode one is much larger than the target signal. Drag compensation is needed, and can be realized, but the problem remains of how to separate with certainty an along track motion of pure gravitational origin whose presence in this experiment would rule out EP violation. We conclude that an EP experiment in space with free falling, uncoupled, test masses would have to face severe limitations.

3. EP violation signal and tidal effects with test masses coupled in the orbit plane

We now show that if the test bodies are coupled in the orbit plane, tidal effects and EP violation signal appear at different frequencies, which makes it possible to separate them out. Let us consider a spacecraft orbiting the Earth with radius r and Keplerian angular velocity

$$\omega_{\rm orb} = \sqrt{\frac{GM}{r^3}}. \tag{11}$$

Let the test masses m_1 and m_2 be separated by Δr in their initial orbital distance, and be coupled to each other with a positive stiffness k (the coupling may be of different nature, e.g., mechanical, electrostatic or magnetic) in

the orbit plane. The suspension is assumed to be rigid (in reality it is only much stiffer) along the orbit normal. We investigate their motion in the reference frame of the orbiting satellite. The frame is centered on the center of mass of the Earth, with the x axis in the Earth-to-satellite direction, the z axis perpendicular to the orbit plane and the y axis to complete the Cartesian system. In this frame we call $\vec{r}_1$ and $\vec{r}_2$ the test masses position vectors with respect to the center of mass of the spacecraft, and $\vec{\rho}_1 = \vec{r} + \vec{r}_1$, $\vec{\rho}_2 = \vec{r} + \vec{r}_2$ their position vectors with respect to the center of mass of the Earth. The bodies have the same inertial mass but different composition. In addition it is assumed that there is a violation of the equivalence principle to the level η, namely: $m_1^i = m_2^i \equiv m$ and $m_1^g = m$, $m_2^g = m(1+\eta)$. The Lagrange function is:

$$L = \frac{1}{2}m\big[\dot{r}_{1x}^2 + \dot{r}_{1y}^2 + 3\omega_{\text{orb}}^2 r_{1x}^2 + \omega_{\text{orb}}(r_{1x}\dot{r}_{1y} - r_{1y}\dot{r}_{1x}) + \dot{r}_{2x}^2 + \dot{r}_{2y}^2 + 3\omega_{\text{orb}}^2 r_{2x}^2 + \omega_{\text{orb}}(r_{2x}\dot{r}_{2y} - r_{2y}\dot{r}_{2x})\big]$$
$$- \frac{1}{2}k\big(r_{1x}^2 + r_{1y}^2 + r_{2x}^2 + r_{2y}^2 - 2r_{1x}r_{2x} - 2r_{1y}r_{2y}\big) - m\omega_0^2 r\eta r_{2x} + \frac{1}{2}m\omega_0^2\eta\big(2r_{2x}^2 - r_{2y}^2\big). \tag{12}$$

Tidal effects can be singled out by putting $\eta = 0$ in (12) (i.e., no EP violation), and then deriving the equations of motion of the test masses in their relative coordinates $X = r_{2x} - r_{1x}$ and $Y = r_{2y} - r_{1y}$:

$$\begin{cases} \ddot{X} - 2\omega_{\text{orb}}\dot{Y} + \big(\omega_n^2 - 3\omega_{\text{orb}}^2\big)X = 0, \\ \ddot{Y} + 2\omega_{\text{orb}}\dot{X} + \omega_n^2 Y = 0. \end{cases} \tag{13}$$

The angular frequency $\omega_n = \sqrt{2k/m}$ appearing in (13) is the natural frequency of oscillation of the test masses relative to one another in the orbit plane due to the coupling stiffness k: the weaker the coupling stiffness, the more sensitive the test bodies are to differential forces, such as those due to tides or EP violation. In space, thanks to weightlessness, the coupling can be very weak, much weaker than on the ground where suspensions must be stiff enough to withstand local gravity. Hence, the natural differential frequency can be much lower in space than in the lab. Yet, it is always much larger than the orbital frequency, which in all proposed space experiments is about 1.7×10^{-4} Hz (typical orbital periods in low Earth orbit are 6000 s). By combining Eq. (13) into one single equation of higher order, we obtain

$$\dddot{X} + \big(\omega_{\text{orb}}^2 + 2\omega_n^2\big)\ddot{X} + \omega_n^2\big(\omega_n^2 - 3\omega_{\text{orb}}^2\big)X = 0, \tag{14}$$

whose eigenvalues are:

$$\Lambda_{1,2,3,4} = \pm i\sqrt{\omega_n^2 + \omega_{\text{orb}}^2/2 \mp 2\omega_{\text{orb}}\omega_n\sqrt{1 + \omega_{\text{orb}}^2/\big(16\omega_n^2\big)}}. \tag{15}$$

These eigenvalues give the angular frequencies of tidal effects in the reference frame of the satellite which orbits around the Earth at ω_{orb}. For the EP experiments in space it is $\omega_n \gg \omega_{\text{orb}}$, and these frequencies become:

$$\Lambda_{1,2,3,4} = \pm i(\omega_n \pm \omega_{\text{orb}}). \tag{16}$$

If seen in the inertial reference frame (centered on the center of mass of the Earth and fixed in space), tidal effect would therefore appear at frequencies:

$$\nu_n, \quad \nu_n \pm 2\nu_{\text{orb}} \tag{17}$$

($\nu = \omega/2\pi$). Hence, the effect of coupling the test masses in the orbit plane is to shift the tidal signal from the orbital frequency ν_{orb} of the uncoupled case (see Fig. 3), to the (typically much larger) natural differential frequency ν_n introduced by the coupling. What about the effect of coupling on an EP violation signal?

In order to answer this question we consider $\eta \neq 0$ in the Lagrange function (12) and find that in this case there exists a position of relative equilibrium of the test masses in the Earth-to-satellite direction (the x axis of the

orbiting reference frame). The coordinates of the test masses at equilibrium are:

$$\begin{cases} r_{1x}^0 = \frac{\omega_n^2 r\eta}{6(\omega_n^2-3\omega_{\rm orb}^2)+2\eta(\omega_n^2-6\omega_{\rm orb}^2)}, \\ r_{2x}^0 = r_{1x}^0\left(1-6\frac{\omega_{\rm orb}^2}{\omega_n^2}\right), \\ r_{1y}^0 = r_{2y}^0 = r_{1x}^0\left(\frac{\omega_n^2}{\omega_n^2+2\eta\omega_{\rm orb}^2}\right). \end{cases} \tag{18}$$

Since the equilibrium position (18) due to an EP violation η is fixed in the orbit plane of the reference frame of the orbiting satellite, it is apparent that in the inertial reference system the EP violation signal is at the orbital frequency (as in the case of uncoupled test masses), while tides are now close to the natural differential frequency due to coupling. Since the orbital frequency is several times lower than the natural one, we conclude that—thanks to coupling in the orbit plane—an EP violation signal can be well separated from classical tidal effects.

4. Signal modulation

For high accuracy EP tests in space the spacecraft should also rotate, so as to modulate the signal at its rotation frequency relative to the Earth (the synodic frequency). EP tests require weak suspensions and large rotation rates: weak suspensions increase the sensitivity of the test masses to applied forces; fast rotation provides high frequency modulation and reduced "$1/f$" noise. Conceptually, the problem is that of a rotating oscillator made of a body of mass m whose center of mass is suspended with stiffness k from a point located a vector $\vec{\varepsilon}$ away from the rotation axis. $\vec{\varepsilon}$ is the inevitable offset due to construction and mounting errors, and is fixed with the rotor. Two frequencies are relevant for equilibrium: the spin frequency ω_s and the natural frequency $\omega_n = \sqrt{(k/m)}$. Equilibrium is achieved at a position $\vec{r}_{\rm eq}$ where the centrifugal force is balanced by the restoring force of the suspension:

$$\vec{r}_{\rm eq} = \frac{1}{1-(\omega_s/\omega_n)^2}\cdot\vec{\varepsilon}. \tag{19}$$

If $\omega_s/\omega_n < 1$ ("sub-critical" rotation), $\vec{r}_{\rm eq} \parallel \vec{\varepsilon}$ and $r_{\rm eq} > \varepsilon$: the equilibrium position moves farther away from the rotation axis than the original offset. If $\omega_s/\omega_n > 1$ ("super-critical" rotation), $\vec{r}_{\rm eq} \parallel -\vec{\varepsilon}$ and $|\vec{r}_{\rm eq}| < |\vec{\varepsilon}|$: equilibrium is achieved on the opposite side of the rotation axis with respect to $\vec{\varepsilon}$ and closer to it than obtained by construction. Note that in this case equilibrium is not possible if the body is constrained to motion in one dimension, as it was demonstrated long time ago in Chapter 6 of [7]. If, moreover,

$$\frac{\omega_s^2}{\omega_n^2} \gg 1 \tag{20}$$

as it is desirable for very accurate EP tests, then:

$$\vec{r}_{\rm eq} \simeq -\vec{\varepsilon}\frac{\omega_n^2}{\omega_s^2} \tag{21}$$

and self-centering occurs since the original offset is reduced by the large factor $\omega_s^2/\omega_n^2 \gg 1$. The same line of reasoning holds for two rotating coupled masses, whose relative position at equilibrium is as in (19), ω_n now being the frequency of differential oscillations. This is the case of the GG experiment design, for which tidal effects and EP violation signal are analyzed in detail in Section 5. Note that, since the offset vector $\vec{\varepsilon}$ is fixed with the rotor, the position vector of relative equilibrium is also fixed with the rotor, and therefore the corresponding tidal effect is (in the rotating reference frame) at twice the spin frequency, just as lunisolar tides on the surface of the Earth have periodicities of 12 h (solar tide) and 12 h 25 min (lunar tide).

5. EP violation signal and tidal effects in the GG space experiment design

Let us now analyze EP violation signal and tidal effects in the case of the GG experiment in space.

5.1. The GG apparatus

The GG satellite is planned to fly at an altitude of about 520 km on a circular sunsynchronous orbit around the Earth with inclination $I = 97.494$ degrees (see [8]). The satellite spins around its symmetry axis at a rather high frequency (2 Hz with respect to the center of the Earth) and this rotation provides passive stabilization of the spacecraft attitude because the axis of symmetry is also the axis of maximum moment of inertia. Because of the flattening of the Earth, the orbit plane of an inclined satellite is known to precess around the normal to the Equator; in sunsynchronous orbits inclination and orbital radius are chosen so that the orbit plane follows the Sun in its annual motion around the Earth (at about 1° per day). Since the spin axis of GG remains fixed in space (due to the very high energy of spin), the angle θ that separates it from the orbit normal will also increase by about 1° per day. In GG θ is maintained within $\pm 10°$, allowing about 20 days duration for each experiment run before realignment of the spin axis along the orbit normal is performed.

The test masses—referred to with subindexes 1 and 2—are two concentric, coaxial hollow cylinders, with the axes along the spin/symmetry axis of the spacecraft and weighing 10 kg each (planned to be made of Pt/Ir and CuBe). They are coupled as in a beam balance by means of mechanical suspensions which are stiff along the spin axis but very soft in the orthogonal plane, where high sensitivity to differential accelerations has to be provided. The mechanical suspensions also allow electric grounding of the test masses, so that no discharging mechanism is required (which would disturb the experiment).

Note that: $\nu_s = \omega_s/2\pi = 2.000175$ Hz is the spin frequency of the satellite around its symmetry axis with respect to a star fixed reference frame; $\nu_{\rm orb} = \omega_{\rm orb}/2\pi = 1.75 \times 10^{-4}$ Hz is the orbital frequency around the Earth and $\nu_{\rm prec} = \Omega_{\rm prec}/2\pi = 3.17 \times 10^{-8}$ Hz is the frequency of precession of the normal to the orbit around the normal to the equator (too small to be detected in 20 days of integration time).

5.2. Whirl motion and tidal frequencies in the sensitive plane

In super-critical regime mechanical suspensions are known to undergo deformations (and therefore to dissipate energy) at the spin frequency. Energy dissipation makes the spin rate to decrease, together with the spin angular momentum. Since the total angular momentum must be conserved, the bodies develop a whirl motion of increasing amplitude around each other at a frequency close to the natural differential one due to the coupling. The smaller the losses (i.e., the higher the quality factor Q), the slower is the growth rate of the whirl. GG relies on high Q (for slow growth) and on active whirl damping (see [9,10, Chapter 6]).

We use a simplified model, as sketched in Fig. 4 and write the equations of motion in the inertial reference frame (X, Y, Z) centered on the center of the Earth, the X-axis along the nodal line of the satellite's orbit at initial time, the Y-axis perpendicular to it in the orbit plane at initial time and the Z-axis along the spin axis, coinciding with the orbit normal at initial time. $\vec{\rho}_1 = (x_1, y_1, 0)$ and $\vec{\rho}_2 = (x_2, y_2, 0)$ are position vectors of the test masses with respect to the center of mass of the Earth while the satellite orbits around it with a constant radius r. The bodies have the same inertial mass but different composition, and there is a violation of equivalence to the level η, namely: $m_1^i = m_2^i \equiv m$ and $m_1^g = m$, $m_2^g = m(1+\eta)$. They are coupled to each other by a dissipative spring with elastic constant k and quality factor Q. An offset vector $\vec{\varepsilon} = \varepsilon(\cos(\omega_s t + \phi), \sin(\omega_s t + \phi), 0)$, due to construction and mounting, locates the suspension point of the spring with respect to the center of mass of body 2; it is fixed with the rotor, and therefore spins with angular frequency ω_s in the inertial reference frame. The dissipative force is proportional to the relative velocity through the coefficient $c_r = k/Q\omega_s$ (sub-index "r" stands for "rotating friction", since it is determined by losses in the rotor).

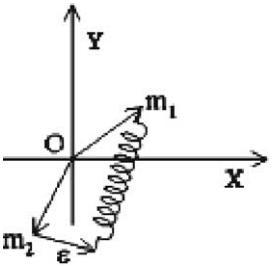

Fig. 4. Simplified model of the GG coupled test masses. The reference system is centered on the center of mass of the Earth; the X-axis is the line of nodes of the satellite orbit at initial time; (X, Y) is the orbit plane of the satellite at initial time; the Z-axis (not shown) is the spin axis, coinciding with the orbit normal at initial time; m_1 and m_2 are the test bodies, connected by a spring, with position vectors $\vec{\rho}_1$ and $\vec{\rho}_2$ from the center of mass of the Earth. The offset error due to inevitable construction and mounting imperfections is indicated as ε. The figure is obviously not to scale.

The equations of motion are:

$$\begin{aligned}
\ddot{\vec{\rho}}_1 &= \frac{k}{m}(\vec{\rho}_2 - \vec{\rho}_1 + \vec{\varepsilon}) - \frac{c_r}{m}\big(\dot{\vec{\rho}}_1 - \dot{\vec{\rho}}_2 - \omega_s \times (\vec{\rho}_1 - \vec{\rho}_2)\big) - \frac{GM\vec{\rho}_1}{|\vec{\rho}_1|^3},\\
\ddot{\vec{\rho}}_2 &= -\frac{k}{m}(\vec{\rho}_2 - \vec{\rho}_1 + \vec{\varepsilon}) + \frac{c_r}{m}\big(\dot{\vec{\rho}}_1 - \dot{\vec{\rho}}_2 - \omega_s \times (\vec{\rho}_1 - \vec{\rho}_2)\big) - \frac{GM\vec{\rho}_2(1+\eta)}{|\vec{\rho}_2|^3},
\end{aligned} \tag{22}$$

which we have integrated numerically with initial conditions:

$$\begin{aligned}
&\vec{\rho}_1(0) = (r + x_0, 0), && \dot{\vec{\rho}}_2(0) = (r - x_0, 0),\\
&\dot{\vec{\rho}}_1(0) = \big(0, \omega_{\text{orb}} r + \sqrt{k/m}\, x_0\big), && \vec{\rho}_2(0) = \big(0, \omega_{\text{orb}} r - \sqrt{k/m}\, x_0\big)
\end{aligned} \tag{23}$$

representing a system in which whirl radius $r_w = 2x_0$ at initial time. ($\omega_n = \sqrt{k/m}$ is the natural differential frequency of the coupling.) For demonstration purposes the numerical integration is carried out with a very large whirl radius $r_w = 2.5 \times 10^{-4}$ m and assuming a very high level of violation $\eta = 10^{-11}$. Instead, the natural differential period of the coupling (also the whirl period) is $T_w = 540$ s as in GG, the quality factor is $Q = 20000$ as originally assumed in GG (though better values have been measured), and $\varepsilon = 10^{-6}$ m. Since at this point we are interested only in frequencies much faster than the precession frequency, the numerical integration timespan is short and precession is not included.

The resulting FFT of the relative displacement between the test bodies is shown in Fig. 5(a) where all four expected peaks are visible: whirl motion appears at $\nu_w = 0.00185$ Hz $\approx \nu_n$, tidal effect at ν_w, $\nu_w + 2\nu_{\text{orb}} = 0.00220$ Hz, $\nu_w - 2\nu_{\text{orb}} = 0.00150$ Hz and EP signal at $\nu_{\text{orb}} = 0.000175$ Hz (EP signal has a peak at ν_s too due to the offset). The FFT of the relative acceleration between the test masses is plotted in Fig. 5(b).

We now derive the same results by analytical methods, taking into account also precession. Let (s_1, s_2, s) be a reference frame fixed with the satellite, where s is in the direction of the spin axis (coinciding with the orbit normal Z at initial time), s_1 is along the nodal line at initial time (same as X-axis) and (s_1, s_2) is therefore the sensitive plane of the instrument. In the reference system identified by the equatorial plane of the Earth and by its rotation axis it is: $s_1 = (1, 0, 0)$, $s_2 = (0, \sin I, \cos I)$ and $s = (0, -\sin I, \cos I)$ and the unit position vector of the satellite at time t is:

$$\hat{r} = \cos(\omega_{\text{orb}} t + \varphi) \begin{pmatrix} \cos(\Omega_{\text{prec}} t) \\ \sin(\Omega_{\text{prec}} t) \\ 0 \end{pmatrix} + \sin(\omega_{\text{orb}} t + \varphi) \begin{pmatrix} -\cos(I)\sin(\Omega_{\text{prec}} t) \\ \cos(I)\cos(\Omega_{\text{prec}} t) \\ \sin(I) \end{pmatrix}, \tag{24}$$

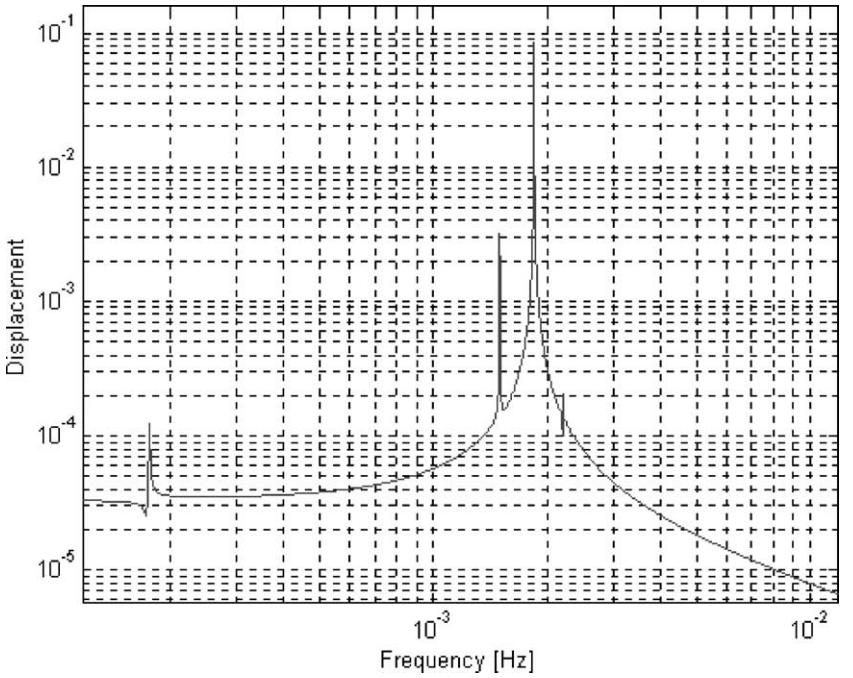

(a)

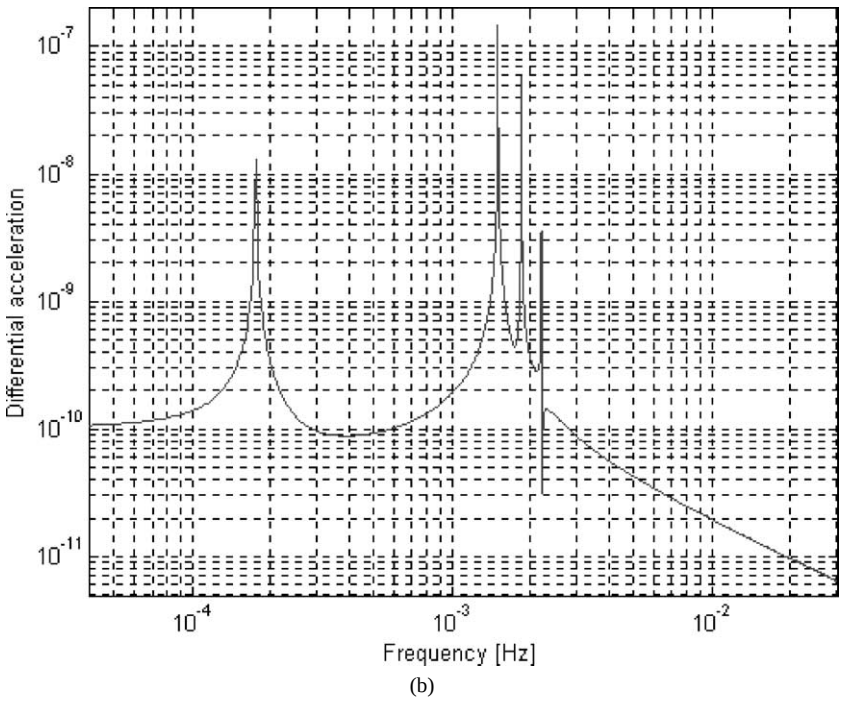

(b)

Fig. 5. (a) FFT of the relative displacement where all four expected peaks are visible, which are assigned to whirl motion at $\nu_w = 0.00185$ Hz $\approx \nu_n$, to the tidal effect at ν_w, $\nu_w + 2\nu_{\rm orb} = 0.00220$ Hz, $\nu_w - 2\nu_{\rm orb} = 0.00150$ Hz and to an EP violation signal at $\nu_{\rm orb} = 0.000175$ Hz. (b) FFT of the relative acceleration in the presence of an EP violation to the level $\eta = 10^{-11}$, which is sensed at $\nu_{\rm orb}$, while whirl motion is at ν_w and tides are at ν_w and $\nu_w \pm 2\nu_{\rm orb}$.

Table 1
Tidal acceleration components in the sensitive plane of the GG system

Component	Frequency
$\frac{GM_\oplus}{r^3}3r_w e^{\omega_w t/(2Q)}\cos(\omega_w t)\cos^2(\omega_{\rm orb}t)\cos^2(\Omega_{\rm prec}t)$	ω_w, $\omega_w \pm 2\omega_{\rm orb} \pm 2\Omega_{\rm prec}$ $\omega_w \pm 2\omega_{\rm orb}$, $\omega_w \pm 2\Omega_{\rm prec}$
$\frac{GM_\oplus}{r^3}\frac{3}{2}r_w e^{\omega_w t/(2Q)}\sin^2(I)\sin(\omega_w t)\sin(2\omega_{\rm orb}t)\cos(\Omega_{\rm prec}t)$	$\omega_w \pm 2\omega_{\rm orb} \pm \Omega_{\rm prec}$
$-\frac{GM_\oplus}{r^3}r_w e^{\omega_w t/(2Q)}\cos(\omega_w t)$	ω_w
$\frac{GM_\oplus}{r^3}3r_w \sin^2(I)\cos(I)e^{\omega_w t/(2Q)}\sin(\omega_w t)\sin^2(\omega_{\rm orb}t)\sin(\Omega_{\rm prec}t)$	$\omega_w \pm \Omega_{\rm prec}$, $\omega_w \pm 2\omega_{\rm orb} \pm 2\Omega_{\rm prec}$
$\frac{GM_\oplus}{r^3}\frac{3}{2}r_w \cos(I)e^{\omega_w t/(2Q)}\sin(\omega_w t)\cos^2(\omega_{\rm orb}t)\sin(2\Omega_{\rm prec}t)$	$\omega_w \pm 2\Omega_{\rm prec}$, $\omega_w \pm 2\omega_{\rm orb} \pm 2\Omega_{\rm prec}$
$-\frac{GM_\oplus}{r^3}\frac{3}{2}r_w \cos(I)e^{\omega_w t/(2Q)}\cos(\omega_w t)\sin(2\omega_{\rm orb}t)\sin(2\Omega_{\rm prec}t)$	$\omega_w \pm 2\omega_{\rm orb} \pm 2\Omega_{\rm prec}$
$\frac{GM_\oplus}{r^3}\frac{3}{2}r_w \cos^2(I)e^{\omega_w t/(2Q)}\sin(\omega_w t)\sin(2\omega_{\rm orb}t)\cos(2\Omega_{\rm prec}t)$	ω_w, $\omega_w \pm 2\omega_{\rm orb} \pm 2\Omega_{\rm prec}$, $\omega_w \pm 2\Omega_{\rm prec}$, $\omega_w \pm 2\omega_{\rm orb}$
$\frac{GM_\oplus}{r^3}\frac{3}{2}r_w \cos^2(I)e^{\omega_w t/(2Q)}\cos(\omega_w t)\sin^2(\omega_{\rm orb}t)\sin^2(\Omega_{\rm prec}t)$	$\omega_w \pm 2\omega_{\rm orb} \pm 2\Omega_{\rm prec}$
$\frac{GM_\oplus}{r^3}\frac{3}{2}r_w \cos^3(I)e^{\omega_w t/(2Q)}\sin(\omega_w t)\sin^2(\omega_{\rm orb}t)\sin(2\Omega_{\rm prec}t)$	$\omega_w \pm 2\Omega_{\rm prec}$, $\omega_w \pm 2\omega_{\rm orb} \pm 2\Omega_{\rm prec}$

while whirl motion is described by the vector

$$\vec{p} = r_w e^{\frac{\omega_w t}{2Q}} \begin{pmatrix} \cos(\omega_w t) \\ \sin(\omega_w t)\cos(I) \\ \sin(\omega_w t)\sin(I) \end{pmatrix}. \tag{25}$$

Then, the tidal (differential) acceleration between the test bodies is:

$$\vec{a} = -\frac{GM}{r^3}\left\{-3r_w e^{\frac{\omega_w t}{2Q}}\sin(\omega_w t)\left[(\hat{r}\times\hat{s})\cdot\hat{s}_1\right]\hat{r} - 3r_w e^{\frac{\omega_w t}{2Q}}\cos(\omega_w t)(\hat{r}\cdot\hat{s}_1)\hat{r} + \vec{p}\right\} \tag{26}$$

and its components in the sensitive plane are:

$$\begin{aligned} a_{s1} &= \vec{a}\cdot\hat{s}_1 = -\frac{GM}{r^3}\left\{-3r_w e^{\frac{\omega_w t}{2Q}}\sin(\omega_w t)\left[(\hat{r}\times\hat{s})\cdot\hat{s}_1\right](\hat{r}\cdot\hat{s}_1) - 3r_w e^{\frac{\omega_w t}{2Q}}\cos(\omega_w t)(\hat{r}\cdot\hat{s}_1)^2 + \vec{p}\cdot\hat{s}_1\right\}, \\ a_{s2} &= \vec{a}\cdot\hat{s}_2 = -\frac{GM}{r^3}\left\{-3r_w e^{\frac{\omega_w t}{2Q}}\sin(\omega_w t)\left[(\hat{r}\times\hat{s})\cdot\hat{s}_1\right](\hat{r}\cdot\hat{s}_2) - 3r_w e^{\frac{\omega_w t}{2Q}}\cos(\omega_w t)(\hat{r}\cdot\hat{s}_2)(\hat{r}\cdot\hat{s}_1) + \vec{p}\cdot\hat{s}_2\right\}. \end{aligned} \tag{27}$$

Using (24) in (27) we can list all the frequencies at which the whirl-related tides take place. Acceleration a_{s1} can be seen as the sum of the nine signals listed in Table 1. The same holds for a_{s2}.

The table shows that tides between the test masses occur at angular frequencies ω_w, $\omega_w \pm 2\omega_{\rm orb}$, $\omega_w \pm 2\Omega_{\rm prec}$, $\omega_w \pm 2\omega_{\rm orb} \pm 2\Omega_{\rm prec}$, and $\omega_w \pm 2\omega_{\rm orb} \pm \Omega_{\rm prec}$. In the case of GG, however, $\Omega_{\rm prec}$ is too tiny to be detected. Thus, the relevant frequencies of the tides in GG are ω_w and $\omega_w \pm 2\omega_{\rm orb}$, in agreement with the numerical simulation.

We conclude this analysis by showing in Fig. 6 the time evolution of the EP violation signal component $a_{s1}^{\rm EP} = -(GM_\oplus/r^3)\eta(\vec{r}\cdot\hat{s}_1)$ as compared to the same component of the tidal effect, giving the corresponding FFT analysis in Fig. 7. It is apparent that the wide separation in frequency allows an EP violation signal to be recovered even if it is much smaller than tidal effects.

5.3. Tides due to relative displacements along the spin/symmetry axis

Even if the GG system is stiff along the spin/symmetry axis Z, perturbations acting along this direction are present (e.g., due to solar radiation pressure or to coupling of the Earth's monopole with higher mass moments of the test bodies) which may produce a displacement between the centers of mass of the test cylinders. Unless the spin axis remains all time exactly perpendicular to the orbit plane (which is not the case in GG), a center of mass separation along its direction will give a tidal signal also in the sensitive plane. We use the same analytical

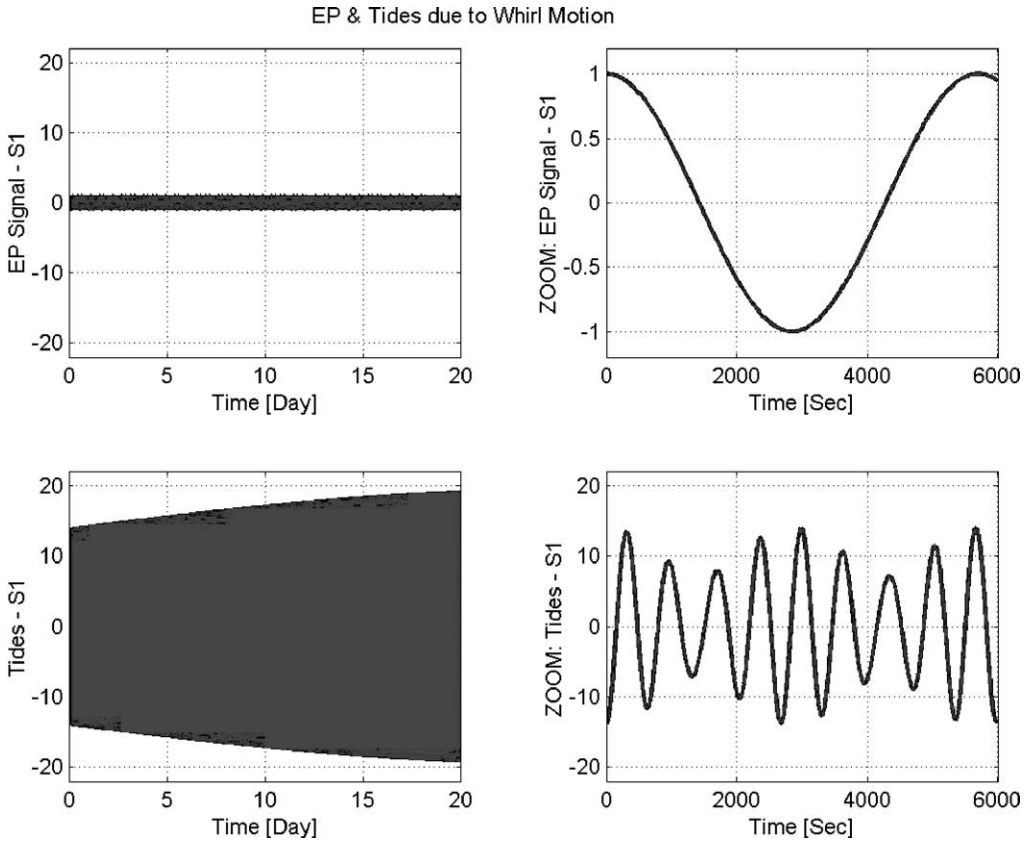

Fig. 6. Time evolution of the EP violation signal (above) and of the tidal signal (below) along the s_1 direction in the sensitive plane. All signals are given in units of $(GM_\oplus/r^2)\cdot\eta = 1$.

procedure as in Section 5.2 to describe the resulting tidal signal. The tidal acceleration $\vec{a}$ corresponding to the relative separation vector $(0, 0, \Delta z)$ with respect to the satellite center-of-mass, can be written as

$$\vec{a} = -\frac{1}{2}\frac{GM_\oplus}{r^3}\Delta z\hat{s} + \frac{3}{2}\frac{GM_\oplus}{r^3}\Delta z\hat{r}(\hat{r}\cdot\hat{s}). \tag{28}$$

In the reference frame (s_1, s_2, s), we have

$$\begin{aligned} a_{s1} &= \frac{3}{2}\frac{GM_\oplus}{r^3}\Delta z r_x\big(r_y\sin(I) - r_z\cos(I)\big),\\ a_{s2} &= \frac{3}{2}\frac{GM_\oplus}{r^3}\Delta z\left[\frac{1}{2}\big(r_y^2 - r_z^2\big)\sin(2I) - r_y r_z\cos(2I)\right]. \end{aligned} \tag{29}$$

The corresponding time evolution and FFT analysis are reported in Figs. 8 and 9. In this case, tidal effects are detected at frequency $2\nu_{\rm orb}$, while the EP signal is still at $\nu_{\rm orb}$. The peak at $2\nu_{\rm orb}$ in Fig. 9 does not resolve the contributions at $2\nu_{\rm orb} \pm \nu_{\rm prec}$ and $2\nu_{\rm orb} \pm 2\nu_{\rm prec}$.

We end this section noticing that, although the frequency analysis of tidal effects is useful in order to understand the physical nature of these subtle perturbations, in the actual GG experiment the measurement data provided by the capacitance bridges, rotating with the test cylinders and the whole spacecraft at a nominal frequency of 2 Hz, are transformed (using the reference signal provided by the Earth elevation sensor onboard the spacecraft) into an Earth pointing, non-rotating reference frame centred in the centre of mass of the spacecraft. In this frame an

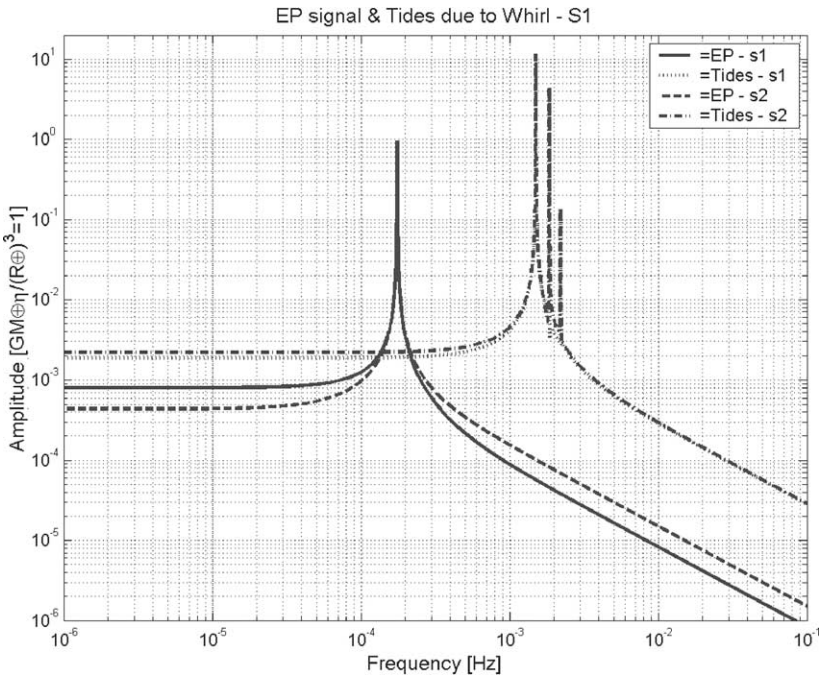

Fig. 7. FFT analysis of the data shown in Fig. 6. The amplitudes of the tidal peaks are about 20 times larger than the EP signal. Nevertheless, the differences between the orbital and the whirl frequency allows us to recover the EP signal from the FFT analysis.

EP violation signal appears as a constant offset (for zero orbital eccentricity) in the satellite-to-Earth direction while tidal disturbances appear at a frequency close to the natural differential frequency of the test cylinders, and therefore average out to zero.

6. EP violation signal and tidal effects with test masses coupled and controlled in one dimension: the STEP and μSCOPE cases

In STEP and μSCOPE the test cylinders are sensitive only along the symmetry axis, which lies and rotates (in order to modulate the signal) in the orbital plane. Being constrained to motions in 1D the test bodies are bound to sub-critical rotation, with no self-centering (see Section 4). Sub-critical rotation is indeed confirmed for STEP by the values of the rotation and oscillation frequencies reported in [11]. Since the original offset ε can hardly be smaller than 1 μm, the residual tidal acceleration would exceed the signal by orders of magnitude. Furthermore, the center-of-mass separation—hence the tidal effect—are not exactly constant because radial oscillations, in the plane perpendicular to the sensitive axis, are excited by residual spacecraft motion. Thus, a component of the large tidal disturbance would appear at the signal frequency as well. This is why tides must be reduced, i.e., the masses must be actively centered.

Let us therefore calculate this control force, assuming no spacecraft rotation at first. In the inertial reference frame (X, Y, Z) centered on the center of mass of the Earth the satellite orbits in the (X, Y) plane and its position vector is $\vec{r} = r(\cos(\omega_{\text{orb}}t), \sin(\omega_{\text{orb}}t), 0)$. For simplicity, the first test mass is assumed to coincide with the center of mass of the satellite, while the second one is separated from it by the vector $\Delta\vec{r} = \Delta r\hat{X}$ along the X direction. A force equal and opposite to the tidal one must be applied in order to maintain the second mass fixed in its position.

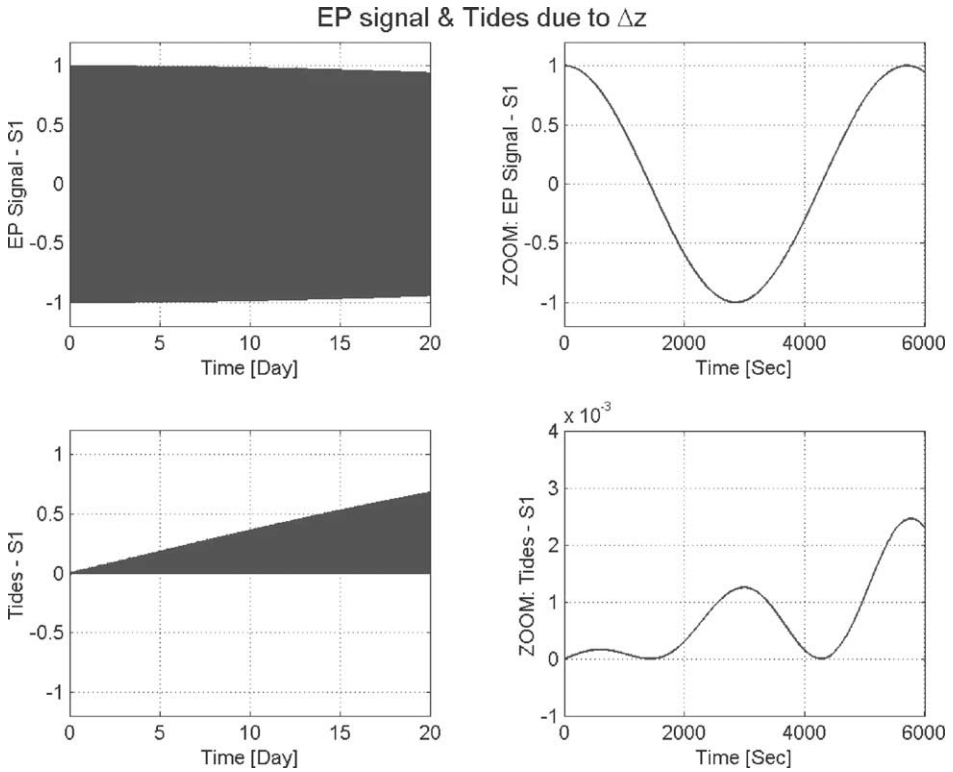

Fig. 8. Time evolution of the EP signal (above) and tidal signal due to a center of mass offset along the spin axis (below) in the s_1 direction of the sensitive plane. All signals are given in units of $(GM_\oplus/r^2)\cdot\eta = 1$.

The tidal force to be reduced to zero is:

$$\vec{F}_2^{\text{Tide}} = -GMm\left(\frac{\vec{r}+\Delta\vec{r}}{|\vec{r}+\Delta\vec{r}|^3} - \frac{\vec{r}}{r^3}\right) = -\frac{GMm}{r^3}\left(\Delta\vec{r} - 3\frac{\vec{r}\Delta\vec{r}}{r^2}\vec{r}\right) = -m\omega_{\text{orb}}^2\left(\Delta\vec{r} - 3\frac{\vec{r}\Delta\vec{r}}{r^2}\vec{r}\right) \tag{30}$$

or else, after making the time-dependence explicit,

$$\vec{F}_2^{\text{Tide}} = -m\omega_{\text{orb}}^2\left[\Delta r\big(1-3\cos^2(\omega_{\text{orb}}t)\big), -\frac{3}{2}\Delta r\sin(2\omega_{\text{orb}}t), 0\right]. \tag{31}$$

It is apparent from (31) that the tidal force, as well as the control force required to make it vanish, are at the frequency $2\nu_{\text{orb}}$ in the inertial reference frame.

Let us now assume that the test masses are perfectly coincident, while there is an EP violation such that $m_2 = m(1+\eta)$. In this case the control force required to maintain the second mass fixed is equal and opposite to the EP violation force

$$\vec{F}_2^{\text{EP}} = -\frac{GMm}{r^3}\eta\vec{r} = -m\omega_{\text{orb}}^2\eta\vec{r}, \tag{32}$$

which is at frequency ν_{orb}. In this case too, as in GG, we can distinguish the tidal effect from the EP violation. However, typical orbital periods of the spacecraft are of the order of 6000 s, resulting in a separation as small as 1.7×10^{-4} Hz in the FFT spectrum. In STEP and μSCOPE too the spacecraft spins in order to modulate the signal. Note, however, that the rotation axis is not the symmetry axis of the test cylinders—which is the sensitive axis—but is perpendicular to it. After demodulation of the output signal (i.e., in the non-rotating reference frame), the EP

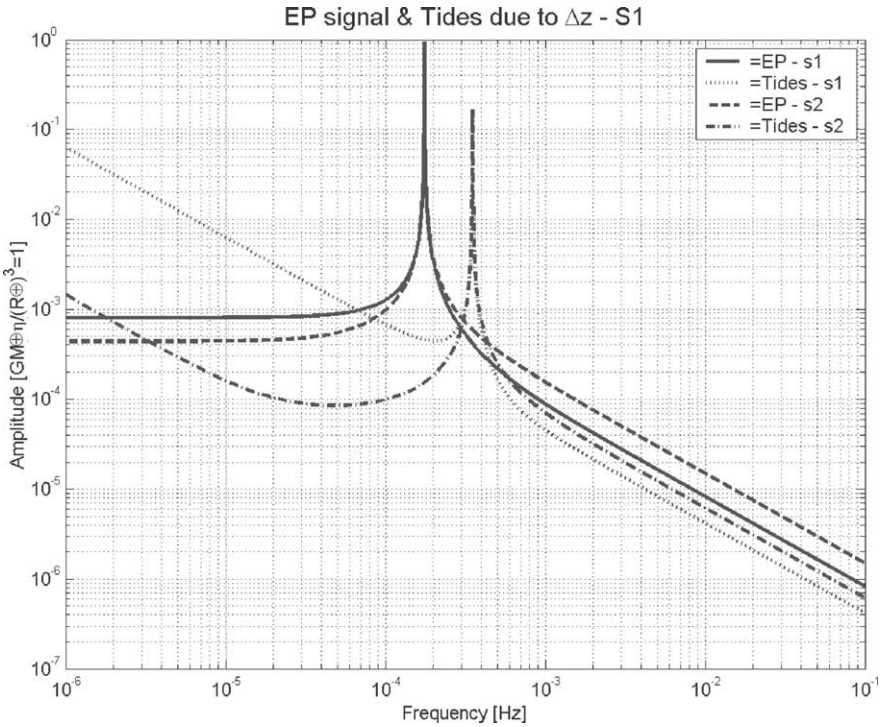

Fig. 9. FFT analysis of the data shown in Fig. 8. For a center of mass separation along the spin axis tidal effects appear in the sensitive plane at frequency $2\nu_{\rm orb}$, while the EP signal is still at $\nu_{\rm orb}$.

violation signal is still at the orbit frequency $\nu_{\rm orb}$, as it is apparent from (32), where the position satellite-to-Earth vector $\vec{r}$ is obviously unaffected by the rotation of the spacecraft. Instead, the tidal force (30) contains the relative position vector $\Delta\vec{r}$ between the test masses, which rotates with the spacecraft at its spin angular frequency ω_s. Its coordinates in the non-rotating frame are:

$$\Delta\vec{r} = \Delta r\big(\cos(\omega_s t), \sin(\omega_s t), 0\big) \tag{33}$$

and the tidal force becomes:

$$\vec{F}_2^{\rm Tide} = \frac{1}{2}m\omega_{\rm orb}^2\Delta r\big[\big(\cos(\omega_s t) + 3\cos\big((\omega_s - 2\omega_{\rm orb})t\big)\big), \big(\sin(\omega_s t) - 3\sin\big((\omega_s - 2\omega_{\rm orb})t\big)\big), 0\big] \tag{34}$$

thus showing that tides are (in the non-spinning frame) at frequencies ν_s and $2\nu_s - \nu_{\rm orb}$. This means that they can be separated from the EP violation signal at frequency $\nu_{\rm orb}$; however, if the spacecraft rotates slowly (with a spin period not much smaller than the orbital one) as it is the case in STEP and μSCOPE the separation in frequency between the two is still small, and due to the difficulties of active centering, the residual tide is still much larger than the target signal. It is also worth noticing that, in this design in which the test masses are actively forced to remain in a fixed relative position, the observable from which a possible EP violation signal can be extracted is the control force equal and opposite to the differential force of an EP violation. However, the latter is in the form (32) if the test masses are allowed to move in the orbital plane around the Earth. Instead, they are forced to move along one direction only (the symmetry axis) of this plane, while the suspension is very stiff in the other direction. How this stiff suspension does influence the motion (hence the control force) along the sensitive axis is a matter of concern for the STEP scientists (see [12,13]).

Electric charging of the test masses is a problem with electrostatic and magnetic suspensions. In μSCOPE a thin gold (conductive) wire is added to ground the masses [14], while the STEP masses need active discharging.

We end this section by noticing that a fixed relative position of the test masses could also be provided by gravitation only. This was suggested in [15] for a short distance EP test exploiting the Lagrangean equilateral configuration of equilibrium for a primary body and two test masses (of different composition) inside a high-altitude spacecraft. In this case a composition-dependent effect would show up as a deviation from the equilateral triangle of classical equilibrium.

7. Conclusions

Experiments to test the equivalence principle inside a spacecraft in low Earth orbit require classical tidal (differential) effects between the test masses to be separated from a non-classical differential signal due to a possible violation of equivalence. If the test bodies are free flying inside the spacecraft tidal effects have the same frequencies as an EP violation signal. However, if the initial conditions are adjusted until the test bodies reach a fixed configuration relative to each other while orbiting around the Earth, then only by measuring their relative displacement it would be possible to tell whether the equivalence principle is violated or not. The displacement measurement can be very accurate, but such a fixed configuration is hard to reach and to maintain due to non-gravitational forces, primarily the electrostatic forces caused by electric charging of the test bodies.

The frequencies of tides can be widely separated from the frequency of an EP violation signal by (weakly) coupling the test masses (concentric coaxial cylinders) in the orbit plane. In this case the signal is at the orbital frequency while tides are at the natural differential frequency of the coupling (several times larger than the orbital one) and at this frequency plus or minus twice the orbital frequency. If the spacecraft spins in order to modulate the signal, weak coupling in 2D allows (fast) rotation in super-critical regime around the symmetry axis of the cylinders. In this regime a self centered position of relative equilibrium exists by physical laws, and tidal effects due to whirl motion around it are again widely separated from the signal (the whirl frequency is very close to the natural differential frequency of the coupling). This is the GG experiment design.

If the test masses are weakly coupled in 1D tides are at twice the orbital frequency, i.e., a factor 2 away from the frequency of EP violation. However, when spinning the spacecraft for signal modulation 1D motion only allows (slow) rotation in sub-critical regime. In this regime the relative distance between the test masses at equilibrium would be far too large to be acceptable (it would produce too large tidal effects), and therefore they need to be centered actively, and to be maintained fixed in that configuration. During rotation tides are at the spin frequency and at the spin frequency minus twice the orbital one, which under this condition of slow rotation are close to each other. Tides are also larger than the signal due to the difficulties of active centering. This is the STEP and μSCOPE experiment design. Its limitations appear to derive from the fact that rotation is not along the symmetry axis of the test cylinders.

Acknowledgements

We thank ASI (Agenzia Spaziale Italiana) for its support of the GG mission studies and INFN for funding the development of a laboratory prototype of the apparatus proposed for space.

Appendix A

Let us start from Eq. (1) in Section 2.1, namely, $a(1-e) = r + \Delta r$.

The angular momentum per unit mass J is expressed as

$$J^2 = GM_{\oplus} a\left(1-e^2\right) \tag{A.1}$$

and is a conserved quantity, so that

$$J^2 = J^2(0) = r_2^2(0)v_2^2(0) = GM_{\oplus}r\left(1+\frac{\Delta r}{r}\right)^2. \tag{A.2}$$

By equating (A.1) and (A.2), it follows:

$$a = \frac{r(1+\Delta r/r)^2}{1-e^2}. \tag{A.3}$$

Eliminating a from (1) and (A.3) we obtain the exact expression

$$e = \frac{\Delta r}{r} \tag{A.4}$$

for the eccentricity of body 2, valid to any order in $\Delta r/r$.

After substituting (A.4) into (A.3) and expanding to second order in $\Delta r/r$, the major semiaxis turns out to be

$$a = r\frac{1+\Delta r/r}{1-\Delta r/r} \simeq r\left(1+2\frac{\Delta r}{r}+2\frac{\Delta r^2}{r^2}\right). \tag{A.5}$$

The mean anomaly n_2 is obtained from Kepler's third law, namely:

$$n_2^2 a^3 = GM_{\oplus} \tag{A.6}$$

with the major semiaxis given by (A.5). To first order in $\Delta r/r$,

$$n_2 = \sqrt{\frac{GM_{\oplus}}{r^3}}\cdot\left(1+2\frac{\Delta r}{r}\right)^{-3/2} \simeq n_1\cdot\left(1-3\frac{\Delta r}{r}\right) \tag{A.7}$$

resulting in the difference Δn

$$\Delta n \equiv n_2 - n_1 \simeq -n_1\cdot\frac{3\Delta r}{r}. \tag{A.8}$$

Appendix B

In the case $\eta \neq 0$, Eq. (A.1) is modified into

$$J^2 = GM_{\oplus}(1+\eta)a\left(1-e^2\right), \tag{B.1}$$

while the initial condition is $J^2(0) = r_2^2(0)v_2^2(0) = GM_{\oplus}r$. The energy per unit of inertial mass is instead

$$E = -\frac{GM_{\oplus}(1+\eta)}{2a} \tag{B.2}$$

and the eccentricity satisfies the relation

$$e^2 = 1 + \frac{2EJ^2}{G^2M_{\oplus}^2(1+\eta)^2}. \tag{B.3}$$

Finally, the Kepler's third law in Eq. (A.6) is changed into

$$n_2^2 a^3 = GM_{\oplus}(1+\eta). \tag{B.4}$$

Combining Eqs. (B.1)–(B.4), expanding to second order in η and retaining only the linear terms, we obtain the relations (6) of the main text.

Appendix C

Eqs. (1) and (A.2) with the initial conditions (8) give us the exact expressions for the Keplerian elements for the orbit of body 2. These are

$$a = \frac{r(1+\Delta r/r)^4}{1-e^2} \tag{C.1}$$

for the major semiaxis,

$$e = \left(1+\frac{\Delta r}{r}\right)^3 - 1 \tag{C.2}$$

for the eccentricity, and

$$n_2 = \sqrt{\frac{GM_\oplus}{(r+4\Delta r)^3}} = n_1\left(1+4\frac{\Delta r}{r}\right)^{-3/2} \tag{C.3}$$

for the mean anomaly. After expansion of equations (C.1)–(C.3) to second order in $\Delta r/r$, we obtain

$$a \simeq r\left(1+4\frac{\Delta r}{r}+18\frac{\Delta r^2}{r^2}\right), \qquad e \simeq 3\frac{\Delta r}{r}+6\frac{\Delta r^2}{r^2}, \qquad \Delta n \simeq -n_1\cdot\frac{6\Delta r}{r}. \tag{C.4}$$

References

[1] A.M. Nobili, et al., “Galileo Galilei-GG”: design, requirements, error budget and significance of the ground prototype, “Galileo Galilei-GG” website: http://eotvos.dm.unipi.it/nobili.

[2] STEP Satellite Test of the Equivalence Principle, 1996, report on the phase A study, ESA-SCI(96)5, STEP website: http://einstein.stanford.edu/STEP.

[3] Microscope website: http://www.cnes.fr/activites/connaissance/physique/microsatellite/1sommaire_microsatellite.htm, http://www.onera.fr/dmph-en/accelerometre.

[4] J.P. Blaser, Class. Quantum Grav. 18 (2001) 2509.

[5] Y. Jafry, Class. Quantum Grav. 15 (1998) 1.

[6] J. Anderson, J.G. Williams, Class. Quantum Grav. 18 (2001) 2447.

[7] J.P. Den Hartog, Mechanical Vibrations, Dover, New York, 1985.

[8] A. Anselmi, G. Catastini, Design of the GG satellite, in press.

[9] S.H. Crandall, A.M. Nobili, On the Stabilization of the GG System (1997), available on line: http://tycho.dm.unipi.it/nobili/ggweb/crandall.

[10] “Galileo Galilei” (GG), Phase A Report, (1998), 2nd Edition, Agenzia Spaziale Italiana, 2000, http://eotvos.dm.unipi.it/nobili/ggweb/phaseA.

[11] J. Mester, et al., Class. Quantum Grav. 18 (2001) 2475.

[12] J.P. Blaser, On the motion of the STEP masses, STEP Note (2000).

[13] J.P. Blaser, Motion of a STEP mass with EP-violation, STEP Note (2001).

[14] P. Touboul, M. Rodrigues, Class. Quantum Grav. 18 (2001) 2487.

[15] A.M. Nobili, A. Milani, in: O. Fackler, Tran Thanh Van (Eds.), Fifth Force and Neutrino Physics, Edition Frontieres, 1998, p. 569.

Errata corrige:

Tidal effect in space experiments to test the equivalence principle: implications on the experiment design, Physics Letters A, 318, 251-269, 2003

Page 266, first line after Eq. (34):

$2\nu_s - \nu_{orb}$ should read $\nu_s - 2\nu_{orb}$

Available online at www.sciencedirect.com
SCIENCE DIRECT®
Physics Letters A 318 (2003) 172–183
PHYSICS LETTERS A
www.elsevier.com/locate/pla

"Galileo Galilei-GG": design, requirements, error budget and significance of the ground prototype

A.M. Nobili [a,b,*], D. Bramanti [a], G.L. Comandi [a,b], R. Toncelli [a,b], E. Polacco [b], M.L. Chiofalo [a,b]

[a] *Space Mechanics Group, Department of Mathematics, University of Pisa, Via F. Buonarroti, I-56127 Pisa, Italy*
[b] *INFN, Sezione di Pisa, Via F. Buonarroti, I-56127 Pisa, Italy*

Received 16 June 2003; accepted 27 July 2003

Communicated by V.M. Agranovich

Abstract

"Galileo Galilei-GG" is a proposed experiment in low orbit around the Earth aiming to test the equivalence principle to the level of 1 part in 10^{17} at room temperature. A unique feature of GG, which is pivotal to achieve high accuracy at room temperature, is fast rotation in supercritical regime around the symmetry axis of the test cylinders, with very weak coupling in the plane perpendicular to it. Another unique feature of GG is the possibility to fly 2 concentric pairs of test cylinders, the outer pair being made of the same material for detection of spurious effects. GG was originally designed for an equatorial orbit. The much lower launching cost for higher inclinations has made it worth redesigning the experiment for a sun-synchronous orbit. We report the main conclusions of this study, which confirms the feasibility of the original goal of the mission also at high inclination, and conclude by stressing the significance of the ground based prototype of the apparatus proposed for space.

Keywords: Equivalence principle; Universality of free fall; Fundamental physics experiments in space

1. Introduction

The equivalence principle (EP) stated by Galileo, reformulated by Newton and reexamined by Einstein to become the founding principle of General Relativity, can be tested from its most direct consequence: the universality of free fall (UFF), whereby all bodies fall with the same acceleration regardless of their mass and composition ($\eta \equiv \Delta a/a = 0$). The most accurate EP experiments have been carried out on the ground with test bodies of different composition suspended on a torsion balance. In the case of Be and Cu it was found $\eta(\mathrm{Be,Cu}) = (-1.9 \pm 2.5) \times 10^{-12}$ [1]. In [2], the differential acceleration between test cylinders of "earth's core" and "moon/mantle" composition in the gravitational field of the Sun ($a_\odot \simeq 0.6\ \mathrm{cm\,s^{-2}}$) is reported with a 1σ statistical uncertainty $\Delta a_\odot = 5.6 \times 10^{-13}\ \mathrm{cm\,s^{-2}}$, hence $\Delta a_\odot/a_\odot \simeq 9.3 \times 10^{-13}$.

Test bodies in low Earth orbit are subject to a driving gravitational (and inertial) acceleration much stronger than on torsion balances on the ground, by about 3 orders of magnitude. Moreover, the absence

* Corresponding author.
E-mail address: nobili@dm.unipi.it (A.M. Nobili).

0375-9601/$ – see front matter
doi:10.1016/j.physleta.2003.07.019

of weight is ideal in small force experiments. There is therefore general agreement on the fact that a very high accuracy test of the equivalence principle can be achieved only by flying the test masses inside a spacecraft in low Earth orbit. It is also agreed that the test bodies should be weakly coupled, concentric, co-axial cylinders, and that they should rotate (the faster the better) for signal modulation. The "Galileo Galilei" (GG) space experiment [3] aims to reach 10^{-17}, which is highly competitive with μSCOPE's goal (10^{-15}) [4]. STEP's goal is the same as that of GG [5], or even 1 order of magnitude more ambitious [6] but the spacecraft is much more massive and the experiment must be performed close to absolute zero rather than at room temperature as GG.

Both GG and STEP would be able to check a possible EP violation predicted by Fischbach et al. [7] at the 10^{-17} level by rigorous calculation of higher order weak interactions, should gravity couple anomalously to weak interaction energy. Beyond the standard model, within string theory, recent work [8] predicts much stronger a deviation, to the level of 10^{-12} for test bodies made of Cu and Be or Pt and Ti. A modest improvement over current torsion balance laboratory tests should be sufficient to either confirm or rule out this prediction.

2. The signal and the accelerometers

Testing the UFF requires two masses of different composition, arranged to form a differential accelerometer, and a read-out system in between them. In GG the test bodies are concentric, co-axial, hollow cylinders weakly coupled like in a beam balance with the beam directed along the symmetry axis, so as to be sensitive to differential accelerations acting between the bodies in the x, y plane perpendicular to it (the weaker the coupling, the higher the sensitivity). Coupling and balancing allow common mode effects to be rejected. Two capacitance bridges in between the test cylinders read their relative displacements (caused by differential accelerations) in the plane of sensitivity. The better the mechanical balance of the bridge capacitance plates halfway in between the test cylinders, the more insensitive is the read-out to common mode effects. Thus, the differential nature of the accelerometer is ensured both by the suspension and by the read-out.

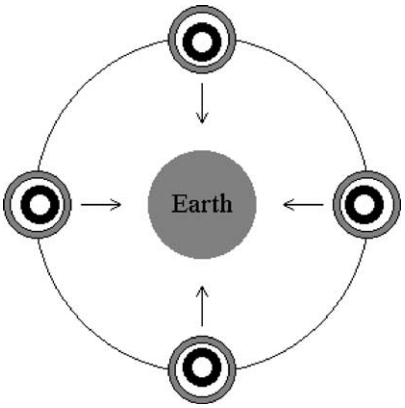

Fig. 1. Section across the spin/symmetry axis of the GG outer and inner test cylinders (of different composition) as they orbit around the Earth inside a co-rotating, passively stabilized spacecraft (not shown). The centers of mass of the test cylinders are shown to be displaced towards the center of the Earth as in the case of a violation of the equivalence principle in the field of the Earth (indicated by the arrows). The signal is therefore at the orbital frequency, and is modulated at the spin frequency of the system with respect to the center of the Earth (2 Hz nominal). The figure is not to scale (taken from [9]).

High frequency modulation of the expected signal—for the reduction of "$1/f$" electronic and mechanical noise—is obtained by spinning the accelerometer around the symmetry axis (the beam of the balance): a cylindrical spacecraft encloses, in a nested configuration, a cylindrical cage with the test cylinders inside, and is stabilized by rotation around the symmetry axis. Once the spacecraft has been given the required rate of rotation at the beginning of the mission (2 Hz nominal with respect to the center of the Earth), no motor is needed in space. Hence, the space experiment is not affected by noise from the motor, contrary to what happens with rotating apparata in ground based laboratories where the motor and its noise are a serious matter of concern. As shown in Fig. 1, an EP violation in the field of the Earth would generate a signal of constant amplitude (for zero orbital eccentricity) whose direction always points to the center of the Earth, hence changing orientation with the orbital period of the satellite. The read-out, also rotating with the system, will therefore modulate an EP violation signal at its spin frequency with respect to the Earth.

The expected signal benefits from the spacecraft orbiting the Earth at low altitude. Having selected 520 km for GG, an orbit inclination of 97.5° ensures

that the spacecraft follows the annual motion of the Sun (sun-synchronous orbit) and makes it possible to use a high latitude, low cost, Russian launcher for orbit injection. By maintaining the spin/symmetry axis of the spacecraft within about 10 degrees from the orbit normal, there is almost no degradation of the signal along both directions in the sensitivity plane of the accelerometer.

For the GG space experiment we have designed 2 concentric differential accelerometers, the inner one for EP testing (with cylinders of different composition) and the outer one for zero check (with cylinders made of the same material). They are sensitive in the x, y plane perpendicular to the symmetry axis which is also the (natural) axis of rotation, so as to provide frequency modulation of the expected signal. Fig. 2 shows a section through the spin/symmetry axis of the accelerometers, and a detailed description is given in the caption. In order to provide an intermediate stage of isolation between the spacecraft and the test cylinders the accelerometers of Fig. 2 are not suspended directly from the spacecraft, but instead from the so-called PGB ("pico gravity box") laboratory: a cylindrical structure which is mechanically suspended from the spacecraft along its symmetry axis (see Fig. 4) so as to provide weak coupling in the plane perpendicular to the axis while being more stiff along it (as in the case of the test cylinders).

In GG the test cylinders are suspended mechanically. However, whatever the nature of the suspensions, there will always be a non-zero offset vector $\vec{\varepsilon}$ from the spin axis (in the reference frame fixed with the system) due to construction and mounting errors. The equilibrium position vector of the centre of mass of the suspended body, for given angular spin frequency ω_s, is given by the equation:

$$\vec{r}_{\mathrm{eq}} = \frac{1}{1-(\omega_s/\omega_n)^2} \cdot \vec{\varepsilon}, \tag{1}$$

where ω_n is the natural frequency of the suspended mass. The system will spin at a frequency either below or above the natural one. From (1), it follows that in the first case the equilibrium position will be farther away from the spin axis than the original offset ε, while in the second case equilibrium will take place closer than ε to the spin axis. The phenomenon is known as auto-centering in super critical rotation. Test masses used for EP testing naturally require $\omega_s > \omega_n$, because they must be weakly coupled (i.e., with low natural frequency for better sensitivity to differential forces) and in rapid rotation (i.e., with high modulation frequency for better reduction of "$1/f$" noise). In space, thanks to the absence of weight, the suspensions can be extremely weak, so that $\omega_s \gg \omega_n$. In this case it is:

$$\vec{r}_{\mathrm{eq}} \simeq -\left(\frac{\omega_n}{\omega_s}\right)^2 \cdot \vec{\varepsilon} \tag{2}$$

which shows that extremely good auto-centering will be achieved (the equilibrium position vector, like the original offset vector, is fixed with the rotor); it also shows that, in order for the system to reach its equilibrium position on the opposite side with respect to the offset vector $\vec{\varepsilon}$, it must have 2 degrees of freedom. Indeed, it is well known that 1D systems are highly unstable if spinning at frequencies above the natural one [10].

As compared to EP testing accelerometers which have only one sensitive axis (the symmetry axis of the test cylinders), the 2D accelerometer of the GG mission has 3 advantages:

(i) it retains the same dimensionality as the physical problem, which is a 2-body problem in the gravitational field of the Earth;
(ii) the plane of sensitivity being perpendicular to the symmetry axis of the test cylinders, the symmetry axis is also the axis of rotation which is the natural choice, and the spin/modulation frequency can be larger than the natural one, providing auto-centering and better reduction of "$1/f$" noise;
(iii) it doubles the amount of output data for any given integration timespan.

The only well-known disadvantage of rotation at frequencies above the natural one is the onset of whirl motions, at the natural frequencies of the system, around the equilibrium position. Whirl is due to losses in the suspensions (the smaller the losses, the slower the growth rate of whirl) and needs to be damped to prevent instability, but it can be separated to recover the equilibrium position thanks to the fact that the whirl frequencies of the system are known [12,13, Chapter 6].

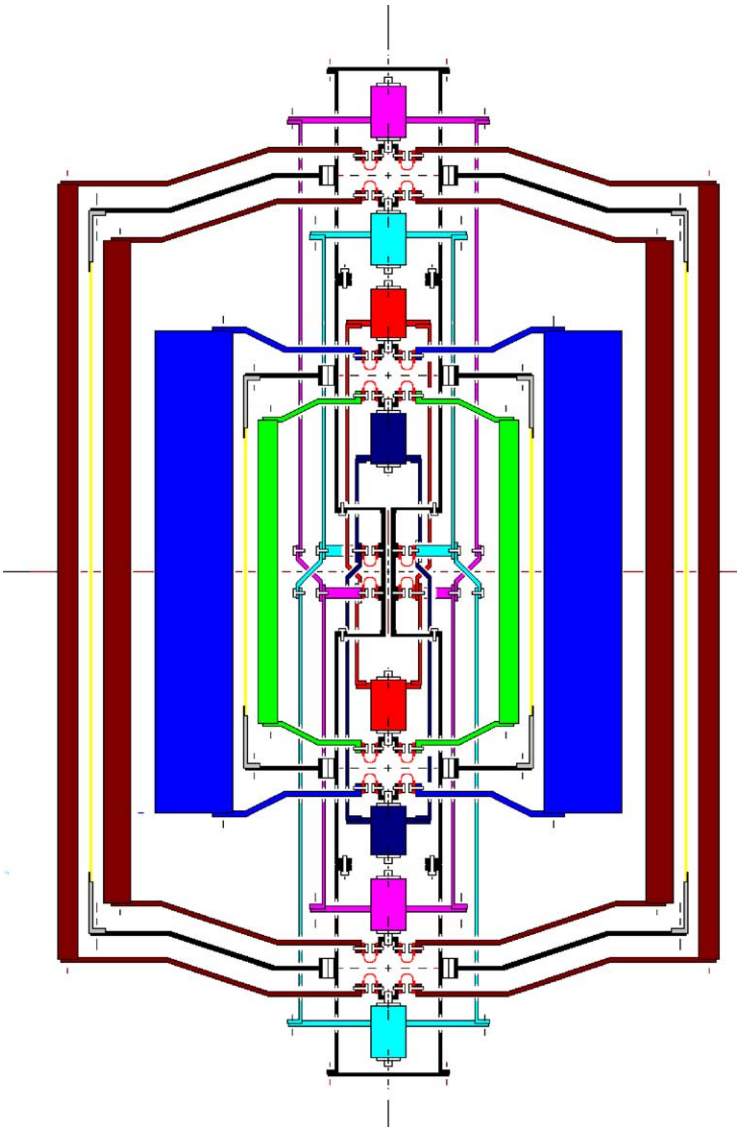

Fig. 2. Section through the spin axis of the differential accelerometers of the proposed GG mission for testing the equivalence principle in low Earth orbit. (Figure is in colour on the web.) There are 4 test cylinders (weighing 10 kg each), one inside the other, all centered at the same point (nominally, the center of mass of the spacecraft) forming 2 differential accelerometers: the inner one for EP testing (cylinders of different composition; shown in green and blue, respectively) and the outer one for zero check (cylinders made of the same material; both shown in brown). In each accelerometer the 2 test cylinders are coupled to form a beam balance by being suspended at their top and bottom from the 2 ends of a coupling arm made of 2 concentric tubes (each tube suspends one test cylinder at each end, which makes it asymmetric top/down; however, the two of them together form a symmetric coupling). All 4 tubes (2 for each coupling arm) are suspended at their midpoints from the same suspension shaft (the longest vertical tube in figure). In all cases the suspensions are $\bigcup$-shape (or $\bigcap$-shape) thin strips (shown in red), to be carved out of a solid piece of CuBe. At each connection there are 3 of them, at 120° from one another (the planar section in figure shows 2 for explanatory purposes only). There are capacitance plates (connected to the suspension shaft) for the read-out of differential displacements in between each pair of test cylinders (shown as yellow lines in section). The 8 small cylinders drawn along the symmetry axis are inchworms for the fine adjustment of the lengths of the coupling arms in order to center each test mass on the center of mass of the spacecraft. The whole system is symmetric around the spin axis as well as top/down. The two accelerometers are both centered at the center of mass of the spacecraft in order to reduce common mode tidal effects and improve the reliability of the zero check. (Taken from [11].)

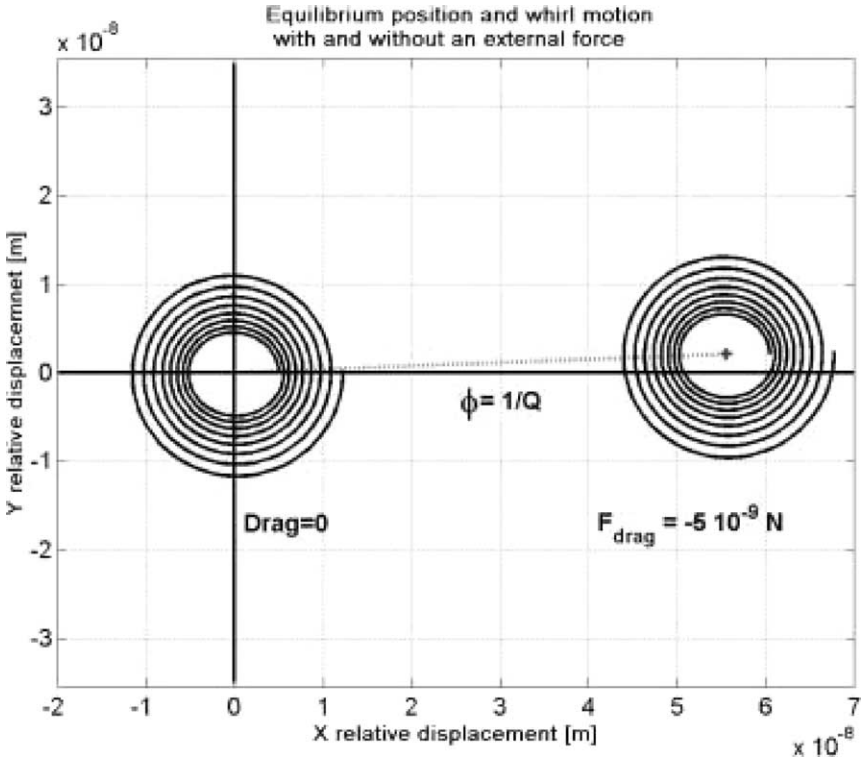

Fig. 3. Relative motion—in the non-rotating reference frame—of two coupled test cylinders spinning at frequency larger than the natural coupling one. The figure shows the plane of motion in two cases: with (right) and without (left) the inertial force deriving from an external residual drag acting on the spacecraft. It shows how the effect of an external force (air drag in this case), is that of displacing the equilibrium position of the system. A small phase lag appears due to energy losses in the suspensions (i.e., finite quality factor Q). Due to these losses whirl motion at the natural frequency of the system arises in either case around the corresponding equilibrium position.

Would a relative displacement of the test bodies caused by an external force be wiped out by auto-centering in supercritical rotation as it happens for the original offset ε? The answer is "No", because the offset vector is fixed in the rotating frame of the system while an external force, such as a possible violation of the equivalence principle, or the disturbing effect due to air drag acting on the spacecraft inside which the test masses are suspended, give rise to a displacement of the equilibrium position of the bodies in the non-rotating reference frame. In the presence of such a force, whirl motion will take place around the displaced position of equilibrium. This phenomenon has been simulated numerically and the result is plotted in Fig. 3 which shows (in the non-rotating reference frame) whirl motion in the absence of an external force, as well as around a displaced equilibrium position as caused by the effect of air drag.

The read-out consists of two pairs of capacitance plates located halfway in between the test cylinders and forming two capacitance bridges in the x, y directions of the plane perpendicular to the spin/symmetry axis. A differential force acting between the cylinders will displace their centers of mass and unbalance the bridges, thus generating an output voltage signal. Ideally, the bridges should sense only differential forces. In practice, they can be rejected only to some extent: the better is the mechanical centering of the plates in between the test cylinders, the more effective is the rejection of common mode forces. As reported in Section 4, a capacitance read-out—which can operate at room temperature—is adequate to the task of the GG mission.

3. The spacecraft and the orbit

The GG spacecraft is designed around the accelerometers and it is meant to provide the rotation of the system around its symmetry axis. It is therefore an axi-symmetric spacecraft passively stabilized by rotation around its axis of maximum moment of inertia (Fig. 4). At 520 km altitude, a sun-synchronous orbit requires an inclination of 97.5° over the equator. The orbit is almost circular. (See [14] for details.)

The sensitive plane of the accelerometers should lie in the plane of the expected signal, that is in the orbital plane. The spin/symmetry axis should therefore be normal to the orbit plane. However, while the spin axis is almost unaffected by external torques and therefore remains fixed in space, regression of the nodes of an inclined orbit due to the flattening of the Earth makes the orbit normal precess around the axis perpendicular to the equator (with a 1 year period in the case of a sun-synchronous orbit). As a result, a spin axis originally aligned with the orbit normal would no longer be so as time goes by. However, it can be shown that if the spin axis stays within about ±10° from the orbit normal, the expected signal is only very slightly diminished (along only one component) with respect to its maximum value. Therefore, the GG spacecraft is equipped with cold gas thrusters (see Fig. 4) to be used to realign its spin axis along the orbit normal every about 20 days of data taking. For the spacecraft to maintain its cylindrical symmetry and its center of mass not to be affected by attitude maneuvers, two tanks have been designed, both of toroidal shape, to be located one above and one below the center of mass. During attitude maneuvers all the masses suspended inside the spacecraft are locked using inchworms placed around their central coupling arms—see Fig. 2).

Since the spin/symmetry axis of the spacecraft is maintained near the axis perpendicular to the sun-synchronous orbit, solar cells for power generation are located on the surface of a dish facing the sun (see Fig. 4). This dish serves also the purpose of shielding the spacecraft body—a compact, 1 m size structure in the shape of a spinning top enclosing the accelerometers—from sunlight, so as to reduce the effects of thermal disturbances on the experiment.

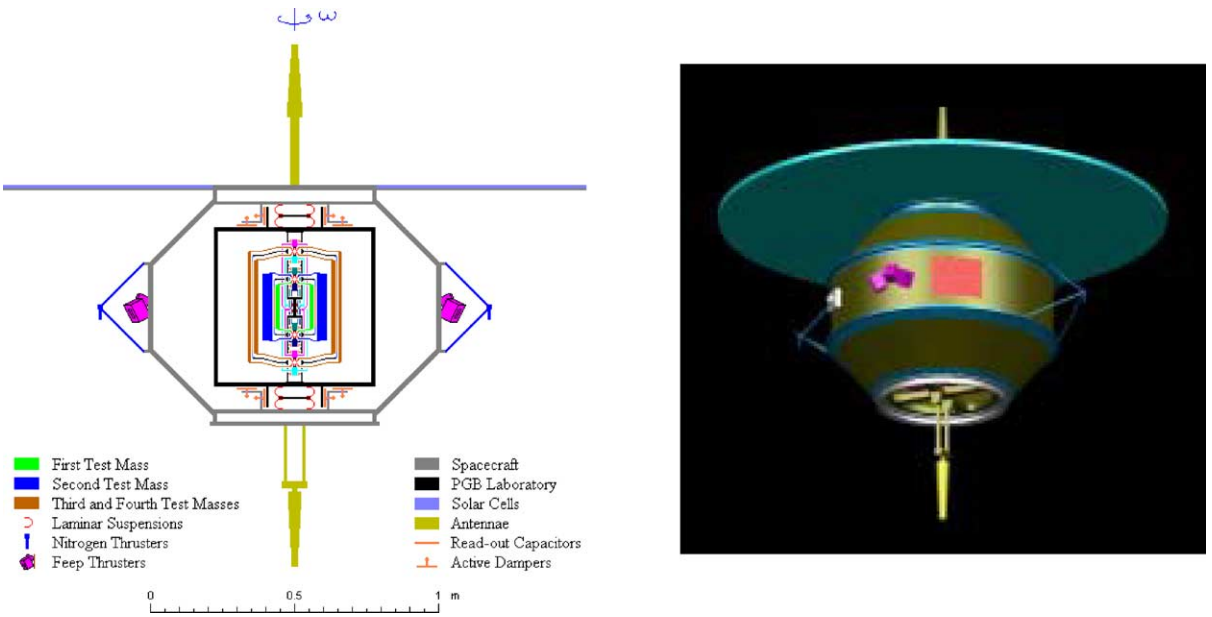

Fig. 4. The GG spacecraft as it has been designed for flight in high inclination, sun-synchronous orbit. (Figure is in colour on the web.) On the right-hand side is a 3D view, while on the left is a section along the spin/symmetry axis—showing the PGB laboratory and the accelerometers inside the spacecraft. The section and the legenda give details on the main parts of the spacecraft and the experimental apparatus. The total mass is 280 kg, the orbit is almost circular, has an altitude of 520 km and an inclination of 97.5° (sun-synchronous orbit).

The largest disturbing acceleration experienced by the accelerometers is due to the effect of residual air drag acting on the spacecraft and not on the test masses suspended inside it, thus resulting in an inertial acceleration equal and opposite to the acceleration caused by air drag on the spacecraft. Moreover, the largest and most "dangerous" air drag effect is due to its "along track" component, which has the same orbital frequency as the signal and differs from it only in phase (the signal is in the radial satellite—center of the Earth direction). The inertial acceleration resulting from air drag—and in general from non-gravitational forces acting on the spacecraft—are in principle the same on the test bodies in each accelerometer. They are known as "common mode" effects and should not produce any differential signal to compete with the target differential signal of an equivalence principle violation. However, this would be so only in the ideal case that the suspensions of the test cylinders in the accelerometers were perfectly identical and the capacitance bridges of the read-out were perfectly balanced, i.e., under conditions of perfect "common mode rejection". In the GG space experiment the strategy chosen is for air drag (and non-gravitational effects) to be *partially compensated* by the spacecraft drag-free control system, and *partially rejected* by the accelerometers themselves. In this way, the burden of reducing to an acceptable level this very large effect is shared between the spacecraft and the experimental apparatus, each of them being given a reasonable task.

Common mode rejection relies on the coupled suspension of the test cylinders and the capacitance differential read-out in between them, and on well established in-flight balancing procedures. Drag compensation requires the spacecraft to be equipped with thrusters and an appropriate control system to force the spacecraft itself to follow the motion of an undisturbed test mass inside it. Since drag compensation must be active during data taking, there are severe limitations on the disturbances it produces which make ordinary impulsive thrusters not suitable. Finely tunable proportional thrusters based on field emission electric propulsion (FEEP) appear to be the best choice, also because of their high specific impulse and consequent need of only a negligible mass of propellant. The test mass which drives the drag-free control system is the PGB (see Fig. 4, left), whose motion relative to the spacecraft in the plane perpendicular to the symmetry axis is read by two capacitance bridges. In terms of frequency, drag must be compensated in a narrow frequency range around the orbital one, in order to reduce its component along track. For this purpose, a control based on a notch filter has been tested in numerical simulations of the GG system and found to be effective [13, Chapter 6]. The PGB can provide the required driving signal to the drag control system because the orbital frequency around which drag must be compensated is below its natural frequency above which disturbances acting on the spacecraft are attenuated (see Fig. 5)

The transfer function of the PGB, given in Fig. 5, shows that effects at the orbital frequency are unaffected by the PGB suspension. They are sensed by the capacitance read-out in between the PGB and the spacecraft through the relative displacements they produce between the two, and these measurements serve as input to the drag free control. Note that the expected signal too is at the orbital frequency (see Fig. 1), hence, it is not attenuated. Instead, the figure shows that disturbances at the spin frequency of the spacecraft (in the non-rotating frame) are significantly reduced. Such disturbances are due primarily to the FEEP thrusters used for drag compensation, because in order to compensate for the effect of drag at the orbital frequency of the spacecraft around the Earth (in the non-rotating reference frame) while spinning with the spacecraft itself, they must fire at the spin frequency relative to the center of the Earth (2 Hz). Since this is also the modulation frequency of the expected signal, its attenuation by the PGB by about 5 orders of magnitude is a considerable advantage for the experiment.

4. Requirements and error budget

In order to be sensitive to differential effects in the plane perpendicular to the spin/symmetry axis, the test cylinders of each accelerometer (see Fig. 2) are weakly coupled to one another. With the suspensions as designed, the natural differential period is 540 s. Instead, all suspensions are stiff along the axis (with a natural period of 30 s) as well as in response to forces acting on both masses in the accelerometer (common mode effects). These mechanical features have been chosen for best sensitivity to differential

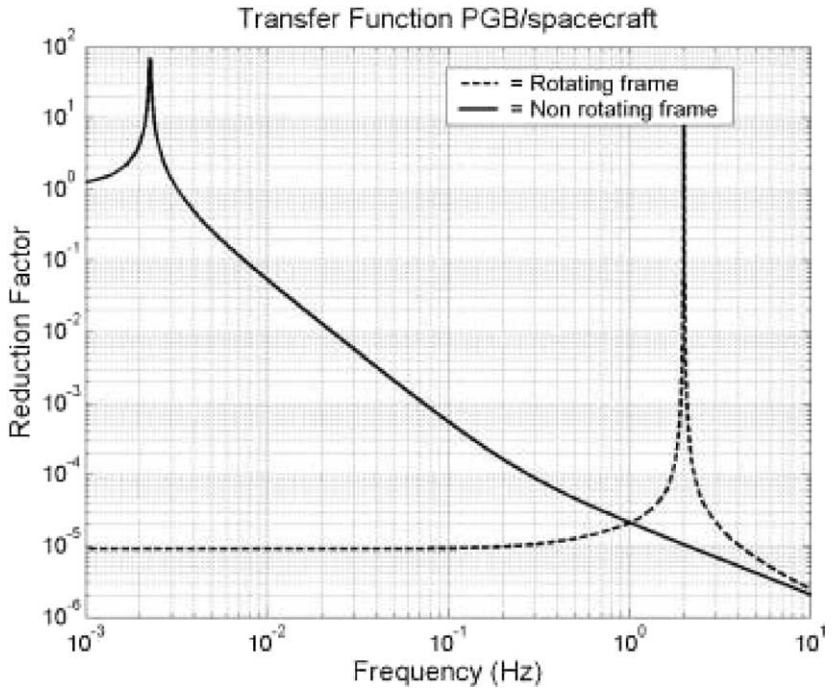

Fig. 5. Transfer function of the PGB laboratory (enclosing the accelerometers), suspended inside the spacecraft. The frequency of natural oscillations in the plane perpendicular to the spin/symmetry axis is 1/360 Hz. The transfer function is shown in the reference frame rotating with the system and also in the non-rotating one. In the non-rotating frame, any effect at frequencies below the natural one (the threshold frequency) is essentially unaffected, while above the threshold, disturbances are attenuated (the higher the frequency, the better the attenuation). These facts can be seen at the corresponding frequencies also in the rotating frame. In the rotating frame the peak near the spin frequency is larger than 1 because it shows (within the resolution of the figure) the transfer function at two nearby frequencies. These are the spin frequency $\pm$ the natural one, and at the natural frequency disturbances are amplified depending on the mechanical quality factor of the suspensions (see the transfer function in the non-rotating frame). It is well known that a better attenuation is obtained with lower quality factors. In this case the value of the quality factor is 90.

forces in the plane, while minimizing the effects of common mode forces in the same plane as well as those of all disturbances along the axes. In particular, the goal of testing the equivalence principle to 1 part in 10^{17} in the gravitational field of the Earth requires to detect the effect of a differential acceleration of $a_{\mathrm{EP}} \simeq 8.4 \times 10^{-17}\ \mathrm{m\,s^{-2}}$ (pointing to the center of the Earth as in Fig. 2), which amounts to a relative displacement between the test cylinders of the inner accelerometer of 0.6 pm.

The main requirements which need to be fulfilled in order to reach the mission goal are concerned with: mechanical balance of the test cylinders; drag compensation; mechanical balance of the capacitance bridges; temperature variations (in space and time); damping of whirl motions and quality factor at the spin frequency.

Each accelerometer is conceptually a beam balance with the beam along the symmetry axis. Ideally, it should be insensitive to common mode forces in the x, y plane of sensitivity perpendicular to it. Perfect rejection is obviously impossible, and we require that all common mode forces in the plane are rejected by a factor $\chi_{\mathrm{CMR}} = 1/10^5$. Much better rejection than this is achieved with ordinary balances on the ground where the common mode force (local gravity) is many orders of magnitude stronger than the largest common mode force (due to residual air drag) acting on the GG test cylinders. The balancing procedure relies on the capacitance bridges in between the test cylinders as sensors and the inchworms on the accelerometer's coupling arms (see Fig. 2) as actuators. Once balancing is completed, the inchworms can be switched off so as not to disturb the measurements. For the resid-

ual effect of air drag at the orbital frequency and in the plane of sensitivity we require a compensation factor of $1/10^4$, using the capacitance bridges between PGB and spacecraft as sensors and FEEP thrusters as actuators. As a result of both compensation and rejection, the residual differential effect of air drag on the test masses of the accelerometers is 10^9 times smaller than its original value, which for the GG spacecraft and orbit is $a_{\text{drag}} \leqslant 2 \times 10^{-7}\ \text{m s}^{-2}$ (worst case). This means that the disturbance due to air drag is larger than the signal by a factor 2.4 at most, and can anyway be distinguished from it because of the large phase difference between the two. The amount of drag effect remaining after compensation by FEEP thrusters gives a common mode effect on the test masses of the accelerometers, which—if the capacitance plates of the read-out are not perfectly balanced in between the test cylinders (i.e., the gaps on the two sides are not equal)—results in a spurious differential signal. For it to be a few times smaller than the target signal the unbalance must be (with a 5 mm gap) of a few μm, which is not a stringent requirement. We also require drag compensation by a factor $1/400$ along the spin/symmetry axis (at the orbital frequency) in order to reduce the separation between the centers of mass of the test cylinders along this axis (see below).

All mechanical balancing will be affected by temperature variations. Since there are about 20 days available for data taking between two successive attitude maneuvers, we require that temperature variations be small enough not to destroy the balancing of the system for that span of time. Temperature time variations must be such that $\dot{T} < 0.1$ K/day, the requirement being set by the mechanical balance of the capacitance bridges, which are affected by the differential thermal expansion of the test masses and bridge frame. Variation of the suspensions stiffness with the temperature are not relevant. Along the z spin/symmetry axis it must be $\Delta T/\Delta z < 4$ K/m, and this requirement is set by the mechanical balance of the test cylinders since it is affected by the expansion/contraction of the coupling arms. Passive thermal isolation is sufficient to avoid temperature variations larger than these, and no active thermal control is needed. Temperature constraints are not very demanding in GG because its rapid rotation averages out azimuthal temperature variations and makes the radiometer effect negligible; much more demanding constraints need to be satisfied in case of slow rotation of the test cylinders [9,11]. During eclipses, when the satellite happens to go in and out of the Earth's shadow, different heating of the outer shell of the spacecraft as compared to the internal apparatus (which is thermally isolated) would produce a differential rotation rate due to changes in the moment of inertia and conservation of angular momentum. This is avoided by means of a small mass compensation system based on a photo-diode sensor to detect the phase lag between the outer and inner part of the spacecraft, and inchworm actuators to displace little masses and compensate moment of inertia changes; the masses required are of a few grams because changes of moment of inertia caused by temperature variations are very small.

Whirl motions (as shown in Fig. 3) of all suspended bodies are damped by means of capacitance sensors/actuators. In the non-rotating frame whirls have the frequencies of natural oscillations (slow), while the sensors/actuators spin fast with the whole system (2 Hz). The spacecraft is equipped with Earth elevation sensors to measure its state of rotation in order to perform the coordinate transformation between the rotating and non-rotating frame which is needed for an accurate reconstruction and damping of the whirl motion [13, Chapter 6]. The growth rate of whirls is determined by losses in the system, essentially in the mechanical suspensions as they undergo deformations at the frequency of spin. The time constant of the growth is $(Q_s/\pi) \cdot T_w$, where Q_s is the quality factor at the frequency of spin and T_w the natural period of the whirl. The force required to damp the whirl is a fraction Q_s of the mechanical coupling force [12]. In GG the requirement is $Q_s = 20000$ (at 2 Hz), which laboratory tests have shown to be achievable: we have recently measured 30000 at 0.9 Hz and about 100000 at 1.4 Hz with the "GG on the Ground-GGG" laboratory prototype. With a Q of at least 20000, whirl growth is so slow that data taking can be performed between successive damping, thus avoiding any disturbance at all from damping forces. In order to reconstruct the position of relative equilibrium of the test cylinders in the non-rotating reference frame, as affected by a low frequency differential force (like an EP violation at the orbital frequency around the Earth) whirl motion at the natural frequency of oscillation can be separated out. Tests with the laboratory prototype demonstrate that a

low frequency differential effect can be detected even in the presence of a much larger whirl [15].

The error budget of the space experiment is performed keeping in mind that both the frequency and phase of the expected signal are well known: once the high frequency signal modulation due to the spin rate of the spacecraft has been eliminated by coordinate transformation to the non-rotating system, the signal must appear as a differential displacement at the orbital frequency, and always pointing to the Earth.

The most dangerous perturbing effects are therefore those which are close to the signal both in frequency and phase. There are two such effects: the Earth monopole coupling to higher mass moments of the test bodies and the radiometer effect. The first is due to the fact that the test bodies are not monopoles; they have non-zero higher mass moments, and the monopole mass moment of the Earth will couple differently to them giving rise to a differential force. Being due to the Earth,—which is the also the source mass of a possible violation of equivalence—this effect cannot in any way be distinguished from the signal. For a given spacecraft altitude and a given target in EP testing, the dominant mass moment of the test cylinders (quadrupole) must be small enough for this effect to be below the signal. The values required (about 0.01) are realistic to obtain by test mass machining. The radiometer effect is caused by the residual gas pressure in the presence of temperature gradients across the test masses generated by the infrared radiation from the Earth. In GG temperature gradients are averaged out by the fast rotation and the radiometer effect is negligible even at room temperature [9,16].

At the same frequency as the signal but, with a phase difference of about 90°, we have the inertial force caused by residual air drag acting on the outer surface of the spacecraft along its orbit. With the requirements given above for drag compensation and common mode rejection, the residual differential acceleration due to air drag is 2–3 times larger than the signal (worst case) and can be separated from it thanks to the large phase difference.

At twice the orbital frequency there is the tidal effect due to a non-zero separation between the centers of mass of the test cylinders along the spin/symmetry axis whenever it is not exactly aligned with the orbit normal [13, Chapter 2.2]. With a compensation of non-gravitational forces (mostly solar radiation pressure) along the spin axis by $1/400$, and with a common mode rejection in that direction of $1/50$ (by suspensions machining only) this tidal effect is almost one order of magnitude smaller than the signal.

At the natural frequency of differential oscillation of the test masses ($1/540$ s) there is a residual whirl motion of their centers of mass which gives rise to a tidal effect from the Earth at the whirl frequency. However, it can be proven that it does not affect the position of relative equilibrium around which whirl motion takes place (see [17]). It causes a small deformation of the whirl orbit which circulates with the motion of the spacecraft around the Earth, does not accumulate in time and does not prevent recovery of the equilibrium position by separation of the whirl motion. Similarly, the whirl orbit is also affected by resonant drag effects due to air granularities along the spacecraft orbit around the Earth. In this case too the equilibrium position is not affected, the deformation of the whirl orbit circulates with the orbital period, it does not accumulate with time and can be separated out.

The accelerometers are designed to be sensitive in the plane perpendicular to the spin/symmetry axis and more stiff along it. However, there is a modest drag compensation requirement along the spin axis because a center of mass separation along it will generate (in the presence of a tilt angle with respect to the orbit normal) a tidal effect in the sensitive plane whose frequency is close to that of the signal.

Mechanical suspensions allow the test masses to be electrically grounded, thus avoiding the need to measure the amount of accumulated charge and to discharge the masses, which inevitably disturbs the measurements. Residual so-called “patch effects” are known to be small and slowly moving. Moreover, their presence can be checked by changing sign to an applied known electric potential corresponding to the resolution achieved: since the force is proportional to the square of the potential, the resulting effect must be the same to rule out a patch effect potential at that level. Requirements on magnetic impurities and magnetic susceptibility for the test masses can be met.

Rotation of the whole system together makes many effects coming from local (fixed) disturbances, (such as local mass anomalies or parasitic capacitances) to become DC signals, and therefore not an issue.

Finally, thermal noise, is compatible with the goal of the experiment thanks to the high frequency of spin, to the high Q of the system and the large mass of the test cylinders (10 kg test bodies compensate for working at 300 K rather than at a few K but with masses of 100 g).

5. Significance of the ground prototype

Since the GG differential accelerometer has two degrees of freedom it is possible to design a ground version of it to be fully operated and tested at 1 g. In the ground version the plane of sensitivity of the accelerometer lies in the horizontal plane of the laboratory while the third dimension is used to suspend the system against local gravity. In this way it can detect the horizontal component of a possible violation of equivalence either in the field of the Earth (a differential force constant in the North–South direction) or in the field of the Sun (a differential force following its 24 hr motion). This is the "Galileo Galilei on the Ground-GGG" prototype, which has been extensively described in [11] and whose recent results are given in [15]. The GGG accelerometer is designed to have the same features as the one proposed for flight, essentially: weak coupling, high frequency supercritical rotation and differential capacitance read-out. However, there are several very important differences to bear in mind.

The main difference is due to the special character of the third dimension—that of local gravity—which makes it impossible for the GGG design to be as symmetric as in space (see Fig. 2), and limits its capability to reject common mode effects. In addition, while no motor is needed in space once the spacecraft has been brought to its nominal rotation rate, GGG requires a motor and its bearings, which are a relevant source of noise. Frequency modulation by fast rotation can be at higher frequency than in space, but while the entire spacecraft spins together with the test bodies and therefore any local mass anomaly gives rise to a DC effect which does not affect (as long as it is constant in time) the modulated signal, nearby mass anomalies in the laboratory and its vicinity give effects which are directly competing with a possible violation of the equivalence principle in the field of the Earth. In order to separate them out, these effects need to be measured and compensated, as in the rotating torsion balance experiment by [1]. In GGG the test bodies are rotors in a non-inertial reference frame (because of the diurnal rotation of the Earth) and the resulting gyroscopic effects would be in the North–South direction like an equivalence principle violation in the field of the Earth and indistinguishable from it, see [11]. However GGG can be used to detect a violation of equivalence in the field of the Sun, because of its 24 hr period, and the driving signal is only slightly weaker than in the field of the Earth. Local mass anomalies are not a problem in this case but the 24 hr component of the tidal effect from the Sun, not being perfectly rejected, would leave a residual differential force which must be separated by measurements at different declinations of the Sun around the equinoxes.

A 24 h signal requires local seismic noise at this frequency (tilts and horizontal accelerations) to be attenuated. This can be done first actively (using a tiltmeter as sensor and PZTs as actuators to maintain the verticality of the rotation axis) and then passively, by means of a cardanic suspension of the whole system. As long as horizontal accelerations are considered, it is worth noticing that in GGG only displacements with respect to the local vertical are relevant, and they can be passively attenuated with a cardanic suspension whose stiffness is only slightly weaker than that of the suspensions currently in use for the test bodies.

Whirl motions need to be damped both on the ground and in space, but in space they can only be damped actively with capacitance sensors/actuators which are fixed in the rotating frame of the whole system. In GGG active damping can be performed also in the non-rotating frame, which is what has been realized so far.

An obvious advantage of the ground experiment is the absence of drag.

Given the stronger driving signal in space (by 3 orders of magnitude), the weaker coupling (and consequent higher sensitivity which can be achieved in absence of weight), the better symmetry of the accelerometer in space and the absence of noise from the motor, it can be convincingly argued that even a relatively modest GGG test of the equivalence principle in the field of the Sun can generate confidence in the capability of the GG space experiment to reach its goal. The space experiment will benefit from sev-

eral key features developed and tested in GGG: the read-out and data analysis, the beam-balance of the accelerometer and its rotation in supercritical regime, the weak and high Q mechanical suspensions, the capacitive active control of whirl motions.

Acknowledgements

Thanks are due to ASI (Agenzia Spaziale Italiana) for funding the GG mission study in sun-synchronous orbit, to Laben space industry for providing laboratory support for the GGG prototype and to INFN (Istituto Nazionale di Fisica Nucleare) for approving GGG as a laboratory experiment starting mid 2003.

References

[1] Y. Su, et al., Phys. Rev. D 50 (1994) 3614.
[2] S. Baeßler, et al., Phys. Rev. Lett. 83 (1999) 3585.
[3] "Galileo Galilei-GG" website: http://eotvos.dm.unipi.it/nobili.
[4] Microscope website: http://www.cnes.fr/activites/connaissance/physique/microsatellite/1sommaire_microsatellite.htm and http://www.onera.fr/dmph-en/accelerometre.
[5] STEP Satellite Test of the Equivalence Principle, 1996, report on the phase A study, ESA-SCI(96)5.
[6] STEP website: http://einstein.stanford.edu/STEP.
[7] E. Fischbach, et al., Phys. Rev. D 55 (1995) 5417.
[8] T. Damour, F. Piazza, G. Veneziano, Phys. Rev. D 66 (2002) 046007.
[9] A.M. Nobili, et al., Phys. Rev. D 63 (2001) 101101R.
[10] J.P. Den Hartog, Mechanical Vibrations, Dover, New York, 1985, first published in 1934.
[11] A.M. Nobili, et al., New Astronomy 8 (2003) 371.
[12] A.M. Nobili, et al., Class. Quantum Grav. 16 (1999) 1463.
[13] "Galileo Galilei" (GG), Phase A Report, 2nd Edition, Agenzia Spaziale Italiana, 1998, 2000, http://eotvos.dm.unipi.it/nobili/ggweb/phaseA.
[14] A. Anselmi, G. Catastini, Design of the GG satellite, Phys. Lett. A 318 (2003) 205, this issue.
[15] G.L. Comandi, et al., "Galileo Galilei on the Ground-GGG": experimental results and perspectives, Phys. Lett. A 318 (2003) 213, this issue.
[16] A.M. Nobili, et al., New Astronomy 7 (2002) 521.
[17] G.L. Comandi, et al., Tidal effects in space experiments to test the equivalence principle: implication on the experiment design, Phys. Lett. A 318 (2003) 251, this issue.

ELSEVIER

New Astronomy 8 (2003) 371–390

New Astronomy

www.elsevier.com/locate/newast

A rotating differential accelerometer for testing the equivalence principle in space: results from laboratory tests of a ground prototype

A.M. Nobili[a,*], D. Bramanti[a], G.L. Comandi[a], R. Toncelli[a], E. Polacco[b]

[a] *Space Mechanics Group, Department of Mathematics, University of Pisa, I-56127 Pisa, Italy*
[b] *Department of Physics, University of Pisa, and INFN, I-56127 Pisa, Italy*

Received 19 August 2002; accepted 1 November 2002
Communicated by F. Melchiorri

Abstract

We have proposed to test the equivalence principle (EP) in low Earth orbit with a rapidly rotating differential accelerometer (made of weakly coupled concentric test cylinders) whose rotation provides high frequency signal modulation and avoids severe limitations otherwise due to operation at room temperature [PhRvD 63 (2001) 101101]. Although the accelerometer has been conceived for best performance in absence of weight, we have designed, built and tested a variant of it at 1-g. Here we report the results of measurements performed so far. Losses measured with the full system in operation yield a quality factor only four times smaller than the value required for the proposed high accuracy EP test in space. Unstable whirl motions, which are known to arise in the system and might be a matter of concern, are found to grow as slowly as predicted and can be stabilized. The capacitance differential read-out (the mechanical parts, electronics and software for data analysis) is in all similar to what is needed in the space experiment. In the instrument described here the coupling of the test masses is 24 000 times stiffer than in the one proposed for flight, which makes it 24 000 times less sensitive to differential displacements. With this stiffness it should detect test masses separations of $1.5 \cdot 10^{-2}$ μm, while so far we have achieved only 1.5 μm, because of large perturbations—due to the motor, the ball bearings, the non-perfect verticality of the system—all of which, however, are absent in space. The effects of these perturbations should be reduced by 100 times in order to perform a better demonstration. Further instrument improvements are underway to fill this gap and also to reduce its stiffness, thus increasing its significance as a prototype of the space experiment.

PACS: 04.80.Cc; 07.10.−h; 06.30.Bp; 07.87.+v
Keywords: Gravitation; Relativity; Instrumentation: detectors; Methods: laboratory; Methods: data analysis

1. Introduction

The equivalence principle (EP) stated by Galileo, reformulated by Newton and reexamined by Einstein to become the founding principle of General Relativity, can be tested from its most direct conse-

*Corresponding author.
E-mail addresses: nobili@dm.unipi.it (A.M. Nobili), bramanti@mail.dm.unipi.it (D. Bramanti), comandi@mail.dm.unipi.it (G.L. Comandi), toncelli@mail.dm.unipi.it (R. Toncelli), polacco@mail.dm.unipi.it (E. Polacco).

1384-1076/02/$ – see front matter
doi:10.1016/S1384-1076(02)00233-6

quence: the universality of free fall (UFF), whereby all bodies fall with the same acceleration regardless of their mass and composition ($\eta = \Delta a/a = 0$). The most accurate EP experiments have been carried out on the ground with test bodies suspended on a torsion balance, finding no violation to about 10^{-13} (Adelberger et al., 1990; Su et al., 1994; Baeßler et al., 1999). (See Note added in proof.) Test bodies in low Earth orbit are subject to a driving gravitational (and inertial) acceleration much stronger than on torsion balances on the ground, by about three orders of magnitude. Moreover, the absence of weight is ideal in small force experiments. As a consequence, space missions can potentially improve by several orders of magnitude the current sensitivity in EP tests. Three such experiments are being considered, and the goals are: 10^{-15} for the French μSCOPE (MICROSCOPE Website: http://www.cnes.fr/activites/activites/connaissance/physique/microsatellite/1sommaire_microsatellite.htm and http://www.onera.fr/dmph-en/accelerometre; Touboul et al., 2001), 10^{-17} for the Italian ''GALILEO GALILEI'' (GG) (''GALILEO GALILEI'' (GG), Phase A Report, 1998; Nobili et al., 1999; ''GALILEO GALILEI'' (GG) Website: http://eotvos.dm.unipi.it/nobili; Nobili et al., 2001), 10^{-18} for the American STEP (Worden, 1978; STEP Satellite Test of the Equivalence Principle, 1993; STEP Satellite Test of the Equivalence Principle, 1996; Step Website: http://einstein.stanford.edu/STEP) [however, STEP studies within the European Space Agency are consistent with a goal of 10^{-17} (STEP Satellite Test of the Equivalence Principle, 1993; STEP Satellite Test of the Equivalence Principle, 1996)]. μSCOPE and GG are room temperature experiments, STEP is cryogenic at very low temperature.

In all the proposed space experiments the test bodies are hollow cylinders one inside the other, with their centers of mass as close as possible for classical differential effects (such as tides) to be reduced. However, in spite of the different arrangement of the test bodies needed in space, the main features of the ground apparata which have so far provided the best sensitivity should be retained. The most relevant of such features is the differential nature of the torsion balance, which makes it ideally insensitive to common mode effects. Its implementation at the end of the 19th century (Eötvös et al., 1922) has provided a major improvement, by about three orders of magnitude, over previous pendulum tests of the EP. However, Eötvös tested the universality of free fall in the field of the Earth, therefore looking for a constant (DC) anomalous acceleration in the North–South direction of the plane of the horizon. Another major improvement (by about three more orders of magnitude) was made possible in the 1960s and 1970s (Roll et al., 1964; Braginsky and Panov, 1972) when a torsion balance was used to search for a deviation from UFF in the field of the Sun, in which case the diurnal rotation of the Earth itself provides a 24-h modulation of the expected signal. Further improvements on the torsion balance, including its rotation faster than the diurnal rotation of the Earth (at $\simeq 1$ h period) and consequent modulation of the signal at higher frequency, have provided the most sensitive tests so far (Adelberger et al., 1990; Su et al., 1994; Baeßler et al., 1999)

It seems therefore appropriate, for an EP experiment in space, that the instrument be designed as a rotating differential accelerometer made of concentric test cylinders, thus leading naturally to a spacecraft of cylindrical symmetry too, and co-rotating with the test cylinders. If the axis of symmetry is the axis of maximum moment of inertia, one-axis rotation provides (passive) spacecraft attitude stabilization. This is how the GG space experiment for testing the EP in the field of the Earth has been designed: the concentric test cylinders spin around the symmetry axis at a rather high frequency (2 Hz with respect to the center of the Earth) and are sensitive to differential effects in the plane perpendicular to the spin/symmetry axis. A cylindrical spacecraft encloses, in a nested configuration, a cylindrical cage with the test cylinders inside, and is stabilized by rotation around the symmetry axis. As shown in Fig. 1, an EP violation in the field of the Earth would generate a signal of constant amplitude (for zero orbital eccentricity) whose direction is always pointing to the center of the Earth, hence changing orientation with the orbital period of the satellite. The read-out, also rotating with the system, will therefore modulate an EP violation signal at its spin frequency.

We have designed and built a differential, rotating accelerometer similar to the one proposed for the GG space experiment. It is a full scale prototype devoted

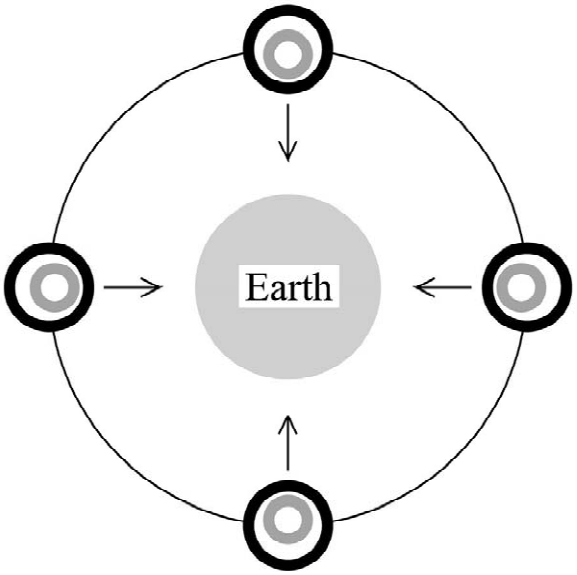

Fig. 1. Section across the spin/symmetry axis of the GG outer and inner test cylinders (of different composition) as they orbit around the Earth inside a co-rotating, passively stabilized spacecraft (not shown). The centers of mass of the test cylinders are shown to be displaced towards the center of the Earth as in the case of a violation of the equivalence principle in the field of the Earth (indicated by the arrows). The signal is modulated at the spin frequency of the system (2 Hz with respect to the center of the Earth). The figure is not to scale (taken from Nobili et al., 2001).

to testing the main features of the proposed instrument, in spite of the fact that the local acceleration of gravity is about eight orders of magnitude bigger than the largest disturbances the accelerometer would be subject to in space (due to the residual air drag and to solar radiation pressure). Here we describe the ground apparatus, show how it is operated and report the results obtained from measurement data so far. To conclude, we discuss the relevance of these results in view of the GG target sensitivity.

2. Design of the apparatus

A schematic view of the apparatus is given in Fig. 2, where a section through the spin/symmetry axis of the accelerometer is shown (enclosed by the vacuum chamber). (The color version of Fig. 2 is available in the article published on the World Wide Web.) Fig. 3 shows a picture of the accelerometer

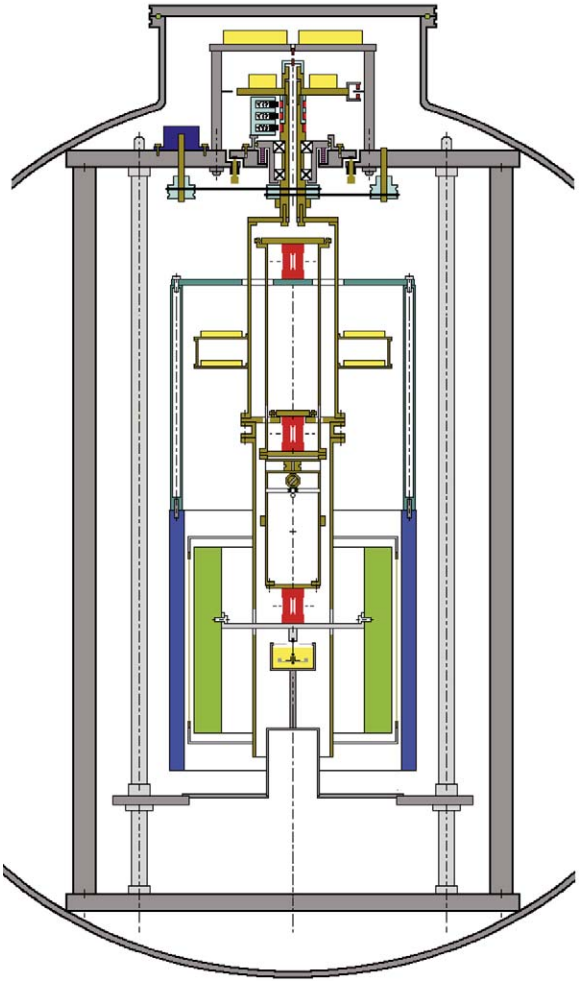

Fig. 2. Section through the spin axis of the differential accelerometer inside the vacuum chamber (drawing to scale; inner diameter of vacuum chamber 1 m; see text for a description of its parts).

mounted inside the chamber. In Fig. 2 the chamber and the frame (not rotating) on which the whole rotor is mounted are drawn in gray. The test cylinders are drawn in green (the inner one) and blue (the outer one). On the top of the frame (at its center) is a shaft turning inside ball bearings (sketched as ''x'' in the section of Fig. 2) to which rotation is transmitted from the motor by means of O-rings on pulleys. This shaft holds the suspension tube, which therefore rotates with the shaft. Inside the suspension tube is the coupling arm (also a tube) suspended at its midpoint from the suspension tube by means of a laminar suspension (drawn in red; see picture in Fig.

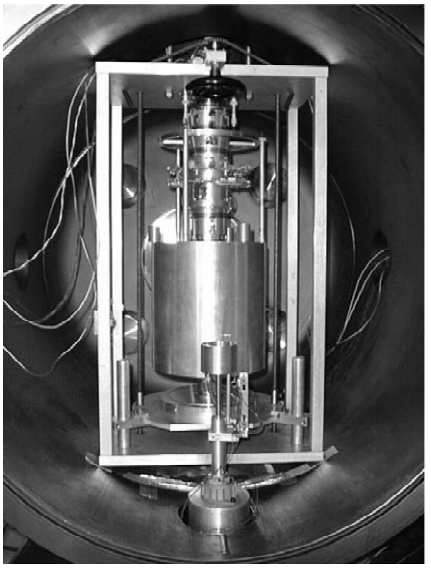

Fig. 3. The rotating differential accelerometer mounted inside the vacuum chamber (in the basement of the LABEN laboratories in Florence).

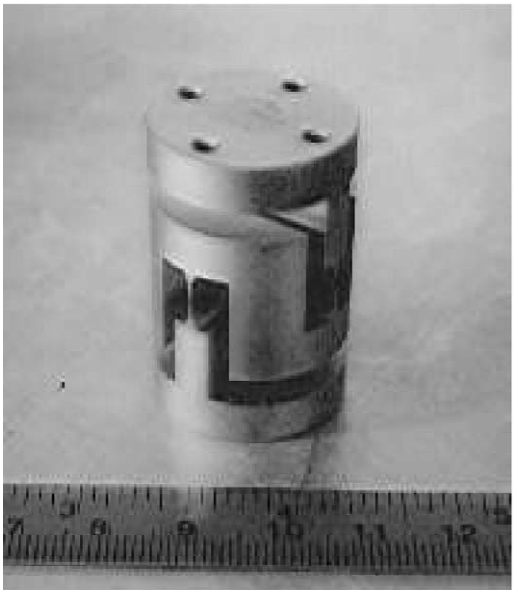

Fig. 4. One of the three laminar suspensions used in the accelerometer (sketched in red in Fig. 2). They are carved out of a solid bar of CuBe by electroerosion in 3D and properly treated for high mechanical quality.

4). The two test cylinders are suspended from the two ends of the coupling arm (the outer one from the top, the inner one from the bottom) by two more laminar suspensions (all three suspensions are manufactured to be equal; they are all drawn in red in Fig. 2). Being metallic, they also ensure passive electrostatic discharging of the test masses. Fig. 3 shows three light vertical bars and a horizontal ring used to connect the outer test cylinder to its suspension at the top of the coupling arm. The suspensions have the property of being soft in both the X and Y directions in the plane perpendicular to the symmetry/vertical axis, while at the same time being strong enough in the vertical direction in order to withstand local gravity. In this way the test cylinders—in spite of being concentric—are in fact suspended like in an ordinary beam balance, but with the beam of the balance (the coupling arm) in the vertical direction rather than in the horizontal one. The central suspension (connecting the midpoint of the beam to the suspension tube) is therefore the one which carries the whole weight of this balance, mostly due to the test cylinders themselves (10 kg each).

The read-out consists of two pairs of capacitance plates located halfway in between the test cylinders and connected to the suspension tube by means of an insulating frame (see picture in Fig. 5 and section in Fig. 2, in which they appear as vertical lines in between the test cylinders). They maintain the cylindrical symmetry of the system, forming two capacitance bridges in the X and Y directions of the plane perpendicular to the symmetry axis (the plane of sensitivity of the instrument). The two annular dishes (in yellow) mounted around the upper half of the suspension tube contain the two capacitance bridge circuits, their preamplifiers, the signal demodulators, the A/D (analog-to-digital) converters and the driver of the optical emitter, which is located at the very top of the rotating shaft (in order to transmit the demodulated signal from the rotor to the non-rotating frame and then outside of the vacuum chamber). In the upper part of the shaft, above the ball bearings, are the rotating contacts for power transmission to the electronics of the rotor and a dish with a circuit for stabilizing this power. To this dish is also attached an optical device which provides a reference signal for the phase of the rotor. The passive damper is shown under the lowest laminar suspension, and is not rotating (see Section 4).

Fig. 5. The four capacitance plates (with their insulating frames) forming the two capacitance bridges of the read-out. They are mounted halfway in between the concentric test cylinders to read their relative displacements (see section in Fig. 2).

A differential force acting between the test cylinders in any direction in the horizontal plane of the laboratory will incline the balance beam—pivoted at its midpoint—with respect to the vertical, thus giving rise to a relative displacement of the centers of mass of the cylinders in the direction of the force. The resulting mechanical displacement will unbalance the capacitance bridges, thus allowing it to be transformed into an electric voltage signal. If the whole system (test cylinders plus read-out) rotates around the vertical shaft, the signal is modulated at the rotation frequency, just as in the GG space experiment (Fig. 1). In case of an EP violation in the field of the Earth, two test cylinders of different composition should show (after transformation to the non-rotating reference frame) a constant, relative displacement in the North–South direction of the horizontal plane. Instead, checking for violation in the field of the Sun requires to detect a (smaller) relative displacement vector in the same plane following the Sun in its daily motion with respect to the Earth fixed laboratory where the test bodies are located.

The instrument is therefore a rotating differential accelerometer sensitive in the horizontal plane. Its differential character comes from two features. The first is that the test cylinders are mechanically coupled so as to be sensitive to differential accelerations acting between them because of the geometry of their mounting. The second is that the read-out too is differential: were all plates mounted exactly halfway in between the test cylinders (same clear gap on either side), it would be totally insensitive to common mode forces (i.e., to forces causing a displacement of both test cylinders together with respect to the capacitance plates). For a non-zero off-centering of the plates between the cylinders, the read-out is anyway less sensitive to common mode displacements than it is to differential ones, by a factor which is the ratio of the off-centering to the average gap: the better the plates are centered, the less sensitive is the read-out to common mode forces, the more suitable it is for EP testing. The sensitivity of the test cylinders to differential accelerations depends on the softness of the laminar suspensions and the balance of arms and masses in their coupled mounting. Soft suspensions and good balancing are needed, providing long natural periods of differential oscillations of the test cylinders with respect to one another. The longer the natural periods of differential oscillations, the larger the mechanical displacements of the test cylinders in response to differential accelerations, the stronger the output voltage signal. Soft suspensions and good balancing are also needed in order to reduce the residual differential fraction of forces which are common mode by their nature but do in fact produce also a differential effect on the test cylinders due to the inevitable imperfections in their mounting and balancing. Ideally, a common mode force should be perfectly rejected by the system, leaving no differential residual. By comparison, the test cylinders of the μSCOPE accelerometer (also based on capacitance sensing) are controlled with respect to the same silica frame but are not coupled, neither by the suspensions (each cylinder has its own electrostatic suspension) nor by the read-out (the differential data of interest are obtained as the difference of the individual readings of the capacitance sensors of each test cylinder (MICROSCOPE Website: http://www.cnes.fr/activites/activites/connaissance/physique/microsatellite/1sommaire_microsatellite.htm and http://www.onera.fr/dmph-en/accelerometre; Touboul et al., 2001, Fig. 1).

Ordinary beam balances are known to be ideal instruments for extremely effective common mode rejection (rejection factors of $10^{-8}-10^{-9}$ can be reached at 1-g). Also in the accelerometer designed for space (see Fig. 6 and its caption; the color

version of Fig. 6 is available in the article published on the World Wide Web) the test cylinders are coupled like in a beam balance—with the plane of sensitivity perpendicular to the beam as in Fig. 2—and have a differential capacitance read-out. The geometry of the space accelerometer is perfectly symmetric, which is possible in the absence of weight because the direction of the beam is not the direction of a force many orders of magnitude larger than any force acting in the sensitivity plane perpendicular to it, as it is the case with the vertical balance of Fig. 2 because of the local acceleration of gravity. In this case the advantage of the coupling of the test cylinders is retained in spite of a lack of symmetry in their suspension arms: the center of mass of the inner cylinder is very close to its suspension point, while the center of mass of the outer one is much farther from its own (see Fig. 2). This asymmetry is a consequence of the special character of the vertical direction when operating at 1-g and it is an inevitable change from the perfect symmetry of the space design.

It is desirable that the spin rate be high, so as to get a correspondingly high frequency modulation of the signal and consequent reduction of $1/f$ mechanical and electronic noise. It is also desirable for the mechanical coupling between the test cylinders to be weak (long natural differential period T_{diff}), for them to be sensitive to differential forces like the one which would result from an EP violation, because the relative displacement due to a differential force increases as T^2_{diff}). This means that typically the system spins at a frequency higher than the natural frequency for differential oscillations of the test cylinders, in which case it is known that the spinning bodies do reduce any original offset vector between their centers of mass (fixed in the rotating system) inevitably due to imperfections in construction and mounting (see e.g. Den Hartog, 1985; Crandall, 1995; Genta, 1993). In simple terms, a weakly coupled and fast spinning rotor is an approximation

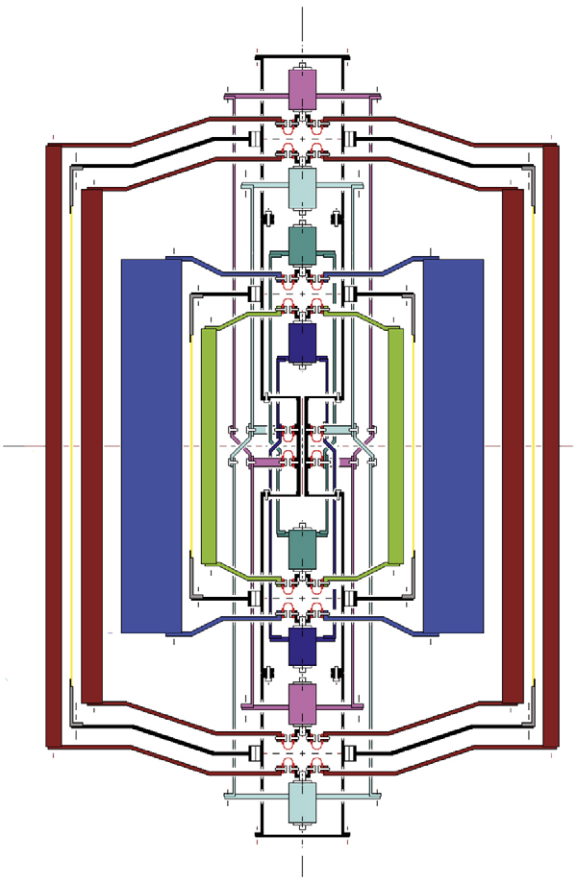

Fig. 6. Section through the spin axis of the differential accelerometers of the proposed GG mission for testing the equivalence principle in low Earth orbit. There are four test cylinders (10 kg each), one inside the other, all centered at the same point (nominally, the center of mass of the spacecraft) forming two differential accelerometers: the inner one for EP testing (cylinders of different composition; shown in green and blue respectively) and the outer one for zero check (cylinders made of the same material; both shown in brown). In each accelerometer the two test cylinders are coupled to form a beam balance by being suspended at their top and bottom from the two ends of a coupling arm made of two concentric tubes (each tube suspends one test cylinder at each end, which makes it asymmetric top/down; however, the two of them together form a symmetric coupling). All four tubes (two for each coupling arm) are suspended at their midpoints from the same suspension shaft (the longest vertical tube in figure). In all cases the suspensions are $\cup$-shape (or $\cap$-shape) thin strips (shown in red), to be carved out of a solid piece of CuBe. At each connection there are three of them, at 120° from one another (the planar section in figure shows two for explanatory purposes only). There are capacitance plates (connected to the suspension shaft) for the read-out of differential displacements in between each pair of test cylinders (shown as yellow lines in section).The eight small cylinders drawn along the symmetry axis are inchworms for the fine adjustment of the lengths of the coupling arms in order to center each test mass on the center of mass of the spacecraft. The whole system is symmetric around the spin axis as well as top/down. The two accelerometers are both centered at the center of mass of the spacecraft in order to reduce common mode tidal effects and improve the reliability of the zero check.

to an ideal unconstrained rotor whose center of mass would have zero offset from the rotation axis.

The natural period $T_{\rm diff}$ for differential oscillations of the test cylinders, one with respect to the other, in the vertical beam balance arrangement of Fig. 2 (in the presence of both local gravity and mechanical coupling) can be written as:

$$T_{\rm diff} \simeq \frac{2\pi}{\sqrt{\left(\frac{3K}{m} + \frac{g\,\Delta l}{l\,2l}\right)}} \qquad (1)$$

with m the mass of the test cylinder, g the local acceleration of gravity, $2l$ the length of the coupling arm (with a difference $\Delta l > 0$ between its lower and upper half respectively) and K the coupling constant (note that, for lateral flexures, K is lower than the elastic constant of the laminar suspensions shown in Fig. 4 and Fig. 2 by a factor given by the ratio, squared, of the length of the laminar suspension itself to the length l of the arm—''lever effect''). In Eq. (1) the ratio $\Delta l/l$ accounts for both the balance of arms and masses ($\Delta m/m$) attached to the beam. The validity of Eq. (1) is confirmed by numerical simulations and measurements, and shows well the relevance of gravity. If $\Delta l > 0$, gravity acts as a positive spring, thus increasing the stiffness of the coupling, i.e. reducing the length of $T_{\rm diff}$. Instead, if $\Delta l < 0$, gravity acts as a negative spring and the ratio $\Delta l/l$ (indeed, $\Delta l/l$ and/or $\Delta m/m$) can be adjusted so as to reduce the denominator of Eq. (1) whereby increasing the value of $T_{\rm diff}$. We have verified this, obtaining differential periods of up to about 90 s, although so far the accelerometer has been operated with differential periods around 10 s.

Natural differential oscillations in the X and Y directions as detected by the capacitance read-out are shown in Fig. 7 (zero spin rate, differential periods of 11 s). When the rotor spins at 3 Hz the differential displacements between the test cylinders measured by the (rotating) capacitance bridges show the same natural periods, in addition to the expected rotation frequency (see Fig. 8). At zero spin the decreasing amplitude of oscillations allows the quality factor Q of the system to be measured, yielding an average value of 510. The dominant losses are due to the laminar suspensions of the rotor as deformed at the low natural differential frequencies, and for large oscillation amplitudes (up to 1 mm). Q measurements for the laminar suspensions alone—before assembling of the accelerometer—when set in horizontal oscillations at higher frequency (5 Hz) and similar oscillation amplitudes, have been performed (in vacuum), yielding Q values of 2000 (''GALILEO GALILEI'' (GG), Phase A Report, 1998, Section 3.4; Nobili et al., 2000). Better (higher) Q values are expected at higher frequencies and for smaller oscillation amplitudes. However, once rotating, the suspensions are deformed at the frequency of spin and losses occur at this frequency, which is higher than the differential frequency, and should therefore result in higher Q's (see Section 5).

Besides the natural frequency for differential oscillations the accelerometer system of Fig. 2 has two additional natural frequencies, one slightly below and one slightly above 1 Hz. The first can be viewed as the pendular frequency (common mode) of the whole system; the second one as due to the inner test cylinder being suspended close to its center of mass and having a non-zero moment of inertia with respect to the symmetry axis (if the inner mass is modeled as a point mass this frequency disappears). The predicted theoretical values of these natural frequencies have been confirmed by experimental measurements. In order to reach the spin rates of interest (above 1 Hz), the system must cross all these natural frequencies, and when passing the two nearby ones it can undergo large resonant disturbances. It has been suggested (Luo, 2000) that the system be simplified by substituting the laminar suspension of the inner test cylinder (the bottom one of the three sketched in Fig. 2; see also Fig. 4) with a solid brass cylinder of the same external dimensions. By simple readjustments of arms and masses we have set up the system for routine measurements with the natural period for differential oscillations close to 8 s and the pendular frequency slightly below 1 Hz. These two values were predicted theoretically and confirmed by measurements. Q measurements at variable residual pressure in the vacuum chamber are reported in Section 5. It is worth noting that in this arrangement the relevant whirl frequency of the test cylinders is split into two: a forward one, increasing with the spin rate, instead of remaining constant (as shown in Figs. 7 and 8) and a backward one. The reason is the following. A

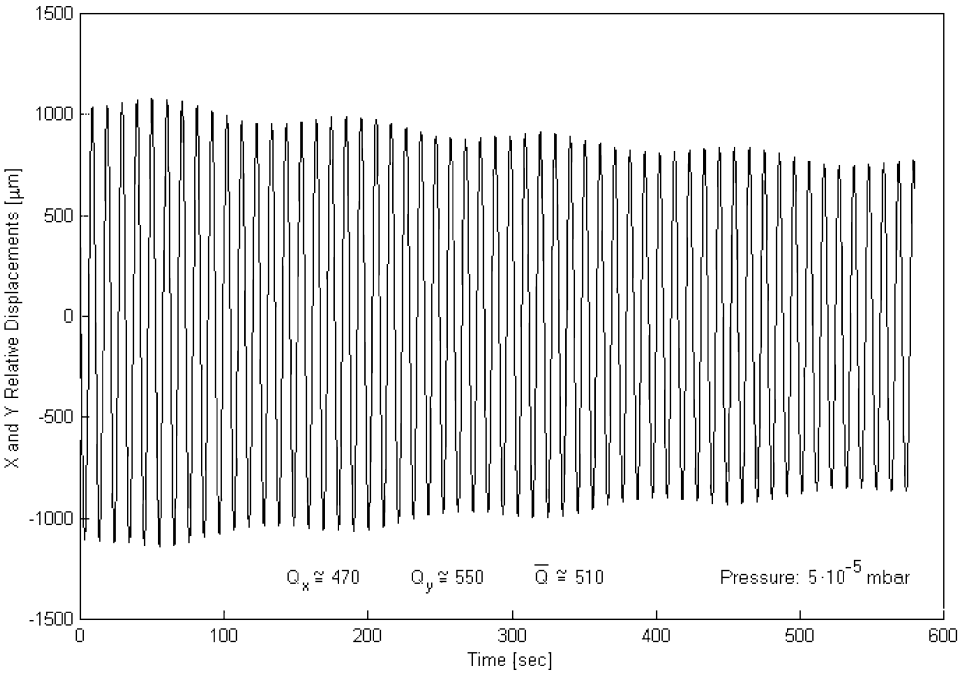

Fig. 7. Relative displacements, in the *X* and *Y* directions of the sensitivity plane, between the centers of mass of the test cylinders at zero spin rate. The natural periods of differential oscillations at 11 s are apparent. The amplitudes of these oscillations are slowly decreasing with time, yielding a quality factor of about 510 (taken from Nobili et al., 2000).

differential force acting between the test cylinders in their vertical beam balance arrangement causes a relative displacement of their centers of mass by inclining the coupling arm of the balance pivoted at its midpoint. In this case, if weakly suspended one at each end of the arm, the test cylinders keep spinning around their axes. However, if the inner test cylinder is rigidly connected to the end of the arm, the inclination of the arm forces it to spin along the arm itself, describing a whirl cone, while the angular momentum of the body would tend to conserve its vertical direction. The result is a stiffer or softer suspension of the inner test cylinder, depending on the sense of rotation and—since the two are coupled—also a period of their whirl motions shorter or longer than that of the natural oscillations, depending on whether whirl motion is in the same sense as the rotation or in the opposite one (see Section 5). The whirl period relevant to the sensitivity of the accelerometer is the shorter one, corresponding to a stiffer coupling.

Spinning bodies are subject to gyroscopic effects, whereby they move not in the direction of the applied force but along the component of the external torque perpendicular to the spin axis. In a ground laboratory the gyroscopic effect for a body of mass *m*, angular momentum $\vec{L}$ and center of mass suspended with an arm $\vec{l}$ is due to the torque generated by the local gravity and to the angular velocity $\vec{\omega}_{\oplus}$ of the Earth's diurnal rotation around its axis:

$$\left(\frac{\mathrm{d}\vec{L}}{\mathrm{d}t}\right)_{\mathrm{lab}} = \left(\vec{\Omega}_g - \vec{\omega}_{\oplus}\right) \times \vec{L}$$

$$\left(\Omega_g = -\frac{mgl}{L},\ \vec{l} \times m\vec{g} = \vec{\Omega}_g \times \vec{L}\right) \qquad (2)$$

Gravity makes the body precess around the local vertical (unless the center of mass lies exactly on the vertical itself), while the non-inertial nature of the laboratory reference frame (because of its diurnal rotation with the Earth) makes it precess around the Earth's rotation vector; the suspensions produce a restoring force towards the vertical. Equilibrium is reached in the North–South direction, the only direction along which the acting torques can balance

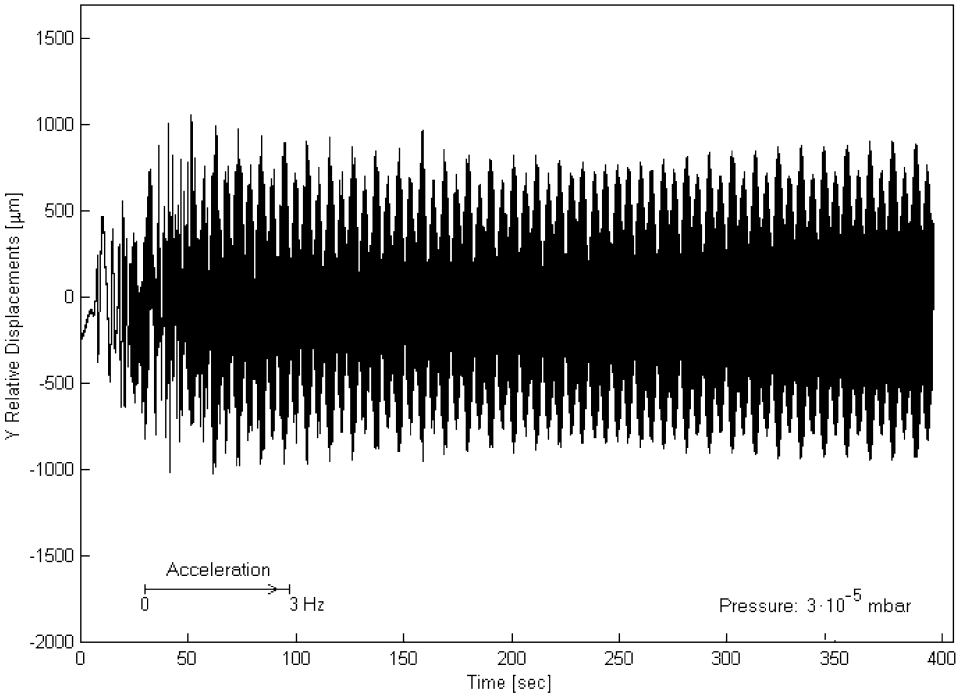

Fig. 8. Relative displacements (for the *Y* direction only, in the rotating reference frame) obtained with the same instrument as in Fig. 7 but having brought it to a rotation rate of 3 Hz. The natural differential oscillation at about 11 s period (the same as at zero spin) is apparent, as it is the faster rotation frequency of the system at 3 Hz.

each other. The test cylinders of Fig. 2 undergo different gyroscopic effects, resulting in a net relative displacement in the North–South direction. Its calculation shows a constant displacement at any given spin rate, and a linear increase with it, reaching several μm at a few Hz; if the laminar suspension of the inner test cylinder is substituted by a rigid connection the differential gyroscopic effect increases by about a factor of 10 (see measurements of gyroscopic effect in Section 5). In both cases it is in the same direction as the effect of an EP violation in the gravitational field of the Earth, and much larger. Instead, a relative displacement due to an EP violation in the field of the Sun would show up as an additional vector following the daily motion of the Sun (the gyroscopic constant displacement can be subtracted away during data analysis or compensated by properly changing the verticality of the suspension shaft in the North–South direction).

For this reason the rotating differential accelerometer of Figs. 2 and 3 can be used as a prototype test instrument of the one proposed for space and for testing the equivalence principle in the field of the Sun, but cannot be used for testing the equivalence principle in the field of the Earth. It is worth stressing that the gyroscopic effect would not affect the space instrument (''GALILEO GALILEI'' (GG), Phase A Report, 1998, Section 2.1.2). Unlike what happens in a ground laboratory, the angular momentum vector of the rotor is almost fixed in space, undergoing only a slow precession (around the orbit normal) due to the fact that the spin axis is not exactly normal to the orbit plane and the moment of inertia with respect to the spin axis is the dominant one (''GALILEO GALILEI'' (GG), Phase A Report, 1998, Eq. (2.11)) (the effect is similar to the luni-solar precession of the Earth's axis around the normal to the ecliptic). The system is symmetrical and the test cylinders are suspended from their center of mass and symmetrically with respect to it (see Fig. 6). The resulting gyroscopic effects are found to be totally negligible (''GALILEO GALILEI'' (GG), Phase A Report, 1998, Section 2.1.2; Comandi, 1999, Section 3.17).

3. Adjustments and settings of the apparatus

Various adjustments can be performed for the rotating differential accelerometer to operate as it is designed to. An inclination of the (rotating) coupling arm, about its midpoint, by a non-zero (constant) angle from the vertical, gives rise to a constant relative displacement of the test cylinders fixed in the rotating frame. It is therefore detected by the (rotating) read-out as a constant offset from zero (in X and Y), which provides the driving signal for this adjustment. In order to reduce this offset the position of the top suspension (the one of the outer test cylinder; see Fig. 2) can be adjusted so as to be as much as possible in line with the other two suspensions at the center and the bottom. This is the coarsest adjustment. Then, on the coupling arm, close to (just below) the central suspension, are mounted two small masses (5 g each) that can be displaced across the arm's axis in the X and Y directions in order to reduce the corresponding offsets, and therefore the inclination of the arm. For yet a finer adjustment there are two additional smaller masses (0.5 g each), also movable in X and Y.

However, a constant offset in the X and Y measurements of the relative displacements between the centers of mass of the test cylinders as performed by the rotating capacitance bridges may also be due to the bridge capacitances being out of balance at zero mechanical displacement; which would require the variable capacitances in each bridge to be adjusted, and no change in the inclination of the coupling arm. In order to separate the two effects, and operate the right adjustment, we perform these measurements by spinning the rotor at a frequency first below and then above the natural one for differential oscillations of the test cylinders. If the offsets are due to the inclination of the coupling arm, i.e. to the test cylinders not being suspended along the same axis, it is known that that they should decrease when spinning above the natural frequency (see e.g. Den Hartog, 1985; Crandall, 1995; Genta, 1993). Once a non-zero inclination of the coupling arm has been ruled out, we can proceed to reduce the offsets of the measurements by adjusting the variable capacitances. A few iterations of this procedure may be necessary.

Around the lower half of the coupling arm is mounted a small solid ring (see section in Fig. 2), movable in the vertical direction. A change in its vertical position, by changing the mass distribution of the beam balance, will change the natural period of the differential oscillations (see discussion on Eq. (1)). Being symmetrical around the arm, the position of the ring does not affect its inclination. From an operational viewpoint, this is the easiest way to change and adjust the differential period of the test cylinders.

In the conceptual design of the differential accelerometer it is very important that the suspension shaft (the tube enclosing the coupling arm, held by a shaft turning inside ball bearings, to which rotation from the motor is transmitted by means of O-rings on pulleys; see Fig. 2) be aligned with the local vertical. In the case of a non-zero inclination of the suspension tube from the local vertical—due to the shaft not being mounted perfectly vertical in the laboratory reference frame—there will be a non-zero lateral deformation of the central suspension which suspends the beam balance (see Fig. 2), and a consequent relative displacement of the test cylinders. The displacement is fixed in the laboratory (non-rotating) frame along the direction identified by the misalignment of the shaft and is modulated by the rotating capacitance bridges at their spin frequency. The X and Y bridge measurements are transformed into the X_{nr} and Y_{nr} relative displacements in the non-rotating frame (see Section 4) where the coordinates of the fixed displacement indicate the direction of the deflection of the suspension shaft. They provide the driving signal for this adjustment, which is performed by means of three vertical micrometric screws (at 120° from one another) which control the inclination of the top plane of the frame around the shaft (see Fig. 3), hence also its verticality. The micrometric screws are differential and allow both coarse and fine adjustments. A still finer adjustment of the verticality of the suspension shaft is performed by means of three (vertical) piezoelectric actuators (PTZs, also at 120° from one another) perpendicular to the horizontal plane at the top of the rotor, on which it rests. They allow finer adjustments of the verticality of the shaft than micrometric screws can do, and moreover they can be remotely controlled from outside the vacuum chamber. In addition, if the central suspension which carries the weight of the whole system is not

centered on the rotation axis, the centrifugal force will compress the same PZTs at the frequency of spin. Their three signals are acquired by means of a National Instruments card and allow us to adjust the position of the central suspension on the rotation axis by means of three micrometric screws mounted horizontally around it, so as to reduce the PZTs signals as much as possible.

As the systems spins the suspensions are deformed at the spin frequency and the relevant loss factors (inverse of quality factor Q) are those of the mechanical suspensions at the spin frequency. The effects of such dissipation are unstable forward whirl motions whose frequencies are close to the natural frequencies of the system. The destabilizing forces which generate the whirl motions are equal to the passive spring forces divided by the Q. The magnitude of the forces is the same in the stationary and in the rotating frame; only their frequencies change. The forces required to achieve neutral equilibrium are equal and opposite to the destabilizing forces. They never exceed the passive spring forces as long as Q is larger than 1. For large Qs the destabilizing forces, as well as the active ones required for stabilization, are much smaller than the passive spring forces. This also means that the instabilities to be damped grow very slowly. The negative Q which determines the growth of the whirl motions is equal (with the opposite sign) to the Q of the suspensions at the frequency of spin (Genta, 1993; Crandall and Nobili, 1997; Nobili et al., 1999).

In the rotating accelerometer of Fig. 2 whirl motions can be stabilized either passively (by providing sufficient non-rotating damping) or actively, by means of small capacitance sensors/actuators which must be controlled to counteract the destabilizing forces which generate the whirl motions. In the GG space experiment, where there are no non-rotating parts (no motor is needed once the spacecraft is set in rotation at the nominal spin rate) whirl motions can only be actively controlled (Nobili et al., 1999; ''GALILEO GALILEI'' (GG), Phase A Report, 1998, Chapter 6). In the differential accelerometer of Fig. 2 a passive, non-rotating damper, made of a very light disk with little radial blades immersed in oil for vacuum, is mounted on the inner test cylinder, below its suspension from the coupling arm (it is shown in yellow and gray in Fig. 2, but only its base is visible in Fig. 3). It stabilizes the whirl motion at the natural differential frequency of the test cylinders, as measurements show (see Section 5). The passive damper is also equipped with a mechanism mounted in the vacuum chamber outside the accelerometer itself (it is clearly visible in Fig. 3 in front of the accelerometer) that can be activated from outside the chamber in order to run the system with or without damping of whirl motion and to measure (when off) the whirl growth rate, which provides the Q of the system at the spin frequency (Section 5). We can also use this on/off mechanism during testing of the active damper. The active damper (not shown in Figs. 2 and 3) is made by eight small capacitance plates facing the outer test cylinder (one layer of four sensors and one of four actuators, the two pairs of sensors forming the two halves of two capacitance bridges in the two coordinates of the horizontal plane). The electronics of these bridges is essentially the same as that of the bridges of the main sensors (Section 4, Fig. 9) except for the fact that here smaller capacitances and less good sensitivity are needed. The signals from these two bridges drive the four (high) voltages for the four actuators.

4. Read-out and data acquisition

The relative mechanical displacements of the test cylinders in the X and Y directions of the plane perpendicular to the spin axis are read by two capacitance bridges, rotating with the system, whose four sensing plates (Fig. 5) are located in between the test cylinders with a clear gap of 5 mm on either side. The electronic circuit of each bridge is sketched in Fig. 9. The smallest fractional capacitance unbalance that the circuit was sensitive to in bench tests corresponds to mechanical displacements of 5 picometer in 1 s of integration time (''GALILEO GALILEI'' (GG), Phase A Report, 1998, Section 2.1.3). A voltage signal of high frequency is applied to the bridge in order to shift the signal of interest to a high frequency band with reduced $1/f$ noise. Since the capacitance bridges rotate with the accelerometer, power and data transfer must be ensured between the rotating and the non-rotating frame. For power

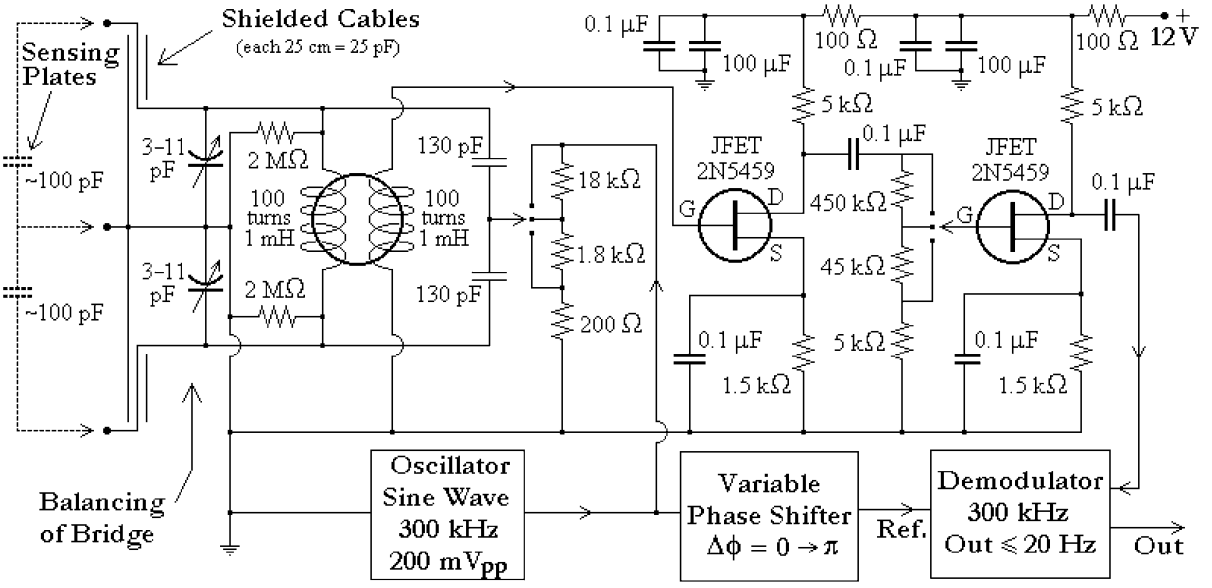

Fig. 9. The capacitance bridge sensor circuits used in the accelerometer of Figs. 2 and 3 for the read-out of the relative displacements of the test cylinders.

transfer we use rotating contacts. The high frequency bridge measurements are first demodulated and then converted from analog to digital to be optically transferred outside the vacuum chamber. The (rotating) electronics which is needed to perform these tasks, as well as the electronics of the bridges, is located on an annular dish mounted around the suspension tube (Figs. 2 and 3).

In order to be able to transform the relative displacements as measured by the bridges in the rotating frame of the rotor to the non-spinning reference frame of the laboratory, we need to know, in correspondence of each data point, also the phase angle of the rotor. For this purpose a simple optical device has been mounted at the top of the rotor which provides a reference signal with the rotor phase information. A microprocessor outside the chamber takes care of combining the reference signal with the X and Y measurements and of providing the resulting combined data in RS232 data format for computer acquisition (through a serial port) as a binary file which is then transformed into a text file for data analysis. The reference signal is also acquired, independently of the capacitance bridges data, by another computer (through a National Instruments card) for independent checks of the spin rate of the system and for various other tests to ensure that the data combination procedure has been performed correctly.

The capacitance bridges are calibrated by displacing the outer test cylinder with respect to the inner one by a known amount (by means of a micrometric screw mounted on the frame for this purpose only; not shown in Fig. 3) and recording the voltage signal read by the capacitance sensors. Displacements are applied in both X and Y directions and linearity checks of the calibration curve are performed in both cases.

The electric zero of the capacitance bridges is first set at its nominal value, by setting the value of the variable capacitance of the circuit (Fig. 9). More accurate checks are performed with the system in rotation, first below and then above the natural frequency of differential oscillations of the test cylinders, as discussed in Section 4.

Mechanical balancing should be achieved to ensure that the capacitance plates of the bridges be located halfway in between the outer surface of the inner test cylinder and the inner surface of the outer one, a configuration which provides the best sen-

sitivity to differential displacements. The capacitance plates shown in Fig. 5 (two for each one of the two bridges in the X and Y directions), are rigidly connected (via an insulating frame) to the suspension tube (see Fig. 2). The linear dimensions of the frame are dictated by the linear dimensions of the test cylinders (outer radius of inner cylinder and inner radius of the outer one), which are chosen on the basis of the desired gap between the two. Since all parts are precisely manufactured according to the design (their dimensions are checked a posteriori to less than 1 μm with a 3D measuring machine equipped with a contact point sensor) it is possible to design and manufacture the insulating frames of the plates (see Fig. 5) so that they provide a configuration as close as possible to the nominal one corresponding to perfect mechanical balancing. This procedure has provided considerable improvement with respect to a previous set up in which all parts of the frame were manufactured, mounted and adjusted independently.

5. Results from measurement data

In this Section we report the results obtained during several months of operation of the rotating differential accelerometer as outlined above, with only two relevant natural frequencies. The results concern the quality factor of the system (at the natural differential frequency and at the spin frequency), the differential gyroscopic effect, the growth rate of whirl motion and the stability in time of the differential displacement vector between the test cylinders.

Fig. 10 shows the differential oscillations of the test cylinders in the X and Y directions (at about 8 s; zero spin rate). The slow decay in the oscillation amplitudes yields a Q value of 1590. This value has been obtained in vacuum with a residual air pressure of $2 \cdot 10^{-5}$ mbar.

By performing Q measurements at different pressures it was possible to establish that residual air in between the test cylinders gives rise to dissipation. Losses due to air friction linearly decrease with pressure until they remain constant and no longer depend on the decreasing pressure (below a few 10^{-5} mbar). Fig. 11 shows well this phenomenon and indicates that, as long as the system is operated at sufficiently low pressure, losses depend on the laminar suspensions only. Note that $Q = 1590$, as from Fig. 10 for oscillations at $\simeq 8$ s, is about three times better than the Q value previously obtained (at 11 s; see Fig. 7).

It is very important to check that gyroscopic effects are as theoretically expected. For this reason numerous measurements have been performed, at various spin frequencies both in clockwise and counterclockwise rotation. Relative gyroscopic displacements of the test cylinders are expected in the North–South direction of the horizontal plane of the laboratory (towards South for counterclockwise rotation, towards North for clockwise rotation), and the amount of the displacement should increase linearly with the spin rate. Measurements reported in Fig. 12 (with a fit to a straight line) show agreement with the theoretical predictions. Each data point in the plot has been obtained from the raw data of the capacitance bridges (in the rotating reference frame) acquired as discussed in Section 4, by coordinate transformation to the non-spinning laboratory frame (see Section 4) and after averaging out of short periodic variations.

The fit is good, but the amount of the displacement is higher than originally expected. The disagreement is explained once the effect is calculated taking into account that the laminar suspension of the inner test cylinder (at the bottom end of the coupling arm) had been replaced by a solid brass cylinder connecting it to the lower half of the coupling arm, suspended from the central laminar suspension. At any given spin rate the relative gyroscopic displacement of the test cylinders, plus any original deviation of the suspension shaft from the local vertical, produce a relative displacement vector fixed in the non-spinning reference frame of the laboratory. Any smaller, slowly changing differential effect must be detected as an additional relative vector moving around this fixed displacement. The smaller the deviation from a fixed displacement, the more sensitive is the accelerometer to low frequency differential effects (such as the one due to an EP violation in the field of the Sun, with a 24-h period). The fixed displacement can be subtracted away during data analysis; however, once the nominal spin rate has

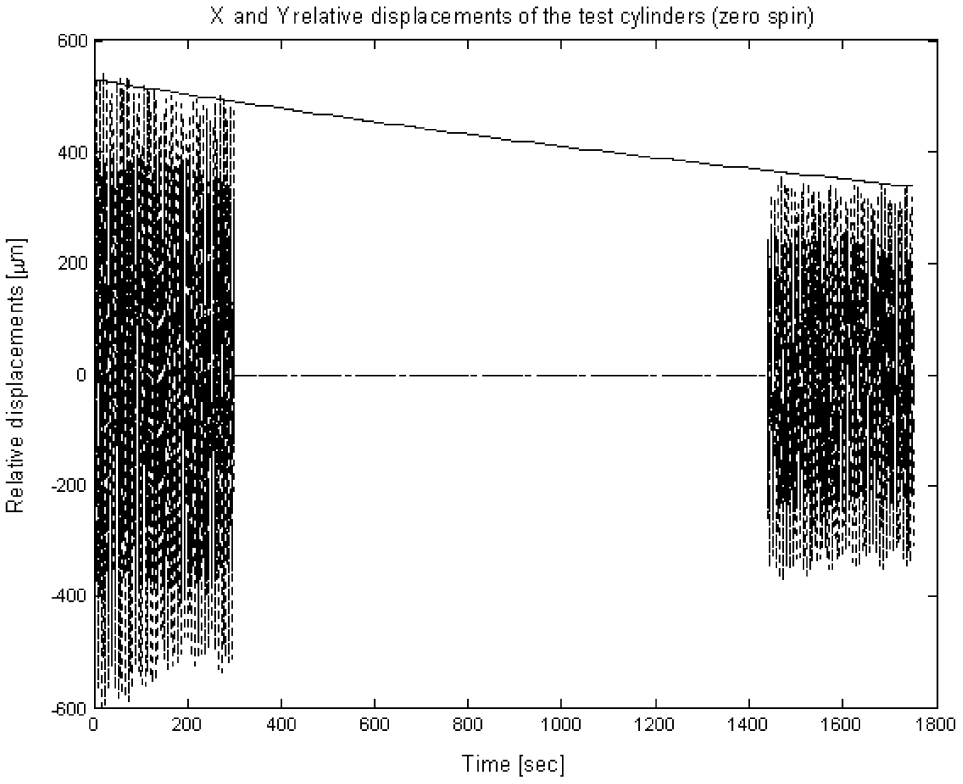

Fig. 10. Relative displacements, in the X and Y directions of the sensitivity plane, between the centers of mass of the test cylinders at zero spin rate. The natural periods of differential oscillations are of about 8 s. The amplitudes of these oscillations are slowly decreasing with time; data sets taken at subsequent times—under no changes in the system—yield a quality factor of about 1590. Residual air pressure during this measurement is of $2 \cdot 10^{-5}$ mbar.

been chosen, the verticality of the suspension shaft (in the laboratory frame) can be adjusted (as discussed in Section 3) so as to compensate for the gyroscopic effect at the working spin rate.

Although whirl motions at the natural frequencies can be damped, it is very important to know how rapidly they grow, i.e. how strong are the destabilizing forces (due to losses in the suspensions at the spin frequency) which need to be counteracted. It is apparent that, the slower is the growth rate of whirl motions, the easier it is to stabilize the system, the smaller are the perturbations caused by the required damping on the signal of interest (Nobili et al., 1999).

We have therefore performed long runs (up to several hours) with the accelerometer spinning at a few Hz and no damping applied (neither passive nor active). Pressure in the chamber was low enough to rule out any dissipation due to residual air (see Fig. 11) and data from the capacitance bridge sensors were taken continuously in order to monitor the growth of oscillation amplitudes (whirl motions at the natural frequencies in the laboratory frame show up as oscillations close to the spin frequency in the reading of the X and Y relative displacements of the test cylinders by the rotating capacitance bridges). We have runs of 3.5 h in which no appreciable growth in the oscillation amplitude could be detected. A shorter run is shown in Fig. 13 (at a spin rate of 2.5 Hz), in which the oscillation amplitude of an undamped whirl motion at 0.74 Hz shows a growth corresponding to a (negative) Q of 4900, which is therefore (with the positive sign) the quality factor of the system at the frequency of spin. We can compare it to a Q of about 2000 measured for the laminar suspension only (Fig. 4), by setting it in

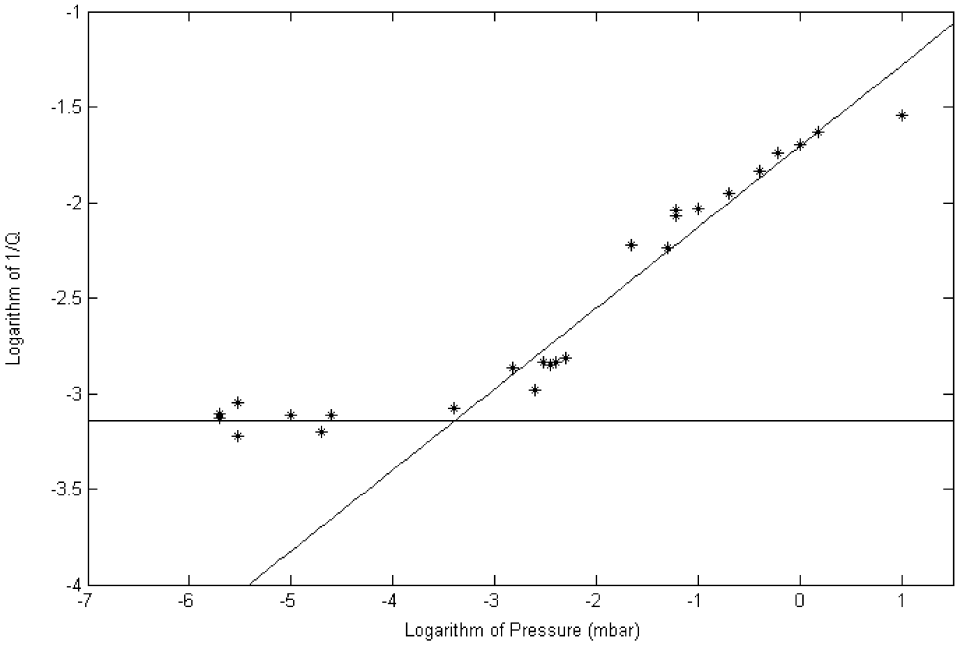

Fig. 11. Log–Log plot of the $1/Q$ value of the natural differential oscillations ($\simeq 8$ s period), at zero spin rate, as function of the residual air pressure in the chamber with linear best fits to the two sets of data, above and below 10^{-3} mbar. Each point refers to a separate run. For pressures greater than about 10^{-3} mbar the value of Q decreases as pressure increases. For lower pressures the value of Q reaches about 1590 and is then independent of pressure since it is the maximum value allowed by losses in the laminar suspensions.

oscillation at 5 Hz and monitoring the decay with time of the oscillation amplitude. The measurement was performed for horizontal oscillation only, for the measured Q not to be affected by local gravity; the amplitude of the oscillations was much larger (''GALILEO GALILEI'' (GG), Phase A Report, 1998, Section 3.4; Nobili et al., 2000).

The relevant physical quantity which remains to be measured is the stability in time of the relative position of the test cylinders in the horizontal plane of the laboratory, non-rotating, frame after short periodic effects have been filtered out. Fig. 14 gives an example. It shows, for a run at 2.5 Hz, the relative displacements of the test cylinders in the horizontal plane of the laboratory after coordinate transformation of the capacitance bridges measurements from the rotating reference frame to the non-rotating one. The curve gives the relative motion as time goes by, roughly represented with color: from blue at the beginning to green at the end of the run. The motion occurs away from the origin (zero relative displacement), around an equilibrium position vector (vector head plotted as a black dot) dominated by the gyroscopic effect (towards the South of the laboratory plane in this case because the accelerometer spins counterclockwise). This equilibrium vector is computed as the average of the vectors (whose heads are plotted as red dots), which are obtained from the average over the whirl period (3.5 s at 2.5 Hz spin frequency; the decrease from the value of the differential period observed at zero spin, shown in Fig. 10, is due to the inner test cylinder being rigidly connected to the bottom end of the coupling arm, as pointed out in Section 2). By performing a continuous run of measurements, with the accelerometer spinning at a given spin rate, we can compute, for various data sets of the same run, the coordinates of the black dot, and check its stability in time. The more stable it is, the better is the instrument sensitivity. The best result obtained so far is a stability of 1.5 μm in 1 h (at a spin rate of 2.5 Hz).

It is worth stressing that the large perturbations that give rise to these displacements are not unexpected: they are due to the motor, to the ball

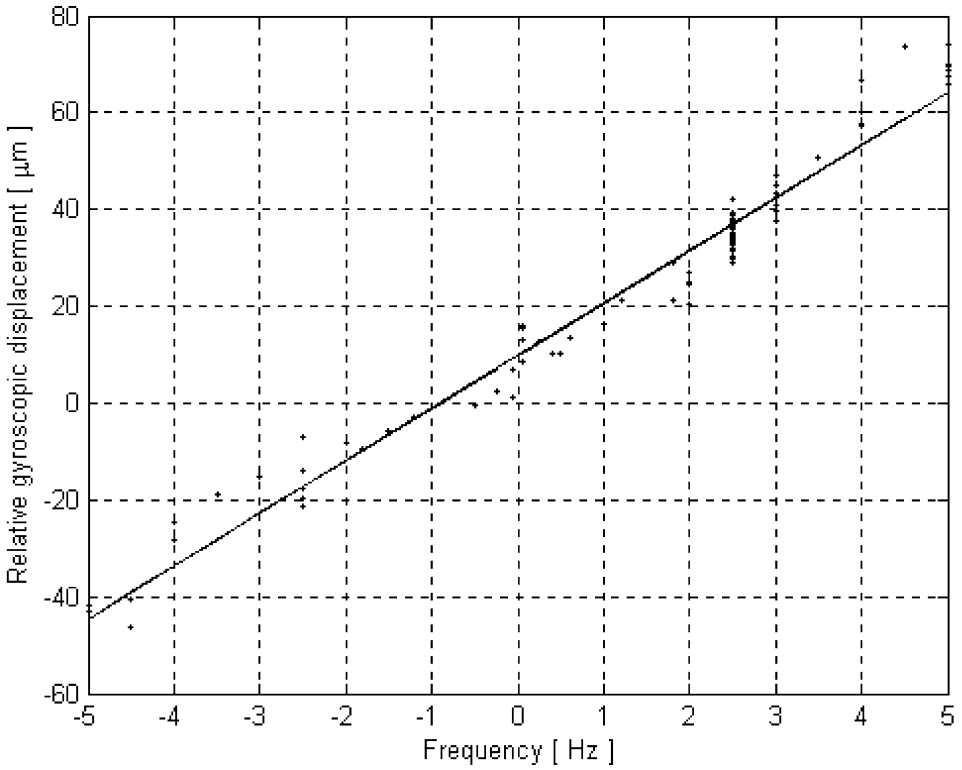

Fig. 12. Relative displacements (crosses) of the test cylinders, fixed in the horizontal plane of the laboratory, as function of the spin frequency and the sense of rotation, with linear fit to a straight line (on the frequency axis, counterclockwise spin frequencies are indicated as positive, clockwise ones as negative). The linear increase with the spin rate and the change of sign can be ascribed to the gyroscopic effect. The offset at zero spin is due to the inclination of the suspension shaft from the vertical.

bearings, to the non-perfect verticality of the system, all causes that will be absent in the space experiment. Firstly, because in the space experiment there is no motor (once the spacecraft has been brought to the desired rotation speed by small tangential jets, these jets can be completely turned off). Then, because there are no bearings, since the whole spacecraft rotates with all its parts at the same rotational speed. Then, because the direction of the rotation axis is not critical, since there is no 1-g force of gravity to withstand. Other perturbations, such as terrain tilts and microseisms, are by far more relevant for the ground prototype than it is residual vibration noise inside the spacecraft. The only perturbations on the ground that have a corresponding perturbation in space, in addition to thermal noise, are the slow whirling instabilities which, according to the measurements reported above, do not appear to be the limiting factor to the observed stability of the relative position of the test cylinders. There is therefore no physical reason to expect that the same perturbations, or other perturbations as large as these, will act on the planned space experiment.

6. Concluding remarks

We have built a rotating differential accelerometer, at room temperature, with fast spinning test cylinders (10 kg each) suspended like in a vertical beam balance so as to be weakly coupled in the horizontal plane. In spite of the need to sustain its weight, the coupled system is very sensitive to differential forces acting between the test cylinders in the horizontal plane; in addition, the read-out is made of capacitance bridges which read the relative displacements

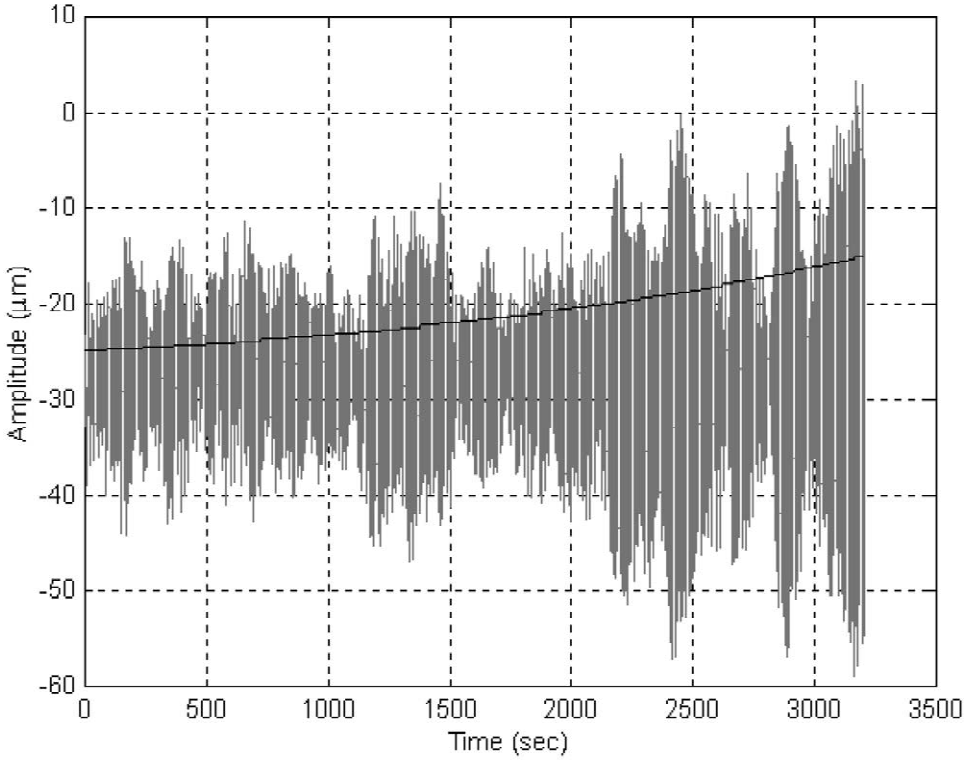

Fig. 13. Amplitude of the relative displacements between the test cylinders once transformed in the non-rotating plane of the laboratory (at a spin rate of 2.5 Hz). The growth in oscillation amplitude is due to an undamped whirl motion at 0.74 Hz. Its growth is represented by the exponential curve, and is due to losses in the system (at the spin frequency) corresponding to a Q value of 4900.

of the test cylinders directly (instead of deriving them as the difference of their individual displacements). This makes the accelerometer well suited for detecting tiny differential effects; by comparison, the proposed μSCOPE accelerometer (also at room temperature and based on capacitance sensors) is not inherently differential because each test cylinder has an independent suspension and sensing system (although both cylinders are controlled with respect to the same silica frame) (MICROSCOPE Website: http://www.cnes.fr/activites/activites/connaissance/physique/microsatellite/1sommaire_microsatellite.htm and http://www.onera.fr/dmph-en/accelerometre; Touboul et al., 2001, Fig. 1). The quality factor of the system has been measured at the spin frequency, as well as at the low frequency of differential oscillations (when at zero spin rate). The results are consistent with those obtained in previous measurements for losses in the mechanical suspensions alone (Nobili et al., 1999, 2000). Unstable whirl motions which are predicted because of such losses have been found to grow very slowly, according to the Q values, and therefore very small forces are needed to stabilize them (see Nobili et al., 1999 for the relevance of this issue). Gyroscopic effects have been measured and shown to be in agreement with their theoretical prediction. Finally, it is found that the stability of the present prototype is such that, at 2.5 Hz spin rate and 3.5 s period of whirl, the 10 kg mass test cylinders remain within 1.5 μm from each other for 1 h.

These results are relevant for the space variant of this instrument, proposed for the GG space mission, in several respects. Losses in the system and whirl motions are in agreement with predictions, giving us confidence in the theoretical analysis and numerical simulations of the GG dynamical system carried out

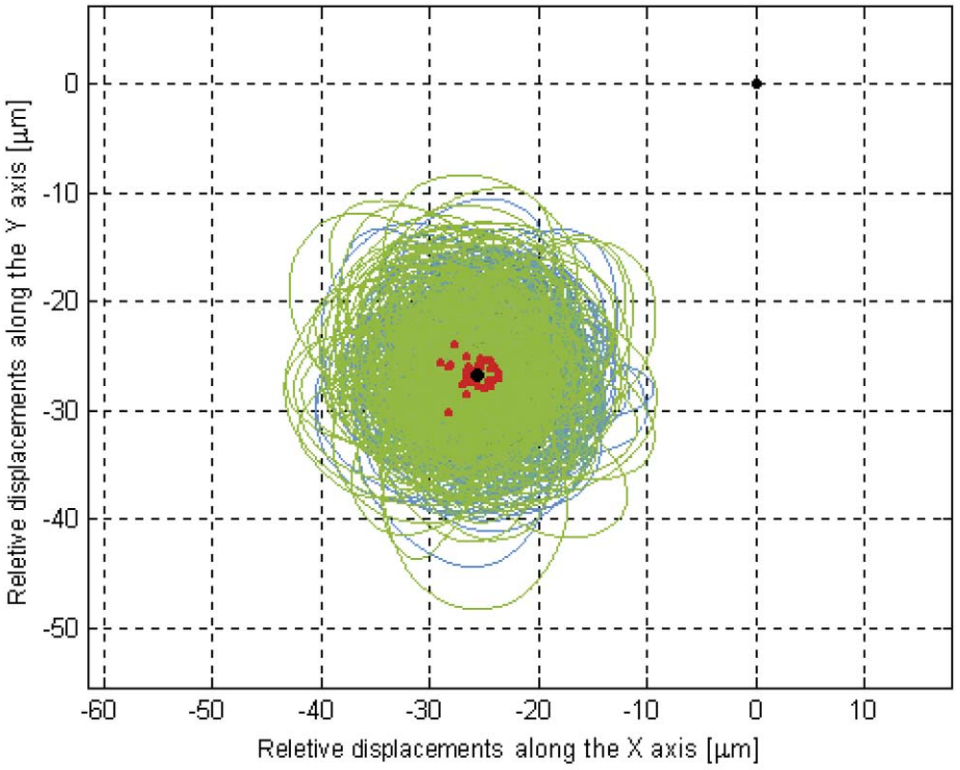

Fig. 14. Relative displacements of the test cylinders in the horizontal (non-rotating) plane of the laboratory with the accelerometer spinning at 2.5 Hz (counterclockwise). The position of relative equilibrium (the black dot at the middle of the figure) is displaced towards South (in this plot North is at 45°, i.e. in the $+X$, $+Y$ direction) because of the gyroscopic effect and short periodic relative motions occur around it. Average over the differential whirl period gives the red dots from whose average the black dot is obtained, thus defining the relative equilibrium vector for this data set (lasting 660 s) of a run lasting about 1 h.

so far (''GALILEO GALILEI'' (GG), Phase A Report, 1998, Chapter 6). The relevant quality factor, as measured with the accelerometer in full operation, is only a factor four smaller than the quality factor required in the GG error budget for its target sensitivity in EP testing of 10^{-17}: 4900 instead of the 20 000 value required (''GALILEO GALILEI'' (GG), Phase A Report, 1998, Section 2.2.7). (Note that we have measured $Q = 19\,000$ for a low stiffness CuBe suspension, suitable for use in space, when set in horizontal oscillation at 5 Hz (Nobili et al., 1999, 2000). The read-out (mechanical parts and electronics), data acquisition and data analysis (including the need for accurate coordinate transformation from the rotating to the non-rotating frame of reference) are of direct relevance to the space instrument and its operation. The stability observed in the relative position of the test cylinders can be compared with the GG requirement as follows. The spin rate is almost the same (the nominal spin rate of GG is 2 Hz), but the test cylinders in space can be coupled much more weakly than on the ground, thanks to the absence of weight. We have 3.5 s whirl period in our recent measurement runs and expect to be able to reach 540 s in space (as in the GG mission baseline at Phase A study level (''GALILEO GALILEI'' (GG), Phase A Report, 1998), the relative displacement of the test cylinders in response to differential forces being proportional to the square of the differential period (and inversely proportional to the stiffness of the suspensions). An EP violation signal would have a well defined signature (frequency and phase), in both the ground and the space experiment, so the relevant sensitivity of the instrument has to be assessed for this target signal. In space (Fig. 1) the signal is a relative displacement vector of fixed length pointing to the Earth and therefore changing direction with the orbital period

of the spacecraft. On the ground it is a fixed displacement in the North–South direction if the source mass under consideration is the Earth; it is a displacement vector whose length and direction change with the daily (and also annual) motion of the Sun if the Sun is the source mass. In all cases, the rotation of the instrument provides higher frequency modulation of the displacement vector. For GG to reach its target sensitivity, the relative displacement of the test cylinders in the satellite-to-Earth direction, modulated at the high frequency of spin and then transformed into a constant signal in the non-rotating reference frame, should not exceed $\Delta r_{GG} = 6.2 \cdot 10^{-11}$ cm (''GALILEO GALILEI'' (GG), Phase A Report, 1998, Section 2.1.1). Bench tests have demonstrated that the sensitivity of our read-out electronics is of $5 \cdot 10^{-10}$ cm in 1 s of integration time (''GALILEO GALILEI'' (GG), Phase A Report, 1998, Section 2.1.3), allowing us to detect the target displacement Δr_{GG} of the space experiment in about 100 s. So, the observed 1.5 μm separation between the centers of mass of the test cylinders is due to the ground perturbations mentioned at the end of the previous section, while the read-out electronics could detect much smaller displacements. The ground prototype, whose measurements of the relative displacements of the test cylinders are reported here, is stiffer than the one proposed for flight by a factor $\lambda = 24\,000$, and consequently it is 24 000 times less sensitive to differential displacements. In order to demonstrate the feasibility of the space experiment to that level of sensitivity it should have detected relative displacements between the centers of mass of the test cylinders of $\lambda \cdot \Delta r_{GG} = 1.5 \cdot 10^{-2}$ μm, while so far we have achieved only 1.5 μm. In order to gain this factor of 100, so as to perform a better demonstration, we need to reduce the effects of the ground perturbations by the same amount. The significance of the ground demonstration improves by reducing the stiffness of the accelerometer (hence the scaling factor λ), together with a corresponding reduction of the effects of the ground perturbations. An improved version of the prototype currently under construction is designed to reach a scaling factor $\lambda = 2400$ and a stability in the relative displacements of the test cylinders of $1.5 \cdot 10^{-3}$ μm. By comparison with the target of the GG space experiment in testing the equivalence principle: $\eta_{GG} = \Delta a/a = 10^{-17}$ ($a = 840$ cm s^{-2}, $\Delta a = 8.4 \cdot 10^{-15}$ cm s^{-2}) this corresponds to a full scale test at the level $\eta_{prototype} = \lambda^2 \eta_{GG} = 5.8 \cdot 10^{-11}$, because $\Delta a = \omega_{diff}^2 \cdot \Delta r_{GG}$, the differential natural frequency ω_{diff} being proportional to the coupling stiffness of the suspensions.

The local acceleration of gravity, because of the need for a stiff suspension in the vertical direction, forces a few asymmetries in the design of the ground accelerometer which are not there in the instrument designed for space (as it is apparent by comparing Fig. 2 and Fig. 6) and reduce the advantages of the instrument for EP testing on the ground. Nevertheless, rotation (especially if at high rate)—and the corresponding frequency modulation of the signal—is extremely important, as the successful experiments by the ''Eöt-Wash'' group have demonstrated, in EP testing (Adelberger et al., 1990; Su et al., 1994; Baeßler et al., 1999) as well as in the measurement of the universal constant of gravity (Gundlach and Merkovitz, 2000) and in testing the inverse square law at sub-mm distances (Hoyle et al., 2001). Our accelerometer shows that fast rotation can be achieved, that it can be achieved with large test masses (which is very important to reduce thermal noise), that it is compatible with small force gravitation measurements and—most importantly—that is suitable for use in space. The dynamics of the system is understood, it can be theoretically anticipated and checked by the measurements. Losses measured with the full system in operation (and with mechanical suspensions of quite a complex shape; see Fig. 4), yield a quality factor only four times smaller than the value that is required for the GG space experiment to reach its target. As for the fact that the prototype can only check for violation in the field of the Sun and not of the Earth (because of the gyroscopic effects discussed in Section 2), it is worth stressing that also the best ''Eöt-Wash'' results have been obtained in the field of the Sun (Baeßler et al., 1999), in spite of the slightly weaker signal and the need for long term measurements in this case. The reason is the difficulty—when searching for an effect in a fixed direction—to model the spurious effects of local mass anomalies (the small ones nearby and the very large ones far away) which obviously do not rotate with the instrument. A difficulty which is totally eliminated in space where the whole spacecraft co-rotates with the test masses.

In summary, we can convincingly argue that

theoretical understanding, numerical modeling and experimental measurements performed so far put on solid grounds the novel idea of a high accuracy space test of the equivalence principle (to one part in 10^{17}) with fast rotating weakly coupled test cylinders as proposed for the GG small mission. It has been shown (Nobili et al., 2001) that fast rotation and large mass of the test bodies are pivotal in making it possible to aim at such a high accuracy test in space with an experiment at room temperature. Among the proposed space experiments, GG is the only one in which the accelerometer devoted to EP testing and the one used for zero check (i.e., with test bodies made of the same material) are both centered at the center of mass of the spacecraft, so as to reduce common mode tidal effects and improve the reliability of the zero check. It is also the only one for which a full scale prototype of the accelerometer has been built and can be operated and tested on the ground.

Note added in proof

Recent work by Damour et al. (2002a,b) suggests that the universality of free fall (hence the equivalence principle) might be violated near $\eta = \Delta a/a \sim 10^{-12}$. The prediction refers to pairs of test masses made of Cu and Be or Pt and Ti. The present experimental limit for Cu and Be is $\eta(\mathrm{Be,Cu}) = (-1.9 \pm 2.5)\cdot 10^{-12}$ (Su et al., 1994). In Baeßler et al. (1999) the differential acceleration between test masses in the gravitational field of the Sun ($a_\odot \simeq 0.6$ cm s^{-2}) has a 1σ statistical uncertainty $\Delta a_\odot = 5.6 \cdot 10^{-13}$ cm s^{-2}, hence $\Delta a_\odot/a_\odot \sim 10^{-12}$. However, since this experiment compares accelerations of ''earth's core'' and ''moon/mantle'' like test bodies, the composition-dependent acceleration Δa_{CD} of the Earth and Moon towards the Sun is smaller than $\Delta a_\odot$ because only a fraction of their mass is contained in their cores and mantles. The authors conclude that $\Delta a_{\mathrm{CD}}/a_\odot = (+0.1 \pm 2.7 \pm 1.7)\cdot 10^{-13}$.

Acknowledgements

This work is funded by the Italian national space agency (ASI), the national Ministry of University, Research and Technology (MURST) and the University of Pisa. Special thanks are due to the Italian space Industry LABEN (Divisione Proel Tecnologie, Firenze) for making available to us their laboratories and infrastructures.

References

Adelberger, E.G. et al., 1990. PhRvD 42, 3267.
Baeßler, S. et al., 1999. PhRvL 83, 3585.
Braginsky, V.B., Panov, V.I., 1972. Sov. Phys. JEPT 34, 463.
Comandi, G., 1999. Laurea degree thesis in Physics (cum laude), University of Pisa available online http://eotvos.dm.unipi.it/nobili/theses/comandi
Crandall, S.H., 1995. Rotordynamics. In: Kliemann, W., Namachchivaya, N.S. (Eds.), Nonlinear Dynamics and Stochastic Mechanics. CRC Press, Boca Raton, FL, pp. 1–44.
Crandall, S.H., Nobili, A.M., 1997. On the Stabilization of the GG System available online http://tycho.dm.unipi.it/nobili/ggweb/crandall
Damour, T., Piazza, F., Veneziano, G., 2002a. PhRvL 89, 081601.
Damour, T., Piazza, F., Veneziano, G., 2002b. PhRvD 66, 046007.
Den Hartog, J.P., 1985. Mechanical Vibrations. Dover, New York, first published 1934.
Eötvös, R.V., Pekar, D., Fekete, E., 1922. Ann. Physik 16, 11.
''GALILEO GALILEI'' (GG), Phase A Report, ASI (Agenzia Spaziale Italiana) (1998), 2nd Edition (2000) (http://eotvos.dm.unipi.it/nobili/ggweb/phaseA).
''GALILEO GALILEI'' (GG) Website: http://eotvos.dm.unipi.it/nobili
Genta, G., 1993. Vibration of Structures and Machines. Springer, New York.
Gundlach, J.H., Merkovitz, S.M., 2000. PhRvL 85, 2869.
Hoyle, C.D. et al., 2001. PhRvL 86, 1418.
Luo, J., 2000. Private communication.
MICROSCOPE Website: http://www.cnes.fr/activites/programmes/microsatellite/1sommaire_microsatellite.htm and http://www.onera.fr/dmph-en/accelerometre
Nobili, A.M. et al., 1999. Class. Quantum Grav. 16, 1463.
Nobili, A.M. et al., 2000. NASA Document D-18925, 309 (http://eotvos.dm.unipi.it/nobili/nasa_fp)
Nobili, A.M. et al., 2001. PhRvD 63, 101101(R).
Roll, P.G., Krotkov, R., Dicke, R.H., 1964. Ann. Phys N.Y. 26, 442.
STEP Satellite Test of the Equivalence Principle, 1993. Report on the Phase A Study, ESA/NASA-SCI(93)4.
STEP Satellite Test of the Equivalence Principle, 1996. Report on the Phase A Study, ESA-SCI(96)5.
STEP Website: http://einstein.stanford.edu/STEP.
Su, Y. et al., 1994. PhRvD 50, 3614.
Touboul, P. et al., 2001. The Microscope mission, Acta Astronautica, in press.
Worden, Jr. P.W., 1978. Acta Astronautica 5, 27.

Proceedings of the XXXVIIIth Rencontres de Moriond "Gravitational Waves and Experimental Gravity",J. Dumarchez and J. Tran Thanh Van Eds., The Gioi Publishers, Vietnam pp. 371-376, 2003

THE FAST ROTATING "GGG" DIFFERENTIAL ACCELEROMETER FOR TESTING THE EQUIVALENCE PRINCIPLE: CURRENT STATE AND ANALYSIS OF SEISMIC DISTURBANCES

A.M. NOBILI†‡, D. BRAMANTI†, G. L. COMANDI†‡, R. TONCELLI†‡, E. POLACCO‡, M.L. CHIOFALO†‡,

† Space Mechanics Group, Department of Mathematics, University of Pisa, Via F. Buonarroti I-56127 Pisa, Italy
‡ INFN, Sezione di Pisa, Via F. Buonarroti, I-56127 Pisa, Italy

Measurements performed with the fast rotating "**G**alileo **G**alilei on the **G**round – **GGG**" differential accelerometer are reported. They show the validity of the main novel features of this instrument which was built as a full scale prototype for the proposed "Galileo Galilei-GG" space experiment aiming to test the equivalence principle to 10^{-17} at room temperature. GGG can also aim to test the equivalence principle to 10^{-13} in the lab. The effects of terrain tilts and local horizontal disturbances are analyzed showing how they can be reduced below the required level.

1 The GGG differential accelerometer: design and current sensitivity

A fast rotating differential accelerometer made of weakly coupled concentric and self centering test cylinders, has been designed to be flown inside the small "Galileo Galilei"-GG [1] satellite with the purpose of testing the equivalence principle to 1 part in 10^{17} at room temperature. The accelerometer is sensitive in 2 dimensions in the plane perpendicular to its spin/symmetry axis. Because of this feature, it has been possible to design a version of it ("**GG** on the **G**round"-**GGG** [2]) to be fully tested in the laboratory: if the spin/symmetry axis is used to suspend the accelerometer against local gravity, its plane of sensitivity lies in the horizontal plane where it could detect the signal of a possible violation of the equivalence principle (Fig. 1). Appropriate cardanic suspensions can withstand gravity along the vertical and also weakly couple the test cylinders in the horizontal plane. The coupling vertical beam is enclosed inside the rotation shaft by means of 3 cardanic suspensions: the central one to suspend the whole system, the top and down ones for the outer and inner test cylinder respectively (see Fig. 1). The relative displacements between the centers of mass of the test cylinders are detected by a differential capacitance read-out. The system spins at frequencies of a few Hz, higher than its natural frequencies. This allows the construction offset errors to be reduced during rotation (self-centering in supercritical regime). It also makes the suspension deformations (and consequent losses) take place at the spin frequency; since this is large, losses are much smaller than they would otherwise be. In Fig. 2 we report the measured values of the quality factor inverse of losses) at the natural frequencies of the system. The largest measured value is Q=95000 at 1.4 Hz.

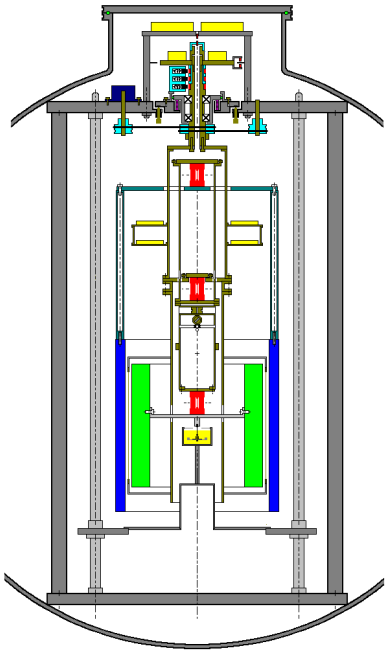

Figure 1: Schematic design of the GGG apparatus (section through the spin/symmetry axis of the system.) The concentric, coaxial test cylinders (green and blue) weigh 10 kg each. The enclosing vacuum chamber has 1 m diameter. Three cardanic suspensions (in red) are shown at the center, top and bottom of the arm which couples the test cylinders thus forming a balance with a vertical beam. So far the spin rate has been of a few Hz with a natural period of oscillation of the test cylinders relative to one another of 10 to 15 sec.

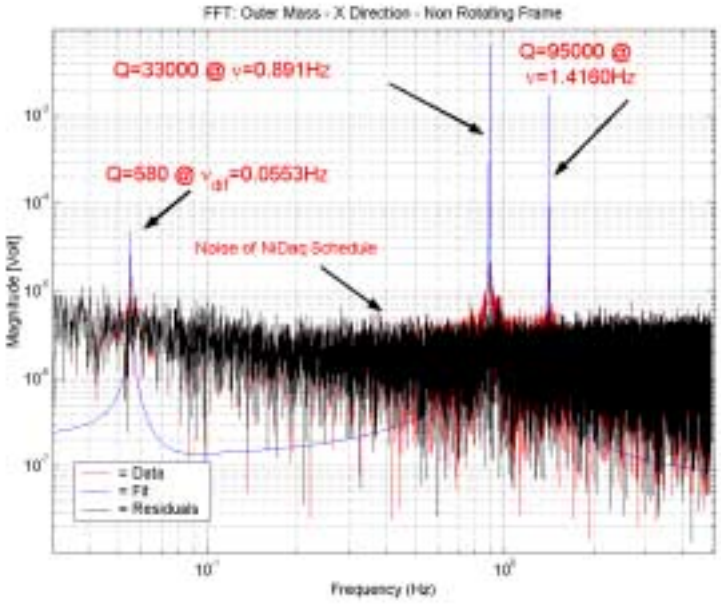

Figure 2: Resulting quality factors of the GGG system at the natural frequencies (at zero spin) obtained by measuring the oscillation decay of the system. The blue curve is the FFT of the fitted output data.

Once in supercritical rotation, the test cylinders show whirl motions at frequencies close to their natural frequencies (in the non rotating horizontal plane of the laboratory) and, primarily, a whirl motion relative to one another at the natural frequency of differential oscillations. The experimental results reported in Fig. 3 (after coordinate transformation to the non rotating reference system) show that whirl motion can be

identified and separated out, so that a low frequency, smaller differential signal can be detected (a violation signal in the field of the Sun would follow its daily motion). In Fig. 4 we show that low frequency residual noise is of about 1.5 μm.

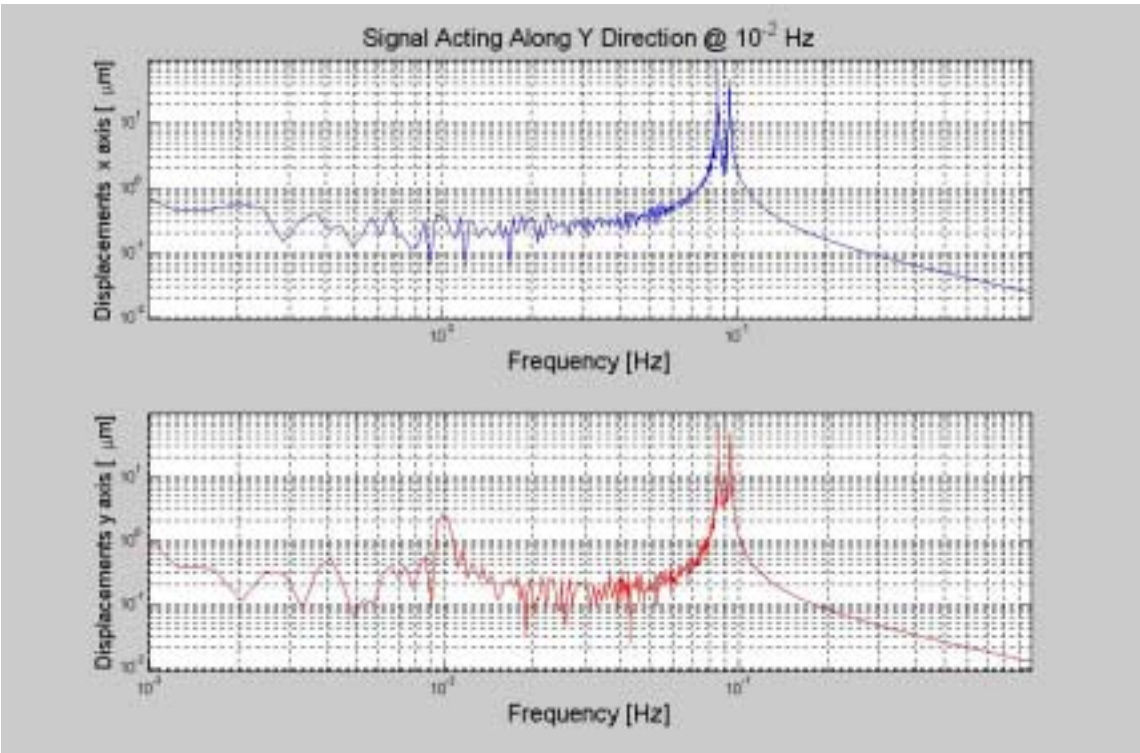

Figure 3: A signal applied in the *y* direction at 0.01 Hz is recovered from the output data though about 400 times smaller than the whirl (more than 100 μm) at about 0.1 Hz (system spinning at 2 Hz).

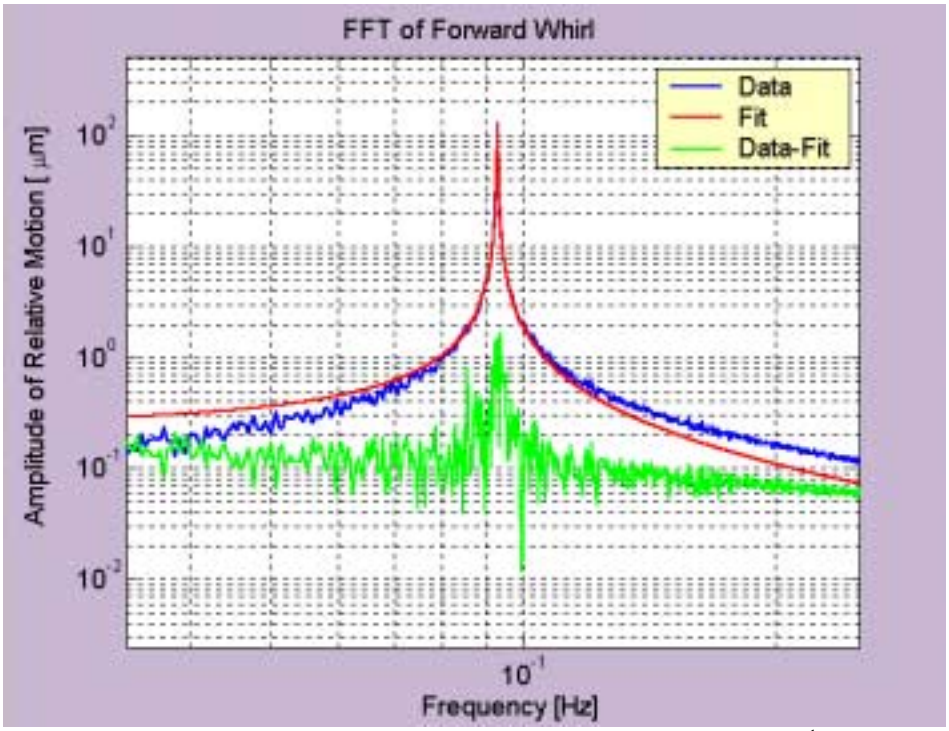

Figure 4: Measured and fitted whirl signal. Residual noise at lower frequencies is a few 10^{-1} μm (2 Hz spin).

In more recent measurements performed with an improved and more accurate control system, the amplitude of whirl motion has been reduced to 0.2 μm, down from 100 μm reported in Figs. 3 and 4. According to the current plan of the GGG experiment as recently funded by INFN, we expect to reach a low frequency stability of 10^{-10} m by the year 2005, corresponding to a sensitivity in testing the equivalence principle in the field of the Sun of 1 part in 10^9.

2 Relevance for a space test to 10^{-17}

A space version of such an instrument, to be used within the GG mission[1] in low Earth orbit, would take advantage of the stronger driving signal (8.4 ms^{-2} from the Earth at 520 km altitude in GG, instead of 0.006 ms^{-2} from the Sun in GGG). It would also allow much weaker suspensions due to absence of weight, and consequent higher sensitivity (which depends on the differential period squared) by a factor about 450. It can be argued that another factor of about 200 can be gained due to the absence of motor and motor/bearings noise, and thanks to the much higher symmetry of the space accelerometer (no 1-g preferential direction, hence much better rejection of common mode forces and consequent higher sensitivity to differential forces). Overall this amounts to about 8 orders of magnitude gain, thus making a 10^{-17} test in space a goal worth pursuing. In point of fact, the error budget of the GG space experiment, as developed within mission studies so far, has turned out to be compatible with this goal [1]. The improvement over current best ground results [3,4] would be of 5 orders of magnitude.

3 Seismic noise attenuation for a ground test to 10^{-13}

Very recently, predictions of violation have been reported [5] at levels close to the current best results, so that even a slight improvement on those experiments on the ground (i..e. to reach the 10^{-13} level) would be significant. The GGG rotating differential accelerometer can be used to test the Equivalence Principle in the gravitational field of the Sun to 1 part in 10^{13}. In GGG this goal requires to detect low frequency (24-hr) relative displacements of the test cylinders of 10^{-13} m, which in turn requires to reduce daily seismic disturbances below this level.

If the terrain where the apparatus is located undergoes low frequency tilts of amplitude α we need to evaluate the effects of such tilts on the experiment and reduce them if necessary. In the presence of a laminar cardanic suspension providing a stiffness k in the horizontal plane the tilt angle β at equilibrium is determined by the condition that the restoring force of the suspension equals the horizontal component of the local acceleration of gravity arising because of the tilt. The equilibrium equation is:

$$mg\beta \simeq k\ell(\alpha - \beta) \quad (\sin\alpha \simeq \alpha\,,\ \sin\beta \simeq \beta) \tag{1}$$

from which the ratio β/α is derived by which the original tilt angle α is reduced because of the suspension:

$$\frac{\beta}{\alpha} \simeq \frac{k\ell}{mg}\left(1+\frac{k\ell}{mg}\right)^{-1} \tag{2}$$

If $k\ell/mg \ll 1$ so that terms of order $(k\ell/mg)^2$ or higher can be neglected, we get that tilts are reduced by the factor:

$$\frac{\beta}{\alpha} \simeq \frac{k\ell}{mg} \ll 1 \tag{3}$$

In terms of the acceleration acting on the mass *m*, in absence of the cardanic suspension, the tilt angle is α and the mass is subject to the *gravitational* acceleration $g\alpha$ in the horizontal plane. With the suspension and the tilt angle β the corresponding acceleration is $g\beta$ (in point of fact, there is also a vertical component, but it is negligible for small tilts). Therefore, the acceleration on the test mass too is reduced, in the presence of the suspension, by the same ratio β/α given by Eq. 3 as the tilt angle.

Let us now consider the case in which, instead of being subject to a terrain tilt, the system is subject to a horizontal disturbing acceleration with the same (low) frequency as the tilt, and amplitude $a = \alpha g$. As a result, the test mass is subject to an *inertial* acceleration equal and opposite to the disturbing one, which defines the direction of a new local vertical as the vectorial sum $\vec{g} - \vec{a}$ forming an angle $\alpha = a/g$ with the original vertical (defined by the direction of local gravity in absence of the disturbing acceleration). In the presence of a suspension providing a stiffness *k* in the horizontal plane, equilibrium is reached at a different angle γ with the original vertical, where the acceleration $g\gamma - a$ acting on the test mass ($\sin\gamma \simeq \gamma$, $\cos\gamma \simeq 1$) is balanced by the restoring force of the suspension according to the equation:

$$mg\gamma - ma \simeq -k\ell\gamma \tag{4}$$

The equilibrium angle with the suspension is therefore:

$$\gamma \simeq \frac{a}{g}\left(1+\frac{k\ell}{mg}\right)^{-1} \simeq \frac{a}{g}\left(1-\frac{k\ell}{mg}\right) \tag{5}$$

And the deviation from the *new* local vertical is

$$\beta \simeq \frac{a}{g}\cdot\frac{k\ell}{mg} = \alpha\cdot\frac{k\ell}{mg} \tag{6}$$

The effect of a suspension with horizontal stiffness *k* is therefore to make the test mass tilt from the *new* local vertical only by the same small angle β as in the case of a terrain tilt by the angle $\alpha = a/g$ (in the same approximation in which terms of the order of $(k\ell/mg)^2$ or higher are neglected). In terms of the acceleration acting on the test mass (in the horizontal, sensitivity plane), this is $g\gamma - a$ which, in the presence of the suspension, amounts to $a(k\ell/mg)$. This means a reduction, with respect to the local disturbing acceleration a acting at the top of the system, by the ratio $k\ell/mg \ll 1$, just as in the case of the terrain tilts. Therefore, because of the equivalence between inertial and gravitational mass which at this level can be assumed to be valid, local terrain tilts cannot be distinguished from horizontal disturbing accelerations. Since in GGG the signal is a relative displacement of the test cylinders around the local vertical, as its direction changes because of horizontal seismic accelerations the beam of the balance will follow it, but these absolute displacements are not relevant for the GGG measurements while those relative to it are reduced by the suspension just like tilts.

Low frequency tilts in the vicinity of the GGG apparatus have been monitored with the ISA tiltmeter/accelerometer. Daily effects turn out to have an amplitude of about 10^{-6} rad (corresponding to horizontal accelerations of about 10^{-6} g). The resulting effect on the GGG test cylinders is to give rise to relative displacements (in the horizontal plane of the laboratory) at the same frequency and with an amplitude of about $4\cdot10^{-7}$ m (the suspension arm relevant for the relative displacements of the test cylinders being about 0.4 m long). The goal of testing the Equivalence Principle to 10^{-13} with GGG requires to detect low frequency (24-hr) relative displacements of the test cylinders of 10^{-13} m, which in turn requires daily seismic disturbances to be reduced below this level. This can be done partly actively and partly passively. Active reduction is done using as sensor a tiltmeter placed inside the vacuum chamber at the top of the GGG

frame (not rotating), and as actuators a set of PZTs (also not rotating, at 120° in the horizontal plane around the symmetry axis, providing tilts of the apparatus through vertical displacements). The tiltmeter currently installed can detect tilts of 10^{-9} rad. At the location of the PZTs the arm length with respect to the symmetry axis is about 0.1 m, and therefore the vertical effect of such tilts would be of about 10^{-10} m, which they can correct by applying a voltage of the order of a mV. If successful, this control would leave a residual relative displacement of the test cylinders of about $4\cdot10^{-10}$ m.

A further reduction by about 4 orders of magnitude, down to $4\cdot10^{-14}$ m, which would bring the effects of tilts and horizontal disturbances well below the target signal, can be obtained using a passive cardanic suspension and the lever effect. If k_s is the intrinsic elastic constant in any direction of the horizontal plane, of a laminar suspension with strip length λ placed at the top of a suspension arm of length ℓ, because of the lever effect the resulting elastic constant in the horizontal plane is $k \simeq (\lambda/\ell)^2 k_s$. With the reduction factor in the tilt angle as given by Eq. 3, it follows that, with $\lambda \simeq 5\cdot10^{-3}$ m , $\ell \simeq 0.5$ m , $m \simeq 40$ kg , $k_s \simeq 8\cdot10^2$ N/m , the reduction is $\beta/\alpha \simeq 10^{-4}$, as required. The laminar suspensions currently used in GGG have $\lambda_{GGG} \simeq 5\cdot10^{-3}$ m , $k_{sGGG} \simeq 10^3$ N/m , thus indicating that it is possible to achieve the required passive attenuation so that, overall, seismic disturbances would not impair a 10^{-13} test of the equivalence principle on the ground with the GGG differential accelerometer.

Acknowledgements

Starting mid 2003 the GGG experiment is under funding by INFN. The GG space mission has been funded for Phase A Study and Advanced Phase A study by ASI. The Italian space industry LABEN has provided support for the GGG prototype in its laboratories in Florence till June 2003.

References

1. GG Report on Phase A Study, ASI, 1998 (2000 second edition; A.M. Nobili *et al.*, *Phys. Lett. A,* in press; GG Website at *http://eotvos.dm.unipi.it/nobili*
2. A.M. Nobili et al., *New Astronomy* **8**, 371-390 (2003)
3. Y. Su *et al.*, *Phys. Rev. D* **50** 3614-3636 (1994)
4. S. Baeßler *et al., Phys. Rev. Lett.* **83** 3585-3588 (1999)
5. T. Damour, F. Piazza, G. Veneziano, *Phys. Rev. D* **66**, 046007-046021 (2002)

REFERENCES.

[1] Genta, G. "Vibration of Structures and Machines", Springer, New York, (1993).
[2] Den Hartog, J.P., (1985), Mechanical Vibrations (Dover Pubblications, Inc., New York, first published 1934).
[3] Darlow, M.S., "Balancing of high speed machinery", Springer, New York, N.Y., (1989).
[4] Gantmacher, F.R., "Lezioni di Meccanica Analitica", Editori Riuniti, (1980).
[5] Goldstein, H., "Classical Mechanics", Addison-Wesley Publishing Company Inc., Massachusetts, USA, (1950).
[6] Landau, L.D., "Meccanica", Editori Riuniti, (1994).
[7] Crandall, S.H., "The role of Damping in Vibration Theory", J.Sound Vib., 11(1), 3-18, (1970).
[8] Nelson, H.D., Crandall, S.H., "Analytic Prediction of Rotordynamic Response", Handbook of Rotordynamics, F.E. Enrich Ed., McGraw Hill, (1992).
[9] Saulson, P.R., Phys. Rev. D 42, 2437, (1990).
[10] Nobili, A.M.,, D. Bramanti, E. Polacco, G. Catastini, A. Anselmi, S. Portigliotti, A. Lenti, P. Di Giamberardino, S. Monaco, R. Ronchini, Class. Quantum Grav., 16,1463, (1999).
[11] Nobili, A.M., D. Bramanti, E. Polacco, G. Mengali, A. Sebasta, A. Anselmi, G. Catastini, S. Portigliotti, V. Ancona, W. Bogo, L. Perachino, S. Di Gennaro, P. Lanza, P. Martella, P. Porta, A. Lenti, R. Ronchi, L. Isabella, A. Severi, M. Minucci, G. Fabri, S. Marcuccio, S. Monaco, P. Di Giamberardino, R. Ronchini, G. Genta, E. Brusa, F. Curti, D. Mortari, F. Cabiati, G.L. Comandi, N. Aversa, M. Bardascino, S. Sabbatini, "Galileo Galilei" (GG), Phase A Report, Agenzia Spaziale Italiana, 2nd Edition, (2000); http://eotvos.dm.unipi.it/nobili/ggweb/phaseA.
[12] Bramanti D., A.M. Nobili, G. Catastini, "Stabilization of Weakly Coupled Rotors: A General Derivation of the Required Forces", (1996), available on line: http://tycho.dm.unipi.it/~nobili/ggweb/pap1/pap1.html.
[13] Nobili, A.M., G. Catastini, D. Bramanti, "Energy Gained by Whirling Motion as Fraction of Energy Lost by Spinning Rotor", (1997), available on line: http://tycho.dm.unipi.it/~nobili/ggweb/ratio/ratiol.html.
[14] Worden Jr., P.W., C.W.F. Everitt, in *Experimental gravitation*, Proceedings of the "Enrico Fermi" Intl. School of Physics, Course LVI, Ed. By B. Bertotti, Academic Press, New York, (1973).
[15] Nobili, A.M., "Precise gravitation measurements on Earth and in space: Tests of the Equivalence Principle", in *Recent Advances in Metrology and Fundamental Constants*, Proceedings of the "Enrico Fermi" Intl. School of Physics, Course CXLVI, Ed. By T.J. Quinn, S. Leschiutta and P. Tavella, p. 609, IOS Press, (2001).
[16] Eötvös, R.V., D. Pekar, E. Fekete, Ann. Physik 68, 11, (1922).
[17] Roll, P.G., R. Krotov, R.H. Dicke, Ann. Physik 26, 442, (1964).
[18] Braginsky, V.B., Panov, V.I., Sov. Phys. JEPT 34, 463, (1972).
[19] Baebler, S., B.R. Heckel, E.G. Adelberger, J.H. Gundlach, U. Schmidt, H.E. Swanson, Phys. Rev. Lett. 83, 3585, (1999).
[20] Damour, T., A.M. Polyakov, Nucl. Phys. B423, 532, (1994).
[21] Damour, T., A.M. Polyakov, Gen. Rel. Grav. 26, 1171, 1(994).
[22] Fischbach, E., D.E. Krause, C. Talmadge, D. Tadic, Phys. Rev. D 52, 5417, (1995).
[23] Damour, T., F. Piazza, G. Veneziano, Phys. Rev. Lett. 89, 081601, (2002).

[24] Touboul, P., M. Rodrigues, Class. Quantum Grav. 18, 2487, (2001).
[25] MICROSCOPE Website: http://www.onera.fr/dmph-en/accelerometre and http://www.cnes.fr/activites/programmes/microsatellite/1sommaire_microsatellite.htm.
[26] ''GALILEO GALILEI'' (GG) Website: http://eotvos.dm.unipi.it/nobili.
[27] Nobili, A.M., D. Bramanti, E. Polacco, I.W. Roxburgh, G.L. Comandi and G. Catastini, Class. Quantum Grav., 17, 2347-2349, (2000).
[28] Nobili, A.M., D. Bramanti, G.L. Comandi, R. Tondelli, E. Polacco, M.L. Chiofalo, Phys. Lett. A, 318, 172-183, (2003).
[29] Nobili, A.M., D. Bramanti, E. Polacco, G.L. Comandi, A. Franzoso, I.W. Roxburgh, A. Brillet, L. Anselmo, P.G. Bizzeti, S.J. Burns, A. Cadez, R. Cowsik, S. H. Crandall, F. Curti, P. Dell'Aversana, J.Van Der Ha, P. Di Giamberardino, A. Di Virgilio, W. Flury, G. Genta, G. Gillies, L.S. Hou, J. Luo, V. Iafolla, N. Khrishan, C. Marchal, G. Mengali, V. Milyukov, S. Monaco, J. Mueller, W.T. Ni, Y. Nie, F. Palmonari, G. Pizzella, R. Ronchini, A.J. Sanders, M. Soffel, C.S. Unnikrishnan, P. Villaggio, Y.Z Zhang, Z. Knezevic, "GALILEO GALILEI (GG): A Small satellite to test the Equivalence Principle of Galileo, Newton and Einstein", proposal for the F2&F3 Competition of ESA, (2000)
[30] STEP Satellite Test of the Equivalence Principle, (1996), report on the phase A study, ESA-SCI(96)5.
[31] STEP website: http://einstein.stanford.edu/STEP.
[32] Comandi, G.L., Laurea degree thesis in Physics, University of Pisa, (1999).
[33] Nobili, A.M., D. Bramanti, G.L. Comandi, R. Tondelli, E. Polacco, New Astronomy, 8, 371, (2003).
[34] Comandi, G.L., A.M. Nobili, D. Bramanti, R. Tondelli, E. Polacco, M.L. Chiofalo, Phys. Lett. A, 318, 213-222, (2003).
[35] A.M. Nobili, D. Bramanti, E. Polacco, I.W. Roxburgh, G.L. Comandi, A. Anselmi, G. Catastini, A. Lenti and A. Severi: "GALILEO GALILLEI" (GG). Proposed Space Experiment to Test the Equivalence Principle and Preliminary Results from the Prototype on the Ground, in Proceedings of 1999 NASA/JPL Conference on "Fundamental Physics in Space", April 29, 30 and May 1, Washington DC, NASA Document D-18925, 309-327, (1999).
[36] Comandi, G.L., M.L. Chiofalo, R. Tondelli, D. Bramanti, E. Polacco, A.M. Nobili, "Dynamical response of the Galileo Galilei rotor for a Ground test of the Equivalence Principle: theory, simulation and experiment. Part I: the normal modes", to be submitted for publication.
[37] Comandi, G.L., M.L. Chiofalo, R. Tondelli, D. Bramanti, E. Polacco, A.M. Nobili, "Dynamical response of the Galileo Galilei rotor for a Ground test of the Equivalence Principle: theory, simulation and experiment. Part II: the rejection behaviour", to be submitted for publication.
[38] Nobili, A.M., D. Bramanti, E. Polacco, G. Catastini, G. Genta, E. Brusa, V.B. Mitrofanov, A. Bernard, P. Touboul, A.J. Cook, J. Hough, I.W. Roxburgh, A. Polnarev, W. Flury, F. Barlier, C. Marchal, New Astronomy, 3, 175, (1998).
[39] Pace, E., F. De Martini, F. Melchiorri, Rev. Sci. Instrum., 63, 3112, (1992).
[40] A.M. Nobili**,** D. Bramanti, G.L. Comandi, R. Toncelli, E. Polacco, M.L. Chiofalo: The fast rotating "GGG" differential accelerometer for testing the equivalence principle: current state and analysis of seismic disturbances, in Proceedings of the XXXVIIIth Rencontres de Moriond "Gravitational Waves and Experimental Gravity",J. Dumarchez and J. Tran Thanh Van Eds., The Gioi Publishers, Vietnam, pp. 371-376, 2003

[41] Iafolla, V., E.C. Lorenzini, V. Milyukov, S. Nozzoli, Rev. Sci. Instrum., 69, 151, (1998).
[42] Iafolla, V., A. Mandiello, S. Nozzoli, "The high sensitive Italian spring accelerometer (ISA) for fundamental physics in space", COSPAR, Nagoya, (1998).
[43] Dattilo, V., et al., The Virgo suspensions: design and recent performance measurements, in press.
[44] Ogata, K., "System dynamics", Prentice-Hall, Englewood Cliffs, (1978).
[45] Ogata, K., "Discrete-time control systems", Prentice-Hall, Englewood Cliffs, (1987).
[46] Ogata, K., "Modern control engineering", Prentice-Hall, Englewood Cliffs, (1990)
[47] Skelton, R.E., "Dynamic systems control: linear systems analysis and synthesis", Wiley, New York, (1988).
[48] Ogata, K., "Designing linear control systems with MATLAB", Prentice-Hall, Englewood Cliffs, (1994).
[49] Ogata, K., "Solving control engineering problems with MATLAB", Prentice-Hall, Englewood Cliffs, (1994).
[50] Ciampi, M., G. Del Corso, L. Verrazzani, "Teoria dei segnali: segnali aleatori", ETS, Pisa, (1994).
[51] Papoulis, A., "Probability, random variables, and stochastic processes", McGraw-Hill, New York, (1965).
[52] Papoulis, A., "Signal analysis", McGraw-Hill, New York, (1977).
[53] Nobili, A.M., D. Bramanti,E. Polacco,G. Mengali, G.L. Comandi, R.Toncelli, A. Franzoso,V. Iafolla,S. Nozzoli,M. Vadim,A. Mandiello, G. Catastini,P. Martella,A. Anselmi,E. Cavazzuti,P. Soravia, R. Ronchi,A. Severi,P. Siciliano,L. Zanin,C. Galli, "PGB (Pico Gravity Box): Enabling Vibration Free Activity on Board the ISS. Final Report.", *ASI Utilizzazione Tecnologica Della Stazione Spaziale*, Project USS-98056, (2000).
[54] Comandi, G.L., A.M. Nobili, R. Toncelli, M.L. Chiofalo, Phys. Lett. A, 318, 251, (2003).
[55] Nobili, A.M., D. Bramanti, G.L. Comandi, R. Toncelli, E. Polacco, G. Catastini, Phys. Rev. D, 63, 101101R, (2001).
[56] Nobili, A.M., D. Bramanti, G.L. Comandi, R. Toncelli, E. Polacco, New Astronomy, 8, 371, (2003).
[57] Bongiovanni, G., G. Roccati, "Le molle: tipi e criteri di calcolo", Levrotto e Bella, (1994).
[58] Carlson, H., "Spring designer's handbook", M. Dekker inc., (1978).
[59] Timoshenko, S., J. Goodler, "Theory of elasticity", McGraw-Hill, (1970).
[60] Brusa, E., "Molle metalliche di connessione", Private communication.
[61] Knudsen, M., "The Kinetic Theory of Gases", Methuen, London, John Wiley, New York, (1952).
[62] Loeb, L., "The Kinetic Theory of Gases", McGraw Hill, New York, (1934).
[63] White, G.K., "Experimental Techniques in Low Temperature Physics", Clarendon, Oxford, (1959).

Dynamical response of the Galileo Galilei on the ground rotor to test the equivalence principle: Theory, simulation, and experiment. I. The normal modes

G. L. Comandi
Istituto Nazionale di Fisica Nucleare (INFN), Sezione di Pisa, Largo B. Pontecorvo 3, I-56127 Pisa, Italy and Department of Physics, University of Bologna, I-40I26 Bologna, Italy

M. L. Chiofalo
Scuola Normale Superiore, Piazza dei Cavalieri 7, I-56100 Pisa, Italy; Istituto Nazionale di Fisica Nucleare (INFN), Sezione di Pisa, Largo B. Pontecorvo 3, I-56127 Pisa, Italy

R. Toncelli and D. Bramanti
Istituto Nazionale di Fisica Nucleare (INFN), Sezione di Pisa, Largo B. Pontecorvo 3, I-56127 Pisa, Italy

E. Polacco and A. M. Nobili
Department of Physics "E. Fermi," University of Pisa, Largo B. Pontecorvo 3, I-56127 Pisa, Italy and Istituto Nazionale di Fisica Nucleare (INFN), Sezione di Pisa, Largo B. Pontecorvo, I-56127 Pisa, Italy

(Received 5 January 2006; accepted 16 January 2006; published online 23 March 2006)

Recent theoretical work suggests that violation of the equivalence principle might be revealed in a measurement of the fractional differential acceleration η between two test bodies—of different compositions, falling in the gravitational field of a source mass—if the measurement is made to the level of $\eta \simeq 10^{-13}$ or better. This being within the reach of ground based experiments gives them a new impetus. However, while slowly rotating torsion balances in ground laboratories are close to reaching this level, only an experiment performed in a low orbit around the Earth is likely to provide a much better accuracy. We report on the progress made with the "Galileo Galilei on the ground" (GGG) experiment, which aims to compete with torsion balances using an instrument design also capable of being converted into a much higher sensitivity space test. In the present and following articles (Part I and Part II), we demonstrate that the dynamical response of the GGG differential accelerometer set into supercritical rotation—in particular, its normal modes (Part I) and rejection of common mode effects (Part II)—can be predicted by means of a simple but effective model that embodies all the relevant physics. Analytical solutions are obtained under special limits, which provide the theoretical understanding. A simulation environment is set up, obtaining a quantitative agreement with the available experimental data on the frequencies of the normal modes and on the whirling behavior. This is a needed and reliable tool for controlling and separating perturbative effects from the expected signal, as well as for planning the optimization of the apparatus. © *2006 American Institute of Physics.* [DOI: 10.1063/1.2173075]

I. INTRODUCTION

Experimental tests of the equivalence principle (EP) are of seminal relevance as probes of general relativity. The equivalence principle is tested by observing its consequence, namely, the universality of free fall, whereby in a gravitational field all bodies fall with the same acceleration regardless of their mass and composition. They therefore require two masses of different compositions, falling in the field of another "source" mass and a readout system to detect their motions relative to one another. An EP violation would result in a differential displacement of the masses in the direction of the source mass, which cannot be explained on the basis of known, classical phenomena (e.g., tidal effects).

The landmark experiment by Eötvös *et al.*[1] has established that a torsion balance is most well suited for the ground tests of the EP, thanks to its inherently differential nature. With the test masses suspended on a torsion balance they improved previous pendulum experiments by almost four-orders of magnitude, showing no violation for η larger than a few 10^{-9}.[1] Several decades later, by exploiting the 24 h modulation of the signal in the gravitational field of the Sun, torsion balance tests have improved to 10^{-11} (Ref. 2) and then to 10^{-12}.[3] More recently, systematic and very careful tests carried out by Su *et al.*[4] and Adelberger *et al.*[5] using *rotating* torsion balances have provided even more firm evidence that no violation occurs to the level of 10^{-12}.

The relevant theoretical question for equivalence principle tests is at which accuracy level a violation, if any, is to be expected? In an earlier work by Damour and Polyakov, based on string theory and the existence of the dilaton,[6] η values at which a violation might be observed have been determined to be in the range $10^{-18} < \eta < 10^{-13}$. Fischbach *et al.*[7] have derived a nonperturbative rigorous result, according to which a violation must occur at the level of $\eta \simeq 10^{-17}$, due to the coupling between gravity and processes of ν-$\bar{\nu}$ exchange which should differently affect masses with

different nuclei. More recent work[8] suggests, in a new theoretical framework for the dilaton, that a violation might occur already at the level of $\eta \simeq 10^{-12} - 10^{-13}$, depending on the composition of the masses.

While an $\eta \simeq 10^{-13}$, and perhaps smaller, should be accessible with rotating torsion balance experiments on the ground, a sensitivity as high as $\eta \simeq 10^{-17}$ could be achieved only by an experiment flying in a low Earth orbit, where the driving acceleration is up to three orders of magnitude larger. Specific instruments have been designed to carry out such an experiment in space: satellite test of the equivalence principle (STEP) microscope, and "Galileo Galilei" (GG).[9–12] They share two features: that the test masses are concentric cylinders and that rotation of the spacecraft provides signal modulation at frequencies higher than the orbital one.

GG is peculiar in that it spins around the symmetry axis and is sensitive to the relative displacements in the plane perpendicular to it: the cylindrical symmetry of the whole system and rotation around the symmetry axis allow a passive attitude stabilization of the spacecraft with no need of a motor after an initial spin up to the nominal frequency (typically 2 Hz). The planar (instead of linear) sensitivity of the instrument is also a crucial feature for allowing us to rotate at supercritical speeds, i.e., faster than the natural frequencies of the system. Faster rotation means modulation of the signal at higher frequency and therefore a reduced $1/f$ noise (for $1/f$ noise see, e.g., the website maintained by Li[13]). GG differs from the other proposed space experiments also in that the test masses are suspended mechanically. We find that in the absence of weight, as it is the case in space, mechanical suspensions too can provide extremely weak coupling, with the additional advantage to electrically ground the test masses.

The GG design naturally allows us to build and test a full scale 1 g version of the apparatus: by suspending the instrument on a rotating platform through its spin/symmetry axis, the sensitive plane lies in the horizontal plane of the laboratory where a component of an EP violation signal might be detected, similarly to a torsion balance experiment. "Galileo Galilei on the ground"[14,15] (GGG) is primarily a prototype for testing the main novel features of the experiment proposed for flight. It is also an EP experiment in its own right aiming to compete with torsion balance tests.[4,5] In this effort, motor noise, low-frequency terrain tilts,[16] and tidal perturbations[17] are the main issues to be addressed.

A full knowledge of the dynamical response of the GGG rotor is needed, especially in view of its condition of supercritical rotation and of its common mode rejection behavior. The theoretical understanding of the dynamical properties of the rotor, together with the construction of a full simulation facility, would allow us to predict and interpret the collected experimental data; they also provide a virtual environment for planning the experiment and optimizing its performance.

With these motivations in mind, we demonstrate that a simple but very effective mathematical model can be set up to quantitatively describe the dynamical properties of the GGG rotor. In this article (Part I), we determine the normal modes in all regimes, from subcritical to supercritical rotation, and address the issue of self-centering in the supercritical rotation. In the following article (Part II), we provide the dependence of the common mode rejection ratio on various system parameters which govern the design of the instrument.

The differential equations in the model are solved by means of a user-friendly simulation program and the numerical solutions are tested against the data available from the experiment. The physical content of the model is also discussed by means of approximate analytical solutions, which provide useful physical insight.

This article is organized as follows: Sec. II describes the main features of the experimental apparatus, Sec. III presents the dynamical model of the system, referring to specific appendixes for details, Sec. IV reports on the numerical method that we have implemented, and Sec. V gives the results obtained on the determination of the normal modes of the system, showing an excellent agreement between the theoretical predictions and experimental data. The details of the calculations are contained in two appendixes, while the third one is specifically devoted to the important concept of self-centering. Concluding remarks are discussed in Sec. VI.

II. THE GGG ROTOR: OVERVIEW OF THE EXPERIMENT

GGG is a rotating differential accelerometer operated in a vacuum chamber (see Fig. 1). It is made of two concentric hollow test cylinders, 10 kg each, weakly coupled by means of a vertical arm—a tube located along the axis of the cylinders—to form a vertical beam balance (from now on we shall always omit the term "hollow" when referring to the test cylinders). The coupling arm is suspended at its midpoint from a rotating vertical shaft in the shape of a tube enclosing it (see Figs. 1 and 2, right hand side). A total of three suspensions are needed (drawn in red in Fig. 1): a central one (see Fig. 2, left hand side) to suspend the coupling arm from the rotating shaft and one for each test cylinder to suspend each of them from the top and bottom ends of the vertical coupling arm.

The suspensions are cardanic laminar suspensions manufactured in CuBe which are stiff in the axial direction $\hat{Z}$, against local gravity, and soft in the plane $\hat{X}$-$\hat{Y}$ orthogonal to the axis so that the geometry is naturally two dimensional, the horizontal plane being sensitive to differential accelerations acting between the test cylinders. In the normal operation mode, the modulation of such a signal is provided by setting the whole system in rotation around the vertical axis in the *supercritical regime*, namely, at frequencies ν_s larger than the natural differential frequencies of the rotor, typically $\nu_s > 1.5$ Hz. The differential character of the instrument is strengthened by two differential readout systems made of four capacitance plates (indicated as IP, internal plates, in Fig. 1) located in between the test cylinders and which are part of two capacitance bridges in two orthogonal directions of the sensitive plane.

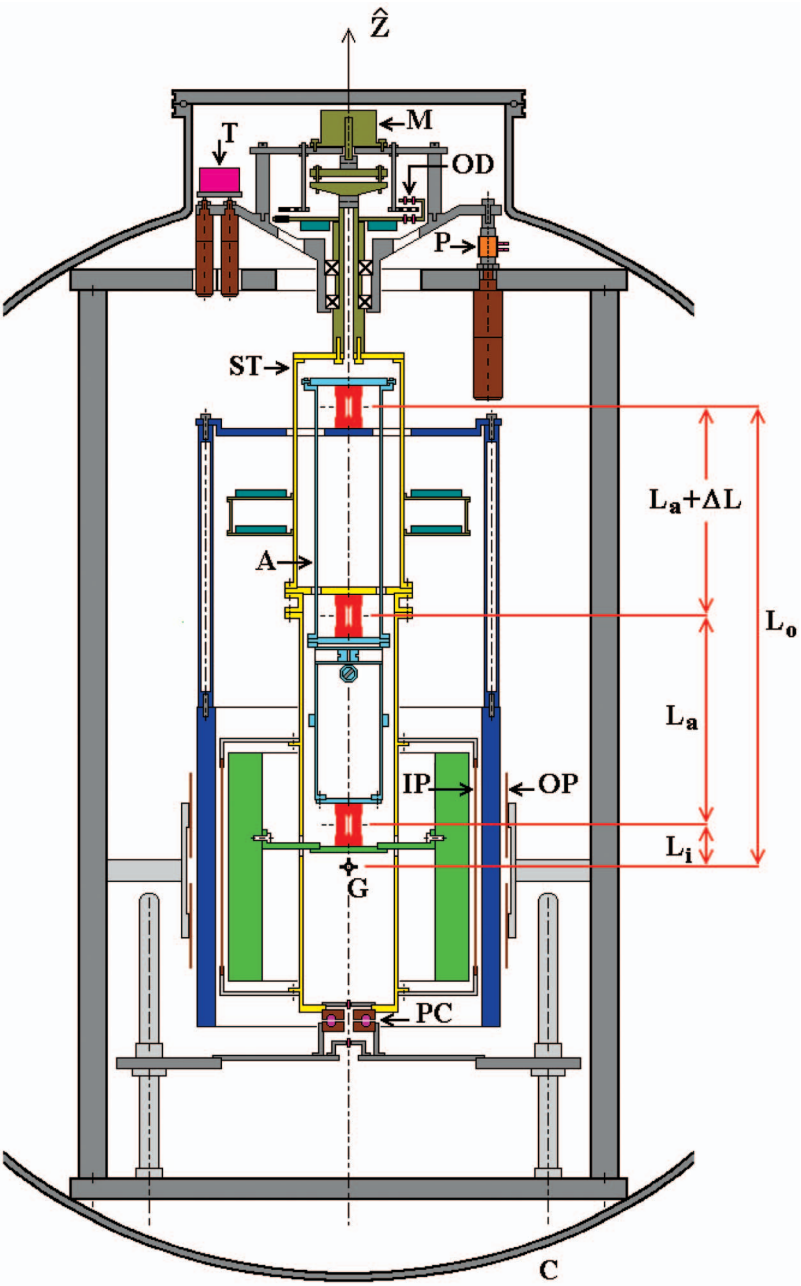

FIG. 1. (Color) Section through the spin axis $\hat{Z}$ of the differential accelerometer inside the vacuum chamber. *C*, vacuum chamber; *M*, motor; OD, optical device (see Sec. II B); **x**, ball bearings; ST, suspension tube; *A*, coupling (balance) arm, located inside the suspension tube, with its three laminar cardanic suspensions (in red); and *G*, center of mass of the two cylinder's system (in blue the outer cylinder, in green the inner one, 10 kg each). IP are the internal capacitance plates of the differential motion detector (Sec. II B), OP are the outer ones for whirl control (Sec. II C 2), and PC is the contactless inductive power coupler providing power to the electronics inside the rotor. The relevant distances, L_i and L_o, of the centers of mass of the inner and outer bodies from their suspension points are also sketched, along with the arm length $2L_a+\Delta L$. *T* and *P*, at the top of the rotor, are the tiltmeter and three-PZTs (at 120° from one another—only one shown) for automated control of low frequency terrain tilts. The drawing is to scale and the inner diameter of the vacuum chamber is 1 m.

A. Description of the mechanical structure of the apparatus

The GGG apparatus is schematically presented in Fig. 1, where a section through the spin-symmetry axis $\hat{Z}$ is shown inside the vacuum chamber *C*. At the top center of the frame is the motor *M* whose shaft is connected to the suspension tube of the rotor ST (drawn in yellow) by means of an appropriate motor-rotor joint and turns in the vertical direction inside ball bearings, indicated by **x** symbols in the figure. From the suspension tube ST rotation is then transmitted to a tube located inside it which constitutes the vertical beam of the balance (also referred to as the coupling arm, Fig. 2, right hand side), the connection between the two being provided at the midpoint of the arm by the central laminar cardanic suspension (see Fig. 2, left hand side).

The coupling arm in its turn transmits rotation to both the test cylinders, since they are suspended (by means of two laminar cardanic suspensions similar to the central one) from its two ends. More precisely, the inner test cylinder (shown in green) is suspended from the bottom of the coupling arm at a distance L_i from the cylinder's center of mass, while the outer one (shown in blue) is suspended from the top of the coupling arm, at a distance L_o from the cylinder's center of mass. In Fig. 1 the three suspensions are drawn in red. It is apparent that the central suspension carries the whole weight of the rotor, mostly the weight of the two test cylinders (10 kg each) plus the small weight of the coupling arm. It is worth noting that the metallic suspensions provide a passive electrostatic discharging of the test masses.

In this way, the symmetry of the whole apparatus is cylindrical, its axis being both the vertical beam of the balance and the axis of rotation, the balance is sensitive in the horizontal plane, and the test masses are concentric.

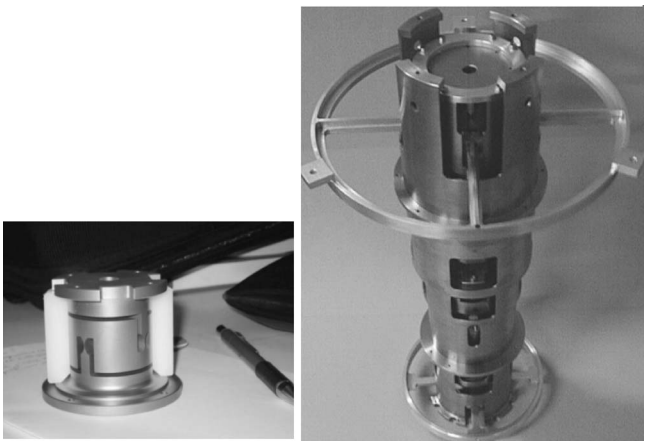

FIG. 2. Left hand side: the central laminar cardanic suspension of the GGG rotor, located at the midpoint to the coupling arm in order to suspend it from the suspension tube (shaft). Right hand side: the coupling arm inside the suspension tube (shaft) as seen from the top. Two cardanic laminar suspensions are located at its top and bottom ends. They suspend the test cylinders (not shown here) through two metal rings. The dimensions of the rings depend on the dimensions of the concentric cylinders, which have equal mass (10 kg) and therefore different sizes. The top and bottom rings refer to outer and inner test cylinders, respectively.

B. The differential motion detector system

The differential motion detector (DMD) reflects the cylindrical symmetry of the system and is composed of the following three parts.

(1) Two capacitance plates IP working as DMD(x) sensors (drawn as vertical lines in between the cylinders in Fig. 1) are located halfway in between the test cylinders in correspondence to the X direction with a clear gap of 5 mm on either side and are connected to the suspension tube by means of an insulating frame. A similar pair of capacitances forming a DMD(y) is placed in the Y direction. A voltage signal is applied to each capacitance bridge in order to shift the signal of interest to a high-frequency band with reduced $1/f$ noise (with phase locked detection). The filtered signal is digitized by an analog-to-digital converter (ADC) before transmission to the nonrotating (laboratory) frame. Calibration and balancing of the capacitance bridge are performed by means of the procedures outlined in Ref. 14. The best sensitivity achieved in bench tests corresponds to mechanical displacements of 5 pm in 1 s of integration time.[11,14] Presently, the sensitivity of the readout system during normal operation is $\simeq 10^{-9}$ m.

(2) An optical device OD located below the motor and above the ball bearings, utilizing a disk with 32 holes and an infrared emitter-detector pair, provides a reference signal for the angular position of the rotor. The reference signal is combined with the X and Y channel data from the DMD and encoded into RS232 format for transmission to a computer. Then a second emitter-detector pair located at the very bottom of the rotor (using a hole along the axis of the power coupler PC, see Fig. 1) transmits the digital signal from the rotor to the nonrotating frame from where it is taken out of the vacuum chamber through electrical feedthroughs.

(3) An annular disk, in two semicircular parts, is mounted around the upper half of the suspension tube and contains the two capacitance-bridge circuits and their preamplifiers (see Fig. 1). The necessary electronics to demodulate the signal and convert it from an analog to digital form as well as the drivers for the optical emitter are also located here.

C. Principle of operation

For detecting an EP violation signal the instrument relies on its sensitivity to the relative displacement of the two test masses, which in the final design will be made of different materials. An acceleration in the horizontal plane of the laboratory acting differently between the test cylinders gives rise to a relative displacement of the two in the direction of the acceleration. This displacement unbalances the capacitance bridges and gives rise to an electric voltage proportional to it.

A modulation of the displacement, as seen by the capacitance plates, is achieved by setting the whole system in rotation around the vertical axis of symmetry passing through the shaft, as shown in Fig. 1. Note that the signal modulation obtained in this way does not affect the centers of mass of the test cylinders; hence, it does not affect their relative displacement, which is the physical quantity measured in the experiment. As a result, this type of modulation reduces the noise but not the signal.

In fact, this signal modulation could be achieved by keeping the test cylinders stationary and rotating only the capacitance plates (located in between the two, indicated as IP in Fig. 1) which form the differential motion detector system described above. However, by rotating the test cylinders together with the capacitors, any irregularity in their mass distribution averages out; moreover, the supercritical regime can be exploited to reduce the rotation noise for all parts of the apparatus (see Sec. II C 2 and Appendix C). As for the experiment in space, the rotation of the whole spacecraft has two more very important advantages. In the first place, it eliminates the need for motor and ball bearings altogether, which are a considerable source of noise in the ground experiment. Secondly, by rotating around the axis of maximum moment of inertia, the spacecraft is *passively* stabilized, thus reducing its weight, cost, and complexity, as well as disturbances on the EP experiment.

An EP violation signal in the gravitational field of either the Earth or the Sun would have a component in the horizontal plane of the laboratory which could be detected by the instrument. Since the test bodies are rotors suspended on the Earth and the Earth rotates around its axis, this diurnal rotation gives rise to large gyroscopic effects on the test bodies resulting in a nonzero differential acceleration which would mask an EP violation signal in the field of the Earth itself. The measurements of such gyroscopic effects have been reported in Ref. 14 (Sec. V, Fig. 12). The instrument—in this ground based version—is therefore used for two purposes: (i) to establish its sensitivity as a prototype of the flight instrument, namely, for an expected signal at the orbital frequency of the satellite ($\simeq 1.75 \times 10^{-4}$ Hz, i.e., about $1\frac{1}{2}$ h period, at an Earth orbiting altitude of $\simeq 520$ km) and (ii) to

look for an EP violation in the gravitational field of the Sun, in which case the signature of the signal (see Ref. 12, Sec. II) would have a dominant Fourier component of a 24 h period due to the diurnal rotation of the Earth.

1. Differential character and common mode rejection

The differential character of the whole instrument, namely, its capability to reject accelerations which are common to both test masses, is in principle ensured by the geometry and mounting of the test masses. It is further augmented by the differential nature of the DMD system.

(i) The sensitivity of the instrument to differential accelerations of the test masses depends on the softness of the laminar suspensions and on the uniform distribution of mass around the spin axis. Soft suspensions and a good balancing of the rotor provide long natural periods for differential oscillations of the test masses relative to each other, giving rise to larger relative displacements between the two and, in turn, to stronger output voltage signals.

The tuning of the natural differential period T_D of the test cylinders is made possible by changing a moment arm in the beam balance. This is accomplished by moving a small solid ring mounted at the lower end of the balance (coupling) arm. Moving this ring vertically along the arm, in the $\hat{Z}$ direction, displaces the center of mass of the balance arm from its suspension point by a quantity ΔL. If $\Delta L=0$ the center of mass of the balance arm is coincident with its suspension point. ΔL can be adjusted to be either slightly positive or negative, resulting in a longer or shorter T_D. However, there is a maximum positive value that ΔL can assume before the system becomes unstable [see Eq. (39) below].

Asymmetric distribution of mass of the rotor in the horizontal plane, resulting in a nonzero inclination of the coupling arm in the rotating reference frame, may also be corrected by two small masses mounted inside the coupling arm itself, one of which is movable in the X direction and the other in the Y.

The tilt of the spin axis with respect to the nonrotating laboratory frame is controlled by 3 μm screws which support the plate on which the rotor shaft is mounted. In addition the tilt can be finely adjusted using piezoelectric actuators (P) attached to the tips of the micrometer screws (see Fig. 1).

(ii) As to the DMD system, a nonzero off centering of the capacitor plates IP located in between the test cylinders—measured by the ratio $(a-b)/a$ where $a(b)$ is the nominal gap between the inner (outer) mass and any one of the capacitance plates—would make a common mode displacement Δx_C of the test masses to produce a differential output signal in addition to that produced by a real differential displacement Δx_D. The larger this off centering, the larger the fraction of the common mode displacement which is turned into a "fake" differential signal, i.e., which contributes to the total unbalance ΔC of the capacitance bridge[11] (GG Phase A Report, Sec. 2.1.3) from the original capacitance value C_o,

$$\frac{\Delta C}{2C_0} \simeq \frac{a-b}{a^2}\Delta x_C - \frac{1}{a}\Delta x_D. \tag{1}$$

2. Signal modulation and whirl motions

Signal modulation in testing the equivalence principle has been first proposed in Ref. 2 in order to improve the experiments of Eötvös *et al.*. By referring to the Sun rather than the Earth as the source mass of the gravitational field, the diurnal rotation of the Earth itself on which the test masses are suspended provides a 24 h modulation with no need to rotate the experimental apparatus, an operation which gives rise to relevant disturbances in such small force experiments. However, higher modulation frequencies are desirable in order to reduce the $1/f$ noise and, in fact, excellent results have been obtained by Refs. 4 and 5 with torsion balances placed on a turntable rotating faster than the Earth. In GGG we try to spin the test masses much faster, at frequencies (typically a few hertz) higher than the natural frequencies ν_n of the system, a condition known as *supercritical rotation*.

The GGG apparatus has three natural frequencies. The differential frequency ν_D of the oscillations of the test bodies relative to one another and two common mode frequencies, ν_{C1} and ν_{C2}, of both test masses together. In the GGG setting reported here their values are $\nu_D=0.09$ Hz, $\nu_{C_1}=0.91$ Hz, and $\nu_{C_2}=1.26$ Hz.

It is well known[18–20] that in supercritical rotation the masses are able to self-center and greatly reduce the original offsets of their centers of mass with respect to their own rotation axes. Any initial offset, which inevitably results from construction and mounting errors, is, in fact, reduced by a factor $(\nu_D/\nu_s)^2$. Such self-centering is a very essential requirement when using fast rotating macroscopic test bodies for the purpose of detecting the effects of extremely small forces between them.

It is also well known that in supercritical rotation, dissipation in the system gives rise to destabilizing *whirl* motions at frequencies ν_w equal (or close) to the natural frequencies of the system, whose amplitude increases with time at a rate $1/\tau_w=\pi\nu_w/\mathcal{Q}(\nu_s)$ scaling as the whirl frequency ν_w and the inverse of the quality factor $\mathcal{Q}$ at the spin frequency ν_s.[20–22]

Whirls can be stabilized by passive and active methods. Passive stabilization is typically used in engineering applications of supercritical rotors, but it produces too large disturbances for our purposes. We have used a passive damper in the past only to stabilize the rotor during resonance crossing (see Ref. 14, Sec. III). With the current improved apparatus, damping at resonance crossing is no longer needed. A much finer whirl stabilization can be performed actively by means of eight small capacitance sensors/actuators (indicated as OP, outer plates, in Fig. 1) placed close to the outside surface of the outer test cylinder, four of them used as sensors and four as actuators in two orthogonal directions of the horizontal plane.[15] In the GGG experiment performed at supercritical speed the relevant $\mathcal{Q}$ value is determined by losses due to

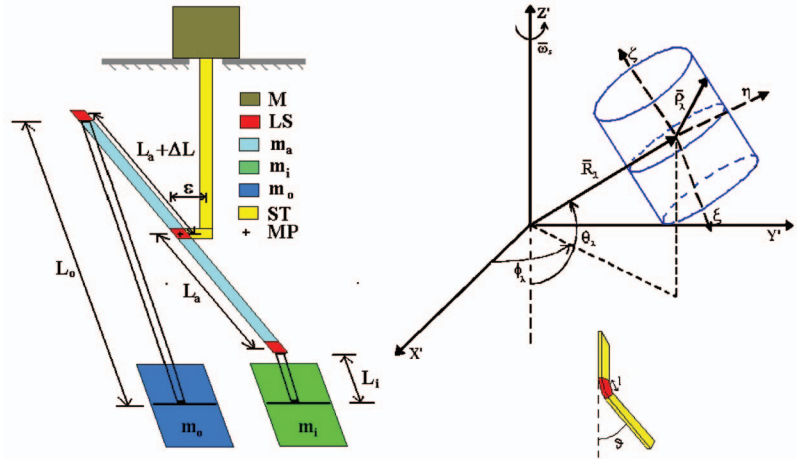

FIG. 3. (Color) Minimal model for the real instrument sketched in Fig. 1 (see text for details). On the left hand side the various parts are drawn with the same colors and labels as in Fig. 1. Here the midpoint of the coupling arm is indicated as MP. L_a, L_o, and L_i refer to the dimensions of the coupling arm and the outer mass and inner mass suspension arms, respectively. $\hat{L}_a$, $\hat{L}_o$, and $\hat{L}_i$ are the unit vectors of the corresponding beams. The offset vector $\boldsymbol{\epsilon}$, due to construction and mounting imperfections, is also indicated. On the right hand side we sketch one of the cylinders in the rotating reference frame $\{X'Y'Z'\}$, showing its principal axes of inertia $\{\xi, \eta, \zeta\}$, the position vector $\mathbf{R}_\lambda$ $(\lambda = a, o, i)$ of its center of mass, and the angles $\theta_\lambda, \phi_\lambda$, which are not the usual Euler angles, as discussed in the text. Below this figure, the small one to the right shows a typical deformation of one of the laminar suspensions of length l, for instance, the central one. None of these figures is to scale.

deformations of the laminar suspensions at the spin frequency. Experimental measurements of $\mathcal{Q}$ are reported in Ref. 14 and, more recently, in Ref. 23.

III. THE MODEL

Having described the real instrument, we are now in a position to outline the minimal model used to describe its dynamical behavior. Figure 3 displays a schematic representation of the model in the reference frame $\{X'Y'Z'\}$ rotating with the shaft at an angular velocity $\omega_s = 2\pi\nu_s$ around the Z' axis $(\boldsymbol{\omega}_s = \omega_s \hat{Z}')$. The relevant parts of the instrument depicted in Fig. 1 are sketched in Fig. 3 with the same colors. The coupling arm, with mass m_a (drawn in cyan as in Fig. 1) and length $2L_a + \Delta L$, is suspended at its midpoint MP from the rotating shaft and suspension tube ST (yellow) by means of the central laminar suspension LS (red) with elastic constant K. The vector $\boldsymbol{\epsilon}$ is the offset of the arm center of mass from the axis, which is unavoidable because of construction and mounting errors. Variations of ΔL, as we have already discussed, produce a change of the mass distribution, hence of the natural differential period of the test masses, T_D. Here, and with no loss of generality, $\boldsymbol{\epsilon}$ is placed along the X' axis.

The outer test cylinder, of mass m_o (blue), is suspended from the top of the coupling arm by means of the laminar suspension with elastic constant K_o and its center of mass is at a distance L_o from the suspension. In a similar manner, the inner test mass m_i (green) is suspended from the bottom of the arm, K_i and L_i being the corresponding parameters. From now on, the label $\lambda = i, o, a$ will be used to refer to the parameters of the inner mass, outer mass, and coupling arm, respectively. The three bodies have moments of inertia $I_{\lambda\xi} = I_{\lambda\eta} = m_\lambda(3R_{\lambda I}^2 + 3R_{\lambda E}^2 + R_{\lambda H}^2)/12$ and $I_{\lambda\zeta} = m_\lambda(R_{\lambda I}^2 + R_{\lambda E}^2)/2$ along their principal axes (ξ, η, and ζ), $R_{\lambda I}$ and $R_{\lambda E}$ being the internal and external radii of the cylinder λ, and $R_{\lambda H}$ its height.

The laminar suspensions have length l, the central one is slightly stiffer than the other two and we assume $K_i = K_o \neq K$. In a refined version of the model, and whenever specified, we also consider an anisotropic central suspension by introducing the parameter Λ such that $K_{Y'} \equiv \Lambda K_{X'}$.

By defining the unit vector $\hat{L}_a$ of the coupling arm as pointing from its midpoint towards the bottom suspension, and the unit vectors $\hat{L}_o$ and $\hat{L}_i$ of the test cylinders each pointing from the suspension to the center of mass of the body (see Fig. 3), the corresponding position vectors in the rotating reference frame $\{X'Y'Z'\}$ of Fig. 3 are

$$\begin{aligned} \mathbf{R}_a &= \boldsymbol{\epsilon} - 0.5\Delta L \hat{L}_a, \\ \mathbf{R}_o &= \boldsymbol{\epsilon} - (L_a + \Delta L)\hat{L}_a + L_o \hat{L}_o, \\ \mathbf{R}_i &= \boldsymbol{\epsilon} + L_a \hat{L}_a + L_i \hat{L}_i. \end{aligned} \tag{2}$$

A. The Lagrangian

The Lagrangian $\mathcal{L}$ in the rotating reference frame $\{X'Y'Z'\}$ can be written as

$$\mathcal{L} = \mathcal{T} - \mathcal{U}, \tag{3}$$

where the kinetic term can be very generally written as

$$\mathcal{T} = \frac{1}{2} \sum_{\lambda=a,o,i} \int_{\tau_\lambda} \boldsymbol{v}_\lambda^2 dm_\lambda, \tag{4}$$

after defining the velocity $\boldsymbol{v}_\lambda$ of the mass element dm_λ in body λ with volume τ_λ. Then, $\mathcal{U}$ includes the potential energies associated with gravity and with the elastic forces, namely,

$$\mathcal{U} = U_g + U_{\mathrm{el}}, \tag{5}$$

where

$$U_g = \sum_{\lambda=a,o,i} - m_\lambda \mathbf{g} \cdot \mathbf{R}_\lambda \quad \text{with } \mathbf{g} \equiv -g\hat{Z}', \tag{6}$$

$$\begin{aligned} U_{\mathrm{el}} = \sum_{\lambda=o,i} & \frac{1}{2} K_\lambda l^2 |\hat{R}_a \times \hat{R}_\lambda|^2 \\ & + \frac{1}{2} L_a^2 (K_{X'} |\hat{R}_a \dot{\hat{X}}'|^2 \\ & + K_{Y'} |\hat{R}_a \dot{Y}'|^2). \end{aligned} \tag{7}$$

For the expression of U_{el} we refer to the small figure at the bottom right of Fig. 3, sketching the laminar suspension and its orientation.

We proceed along the main steps to derive the operational expression for $\mathcal{L}$. The bodies are rotating around their

own axis with angular velocity ω_s in a reference frame which is rotating as well, as sketched in Fig. 3, right hand side. Thus, we define as $\mathbf{\Omega}_\lambda$ the angular-velocity vector of the element dm_λ in the $\{X'Y'Z'\}$ frame and $\boldsymbol{\omega}_s=\omega_s\hat{Z}'$, so that

$$\boldsymbol{v}_\lambda=\mathbf{V}_\lambda+\mathbf{\Omega}_\lambda\times\mathbf{r}_\lambda=\mathbf{V}_\lambda+\mathbf{\Omega}_\lambda\times(\mathbf{R}_\lambda+\boldsymbol{\rho}_\lambda), \tag{8}$$

where $\mathbf{V}_\lambda$ is the velocity of the center of mass of body λ and $\mathbf{r}_\lambda$ is the vector pointing to the element dm_λ, composed by $\mathbf{R}_\lambda$ and $\boldsymbol{\rho}_\lambda$, as drawn in Fig. 3. By inserting Eq. (8) into Eq. (4), we can write $\mathcal{T}$ as

$$\mathcal{T}=T_{\rm kin}+T_{\rm cor}+U_{\rm cor}+U_c, \tag{9}$$

where the only nonzero terms are (see Appendix A for details)

$$T_{\rm kin}=\frac{1}{2}\sum_\lambda\left(m_\lambda V_\lambda^2+\sum_{\alpha=\xi,\eta,\zeta}I_{\lambda\alpha\alpha}\Omega_\alpha^2\right), \tag{10}$$

$$T_{\rm cor}+U_{\rm cor}=\sum_\lambda m_\lambda\mathbf{V}_\lambda\cdot(\boldsymbol{\omega}_s\times\mathbf{R}_\lambda)+\sum_\lambda\int_{\tau_\lambda}(\mathbf{\Omega}_\lambda\times\boldsymbol{\rho}_\lambda)\cdot(\boldsymbol{\omega}_s\times\boldsymbol{\rho}_\lambda)dm_\lambda, \tag{11}$$

$$U_c=\frac{1}{2}\sum_\lambda\int_{\tau_\lambda}[\boldsymbol{\omega}_s\times(\mathbf{R}_\lambda+\boldsymbol{\rho}_\lambda)]^2dm_\lambda. \tag{12}$$

In Eq. (11) the terms coming from Coriolis forces have been split into the $U_{\rm Cor}$ potential energy, which contains only the position vectors, and $T_{\rm Cor}$ which contains also the velocities. The centrifugal part U_c has been indicated as a potential energy. To proceed further, we now have to specify the choice of the generalized coordinates.

B. Choice of the generalized coordinates

The GGG rotor model shown in Fig. 3 is composed of $n_b=3$ coupled bodies, for a total of 18 degrees of freedom. However, the central suspension prevents them from performing translational motions, thereby reducing the degrees of freedom to 9. In addition, the motor forces the three bodies to rotate at a constant angular velocity, so that the number of degrees of freedom for the model is $n=6$.

We have chosen as generalized coordinates for each body the two angles θ_λ and ϕ_λ (see Fig. 3, right hand side). These angles are defined slightly differently from the usual Euler angles: θ_λ is the angle between $\mathbf{R}_\lambda$ and the axis $-\hat{Z}'$ and runs in the interval $[0,\pi]$; ϕ_λ is the angle from the $\hat{X}'$ axis to the projection of $\mathbf{R}_\lambda$ on the $X'Y'$ plane and runs in the interval $[0,2\pi]$. We thus define the vector Q of the generalized coordinates and the corresponding velocities $\dot{Q}$

$$Q=\{q_1,q_2,q_3,q_4,q_5,q_6\}=\{\theta_a,\phi_a,\theta_o,\phi_o,\theta_i,\phi_i\}. \tag{13}$$

With these definitions in hand, we have that

$$\hat{L}_a=\{\sin\theta_a\cos\phi_a,\ \sin\theta_a\sin\phi_a,-\cos\theta_a\}, \tag{14}$$

and similar expressions for $\hat{L}_o$ and $\hat{L}_i$. Equation (14) turns Eqs. (2) into expressions for the $\mathbf{R}_\lambda(Q)$ and the corresponding velocities $\mathbf{V}_\lambda=\dot{\mathbf{R}}_\lambda(Q,\dot{Q})$. We then conveniently write all the vectors in the $\{X'Y'Z'\}$ reference frame in terms of their components in the $\{\xi\eta\zeta\}$ frame by means of the rotation matrix $\mathcal{M}$ (Eq. (A2)), namely, $\mathbf{\Omega}_\lambda=\vec{\mathcal{M}}\mathbf{\Omega}_{\lambda,\xi\eta\zeta}$ and $\boldsymbol{\rho}_\lambda=\vec{\mathcal{M}}\boldsymbol{\rho}_{\lambda,\xi\eta\zeta}$.

After noting that $\mathbf{\Omega}_{\lambda,\xi\eta\zeta}=\{-\dot{\theta}_\lambda,\dot{\phi}_\lambda\sin\theta_\lambda,\omega_s\}$ and performing all the integrals over the three bodies, we finally obtain (Appendix A) the operative expression for $\mathcal{L}(Q,\dot{Q})$ in the rotating reference frame,

$$\mathcal{L}(Q,\dot{Q})=T(Q,\dot{Q})-U(Q), \tag{15}$$

where we have defined

$$T(Q,\dot{Q})\equiv T_{\rm kin}(Q,\dot{Q})+T_{\rm Cor}(Q,\dot{Q}), \tag{16}$$

$$U(Q)\equiv U_g(Q)+U_{\rm el}(Q)-U_{\rm Cor}(Q)-U_c(Q). \tag{17}$$

The terms entering (15) and (17) are

$$T_{\rm kin}=\frac{1}{2}\sum_\lambda[m_\lambda V_\lambda(Q,\dot{Q})^2+I_{\lambda\xi}(\dot{\phi}_\lambda^2\sin^2\theta_\lambda+\dot{\theta}_\lambda^2)],$$

$$T_{\rm Cor}=\sum_\lambda m_\lambda\mathbf{V}_\lambda(Q,\dot{Q})\cdot[\boldsymbol{\omega}_s\times\mathbf{R}_\lambda(Q)]+\sum_\lambda I_{\lambda\xi}\omega_s\dot{\phi}_\lambda\sin^2\theta_\lambda, \tag{18}$$

$$U_{\rm Cor}=-\sum_\lambda I_{\lambda\zeta}\omega_s^2\cos\theta_\lambda,$$

and

$$U_c=\frac{1}{2}\sum_\lambda m_\lambda[\boldsymbol{\omega}_s\times\mathbf{R}_\lambda(Q)]^2+\frac{1}{2}\sum_\lambda(I_{\lambda\xi}\sin^2\theta_\lambda+I_{\lambda\zeta}\cos^2\theta_\lambda)\omega_s^2. \tag{19}$$

To these equations we have to add the expressions (6) and (7) written in terms of $\mathbf{R}_\lambda(Q)$ through (2) and (14).

Equation (15) together with Eqs. (17)–(19) yield the Lagrange function of the model in Fig. 3.

C. Equilibrium positions and second-order expansion

During normal and successful operation of the GGG rotor only very small amplitude motions take place. The Lagrange function (15) can thus be expanded to second order in $(Q,\dot{Q})$ around the equilibrium solution $(Q^0,\dot{Q}=0)$, $Q^0=\{q_1^0,\ldots,q_6^0\}$ to derive linearized equations of motion.

In order to do this, we first determine the equilibrium positions from the equation

$$\left.\frac{\partial U}{\partial q_j}\right|_{q_j=q_j^0}=0,\quad j=1,\ldots,n. \tag{20}$$

We then use the physical assumption that during the motion, the Q's are slightly perturbed from their equilibrium values Q^0. This results in the substitutions

$$Q\to Q^0+Q, \tag{21}$$

$$\dot{Q}\to\dot{Q}, \tag{22}$$

into (15) to obtain a linearized version of the Lagrange function. $\mathcal{L}(Q,\dot{Q})$ can now be expanded to second order, namely,

$$\mathcal{L}(Q,\dot{Q}) = a_0 + \sum_{j<k}^{n} a_{jk} q_j q_k + \sum_{j<k}^{n} b_{jk} \dot{q}_j \dot{q}_k + \sum_{j,k=1}^{n} c_{jk} q_j \dot{q}_k + \sum_{j=1}^{n} d_j \dot{q}_j + O(q_j,\dot{q}_k)^4, \tag{23}$$

where we remark that now the q_j's are small according to the substitutions (21) and (22), and that the linear terms have canceled out because of (20). The matrix coefficients a_{jk}, b_{jk}, and c_{jk} are known functions of the Q^0 and of the governing parameters of the system and, in general, are to be numerically evaluated.

D. Linearized equations of motion

The equations of motion in terms of the known a_{jk}, b_{jk}, and c_{jk} coefficients are

$$\frac{d}{dt}\frac{\partial \mathcal{L}}{\partial \dot{q}_j} - \frac{\partial \mathcal{L}}{\partial q_j} = \mathcal{F}_j, \quad j = 1, \ldots, n, \tag{24}$$

where we have introduced the generalized forces

$$\mathcal{F}_j = \sum_{d=1}^{3} \mathbf{F}_{\lambda d} \frac{\partial \mathbf{R}_{\lambda d}}{\partial q_j}, \tag{25}$$

starting from the Cartesian components $\mathbf{F}_{\lambda d}$ of the forces acting on each body. The $\mathcal{F}_j$ are to be consistently expanded to first order, namely,

$$\mathcal{F}_j = \sum_{k=1}^{6} \alpha_{jk} q_k + \sum_{k=1}^{6} \beta_{jk} \dot{q}_k. \tag{26}$$

By combining Eqs. (23)–(26) together, the equations of motion can be written in a compact matrix form as

$$\mathbb{M}\ddot{Q} = \mathbb{S}\begin{pmatrix} Q \\ \dot{Q} \end{pmatrix}, \tag{27}$$

with the obvious notation $\ddot{Q} = \{\ddot{q}_1, \ldots, \ddot{q}_6\}$. In Eq. (27), $\mathbb{M}$ is the $n \times n (n=6)$ "mass-matrix" composed by the b_{jk} coefficients

$$\mathbb{M}_{jk} = 2b_{jk}\delta_{jk} + b_{jk}(1 - \delta_{jk}), \tag{28}$$

where the factor of 2 on the diagonal elements is a consequence of the restricted $j<k$ sum in the expansion (25). $\mathbb{S}$ is a $n \times 2n$ matrix containing the a_{jk}, c_{jk}, α_{jk}, and β_{jk} coefficients,

$$\mathbb{S} = \mathbb{A}_2 + \mathbb{C}_2 + \mathbb{A}_1 + \mathbb{B}_1, \tag{29}$$

with

$$\mathbb{A}_{2jk} = \mathbb{A}_{2kj} = 2a_{jk}\delta_{jk} + a_{jk}(1 - \delta_{jk}), \quad k \leqslant n$$
$$= 0, \qquad n < k \leqslant 2n, \tag{30}$$

$$\mathbb{C}_{2jk} = 0, \qquad k \leqslant n$$
$$= -\mathbb{C}_{2kj} = c_{jk} - c_{kj}, \quad n < k \leqslant 2n, \tag{31}$$

$$\mathbb{A}_{1jk} = \mathbb{A}_{1kj} = \alpha_{jk}, \quad k \leqslant n$$
$$= 0, \quad n < k \leqslant 2n, \tag{32}$$

and

$$\mathbb{B}_{1jk} = 0, \qquad k \leqslant n$$
$$= \mathbb{B}_{1kj} = \beta_{jk}, \quad n < k \leqslant 2n. \tag{33}$$

Note that while $\mathbb{M}$ and the submatrix defined by the first $n=6$ columns of $\mathbb{A}_2$ are symmetric, the submatrix defined by the second $n=6$ columns of $\mathbb{C}_2$ is antisymmetric, as expected after inspection of the expansion (23).

For all practical purposes, it is convenient to turn (27) into a more symmetric form involving only first-order time derivatives. To this aim, we define the $2n=12$-component vector X as

$$\begin{aligned} X_{2j-1} &= q_j, \\ X_{2j} &= \dot{q}_j, \end{aligned} \quad j = 1, \ldots, n = 6. \tag{34}$$

By inserting the definition (34) into (27), we finally obtain

$$\dot{X} = AX, \tag{35}$$

where A is now the square $2n \times 2n$ dynamical matrix defined from $\mathbb{M}^{-1}$ and $\mathbb{S}$ after inserting rows of zeros.

$$A_{jk}\begin{cases} (\mathbb{M}^{-1}\mathbb{S})_{j1+k-1/2}, & j \text{ even and } k \text{ odd} \\ (\mathbb{M}^{-1}\mathbb{S})_{j7+k-2/2}, & j \text{ even and } k \text{ even} \\ 1, & j \text{ odd and } k = j+1 \\ 0, & j \text{ odd and } k \neq j+1. \end{cases} \tag{36}$$

The relations (35) and (36) are central equations, written in a form amenable for numerical evaluation. The eigenvalues of the A matrix (36) correspond to the normal modes of the rotor and the solution of the set of differential equations (35) completely determines the small-amplitude dynamical behavior of the rotor modeled in Fig. 3. Before turning to the description of the numerical method, we introduce rotating and nonrotating dampings.

1. Rotating and nonrotating dampings

By means of (25) and (26) we can in principle introduce any known force determining the dynamical behavior of the rotor. In the following we include dissipative forces $\mathcal{R}_R$ and $\mathcal{R}_{\mathrm{NR}}$ due to rotating and nonrotating damping mechanisms respectively, (see Refs. 19 and 20). The rotating part of the dissipative force is to be ascribed to dissipation of the laminar suspensions. In supercritical rotation, this kind of dissipation is known to destabilize the system, generating whirl motions. It can be expressed as

$$\mathcal{R}_R(Q,\dot{Q}) = -\Gamma_{Ra}[\dot{\hat{L}}_a - (\dot{\hat{L}}_a \cdot \hat{Z}') \cdot \hat{Z}'] - \sum_{\lambda=o,i} \Gamma_{R\lambda}[\dot{\hat{L}}_\lambda - (\dot{\hat{L}}_\lambda \cdot \hat{R}_a(Q)\ ][\hat{R}_a(Q)], \tag{37}$$

where the velocities $\dot{\hat{L}}_\lambda$ are functions of $(Q,\dot{Q})$. Instead, nonrotating damping has the effect of stabilizing a system in supercritical rotation and can be written as

$$\mathcal{R}_{\mathrm{NR}}(Q,\dot{Q}) = -\Gamma_{\mathrm{NR}}[\mathbf{V}_i(Q,\dot{Q}) + \boldsymbol{\omega}_s \times \mathbf{R}_i(Q)]. \tag{38}$$

Other forces acting on the rotor, such as external disturbances due—for instance—to tides and seismic noise, or control forces applied in order to control the rotor dynamics, can also be included, as described in Sec. IV.

IV. THE NUMERICAL METHOD

A. General considerations

The simulation method that we have implemented rigorously follows the derivation outlined in Sec. III. We have found very convenient to use the MATLAB environment, with SYMBOLIC TOOLBOX and SIMULINK packages, as it allows us to perform all the needed symbolic calculations and numerical evaluations, together with the analysis of experimental data.

We start from the formal Lagrange function written in a user-friendly way as in (3)–(7) and (10)–(12) by means of symbolic vector operations. We specify the choice (13) for the generalized coordinates with respect to the $\{X'Y'Z'\}$ reference frame and define accordingly all the vectors entering $\mathcal{L}$. We then move on to the symbolic computation by linearizing and expanding the Lagrange function as in (23) and define the matrices $\mathbb{M}$, $\mathbb{A}_2$, $\mathbb{C}_2$, $\mathbb{A}_1$, $\mathbb{B}_1$, and A.

Once the system parameters are fixed (see below), the numerical computation is carried out using standard packages to find eigenvalues and eigenvectors of the A matrix, which are the normal frequencies and modes of the spinning rotor. The A matrix is then inserted as input to perform the dynamical simulation within standard transfer-function method used in the SIMULINK toolbox.

The advantage of this strategy is apparent, in that it easily allows us to make any changes in the model that correspond to changes in the experiment we would like to test before implementation. Since the number of bodies n_b and of the generalized coordinates n are symbolically defined and specified only once, all what is to be done in order to introduce any changes or new features amounts to modification or addition of pieces of the Lagrangian after having symbolically written them in terms of vector operations.

The description of the method used to introduce external forces is postponed to Part II of this work, where it is used to evaluate the common mode rejection function. We now turn to listing the system parameters.

B. System parameters

The parameters which govern the physics of the GGG rotor are the geometrical dimensions of the three bodies, their weight, the mounting error ϵ, the elastic constants, length and anisotropy factor Λ of the three laminar suspensions, and the quality factor $\mathcal{Q}$. To these parameters—which are fixed after construction—we must add the spin frequency $\nu_s=\omega_s/2\pi$ that can be varied in the course of the experiment. The balancing of the beams and the natural period T_D of oscillation of the test cylinders relative to one another can also be adjusted, as discussed earlier by moving small masses along the balance (coupling) arm.

We have inserted as inputs to the numerical calculation all the above parameters as determined in the real GGG instrument. They are listed in Tables I and II. As for the spin frequency, in the experiment it varies in the range $(0 \leqslant \nu_s \leqslant 3.9)$ Hz, while in the model calculations it can be assumed in a wider range $(0 \leqslant \nu_s \leqslant 10)$ Hz.

TABLE I. Input parameters for the numerical calculations: geometrical dimensions of the real bodies. (A mounting error of $\epsilon=20$ μm has also been used.)

Body	m_λ (kg)	$R_{\lambda I}$ (cm)	$R_{\lambda E}$ (cm)	L_λ (cm)	$R_{\lambda H}$ (cm)
Arm (a)	0.3	3.3	3.5	19 ($\Delta L=-0.1353$)	$2L_a+\Delta L$
Outer cyl. (o)	10	12.1	13.1	$2L_a+L_i+\Delta L$	29.8
Inner cyl. (i)	10	8.0	10.9	4.5	21.0

The differential periods T_D corresponding to the value ΔL listed in Table I are measured to be 11.7 and 10.8 s in the X and Y directions, respectively. These values are in reasonable agreement with the following simple formula:

$$T_D = \frac{2\pi}{\sqrt{(K+K_i+K_o)l^2/(m_i+m_o)L_a^2 - (g/2L_a)(\Delta L/L_a)}}, \tag{39}$$

which can be derived from the general equations of motion (24) describing the small oscillations of the θ_λ angles, in the very simplified case in which the bodies are neither rotating nor subjected to any dissipative or other external forces, except gravity, and under the reasonable assumption that $\theta_i=\theta_o=0$ and that ϕ_λ's are constant, e.g., $\phi_\lambda=0$.

Of the whole set of parameters used, only the anisotropy factor Λ of the suspensions and the construction and mounting error ϵ are not measured from the instrument. Λ is tuned, together with the balancing ΔL, so as to reproduce the natural frequencies of the nonspinning instrument. A conservative value $\epsilon=20$ μm is assumed for the offset, and it is checked *a posteriori* not to have any sizable effect on these results.

V. RESULTS: THE NORMAL MODES

We have solved for the eigenvalues ν_n of the matrix A in (35), using the system parameters listed in Sec. IV B.

Figure 4 summarizes our results by plotting the normal modes of the system (ν_n in the nonrotating frame) as functions of the spin frequency $\nu_s=\omega_s/2\pi$ of the rotor. In this figure, theoretical results for $\nu_n(\nu_s)$'s are displayed by the solid lines in the case of zero rotating damping (i.e., no dissipation in the suspensions) and by the open circles in the case of nonzero rotating damping $[\mathcal{Q}(\nu_s)=510]$. At zero damping there are 12 lines, 6 horizontal and 6 inclined; start-

TABLE II. Input parameters for the numerical calculations: laminar suspensions data. In addition, a conservative value $\mathcal{Q}(\nu_s)=510$ has been used taken from previous measurements of whirl growth (Ref. 14, Fig. 7).

Suspension	l (cm)	K (dyn/cm)	Anisotropy ($\Lambda=K_{Y'}/K_{X'}$)
Central	0.5	$10^6(l/L_a)^2$	2.6
Outer cyl. (o)	0.5	10^6	1.0
Inner cyl. (i)	0.5	10^6	1.0

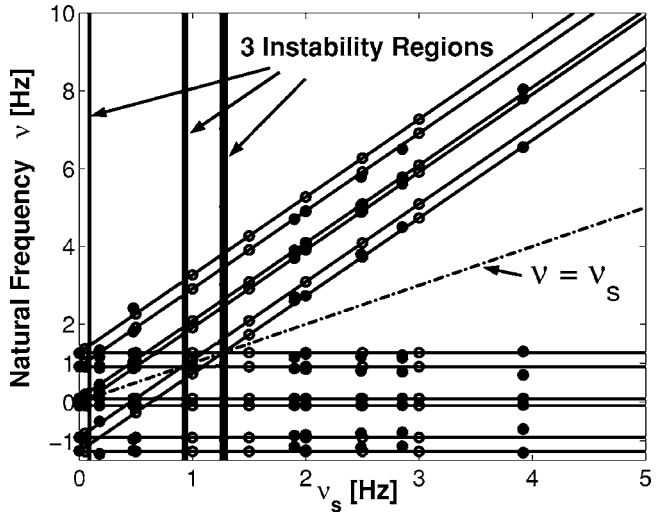

FIG. 4. Normal modes of the GGG rotor: the frequencies of the normal modes are plotted as functions of the spin frequency ν_s. The normal modes as predicted theoretically assuming anisotropic suspensions are shown as 12 solid lines in the case of zero rotating damping and as open circles in the case of nonzero damping (see text). The experimental results are plotted as filled circles and clearly agree with the theoretical predictions. The bisecting dot-dashed line $\nu=\nu_s$ separates the supercritical ($\nu_s>\nu$) from the subcritical ($\nu_s<\nu$) region. Three vertical thick lines are plotted in correspondence of three instability regions, their thickness referring to the width of the regions (see Sec. V G).

ing from the three natural frequencies (Sec. II C 2) of the system, we get $3\times2\times2=12$ normal mode lines, a factor of 2 being due to anisotropy of the suspensions in the two orthogonal directions of the plane, and the other to the positive and negative signs (i.e., counterclockwise or clockwise whirl motion). For the nonzero damping case (open circles) a conservative low value $\mathcal{Q}(\nu_s)=510$ has been assumed (see Table II), referring to a comparatively large dissipation. This value has been obtained from previous not so favorable measurements of whirl growth, while much higher $\mathcal{Q}$ values (namely, much smaller dissipations) are expected (see discussion on this issue in Ref. [15], Sec. III). In Fig. 4, to be compared with the above theoretical results, we plot, as filled circles, the experimental results too, finding an excellent agreement between theory and experiments. Since Fig. 4 contains the crucial results of this work, it is worth discussing its main features in detail. The main features are the comparison with the experiment, the role of damping, the behavior at low spin frequencies, the so-called scissors's shape, the splitting of the normal modes, and the presence of three instability regions.

A. Comparison with the experiment

In the experiment, the rotor is first accelerated to spin at a given frequency ν_s. Then, the natural modes are excited by means of capacitance actuators (indicated as OP in Fig. 1) in the X' or Y' directions at frequencies close to the natural frequencies $\nu_n^0\equiv\nu_n(\nu_s=0)$ of the system at zero spin. The excitation is performed for several (typically ten) fundamental cycles $1/\nu_n^0$ by means of voltages applied to four of the eight outer plates (OP in Fig. 1). The actuators are then switched off and the bodies's displacements are recorded as functions of time by means of the readout described in Sec. II B. A standard data analysis is then performed by fitting the measurement data to extract oscillation frequencies and damping of the modes.

The experimental data, resulting from averaging over several measurements, are represented as filled circles in Fig. 4. The agreement between theory and experiments is excellent, thus validating the model developed in Sec. III.

In the experimental spectra as well as in the theory, it is found that the amplitudes of the modes in the subcritical region $\nu_s<\nu$—represented by the inclined lines, with their open and filled circles—are quite small, while the nondispersive modes (the horizontal lines, not varying with the spin frequency) are preferably excited. When the horizontal lines cross the inclined ones, the latter modes can also be excited. Since the excited modes must obviously be avoided in operating the experiment, this information is very useful, in that it is telling us that we should avoid to spin the system at frequencies where these line crossings occur. Even more so, spin frequencies lying in the instability regions must be avoided (see Sec. V G).

B. Role of damping

We have numerically checked that the dissipation present in the system does not significantly shift the natural mode frequencies. This is apparent in Fig. 4, where the results obtained with damping (open circles) stay on the solid lines obtained in the absence of damping. It is worth stressing that this result is especially good because, as discussed above, we have used a low value $\mathcal{Q}(\nu_s)=510$, corresponding to comparatively large dissipations. As expected, the dissipation affects the line shape of the peaks, making them wider than in the absence of damping.

C. Low-frequency limit

At zero spin frequency we have recovered the theoretical and experimental results previously obtained for the nonrotating system. On the left hand side of Fig. 5, a zoom from Fig. 4 at very low spin frequencies, we can see that the nonspinning rotor is characterized by three natural frequencies for the instrument with ideally isotropic springs, the three bodies oscillating in a vertical plane. The frequency $\nu^0=0.09$ Hz corresponds to the differential mode, where the centers of mass of the two test bodies oscillate in opposition of phase; the frequencies $\nu^0=0.91$ Hz and $\nu^0=1.26$ Hz correspond to common modes, in which the common center of mass of the two test bodies is displaced from the vertical. During rotation, the number of degrees of freedom increases to six, as discussed in Sec. III B, leading to the six lines plotted in the same figure.

We may get a flavor of the ν_s dependence of the modes in the $\nu_s\ll\nu_n$ limit, by evaluating the natural frequencies of only one spinning cylinder with mass m and moments of inertia I_ξ and I_ζ. The cylinder is suspended at distance L and with offset ϵ from a fixed frame by means of a cardanic suspension with isotropic elastic constant K and length l. The calculation is performed by following the steps outlined in

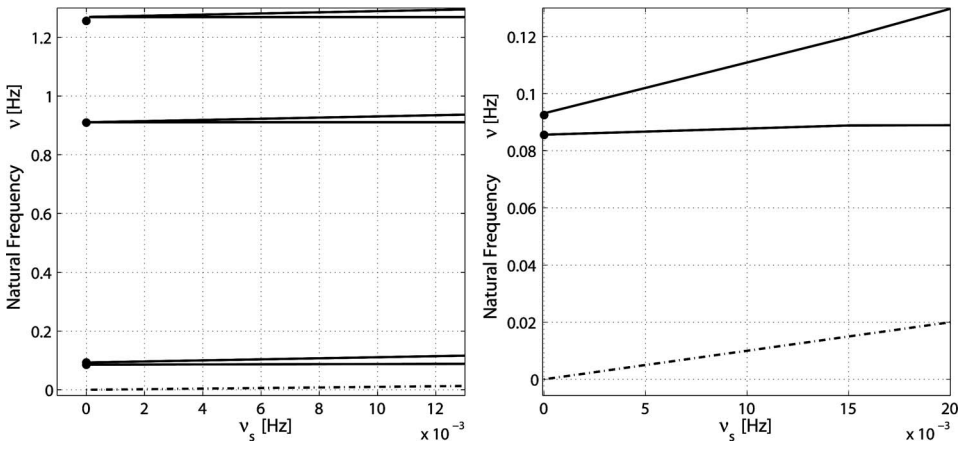

FIG. 5. Normal modes of the GGG rotor. On the left hand side we show a zoom from Fig. 4 in the very low spin frequency region, showing, in particular, the three-natural frequencies of the system in the zero spin case. On the right hand side, we plot a zoom from Fig. 4 in the small frequency region of both axes, showing the splitting into two lines of the low frequency mode because of anisotropy of the suspensions (the dashed line is the $\nu_s=\nu$ line as in Fig. 4).

Sec. III with $n_b=1$ and thus $n=4$. After evaluating the A matrix [Appendix B, see Eq. (B10)] and solving $\det(A-sI)=0$, we obtain the two double solutions

$$\nu_{n1,2,3,4}=\pm\tilde{\nu}_n^0\frac{L}{L'}, \tag{40}$$

for the four $\nu_n(\nu_s/\nu_n\to 0)$ in the nonrotating frame. In Eq. (40), $\tilde{\nu}_n^0=(2\pi)^{-1}\sqrt{g/L+Kl^2/mL^2}$ is the natural frequency for the nonspinning pointlike mass. $L'=\sqrt{L^2+(I_\xi-2I_\zeta)/m}$ (with $I_\zeta<0.5mL^2+I_\xi$, see Appendix B) takes into account the extended nature of the body and the ratio L/L' modifies ν_n with respect to $\tilde{\nu}_n^0$.

D. Anisotropy

If the suspensions are not isotropic in the two orthogonal directions, as it is indeed the case for our real cardanic suspensions, each natural frequency is expected to split up. This is clearly shown on the right hand side of Fig. 5. It is worth noting that the splitting is larger for the lowest-frequency mode.

E. Scissors's shape

Figure 4 shows that each natural frequency of the nonspinning system splits up into two branches at $\nu_s>0$, a lower branch remaining approximately constant and an upper branch increasing with $2\nu_s$.

This characteristic scissors's shape can be traced back to the general properties of spinning bodies (see also Part II). We again use the one-cylinder simple case (see Appendix B) to prove this statement. By following the same procedure which has led to Eq. (40) we obtain [see Eq. (B9)]

$$\nu_{1,2}=\pm\sqrt{\nu_s^2-2\nu_n\nu_s\frac{L}{L'}}\simeq\pm\nu_s\left(1-\frac{\nu_n}{\nu_s}\frac{L}{L'}\right), \tag{41}$$

$$\nu_{3,4}=\pm\sqrt{\nu_s^2+2\nu_n\nu_s\frac{L}{L'}}\simeq\pm\nu_s\left(1+\frac{\nu_n}{\nu_s}\frac{L}{L'}\right), \tag{42}$$

showing that in the rotating frame $\nu_n\propto\nu_s$ to zeroth order. After taking the $\nu_s/\nu_n\to\infty$ limit and tranforming back to the nonrotating frame by means of the substitution $s_n=2\pi i\nu_n\to 2\pi(i\nu_n+i\nu_s)$, we finally have

$$\nu_{1,3}\simeq\pm\nu_n\frac{L}{L'}, \tag{43}$$

$$\nu_{2,4}\simeq 2\nu_s. \tag{44}$$

F. Mode splitting

The two branches may cross at selected frequencies. Crossing and anticrossing of degenerate modes are a very general concept, which applies to a variety of physical systems, from classical to quantum mechanics, from single to many-particle physics. As it is well known,[24] splitting of the modes is expected in correspondence of such crossings. In our numerical results we have found all the 15 splittings expected for our system (see Fig. 4). Figure 6 shows a particular case of anticrossing of two modes.

G. Instability regions

Dynamical instability may occur whenever the values of the natural frequencies are in proximity of the spin frequency. In such regions the oscillation amplitude grows exponentially.

This is a well-known characteristic of rotating machines; in engineering books it is usually described within the simple model of the so-called Jeffcott rotor.[21] The number of instability regions can be predicted from Fig. 4 after drawing the dotted-dashed line $\nu=\nu_s$. We have found indeed three insta-

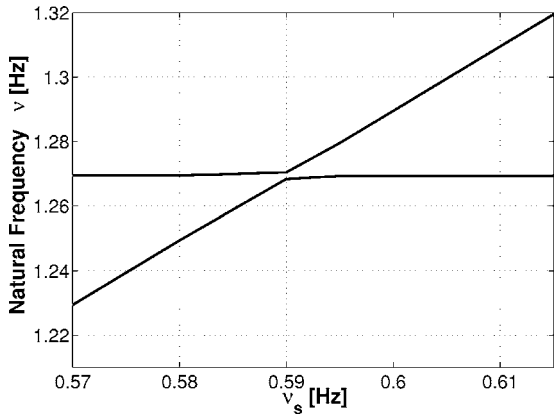

FIG. 6. Normal modes of the GGG rotor. A zoom from Fig. 4 showing one particular case of anticrossing of two modes.

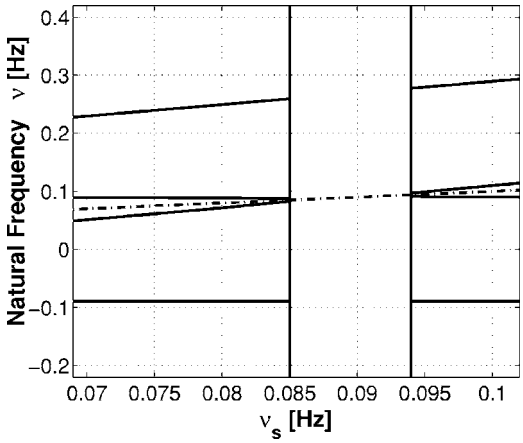

FIG. 7. Normal modes of the GGG rotor. The lowest-frequency instability region is zoomed in from Fig. 4.

bility regions. Figure 7 displays in detail the one at the lowest frequency; as shown in Fig. 4, the two at higher frequencies are found to be wider and closer to each other. These theoretical results do explain why in the experiment we can increase the spin frequency and cross the low-frequency instability region easily, while it is much more difficult to cross the frequency range $0.9 \rightarrow 1.3$ Hz. In the past we solved this problem by designing and installing passive dampers to be switched on from remote just before resonance crossing, and then turned off at higher spin frequencies; the least noisy was a special, no oil damper described in Ref. 25, p. 45. Later on the GGG rotor imperfections have been reduced so that all instability regions can now be crossed, if the crossing is sufficiently fast, without producing any relevant disturbances even in absence of a passive damper. The physical space previously occupied in the vacuum chamber by the passive damper is now used for the inductive power coupler, indicated as PC in Fig. 1, which provides the necessary power to the rotating electronics and has allowed us to avoid noisy sliding contacts.

VI. CONCLUDING REMARKS

We have demonstrated that the linearized model set up in Sec. III can quantitatively account for the dynamical response of the GGG rotor, an apparatus designed to test the equivalence principle with fast rotating, weakly coupled, macroscopic, concentric cylinders (Sec. II). The model developed here can be expanded to include external disturbances whose effects need to be taken into account in testing the equivalence principle. A qualitative understanding has been provided, by means of helpful analytical solutions of the simplified model under special limits, of relevant features observed in the simulations as well as in the experimental data.

We have acquired a detailed knowledge of the instrument's features and the way it works, the main feature being the normal modes of the system (Sec. V) in the whole range of spin frequencies, from subcritical to supercritical regime, and as functions of the governing parameters (see Sec. IV B).

In particular, we have established the location and characteristics of the instability regions; we have verified quantitatively the effects of dissipation in the system, showing that losses can be dealt with and are not a matter of concern for the experiment; we have established the split up of the normal modes into two scissorlike branches, distinguishing modes which are preferentially excited (the horizontal lines) from those whose spectral amplitudes are typically small (the inclined lines), thus learning how to avoid the spin frequencies corresponding to their crossings, in order not to excite the quiet modes too by exchange of energy; we have investigated the self-centering characteristic of the GGG rotor when in the supercritical rotation regime, gaining insight on how to exploit this very important physical property for improving the quality of the rotor, hence its sensitivity as a differential accelerometer.

In the following Part II of this work we apply the same model and methods developed here to investigate the common mode rejection behavior of the GGG rotor, a crucial feature of this instrument devoted to detect extremely small differential effects.

ACKNOWLEDGMENT

Thanks are due to INFN for funding the GGG experiment in its Laboratory of San Piero a Grado in Pisa.

APPENDIX A: THE LAGRANGE FUNCTION IN THE ROTATING REFERENCE FRAME

In the following, in order to simplify the notation we drop the λ indices everywhere and restrict our reasoning to only one body. Let us begin with the expression (4). After using Eq. (8) into (4), we have

$$\mathcal{T} = \frac{1}{2}\int_{\tau_i} [\mathbf{V}^2 + (\boldsymbol{\Omega} \times \boldsymbol{\rho})^2 + 2\mathbf{V} \cdot (\boldsymbol{\Omega} \times \boldsymbol{\rho})] dm. \tag{A1}$$

We conveniently represent the vectors $\boldsymbol{\Omega} = \overleftrightarrow{\mathcal{M}} \boldsymbol{\Omega}_{\xi\eta\zeta}$ and $\boldsymbol{\rho} = \overleftrightarrow{\mathcal{M}} \boldsymbol{\rho}_{\xi\eta\zeta}$ in the $\{\xi\eta\zeta\}$ frame by means of the rotation matrix

$$\overleftrightarrow{\mathcal{M}} = \begin{pmatrix} \sin\phi & \cos\theta\cos\phi & -\sin\theta\cos\phi \\ -\cos\phi & \cos\theta\sin\phi & -\sin\theta\sin\phi \\ 0 & \sin\theta & \cos\theta \end{pmatrix}, \tag{A2}$$

with respect to the $\{X'Y'Z'\}$ reference system.

Thus, by exploiting the properties of the vectorial product and the definition of center of mass, namely, $\int_{\tau_i} \rho_\xi = \int_{\tau_i} \rho_\eta = \int_{\tau_i} \rho_\zeta = 0$, we find the following results for the integrals appearing in Eq. (A1):

$$\frac{1}{2}\int_{\tau_i} \mathbf{V}^2 dm = \frac{1}{2} m \mathbf{V}^2,$$

$$\frac{1}{2}\int_{\tau_i} (\boldsymbol{\Omega} \times \boldsymbol{\rho})^2 dm = \frac{1}{2}\sum_\alpha I_{\alpha\alpha}\Omega_\alpha^2,$$

$$\frac{1}{2}\sum_\alpha I_{\alpha\alpha}\Omega_\alpha^2 = \frac{1}{2} I_\xi (\dot{\phi}^2 \sin^2\theta + \dot{\theta}^2),$$

$$\int_{\tau_i} \mathbf{V}\cdot(\boldsymbol{\Omega}\times\boldsymbol{\rho})dm = (\mathbf{V}\times\boldsymbol{\Omega})\cdot\int_{\tau_i}\boldsymbol{\rho}dm = 0,$$

$$\int_{\tau_i} \mathbf{V}\cdot(\boldsymbol{\omega}_s\times\mathbf{R})dm = m\mathbf{V}\cdot(\boldsymbol{\omega}_s\times\mathbf{R}),$$

$$\int_{\tau_i} \mathbf{V}\cdot(\boldsymbol{\omega}_s\times\boldsymbol{\rho})dm = (\mathbf{V}\times\boldsymbol{\omega}_s)\cdot\int_{\tau_i}\boldsymbol{\rho}dm = 0,$$

$$\int_{\tau_i} (\boldsymbol{\Omega}\times\boldsymbol{\rho})\cdot(\boldsymbol{\omega}_s\times\mathbf{R})dm = (\boldsymbol{\omega}_s\times\mathbf{R})\cdot\int_{\tau_i}(\boldsymbol{\Omega}\times\boldsymbol{\rho}) = 0,$$

$$\int_{\tau_i} (\boldsymbol{\Omega}\times\boldsymbol{\rho})\cdot(\boldsymbol{\omega}_s\times\boldsymbol{\rho})dm = I_\xi\omega_s\dot{\phi}\sin^2\theta + I_\zeta\omega_s^2\cos\theta,$$

$$\frac{1}{2}\int_{\tau_i} (\boldsymbol{\omega}_s\times\mathbf{R})^2 dm = \frac{1}{2}m(\boldsymbol{\omega}_s\times\mathbf{R})^2,$$

$$\frac{1}{2}\int_{\tau_i} (\boldsymbol{\omega}_s\times\boldsymbol{\rho})^2 dm = \frac{1}{2}[I_\xi\sin^2\theta + I_\zeta\cos^2\theta]\omega_s^2,$$

$$\int_{\tau_i} (\boldsymbol{\omega}_s\times\mathbf{R})\cdot(\boldsymbol{\omega}_s\times\boldsymbol{\rho})dm = (\boldsymbol{\omega}_s\times\mathbf{R})\cdot\int_{\tau_i}(\boldsymbol{\omega}_s\times\boldsymbol{\rho})dm = 0.$$

By collecting all these results, one ends up with the final forms (17)–(19) for the original $\mathcal{T}$ function (4).

APPENDIX B: THE ONE-CYLINDER SOLUTION

It is useful to study (along the lines of Sec. III) the simplified case of only one spinning cylinder with mass m and moments of inertia I_ξ and I_ζ. This amounts to setting $n_b=1$ and thus $n=4$ for the number of generalized coordinates.

The A matrix turns out to be

$$A = \begin{pmatrix} 0 & 1 & 0 & 0 \\ \mathcal{L}_{11}/\mathcal{L}_{22} & \mathcal{R}_{12}/\mathcal{L}_{22} & \mathcal{R}_{13}/\mathcal{L}_{22} & (\mathcal{L}_{14}-\mathcal{L}_{23})/\mathcal{L}_{22} \\ 0 & 0 & 0 & 1 \\ \mathcal{Q}_{31}/\mathcal{L}_{44} & (\mathcal{L}_{23}-\mathcal{L}_{14})/\mathcal{L}_{44} & \mathcal{L}_{33}/\mathcal{L}_{44} & \mathcal{R}_{34}/\mathcal{L}_{44} \end{pmatrix}, \tag{B1}$$

where the coefficients of $\mathcal{L}$ and $\mathcal{R}$ are defined in terms of the system parameters and of the equilibrium positions θ_0 and ϕ_0 as

$$\mathcal{L}_{11} = m\omega_s^2 L(L\cos 2\theta_0 + \epsilon\sin\theta_0) - mgL\cos\theta_0 - Kl^2\cos 2\theta_0 + (I_\xi - I_\zeta)\omega_s^2\cos 2\theta_0 - I_\zeta\omega_s^2\cos\theta_0, \tag{B2}$$

$$\mathcal{L}_{22} = mL^2 + I_\xi,$$

$$\mathcal{L}_{33} = m\omega_s^2\epsilon L\sin\theta_0,$$

$$\mathcal{L}_{44} = (mL^2 + I_\xi)\sin^2\theta_0, \tag{B3}$$

$$\mathcal{L}_{14} = \mathcal{L}_{41} = I_\zeta\omega_s\sin 2\theta_0 - m\omega_s\epsilon L\cos\theta_0 + m\omega_s^2 L^2\sin 2\theta_0,$$

$$\mathcal{L}_{23} = \mathcal{L}_{32} = -m\omega_s\epsilon L\cos\theta_0,$$

and

$$\mathcal{R}_{12} = -(\Gamma_R + \Gamma_{\mathrm{NR}})L^2,$$

$$\mathcal{R}_{13} = -\Gamma_{\mathrm{NR}}\omega_s L\epsilon\cos\theta_0, \tag{B4}$$

$$\mathcal{R}_{31} = -\Gamma_{\mathrm{NR}}\omega_s L(L\sin 2\theta_0 + \epsilon)$$

$$\mathcal{R}_{34} = -(\Gamma_R + \Gamma_{\mathrm{NR}})L^2\sin^2\theta_0. \tag{B5}$$

In the case of negligible dissipation, the eigenvalue equation $\det(A-sI)$ for $s=2\pi i\nu$ reads

$$s^4 - s^2(a_{21} + a_{43} + a_{24}a_{42}) + a_{21}a_{43} = 0. \tag{B6}$$

In the $\omega_s \gg \omega_n$ limit, the equilibrium solutions are

$$\theta_0 \simeq \frac{\epsilon L}{L'^2}\left[1 + \left(\frac{L}{L'}\right)^2\left(\frac{\tilde{\omega}_n^0}{\omega_s}\right)^2\right], \quad \phi_0 = 0, \tag{B7}$$

where $L' = \sqrt{L^2 + (I_\xi - 2I_\zeta)/m}$, $I_\zeta < 0.5mL^2 + I_\xi$, and

$$\tilde{\omega}_n^0 = \sqrt{\frac{g}{L} + \frac{Kl^2}{mL^2}} \tag{B8}$$

is the natural frequency of the pointlike mass. Equation (B6) becomes then

$$s^4 + 2s^2\omega_s^2\left[1 + \left(\frac{\omega_n^0}{\omega_s}\right)^2\right] + \omega_s^4\left[1 - 2\left(\frac{\omega_n^0}{\omega_s}\right)^2\right] = 0, \tag{B9}$$

where we have defined the natural frequency of the cylinder mass as $\omega_n^0 \equiv (L/L')\tilde{\omega}_n^0$.

In the $\omega_s \ll \omega_n$ limit, the eigenvalue equation becomes instead

$$s^4 + 2s^2\left(\frac{L}{L'}\right)^2\tilde{\omega}_n^{02} + \left(\frac{L}{L'}\right)^4\tilde{\omega}_n^{04} = 0. \tag{B10}$$

Equations (B9) and (B10) are used to derive the results (40)–(44) in the main text.

APPENDIX C: THE SELF-CENTERING

This appendix is devoted to a key feature of the GGG experiment, namely, the concept of self-centering of the rotor in supercritical rotation. Let us analyze the one-cylinder case, by numerically integrating the equations of motion in the presence of nonrotating damping, to make the rotor asymptotically stable (Sec. III D 1). Figure 8 shows the resulting motion of the cylinder in the horizontal plane of the rotating reference frame: its center-of-mass spirals inward towards an equilibrium position much closer to the origin, i.e., to the rotation axis. The equilibrium position always lies in the same direction as the initial offset vector $\boldsymbol{\epsilon}$, which in this simulation was assumed to be in the X' direction. The center of mass of the cylinder will eventually perform small-amplitude oscillations around the asymptotic value $\{X_0' = \epsilon - L\sin\theta_0, Y_0' = 0\}$.

In the limit of small angles we obtain

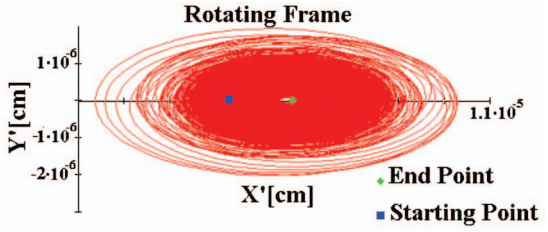

FIG. 8. (Color) Self-centering of one cylinder in the presence of nonrotating damping. Simulated $X'(t)$-$Y'(t)$ plot showing the motion of the center of mass of the cylinder in the rotating reference frame (one cylinder model, ν_s=5 Hz). The center of mass spirals inward from the initial offset value and large initial oscillations to a final value, much closer to the rotation axis.

$$\theta_0 \simeq \pm \frac{\epsilon}{L}\left[\frac{1}{(L'/L)^2-(\omega_n/\omega_s)^2}\right], \tag{C1}$$

with

$$\phi_0 = 0(\pi), \tag{C2}$$

in the case of the lower (upper) sign in Eq. (C1), respectively (angles defined as in Fig. 3). The cylinder's center of mass is eventually located at a distance

$$\Delta X \simeq \epsilon \pm L\theta_0 = \epsilon - \left[\frac{\epsilon}{(L'/L)^2-(\omega_n/\omega_s)^2}\right], \tag{C3}$$

from the rotation axis.

In Fig. 9 we plot, as function of the spin frequency ν_s, the self-centering distance ΔX in the one-cylinder case discussed above and in the point masss case. According to the previous appendix, if $L' \neq L$ we have the cylinder, while if $L=L'$ we have the point mass. The two curves are worth comparing. They have a similar behavior till the resonance peak (in this case, at about $\nu_s \approx 1$ Hz); the distance from the rotation axis remains constant till, at spin frequencies slightly below the natural one, it starts increasing showing a typical peak at the resonance. For the cylinder and the point mass

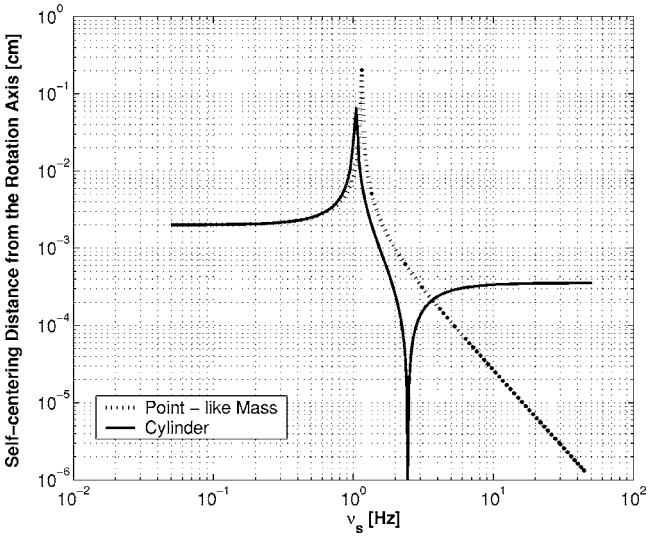

FIG. 9. Self-centering of one cylinder in the presence of nonrotating damping. The distance ΔX of the center of mass of the cylinder from the rotation axis is plotted as function of the spin frequency ν_s, in agreement with Eq. (C3). The same distance in the case of a point mass is plotted as a dashed line. See text for comments on their comparison.

the peaks are slightly shifted. The constant value can be obtained from Eq. (C3) in the limit of small spin frequencies $\omega_s \ll \omega_n$, finding

$$\Delta X \simeq \epsilon. \tag{C4}$$

We can also recover the position and relative shift of the resonance peaks in the two cases from the values ν_s^p (the spin frequency at the peak) taken by the poles of ΔX in Eq. (C3), namely,

$$\nu_s^p = \pm \frac{L}{L'}\nu_n. \tag{C5}$$

Thus, the position of the peaks is dictated by the natural frequency ν_n, while the shift is due to the difference between L and L'.

At rotation speeds above the resonance and in the highly supercritical regime $\omega_s \gg \omega_n$, the behavior of the cylinder and that of the point mass are remarkably different.

For the cylinder, ΔX drops to a minimum and then saturates at a constant value, while for the point mass it keeps decreasing monotonically. The minimum for the cylinder is related to the presence of a zero in Eq. (C3), namely,

$$\nu_s^z = \pm \frac{L}{\sqrt{L'^2-L^2}}\nu_n, \tag{C6}$$

which is valid only if $L' > L$. Instead, for the point mass we have the finite value $\Delta X = \epsilon/(1-\omega_s^2/\omega_n^2)$. Note that the position of the minimum shifts towards higher spin frequencies as $L' \to L$, namely, as the finite cylinder case approaches a point mass. In the limit $\omega_s \gg \omega_n$ (i.e., highly supercritical speeds) Eq. (C3) yields

$$\Delta X \simeq \epsilon\left[1-\left(\frac{L}{L'}\right)^2\right], \tag{C7}$$

which explains the saturation to a constant self-centering value in the case of a finite cylinder, whereas a point mass would monotonically approach perfect centering (i.e., $\Delta X = 0$).

In fact, it is very interesting to note that ΔX depends slightly on the point that we are considering along the cylinder's axis. In particular, in the limit $\omega_s \to \infty$, where ΔX of the cylinder's center of mass saturates, the point at distance $\tilde{L} = L'^2/L$ from the suspension point along the axis has instead perfect self-centering, namely, $\Delta X = 0$. This is easily seen from Eq. (C3) after substituting $\epsilon \pm L\theta_0$ with $\epsilon \pm \tilde{L}\theta_0$ and imposing $\Delta X = 0$. We plan to exploit this property in order to obtain better self-centering, though it needs further investigation in the actual GGG rotor.

We can consider a plot similar to that of Fig. 9 in the GGG case with two concentric cylinders and a coupling arm, where there are three natural frequencies (one differential and two common modes).

It happens that the common mode behavior is similar to that of the one-cylinder case (shown as a solid line in Fig. 9); namely, for each common mode frequency there is a resonance peak and a minimum peak. Instead, the differential frequency behavior is similar to that of a point mass (shown as a dashed line in Fig. 9). This latter fact is because in the

differential mode the coupling arm oscillates and the cylinders's centers of mass move in the horizontal plane with the opposite phase, while $\theta_{i,o}=0$; under these conditions, their moment of inertia is irrelevant in determining the dynamics, which therefore is very much alike the case of a point mass. As a result, the ΔX of the GGG rotor for intermediate values of the spin frequency is characterized by one peak at low frequency, in correspondence to the differential mode, and two peaks and two minima, in correspondence to the common modes. Instead, in the limit of very low and very high spin frequencies, it has a behavior similar to that displayed in Fig. 9, depending on the values and directions assumed for the initial offsets of the three bodies.

Thus, in order to obtain the best possible centering of the test cylinders in the GGG rotor, one can either spin at a frequency close to the minima of the common modes, or above both of them, in such a condition that the two cylinders are better centered on their own rotation axes than both of them are, together, in a common mode. Self-centering on the rotation axes is very important in order to reduce rotation noise, because we are dealing with rapidly spinning macroscopic bodies and aiming at measuring extremely small effects. The issue therefore needs a careful investigation, and to this end realistic numerical simulations of the apparatus are an essential tool.

Finally, concerning the use of supercritical rotors for EP testing, it is worth mentioning a frequently asked question: Would a relative displacement of the test bodies caused by an external force—such as that resulting from an EP violation—be reduced by self-centering in supercritical rotation as it happens for the original offset ϵ? The answer is "no" because the offset vector is fixed in the rotating frame of the system, while an external force gives rise to a displacement of the equilibrium position of the bodies in the nonrotating reference frame. In the presence of such a force, whirl motion will take place around the displaced position of equilibrium. A numerical simulation, showing this important feature is reported and discussed in Ref. 11, PLA paper, p. 176.

[1] R. V. Eötvös, D. Pekar, and E. Fekete, Ann. Phys. (N.Y.) **68**, 11 (1922).
[2] P. G. Roll, R. Krotov, and R. H. Dicke, Ann. Phys. (N.Y.) **26**, 442 (1964).
[3] V. B. Braginsky and V. I. Panov, Sov. Phys. JETP **34**, 463 (1972).
[4] Y. Su *et al.*, Phys. Rev. D **50**, 3614 (1994).
[5] S. Baebler, B. R. Heckel, E. G. Adelberger, J. H. Gundlach, U. Schimidt, and H. E. Swanson, Phys. Rev. Lett. **83**, 3585 (1999).
[6] T. Damour and A. M. Polyakov, Nucl. Phys. B **423**, 532 (1994); Gen. Relativ. Gravit. **26**, 1171 (1994).
[7] E. Fischbach, D. E. Krause, C. Talmadge, and D. Tadic, Phys. Rev. D **52**, 5417 (1995).
[8] T. Damour, F. Piazza, and G. Veneziano, Phys. Rev. Lett. **89**, 081601 (2002).
[9] P. W. Worden, Jr. and C. W. F. Everitt, in *Experimental Gravitation*, Proceedings of the "Enrico Fermi" International School of Physics, Course LVI, edited by B. Bertotti (Academic, New York, 1973); J. P. Blaser *et al.*, ESA SCI Report No. (96)5, 1996 (unpublished); see also the STEP website http://einstein.stanford.edu/STEP/step2.html
[10] See the MICROSCOPE website http://www.onera.fr/dmph/accelerometre/index.html
[11] A. M. Nobili, D. Bramanti, G. L. Comandi, R. Toncelli, E. Polacco, and M. L. Chiofalo, Phys. Lett. A **318**, 172 (2003); "Galileo Galilei" (GG), Phase A Report, ASI (November 1998), 2nd ed. January 2000. A. M. Nobili, D. Bramanti, G. Comandi, R. Toncelli, E. Polacco, and G. Catastini, Phys. Rev. D **63**, 101101 (2001); for a review see, e.g., Ref. 12; see also the GG website http://eotvos.dm.unipi.it/nobili
[12] A. M. Nobili, in *Recent Advances in Metrology and Fundamental Constants*, Proceedings of the "Enrico Fermi" International School of Physics, Course CXLVI, edited by T. J. Quinn, S. Leschiutta, and P. Tavella (IOS Press, 2001), p. 609.
[13] W. Li, http://linkage.rockfeller/edu/wli/1fnoise
[14] A. M. Nobili, D. Bramanti, G. L. Comandi, R. Toncelli, and E. Polacco, New Astron. **8**, 371 (2003).
[15] G. L. Comandi, A. M. Nobili, D. Bramanti, R. Toncelli, E. Polacco, and M. L. Chiofalo, Phys. Lett. A **318**, 213 (2003).
[16] A. M. Nobili, D. Bramanti, G. L. Comandi, R. Toncelli, E. Polacco, and M. L. Chiofalo, in *Proceedings of the XXXVIIIth Rencontre de Moriond Gravitational Waves and Experimental Gravity*, edited by J. Dumarchez and J. Tran Thanh Van (The Gioi, Vietnam, 2003), p. 371.
[17] G. L. Comandi, A. M. Nobili, R. Toncelli, and M. L. Chiofalo, Phys. Lett. A **318**, 251 (2003).
[18] J. P. Den Hartog, *Mechanical Vibrations* (Dover, New York, 1985).
[19] S. H. Crandall, in *Nonlinear Dynamics and Stochastic Mechanics*, edited by W. Kliemann and N. S. Namachchivaya (CRC, Boca Raton, FL, 1995).
[20] G. Genta, *Vibration of Structures and Machines* (Springer-Verlag, New York, 1993).
[21] S. H. Crandall and A. M. Nobili, http://eotvos.dm.unipi.it/nobili/ggweb/crandall
[22] A. M. Nobili *et al.*, Class. Quantum Grav. **16**, 1463 (1999).
[23] A. M. Nobili, G. L. Comandi, S. Doravari, D. Bramanti, E. Polacco, and F. Maccarrone (unpublished).
[24] This concept was originally introduced by G. C. Wigner and V. F. Weisskopf.
[25] G. L. Comandi, Ph.D. thesis, University of Pisa, 2004; http://eotvos.dm.unipi.it/nobili/comandi_thesis

Dynamical response of the Galileo Galilei on the ground rotor to test the equivalence principle: Theory, simulation, and experiment. II. The rejection of common mode forces

G. L. Comandi
Istituto Nazionale di Fisica Nucleare (INFN), Sezione di Pisa, Largo B. Pontecorvo 3, I-56127 Pisa, Italy and Department of Physics, University of Bologna, Bologna, Italy

R. Toncelli
Istituto Nazionale di Fisica Nucleare (INFN), Sezione di Pisa, Largo B. Pontecorvo 3, I-56127 Pisa, Italy

M. L. Chiofalo
Scuola Normale Superiore, Piazza dei Cavalieri 7, I-56100 Pisa, Italy and Instituto Nazionale di Fisica Nucleare (INFN), Sezione di Pisa, Largo B. Pontecorvo 3, I-56127 Pisa, Italy

D. Bramanti
Istituto Nazionale di Fisica Nucleare (INFN), Sezione di Pisa, Largo B. Pontecorvo 3, I-56127 Pisa, Italy

A. M. Nobili
Department of Physics "E. Fermi," University of Pisa, Largo B. Pontecorvo 3, I-56127 Pisa, Italy

(Received 5 January 2006; accepted 16 January 2006; published online 23 March 2006)

"Galileo Galilei on the ground" (GGG) is a fast rotating differential accelerometer designed to test the equivalence principle (EP). Its sensitivity to differential effects, such as the effect of an EP violation, depends crucially on the capability of the accelerometer to reject all effects acting in common mode. By applying the theoretical and simulation methods reported in Part I of this work, and tested therein against experimental data, we predict the occurrence of an enhanced common mode rejection of the GGG accelerometer. We demonstrate that the best rejection of common mode disturbances can be tuned in a controlled way by varying the spin frequency of the GGG rotor. [DOI: 10.1063/1.2173076]

I. INTRODUCTION

The relevance of equivalence principle (EP) tests as the most sensitive probe of general relativity has been strongly motivated from a theoretical point of view.[1,2] In Part I of this work we have discussed the motivation behind the Galileo Galilei on the ground (GGG) experiment for testing the EP at 1 g with macroscopic (10 kg) concentric test cylinders in rapid rotation. The instruments which have provided the best EP tests to date are rotating torsion balances,[3,4] their essential features being the differential nature of the instrument (i.e., its capability to reject common mode effects) and the modulation of the signal through rotation. It has also been established that very high accuracy tests can be achieved only by performing an experiment in space, inside a spacecraft orbiting the Earth at low altitude.[5–7] The GGG experiment embodies the key features of the rotating torsion balances, with the addition of being suitable for flight.

The GGG experiment[8,9] has been described in Part I, and its underlying physics has been embodied in an effective model that fully accounts for the measured normal modes of the GGG rotor in the whole range of spin frequencies, from subcritical to supercritical rotation.

Here, we apply the model to evaluate the common mode rejection capability of the GGG rotor as determined by all the system parameters which govern the design of the instrument. This study naturally provides an effective tool to optimize the real instrument in response to external disturbances such as tidal forces[10] and seismic noises.[11]

We refer to Part I for all the definitions and the description of the experiment, as well as of the model. This Part II is organized as follows. In Sec. II the numerical method developed in Part I is completed by including external forces, in common mode and in differential mode. In Sec. III, we compute the common mode rejection factor, first at zero spin, through an analytical solution depending on one scaling parameter, and then in rotation, through our numerical simulation model; numerical simulations show the relevance—in wide ranges of the spin frequency—of the analytical scaling parameter and demonstrate the existence of an enhanced common mode rejection. In Sec. IV we apply these results to the realistic range of parameters of the GGG rotor and discuss how the enhanced rejection of common mode effects can be exploited for optimizing the performance of the instrument in testing the equivalence principle. Concluding remarks and perspectives after both Parts I and II are given in Sec. V.

II. THE NUMERICAL METHOD

A. Dynamical equations: External forces and transfer function

In Sec. IV of Part I we have discussed the numerical simulation method of the model used to describe the GGG

instrument and the parameters of the system (see Figs. 1 and 3 of Part I for the GGG instrument and its model). Here we describe the transfer matrix method, in the presence of external forces—acting on the system in common mode as well as in differential mode—which determine the dynamical behavior of the rotor. External forces are added to the right-hand side of the equations of motion, written as in Eq. (37) of Part I, which now becomes

$$\dot{X} = AX + BU, \tag{1}$$

where A is the $2n \times 2n$ dynamical matrix already appearing in Eq. (38) of Part I, X is the vector of generalized coordinates and velocities defined in Eq. (36) of Part I, while the $2n \times m$ input matrix B and the input vector U have been added, the m components of U representing the external forces. The definition of the problem is completed after specifying the p component output vector Y by means of the general relationship

$$Y = CX + DU, \tag{2}$$

where C is the $p \times 2n$ output matrix and D is the $p \times m$ input-output coupling matrix. In our problem, $D=0$ and the Y's are the displacements of the masses from their equilibrium positions.

Equations (1) and (2) are solved in the frequency domain, after Laplace transform to the variable $s=i\omega$. By combining them into a single equation, we have the direct link between the output vector and the input forces,

$$Y(s) = C(sI - A)^{-1}BU(s) \equiv H(s)U(s). \tag{3}$$

Equation (3) defines the $p \times m$ transfer matrix H, in the rotating reference frame, in terms of the matrices A, B, and C (I is the identity matrix). The derivation of matrices C and B is given in the Appendix.

The poles p_r and the zeros z_r of the transfer matrix fully determine the dynamical response of the rotor: the poles are located at the excitation energies, and the zeros tell us where external effects are suppressed.

The signal of an EP violation would be a relative displacement of the GGG test cylinders in the nonrotating reference frame of the laboratory. Therefore, we need to transform the output vector given by (3) in the rotating frame into the $Y^{\mathrm{NR}}(s)$ displacement vector in the nonrotating laboratory frame. We show in the Appendix how the transfer matrix and thus the output are transformed into the nonrotating frame. This obviously results into shifting the poles from $p_r \pm i\omega_s$ to p_r and $p_r + 2i\omega_s$, namely, to zero and twice the angular spin frequency ω_s. The latter behavior, expected in the nonrotating frame, has already been outlined in Fig. 4 of Part I (also reported in Fig. 3 of Ref. 8) where the normal modes of the GGG rotor are given as functions of the spin frequency $\nu_s = \omega_s/2\pi$, showing the existence of horizontal normal mode branches and of inclined ones (at $2\nu_s$ angle), as well as the presence of three instability regions at values of the spin frequency which are resonant with the three natural frequencies of the GGG system.

In the GGG setting reported here the values of the natural frequencies are $\nu_D \simeq 0.09$ Hz for the differential one and $\nu_{C1} \simeq 0.9$ Hz and $\nu_{C2} \simeq 1.26$ Hz for the two common mode ones. The normal mode behavior defines two main spin frequency regions. One region—that we call the region of "intermediate spin frequencies"—is where $|p_r \pm 2i\omega_s| < |p_r|$ or $|z_r \pm 2i\omega_s| < |z_r|$ (i.e., $0.09 < 2\nu_s < 1.26$ Hz in our case). The other region—that we call the region of "low and very high spin frequencies"—is where $|p_r \pm 2i\omega_s| > |p_r|$ and $|z_r \pm 2i\omega_s| > |z_r|$, namely, on either side of the intermediate frequency region. As we have seen in Part I, the intermediate frequency region is where mode crossings occur; we therefore expect that in this region the rejection of common mode forces will depend very much on the particular frequency at which the system is spinning, while it should not be so in the region of low and high frequencies. The rejection of common mode forces will depend on the frequency region.

III. RESULTS

A. The common mode rejection factor

In this section we define and evaluate the common mode rejection factor χ which describes the rotor's capability, as a differential instrument, to reject common accelerations as compared to those acting in a differential manner on the test bodies. The smaller the rejection factor χ, the better the performance of the instrument. The rejection is a function of the frequency ν of the external force applied, as it is the dynamical response of the system.

We have proceeded to evaluate numerically $\chi(\nu)$ by first determining the transfer function in the rotating reference frame for the two cases of common and differential accelerations acting on the test cylinders. The common H_C^{NR} and differential H_D^{NR} transfer functions are then calculated in the nonrotating frame, yielding the corresponding *relative* displacements $\{\Delta x_C^{\mathrm{NR}}, \Delta y_C^{\mathrm{NR}}\}$ and $\{\Delta x_D^{\mathrm{NR}}, \Delta y_D^{\mathrm{NR}}\}$ in the X' and Y' directions of the nonrotating, horizontal plane of the laboratory. It is worth stressing that we are always computing displacements of the test cylinders relative to one another, also in response to an external force acting in common mode; this is precisely because we wish to quantitatively establish how far is our actual instrument from being an *ideal* differential accelerometer which would give no relative displacement of the test cylinders in response to common mode forces. The relative displacements resulting in both directions of the horizontal plane and depending on the nature of the applied force (either common mode or differential mode) are

$$\begin{bmatrix} \Delta x_C^{\mathrm{NR}}(s) \\ \Delta y_C^{\mathrm{NR}}(s) \end{bmatrix} = H_C^{\mathrm{NR}}(s - i\omega_s)\frac{1}{m_i}\begin{bmatrix} F_X(s) \\ F_Y(s) \end{bmatrix}, \tag{4}$$

$$\begin{bmatrix} \Delta x_D^{\mathrm{NR}}(s) \\ \Delta y_D^{\mathrm{NR}}(s) \end{bmatrix} = H_D^{\mathrm{NR}}(s - i\omega_s)\frac{1}{2m_i}\begin{bmatrix} F_X(s) \\ F_Y(s) \end{bmatrix}. \tag{5}$$

The factor $1/2$ in (5) is introduced because in this way, if $a_C = F/m_i = F/m_o$ is the acceleration acting in a common manner on the two masses, the differential accelerations are $a_{Di} = F/(2m_i)$ and $a_{Do} = -F/(2m_o) = -a_{Di}$, and then $\Delta a \equiv a_i - a_o = F/m_i$.

The rejection factors along the X' and Y' directions of the plane (not rotating) are therefore defined as follows:

$$\chi_{X'}(s) = \frac{\Delta x_C^{\mathrm{NR}}(s)}{\Delta x_D^{\mathrm{NR}}(s)}, \tag{6}$$

$$\chi_{Y'}(s) = \frac{\Delta y_C^{\mathrm{NR}}(s)}{\Delta y_D^{\mathrm{NR}}(s)}. \tag{7}$$

As discussed in Sec. II C of Part I, the GGG instrument must be as sensitive as possible to low frequency effects (between 10^{-5} and 10^{-4} Hz). For this reason, in the following we shall focus on the $\chi(s\to 0)\equiv\chi_0$ behavior of the rejection factor for different values of the spin frequency ν_s of the GGG rotor.

B. Nonspinning rotor: Analytical solution and scaling parameter

We first compute the rejection factor in the particular case of zero spin rate, i.e., for the nonspinning GGG apparatus, showing that the capability of the system to reject common mode forces can be predicted analytically, and that rejection is quantitatively expressed by a simple scale parameter. The model we use to describe the GGG apparatus is the same as in Fig. 3 of Part. I

The relative displacement Δx_D of the test cylinders in response to an external acceleration a_D, acting in differential mode, can be written as

$$\Delta x_D = \frac{a_D T_D^2}{(2\pi)^2} = \frac{a_D m_t L_a^2}{K_t l^2 - g m_t \Delta L/2}, \tag{8}$$

where the second equality is obtained by using the expression for the natural period of differential oscillation of the test cylinders T_D as computed in Part I, Eq. (41), namely,

$$T_D = \frac{2\pi}{\sqrt{[(K+K_i+K_o)l^2/(m_i+m_o)L_a^2] - (g/2L_a)(\Delta L/L_a)}}, \tag{9}$$

and introducing the total mass of the test bodies $m_t=m_i+m_o$ and the total elastic constant $K_t=K+K_i+K_o$ (assuming isotropic suspensions).

Let us now see how an external acceleration a_C, albeit applied in common mode (i.e., the same on both test cylinders), will nevertheless affect their relative position giving rise to a relative displacement Δx_C. Note that the system is at equilibrium, it is not rotating, and we are limiting the calculation to small angles and to constant applied forces (i.e., to forces which are dc in the nonrotating laboratory frame). We then have

$$\Delta x_C = L_o\theta_o - L_i\theta_i - (2L_a+\Delta L)\theta_a. \tag{10}$$

We now need the values of θ_λ in the presence of a common mode force (the label $\lambda=i,o,a$ refers to the inner mass, outer mass, and coupling arm, respectively, as in Part I). They can be obtained from the equation

$$\left.\frac{\partial U}{\partial q_j}\right|_{q_j=q_j^0} = 0, \quad j=1,\ldots,n, \tag{11}$$

[already given as Eq. (22) in Part I] in the limit of small angles, having added to the potential energy U, the work done by the external forces. After some algebra, this procedure leads to the following equations:

$$\begin{aligned}
&m_i g L_i\theta_i - K_i l^2(\theta_a-\theta_i) - m_i a_C L_i = 0,\\
&m_o g L_o\theta_o - K_o l^2(\theta_a-\theta_o) - m_o a_C L_o = 0,\\
&\left[K_t l^2 - \frac{1}{2}(m_t+m_a)g\Delta L\right]\theta_a - K_i l^2\theta_i - K_o l^2\theta_o + \frac{1}{2}(m_t\\
&\quad + m_a)a_C\Delta L = 0.
\end{aligned} \tag{12}$$

After some additional manipulations, Eqs. (12) yield the approximated values of the angles as

$$\begin{aligned}
\theta_i &\simeq \frac{mL_i}{K_i l^2 + mgL_i}a_C,\\
\theta_o &\simeq \frac{mL_o}{K_o l^2 + mgL_o}a_C,\\
\theta_a &\simeq -\frac{(1/2)m_t\Delta L - \sum_{\lambda=i,o} K_\lambda l^2(mL_\lambda/K_\lambda l^2 + mgL_\lambda)}{K_t l^2 - (1/2)m_t g\Delta L}a_C.
\end{aligned} \tag{13}$$

After expanding Eqs. (13) in the small parameters $K_\lambda l^2/m_\lambda g L_\lambda$ and substituting the resulting equations into (10) using the relation $L_o=2L_a+\Delta L+L_i$, we eventually obtain

$$\Delta x_C \simeq \frac{(2L_a+\Delta L)Kl^2}{[K_t l^2 - (1/2)m_t g\Delta L]g}a_C. \tag{14}$$

The ratio of the relative displacement ΔX_D caused by a differential force, over the relative displacement ΔX_C caused by a common mode force (along the X' direction of the non rotating frame), is therefore

$$\frac{\Delta X_D}{\Delta X_C} = \frac{m_t g L_a^2}{(2L_a+\Delta L)Kl^2}\frac{a_D}{a_C}, \tag{15}$$

which, for $a_D=a_C$, gives us the inverse of the rejection factor along the same direction of the horizontal plane,

$$\frac{1}{\chi_0} = \frac{m_t g L_a^2}{(2L_a+\Delta L)Kl^2}, \tag{16}$$

that is, an external acceleration acting on the GGG test cylinders in common mode would produce a relative displacement of the cylinders with respect to one another $1/\chi_0$ times smaller than the same acceleration would produce if acting in differential mode. For a perfectly differential instrument, $1/\chi_0$ would be infinite, namely, a common mode force would not produce any relative displacement of the test masses. Here we indicate the rejection factor with the subscript zero because this analytical calculation refers to the rejection of dc external forces (i.e., of forces which act at zero frequency in the laboratory frame). In the following numerical computation we will also show the dependence of the rejection factor on the frequency of the applied force, as well as on the rotation speed of the GGG rotor.

The rejection factor (16) takes a very simple form in the limits $\Delta L/L_a\to 0$ and $m_a/m_{i,o}\to 0$, that are verified in our experiment. This is

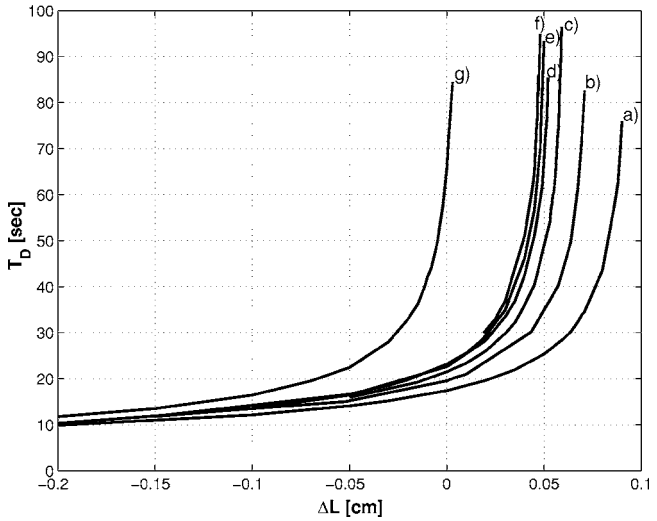

FIG. 1. Differential period T_D as a function of the balancing parameter ΔL. The various curves refer to different values of the other parameters of the system, as given in Table I (all simulations were performed with the rotor spinning at ν_s=2.5 Hz).

$$\frac{1}{\chi_0} \simeq \frac{m_{i,o} g L_a}{K l^2}. \tag{17}$$

Thus, at zero spin, the inverse of the common mode rejection factor $1/\chi_0$ is given by the simple scaling parameter (17), where the relevant energy scales are the gravitational energy of the inner and outer test cylinders (at the numerator) and the elastic energy stored by the central suspension (at the denominator). The larger is this ratio, the better the instrument will reject common mode forces, the more suitable it will be to detect differential effects such as that of an equivalence principle violation. In the following we show that, far from being limited to the very particular case of zero spin rate, this result holds also for the spinning rotor in the region of low and high spin frequencies, as defined in Sec. II A.

C. Region of low and high spin frequencies

Expression (17), for the rejection factor of dc common mode forces, results from a number of approximations performed in describing the system in the case of zero spin rate. We devote this section to evaluate numerically to which extent it is valid also in the low and high spin frequency regions (see Sec. II A). The more complex case of the rejection behavior, when the rotor is spinning at intermediate frequencies, will be addressed in Sec. III D.

1. The differential period T_D

In order to calculate the dependence of the rejection on the scaling parameter $Kl^2/m_{i,o}gL_a$, we proceed by varying one at a time its governing parameters. We do that while keeping the differential period T_D fixed, by also varying ΔL (see Fig. 1, where T_D vs ΔL is displayed under the different experimental conditions listed in Table I). T_D must be kept fixed because its variation would mean a variation of the stiffness of the coupling between the test cylinders, and therefore a different response, in terms of relative displacement, under the action of a given external force. The softer the coupling, the longer the differential period, the larger the relative displacement between the test cylinders in response to a given force.

TABLE I. Legend corresponding to Fig. 1.

Curve	$K_{X'}$ (dyn/cm)	Λ $(K_{Y'}/K_{X'})$	l (cm)
a	10^6	2.58	0.5
b	10^6	1	0.5
c	5×10^5	1	0.5
d	2.5×10^5	1	0.5
e	1.5×10^5	1	0.5
f	5×10^4	1	0.5
g	10^6	1	0.15

2. Spectra of the test mass differential displacements

Once the differential period is fixed, we need to set the observables that are needed in order to extract the rejection factor. We first need to establish how the signal of the relative displacements of the test cylinders (in the nonrotating frame) responds to the frequency of the external force applied, either in common mode or in differential mode [see Eqs. (4) and (5)], for a given spin frequency ν_s of the rotor.

We evaluate numerically Eqs. (4) and (5). Figure 2 shows the magnitude of the relative displacement resulting from the application, along the X' direction of the nonrotating frame, of a common mode acceleration (top panel) and of a differential one (bottom panel), of the same intensity, varying at a frequency that ranges between 10^{-5} and 10 Hz, with the rotor spinning at frequency ν_s=2.5 Hz. Though the force is applied in the X' direction, there will be some effect also in the perpendicular Y' direction, as discussed below in relation to Fig. 3. Here we show only the effect in the direction X' of the force.

In the case of common mode input accelerations (Fig. 2, top panel), the test masses of the rotor are seen to respond with a relative displacement at all the natural frequencies. The plot shows peaks at the frequencies ν_{pole} corresponding to the differential frequency $\nu_D \simeq 0.09$ Hz, to the common ones $\nu_{C1} \simeq 0.9$ Hz and $\nu_{C2} \simeq 1.26$ Hz, and to their combinations with $2\nu_s$, namely, $2\nu_s \pm \nu_D$, $2\nu_s \pm \nu_{C1}$, and $2\nu_s \pm \nu_{C2}$. Two zeros of the transfer function are also apparent, the first located in between ν_D and ν_{C1} and the second in between ν_{C1} and ν_{C2}.

In the case of differential input accelerations (Fig. 2, bottom panel), no zeros are present in the transfer function, and only the mode at frequency ν_D is significantly excited, while the effect at $2\nu_s \pm \nu_D$ is negligible. The value of the relative displacement for $\nu \to 0$ (i.e., as the applied force becomes almost dc) turns out to be in perfect agreement with the value predicted by Eq. (8) for the zero spin case, though this figure refers to the system spinning at ν_s=2.5 Hz.

The corresponding inverse rejection factor, as given by Eqs. (6) and (7) for the two directions of the horizontal plane, is displayed in Fig. 3. Even though the external forces (both common and differential) have been applied along the X' direction only, differential displacements occur also along Y', because of losses in the test mass suspensions while ro-

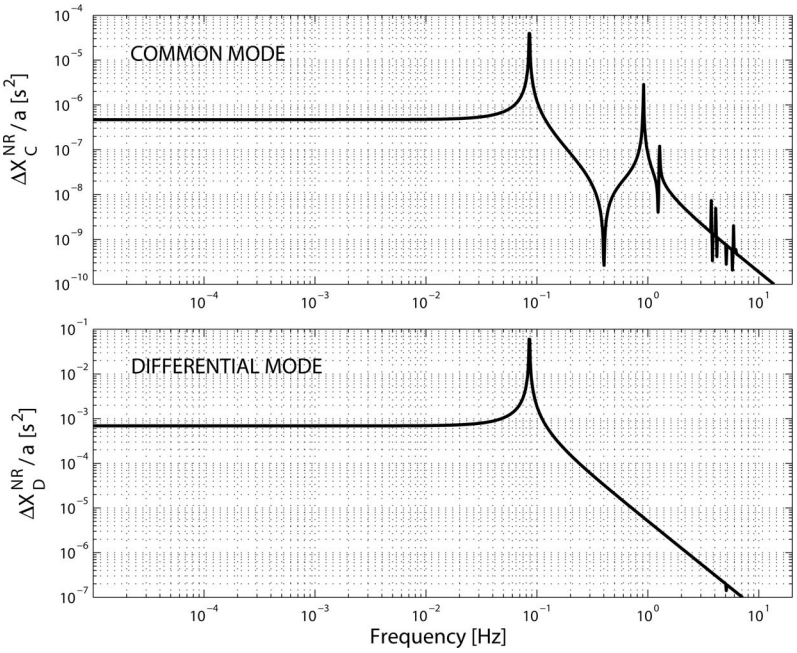

FIG. 2. Common mode Δx_C^{NR} (top panel) and differential mode Δx_D^{NR} (bottom panel) relative displacements, divided by the intensity a of the acceleration applied, in common mode or differential mode, respectively, as functions of the frequency of the applied force. The rotor is spinning at $\nu_s=2.5$ Hz. The other parameters of the system are typical of the present instrument: $T_D=12.5$ s, $K=K_i=K_o=10^6$ dyn/cm, $l=0.5$ cm, $L_a=19$ cm, $m_{i,o}=10$ kg, and $L_i=4.5$ cm.

tating (as discussed in Part I, the quality factor Q is finite in our simulations). For this reason, the spectrum along the Y' direction shows an additional peak at the differential mode frequency. However, the magnitudes of both the common and differential Y' displacements are very small, reduced by a factor Q with respect to those along X' (their ratio remaining of the same order of magnitude as that in the X' direction).

3. Rejection of dc forces versus the governing parameters

We now vary—one at a time—all the four governing parameters which appear in the scaling parameter (17), plus the anisotropy factor Λ of the suspensions introduced in Part I, Sec. IV. If $\Lambda=1$ the suspensions have the same stiffness in both directions of the horizontal plane; if not, there is an anisotropy (see Table I). The purpose is to determine how the rejection factor of dc common mode forces, $|1/\chi_0|$, depends on these parameters both at zero and high spin frequencies. In doing this we need to keep the natural differential period T_D fixed, as discussed above. Figure 4 displays, in its five panels, the dependence of $|1/\chi_0|$ on the five relevant parameters (the balancing arm length L_a, the mass $m_{i,o}$ of the suspended cylinders, the elastic constant K of the central laminar suspension, its length l, and the anisotropy factor Λ). In each panel, the solid lines give the value of $|1/\chi_0|$ for the zero spin case, while the filled circles give its value for the rotor spinning at 2.5 Hz. We are therefore investigating the rejection of dc forces in what we call the very low and very high spin frequency regions of the rotor.

As all five panels in Fig. 4 show, there is almost no difference between the zero spin and 2.5 Hz spin frequency cases. This result had to be expected from our analysis of the normal modes of the GGG system developed in Part I (and reported in Fig. 4 therein), where it was apparent that the horizontal branches and the inclined ones (at $2\nu_s$) of the normal modes do not cross in the low and high spin frequency regions. By performing a spectral analysis of the experimental data we have verified that the horizontal branches of the normal modes are typically excited, while the inclined ones are not. Thus, if no crossing occurs, also no energy transfer occurs from the former to the latter.

We expect this not to be the case in the intermediate spin frequency region, where the horizontal and the inclined branches of the normal modes do cross (see the analysis of this region in Sec. III D below).

4. Validation of the scaling parameter

We can now collect all the results discussed so far in order to quantify the validity of the scaling parameter (17) in determining the rejection of dc common mode forces. The results of our numerical simulations are reported in Fig. 5, where we plot $|1/\chi_0|$ as a function of the scaling parameter

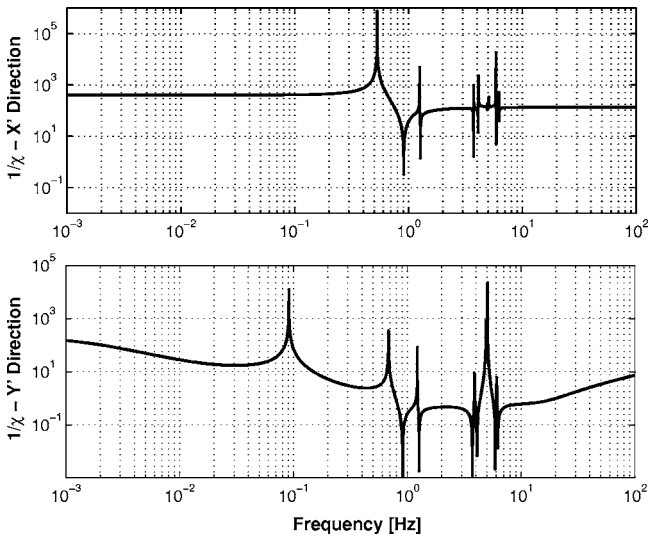

FIG. 3. Inverse rejection function $1/\chi(\nu)$ vs frequency in the X' (top) and Y' (bottom) directions for the rotor spinning at $\nu_s=2.5$ Hz. The other system parameters are the same as in Fig. 2.

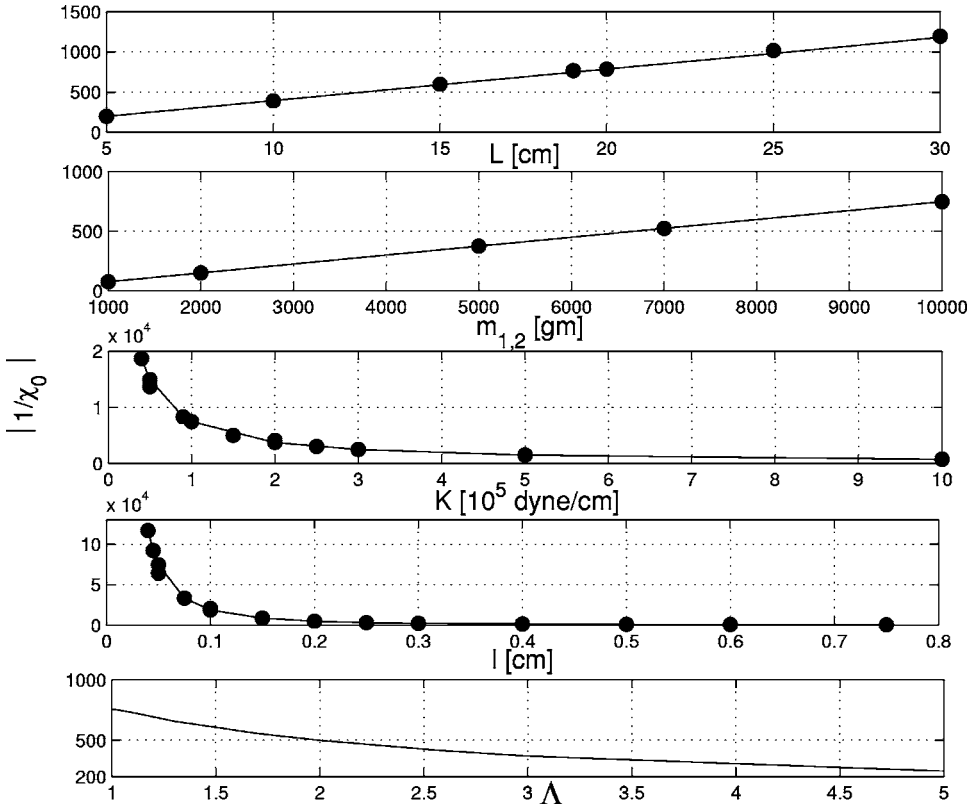

FIG. 4. Inverse rejection factor of dc forces, $1/\chi_0$, as a function of various system parameters. From top to bottom, the varying parameters are L_a, $m_{i,o}$, K, l, and the anisotropy Λ. Solid line: nonspinning rotor. Points: rotor spinning at $\nu_s=2.5$ Hz. The parameters are changed one at a time from the values reported in the caption of Fig. 2.

(17). The solid line at 45° represents $|1/\chi_0|$ in the case of a nonspinning rotor with isotropic suspensions ($\Lambda=1$), and it has been found to be valid also for the isotropic spinning rotor in the low and high spin frequency regions. If then anisotropy is taken into account, the resulting values of $|1/\chi_0|$ still lie on the 45° line as long as the spin frequency is very low (filled circles), while they lie on a lower inclination line if the spin frequency is very high (filled triangles). That is, in the latter case, the inverse rejection factor of dc common mode forces $|1/\chi_0|$ is still proportional to the scaling parameter (17), but through a coefficient smaller than unity. The amount of the deviation depends on Λ, as shown in the bottom panel of Fig. 4.

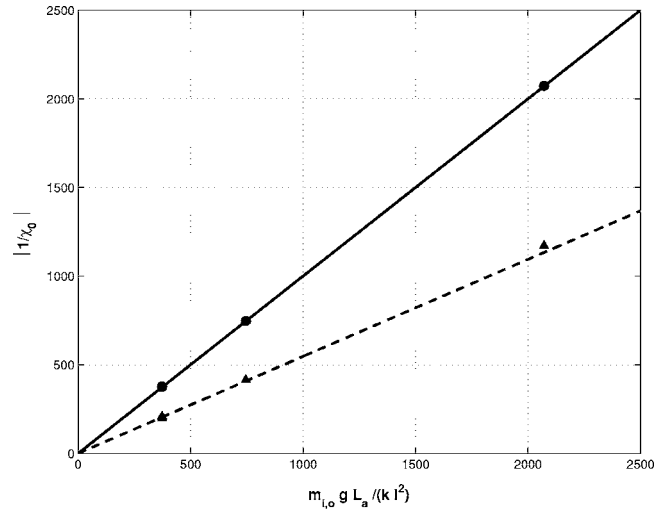

FIG. 5. Results from numerical simulations of the inverse rejection factor of dc forces, $1/\chi_0$, as a function of the scaling parameter $m_{i,o}gL_a/(Kl^2)$. The solid line refers to the zero spin case with isotropic suspensions ($\Lambda=1$), and also to the isotropic rotor in the low and high spin frequency regions. Once anisotropy of the suspensions is taken into account (e.g., with $\Lambda=2.58$), the rotor spinning at low frequencies gives the results shown as filled circles, while the one spinning at high frequencies gives the results shown as filled triangles. The dashed line has no physical meaning; it simply shows that the filled triangles still lie on a line, though at lower inclination. The system parameters reported in Fig. 2 correspond to $m_{i,o}gL_a/(Kl^2)=745$.

D. Region of intermediate spin frequencies

We now compute the inverse rejection factor $1/\chi(\nu)$ for a wide range of frequency ν of the applied force, in the region of intermediate values of the spin frequency of the rotor (as defined in Sec. II A). The calculations are similar to those which led to Fig. 3 in the case of high spin frequency (2.5 Hz in that case). Since we are interested in applied forces of very low frequency, only the value $|1/\chi_0|$ of the inverse rejection factor for a dc applied force is plotted as a function of the spin frequency ν_s (Fig. 6, top panel). This figure shows very clearly that the best performance of the instrument (i.e., best rejection of common mode dc forces) is to be expected, with the current parameters of the instrument, at the values $\nu_s \simeq 0.36$ Hz $> \nu_D$ and $\nu_s \simeq 0.6$ Hz $> \nu_D$, where the value of $1/\chi_0$ is as high as 10^6. The difference between the values of $|1/\chi_0|$ at the two ends of the spin frequency (for $\nu_s \to 0$ and $\nu_s \to \infty$) is due to the anisotropy of the central suspension, as already shown in Fig. 5. We have run the same system as in Fig. 6, but with isotropic elastic constants, and have numerically verified that $|1/\chi_0(\nu_s=0)|=|1/\chi_0(\nu_s=\infty)|$, the positions of the peaks being slightly changed according to the corresponding change in the differential period.

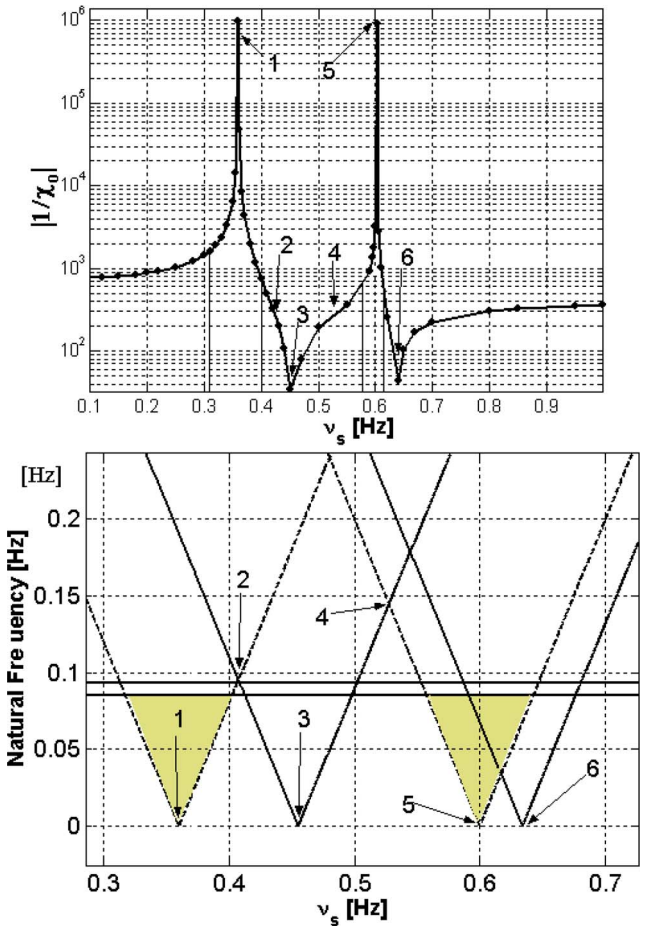

FIG. 6. Top panel: the inverse rejection factor of common mode dc forces, $1/\chi_0$, as a function of the spin frequency ν_s. The system parameters are the same as in Fig. 2. The numbered arrows indicate crossing points and minima (see text) and correspond to those shown in the bottom panel. Bottom panel: absolute values of the zeros (dashed lines) and of the poles (solid lines) of the transfer function vs ν_s. The horizontal branches correspond to the differential frequencies ν_D, and split because of the anisotropy. For ν_s within the shaded areas, the response is dominated by the zeros of the transfer function $H(s)$, and therefore the relative displacement in response to common mode dc forces, $\Delta x_C(\nu \to 0)$, is strongly suppressed.

The enhanced rejection behavior at intermediate spin frequencies is related to the dependence of the zeros and of the poles of the transfer matrix on ν_s, as we are going to discuss below. As it happens in the case of the poles of the transfer function, also the values of its zeros change with the spin frequency, showing the typical two branch behaviors, namely, a flat branch and an inclined one with $2\nu_s$ coefficient. This is apparent in the bottom panel of Fig. 6, where we plot the absolute values of the zeros and of the poles of the transfer function, $|\nu_{\text{zero}}|$ and $|\nu_{\text{pole}}|$, as dashed and solid lines, respectively.

The nondispersive branches in Fig. 6, bottom panel, shown as solid horizontal lines, correspond to the poles at the differential frequencies ν_D (there are two of them because of the anisotropy in the suspensions). The zero branches, represented by dashed lines in the same figure, are characterized by minima located at $0.5|\nu_{\text{zero}}(\nu_s=0)|$ and marked with the numbers 1 and 5. The zero minima are shifted from the minima of the pole branch, that are located at the points marked as 3 and 6. At the points marked as 2 and 4, the zero branch with $-|\nu_{\text{zero}}|+2\nu_s$ crosses the pole branch with $-|\nu_{\text{pole}}|+2\nu_s$.

We thus see that there are ranges of spin frequencies for which $|\nu_{\text{zero}}| < \nu_D$. This occurs within the shaded region of the frequencies indicated in the bottom panel of Fig. 6, whose width is easily evaluated to be precisely ν_D. When $|\nu_{\text{zero}}| < \nu_D$, the low frequency rotor response is dominated by the position of the zero, hence the value of the relative displacement $\Delta x_C(\nu \to 0)$ of the test cylinders in response to a low frequency common mode force is strongly suppressed (i.e., the disturbance is strongly rejected).

In order to make the correspondence clear, we have reported in the top panel of Fig. 6 the same points 1–5 marked in the bottom one. We thus see that the peaks of $|1/\chi_0|$ correspond to the minima 1 and 5 of the zero branches, the valleys of $|1/\chi_0|$ correspond to the minima 3 and 6 of the pole branches, and finally the saddle points of $|1/\chi_0|$ correspond to the crossings 2 and 4 between zero and pole branches.

The fundamental question then arises as to how we can move the location of the peaks shown in the top panel of Fig. 6 in order to enhance the capability of the instrument to reject common mode forces at larger supercritical values of the spin frequency ν_s, since rotation provides signal modulation and higher frequency modulation is preferable. We are going to address this question in the next section.

IV. ENHANCED REJECTION BEHAVIOR OF THE GGG ROTOR

In Sec. III C we have shown that in the region of low and high spin frequencies the scaling parameter $m_{i,o}gL_a/(Kl^2)$ precisely describes the rejection behavior of the GGG rotor, the differential period being adjusted for every set of parameters by varying ΔL. Then, in Sec. III D we have investigated the region of intermediate spin frequencies showing how the spin frequency can be tuned so as to obtain a considerably enhanced rejection of common mode forces in a nontrivial manner. We now need one more independent "knob" in order to move the $1/\chi_0$ peaks towards higher spin frequencies, where we expect a better performance of the GGG experiment.

If we vary the scaling parameter in the region of intermediate spin frequencies, the results obtained are shown in Fig. 7: as the value of the scaling parameter increases, the inverse rejection factor somewhat improves at the two ends of the plot, but the position of the peaks, namely, the spin frequencies at which rejection is strongly enhanced, is unaffected.

However, we can still vary the remaining free parameters $L_{i,o}$ while keeping $m_{i,o}gL_a/(Kl^2)$ fixed. Figure 8 shows that, as the values of L_i (Ref. 12) increase in going from the bottom to the top panel of the figure, the separation in spin frequency between the peaks of $1/\chi_0$ increases too.

All the cases displayed in Fig. 8 refer to a realistic GGG apparatus. In particular, in all three panels the scaling parameter has always the same value $m_{i,o}gL_a/(Kl^2)=370$ (with $K=10^5$ dyn/cm, $L_a=19$ cm, $l=1$ cm, and $m_{i,o}=10$ kg). Only the value of L_i increases from 4.5 to 9.0 to 15 cm in going

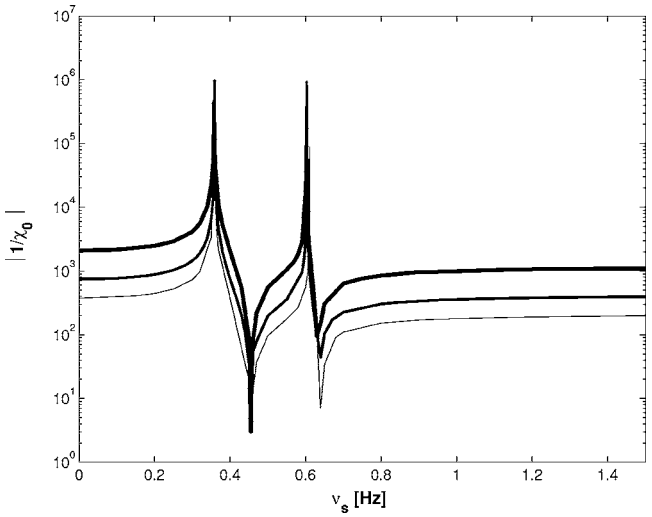

FIG. 7. Inverse static rejection $1/\chi_0$ as a function of the spin frequency. Curves of increasing thickness refer to increasing values of the scaling parameter $m_{i,o}gL_a/(Kl^2)=370$, 745, and 2070, while keeping $L_i=4.5$ cm fixed. We note that $1/\chi(\nu_s\rightarrow 0)\neq 1/\chi(\nu_s\rightarrow\infty)$ because of the anisotropic central suspension. Note that different values of $m_{i,o}gL_a/(Kl^2)$ leave the position of the peaks unaffected.

from the bottom to the top panel. At the top panel, with $L_i=15$ cm, the inverse rejection factor of common mode dc forces has a peak as high as $1/\chi_0=1.5\times 10^5$ at a spin frequency $\nu_s=1.12$ Hz.

Figure 8 summarizes the main result of this work, as it shows the way to perform a controlled tailoring of the rejection capability of the GGG apparatus. This can be done essentially by tuning L_i and ν_s. In the experiment, the most convenient way is to first fix $m_{i,o}gL_a/(Kl^2)$ and L_i in such a way that $|\nu_{\text{zero}}(\nu_s=0)|\simeq 2\nu_s^{\max}$, where $\nu_s^{\max}$ is the spin frequency at which the rotor is finally operated (and at which we want the best performance). A finer tuning is then done

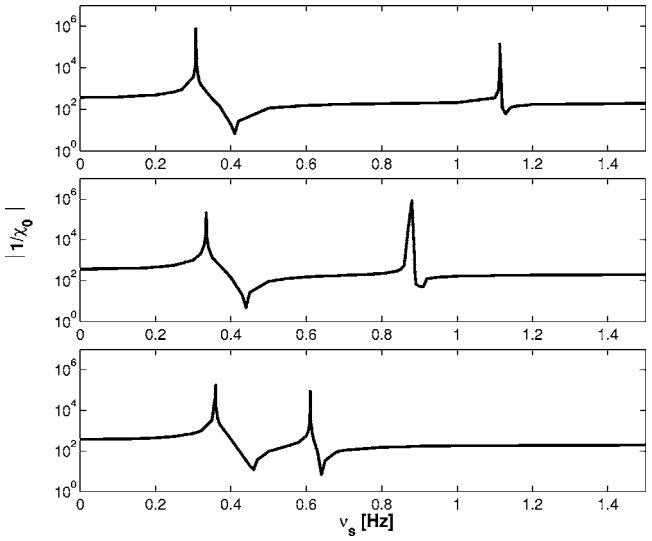

FIG. 8. Inverse rejection factor of common mode dc forces, $1/\chi_0$, as a function of the spin frequency at different values of L_i [with the scaling parameter fixed at $m_{i,o}gL_a/(Kl^2)=370$]. From bottom to top: $L_i=4.5$ cm, $L_i=9.0$ cm, and $L_i=15.0$ cm. Note the increasing separation in frequency between the peaks from bottom to top, leading to enhanced rejection at higher spin frequencies. For the maximum separation case (top panel) enhanced rejection takes place at $\nu_s=1.12$ Hz.

by adjusting ν_s so as to bring the first zero below the differential frequency ν_D, as shown in the bottom panel of Fig. 6. This can be done in a highly controlled way, allowing us to place the system in correspondence to the peaks of $|1/\chi_0|$.

V. CONCLUDING REMARKS AND PERSPECTIVES

We have investigated the frequency-dependent response of the GGG rotating differential accelerometer for testing the equivalence principle using an effective physical model (Part I, Sec. III) along with a simulation procedure (Part I, Sec. IV and Part II, Sec. II). This method has been demonstrated to quantitatively account for the available experimental data (Part I, Sec. II) and to provide analytical insights helpful for a qualitative understanding of the underlying physics.

In Part I we have shown, among other things, the split up of the normal modes into two scissor like branches, distinguishing modes which are preferentially excited from those whose spectral amplitudes are typically small, thus learning how to avoid the spin frequencies corresponding to their crossings, in order not to excite the quiet modes too by exchange of energy. We have also investigated the self-centering characteristic of the GGG rotor when in supercritical rotation regime, gaining insight on how to exploit this very important physical property for improving the quality of the rotor, hence its sensitivity as differential accelerometer. Here we can add a major result. The rejection of common mode dc forces is characterized by two distinct behaviors, depending on the region of spin frequency ν_s at which the rotor is operated. For low and high values of ν_s, the dependence of the inverse rejection factor $1/\chi_0$ is quantitatively expressed by the scaling factor $m_{i,o}gL_a/(Kl^2)$, with all the relevant parameters combined in it. In the case of intermediate values of ν_s, $1/\chi_0$ can reach peaks as high as 10^5-10^6, whose positions are affected by the remaining parameters $L_{i,o}$ and $K_{i,o}$. This conclusion allows us to tailor the features of the real instrument for best performance in terms of rejection of external disturbances such as tidal forces and seismic noise. Future experimental tests can probe this conclusion.

Results from both Parts I and II indicate that we can aim at a more realistic simulation model, to be used online with the experiment, as the latter becomes more sensitive (e.g., by reduction of the motor disturbances, by remote adjustment of the verticality of the spin axis, by active control of low frequency terrain tilt noise, etc.). The key point is that changes can be easily implemented in our numerical method and simulation environment, since any modification of the model corresponds to modifying only the part of the code where the Lagrange function is clearly written in terms of vector operations. The possibility to perform such realistic simulations, before applying any real changes to the apparatus, allows us to implement those which provide the best results so as to optimize the experiment. Along these lines, the present approach can be adapted to the "Galileo Galilei" (GG) experiment in space, where we expect a much more sensitive test of the equivalence principle.[7]

ACKNOWLEDGMENT

Thanks are due to INFN for funding the GGG experiment in its laboratory of San Piero a Grado in Pisa.

APPENDIX: THE TRANSFER FUNCTION

1. The *C* matrix

In our experiment, Eq. (3) is characterized by two inputs, namely, the X' and Y' components of the external forces, and two outputs Y, that are the relative displacements of the two test cylinders from their equilibrium positions in the sensitivity plane as measured in the rotating $X'Y'$ frame. That is, $Y \equiv \{Y_1, Y_2\} = [\Delta \mathbf{R}_o(t) - \Delta \mathbf{R}_i(t)] \cdot \{\hat{X}', \hat{Y}'\}$, where $\Delta \mathbf{R}_\lambda(t) = \mathbf{R}_\lambda(t) - \mathbf{R}_\lambda^0$. In order to determine the coefficients of the C matrix, we thus have to combine Eq. (2) of Part I for the vectors pointing to the three bodies and written in terms of the unit vectors $\hat{L}_a$, $\hat{L}_o$, and $\hat{L}_i$ together with the expression (16) of Part I for the unit vectors in terms of the generalized coordinates $X = \{x_1, \ldots, x_{12}\}$, thereby obtaining expressions for $\mathbf{R}_\lambda(\{x_1, \ldots, x_{12}\})$. In the linearized theory, we then have $\Delta \mathbf{R}_\lambda(t) = \mathbf{R}_\lambda(\{x_1 + x_1^0, \ldots, x_{12} + x_{12}^0\}) - \mathbf{R}(x_1^0, \ldots, x_{12}^0)_\lambda$, so that we can explicitly form the differences

$$Y_1 = \hat{X}' \cdot [\mathbf{R}_o(X + X^0) - \mathbf{R}_o(X^0) - \mathbf{R}_i(X + X^0) + \mathbf{R}_i(X^0)],$$

$$Y_2 = \hat{Y}' \cdot [\mathbf{R}_o(X + X^0) - \mathbf{R}_o(X^0) - \mathbf{R}_i(X + X^0) + \mathbf{R}_i(X^0)].$$

After imposing

$$\begin{pmatrix} Y_1 \\ Y_2 \end{pmatrix} = C \begin{pmatrix} x_1 \\ x_2 \\ \cdots \\ x_{12} \end{pmatrix}, \tag{A1}$$

we obtain the coefficients C_{jk} of the $2 \times 2n$ matrix as

$$C_{1k} = \gamma_k \cos x_k^0 \cos x_{k+6}^0, \quad k \leqslant 6,$$

$$C_{1k} = \gamma_k \sin x_{k-6}^0 \sin x_k^0, \quad k > 6,$$

$$C_{2k} = \gamma_k \cos x_k^0 \sin x_{k+6}^0, \quad k \leqslant 6,$$

$$C_{2k} = -\gamma_k \sin x_{k-6}^0 \cos x_k^0, \quad k > 6,$$

$$\gamma_{2k} = 0, \quad \forall\, k \leqslant 6, \tag{A2}$$

where $\gamma_1 = -\gamma_7 = -(2L_a + \Delta L)$, $\gamma_3 = -\gamma_9 = L_2$, and $\gamma_5 = -\gamma_{11} = -L_1$.

2. The *B* matrix: Case of differential and common accelerations

The vector U in Eq. (1) is defined as the components of the given external force $\mathbf{F}$ on the sensitivity plane in the rotating $X'Y'$ frame, namely, $U \equiv \{U_1, U_2\} = \mathbf{F}_e \cdot \{\hat{X}', \hat{Y}'\}$. The matrix B transforms the two-component U vector into its $2n = 12$-component counterpart $U(X)$.

In the case of a differential external force, we may figure out $\mathbf{F}_e$ as having opposite signs when acting on the two test cylinders. The B matrix is expressed as

$$B_{i1} = \sum_{r=1}^{2n} \mathbb{M}_{ir} \mathcal{B}_{r1} \quad \text{for even } i = 1, \ldots, 2n,$$

$$B_{i2} = \sum_{r=1}^{2n} \mathbb{M}_{ir} \mathcal{B}_{r2} \quad \text{for even } i = 1, \ldots, 2n,$$

and

$$B_{ij} = 0 \quad \text{for odd } i = 1, \ldots, 2n \text{ and } j = 1, 2, \tag{A3}$$

where $\mathbb{M}$ is the "mass" matrix defined in Eq. (29) of Part I. We find

$$\mathcal{B} = (\mathcal{B}_{j1}\ \mathcal{B}_{j2}), \tag{A4}$$

where $\mathcal{B}_{j1}$ is the column vector defined as

$$\mathcal{B}_{j1} = \begin{pmatrix} \partial[(\mathbf{R}_i - \mathbf{R}_o) \cdot \hat{X}']/\partial\theta_a \\ -\partial[\mathbf{R}_o \cdot \hat{X}']/\partial\theta_o \\ +\partial[\mathbf{R}_i \cdot \hat{X}']/\partial\theta_i \\ \partial[(\mathbf{R}_i - \mathbf{R}_o) \cdot \hat{X}']/\partial\phi_a \\ -\partial[\mathbf{R}_o \cdot \hat{X}']/\partial\phi_o \\ +\partial[\mathbf{R}_i \cdot \hat{X}']/\partial\phi_i \end{pmatrix}, \tag{A5}$$

and $\mathcal{B}_{j2}$ is obtained from $\mathcal{B}_{j1}$ after substitution of $\hat{X}'$ with $\hat{Y}'$.

Common accelerations instead would act on both test bodies and the coupling arm. The resulting $\mathcal{B}$ matrix is then composed by the column vectors,

$$\mathcal{B}_{j1} = \begin{pmatrix} \partial[(\mathbf{R}_a(m_a/m_i) + \mathbf{R}_o + \mathbf{R}_i) \cdot \hat{X}']/\partial\theta_a \\ \partial[\mathbf{R}_o \cdot \hat{X}']/\partial\theta_o \\ +\partial[\mathbf{R}_i \cdot \hat{X}']/\partial\theta_i \\ \partial[(\mathbf{R}_a(m_a/m_i) + \mathbf{R}_o + \mathbf{R}_i) \cdot \hat{X}']/\partial\phi_a \\ -\partial[\mathbf{R}_o \cdot \hat{X}']/\partial\phi_o \\ +\partial[\mathbf{R}_i \cdot \hat{X}']/\partial\phi_i \end{pmatrix}, \tag{A6}$$

and the same for B_{j2} containing the Y' components. In Eq. (A6), the factor m_a/m_i has been introduced so that the external force produces on the arm the same acceleration as on the inner and outer bodies.

3. The transfer function in the nonrotating frame

We show here how to transform the transfer function into the nonrotating frame. In our setting, we may write for the two-component $(X'Y')$ outputs Y^{NR} and inputs F^{NR} in the nonrotating frame,

$$Y^{\mathrm{NR}}(t) = \mathbb{R}(t) Y(t), \tag{A7}$$

$$F^{\mathrm{NR}}(t) = \mathbb{R}(t) U(t), \tag{A8}$$

where the rotation matrix $\mathbb{R}$ is

$$\mathbb{R}(t) = \begin{pmatrix} \cos\omega_s t & -\sin\omega_s t \\ \sin\omega_s t & \cos\omega_s t \end{pmatrix}. \tag{A9}$$

After introducing the complex variable $Z(t) = Y_1(t) + iY_2(t)$, from (A7) and (A9) we have $Z^{\mathrm{NR}}(t) = \exp(i\omega_s t) Z(t)$ and fi-

nally in the frequency domain $Z^{\mathrm{NR}}(s)=Z(s-i\omega_s)=Y_1(s-i\omega_s)+iY_2(s-i\omega_s)$ or else

$$Z^{\mathrm{NR}}(s)=\Re[Z(s-i\omega_s)]+i\Im[Z(s-i\omega_s)]. \tag{A10}$$

In a similar manner, we also have

$$W(s)=\Re[F^{\mathrm{NR}}(s+i\omega_s)]+i\Im[F^{\mathrm{NR}}(s+i\omega_s)], \tag{A11}$$

with $W(s)=U_1(s)+iU_2(s)$ and $F^{\mathrm{NR}}(s)\equiv F_1^{\mathrm{NR}}(s)+iF_2^{\mathrm{NR}}(s)$.

We now evaluate the right-hand side of Eq. (A10) by inserting the expressions of Eq. (3) for $Y_1(s-i\omega_s)$ and $Y_2(s-i\omega_s)$ and using Eq. (A11) for $W(s)$ (thus U_1 and U_2). After some simple algebra we obtain

$$Z^{\mathrm{NR}}(s)=H^{\mathrm{NR}}(s)F^{\mathrm{NR}}(s) \tag{A12}$$

for the nonrotating output $Y^{\mathrm{NR}}(s)$ in response to the nonrotating forces F^{NR}. The non-rotating transfer matrix H^{NR} turns out to be formed by a combination of the coefficients of the rotating H, that is,

$$H^{\mathrm{NR}}(s)=\begin{pmatrix}\Re[H_{11}(s_-)+iH_{21}(s_-)] & \Re[H_{12}(s_-)+iH_{22}(s_-)]\\ \Im[H_{11}(s_-)+iH_{21}(s_-)] & \Im[H_{12}(s_-)+iH_{22}(s_-)]\end{pmatrix}, \tag{A13}$$

where we have introduced the shorthand notation $s_-\equiv s-i\omega_s$.

Let us now look at the poles p_{lm}^r and zeros z_{lm}^r of the rotor response. The rotating H_{lm} can be expressed as

$$H_{lm}(s)=\frac{\Pi_r(s-z_{lm}^r+i\omega_s)(s-z_{lm}^{r*}-i\omega_s)}{\Pi_{r'}(s-p_{lm}^{r'}+i\omega_s)(s-p_{lm}^{r'*}-i\omega_s)}, \tag{A14}$$

showing that poles (zeros) in the rotating frame are calculated by shifting the nonspinning values $p_{lm}^r(z_{lm}^r)$ by $\pm i\omega_s$, namely, $p_{lm}^r\pm i\omega_s$ $(z_{lm}^r\pm i\omega_s)$. By inspection from Eq. (A13), it follows that the poles (zeros) of H^{NR} in the nonrotating frame can be expressed in terms of the $p_{lm}^r(z_{lm}^r)$ nonspinning values as combinations of a dc component p_{lm}^r and of a term $p_{lm}^r+2i\omega_2$ modulated at twice the spin frequency (z_{lm}^r and $z_{lm}^r+2i\omega_2$).

[1] E. Fischbach, D. E. Krause, C. Talmadge, and D. Tadic, Phys. Rev. D **52**, 5417 (1995).

[2] T. Damour, F. Piazza, and G. Veneziano, Phys. Rev. Lett. **89**, 081601 (2002).

[3] Y. Su *et al.*, Phys. Rev. D **50**, 3614 (1994).

[4] S. Baebler, B. R. Heckel, E. G. Adelberger, J. H. Gundlach, U. Schimidt, and H. E. Swanson, Phys. Rev. Lett. **83**, 3585 (1999).

[5] P. W. Worden Jr. and C. W. F. Everitt, in *Experimental Gravitation*, Proceedings of the "Enrico Fermi" International School of Physics, Course LVI, edited by B. Bertotti (Academic, New York, 1973); J. P. Blaser *et al.*, ESA SCI Report No. (96)5, 1996 (unpublished); see also the STEP website http://einstein.stanford.edu/STEP/step2.html

[6] See the MICROSCOPE website http://www.onera.fr/dmph/accelerometre/index.html

[7] A. M. Nobili, D. Bramanti, G. L. Comandi, R. Toncelli, E. Polacco, and M. L. Chiofalo, Phys. Lett. A **318**, 172 (2003); Galileo Galilei (GG) Phase A Report, ASI, 2nd ed., January 2000; A. M. Nobili, D. Bramanti, G. Comandi, R. Toncelli, E. Polacco, and G. Catastini, Phys. Rev. D **63**, 101101 (2001); for a review see, e.g., A. Nobili, in *Recent Advances in Metrology and Fundamental Constants*, Proceedings of the "Enrico Fermi" International School of Physics, Course CXLVI, edited by T. J. Quinn, S. Leschiutta, and P. Tavella (IOS, IOS Press, 2001), p. 609; see also the GG website http://eotvos.dm.unipi.it/nobili

[8] A. M. Nobili, D. Bramanti, G. L. Comandi, R. Toncelli, and E. Polacco, New Astron. Rev. **8**, 371 (2003).

[9] G. L. Comandi, A. M. Nobili, D. Bramanti, R. Toncelli, E. Polacco, and M. L. Chiofalo, Phys. Lett. A **318**, 213 (2003).

[10] G. L. Comandi, A. M. Nobili, R. Toncelli, and M. L. Chiofalo, Phys. Lett. A **318**, 251 (2003).

[11] A. M. Nobili, D. Bramanti, G. L. Comandi, R. Toncelli, E. Polacco, and M. L. Chiofalo, in *Proceedings of the XXXVIIIth Rencontre de Moriond "Gravitational Waves and Experimental Gravity,"* edited by J. Dumarchez and J. Tran Thanh Van (The Gioi, Vietnam, 2003), p. 371.

[12] Note that K_i and K_o are bound to be very similar to K for symmetry reasons, and that L_o is related to L_i through $L_o=2L_a+\Delta L+L_i$. Thus L_i (or else L_o) is the remaining independent parameter.